A UNITED STATES DEPARTMENT OF COMMERCE PUBLICATION

U.S. DEPARTMENT OF COMMERCE
National Oceanic and Atmospheric Administration

COLLECTED REPRINTS-1972
Volume II

ATLANTIC OCEANOGRAPHIC AND METEOROLOGICAL LABORATORIES

U.S. DEPARTMENT OF COMMERCE
Frederick B. Dent, Secretary

NATIONAL OCEANIC AND ATMOSPHERIC ADMINISTRATION
Robert M. White, Administrator
ENVIRONMENTAL RESEARCH LABORATORIES
Wilmot N. Hess, Director

Collected Reprints-1972
Volume II

ATLANTIC OCEANOGRAPHIC AND METEOROLOGICAL LABORATORIES

ISSUED JULY 1973

Atlantic Oceanographic and Meteorological Laboratories
Miami, Florida 33149

For sale by the Superintendent of Documents, U. S. Government Printing Office, Washington, D. C. 20402

FOREWORD

The end product of research is new knowledge. To be useful to anyone other than the investigator himself, however, this knowledge must somehow be made widely available. This routinely is done through the publication of research results in scientific journals. The published papers of the researchers at NOAA's Atlantic Oceanographic and Meteorological Laboratories appeared in so many different journals that many people who could benefit from the knowledge were in fact unaware it existed. For this reason we began in 1966 to bring these papers together as a set of collected reprints. The response from the scientific community has justified continuing this publication, and this volume, the seventh in the series, contains the published research results of NOAA's Atlantic Oceanographic and Meteorological Laboratories for the year 1972.

Harris B. Stewart, Jr.
Director, Atlantic Oceanographic
and Meteorological Laboratories

CONTENTS

VOLUME I

Page

Foreword iii

Table of Contents v

General

1. Carrodus, R. L.

History of Maps: Muse News *III*, No. 12, 479-512 1

2. Cox, Doak C., and Harris B. Stewart, Jr.

Technical Evaluation of the Seismic Sea Wave Warning System: The Great Alaska Earthquake of 1964; Oceanography and Coastal Engineering ISBN 0-309-1605-3. National Academy of Sciences, 229-245. 7

3. Henderson, J. Welles, and Harris B. Stewart, Jr.

A Recently Discovered CHALLENGER Sketchbook: Proceedings of the Royal Society of Edinburgh, Section B, *72*, No. 20, 223-229. 24

4. Stewart, Harris B., Jr.

Cicar's NOAA-CARIB, a New Experiment in International Scientific Cooperation: Environmental Data Service, February, 10-12. 36

5. Stewart, Harris B., Jr.

Eyewitness Pictures of the CHALLENGER Expedition Discovered: Environmental Data Service, October, 3-7. 39

Physical Oceanography

6. Apel, J. R. Editor

Sea Surface Topography from Space: Volume I - NOAA TR ERL 228-AOML 7, Volume II - NOAA TR ERL 228-AOML 7-2 (Summary) 44

7. Chew, Frank, and George A. Berberian

Neighbor Diffusivity as Related to Lateral Shear in the Florida Current: Deep-Sea Research *19*, 493-506 50

8. Chew Frank, William S. Richardson, and George A. Berberian

A Comparison of Direct and Electric-Current Measurements in the Florida Current: Journal of Marine Research *29*, No. 3, 339-346. 64

9. Hansen, Donald V., and Maurice Rattray, Jr.

Estuarine Circulation Induced by Diffusion: Journal of Marine Research *30*, No. 3, 281-294. 72

10. Maul, George A., and Donald V. Hansen

An Observation of the Gulf Stream Surface Front Structure by Ship, Aircraft, and Satellite: Remote Sensing of Environment *2*, No. 2, 109-116. 86

11. Maul, George A., and Miriam Sidran

Comment on "Estimation of Sea Surface Temperature from Space" by D. Anding and R. Kauth: Remote Sensing of Environment *2*, 165-169. 94

12. Molinari, Robert L., and Donald V. Hansen

Formulation of Drifting Limited Capability Buoy Placement and Retrieval Concepts: NOAA Tech Memo ERL AOML-18. (Originally published in National Data Buoy Center's Statement of work 0134EC.) 99

13. Zetler, Bernard D.

Comments on Paper by A. A. Nowroozi, "Long-Term Measurements of Pelagic Tidal Height Off the Coast of Northern California": Journal of Geophysical Research 77, No. 24, 4590. 129

14. Zetler, Bernard D., and Robert A. Cummings

Tidal Observations Near an Amphidrome: Geophysical Surveys *1*, 85-98. 130

Meteorology

15. Anthes, R. A.

Non-Developing Experiments with a Three-Level Axisymmetric Hurricane Model: NOAA Tech Memo ERL NHRL-97. 144

16. Black, Peter G.

Some Observations from Hurricane Reconnaissance Aircraft of Sea-Surface Cooling Produced by Hurricane Ginger (1971): Mariners Weather Log *16*, No. 5, 288-293. 164

17. Black, Peter G., H. V. Senn, and C. L. Courtright

Airborne Radar Observations of Eye Configuration Changes, Bright Band Distribution, and Precipitation Tilt During the 1969 Multiple Seeding Experiments in Hurricane Debbie: Monthly Weather Review *100*, No. 3, 208-217. 170

18. Carlson, T. N., and J. M. Prospero

The Large-Scale Movement of Saharan Air Outbreaks Over the Northern Equatorial Atlantic: Journal of Applied Meteorology *11*, No. 2, 283-297. 180

19. Hawkins, H. F., Jr.

Development of a Seven-Level, Balanced, Diagnostic Model and Its Application to Three Disparate Tropical Disturbances: NOAA Tech Memo ERL NHRL-98 (Summary Only) 195

20. Hawkins, H. F., Jr., K. R. Kurfis, B. M. Lewis, and H. G. Ostlund

Successful Test of an Airborne Gas Chromatograph: Journal of Applied Meteorology *11*, No. 1, 221-226. 197

21. Lamb, D., and W. D. Scott

Linear Growth Rates of Ice Crystals Grown from the Vapor Phase: Journal of Crystal Growth *12*, 21-31. 203

22. Lubin, S. J., and B. M. Lewis

Effects of Weather on Airborne Omega: Navigation Journal of the Institute of Navigation *19*, No. 2, 175-180. 214

23. Moss, M. S., and S. L. Rosenthal

On the Role of the Organizational Periods in the NHRL Circularly Symmetric Hurricane Model: NOAA Tech Memo ERL NHRL-99 220

24. Scott, William D.

An Assessment of the Present Instrumentation for the Measurement of Cloud Elements and our Needs: Second Symposium on Meteorological Observations and Instruments, March 27-30, 1972, San Diego, California, 205-216 244

25. Scott, Williams D.

Details for Constructing a Miniature Solid State Electrometer Probe: The Review of Scientific Instruments *43*, No. 1, 152-153. 256

26. Scott, Williams D., and Z. Levin

Open Channels in Sea Ice (Leads) as Ion Sources: Science *177*, 425-426. 258

27. Smith, Clark L.

On the Intensification of Hurricane Celia (1970): NOAA Tech Memo ERL NHRL-100. 259

28. Staff

Project STORMFURY 1971 Annual Report. 296

Volume II

Marine Geology and Geophysics

29. Cronan, D. S., T. H. Van Andel, G. R. Heath, M. G. Dinkelman, R. H. Bennett, and D. Bukry

Iron-Rich Basal Sediments from the Eastern Equatorial Pacific: Leg 16, Deep Sea Drilling Project: Science *175*, 61-63. 477

30. Dietz, Robert S.

Book Review of: The Face of the Deep, by B. C. Heezen and C. D. Hollister: EOS *53*, No. 2, 200-201. 480

31. Dietz, Robert S.

Geosynclines, Mountains and Continent-building: Scientific American *226*, No. 3, 30-38. 481

32. Dietz, Robert S.

Plate Tectonics, Sea-Floor Spreading and Continental Drift: Journal College Science Teaching *2*, No. 1, 16-19. 490

33. Dietz, Robert S.

Shatter Cones (Shock Fractures) in Astroblemes: 24th IGC Section *15*, 112-118. 494

34. Dietz, Robert S.

Sudbury Astrobleme, Splash Emplaced Sub-Layer and Possible Cosmogenic Ores: New Developments in Sudbury Geology, J. Guy-Bray, Editor. Geological Association of Canada, Special Paper 10, 29-40. 501

35. Dietz, Robert S.

Walter H. Bucher Medal, Fourth Presentation to Robert S. Dietz, Citation by J. T. Wilson and REPLY by Dietz: EOS *52*, No. 7, 540-541. 513

36. Dietz, Robert S., and D. C. Krause

Book Review of: The Earth's Tectonosphere. Its Past Development and Present Behavior, by J. H. Tatsch: EOS *53*, No. 11, 940-942. 515

37. Dietz, Robert S., and J. F. McHone, Jr.

Laguna Guatavita: Not Meteoritic, Probable Salt Collapse Crater: Meteoritics *7*, No. 3, 303-307. 516

38. Dietz, Robert S., and W. P. Sproll

Overlaps and Underlaps in the North America to Africa Continental Drift Fit: ICSU/SCOR Working Party 31 Symposium, Cambridge 1970: The Geology of the East Atlantic Continental Margin, edited by F. M. Delany, 1970. Institute of Geological Sciences Report No. 70/13, 143-151. 521

39. Dietz, Robert S., J. C. Holden, and W. P. Sproll

Antarctica and Continental Drift: Proceedings SCAR/IUGS Symposium on Antarctic Geology and Solid Earth Geophysics, Oslo, Norway 1970, 837-842. 529

40. Duane, David B., Michael E. Field, Edward P. Meisburger, Donald J. P. Swift, and S. Jeffress Williams

Linear Shoals on the Atlantic Inner Continental Shelf, Florida to Long Island: Shelf Sediment Transport, edited by Swift, Duane, and Pilkey © Dowden, Hutchinson and Ross, Inc., Stroudsburg, Pa., 447-498. 544

41. Freeland, G. L., and Robert S. Dietz

Plate Tectonics in the Caribbean: A Reply (Mattson's Critique): Nature *235*, 156-157. 596

42. Grim, P. J., G. H. Keller, and R. J. Barday

Computer Produced Profiles of Microtopography as a Supplement to Contour Maps: International Hydrographic Review *XLIX*, No. 1, 81-94. 598

43. Holden, J. C., and R. S. Dietz

Galapagos Gore, NazCoPac Triple Junction and Carnegie/Cocos Ridges: Nature *235*, 266-269. 612

44. Keller, George H.

Engineering Properties of Greenland and Norwegian Basin Sediments: Proceedings First International Conference on Port and Ocean Engineering Under Arctic Conditions *II*, 1285-1311. 616

45. Keller, George H., Douglas N. Lambert, Richard H. Bennett, and James B. Rucker

Mass Physical Properties of Tobago Trough Sediments: VI Conferencias Geologica del Caribe, Margarita, Venezuela, Memorias - 405-408. 643

46. Lambert, D. N., and R. H. Bennett

Tables for Determining Porosity of Deep-Sea Sediments from Water Content and Average Grain Density Measurements: NOAA Tech Memo ERL AOML-17. (Summary Only) 647

47. Long, L. T., S. R. Bridges, and L. M. Dorman

Simple Bouguer Gravity Map of Georgia: Geological Survey of Georgia, State of Georgia Department of Natural Resources. 652

48. McDonald, V. J., R. E. Olson, A. F. Richards, and G. H. Keller

Measurement and Control System for Deep Sea Vane-Shear Device: Ocean *72*, IEEE International Conference on Engineering in the Ocean Environment, 474-479. 654

49. Peter, George

Geology and Geophysics of the Venezuelan Continental Margin Between Blanquilla and Orchilla Islands: NOAA TR ERL 226-AOML 6. 660

50. Prospero, J. M., and T. N Carlson

Vertical and Areal Distribution of Saharan Dust Over the Western Equatorial North Atlantic Ocean: Journal of Geophysical Research *77*, No. 27, 5255-5265. 747

51. Rona, P. A.

Exploration Methods for the Continental Shelf: Geology, Geophysics, Geochemistry: NOAA TR ERL 238-AOML 8. 758

52. Scott, R. B., P. A. Rona, L. W. Butler, A. J. Nalwalk, and M. R. Scott

Manganese Crusts of the Atlantis Fracture Zone: Nature Physical Sciences *239*, No. 92, 77-79. 807

53. Shideler, G. L., and Donald J. P. Swift

Seismic Reconnaissance of Post-Miocene Deposits, Middle Atlantic Continental Shelf-Cape Henry, Virginia to Cape Hatteras, North Carolina: Marine Geology *12*, 165-185 814

54. Shideler, G. L., Donald J. P. Swift, G. H. Johnson, and B. W. Holliday

Late Quarternary Stratigraphy of the Inner Virginia Shelf: A Proposed Standard Section: Geological Society of America Bulletin *83*, 1787-1804. 835

55. Swift, Donald J. P.

Implications of Sediment Dispersal from Bottom Current Measurements; Some Specific Problems in Understanding Bottom Sediment Distribution and Dispersal on the Continental Shelf-a Discussion of Two Papers: Shelf Sediment Transport, edited by Swift, Duane, and Pilkey © Dowden, Hutchinson and Ross, Inc., Stroudsburg, Pa., 363-371. 853

56. Swift, Donald J. P., and W. R. Boehmer

Brown and Gray Sands on the Virginia Shelf: Color as a Function of Grain Size: Bulletin of Geological Society of America *83*, No. 4, 877-883. 862

57. Swift, Donald J. P., John C. Ludwick, and W. Richard Boehmer

Shelf Sediment Transport: A Probability Model: Shelf Sediment Transport, edited by Swift, Duane and Pilkey © Dowden, Hutchinson and Ross, Inc., Stroudsburg, Pa., 195-223. 869

58. Swift, Donald J. P., J. R. Schubel, and R. W. Sheldon

Size Analysis of Fine-Grained Suspended Sediments: A Review: Journal of Sedimentary Petrology *42*, No. 1, 122-134. 897

59. Van Andel, T. H., G. R. Heath, Richard H. Bennett, S. Charleston, D. W. Cronan, Kelvin S. Roldolfo, R. S. Yeats, D. Bukry, M. Dinkelman, and A. Kaneps

Deep Sea Drilling Project - Leg 16: Geotimes, 12-14. 910

Sea-Air Interaction

60. Hanson, Kirby J.

Remote Sensing of the Ocean: Remote Sensing of the Troposphere, edited by V. E. Derr, U. S. Dept. of Commerce and the Electrical Engineering Dept., Univ. of Colo., Boulder, Colo. 913

61. Hanson, Kirby J., and Monte F. Poindexter

Attenuation of Broad-Band Solar Irradiance in the Ocean: Conference on Atmospheric Radiation, August 7-9, 1972, Fort Collins, Colo. (AMS, Boston, Mass.). 969

62. Hanson, Kirby J., and Monte F. Poindexter

The Solar Irradiance Environment of Florida Coastal Water During Flare: NOAA Tech Memo ERL AOML-16. 973

63. Ostapoff, Feodor

Observation of Laminae in the Thermocline of the Tropical Atlantic: Presented at the ICES Symposium on "Physical Variability in the North Atlantic" held in Dublin, Ireland, September 1969. Paper 8. 997

Reprinted from Science *175*, 61-63.

Iron-Rich Basal Sediments from the Eastern Equatorial Pacific: Leg 16, Deep Sea Drilling Project

Abstract. *Iron-rich sediments chemically similar to those forming at present on the crest of the East Pacific Rise have been found just above basement at widely separated drill sites in the eastern equatorial Pacific, including three sites of Leg 16 of the Deep Sea Drilling Project. These sediments were probably formed when the basement was at the crest of this rise and have moved to their present location as a result of sea-floor spreading.*

The program for Leg 16 of the Deep Sea Drilling Project (DSDP) was designed around three principal objectives: (i) an examination of the tectonic and depositional history of the Panama Basin, (ii) supplementary drilling for the study of the Cenozoic depositional history of the eastern equatorial Pacific, and (iii) a search for Fe-rich sediments directly above basement similar to those found previously by drilling in the eastern equatorial Pacific. In connection with the first objective, DSDP sites 155 through 158 were drilled on shallow ridges surrounding the Panama Basin (*1*); DSDP sites 159 through 163 were drilled to supplement a north-south traverse of drill sites along 140°W which was begun on Legs 5 and 8, and to add to the network of equatorial drill sites extending across the eastern and central Pacific. The evaluation of these aspects of Leg 16 results awaits publication of the results of earlier legs.

In addition, the Leg 16 sites were designed to test the distribution of ferruginous sediments that have been reported immediately overlying basement at several sites of Legs 5 and 9 (*2*). These deposits may be analogous to the iron-rich sediments now forming on the crest of the East Pacific Rise. Similar deposits were found at sites 159 through 162 in the area between the discoveries of Legs 5 and 9 to the north and south, respectively. We present here the results of some analyses of these deposits and a preliminary discussion of their origin.

The basal sediments of sites 159 through 163 consist predominantly of clays and chalk oozes. At both site 159 and site 160 a thin basal clay unit may be present, but it is difficult to be sure since an undisturbed contact between basalt and the overlying sediments was not recovered. The lowermost core from each of these sites consists of slurried carbonate, clay, and basalt chips, whereas the deepest sediment preserved in a reasonably undisturbed state is a nannofossil chalk ooze. At site 161 the basal sediment is a locally calcareous indurated

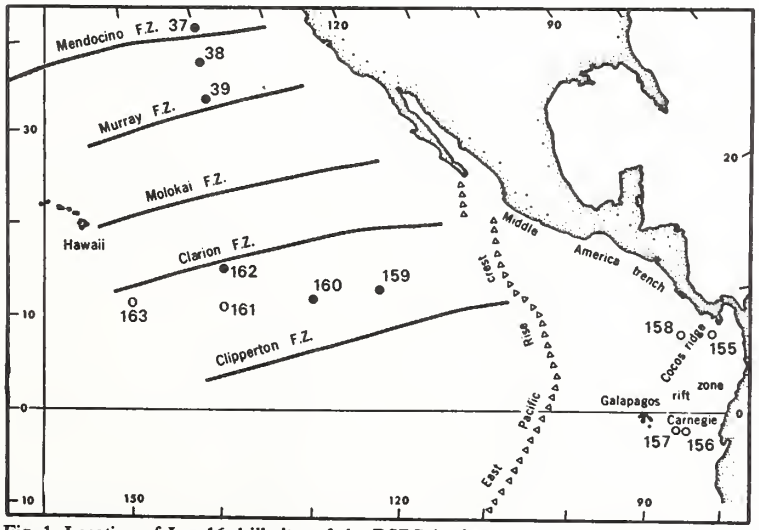

Fig. 1. Location of Leg 16 drill sites of the DSDP in the eastern equatorial Pacific (sites 155 through 163). Solid circles are sites at which sediments enriched in Fe and trace metals were recovered immediately above basement. Also shown are sites 37 through 39 of Leg 5 at which similar deposits were encountered; *F.Z.*, fracture zone.

Table. 1. Composition of basal sediments collected during DSDP Leg 16. Site 159, 12°20'N, 122°17'W; site 160, 11°42'N, 130°53'W; site 161A, 10°40'N, 139°57'W; and site 162, 14°52'N, 140°03'W; ppm, parts per million.

Site	Core	Section	Interval (cm)	Depth below sea floor (m)	Distance above basalt (m)	Fe (% by weight)	Mn (% by weight)	Ni (ppm)	Co (ppm)	Cu (ppm)	Pb (ppm)	Zn (ppm)	Stratigraphic age	Lithology
159	2	1	38–43	9	99	4.74	0.72	336	183	816	40	219	Late Miocene	Radiolarian clay
159	10	6	90–95	89	19	18.27	4.60	438	78	1044	130	443	Early Miocene	Nannofossil marl
159	12	1	25–30	99	9	16.77	4.48	472	76	762	122	427	Early Miocene	Nannofossil marl
159	12	6	103–108	107	1	19.10	5.15	436	95	840	152	458	Early Miocene	Nannofossil marl
159	13	2	95–100	107	1	15.96	3.56	385	79	611	106	518	Early Miocene	Nannofossil marl
159	13	4	133–137	108	0	15.96	3.16	345	79	744	106	438	Early Miocene	Nannofossil marl
160	3	4	78–83	23	86	6.42	1.10	187	64	749	42	230	Early Miocene	Zeolitic clay
160	10	6	125–130	90	19	2.06	0.36	243	121	364	304	206	Early Oligocene	Nannofossil chalk ooze
160	11	6	135–140	99	10	2.29	0.36	241	120	362	302	205	Early Oligocene	Nannofossil chalk ooze
160	12	5	135–140	106	3	3.09	0.35	158	71	431	179	179	Early Oligocene	Nannofossil chalk ooze
160	13	1	99–103	109	0	8.52	1.86	934	56	994	56	262	Early Oligocene	Nannofossil marl
161A	12	1	59–64	218	26	5.94	1.04	113	27	475	34	183	Late Eocene	Radiolarian ooze
161A	12	1	139–144	219	25	6.48	1.09	108	27	536	37	189	Late Eocene	Radiolarian ooze
161A	13	1	136–141	227	17	3.91	0.84	61	20	350	29	95	Late Eocene	Radiolarian ooze
161A	14	1	148–150	236	8	4.74	1.10	169	33	508	58	183	Middle Eocene	Radiolarian ooze
161A	14	2	149–151	238	6	4.48	0.92	105	17	402	34	149	Middle Eocene	Radiolarian ooze
162	12	2	104–109	102	51	6.04	0.63	56	12	226	31	126	Middle Eocene	Clayey marl ooze
162	16	3	76–81	138	25	3.87	1.03	86	15	244	28	91	Middle Eocene	Clayey radiolarian ooze
162	17	1	62–67	145	8	19.42	7.10	488	99	1498	149	33	Middle Eocene	Ferruginous clay
162	17	4	101–106	150	3	30.56	9.55	1680	171	1814	229	515	Middle Eocene	Clayey marl
Average of 11 ferruginous sediments from sites 159, 160, and 162						17.50	4.52	535	83	917	145	358		
Average of carbonate-free surface cores from the East Pacific Rise, 12° to 14°S (6)						18.00	6.00	430	105	730		380		
Average surface Pacific pelagic clay (10)						5.06	0.48	211	101	323	68			

radiolarian ooze, at site 162 a zeolitic brown clay overlying a foraminiferal nannofossil chalk, and at site 163 a slightly dolomitized chalk. All these sediments, other than those at site 163, contain a relatively high proportion of small yellow to reddish-brown amorphous ferruginous aggregates, grains, and globules. These are as large as a few tens of micrometers in diameter and are generally spherical. They are also found, usually in low concentrations, elsewhere in the sediment column at each of the sites, but are most abundant in basal sediments.

Eighteen samples of basal and near basal sediments from sites 159 through 162 were selected for analysis, together with two shallower samples from sites 159 and 160 for comparison. The elements Fe, Mn, Ni, Co, Cu, Pb, and Zn were determined by standard atomic absorption spectrophotometric techniques (*3*) after digestion in aqua regia. The results are presented on a carbonate-free basis in Table 1.

The data show that the basal sediments at sites 159 and 162 are markedly more ferruginous than those higher in the sediment column, whereas only a slight basal enrichment of Fe occurs at site 160 (Table 1). Smear-slides of these samples contain high concentrations of the yellow to reddish-brown grains mentioned above. The apparent lack of basal Fe enrichment at site 161 may reflect dilution by opaline silica, since ferruginous grains are common here also. Recalculation of the analyses on a biogenous silica-free basis would reveal an enrichment similar to those in the other cores, since the opal content of sediment in section 1 of core 14, for example, is 65 to 70 percent (by weight).

Elements other than Fe are also enriched in the basal sediments from sites 159, 160, and 162, Manganese is concentrated severalfold at the base of the sediments at sites 159 and 162 relative to its abundance higher in these sections, whereas Zn, Ni, Cu, Co, and Pb are concentrated in some, but not all, of the ferruginous sediments (Table 1).

Metal-rich recent sediments from the crests of mid-oceanic ridges are well documented (*4*), but it is only with the advent of the deep-drilling techniques of the Deep Sea Drilling Project that such sediments have been found in older subsurface formations. The basal sediments analyzed in this work range in age from early Miocene at site 159 to middle Eocene at site

162, and are very similar in composition to recent sediments at the crest of the East Pacific Rise. Boström (*5*) has reported Fe concentrations in excess of 20 percent on a carbonate-free basis in East Pacific Rise deposits, and Boström and Peterson (*6*) have found that these sediments contain concentrations of Mn, Cu, Zn, Ni, and Co similar to those occurring in the sediments described here (Table 1). The high metal concentrations in East Pacific Rise sediments are thought by Boström (*5*) to result from submarine hydrothermal activity associated with the generation of new ocean floor at the rise crest. Corliss (*7*) has proposed that these hydrothermal solutions originated by the leaching of the newly extruded basalt. However, Turekian and Bertine (*8*) have suggested that some metal enrichments in ocean ridge sediments may result from their deposition under anaerobic conditions. Such a mechanism is unlikely to apply to the sediments described in this report, since they are oxidized throughout and contain the bulk of their Fe in the ferric state. In any event, according to current theories of sea-floor spreading, new ocean floor moves away from ridge crests, thereby carrying away sediment deposited on it irrespective of its origin. The ferruginous sediments described here are probably the Tertiary equivalents of those forming at the crest of the East Pacific Rise at the present time (*9*).

D. S. Cronan
Department of Geology, University of Ottawa, Ottawa 2, Ontario, Canada
T. H. van Andel, G. Ross Heath
M. G. Dinkelman
Department of Oceanography, Oregon State University, Corvallis 97331
R. H. Bennett
National Oceanic and Atmospheric Administration, Atlantic Oceanographic Meteorological Laboratory, Miami, Florida 33130
David Bukry
U.S. Geological Survey, La Jolla, California 92037
Santiago Charleston
Mexican Petroleum Institute, Mexico 14, D.F., Mexico
Ansis Kaneps
Scripps Institution of Oceanography, La Jolla, California 92037
K. S. Rodolfo
Department of Geology, University of Illinois, Chicago 61680
R. S. Yeats
Department of Geology, Ohio University, Athens 45701

7 JANUARY 1972

References and Notes

1. T. H. van Andel, G. R. Heath, B. T. Malfait, D. F. Heinrichs, J. Ewing, *Geol. Soc. Amer. Bull.* **82**, 1489 (1971).
2. C. C. von der Borch and R. W. Rex, in D. A. McManus *et al.*, *Initial Reports of the Deep Sea Drilling Project* (Government Printing Office, Washington, D.C., 1970), vol. 5, p. 541.
3. E. E. Angino and G. K. Billings, *Atomic Absorption Spectrometry in Geology* (Elsevier, Amsterdam, 1967).
4. K. Boström and M. N. A. Peterson, *Econ. Geol.* 61, 1258 (1966).
5. K. Boström, *Earth Planet. Sci. Lett.* **9**, 348 (1970).
6. ——— and M. N. A. Peterson, *Mar. Geol.* **7**, 427 (1969).
7. J. Corliss, thesis, University of California, San Diego (1970).
8. K. K. Turekian and K. Bertine, *Nature* **229**, 250 (1971).
9. The Deep Sea Drilling Project is an NSF-funded program to explore the geologic history of the deep ocean basins by means of standard oil-field drilling techniques. Scripps Institution of Oceanography is the managing institution for the project. Actual drilling is done by Global Marine, Inc. (their vessel is the *Glomar Challenger*). Scientific planning is based on advice from a number of panels representing interested scientific disciplines and including representatives from universities, government agencies, and industry.
10. D. S. Cronan, *Geochim. Cosmochim. Acta* **33**, 1562 (1969).

16 August 1971; revised 5 October 1971

Reprinted from EOS 53, No. 2, 200-201.

The Face of the Deep, Bruce C. Heezen and Charles D. Hollister. Oxford University Press, New York, 659 pp., 1971, $25.00.

The Face of the Deep is an elegant, large-format tome organized around some 600 deep-sea photographs, including an eight-page signature in color, selected and culled from a study of many tens of thousands. The scenery of the abyss is treated in an authoritative, easy-flowing and pleasantly readable manner. It will excite both the scientist and the general reader. It is remarkable how far deep-sea photography has progressed since the first abyssal photograph taken a mere two decades ago. The book is a great leap forward since Brackett Hersey's (editor) fine book, *Deep-Sea Photography*, published in 1967.

If a picture is worth a thousand words, then this weighty volume is two-thirds of a million words long. About half of the text is a verbal accompaniment to the photos, but the remainder is an exposition of marine geology generally supported by a profusion of physiographic diagrams, clear illustrations, and fine drawings. It could serve as a useful text, or at least as a supplement, to a marine geology course. To make for good reading, each chapter has its own frontispiece and each has a poetic introduction. Names of persons, reference, and credits are relegated to sections at the ends of chapters or at the end of the book.

Each photograph covers only a few square meters, equivalent to that of a bed sheet. Nevertheless, one can nearly always distinguish the type of region: a stagnant basin, the top of a seamount, pillow basalts of the central rift, or a sterile expanse of red clay. A shelf photo is invariably distinguishable from an abyssal scene A strewn field of manganese nodules may typify a million square kilometers.

Chapters are devoted to the following subjects: (1) portraits of the various animals that people the abyss from lowly sponges to the giant sleeper shark; (2) tracks and trails, many without explanation although the authors are experts on *Lebensspuren;* (3) identification of fecal pellets and coprolites that litter the bottom; (4) interpretation of mounds, holes, and bioturbation; (5) depiction of the great variety of junk that litters the bottom, both natural and man-made, and running the gamut from iceberg-rafted boulders to shipwrecks and even including the proverbial kitchen sink; (6) a visual study of the effects of turbidity currents; (7) ripples, scours, and so forth, caused by the planetary currents that sweep the bottom; (8) manganese nodules, philipsite, phosphorite and other authigenic chemically deposited substances; (9) visual effects of tectonism under the sea; (10) a look at seamounts and underwater plateaus; and (11) the mid-ocean rifts and fracture zones. Finally, there are seven appendices that support the text. Among the more remarkable photos are those of pillow basalts in rift zones, whale bones, strewn fields of manganese nodules, and giant sea spiders (pycnogonids).

There is a pleasant dash of whimsey in the book, such as a cartoon of Winnie-the-Pooh puzzling over his own tracks with the caption 'It is not always possible to identify tracks, not even your very own.' Early bathyscaph divers are termed 'submarine mountain climbers.' Hollister, however, must know this nonscientific aspect of human challenge quite well, for he was a member of the American team that first conquered the highest mountain in Antarctica.

Advance publicity indicated that a $12.50 (or one-half price) paperback edition would also be issued. Unfortunately this did not materialize, and now the book is priced beyond the means of most scientists as private buyers. Apparently the real cost of turning out a hard-cover edition is only $1 more than a paperback The large additional markup stems from the wholly different scheme of merchandizing.

This magnificent compendium will become a *vade mecum* for the deep-submergence-vehicle diver. It will enthrall the geologist, the biologist (those who are not perturbed by the limitations of photography), and the just plain curious to see a world that has never been seen before.

Robert S. Dietz

NOAA, Atlantic Oceanographic and Meteorological Laboratories
901 South Miami Avenue
Miami, Florida 33130

Reprinted from Scientific American 226, No. 3, 30-38.

Geosynclines, Mountains and Continent-building

A geosyncline is a huge deposit of sedimentary rock that forms at the edge of a continent. When it is compressed, it buckles up into a mountain range. It also enables a continent to grow by accretion

by Robert S. Dietz

A geosyncline is a long prism of sedimentary rock laid down on a subsiding region of the earth's crust. It has long been recognized that geosynclines are fundamental geologic units. Furthermore, it has been a dictum of geology that they eventually evolve into mountains consisting of folded sedimentary strata. The laying down of such sediments and their subsequent folding constitute a basic geologic cycle that requires a few hundred million years. Until recently the original nature of geosynclines has been inferred only by studying folded mountains. It was commonly believed that there are no nascent (unfolded) geosynclines in the world today, but this would defy another geologic dictum: that the present is the key to the past.

In recent years the study of marine geology has been revolutionized by the concept of plate tectonics, which holds that the earth's crust is divided into a mosaic of about eight rigid but shifting plates in which the continents are embedded and drift along as passive passengers. With this concept the evolution of ocean basins has been rather clearly resolved. The question arises: Must plate tectonics stay at sea, or is it also the prime mover of the geosyncline mountain-building cycle? In other words, can it account for the collapse of geosynclines and the growth of continents? I am among those who believe it can. Some notable advocates of this new concept of continental evolution are John Dewey and John M. Bird of the State University of New York at Albany, Andrew Mitchell and Harold Reading of the University of Oxford and William R. Dickinson of Stanford University.

When one examines the structure of ancient folded mountains, one finds that the classic geosyncline is divided into a couplet: two adjacent and parallel structures consisting of a eugeosyncline (true geosyncline) and a miogeosyncline (lesser geosyncline), often shortened to eugeocline and miogeocline. Now that the ocean floor is becoming better known, one need not look far to find an example of the geosynclinal couplet in process of formation. A probable example of a "living" eugeocline is the continental rise that lies seaward of the continental slope off the eastern U.S. Landward of the rise and capping the continental shelf is a wedge of sediments that becomes progressively thicker as it extends toward the shelf edge. This wedge seems to be a living miogeocline.

In dimensions and in the overall character of its rocks and stratigraphy the modern continental-rise prism closely matches typical ancient eugeoclines. It parallels the Atlantic seaboard for 2,000 kilometers, forming an apron 250 kilometers wide from the continental slope to the abyssal plain [*see illustrations on pages 34 and 35*]. Seismic studies reveal that the rise is the top of a huge planoconvex lens of sediments whose maximum depth is about 10 kilometers. The sediments are turbidites, deposited by the muddy suspensions known as turbidity currents. Such suspensions periodically cascade down submarine canyons and pour across the continental rise, depositing sedimentary fans that eventually coalesce into an apron. Turbidites consist of thin graded beds of poorly sorted particles of silt and sand in which coarse material is at the base and finer material is at the top. The gradation in particle size reflects the differential rate of settling from a single injection of muddy sand. Interlayered with the graded beds are fine clays (pelagites) that slowly settle from the overlying water as a "gentle rain" between major influxes of turbidity currents.

Collapsed eugeoclines in ancient folded mountains are similarly composed of thick and repetitive sequences of turbidites; these strata are usually termed flysch or graywacke. Mixed with the graywackes are thin limestones, ironstones and cherts formed from the skeletons of radiolarians, indicating that the sediments were deposited in deep water. True fossils are sparse, but many eugeoclinal sequences of the lower Paleozoic era contain graptolites: extinct plantlike animals that settled down from the surface.

Close examination of the graded beds also reveals what are called sole mark-

COLLISION OF CONTINENTS is depicted in this view of the Zagros Mountains in Iran along the Persian Gulf taken from the spacecraft *Gemini 12* in November, 1966. The mountains are uplifted folds of sedimentary strata, originally deposited as a geosyncline, whose cores have been exposed by erosion. The foldbelt has apparently been thrown up by the collision of the Arabian block, rotating counterclockwise, with the Eurasian block, rotating clockwise. Since the Arabian block is part of the African block, the folding represents the collision between Africa and Eurasia. The Zagros Mountains and the shallow Persian Gulf are both part of the Arabian block that extends to the Red Sea. The suture between the Arabian block and the Eurasian block is marked by a major thrust fault that passes through the upper right corner of the photograph just beyond the mountain chains.

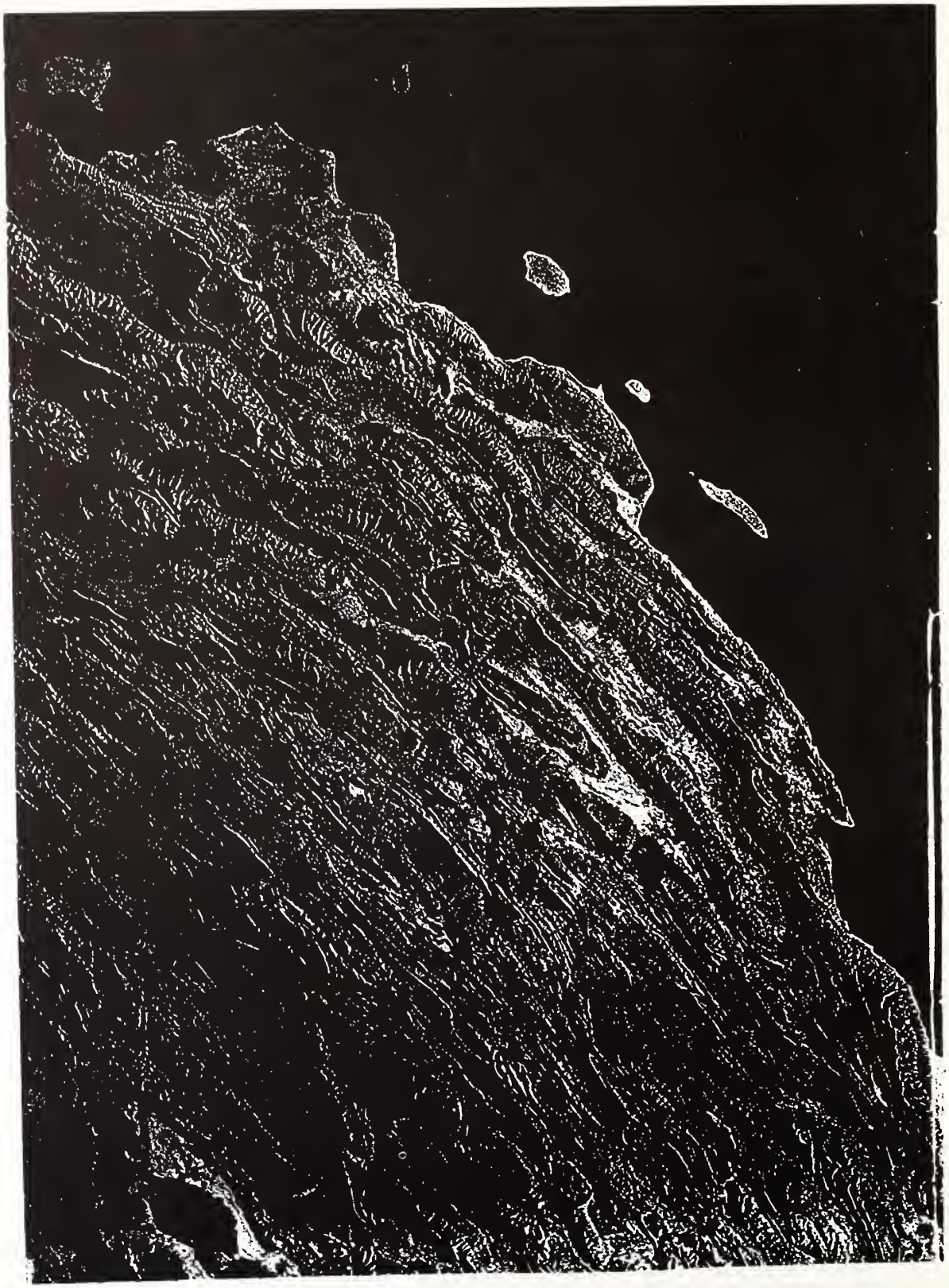

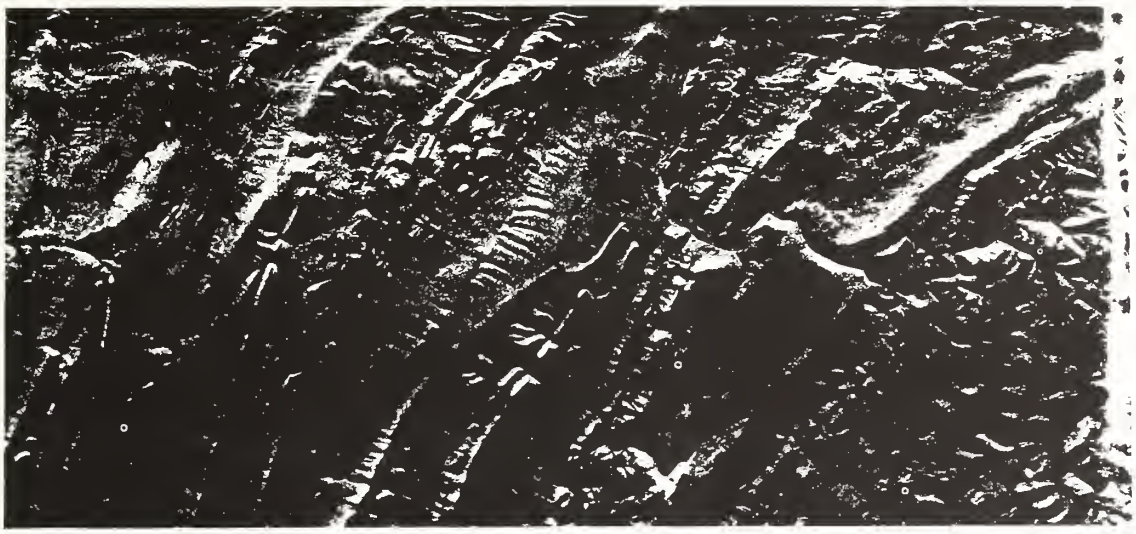

FOLDED APPALACHIAN MOUNTAINS in western Pennsylvania are depicted in this image produced by side-looking radar. The picture covers a region 25 miles long parallel to the Maryland border, centered approximately at 78 degrees 45 minutes west longitude. The picture is printed with north at the bottom so that the landscape appears to be lighted from the top. (The illuminant, of course, is the radar beam transmitted from an airplane.) If the picture is inverted, features that are actually elevated appear depressed and vice versa. This image and the sequence of three views at the bottom of these two pages were made by the National Aeronautics

ings or "flysch figures," for example ripple marks of a kind that could have been produced by turbidity currents. There can be little doubt that most of these sequences are the uplifted and eroded remnants of former continental-rise prisms. The crystalline Appalachians, which are that part of the Appalachians lying seaward of the Blue Ridge Mountains and equivalent ranges to the north and south, bear the clear imprint of being a collapsed continental-rise prism laid down in the early Paleozoic some 450 to 600 million years ago. The original prism has been much altered by intrusions and metamorphism.

The sedimentary wedge that underlies the coastal plain and continental shelf along the Atlantic seaboard appears to be an actively growing miogeocline. The wedge thickens as it progresses seaward, attaining a total thickness of between three and five kilometers along the shelf edge. Laid down on a basement of Paleozoic rocks, the wedge is composed of well-sorted shallow-water sediments deposited during the past 150 million years under conditions much like those of today. The stratified beds exhibit characteristics indicating they were deposited across the continental shelf in alluvial plains, in lagoons, along shorelines and offshore. Taking into account expected changes in the pattern of sedimentation over geologic time, the present Atlantic marine

APPALACHIAN FOLDBELT north of Harrisburg, Pa., is an extension of the foldbelt shown at the top of the page. In these side-looking radar views north is at the right. The three pictures cover a distance of 75 miles from just south of Mechanicsburg to the vicinity of a town called Jersey Shore on the West Branch of Susquehanna River. The Susquehanna River itself appears in the first frame at the left. The folded Appalachians were probably created in a late compressional stage of the collision between Africa and North America more than 450 million years ago, which caused "rugfolds" in the strata of sedimentary rock that formed part of a

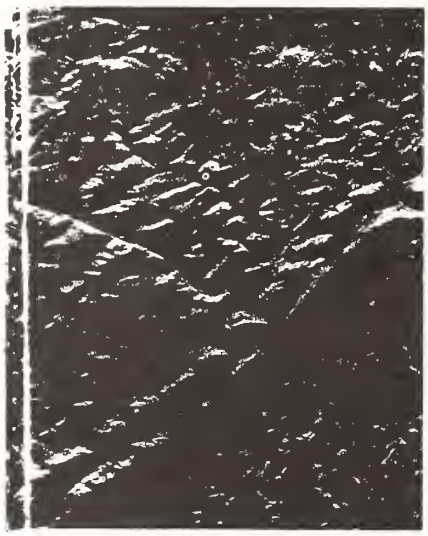

and Space Administration in collaboration with the Remote Sensing Laboratory of the University of Kansas. The *K*-band radar system that produced the images was built by the Westinghouse Electric Corporation.

deposits closely resemble the ancient miogeoclinal foldbelts of the Paleozoic era and earlier. For example, the modern sedimentary wedge is much like the one found in the folded Appalachians of Pennsylvania. Both wedges are characterized by "thickening out," signifying that they grow steadily thicker toward the east before they abruptly terminate.

If the foregoing analysis is correct, one must conclude that geosynclines are actively forming along many continental margins today: eugeoclines at the base of the continental slope and miogeoclines capping the continental shelves. It remains to be shown, however, that the crustal shifting associated with plate tectonics can convert these sedimentary prisms into the mountainous foldbelts that make up the fabric of the continents, mostly as ancient eroded mountain roots rather than as modern mountain belts. In order to examine this possibility we must first summarize some of the basic concepts of plate tectonics.

The approximately eight rigid but shifting plates into which the earth is currently divided are thought to be about 100 kilometers thick. Most of the plates support at least one massive continental plateau, often referred to as a craton. We can visualize the ideal plate as being rectangular, although only the plate supporting the Indian craton approaches this simple shape. Along one edge of a crustal plate there is a subduction zone, usually marked by a trench, where the plate dives steeply into the earth's mantle, attaining a depth as great as 700 kilometers before being fully absorbed into the mantle. On the opposite side of the plate from the subduction zone is a mid-ocean rift, or pull-apart zone. As the rift opens, the gap is quickly healed from below by the inflow of liquid basalt and quasi-solid mantle rock. The other two opposed sides of the plate, connecting the rifts to the trenches, are shears called transform faults.

Hence three types of plate boundary are possible: divergent junctures (the mid-ocean rifts where new ocean crust is created), shear junctures (the transform faults where the plates slip laterally past one another, so that crust is conserved) and convergent junctures (trenches where two plates collide, with one being subducted and consumed). Only the last of the three, the convergent juncture, can help to explain how the sedimentary prism of a submarine geosyncline might be collapsed into a folded range of mountains. As the plate carrying a prism collides with a plate carrying a continental craton one would expect the prism to be compressed into folds. Thrusting and crustal thickening would follow, assisted by isostatic forces that act to keep adjacent crustal masses in balance. Such forces would cause the collapsed prism to be uplifted. The entire process would be accompanied by the generation and intrusion of magma, together with extensive metamorphism of the crustal rocks.

A grand theme of plate tectonics is that ocean basins are not fixed in size or shape; they are either opening or closing. Today the Atlantic Ocean is opening and the Pacific Ocean is closing. The drifting of the continents is another theme; every continent must have a leading edge and a trailing edge. For the past 200 million years the Pacific coast of North America has been the leading edge and the Atlantic coast the trailing edge. The trailing margin is tectonically stable, and since the continental divide is near the mountainous Pacific rim, most of the sediments are ultimately dumped into the Atlantic Ocean, including the Gulf of Mexico. Therefore it is primarily along a trailing edge that the great geosynclinal prisms are deposited.

Consider, however, what would hap-

Paleozoic geosyncline (*see illustration on page 36*). After folding the region was eroded to a level plain and then uplifted. The modern mountains were subsequently etched out according to the hardness of the various strata. Thus the ridges are composed mainly of dense sandstone and can be either synclines (troughs) or anticlines (arches). The *V*-shaped chevrons in the first frame are synclines that plunge to the northeast. The Susquehanna River established its course when the entire region was reduced to a level surface, so that its course has been superimposed on the folded structure, thereby cutting directly across the folds and creating water gaps.

pen if, with the changing patterns of plate motions, a subduction zone (a trench) were created along a former trailing edge, forming a new plate boundary. The Atlantic would be transformed into a closing ocean with its geosynclinal prisms riding toward the trench. The continental margin and the trench would eventually collide, collapsing the eugeocline into a contorted mountainous foldbelt and also folding the miogeocline to a much lesser extent. Before that happened the continental margin would encounter and incorporate an island arc, similar to the island arcs found along the perimeter of the western Pacific. These arcs are created by tectonic and magmatic activity triggered by the plunging crustal plate. It is also quite possible that the Atlantic Ocean would close entirely, causing North Africa to collide with eastern North America. The collision of India with the underbelly of Asia, throwing up the Himalaya rampart, would be a present-day analogy. One can imagine many possible scenarios, depending on the geometry of plate boundaries and other variables.

The creation of a eugeoclinal foldbelt is of course considerably more than simply the accordion-like collapse of a continental-rise prism. The foldbelt is sheared into thrust faults and the landward edge of the eugeocline is commonly thrust onto the adjacent miogeocline. The descending crustal plate is not entirely consumed within the earth's hot mantle, with the result that low-density magmas buoyantly rise and invade the eugeocline. This leads to intrusions of granodiorite (a granite-quartz rock) and the growth of volcanic mountains consisting of andesite (the rock characteristic of the Andes). This lava is highly explosive because it is charged with water sweated out of the descending plate. Magma is not generated from the plunging lithosphere until it has reached a considerable depth. As a result the eugeocline can be subdivided into two parallel geologic belts. Toward the sea one finds sedimentary rock transformed at high pressure and low temperature; farther inland the sedimentary rock has been altered predominantly at low pressure and high temperature by the numerous intrusions of magma. From the new marginal mountain range, delta and river deposits sweep back across the continent, covering the miogeocline with a suite of continental shales and conglomerates collectively called molasse.

The concept that the geosynclinal cycle is controlled by plate tectonics provides some new answers to old questions about geosynclines. For example, is mountain-building periodic and worldwide or is it random in space and time? The answer must be both yes and no. On the one hand, the crustal plates are highly intermeshed; the drift of any one plate has global repercussions, giving rise to synchronous mountain-building. Any brief interval of rapid plate motion would also be one of widespread mountain-building. On the other hand, the rate of plate convergence is highly dependent on the latitudinal distance from the relative pole of rotation of that plate and on the particular geometry of the plate boundary.

A law of plate tectonics states that seafloor spreading (injection of new ocean crust) proceeds at right angles to a rift; the crustal plate, however, may be subducted into a trench at any angle. The rate of subduction and the attendant distorting of the crust therefore vary greatly from place to place, as can be observed on the perimeter of the Pacific today. Thus it would seem that although mountain-building over the span of geologic time may reach crescendos, it must also be continuous and random.

The plate-tectonic version of the geosynclinal cycle predicts that miogeoclines are ensialic, or laid down on continental crust (sial), whereas eugeoclines are ensimatic, or deposited on oceanic crust (sima). This differs from the earlier view that all geosynclines are ensialic,

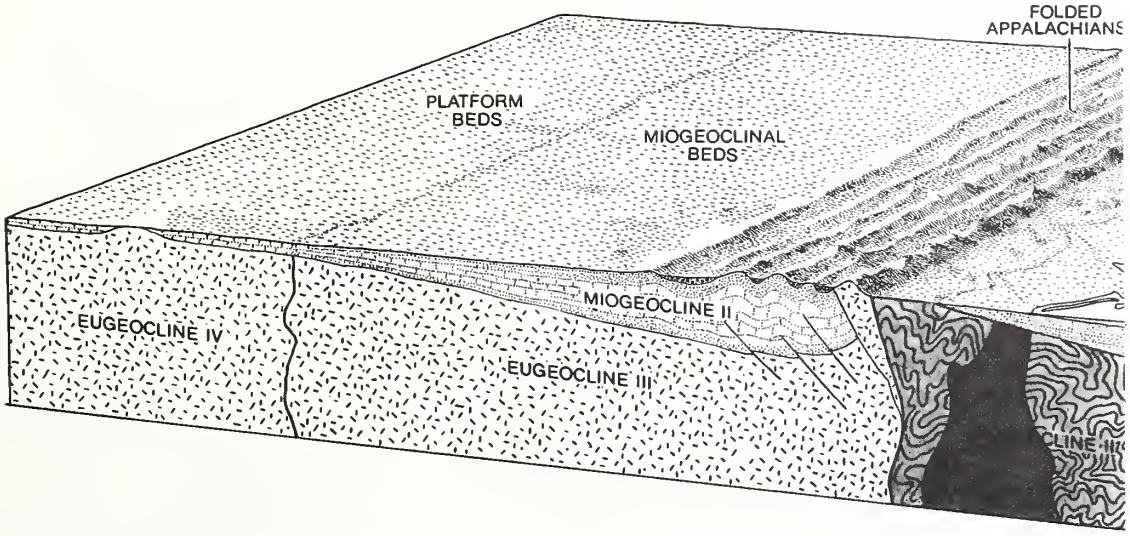

SUCCESSION OF EUGEOCLINES underlies nearly all North America below the relatively undisturbed cover beds. These contorted and intruded prisms constitute the fundamental fabric of continents, known as the basement complex. A new geosynclinal couplet is being deposited today. It consists of a miogeocline (lesser geosyncline) of shallow water beds that caps the coastal plain and continental shelf paralleled by a eugeocline (true geosyncline) that is formed at the base of the continental slope by detritus

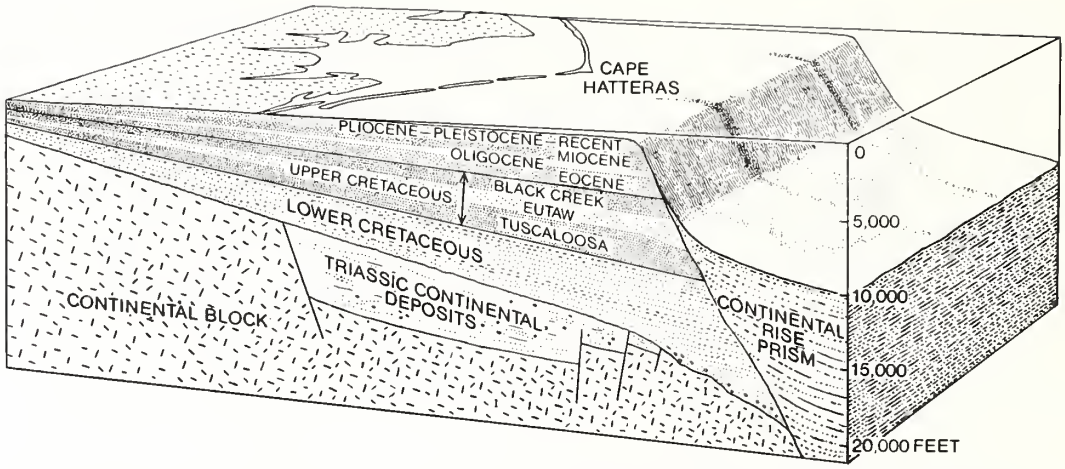

LIVING GEOSYNCLINAL COUPLET off the Atlantic coast of the U.S. consists of a miogeocline, strata laid down on the shallow continental shelf during the past 150 million years, and a eugeocline prism (*dark color*), consisting of thin beds of sand and mud deposited by turbidity currents flowing down the continental slope. The material in the Triassic basin represents continental deposits laid down before the foundering of the continental margin under tension 190 million years ago, prior to opening of Atlantic Ocean.

which is certainly incorrect. Early investigators observed that a granitic basement is invariably present under miogeoclines and evidently reasoned that a similar sialic basement, although it was unseen, must also be present under eugeoclines. A collapsed eugeocline is as thick as the continental plate, about 35 kilometers, so that its basement is beyond the depth of even the deepest boreholes. We can infer that the ultimate basement is simatic, however, by observing detached fragments that are caught up in the contorted mélange of the eugeoclinal pile. These fragments include samples of oceanic crust (for example radiolarian cherts and sodium-altered lavas) and upper-mantle rocks (for example serpentinites and peridotites).

The ensimatic location of eugeoclines can also account for their tectonic style. They are tightly folded, faulted, tumbled and dynamically metamorphosed into an almost unmappable mélange. This contorted state is understandable, since the ocean floor is shearing under the eugeocline and thrusting the sedimentary pile against the continental slope. Extensive tectonic thickening and interleaving must occur before the pile will rise to mountainous altitudes. On the other hand, the miogeocline beds are protected by the stable continental slab, so that they are simply thrown into a series of loose, open, ruglike folds.

It now seems amusing to recall that 19th-century geologists, using a wrinkled apple as an analogy, interpreted folded mountains to mean that the earth was shrinking. Today it seems clear that eugeoclines are deposited at the edge of a continent on oceanic crust seaward of the continental slope, so that folded mountains really show that the continents are growing larger through marginal accretion. Mountain-building is therefore evidence of an even more fundamental geologic process: the growth of continents. The continents grow not as a layer cake but as a craton that is divided vertically into zones with an old nucleus and young margins.

An important aspect of geosynclines requiring explanation is that they are laid down on foundations that are continuously subsiding. This aspect is par-

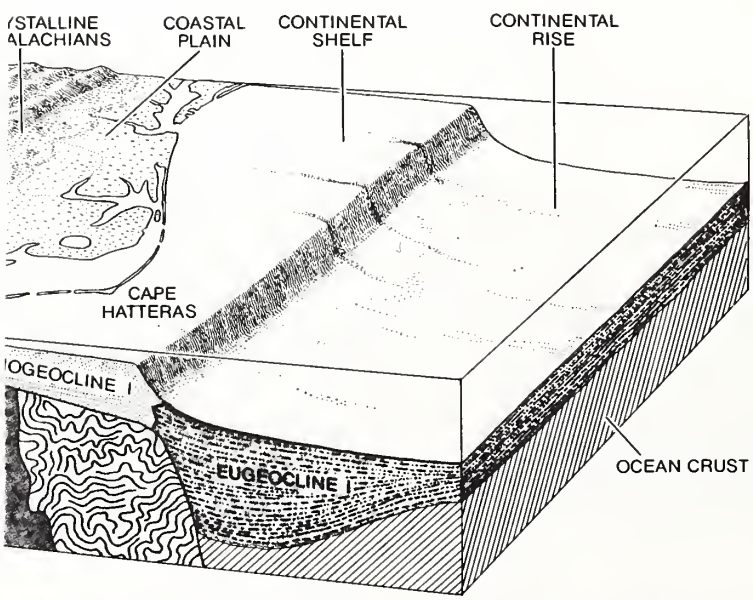

washed over the shelf edge. If at some future time the sea floor were to thrust against the continent, the modern eugeocline (*I*) would collapse into a new foldbelt like the earlier ones. The hypothetical mechanism that creates foldbelts is shown on page 37. This diagram and others are based on drawings by the author's colleague John C. Holden.

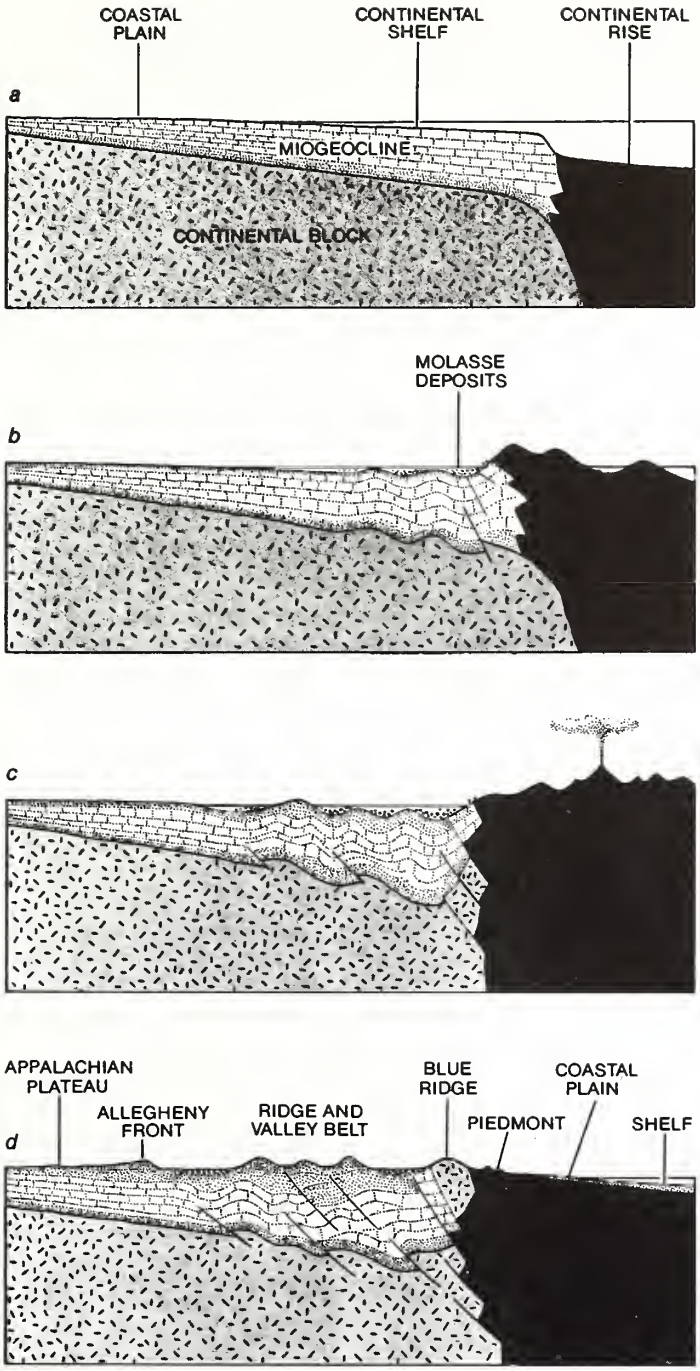

CRUMPLING OF EARLIER GEOSYNCLINAL COUPLET, appareutly laid dowu iu late Precambrian and early Paleozoic time more than 450 milliou years ago, produced the Appalachian foldhelt. The four-part sequence shows how the miogeocline, or western part of the geosyncliual couplet, was folded into the series of ridges betweeu the Blue Ridge line and the Allegheuy frout. The eugeocline, altered by heat, pressure and volcanism, formed a lofty range of mountains, uow almost completely eroded, east of the Blue Ridge line.

ticularly evident in miogeoclines, which can attain a total thickness at their seaward edge of five kilometers even though they are entirely composed of beds deposited in shallow water. This phenomenon is nicely accounted for by plate tectonics: the margins of rift oceans inherently have, as one geologist has expressed it, a "certain sinking feeling."

Let us take as an example the Atlantic Ocean between the U.S. and the bulge of Africa. This new ocean basin was created about 180 million years ago by the insertion of a spreading rift that split North America away from Africa [*see illustration on opposite page*]. Attendant swelling of the mantle arched the continents upward along the rift line by about two kilometers. Erosion then beveled the raised edges, thinning the margins of the two continental plates.

A modern example of crustal arching associated with incipient rifting of the crust can be observed in the high dorsal of Africa from Ethiopia southward. The Red Sea provides a more advanced stage of a newly opening ocean basin. Along the flanks of this linear trough crustal arching has stripped away young rocks, exposing "windows" of Precambrian basement.

With the insertion of new oceanic crust by sea-floor spreading, the ocean grew ever wider. In the process the continental edges subsided, as is demonstrated by the sloping flanks of the mid-Atlantic ridge today. When the ocean was smaller, the continental edges had to ride down a similar slope. Eventually the inflated mantle under the ridge reverts to normal mantle, but this takes 100 million years or more. Therefore as a geosyncline is laid down on the trailing edges of a drifting continent it slowly subsides for reasons external to the sedimentary deposit itself.

Additional subsidence, however, is caused by the steadily growing mass of the sedimentary apron, which must be isostatically compensated because the earth's crust is not sufficiently strong to sustain the load. For every three meters of sediment deposited the crust sinks about two meters. This crustal failure, however, is spread over a large geographic area, so that the growth and subsidence of a huge continental-rise prism causes a sympathetic downward flexing of the adjacent continental margin. As the continental shelf slowly tilts, wedges of shallow-water sediments are deposited.

Over the millenniums, as the shoreline transgresses and regresses repeatedly across the shelf, a large composite

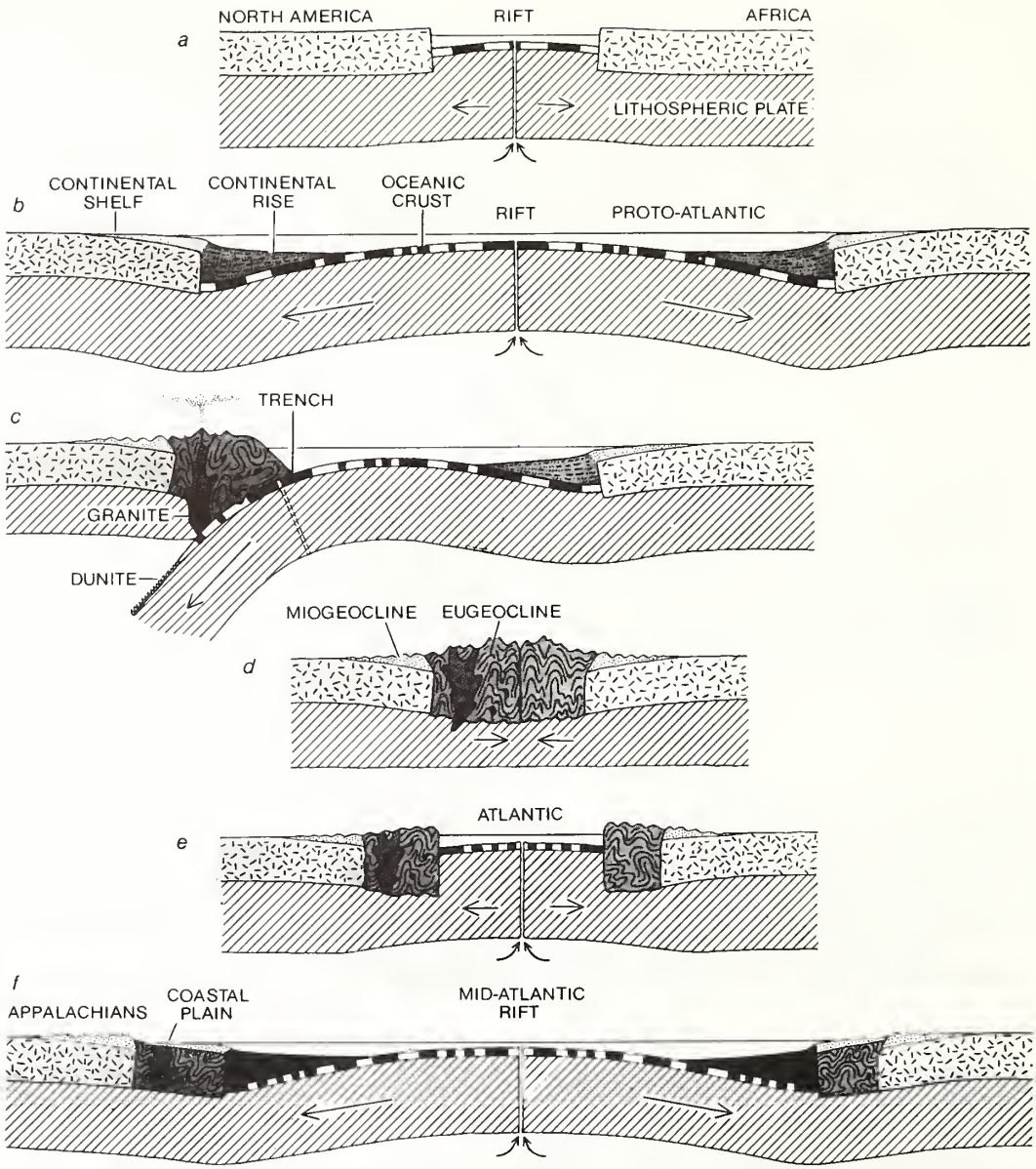

MECHANISM OF CRUMPLING that produced the Appalachian foldbelt is depicted on the hypothesis that the Atlantic Ocean has opened, closed and reopened. In the late Precambrian (*a*), North America and Africa are split apart by a spreading rift, which inserts a new ocean basin. By the process of sea-floor spreading (*b*) the ancestral Atlantic Ocean opens. New oceanic crust is created as the plates on each side move apart. As the crust cools, its direction of magnetization takes the sign of the earth's magnetic field; the field periodically reverses, and the reversals are represented by the striped pattern. On the margin of each continent sediments produce the geosynclinal couplet: miogeocline on the continental shelf, eugeocline on the ocean floor itself. The ancestral Atlantic now begins to close (*c*). The lithosphere breaks, forming a new plate boundary, and a trench is produced as the lithosphere descends into the earth's mantle and is resorbed. The consequent underthrusting collapses the eugeocline, creating the ancient Appalachians. The eugeocline is intruded with ascending magmas that create plutons of granite and volcanic mountains of andesite. The proto-Atlantic is now fully closed (*d*). The opposing continental masses, each carrying a geosyncline couplet, are sutured together, leaving only a transform fault (*vertical black line*). The shear contains squeezed-up pods of ultramafic mantle rock. Sediments eroded from the mountain foldbelt create deltas and fluvial deposits collectively called molasse. North America and Africa were apparently joined in this way between 350 million and 225 million years ago. About 180 million years ago (e) the present Atlantic reopened near the old suture line. Today (*f*) the central North Atlantic is opening at the rate of three centimeters per year, creating new geosynclines.

megawedge of shallow-water sediments caps the shelf. The abundant supply of sediment usually ensures that the top of the prism is maintained close to sea level. Excess detritus bypasses the shelf, is temporarily dumped on the continental slope and is then carried onto the continental rise by turbidity currents. The shelf edge and the continental-rise prism comprise a couplet within which there is constant interplay.

Like the sedimentary wedge under the Atlantic coastal plain today, the early Paleozoic Appalachian miogeocline thickens in the seaward direction. The abrupt termination of this miogeocline was long a mystery to early geologists who mapped it. They suggested that a missing seaward limb had been thrust upward and completely eroded away or that it had foundered into an ancient oceanic basin. This hypothetical land mass of Appalachia was the geological equivalent of the legendary Atlantis. The wedgelike structure of the existing continental-plain prism provides a satisfactory solution to the puzzle: the hypothesized seaward limb never existed. We now see that the thickening out of sedimentary deposits at the shelf edge is a normal mode of sedimentation. One way in which this may happen is that reefs of coral and algae build up along the margin of the continental shelf, creating a carbonate dam behind which other shelf sediments accumulate.

The mechanism of building continents by the peripheral accretion of collapsed continental rises seems also to ensure that the sedimentary deposits become dry land. (We take for granted that continents are above sea level, but it should be remembered that the mid-ocean ridge system, which approaches the continents in importance as a topographic feature, almost never rises above the sea surface.) The sedimentary apron gradually thickens until it approaches the height of the continental slope (about five kilometers), but upward growth ceases once the slope is completed and sea level is attained.

As we have seen, however, isostasy is at work, causing the oceanic crust to subside under the sedimentary load. The result is that a fully developed sedimentary prism attains an overall thickness of about 15 kilometers. When the prism is subsequently collapsed into a eugeosynclinal foldbelt, it becomes thicker still. The attendant metamorphism and granitic intrusion (which increases the total mass of rock) give rise to a monolithic structure that is more than 35 kilometers thick, thicker than a continental plate. Thus new foldbelts not only rise above sea level but also throw up rugged mountain ranges.

The hypothesis that geosynclines are deposited along a continental margin and then crushed against the continent as a result of plate tectonics seems to explain satisfactorily how geosynclines are transformed into folded mountains. The close relation between eugeoclines and foldbelts is not one of cause and effect but a simple consequence of location: geosynclines are laid down along continental margins and such margins are the locus of interaction between continents and subduction zones.

In spite of the vast span of geologic time and the rigors of erosion, the continents remain in a good state of health. We can predict that they always will be: detritus lost to the oceans is eventually carried back to the continents and collapsed into accretionary belts that also incorporate new igneous rock. Although the earthquakes that punctuate mountain-building are sometimes disastrous to man's culture, they are acts of continental construction. The great flood—the complete inundation of the erosionally leveled continents—will always threaten but will never come to pass.

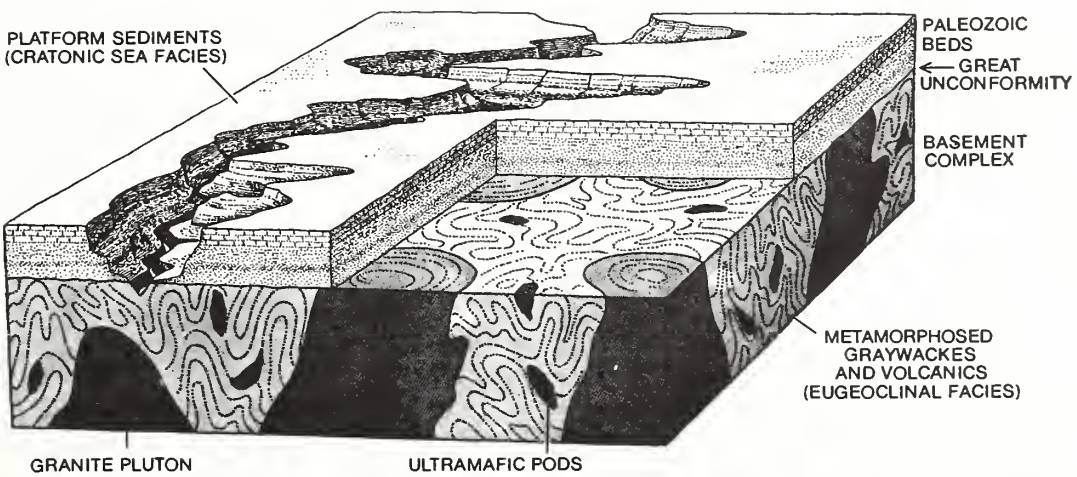

DEEP FABRIC OF CONTINENTS, the basement complex, is the fundamental rock unit of the continental plateaus, or cratons. This complex is usually obscured from view by miogeoclinal beds or by the coating of shallow-sea deposits that have invaded the continents from time to time. (Hudson Bay is a modern example of such an invading shallow sea.) Long a puzzle to geologists, the basement is composed of eugeoclinal foldbelts that have undergone intensive folding, metamorphism and intrusion. Geologists once thought that these "roots of mountains" indicated that the earth had contracted while cooling. The folds were likened to the skin of a dried apple. The present interpretation is that the eugeoclinal facies was laid down on the ocean floor and subsequently was crumpled against the continental margin, building up an onion-like vertically zoned craton. On this view the continents have grown larger rather than smaller with time. Moreover, the basement complex need not be Archean (composed of the oldest rocks) as formerly supposed, because the high degree of metamorphism does not necessarily indicate great antiquity and repeated mountain-building events. Instead it reflects the intensity of the collapsing process; once accreted, the foldbelt is not usually mobilized again. It has long been known that the granites of the basement complex are always younger than the metamorphosed sediments they intrude. On the other hand, the included pods of ultramafic rocks are always older, since they are detached fragments of the oceanic foundation on which the eugeocline was deposited. If geologists ever find "the original crust of the earth," it will be one of these pods within the oldest foldbelts.

Reprinted from the JOURNAL OF COLLEGE SCIENCE TEACHING, October 1972.

Plate Tectonics, Sea-Floor Spreading, and Continental Drift

Robert S. Dietz

The debate between the fixists and the mobilists which dragged along for a few decades was suddenly marked by a wholesale conversion to drift in 1967.

Over the past decade a geologic revolution has transpired. It can be summarized in the expression, "the new global tectonics," or more succinctly as *plate tectonics.* This, in turn, involves sea-floor spreading, descending lithospheric slabs, transform faulting, and continental drift. It has added a fourth dimension to classical geotectonics which was formerly concerned with uplift, subsidence, and time; but now we have added great horizontal shifts as well.

Of course, geologists have always accepted a limited amount of horizontal displacement by strike-slip faulting, but never before as the dominant dimension of tectonics. Consider the Bahama platform, where post-mid-Jurassic carbonates all deposited in shallow water have a thickness of about six kilometers. This reveals a history of great subsidence. But during this time, according to the plate tectonic-continental drift solution, the Bahama platform has drifted 5,000 km from an original geographic position near Ascension Island in the equatorial central Atlantic Ocean. Consider also the displacement of 6.5 cm/yr along the San Andreas fault, a transform fault separating the North American plate from the Pacific plate. This rate may seem ponderous, but it is a remarkably rapid geologic process compared to the upheaval of mountains or the peneplanation of continents. It is sufficient to shunt Los Angeles (on the Pacific plate) with respect to San Francisco (on the North American plate) entirely around the circumference of the earth in 600 million years, the time span of the Phanerozoic era.

Earth's Mosaic Carapace The plate tectonics concept holds that the earth is divided into about eight rigid spherical caps 100 km thick, riding on the weak asthenosphere and in which the continents are embedded and drift as passive passengers. We can visualize the ideal plate as rectangular, although perhaps only the Indian plate attains this simplicity. Along one edge there is a subduction zone, usually marked by a trench, where the cold crustal plate dives steeply into the earth's mantle, reaching a depth of 700 km before being fully resorbed. Opposing the subduction zone is a mid-ocean rift, or pull-apart zone. As the rift opens, the gap is quickly healed by the inflow of liquid basalt and quasi-solid mantle rock. The other two antithetical sides of the plate, connecting the rifts to the trenches, are crust-piercing shears called transform faults. Three types of plate boundaries are possible: (1) divergent junctures, the mid-ocean rifts where new simatic crust is created; (2) shear junctures, the transform faults where plates slip laterally past one another so that crust is conserved; and (3) convergent junctures, the trenches where two plates overlap, with one plate descending and being consumed. This subducting

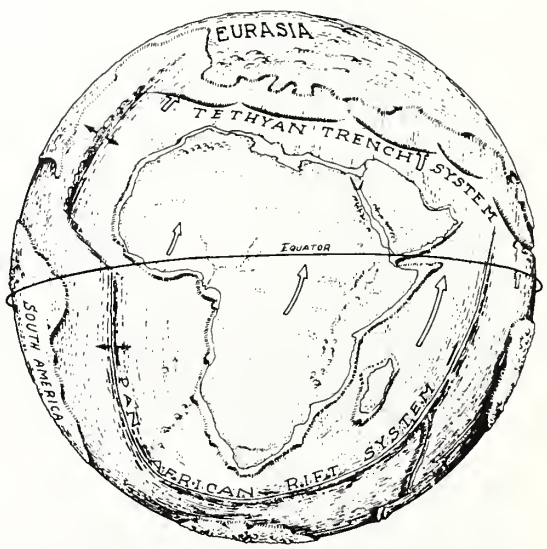

Figure 1—The African plate has drifted north and counterclockwise, closing up the Tethys seaway and leaving the Mediterranean Sea as a remnant. The northern margin of the plate has been subducted into the Tethyan trench; the mid-Atlantic ridge has been a spreading ridge; the Indian rift has acted mainly as a transform fault along which shearing has occurred.

Dr. Dietz is a marine geologist in the National Oceanic and Atmospheric Administration, Atlantic Oceanographic and Meteorological Laboratories, Miami, Florida. *Dr. Dietz' paper, "Plate Tectonics, Sea-Floor Spreading, and Continental Drift," was presented under the Sunoco Science Seminar Program at the 1972 national convention of the National Science Teachers Association. The author wishes to thank John Holden for the preparation of the figures which appear in this paper.*

plate is not fully digestible by the mantle, so that the sialic hyperfusible rocks rise to the surface as the andesitic volcanics and granodiorite plutons of island arcs.

All plates, except the great Pacific plate, may be identified by the particular continent embedded within the plate. Thus, in addition to the Pacific plate, there is the North American plate, the South American plate, the Eurasian plate, the African plate, the Indian plate, the Australian plate, and the Antarctic plate. Additionally, there are many small plates: e.g., Nazca, Cocos, Farallon, Caribbean, etc. There is even one plate, the Kula plate (from an Indian word meaning "all gone"), which has disappeared down the Aleutian trench. We know about its demise through the so-called Great Magnetic Bight in the northeast Pacific. Within the Pacific Ocean there probably was originally a West Pacific plate, an East Pacific plate, and a North Pacific plate (the Kula plate). The Antarctica plate is curious in that it contains no subduction zone along its perimeter, which in turn suggests that it is the most stationary of all the plates, having no place to go.

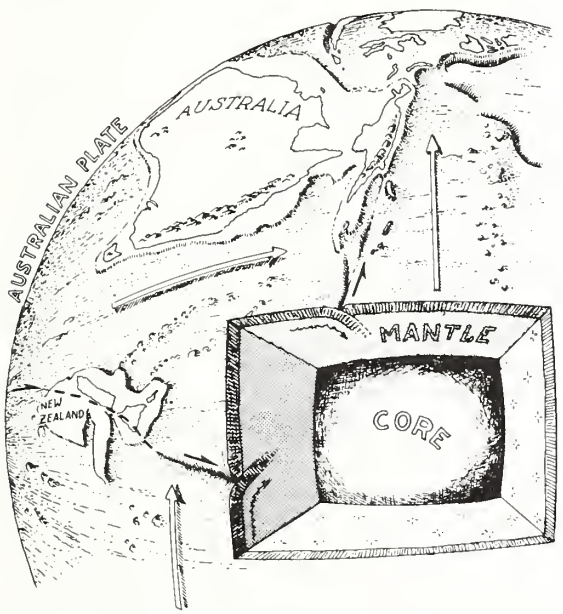

Figure 2—The Australian plate is drifting north about 8 cm/yr. Australia was detached from Antarctica only about 50 million years ago in the Eocene. This plate is moving nearly at right angles to the Pacific plate so that the northern boundary is a subduction zone for the Australian plate and a shear transform zone for the Pacific plate. The reverse holds true for the eastern margin of the Australian plate.

The South American and North American plates plus the Australian and Indian plates seem to be moving in unison and joined today so that, in terms of the major plates, the earth may be described as a highly distorted, spherical hexahedron or "cube." A few years ago S. W. Carey reviewed the various symmetries of the earth, including a listing of many historical comparisons that have been made about the earth with respect to various, regular polyhedrons and other solid forms. Of these, the tetrahedral hypothesis of Lowthian Green in the 1880s is especially well known. It is curious that a comparison with a hexahedron apparently has never been made.

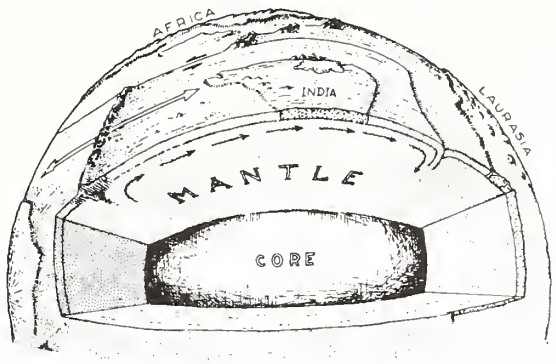

Figure 3—The Indian plate. The Indian subcontinent has undergone a remarkable drift since being detached from Antarctica. New ocean floor has been emplaced between the mid-ocean ridge which has maintained its position equidistant between Antarctica and India, while the northern portion of the plate has been consumed in the Himalayan trench. About 20 million years ago India collided with Asia, throwing in the Himalayan rampart. These mountains are as high as a continental slope (ca. 4,500 m), indicating that the underlying sialic slab is two continents thick due to underthrusting and dovetailing.

A cube, of course, has eight corners or coigns as well as six faces. Similarly, the crustal plates intersect in so-called *triple junctions*. These play a fundamental role in geotectonics which still remains to be fully elucidated. A few types of triple junctions are inherently unstable, that is, they will change their geometry with time, while most are stable. Near the Azores, for example, is the Am/Eur/Af triple junction marking the intersection of the North American, Eurasian, and African plates. It is classified as a ridge/ridge/fault triple junction, as two of its arms are mid-ocean, spreading ridges, while the third is the Azores-Mediterranean transform fault.

Another triple junction near the Galapagos Islands in the east-central Pacific is the Naz/Co/Pac ridge/ridge/ridge nexus marking the intersection of the Nazca, Cocos, and Pacific plates. John Holden and I have inferred that, although this junction has maintained a stable geometry, the juncture itself has migrated 1,000 km westward since its inception 20 to 40 million years ago.

Shifty Continents Continental drift is a corollary to plate tectonics since these 35-km-thick, sialic slabs drift passively, embedded in the even larger lithospheric plates. The rotational translations of the continents across the face of the globe quite naturally, however, are of especial interest to man.

According to the continental drift theory, the continents were combined into the universal landmass of Pangaea 200 million years ago in Triassic time. It is probably more correct to say that the continents were sutured together as of this time, for it is likely that the continents were sundered apart and drifted in earlier geologic time, although the details of this "pre-drift drift" remain unclear. As measured to the 2,000-m isobath (the true mar-

gin of the continents), Pangaea covered 40 percent of the earth while the universal ocean, Panthalassa (the ancestral Pacific) covered the remainder. With Africa as the heartland, the continents were generally farther south and farther east than today. New York and London were only slightly north of the equator. The ovoid plan of Pangaea was interrupted by a great bight called the Sea of Tethys which separated Eurasia from Africa.

The breakup and dispersal of the continents can best be visualized in a general way by reference to Figure 5. There the drift is shown in absolute coordinates as controlled by "hot spots"—plumes of lava which have pierced

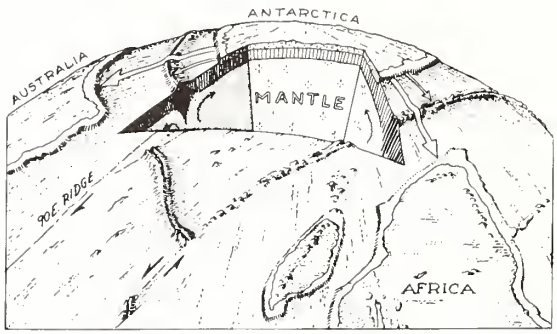

Figure 4—The Antarctic plate, because it is surrounded entirely by a system of ridges and transform faults and without any trench, is the most fixed of all of the plates, but has grown ever larger by peripheral addition of new oceanic crust. The detachment of Australia and Africa from Antarctica and their northward drift has been accommodated by migrating, mid-ocean ridges which have moved one-half the velocity of the drifting continents.

the lithosphere and laid down strings of islands as the crust moved over a fixed hot spot—or one at least assumed to be fixed. This effect can best be observed in the case of the Hawaiian Chain where a stream of islands and seamounts extends from Hawaii to Milwaukee Seamount, well past Midway Island. There are other methods of tracking the drift of continents (magnetic reversal anomalies on the ocean crust; the strike of fracture zones; and matching conjugate points on opposing continental margins across a rift ocean, e.g., the South Atlantic), but these methods give only relative solutions to drift rotations.

The major aspects of drift can be summarized as follows. The Atlantic Ocean (including the Gulf of Mexico and the Caribbean Sea) is a new ocean basin, as is the Indian Ocean. The Mediterranean Sea is a remnant of Tethys, as it is still undergoing closure. The Pacific Ocean is a closing ocean, for the earth as a whole is growing no larger. For each addition of new oceanic crust (ca. 1.5 km^2/yr), an equal amount of crust is lost by subduction in the oceanic trenches. At this rate the entire ocean basin undergoes renewal, on an average, once every 200 million years.

Turning now to the continents, the New World has drifted west while those continents around the Indian Ocean have moved north. Antarctica has remained almost stationary, as has Eurasia, while undergoing clockwise rotation such that Europe has moved north and China southward. The latest major event was the detachment of Australia from Antarctica in the Eocene only about 55 million years ago.

Actualistic Geosynclines, Mountains, and Continent Building Plate tectonics also provides fresh insight into the geosyncline-mountain building cycle. A drifting continent has a leading and a trailing edge—for North America, the west coast leads while the Atlantic coast trails. The trailing margin, fully coupled with the crustal plate, is tectonically stable; and, since the continental divide is near the mountainous Pacific perimeter, most sediments are dumped onto the Atlantic floor (including the Gulf of Mexico). So that, along this trailing edge, a thick prism of sediments has been deposited at the base of the continental slope, the continental rise. This prism appears to be a living eugeosyncline, or, as plate tectonicists are inclined to say, eugeocline. The Atlantic Ocean is now opening, but suppose the Atlantic crust eventually becomes heavy and unstable along the Atlantic margin. The lithosphere would then form a new break and dive, creat-

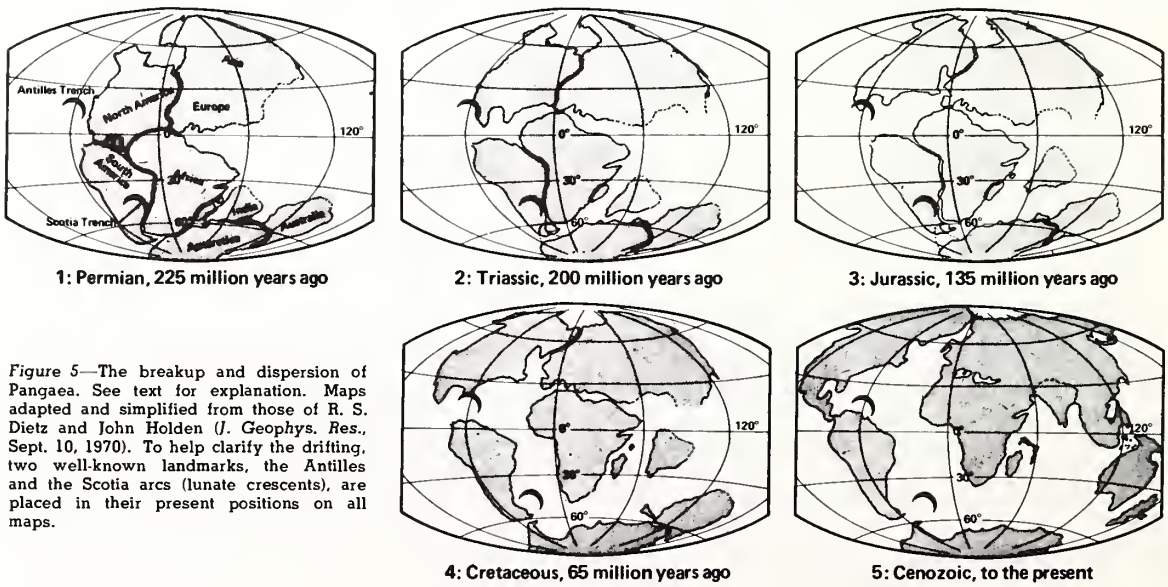

Figure 5—The breakup and dispersion of Pangaea. See text for explanation. Maps adapted and simplified from those of R. S. Dietz and John Holden (*J. Geophys. Res.*, Sept. 10, 1970). To help clarify the drifting, two well-known landmarks, the Antilles and the Scotia arcs (lunate crescents), are placed in their present positions on all maps.

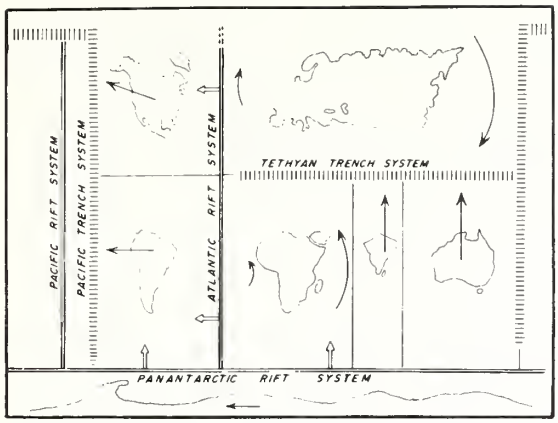

Figure 6—A summary of the drift motion of the continents. The New World has drifted west. Africa has moved north and counterclockwise, India and Australia both have moved north. Eurasia has rotated clockwise so that Great Britain has moved from the tropics to a northern clime, while Japan has become more tropical. Antarctica has remained almost stationary.

ing a trench, and the Atlantic would revert to being a closing ocean. Eventually, the continental rise prism would collide with this convergent juncture, and the continental rise would collapse into a classical eugeoclinal foldbelt.

The probable reality of this story line is enhanced by the fact that this sequence of events apparently has already transpired once before with the creation in the lower Paleozoic of the crystalline Appalachian eugeoclinal foldbelt. The Atlantic Ocean seems to have opened, closed, and reopened again (the last-named event commencing 190 million years ago), and in the future it may once more undergo closure. One of the grand themes of plate tectonics is that ocean basins are transient features, constantly changing their size and shape, while the continents not only persist, but also grow by the accretion to their margins of new eugeoclinal foldbelts.

Paired with the ancient, folded eugeoclines are miogeoclines (or miogeosynclines) of which the loosely folded Appalachians, lying parallel and inside of the crystalline Appalachians, is the type example for North America. The thick wedge of Cretaceous and Cenozoic sediments underlying the coastal plain and capping the Atlantic shelf provides an actualistic example paired to the modern continental rise. Plate tectonics also provides an explanation for the extensive downwarping needed for the deposition of this wedge entirely laid down in shallow water. With the initial splitting of North America from Africa, a spreading ridge must first be inserted beneath the craton like that under high Africa today. Erosion ensues, thinning the cratonic slab along the new rift. Then, as the new ocean basin opens and the underlying upper mantle detumesces, the continental margin subsides, providing a submerged platform on which a wedge of sediments accumulates. Thus, a living miogeocline is deposited.

A Unifying Model The debate between the fixists and the mobilists dragged along for a few decades. Then it was suddenly marked by a wholesale conversion to drift in 1967. Now the burden of proof lies with those who prefer to hold the continents still. A revolution has been

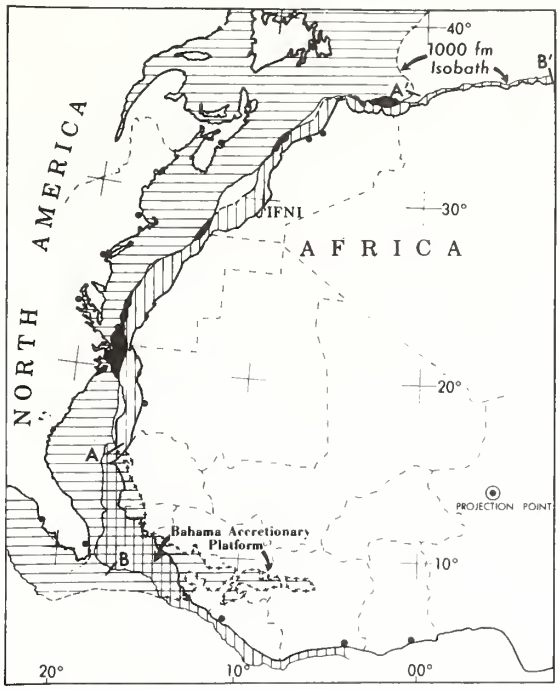

Figure 7—A computerized fit between Africa and North America matched to minimize total overlap (black areas) and underlap (white areas). The margin of North America was matched between points A-A′ and Africa between B-B′. The Bahama platform was permitted to overlap on the premise that it is a post-breakup sedimentary deposit lying directly on oceanic crust. The fit achieved seems remarkably good.

wrought. The new global tectonics now is having a salubrious and unifying effect on the geosciences. As Sir Edward Bullard has noted, "the acquisition of new data is likely to re-establish the usual chaos in earth sciences, but at least we do now have a universal model as a point of departure."

The transformation of geology has been so complete that Kenneth Deffeyes of Princeton has said, "Ninety-nine per cent of the profession has had to admit that they were wrong, including a great many who were in print saying continental drift couldn't possibly happen. . . . Everything has got to be re-written. We've been caught with our textbooks down." ■

Bibliography

Dewey, J. "Plate Tectonics." *Scientific American* 226(5):56. 1972.

Dewey, J., and J. Bird. "Mountain Belts and The New Global Tectonics." *Journal of Geophysical Research* 74(14):2625. 1970.

Dietz, R. S. "Geosynclines, Mountains and Continent Building." *Scientific American* 232(3):30-38. 1972.

Dietz, R. S. and J. Holden. "The Breakup of Pangaea." *Scientific American* 223(4):30-41. 1970.

Irving, *E. Paleomagnetism.* John Wiley and Sons, New York. 1964.

MacKenzie, D. P. and W. J. Morgan. "Evolution of Triple Junctions." *Nature* 224(5215):125-133. 1969.

Runcorn, S. K., Editor. *Continental Drift.* Academic Press, New York, N. Y. 1942.

Takeuchi, H., S. Uyeda, and H. Kanamori. *Debate About The Earth.* Freeman, Cooper and Co., San Francisco, Calif. 1967.

Tarling, D. and M. Tarling. *Continental Drift: A Study of The Earth's Moving Surface.* Doubleday and Co., New York. 1971.

Vine, F. J. "Spreading of The Ocean Floor." *Science* 154(3755): 1405-1415. 1966.

Wilson, J. T., Editor. *Continents Adrift: Readings from Scientific American.* W. H. Freeman and Co., San Francisco, Calif. 1972.

Reprinted from 24th IGC Section 15, 112-118.

Shatter Cones (Shock Fractures) in Astroblemes

ROBERT S. DIETZ,
U.S.A.

ABSTRACT

Shatter cones, conical shock fractures, are known from more than a score of cryptoexplosion structures, presumed to be astroblemes (ancient meteorite or comet-head impact scars). These structures include: Steinheim Basin and Ries Basin in Germany; Vredefort Ring in South Africa; Gosses Bluff in Australia; Rochechouart in France; Kentland, Wells Creek Basin, Crooked Creek, Serpent Mound, Flynn Creek, Sierra Madera, Decaturville and Middlesboro in the U.S.A.; and Sudbury, Manicouagan, Nicholson Lake, Carswell Lake, Clearwater Lake West, Lake Mistastin and Charlevoix in Canada. In addition, they occur at Kaalijarv and Lake Bosumtwi, which are modern meteorite craters. Besides indicating shock overloading in excess of that which can be caused by endogenic explosions (e.g., cryptovolcanism), they permit vectoring of the force field, as the cones point toward the oncoming shock wave.

At several locations (Vredefort, Sudbury, Decaturville, Wells Creek, Sierra Madera, Kentland, Gosses Bluff), they indicate that the explosion focus (ground zero) was either from above and/or inward toward the center of the structure. At Charlevoix the finding of shatter cones by Rondot led to the discovery of the associated cryptoexplosion structure.

Shatter cones are an especially useful criterion of shock in carbonate terranes, where petrographic shock metamorphic effects commonly are absent.

INTRODUCTION

THE INTENT OF THIS PAPER is to review briefly the status of shatter cones as a criterion for identifying astroblemes, as well as adding new information. This paper will also update a previous summary of this fascinating problem (Dietz, 1968). The term astrobleme, as coined by the author (Dietz, 1961), pertains to the geologic scars of ancient impacts on the earth by cosmic objects (giant meteorites, comet heads and ?). Impact structures, a more general term, would then include both astroblemes and meteorite craters (still crater-form and hence created within the last few million years). Although somewhat transitional between meteorite craters and astroblemes, the Ries and Steinheim basins of West Germany may usefully be regarded as type examples of astroblemes, as their crater-like form has been partially erased by erosion and deposition of lake beds since their impact creation 14 million years ago. The youth of these impact structures and their excellent exposure make them ideal for extrapolating to more ancient putative astroblemes.

GENERAL DESCRIPTION

Shatter cones are conical fracture surfaces with striae which fan outward from the apex in horsetail-like packets. The striae are sharp grooves between intervening, rounded ridges — or the reverse on negative mold faces. Small, para-

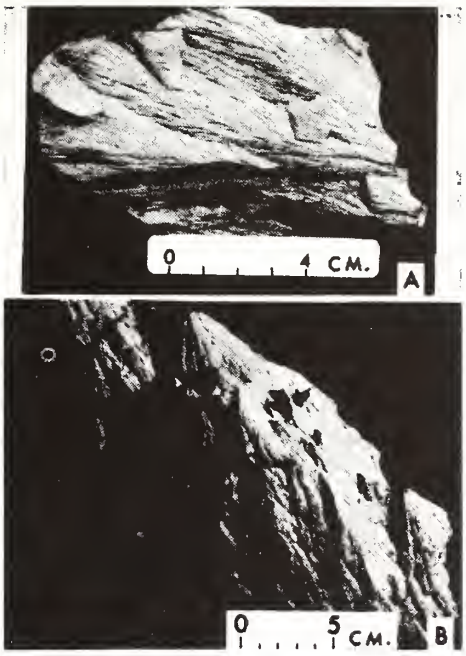

FIGURE 1 — A. Fragment of shatter-coned Permian dolomite from the Sierra Madera astrobleme in Texas. The horse-tail-like packets of converging striations are a hallmark of this type of shock fracturing.

B. A nest of shatter cones about 10 inches across in a fragment of Knox dolomite from the central uplift of the Wells Creek Basin astrobleme of Tennessee. The stacked, shoulder-upon-shoulder aspect of the cones, the striations and the common orientation of the apexes are characteristic of shatter coning. The specimen consists of two main cones with numerous tributary cones.

FIGURE 2 — A large shatter cone (1.5 m) in Ordovician limestone at Kentland quarry, Indiana. The strata are vertically upturned with their tops to the right. If returned to horizontality (the pre-event position), the cone would point upward, showing that the shock wave came from above.

sitic half-cones are shingled on the face of the master cone. Cones vary greatly in length from less than 1 cm to more than 12 m for one shale cone at Kentland. Typical shatter cones are shown in Figure 1 (A and B) and Figure 2. They are best developed in aphanitic and dense rocks, especially carbonates, but are also known from shale, sandstone, quartzite, granite, gneiss and other lithologies. Because of their fine display in carbonates and because of the difficulty of recognizing shock metamorphic damage in carbonates, the shatter cone criterion will continue to find greatest use in limestone terranes. An advantage of shatter cones over shock metamorphic effects is that they can be readily observed in the field.

Some natural cones which are sometimes confused with shatter cones are: cone-in-cone, coal cones, serpentinite cones, spalling cones in granite, conical packets of a fibrous mineral (e.g. pectolite). Weathering or wind fluting may

also sometimes be confused with shatter cones (Elston *et al.*, 1968), but this can be tested by breaking the rock with a hammer. A shatter-coned rock will break so as to display a fresh striated surface.

The worldwide inventory of Short and Bunce (1968) lists 52 putative impact structures based upon a variety of rather substantial criteria. Today this list could probably be extended to about 62 (Millman, 1971), of which, by the listing here (Fig. 3), 23 display shatter cones (or about one-third).

Some general observations based on field studies and theoretical analysis are the following. (1) Shatter cones are a unique type of fracture created along the boundary between an elastic and a plastic shock wave; the horsetail-like striation is caused by the plastic domain moving relative to the elastic domain (Johnson and Talbot, 1964). (2) Shatter cones apparently are formed by tensional release in an axially symmetrical field, following compression by an expanding shock wave (Manton, 1965). (3) A shatter cone is created by the interaction of the elastic precursor shock wave with some inhomogeneity. In a few instances (especially at Sudbury), a pebble or nodule is present at the apex of a shatter cone. (4) The susceptibility of a stratum to shatter coning is a function of the shape of the Hugoniot for the rock in which the shock wave is propagating. (5) Shatter coning requires shock overpressure usually in the range from 20 to 80 kb, or much higher than is ever produced in a volcanic explosion. (6) The shatter cone which formed last (farthest along the shock-wave front) truncates earlier shatter cones.

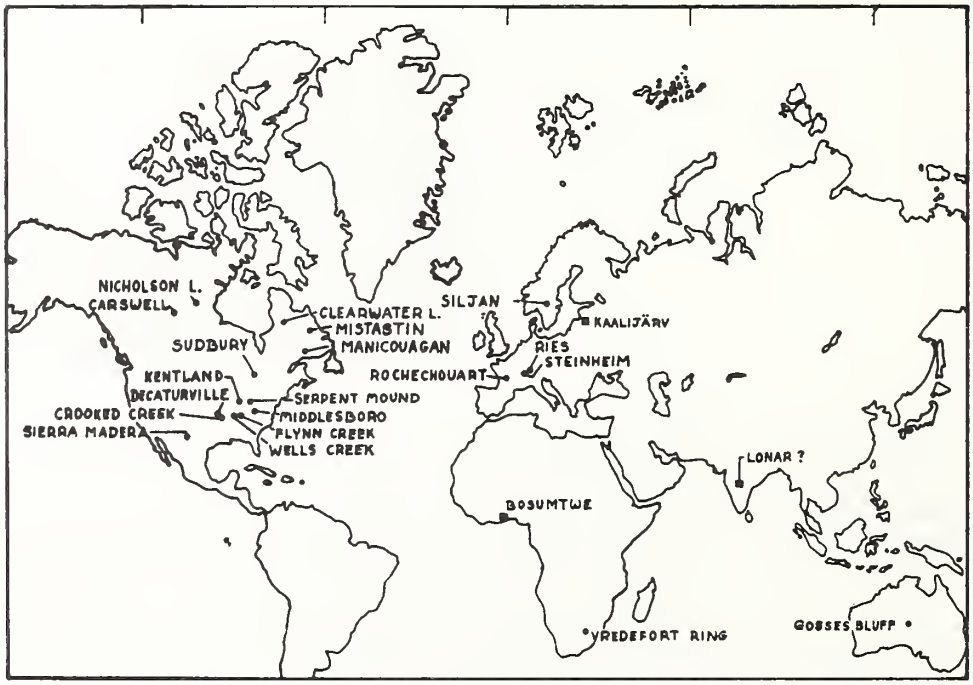

FIGURE 3 —Map showing the world distribution of shatter-coned cryptoexplosion structures presumed to be astroblemes (solid circles) and meteorite craters (solid squares) with shatter cones. Shatter cones have been identified at about one-third of the putative impact structures on earth.

This accounts for the stacked appearance of a thoroughly shatter-coned rock. (7) Shatter cones may vary widely in size, but usually are of a uniform size in any particular stratum. (8) Although varying widely, and sometimes being curved or splayed, the apical angle of the cone is typically around 90°. Nearly 900 measurements of cones at Wells Creek Basin showed a median apical angle of 56° (Wilson and Stearns, 1968). At Sierra Madera the shatter cones have apical angles varying from 75° to 108° and averaging 88.5° (Howard and Offield, 1968). Those at Vredefort varied between 90° and 110° (Manton, 1965). (9) The distribution of shatter coning is symmetrical around ground zero. (10) Shatter cones are nearly always oriented so that their apexes point toward the point of impact. However, reflected waves may sometimes produce shatter cones with apexes inverted by 180°. Such inverted cones have been observed at Kentland, Decaturville, Wells Creek, Charlevoix and Sierra Madera. (11) In small astroblemes the shatter cones are limited to the central uplift. In the larger structures (e.g. Sudbury, Vredefort) they may extend outward for 20 to 35 km from ground zero. A new theory of shatter coning has recently been offered by Syme Gash (1971) which suggests that shock overpressures of 20-40 kb or more are required to produce reasonably perfect examples and also that the apical angle is highly dependent upon the degree of shock, with acute angles indicating higher shock pressures.

SHATTER CONE ORIENTATION

As well as indicating shock overpressures, shatter cones may be used to reconstruct the force field at an impact site. In principle, the apexes of the shatter cones should point toward ground zero (the point of impact) once the rocks are returned to their pre-event attitude (usually horizontal). In the partitioning of the impact event, the creation of shatter cones precedes the upheaval of the rock by the plastic pulse so that the shock wave vector field is frozen into the geologic record. Many practical difficulties (lack of outcrop, etc.) interfere with orientation studies, but they have been carried out successfully at Kentland (Dietz, 1947), Crooked Creek (Hendricks, 1954), Vredefort (Hargraves, 1961; Manton, 1965), Wells Creek Basin (Wilson and Stearns, 1968), Gosses Bluff (Dietz, 1967), Sierra Madera (Howard and Offield, 1968) and Sudbury (Dietz and Butler, 1964; Bray, 1966). These all provide the solution that the source of the shock event was centrally located within the structure and/or the force came from above. (At Mistastin Lake, Labrador, Currie (1968) reports that poorly developed shatter cones in anorthosite point downward near the center of the structure. Without bedded rocks for guidance, however, it is not possible to establish original orientation within a jumbled central uplift.)

The Gosses Bluff astrobleme in central Australia provides especially impressive evidence that the force field can be reconstructed from shatter cone orientation (Dietz, 1967). In this 20-km-diameter ring structure, the shatter cones can be observed in the central uplift out to a range of about 4 km from ground zero. In the center the shatter cones are oriented normal to the bedding and point upward. Although maintaining this generally upward orientation and pointing generally inward, the cones decrease their angle to the bedding until they are parallel to bedding at the 4-km range. This would seem to demonstrate that the shock force which created the structure came from above and was centrally impressed. This, of course, is consistent with a cosmic impact as from a comet head.

CANADIAN ASTROBLEMES

Shatter coning did not at first prove useful in identifying Canadian astroblemes. This relates in part to the rude development of shatter cones in the crys-

talline rocks of the Precambrian basement. However, shatter cones were eventually identified at Manicouagan, Carswell, Clearwater Lake West, Nicholson Lake, Mistastin Lake, the Sudbury basin and Charlevoix.

The validity of the shatter cone criterion is strengthened if it proves useful in prediction. The 1967 discovery of the Charlevoix (or La Malbaie) astrobleme near Quebec City is a case in point. Striated cones in limestone and gneiss were first discovered by a local geologist (Rondot), who did not at first realize their special significance and termed them "cat's claws". They were, in turn, shown to another geologist (Murtaugh), who immediately recognized them as shatter cones. Then Robertson (1968), of the Dominion Observatory "fossil crater" working group, quickly was able to demonstrate the existence of a 37-km-diameter, deeply eroded probable astrobleme of early Paleozoic age. Rondot (1968; 1970), after further extensive study, also supports this view. This was the first time that shatter cones actually triggered the discovery of a previously unnoticed cryptoexplosion structure.

Charlevoix also shows that shatter cones may be best developed in rocks shocked to a level where there is a clear separation between the plastic and elastic shock waves. There is a progressively better development of shatter cones outward from the central peak to about 7 km, which appears to have been the region most favorable for shatter cone formation. Beyond this zone, shatter cone development weakens until it gradually dies out about 12 km from ground zero. Charlevoix tends to confirm shatter coning as a low-grade shock phenomenon; also, only the low-grade shock effect in quartz is associated with the best development of cones. This shock level corresponds to upper Stage 0 and lower Stage 1, with the level of best shatter cone development in granitic rocks being near the boundary of these two stages (Stöffler, 1971). Elsewhere, shock-damaged quartz and other minerals, although noted at Sudbury and Vredefort, are usually absent in shatter cones. On the other hand, shatter-coned basement rocks at Ries seem to show rather high levels of shock.

The shatter cones at Sudbury, in addition to recording shock overpressure and showing that the shock force was centrally positioned, provide good information as to relative timing of the geologic events associated with the presumed impact. If the Sudbury structure is an astrobleme, shatter cones should be present (and are) in the pre-event country rocks, older than 1720 million years, which make up the framework of the inferred Sudbury basin crater. They should also be present in clasts in the Onaping microbreccia if it is a suevite (impact breccia) (French, 1967), but they should not invade the matrix of the formation. W. Peredery (personal communication) has found such shatter-coned quartzite clasts in the Onaping. Shatter cones should also be present (and are) as clasts in the Sudbury breccia emplaced against the Sudbury basin wall and in radial fissures (J. G. Bray, personal communication).

On the other hand, shatter cones should be absent (and are) from the irruptive, as these igneous rocks would have solidified after impact. They must not occur (and do not) in formations south of the Grenville Front, as these are much younger rocks or rocks remobilized and metamorphosed since the Sudbury event. They also must not occur (and do not) in the Whitewater sediments, as these were laid down (by the impact model) since the formation of the Sudbury basin, resulting in the Sudbury lopolith and extrusive lopolith. In short, the shatter cones at Sudbury, by their presence as shock indicators, their orientation and position in the superposition sequence (timing), support the origin of this structure as an astrobleme.

RIES AND STEINHEIM BASINS

Although contrasting strongly, etc., the Ries Basin and the Steinheim Basin, collectively, provide nearly all of the criteria geologists need to establish astroblemes, including tectonic style, shock metamorphic effect and shatter coning. The Steinheim Basin is the type locality for shatter cones; they are excellently displayed and have been known since 1905. At Steinheim these shock fractures were originally termed *Strahlenkalk* (striated limestone) by Branca and Fraas (1905) and later *Drucksuturen* (pressure sutures). It remained for Bucher (1936) to coin the modern and more descriptive term, *shatter cone*, still something of a misnomer, as *shock cone* would be more exact. Without doubt it was the observation of shatter cones at Kentland and Wells Creek Basin, which were identical to those he had earlier been shown at Steinheim, that led him to identify these American structures as, in his opinion, cryptovolcanic. Until the last few years, shatter cones were thought to be absent at the Ries Basin, but recently convincing examples have been found there by von Engelhardt and others (personal comm.). In 1971, this writer observed reasonably good examples at the Otting quarry and at Mueller's Keller as allochthonous explosion debris in basement granites and gneisses. This again emphasizes the point that shatter cones attain their most perfect development in carbonates and their poorest development in coarse-grained intrusive rocks.

CONCLUSIONS

In summary, shatter coning appears to be a valid criterion for showing that a particular geologic structure is created by intense shock, and orientation studies also commonly show that the shock came from above and was central with respect to the structure. Although normal volcanic steam explosions appear to be eliminated as a cause for shatter coning, there remains an outside chance that some unknown geologic shock process could create them. To be quite sure that we are dealing with astroblemes, we still need to find certain remnants of the cosmic missile. Like traces of TNT in a bomb crater, these still elude our search. Shatter coning is now generally accepted by astrogeologists as a valid criterion for impact, but some skepticism remains in other sectors of the geologic community (e.g., Currie, 1968; Zimmermann, 1971).

REFERENCES

Branca, W., and Fraas, E., 1905. Das kryptovulkanische Becken von Steinhem. K. Preuss. Akad. Wiss. Abh., Berlin, p. 1-64.

Bray, J. G., 1966. Shatter cones at Sudbury. J. Geol., 74, (2), p. 243-245.

Bucher, W. H., 1936. Cryptovolcanic structures in the United States. 16th Int. Geol. Congr., Rept. 2, p. 1055-1084.

Currie, K., 1968. Mistastin Lake, Labrador, a new Canadian crater. Nature, 22, p. 776-777.

Dietz, R. S., 1947. Meteorite impact suggested by orientation of shatter cones at the Kentland, Indiana, disturbance. Science, 105, p. 2715.

Dietz, R. S., 1961. Astroblemes. Sci. Amer., 205, p. 50-58.

Dietz, R. S., 1967. Shatter cone orientation at Gosses Bluff astrobleme. Nature, 216, p. 1082-1084.

Dietz, R. S., 1968. Shatter cones in cryptoexplosion structures. *In* French, B., and Short, N. (*Editors*). Shock metamorphism of natural materials. Mono Book Corp., Baltimore, p. 267-285.

Dietz, R. S., and Butler, L., 1964. Orientation of shatter cones at Sudbury, Canada. Nature, 204, (4955), p. 280-281.

Elston, W., Lambert, P., and Smith, E., 1968. Striated cones: Wind-abrasion features, not shatter cones. *In* French, B., and Short, N. (*Editors*). Shock metamorphism of natural materials. Mono Press, Baltimore, p. 287-290.

French, B., 1967. Sudbury structure, Ontario: some petrographic evidence for origin by meteorite impact. Science, 156, (3778); p. 1094-1098.

Hargraves, R. B., 1961. Shatter cones in rocks of Vredefort Ring. Geol. Soc. S. Africa Trans., 64, p. 147-153.
Hendricks, H. E., 1954. The geology of the Steelville quadrangle, Missouri. Missouri Geol. Surv., 36, 2nd ser., 88 p.
Howard, K., and Offield, T., 1968. Shatter cones at Sierra Madera, Texas. Science, 162, p. 261-265.
Johnson, G., and Talbot, R., 1964. Theoretical study of shock wave origin of shatter cones. Air Force Inst. Tech., M.S. thesis, Wright-Patterson AFB, Ohio.
Manton, W. I., 1965. The orientation and origin of shatter cones in the Vredefort Ring. New York Acad. Sci. Annals, 123, Art. 2, p. 1017-1049.
Millman, P. M., 1971. The space scars of Earth. Nature, 232, p. 161-164.
Robertson, P. B., 1968. La Malbaie structure, Quebec: a Paleozoic meteorite impact site. Meteoritics, 4, (2), p. 1-24.
Rondot, J., 1968. Nouvel impact météoritique fossile?: La structure semi-circulaire de Charlevoix. Can. J. Earth Sci., 5, (5), p. 1305-1317.
Rondot, J., 1970. La structure de Charlevoix comparée à d'autres impacts météoritique. Can. J. Earth Sci., 7, (5), p. 1194-1202.
Short, N., and Bunce, T., 1968. Worldwide inventory of presumed meteorite impact structures. *In* Short, N., and French, B. (*Editors*). Shock metamorphism of natural materials. Mono Book Corp., Baltimore, p. 255-266.
Stöffler, D., 1971. Progressive metamorphism and classification of shocked and brecciated crystalline rocks at impact structures. J. Geophys. Res., 73, (23), p. 5541-5551.
Syme Gash, P. J., 1971. Dynamic mechanism for the formation of shatter cones. Nature, 230, p. 32-35.
Wilson, C. W., and Stearns, R., 1968. Geology of the Wells Creek structure, Tennessee. Bull. 68, Tenn. Div. Mines, Nashville, 236 p.
Zimmermann, R. A., 1971. Formation of shatter cones in the Steinheim Basin. N. Jb. Miner. Mh., 1, p. 19-25.

Reprinted from Geological Association of Canada, Special Paper 10, 29-40.

SUDBURY ASTROBLEME, SPLASH EMPLACED SUB-LAYER AND POSSIBLE COSMOGENIC ORES

Robert S. Dietz
NOAA, Atlantic Oceanographic and Meteorological Laboratories,
Miami, Florida 33130, U. S. A.

ABSTRACT

Shock metamorphism studies by French and geologic investigations by Bray have added strong support to this writer's original interpretation of the Sudbury structure as a "wet" (magma-triggering) astrobleme, or ancient meteorite impact scar. This evidence is reviewed and extended especially to show that the timing of events, as rigorously demanded by the impact model, appears to be met. Also, in recent years shatter coning, as extensively displayed at Sudbury, has achieved full status as a criterion of shock uniquely caused by meteorite impact.

My additional suggestion, however, – that the Sudbury nickel sulphide ores may be of meteoritic parenthood – apparently has received no adherence. Despite some geochemical and petrologic difficulties, the following points support a cosmogenic origin for the ores. (1) The distribution of the ore bodies against the lopolith wall (the crater wall under the impact concept) and in radial cracks in the surrounding country rock suggest splash emplacement of the sub-layer ("noritic" matrix, inclusions, and sulphides). (2) The density gradient of the component sulphide and sub-layer rocks across the ore bodies is consistent with hypervelocity emplacement, with the substances of greatest inertia traveling farthest. (3) The symmetrical positions of the sub-layer deposits and the mineralogical uniformity of the sulphides suggest emplacement by a symmetrical explosive centrifugal field rather than control by the vertical gravity field. (4) The sulphur isotope ratio ($S^{32}:S^{34}$) is close to the primordial value as found in meteorites. (5) The high content of cobalt and platinum group metals is similar to that found in meteorites.

Like the now-discredited hypothesis of hydrothermal origin for the ores, the "rain of sulphide" concept (gravity fallout of immiscible sulphide from the lopolithic magma) has run into difficulties. Sulphide differentiation within a deep magma chamber followed by injection seems now preferred. This latter concept infers a post-lopolith injection of the sub-layer. This model, however, cannot reasonably account for the remarkable preferred locus of emplacement solely against the lopolith wall or injected into the surrounding country rock. This difficulty is compounded once the probably impulsive emplacement of the sub-layer is recognized, as indicated by the giant inclusions. Impact emplacement of the sub-layer, as a solid, liquid, gaseous, and plasma mix of bolide and target rock, just prior to the extrusion of the lopolith offers a reasonable solution.

If the Sudbury basin is an astrobleme and the sub-layer was emplaced by splash, then the sulphide deposits which form an intimate part of the sub-layer may be cosmogenic. An impact is a short-life event without sequels so the ores, too, most likely also were generated by the impact. Regarding the composition of the hypothetical Sudbury bolide, it could not have been a chondrite – i.e., a primordial undifferentiated body reflecting cosmic abundances of the elements; also, it could not have been like any known meteorite, because a high copper content is indicated. One possible model is a differentiated body with both siderophyllic and chalcophyllic phases – hence, neither a usual meteorite nor a comet head, but most likely a 4-km-diameter Apollo asteroid – a Sudbury "moon."

INTRODUCTION

Nearly a decade ago, I (Dietz, 1962; 1964) suggested that the Sudbury Basin was an astrobleme, or ancient meteorite scar. Many geologists regarded this interpretation as bizarre, for it is alien to geologic philosophy to accept an origin which is both catastrophic and exogenic. The creation of the Sudbury Basin by impact, however, seems now to have achieved some measure of acceptance. H. F. Zurbrigg, Vice President, Exploration for The International Nickel Company, stated in a recent trade journal interview, "We have found convincing evidence that the geological events at Sudbury were triggered by a meteoritic impact that fractured the earth's crust and led to the upward movement of basic rock with associated nickel mineralization." This statement echoes the opinion of many geologists who now accept the impact origin of the Sudbury basin but would then call upon some conventional mode of ore genesis. Apparently my secondary speculation that the sulphide ores have a meteoritic parenthood has been assigned to limbo. For example, Thomson (1969), revising his earlier model, now agrees that a meteorite impact created the Sudbury Basin, but he then reasoned that all subsequent events were purely endogenic. Zurbrigg's interpretation would seem to follow a similar path. The burden of proof for any unusual concept without precedent, of course, lies with the proposer. My purpose in this paper is to update and extend the astrobleme concept of Sudbury and to attempt to further specify why an exogenic origin for the Sudbury ores remains a viable or at least a possible supposition.

GEOLOGIC HISTORY: A SYNOPSIS

For brevity, a summary of my views on the geologic history of Sudbury is outlined below. Figures 1 and 2 diagram this proposed history. The impact concept requires a rigorous sequence of events superimposed in time, often at short intervals. This sequence must be valid if Sudbury is an astrobleme.

1. Deposition of the Huronian sediments probably as a miogeosynclinal prism on the margin of the Superior craton (Dietz and Holden, 1966), commencing about 2500 million years before present (mybp).

2. Impact of the Sudbury "moon," probably an Apollo asteroid (one crossing the earth's orbit), 1720 mybp (Fairbairn *et al.*, 1969). Hemispherical spreading of the impact shock wave, creating shatter cones pointing toward ground zero.

3. Formation by the 4-km-diameter bolide of an impact crater about 40 km in diameter and 4 km deep (from Baldwin's, 1963, formulas). (This calculation has been explained elsewhere (Dietz, 1964) and is based upon the present margin of the Sudbury basin marking the crater wall. J. G. Bray, Bevan French, and Michael Dence (personal communications) prefer models which provide a much larger crater diameter as might be marked by the Huronian "ring" north of the basin and giving a diameter of about 100 km. French supposes that the present basin may represent only the

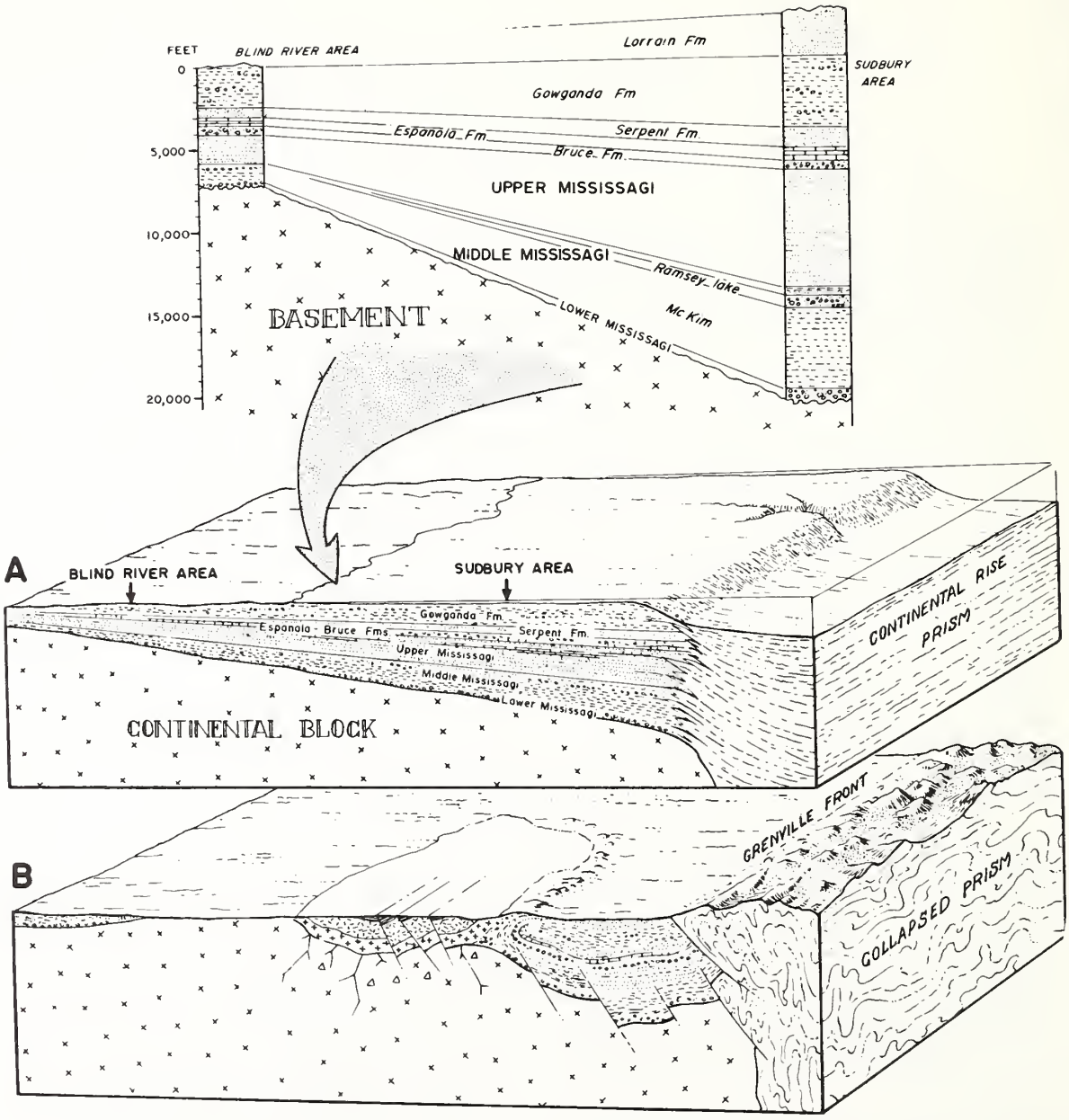

Figure 1: Regional geologic setting of the Sudbury region as postulated.

A. Regional view 1720 m. y. ago, just prior to the asteroid impact. A miogeosynclinal prism is present in the Sudbury region margined by continental slope to the southeast.

B. Sudbury Basin as erosionally exposed today. The Sudbury impact caused major disruption of the miogeosyncline, creating a crater filled by a lopolith surrounded by a toroid of upturned country rock. The Grenville foldbelt is shown emplaced against the Grenville front by an orogeny that occurred about 1000-1400 mybp. The originally circular Sudbury crater was slightly deformed.

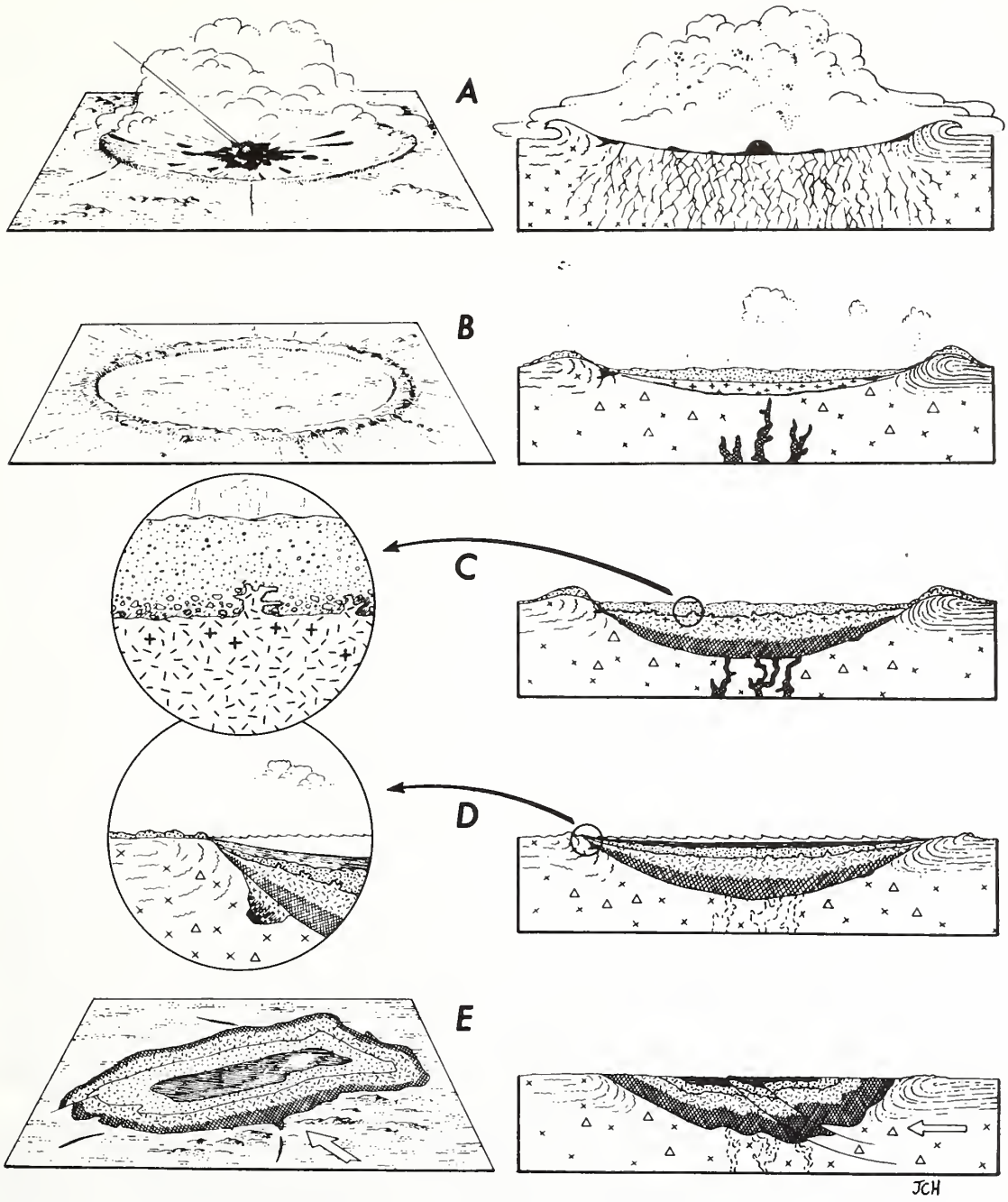

Figure 2: Development of the Sudbury Basin by asteroidal impact, a time-sequence diagram.

A. Asteroidal impact 1720 million years ago, producing a crater and radial tension cracks.

B. Laying down of the Onaping microbreccia as a fallout blanket or suevite. A pool of magma is also generated from the target rocks.

C. Ascent of the Sudbury Irruptive as an impact-triggered magma from the deep crust. The shock-generated melt rock is incorporated into the micropegmatite. The Irruptive differentiates with micropegmatite above and norite below. Apophyses of micropegmatite invade the overlying Onaping suevite. Emplacement of Irruptive is accompanied by foundering.

D. The Whitewater sediments (Chelmsford Formation) are laid down as a greywacke deposit in the Sudbury Basin. Detailed sketch shows sulphide deposit emplaced as an impact splash in footwall along with breccia and noritic matrix.

E. Geologic situation today after distortion by Grenville orogeny and erosional deleveling.

foundered central uplift. These views have considerable merit; hence the values I quote may be only minima.)

4. Quaquaversal upheaval of the country rock approaching a near vertical attitude near the crater rim. Simultaneous emplacement of the sub-layer as the impacting bolide literally turned inside out and swept up the side walls of the forming crater. The sub-layer would tend to fill the concave swales in the crater wall and be injected into spoke-like radial tension cracks (offsets). The sub-layer would be a mix of country rock breccia, country rock melt (liquid, vapor and plasma phases) creating the "quartz diorite" and other noritic sub-layer variants, and bolide phases providing parenthood substances for the iron-nickel-copper ores. The full penetration of the bolide would be several miles, or much deeper than final crater depth, especially after rebound and isostatic uplift. Hence, rocks from deep within the crust would be included in the breccias splashed or smeared against the footwall. This deep source would account for the common exotic basic and ultramafic clasts encountered in the sub-layer at the Irruptive contact and in the offsets (e.g., Frood-Stobie). Another type of breccia would form within the surrounding ring of country rock and extend outward for 10 to 15 miles. At nodes along the shock wave front, pods of country rock would be fluidized or melted in pods which would then entrap fragments of local rock (monomict Sudbury breccia; Speers, 1957).

5. Fallback into the crater of shocked and comminuted country rock from the explosion cloud. This deposited the Onaping microbreccia as a suevite including glass bombs (*Fladen*) and fragments coated with glass (cored bombs). As the impact event probably occurred in a shallow epeiric sea, much of the suevite deposited from the base surge was washed back into the crater eventually building up a deposit 6,000 feet thick and with a remnant modern area of 350 square miles and volume of 400 cubic miles. Large blocks of country rocks fell first, forming a polymict megabreccia mixed with melt rock and included giant clasts of quartzite as large as 100 feet across (Lorraine quartzite?) (Peredery, this volume). A pool of silicic melt rock also resulted which was later incorporated into the granophyric upper layer of the Irruptive. As the Onaping is rich in sulphides (nearly 1 per cent) high in nickel, I suggest that these sulphides were originally derived as droplets from the explosion cloud and represent bolide substance (iron, copper, and nickel sulphides) plus target rock sulphides (lead and zinc sulphides). The possibly oxygen-free reducing atmosphere at this time in earth history would enhance the probability of their preservation.

6. Emplacement of the Irruptive melt rock, its lopolith form being shaped by the saucer-shaped crater. This magma would be, in part, a surficial shock melt, but, more importantly, it would be the result of conventional magmatism from depth simply triggered by the impact due to shock decay heat and static offloading of the deep crust and upper mantle. This magma generation primarily would involve the lower crust, so would not be a normal tholeiite, but instead would be more silicic. The magma pool filling the crater would be essentially an extrusive lopolith rather than an intrusive lopolith of the classical model. The suevite would be floated upward on top of the magma.

7. Differentiation of the Irruptive into micropegmatite and norite, and gradual cooling. As the Irruptive was extruded shortly after the impact and while the sub-layer was still warm, no marked chill contacts developed.

8. Modification of the crater's bowl-shaped form owing to collapse over a magma chamber, and isostatic adjustments.

9. Deposition of the Whitewater sediments in a closed cratonic salt water basin. The underlying Onwatin slates formed as a continuation of the Onaping wash-in but with an increasing admixture of normal clastic components from the surrounding terrane. As the basin remained deep possibly due to foundering, this deposition was followed by the turbidity-current injection of the Chelmsford greywacke which displays 188 Bouma turbidite units within its thickness of about 2,800 ft. (Rousell, this volume). The age of the Chelmsford, as determined by Rb-Sr methods, is 1720 $\pm$ 30 m.y. or essentially synchronous with the age of the Irruptive (Fairbairn *et al.*, 1968) in agreement with the model proposed here. (The alternate supposition that the Whitewater sediments are pre-Irruptive creates a major space problem and so is unlikely. The Irruptive would have to have been emplaced uniquely beneath these sediments and then, instead of creating a mushroom-like laccolithic dome, caused great subsidence to account for their depressed position today.)

10. Folding and metamorphism of the Sudbury Basin as a peripheral effect of the Grenville orogeny (1000-1400 mybp), squashing the circular basin into an oval form and upturning the southern rim. Although the history is in detail much more complex, the Grenville rocks are envisioned here as an accretionary foldbelt (Figure 1). Emplacement of diabase dikes in the Sudbury region then followed –

11. Erosional truncation and peneplanation to the exposure level of today.

Some amplification of this summary of geologic history follows. Studies by French (1967; 1968; 1970) make an excellent case for the Onaping Formation being not volcanic tuff, as originally supposed, but a fallback microbreccia (shocked and comminuted country rock) or *suevite* – this name taken from the type locality at the Ries Basin astrobleme in West Germany. Shock metamorphic effects within mineral grains and glass bombs (*Fladen*) are part of the evidence. Of course, the two concepts are not necessarily mutually exclusive, and it may be that large amounts of tuff associated with the degassing of the Irruptive, as an *extrusive* lopolith (Hamilton, 1960), also are present.

Hamilton (1970) states that the weighted bulk composition of the known irruptive components (SiO_2 content 63 per cent) precludes its differentiation from a basaltic magma, but could result from the fusion of crustal rocks (Naldrett *et al.*, 1970). He also notes that the initial Sr^{87}/Sr^{86} ratio of 0.705 (Fairbairn *et al.*, 1968) is somewhat too high for a mantle origin, but is consistent with derivation from the sialic crust.

Recent radiometric dating (Fairbairn *et al.*, 1968) supports the consanguinity of the entire Sudbury complex and rapid emplacement of the Irruptive, the Onaping microbreccia and the Whitewater slate-greywacke sequence. Thus, the Sudbury lopolith, indeed, appears to be an extrusive lopolith crusted over with the Onaping suevite as required by the astrobleme concept – i.e., a magma that was laid down in a saucer-shaped basin and onto which the concordant Whitewater sediments were quickly deposited. This is a reversal of the earlier opinion of Fairbairn *et al.*, (1960), that interpreted the Sudbury lopolith as intrusive and post-Whitewater sedimentation.

As previously suggested (Dietz, 1964), Sudbury may be analogous to a small lunar "wet" mare; that is, one which contains a pool of melt rock. Although somewhat larger, the 120-km diameter crater Tsiolkovsky, on the averted hemisphere of the Moon, would seem to provide a good lunar counterpart. As this crater is isolated within a broad expanse of terra, it seems quite probable that its filling of dark mare material was a direct result of the impact. The answer as to why there are not more large impact sites on the earth seems to be that the lunar surface is old in the extreme and largely "pre-geologic." One of the youngest events on the Moon created the giant bull's-eye structure called Mare Orientale. But this "young" impact was caused by a bolide that struck

the Moon ca. 3700 mybp (T. Offield, personal communication).

SHATTER CONES

Although commonly only crudely developed, as is characteristic of their appearance in massive igneous and metamorphic rocks, shatter cones are widely present around the Sudbury Basin (Plate 1). Since the original discovery (Dietz, 1964; Dietz and Butler, 1964) observations on their distribution and orientation have been greatly extended, especially by Bray (1968). There is no doubt that the Sudbury shatter cones are bona fide examples of this mode of shock fracturing. More than a score of other shatter-coned, cryptoexplosive structures are now known around the world (Dietz, 1968). There is now good evidence that these are all astroblemes and that this style of fracturing in natural cryptoexplosion structures is uniquely formed by the shock waves emanating from a cosmic impact. They are not known from any structure which is clearly volcanic or otherwise endogenic (Dietz, 1968).

By the impact model there can be only one brief instant of shatter cone creation as the shock front interacts with the target rock. Clearly the imprint of shatter coning must affect pre-event strata but is prohibited from any post-event rocks. (It would be highly fortuitous for the effects of a second "cosmic cannonball" to overlap an earlier site, but apparently this *has* happened at Sudbury. Lake Wanapitei near Sudbury appears to be a Mesozoic or Paleozoic impact site (Dence and Popelar, this volume). However, the overlapping effects are minor and do not cause any important geologic confusion.) By the history proposed above, shatter cones should be present (and are) in the country rocks older than 1720 mybp, which make up the framework of the inferred Sudbury Basin crater. They also should be present in clasts in the Onaping microbreccia if it is a suevite, but they should not invade the matrix of this formation. W. Peredery (personal communication) has found four such shatter-coned clasts (Plate II). Shatter cones should also be present among the clasts in the Sudbury breccia that cuts the footwall rocks. G.

PLATE I

Large shatter cones in upturned Mississagi quartzite near Kelly Lake south of the Sudbury Basin. When strata are returned to a horizontal (pre-event) position the cones point towards the Sudbury Basin indicating that the shock wave arrived from that direction.

PLATE II

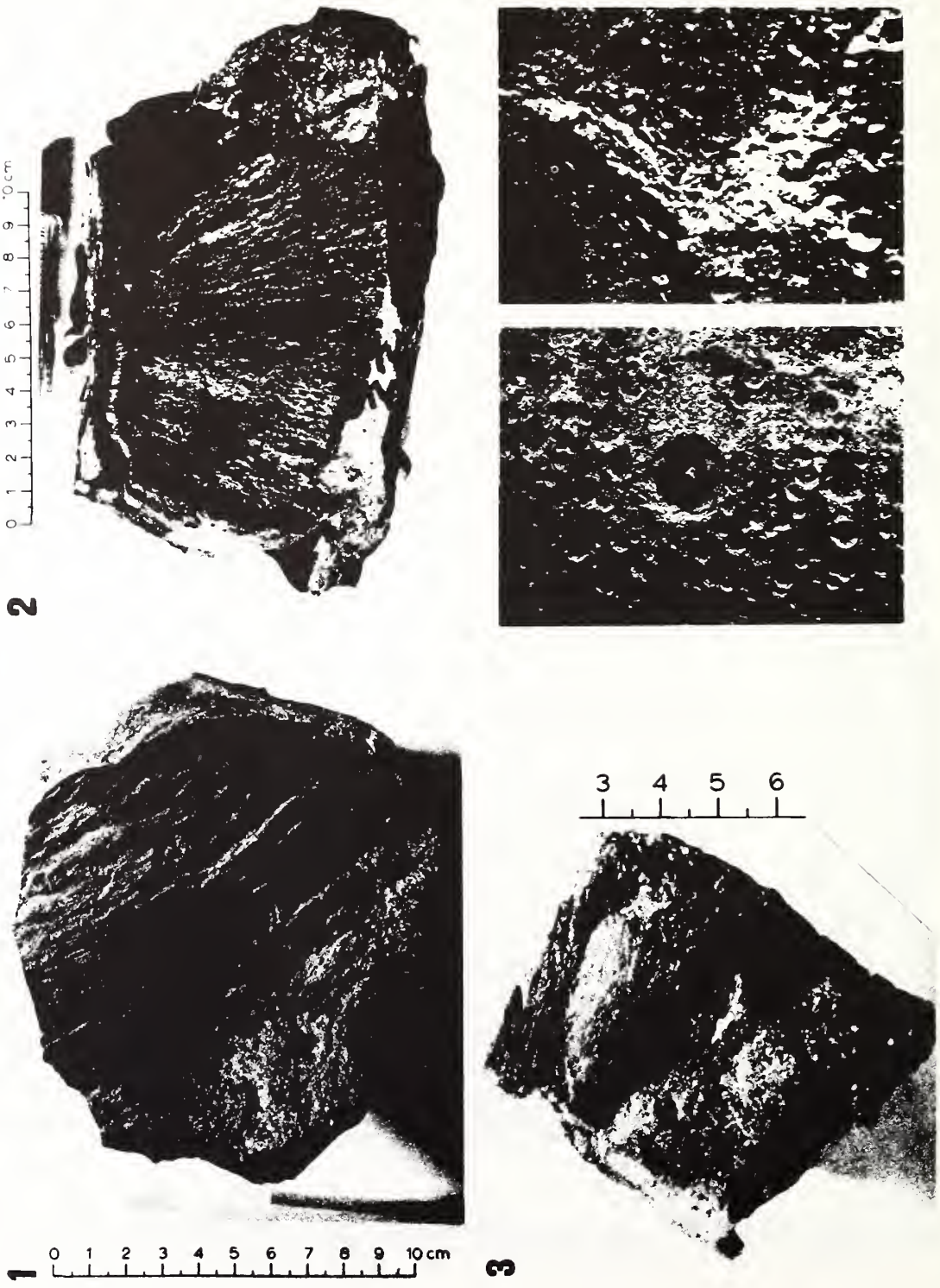

Bray (personal communication) reports that there are examples.

On the other hand, shatter cones should be absent (and are) from the Irruptive, as those igneous rocks solidified after the impact. They must also be absent (and are) in the Whitewater sediments, as these were laid down in the Sudbury crater after the impact. They must not occur (and do not) in the formations south of the Grenville front, as these are a post-impact emplacement. Finally, as the passage of the shock front precedes upheaval, the orientation of the shatter cones must be such that their apices point inward toward the centre of Sudbury Basin ("ground zero") when the strata are rotated to a flat-lying position (under the assumption that they were essentially in this attitude prior to the impact). This condition apparently is also met (Dietz and Butler, 1964; Bray, 1968) although the strata may have been slightly folded prior to impact.

In summary, both the shatter cones' orientation and distribution support the impact concept. They occur only in the pre-impact rocks or in breccia clasts (basal Onaping and Sudbury breccia) associated with the overall impact event – produced by the shock front and then immediately incorporated into disrupted rock. They are wholly absent from post-impact rocks – Whitewater sediments, Irruptive and Grenville rocks.

SUB-LAYER

The Irruptive is almost everywhere separated from the encircling rocks, or footwall, of the Sudbury Basin by the discontinuous unit recently termed the *sub-layer* (Souch and Podolsky, 1969). The sub-layer also makes up the filling within all of the offsets. It is a distinct multi-phase lithologic unit rather than a differentiated phase or a chill zone of the overlying norite. This sub-layer consists of three phases: igneous noritic silicate matrix, polymict fragments of subangular country rocks and exotic inclusions and sulphides of iron, nickel and copper. In many layered complexes, e.g., Muskox and Skaergaard, it is possible to infer the bulk composition of the lopolith from that of the chill zones. But this is not possible at Sudbury, owing to the absence of any such chill zone and because the sub-layer is an entirely separate intrusion or intrusions of variable composition.

Under my impact concept, the sub-layer was emplaced as the splash product of the bolide impact, whereby jets of plasma, gas, liquid, and brecciated rock fragments were injected against the Sudbury crater wall prior to the extrusion of the lopolith. The sub-layer would thus incorporate substances from the meteoroid as well as liquefied country rock which is generally of a greywacke bulk composition as the precursor of the sub-layer silicate matrix. The heterogeneity of the country rock would introduce some variation, as is actually observed, in the compostion of this matrix.

The various conventional concepts of ore genesis (magmatic segregation, hydrothermal alteration, or differentiation in a deep chamber followed by injection) generally envision *post*-Irruptive injection of the sub-layer. In contrast, an origin by impact splash envisions *pre*-Irruptive emplacement of the sub-layer. Hence, a test is offered, but unfortunately chill relationships and time relationships as might be revealed by apophyses are not clearly defined. On the other hand, the perfection with which the sub-layer hugs the wall of the Sudbury Basin, seeks out concavities in the footwall, and fills radial cracks (offsets) in the footwall alone and not in the Irruptive suggests that the sub-layer is pre-Irruptive (Figure 3). The propensity for intrusive dikes to seek out contacts is well known to the field geologist but not to the extent observed around the Sudbury Basin. Also Vos (1966) has found that the sub-layer on the northern rim, away from the effects of the regional metamorphism which affected the south rim, has a thermally recrystallized texture. An explanation might be that the sub-layer was recrystallized by the heat accompanying the later emplacement of the Irruptive body. According to J. G. Bray (personal communication), however, this relationship is not generally true.

The sub-layer deposits are pod-shaped lenses that thicken, thin, and pinch out. The xenolithic clasts often are exceedingly large. In the Frood offset one such block of mica peridotite measures 40 m across, another 20 x 10 x 5 m. This type of ultrabasic rock is not known from the surrounding terrane, so that it must have been transported for a considerable distance. Their high density makes difficult their having been floated up carried by a magma, unless streaming rapidly. Explosive injection could easily account for these curious aspects of the sub-layer.

J. G. Bray (personal communication), while subscribing to a deep terrestrial source for the sub-layer after impact, does not exclude the emplacement of the sub-layer as *pre*-Irruptive. I find it difficult to envision such a model, as the Irruptive must have been quickly generated after impact. Perhaps a "squirt" (between rock formations) rather than a "splash" (via an air path) is envisioned – but again the selectivity of the sub-layer emplacement argues against any such squirt. However, a splash variant seems an outside possibility as follows. It may be that the impact shock selectively mobilized and squeezed out terrestrial metallic sulphides from the target country rock, and this in turn became an important component of the sub-layer splash. If a mechanism of this type was operative, it still would not be a wholly satisfactory alternative to the cosmogenic origin offered here, as one would expect abundant associated zinc and lead sulphides. It is interesting to note that the centre of Decaturville and Serpent Mound astroblemes contain such sulphides.

Of course, the mechanics of impact on the scale envisioned at Sudbury remain poorly known so that almost any scheme remains possible. Many surprises await. One wonders, for example, what geologic role a plasma, the fourth state of matter, might play. Other than a lightning stroke, meteorite impact would seem to be the only geologic process capable of creating a plasma on earth. What would be the effect of this as a part of the splash? And is there any way to determine if any components of the sub-layer were once a plasma?

Finally, two bold speculations concerning the sub-layer seem worth mentioning. Firstly, the distribution of sulphide in the sub-layer is not entirely symmetrical, as the ore deposits seem to favour the south rim which contains thirty-one of the

PLATE II

Figures 1 – 3: Shatter coned fragments collected by Walter Peredery from the quartzite megabreccia at the base of the Onaping Formation. This shock fracturing shows that the impact preceded the deposition of the Onaping, presumably as fallback breccia so that the Irruptive is an extrusive lopolith. In other words, the Onaping is not a member of the old Huronian sequence into which the Irruptive was intruded.

Figure 4A: The crater Tsiolkovsky on the far side of the Moon, which may be a lunar analogy to Sudbury. Note that the region of melt rock does not fill the crater and that it is not circular.

Figure 4B: Base surge deposits outside of the southeast rim of Tsiolkovsky which may be similar to the wash-in upper portion of the Onaping suevite.

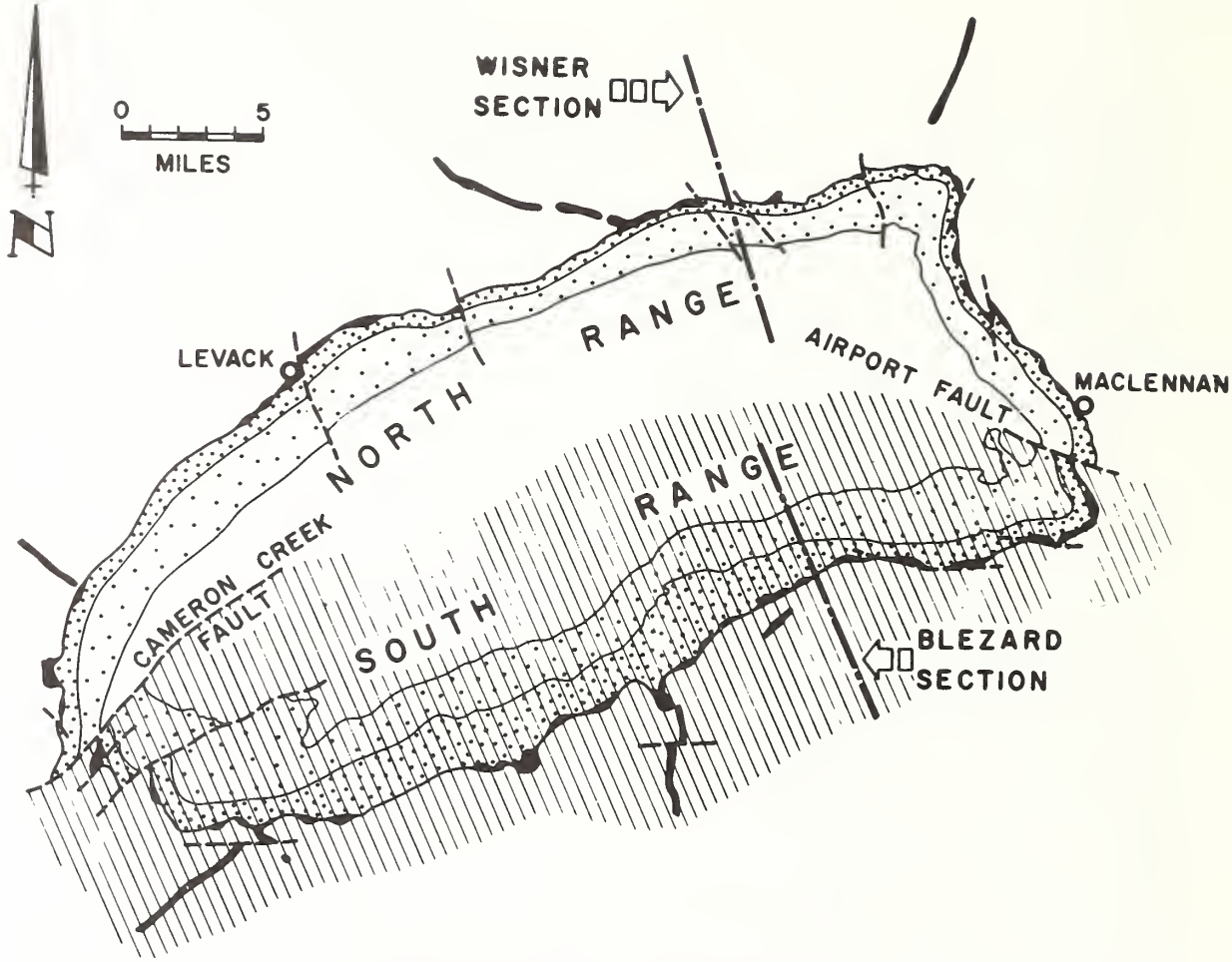

Figure 3: The Sudbury lopolith showing the distribution of the sub-layer (in black) along the margin of the Irruptive and in radial fractures ("offsets"). Diagonal ruling shows the extent of more highly metamorphosed and tectonically disturbed rock associated with the South Range. This metamorphic aureole extends northward from the nearby Grenville front (Souch and Podolsky, 1969).

fifty known sulphide occurrences. This may possibly mean that the bolide arrived from the north so that its substance was preferentially splashed against the south wall. Secondly, one wonders if the common mafic and ultramafic xenoliths which are not traceable to known formations could be preserved fragments of the cosmic bolide, and hence "cosmoliths"? By reflection and interference of shock waves along the rear margin of an impacting bolide, fragments may escape shock destruction. This effect apparently explains the preservation of unshocked fragments of the Canyon Diablo meteorite, which created the Barringer (Meteor) Crater in Arizona (Anders, 1965). However, the wide variety of these rock types at Sudbury argues against this possiblity and makes the deep-crust source more likely. Also, Sidney Pollack (personal communication) has been unable to find any stacking disorder in their orthopyroxenes such as is found in some meteoritic pyroxenes in chondrites.

HYPERVELOCITY AND CENTRIFUGAL INJECTION

By the proposed impact model, the sub-layer would be emplaced at hypervelocity and injected centrifugally with respect to ground zero – the centre of the Sudbury Basin. Distribution of the sub-layer components would reflect inertial or density differences and would not be appreciably influenced by the gravitational field.

Both theory and small-scale experiments show that hypervelocity bolides traveling many kilometres per second upon impact are literally turned inside out. There is almost complete destruction of the bolide as it is converted into a spray of plasma, liquid, and gas phases which sweep up along the walls of the crater. Experiments and the rayed craters on the Moon both indicate that, instead of a uniform sheet, discrete coherent jets are formed.

Figure 4, adapted from a diagram of the Levack Mine by Souch and Podolsky (1969), shows the zonation expected with a hypervelocity injection of the sub-layer vectored normal to the gravity field. The densest substances would travel farthest, giving an order of zonation as follows: sub-layer silicate matrix, a mixed zone (breccia with disseminated sulphide and some silicate matrix), and massive sulphide. The innermost zone would be pyrrhotite-rich (Fe at. wt. = 55.8), followed by a zone enriched in pentlandite (Fe at. wt. = 58.7), and finally a chalcopyrite-rich zone nearest the

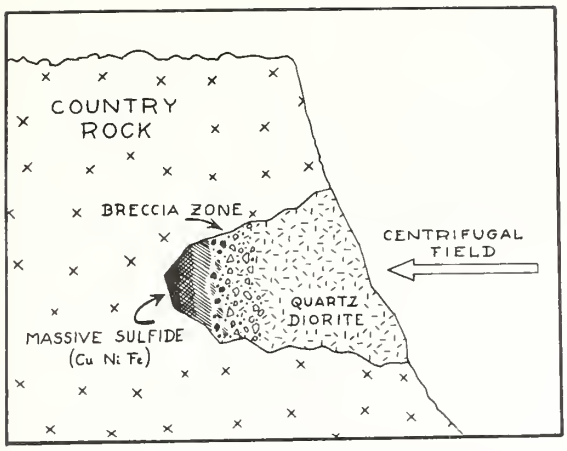

Figure 4: Zonation of sub-layer rocks expectable with emplacement by hypervelocity jet (meteorite splash against the wall of the Sudbury Crater). The denser substances seek the most distant recesses within the footwall; hence, the order of zonation would tend to be Irruptive silicate matrix, a mixed zone with breccia, pyrrhotite, pentlandite, and chalcopyrite. The heavy Pt-metals would tend to associate with the chalcopyrite. Sketch is adapted from a diagram of the Levack Mine by Souch and Podolsky (1969).

footwall (Cu at. wt. = 63.6). The very dense platinum group metals (sperrylite – $PtAs_2$, etc.) in turn would tend to hug the footwall and be associated with the chalcopyrite. This type of zonation seems generally to hold true for the footwall mines if the mine diagrams of Souch and Podolsky (1969) are used as a guide. Hawley (1962, p. 124) reports that the platinum-group metals are in fact found principally associated with chalcopyrite and usually remote from the Irruptive contact. The Pt-metals sometimes also extend far into the footwall rocks where they are in sulphide veins.

The distribution of the sub-layer components at the Frood offset mine is quite different from the footwall mines. This may be due to the sub-layer substances within this offset having been injected parallel to force field. Accordingly, the Frood ores do not show a zonation like that of the footwall mines, or like that expected by deposition controlled either by gravity or by a heat gradient increasing with depth. This may explain why the Frood lode is an "upside-down deposit" (Hawley, 1965).

The Sudbury lopolith is strongly deformed, presumably by compression associated with the nearby Grenville orogeny (and possibly also the Penokean orogeny), so that, at the bottom of the mines along the south rim, a section of the lopolith is exposed that was originally 5-1/2 miles deeper than that outcropping along the east rim (Souch and Podolsky, 1969). A remarkable aspect of the ores is that they are uniform in mineralogical and chemical composition without any hint of overall gravitational differentiation or variation with distance from a hypothetical deep thermal source. This uniformity is consistent with the astrobleme concept, as the ores would be emplaced symmetrically with respect to ground zero and without appreciable control by the gravity field.

POSSIBLE METEORITIC PARENTHOOD OF SUDBURY ORES

I turn now to the evidence that the Sudbury copper-nickel-iron sulphides have a cosmic or exogenic origin. It would be more in conformance with classical geologic interpretations to argue, at most, for an indirect meteoritic parenthood whereby the Sudbury impact resulted in the contamination of a terrestrial magma after which ore emplacement proceeded in some usual endogenic fashion. For example, the impact may have triggered magmatism, causing the Irruptive to well up into the Sudbury Basin, after which the meteoritic contaminants were cleansed by a gravitational "rain" of sulphide. This path, however, would not account reasonably for the stratigraphic position of the lodes as just elaborated above. A virtually direct meteoritic parenthood by splash emplacement appears preferable.

There apparently is a growing consensus among geologists that the Sudbury sulphide ores are magmatic and that a hydrothermal origin is wholly untenable. It seems also agreed that there are serious objections to the classical "rain of sulphide" (magmatic differentiation) concept whereby the ores gravitationally settled from the Irruptive as immiscible droplets. One point is that the Irruptive seems unlikely to have held the requisite amount of sulphur. Another is the acidity of the Irruptive with its free quartz which prohibits the presence of olivine. This mineral is the usual hiding place for nickel substituting within the lattice for iron or magnesium. Pyroxenes, such as the hypersthene of the Sudbury norite, commonly contain only about one tenth as much nickel as olivine. The preferred solution to such difficulties appears to be to suggest that the sub-layer, with all of its components, including the sulphide ores, was differentiated at depth from the main magma pool and separately injected. This variant has the questionable advantage of removing much of the evidence beyond the reach of the geologist's hammer. I offer here still another variant of magmatic ore origin whereby the ores have meteoritic parenthood – directly derived by an impact melt. It would be possible, of course, to marry the two views by having the meteorite both create and contaminate a large pool of magma at great depth within the crust, but this raises more inconsistencies than it solves. The Sudbury ores include all variants of a mix composed of country rock and exotic rocks (basic and ultrabasic rocks), breccia, Irruptive silicate (matrix) rocks and sulphides. The iron-nickel-copper sulphides are so intimately intermixed with other components of the sub-layer that it seems not unreasonable to assume that they were derived more or less directly from the shock-melted substance of the bolide.

I suggest also that the sulphur largely is derived from the impacting bolide, although doubtless with some terrestrial addition. This may seem gratuitous, as sulphur is the second most common anion on earth, but it is even more common in meteorites. The Soroti, a Uganda fall, is an example of a high sulphur meteorite. More importantly, there apparently are difficulties in obtaining the sulphur from the Irruptive. Basic rocks are notably sulphur poor compared to acidic rocks. Apparently so much so that Cheney and Lange (1967) argued that the Sudbury lopolith could not possibly provide the sulphur necessary to explain the Sudbury ores. They suggested the sulphur must in some manner have migrated in from the surrounding granitic country rocks by a process called sulphurization. However, (1) the process invoked is doubtful, (2) zinc is equally available with copper and nickel in the country rock, but virtually no zinc is found in the Sudbury sulphides, and (3) the sulphur isotope ratio is not consistent with the Cheney and Lange model.

The isotopic composition of the sulphur at Sudbury should be useful in assessing whether or not it is cosmogenic. In fact, the sulphur isotope ratio within the ore bodies lies very close to the meteoritic value of 22.41 $S^{32}:S^{34}$, for which the troilite in the Canyon Diablo siderite is used as the standard. (Using Canyon Diablo, a differentiated meteorite, as the standard is presumably a matter of convenience. It seems more proper to use a chondrite as the standard, as these are believed

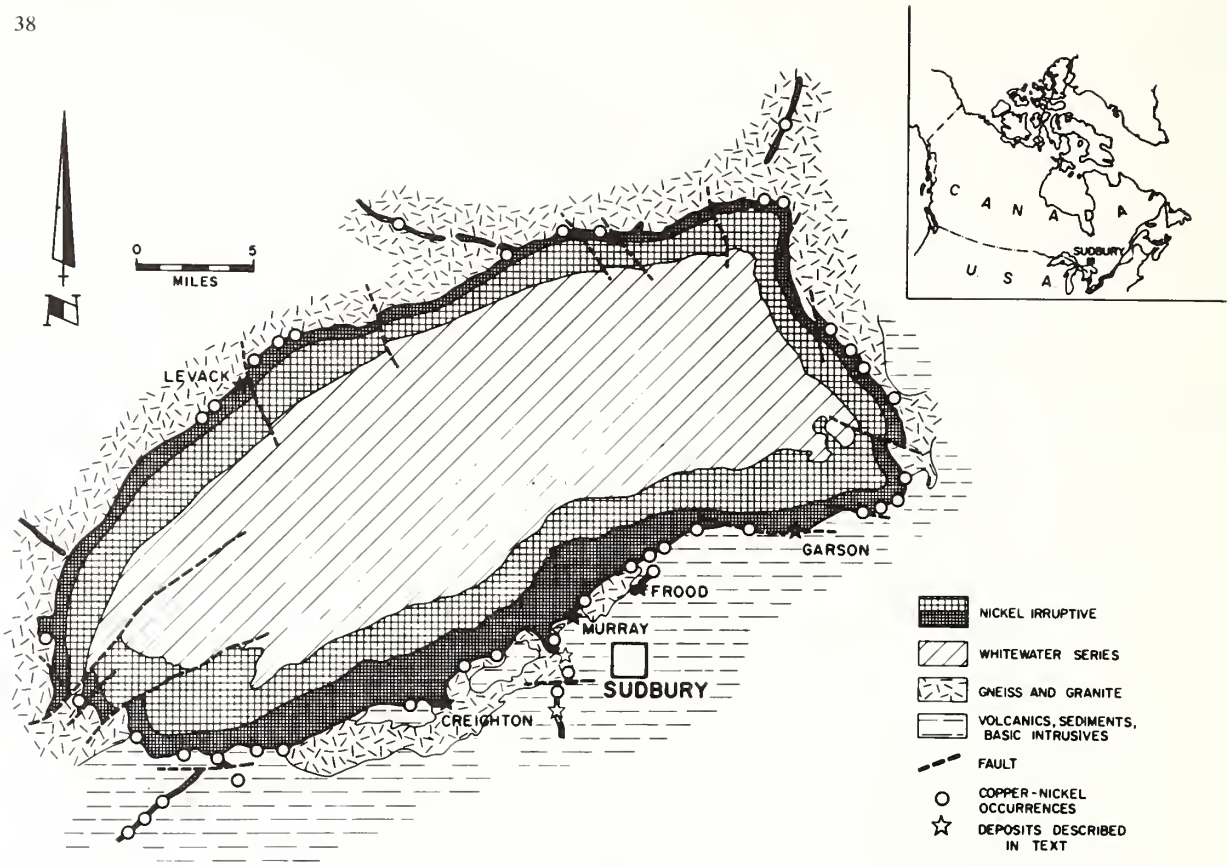

Figure 5: Geologic map of the Sudbury lopolith showing fifty-one occurrences of copper-nickel sulphide lodes along the Irruptive contact (after Souch and Podolsky, 1969).

to be undifferentiated primordial substances. The difference appears to be negligible.) A grand average of seventeen samples analyzed by Thode (1963) shows a plus 1.3 per mil δS^{34} value, or one which is close to the primordial meteoritic standard. Thus, a meteoritic origin for the Sudbury sulphur is at least permissible. On the other hand, it cannot be construed as proof, as many magmatic sulphide bodies which are obviously of terrestrial origin also have isotopic ratios that are close to the Canyon Diablo troilite standard.

In principle, the lead isotope values also should be useful, as their ratios in meteorites are distinctive. However, the lead content of a siderite is exceedingly low – only about 1/25 of that present in the earth's crust. Any interpretation of the lead isotope ratios as a criterion for cosmic origin is probably vitiated by contamination with terrestrial lead.

SUDBURY "MOON"

As noted above, the Sudbury bolide would have had a diameter of 4 km. This is calculated from the basic assumptions that the impact velocity was 15 km/sec (a typical asteroidal velocity), that the original crater diameter was 40 km, and that the object was an iron meteorite of density 7.8. In turn, the original apparent crater depth was 12,500 ft, which is the sum of the true depth of 8,500 ft plus a rim height of 4,000 ft (Dietz, 1964).

We may classify possible giant cosmic bodies into two types, (1) comet heads and (2) Apollo asteroids – i.e., those whose orbits cross the Earth's. Comet heads, because of their extreme hypervelocity and low density (circa 0.8, owing to their composition of ice and free radicals), probably explode surficially. This shallow focus of burst creates a shallow crater with a prominent central uplift (Sun, 1968). Quite likely, comet heads caused most of the known astroblemes, as, unlike Sudbury, these impact scars typically display a central dome. In contrast, an asteroidal siderite, owing to its low hypervelocity and high density (circa 7.8), penetrates the rock strata to a depth of one bolide diameter or more, causing a deep focus explosion. A bowl-shaped crater results without any central uplift, as exemplified by the Barringer Meteor Crater. A similar geomorphic style is found at other modern craters with associated siderite fragments (e.g., Henbury, Wolf Creek, etc.). The lack of any known central uplift at Sudbury suggests that this basin was caused by a low-velocity high-density asteroid rather than a comet head. This type of impact may also account for the extensive melting at Sudbury, making it a remarkably "wet" astrobleme. It should be mentioned, however, that Dence (1968) offers quite a different explanation for simple bowl craters and the large complex craters with central uplifts and peripheral annular depressions.

A pure siderite would hardly qualify as the proposed Sudbury "moon." A differentiated meteorite is required, most plausibly one that contains a mix of both a chalcophyllic phase (to supply the copper and sulphur) and a siderophyllic phase (to supply the iron, nickel, cobalt, and Pt-metals). The ratio of iron to nickel in the Sudbury sulphides is about 10:1,

or similar to that of a medium octahedrite. Among the nearly two thousand finds and falls catalogued in modern collections, however, no meteorite is known which would supply the high copper-to-nickel ratio observed at Sudbury (nearly 1:1). Known meteorites display only an occasional grain of native copper. But, as meteorites overall are considered to reflect cosmic abundances of the elements, copper-rich meteorites must be present in the cosmic inventory. From time to time these must strike the Earth. Need a giant meteorite which fell 1.7 aeons ago have a composition similar to the specimens in modern collections? Ninety per cent of all falls are stones, but all fully established modern meteorite craters were formed by irons. This offers a clear example of change in composition of meteorites with an increase in size. The Sudbury bolide may have been quite unlike any meteoritic samples we know today. If, as commonly agreed, the average composition of meteorites should reflect solar abundances, museum collections show a large copper deficit so that high copper meteorites probably exist in space.

It has been recently suggested that the anomalously low density of the core of the Earth and Mars, with respect to the pure nickel-iron model, is due to the presence of the light element sulphur rather than silicon (Rama Murthy and Hall, 1970; Anderson and Jordan, 1971). If this is true, it seems likely that this sulphur scavenged copper as it descended as a differentiate into the planetary core. Hence, it seems not unreasonable to postulate a giant meteorite with both siderophyllic and chalcophyllic components.

The composition of the bolide that created the six-mile-diameter Bosumtwi Crater in Ghana, the largest of the Quaternary meteorite craters, remains unknown, for no unaltered meteorite fragments have been recovered. It is interesting, however, that Bosumtwi impact glass contains opaque spherules composed of pyrrhotite, chalcopyrite, and iron-nickel-cobalt particles (El Goresy, 1968).

Any such speculations as to the nature of the Sudbury bolide, at the present state of our knowledge, are almost certain to be incorrect. I have simply offered a model in an attempt to account for all of the ore components. Alternatively, for example, it may be necessary to bring in only the nickel, iron, and Pt-metals exogenically from an ordinary iron meteorite, e.g., an octahedrite, with the copper and sulphur being terrestrial. The basic argument remains, that the ores are so intimately associated with the sub-layer that they must have been emplaced along with the sub-layer.

One characteristic of an impact is an abundant supply of energy producing geologic "overkill"; and this we seem to observe at Sudbury. Another is that, unlike the involved "scenarios" of endogenic cryptovolcanism, once the astrobleme is created there are no sequels. Hence, the emplacement of the sulphides seems most likely a part of the main impact event.

UNIQUENESS OF SUDBURY ORES

It is clear that an exogenic origin is not tenable for nickel deposits generally. In the first place, it is quite evident that the nickel silicate (garnierite) and oxide deposits are found in weathered and lateritized outcrops of ultramafic rocks which generally may be inferred to be tectonically detached outcroppings of the Earth's mantle. So far as the nickel sulphides are concerned, their mineralogy is, in general, quite similar to that of Sudbury—a mix of pyrrhotite, chalcopyrite, and pentlandite. This similarity develops, I believe, because of a convergence in the evolution of sulphide ores regardless of differing initial starting conditions. Why, then, should Sudbury be singled-out for a separate mode of genesis? In fact, Sudbury is unique, or is virtually so, in many ways.

(1) Among nickeliferous sulphides, the Sudbury ores are unique in their grand scale.

(2) The Sudbury ores are associated with a miogeosynclinal suite. All other major nickel deposits, with the exception of Norilsk which is in Cretaceous "traps" (picrites) on a platform, are associated with tectonized eugeosynclinal deposits.

(3) Uniquely, the Sudbury ores have no obvious ultramafic association. The ultramafic xenoliths found in the sub-layer probably are adventitious and probably have no direct bearing on the origin of the ore. The melt rocks of the Irruptive are quite acidic with free quartz, prohibiting the presence of olivine, usually the ultimate source of the nickel. There is no gravity evidence for any ultramafic layer within the lopolith at depth or of any deep chamber that could have generated the Irruptive (Popelar, 1971).

(4) The Sudbury ores contain the only nickel deposits which apparently are associated with an astrobleme. It can hardly be simply fortuitous that the world's richest nickel deposit is associated with a meteorite, an object known to be rich in nickel. It is more likely that the nickel is, even if in some manner not yet clearly understood, derived from that meteorite. The ores are too intimately associated with the apparently splash-emplaced sub-layer for one to accept an indirect path – such as the nickel being first incorporated into a deep magma chamber and later being injected into the sub-layer.

CONCLUSIONS

In the past decade, by using shock criteria, considerable progress has been made in identifying astroblemes, ancient impact structures created by the impact of cosmic bodies. The Sudbury Basin would seem to be a prime example. As leaders in this field, Canadian scientists have been especially successful in identifying about a score of these "fossil meteorite craters" on the Canadian Shield. The excellent work of C. S. Beals, Michael Dence, M. J. S. Innes, Ian Halliday, and others has led the way. In spite of this success, we have as yet been unable to find in any astrobleme unaltered remnants of the projectile. In this paper I have attempted to build a case for an indirect preservation of the "cosmic cannonball" as incorporated into the sulphide ores. Further testing of this thesis could be provided by a sophisticated geochemical analysis. In the interim there seems to be at Sudbury a reasonable geologic case for not only "pennies from heaven," but nickels as well.

ACKNOWLEDGEMENTS

In learning about the problems of Sudbury geology, I have profited by discussions and correspondence with W. Hamilton, M. Dence, U. Marvin, M. Short, B. French, J. Guy Bray, W. Peredery, D. Phipps, and T. Podolsky. This, of course, does not necessarily mean that these persons concur in the views expressed here. J. Holden has prepared the illustrations.

REFERENCES

Anders, E. (1965) – Diamonds in meteorites; Sci. Amer., vol. 213, pp. 26-36.

Anderson, D. L., and Jordan, T. H. (1971) – The composition and evolution of Earth and Mars; EOS, Trans., Amer. Geophys. Union, vol. 52, no. 4, p. 350.

Baldwin, R. (1963) – The measure of the moon; Univ. Chicago Press.

Bray, J. G., and geological staff (1968) – Shatter cones at Sudbury; J. Geol., vol. 74, pp. 243-245.

Cheney, E., and Lange, I. (1967) – Evidence for sulfurization and the origin of some Sudbury-type ores; Mineralium Deposita, vol. 2, pp. 80-94.

Dence, M. (1968) – Shock zoning at Canadian craters: petrography and structural implications; *in* Shock Metamorphism of Natural Materials, (French and Short, editors), Mono Book Corp., pp. 169-184.

Dietz, R. S. (1962) – Sudbury Structure as an astrobleme; Trans. Am. Geophys. Union, vol. 43, pp. 445-446.

. . . . . (1964) – Sudbury structure as an astrobleme; J. Geol., vol. 72, pp. 412-434.

. . . . . (1968) – Shatter cones in cryptoexplosion structures; *in* Shock Metamorphism of Natural Materials, (French and Short, editors), Mono Book Corp., Baltimore, pp. 267-285.

Dietz, R. S., and Butler, L. (1964) – Orientation of shatter cones at Sudbury, Canada; Nature, vol. 204, pp. 280-281.

Dietz, R. S., and Holden, J. C. (1966) – Miogeoclines in space and time; J. Geol., vol. 74, no. 5, pp. 566-583.

El Goresy, A. (1968) – Opaque minerals in impactite glasses; *in* Shock metamorphism of natural materials, (French and Short, editors), Mono Book Corp., Baltimore, pp. 521-533

Fairbairn, H. W., Faure, G., Pinson, W. H., Jr., and Hurley, P. M. (1968) – Rb-Sr whole-rock age of the Sudbury lopolith and basin sediments; Can. J. Earth Sci., vol. 5, pp. 707-714.

Fairbairn, H. W., Hurley, P. M., and Pinson, W. H., Jr. (1960) – Mineral and rock ages at Sudbury-Blind River, Ontario; Proc. Geol. Assoc. Can., vol. 12, pp. 41-46.

French, B. (1967) – Sudbury structure, Ontario – some petrographic evidence for origin by meteorite impact; Science, vol. 156, pp. 1094-1098.

. . . . . (1968) – Sudbury structure, Ontario – some petrographic evidence for an origin by meteorite impact; *in* shock metamorphism of natural materials, (French and Short, editors), Mono Book Corp., Baltimore, pp. 383-412.

. . . . . (1970) – Possible relations between meteorite impact and igneous petrogenesis, as indicated by the Sudbury structure, Ontario, Canada; Bull. Volcanologique, vol. 25, no. 2, pp. 466-517.

Hamilton, W. (1960) – Silicic differentiates of lopoliths; 21st Int. Geol. Cong. Rept., Copenhagen, vol. 13, pp. 59-67.

. . . . . (1970) – Bushveld complex – products of impacts?; Geol. Soc. South Africa, Spec. Publ. 1, pp. 367-379.

Hawley, J. (1962) – The Sudbury ores, their mineralogy and origin; Canadian Mineralogist, vol. 7, pt. 1.

. . . . . (1965) – Upside-down zoning at Frood, Sudbury, Ontario; Econ. Geol., vol. 60, pp. 529-575.

Naldrett, A. J., Bray, J. G., Gasparrini, E. L., Podolsky, T., and Rucklidge, J. C. (1970) – Cryptic variation and the petrology of the Sudbury Nickel Irruptive; Econ. Geol., vol. 65, pp. 122-155.

Peredery, W. V. (1971) – Volcanic rocks, chilled micropegmatite, or impact breccias and melt rocks in the Onaping formation; Geol. Assoc. Can., Mineral Assoc. Can, Sudbury meeting, p. 55 (abs).

Popelar, J. (1971) – Gravity measurements in the Sudbury area; Gravity map series no. 138, Dept. Energy, Mines and Resources, Ottawa.

Rama Murthy, V., and Hall, H. T. (1970) – The chemical composition of the Earth's core – possibility of sulphur in the core; Physics Earth and Planet. Interiors, vol. 2, no. 4, pp. 276-282.

Rousell, D. H. (1971) – Chelmsford formation of Sudbury basin – a Precambrian turbidite; Geol. Assoc. Can., Mineral Assoc. Can., 1971 meeting, Sudbury, pp. 62-63 (abs).

Souch, B., Podolsky, T., and Geological Staff (1969) – The Sulphide ores of Sudbury: their particular relationship to a distinctive inclusion-bearing facies of the nickel irruptive; Econ. Geol., Monog. 4, pp. 252-261.

Speers, E. (1957) – Age relation and origin of common Sudbury breccia; J. Geol., vol. 65, pp. 497-514.

Sun, J. (1968) – Cometary origin of Copernicus; J. Geophys. Res., vol. 72, pp. 2721-2728.

Thode, H. G. (1963) – Sulphur isotope geochemistry; *in* Studies in analytical geochemistry, Roy. Soc. Can., Spec. Publ. 6, pp. 25-41.

Thomson, J. E. (1969) – Discussion of Sudbury geology and sulfide deposits; Ontario Dept. Mines, Misc. Publ. 30.

Vos, M. A. (1966) – Petrology of some "quartz diorites" of the Sudbury Basin, Ontario; PhD thesis, U. Leiden library, 50 p.

Reprinted from EOS 52, No. 7, 540-541.

Fourth Presentation

WALTER H. BUCHER MEDAL

to

Robert S. Dietz

for original contributions to the basic knowledge of the earth's crust

ROBERT S. DIETZ is at once versatile and imaginative. There are few places that he has not visited, and many and original have been his contributions to earth science.

In 1941, after receiving his Ph.D. from the University of Illinois, he joined the United States Air Force and served until 1946 when he became a member of Admiral Byrd's last expedition to Antarctica.

After joining the Navy Electronics Laboratory, he worked with the United States Coast and Geodetic Survey and spent the 1950's as one of the leaders in that group of scientists whose explorations revealed the nature of the Pacific Ocean basin. Alone or with others, he found Mesozoic fossils and wave-formed pebbles on the top of guyots; he mapped the moat and arch structure that sur-

rounds the Hawaiian Islands and noted the smooth archipelagic aprons around other islands. He and H. W. Menard discovered the submarine scarp off Cape Mendacino and identified it as the first of a new class of tectonic features called fracture zones which have since been found to be numerous and important.

He drew attention to the great group of seamounts running southeast from Kamchatka and named them after the Japanese emperors. He analyzed manganese nodules, discovered the extension of marginal basins behind island arcs, noted submarine channels in the Indian Ocean, promoted the use of bathyscaphs, and identified some of the small animals whose presence in swarms causes deep scattering in the sea.

He participated in the discovery of new chains of seamounts in the Gulf of Alaska, noting that the northernmost were tilted and bowed down into the Aleutian trench. He also observed that the sediments on Kodiak Island had probably originated within the Aleutian trench and been uplifted. He commented on the nature and origin of continental shelves.

In the early 1960's he was one of the first to recognize sea-floor spreading. He gave that process its name and combined the idea with his earlier work to suggest the nature of continental margins. He went on to propose that the Alpine serpentinites are ocean floor that has been thrust on to land. By these developments he did much to relate former continental margins to geosynclines and to introduce uniformitarian concepts into geotectonics.

More recently he has computed the best fit between the several continents that constituted Gondwanaland and discussed the break-up of that supercontinent. This led him to recognize areas of particularly old sea floor and the special place of several groups of islands. In particular he has drawn attention to the probable continental nature of two of the Canary Islands, the origin and unusual history of the Bahama Islands at a triple point and role of volcanic islands as tracers of the past movements of continents.

Throughout his career, since he was a student in Illinois, he has taken a special interest in the scars formed by meteoric impacts which he named astroblemes. He recognized shatter cones as a means of identifying them, and of the first fourteen sites at which this relationship was shown to exist he was responsible for finding shatter zones at seven, including the Vredefort Dome and Sudbury Basin structures. When Robert Dietz began his work, Walter Bucher could only list a handful of cryptoexplosion structures and craters and few believed in a meteoric origin for any of them. Today more than sixty structures are well authenticated and accepted as astroblemes.

This brief account highlights Dietz's contributions. His travels have taken him to all parts of the world. His interests and discoveries have ranged from the tectonics of the Alps to the origin of submarine fracture zones and the explanation of enigmatic cryptoexplosion structures. His work has been characterized by a quickness to recognize and to accept new and unusual ideas. Typically one of his latest papers deals with the shape of things to come: the earth in 20,000,000 A.D. His clear and imaginative presentations have included many popular articles and have placed him in demand as a public lecturer.

His many contributions to tectonics and their originality fully qualify him for this award, and it is particularly satisfying to recall that Walter Bucher and Robert Dietz were friendly protagonists in vigorous debates together.

J. T. Wilson

Acceptance and Response

The writings of Walter H. Bucher on geotectonics have exerted a strong influence on my career as a geologist. Also, for 30 years I have followed in his footsteps to the Steinheim basin in Germany, Jeptha knob in Kentucky, Wells Creek basin in Tennessee, and Serpent mound in Ohio to examine these cryptoexplosion structures which he mapped in such exquisite detail. We gave these remarkable structures opposite interpretations: he regarded them as cryptovolcanic, while I suggested that they were astroblemes (that is, ancient meteoritic impact scars). Stimulating exchanges followed, but always without polemics or rancor, finally culminating in a published debate in the *American Journal of Science* of 1963. Through this common interest I came to know and to admire Bucher and to be caught up by his enthusiasm, zestful manner, and especially his love of the earth. And we had all better love Spaceship Earth, for within the continuum of space we are alone, or nearly so. I am too aware of the earth's frailties to be more than cautiously optimistic about her future. The human spirit will not burn brightly in a world of squandered resources, of despoiled environment, and with standing room only.

My last visit with Bucher, just prior to his death, was here at the AGU Washington meeting. As with all of us here today, he wanted to learn 'what's new on earth' and to be where the action is. The AGU *is* the focal point of this action. The wholesale, overnight conversion of American earth scientists to continental drift can be rather clearly identified with the 1967 meeting here in Washington at the symposia organized by Lynn Sykes and others. It is a privilege to be a student of the rocks in these times when earth science is a frontier science—and to play a small part in contributing. It behooves us all to continue this conversation with the rocks, for they have much to tell us about the history of the earth. As the magnetic reversal anomalies on the ocean floor once again so elegantly reminded us, the first law of geology, perhaps, is: the rocks remember while liquids and gases forget.

If Leonardo da Vinci were called back to life after five centuries, it is doubtful that he would recognize much progress in fine art. But if Walter Bucher were called back after just five years, he would readily agree that his treatise on geotectonics, 'Deformation of the Earth's Crust,' has been largely rendered obsolete by the new revolution in earth sciences.

It is with much pleasure that I accept the 1971 Walter H. Bucher medal of the American Geophysical Union.

Robert S. Dietz

Reprinted from EOS 53, No. 11, 940-942.

The Earth's Tectonosphere: Its Past Development and Present Behavior, J.H. Tatsch. Tatsch Associates, Sudbury, Massachusetts, 889 pp., 1972.

In this privately published book, J.H. Tatsch attempts to relate geotectonics to his dual primitive planet hypothesis. The essence of this hypothesis is that the earth is fractured into octants by three mutually othogonal planes—a triplane—so that the earth is really a spherical octahedron. To explain this fractured earth, Tatsch invents a cosmological model whereby two proto-earths occupy the same orbit around the sun. When they approach, they both tidily fracture into octants, but only one disrupts into its eight parts. Two of these in hyperbolic orbit escape from the solar system, another becomes the moon, and the remaining five collide and add themselves to the present earth. These five octants then somehow provide an outer 1000-km mantle shell while preserving the octagonal fracture pattern of the primitive earth's interior. (He fails to account for the present location of the destroyed planet's core; also, the moon has only 1.3% of the earth's mass, not one-eighth.)

Tatsch thus divides the earth's core and deep mantle into octants over which the upper mantle, also octahedrally fractured, slips and slides. Interaction along the margins of his eight 'plates,' which have existed for the past 4.6 billion years, causes vertical and horizontal tectonics in a manner vaguely reminiscent of plate tectonics. He attributes the magnetic field to the rise of volatiles and heat along the planes. He develops an obscure explanation for magnetic reversals based on doubtful physics. He states that the spherical harmonics of the gravity geoid fit his model better when axes are transferred from the present spin axis to one aligned with his vertexes, but he offers no evidence.

Tatsch presumably has erected his octahedron in terms of probable great circle lineaments along active tectonic elements—mountain belts, earthquakes, trenches, mid-ocean rifts, and volcanoes. But his selection seems little better than any great circle lineations selected at random, except that they traverse the North Pacific 'rim of fire' and the Mediterranean region. This octahedron necessarily has six vertexes or coigns—namely, Bouvet Island, Gibraltar, Bengal, Kermadecs, Aleutians, and Galapagos. Again, these points have no great geotectonic merit. Each of these marks the orthogonal intersection of two global fractures and is therefore a quadruple point. (In conventional plate tectonics only triple points exist; and there are six major plates, which may suggest that a comparison of the earth to a spherical hexahedron, or 'cube,' has more validity.) Tatsch's octahedron is not symmetrical with respect to the earth's spin axis, although the Galapagos and Bengal coigns do lie on the equator; the antipodes at Bouvet and the Aleutians provide his pole points. Unfortunately, his numerous felt pen sketches are so crudely drawn that it is difficult to be entirely sure of his intended terrestrial geometry.

Tatsch continues in this vein, piling unlikely (or entirely false) model upon model, building an extremely unsteady house-of-cards, all to account for his single observation that the earth is tectonically octahedral. His work is intuitive and purely descriptive and without rigor; no mathematical proofs or derivations are offered. We are asked simply to accept the assumption that celestial disruptions and mantle rheology act in the manner he describes. However, the author is well read and seems fully aware of the pertinent literature, and the work shows flashes of insight. Perhaps there are a few genuine diamonds within this heap of paste brilliants, but we have failed to discern them.

From the author's previous publication record (only 17 abstracts are listed), we surmise that he has experienced some difficulty in the publication of his ideas in the usual scientific journals. If so, we applaud this method of private publication. This monograph makes his unorthodox ideas a matter of record and, hopefully, obviates any bitterness against the 'scientific establishment.'

Robert S. Dietz
Dale C. Krause

NOAA-Atlantic Oceanographic and Meteorological Laboratories
Miami, Florida 33149

Reprinted from Meteoritics 7, No. 3, 303-307.

LAGUNA GUATAVITA: NOT METEORITIC, PROBABLE SALT COLLAPSE CRATER

Robert S. Dietz and John F. McHone

NOAA, Atlantic Oceanographic & Meteorological Laboratories
Miami, Florida 33149
and
Old Dominion University
Norfolk, Virginia 23508

Laguna Guatavita (Colombia), a crater 700 m across and 125 m deep containing a central lake, appears not to be a meteorite crater as widely supposed. The tectonic style is not that of an impact site and there is no raised rim or ejected debris. We could find no impactite, shock metamorphic effects or shock fractures (shatter cones). Most likely it is a collapsed crater caused by the solution and withdrawal of salt from an underlying anticline.

The Guatavita Crater, lat 4° 59′ N.; long 73° 47′ W., occupied by Laguna Guatavita, is an extraordinary, impressive and unique feature of the Colombian high-Andes landscape. This crater lake is located near the 3000-m level of the Cordillera Orientale in the *paramó* ecological zone, 50 km northwest of Bogotá, Colombia. More exactly the lake lies at the 2988-m level and has a depth of about 15 m by our measurements.

The crater is 700 m across at rim level and 375 m in diameter at lake level. The inner slope is steep, attaining 32° in some places. The crater has a maximum relief, from rim to lake bottom, of 125 m and a minimum relief of 100 m. Although now only rudely circular, both the crater at rim level and the crater lake were, doubtless, originally highly circular. This original roundness has been destroyed by headward valley cutting and especially by a large landslip of the northwest wall. The northeast wall of the crater is breached by a stream which now controls the lake level.

Geologically, the crater is positioned on or very near the axis of northeast-plunging anticline and exposes the top three members (sandstones, siltstones and cherts) of the Guadalupe Formation of uppermost Cretaceous age. This is the top of an enormously thick Upper Mesozoic clastic miogeosynclinal section which contains no thick limestones but some salt in the Chipaque Formation which lies immediately beneath the Guadalupe Formation.

HISTORICAL BACKGROUND

Nearly all lakes were sacred to the aborigines of this land, the Chibcha or Muisca Indians; but of all these lakes, Laguna Guatavita was the most

Fig. 1 **Laguna Guatavita Crater, Colombia, looking southward, obliquely across a northeast-ward plunging anticline. The crater is breached by a stream in the northeast quadrant. A large slump block can be seen within the crater and the southwest wall is deeply dissected. The crater lacks a raised debris rim and there is no ejecta blanket. Photo by H. Raasveldt.**

sacred. It is widely regarded as *the* lake upon which El Dorado, the man-god dusted with gold, sailed aboard a raft while he cast gold ornaments into the water. This legend has recently received new support by the new discovery of the model of such a raft with the man-god and his retinue aboard. This artifact is now the prize exhibit of Colombia's National Gold Museum in Bogotá. For four centuries, treasure hunters have scavenged Laguna Guatavita and its environs. A scuba diver reported that the lake bottom is pitted and scarred by treasure hunters. It is well known in Colombia that a grand attempt was made by Spaniards about 1820 to deepen the stream exit and thus drain the lake but landslides defeated the effort. It is virtually unknown that a draining was successfully and apparently secretly accomplished in the early 1900's by a British syndicate. After eight years of labor, they succeeded in driving a 400-m drainage tunnel. Numerous artifacts were recovered, but no gold treasure hoard. The drainage is clearly established by a 1910 photograph published in a rare German travel book (Weisswanger, 1911) which shows the lake bottom to be flat and occupied by a now drowned stream channel running across a graded plain. Evidently the lake once was naturally drained by the downcutting of the exiting stream only to be later dammed by landslides. The bottom fill plus the well developed valleys cut

into the crater wall, indicating at least a modest geomorphic antiquity of several tens of thousands of years. Clearly the crater-forming process is dead and not going on today.

EVIDENCE CONCERNING METEORITIC IMPACT ORIGIN

A meteorite-impact origin was first suggested by Raasveldt (1954), and today the crater is widely regarded as an impact site by Colombian scientists as well as the general populace. The crater is, however, little known outside of Colombia and has not been listed on the various lists of possible meteorite craters of the world (e.g., Freeburg, 1965).

The evidence for an impact origin is apparently largely morphologic, as the dimensions and geomorphic appearance are generally consistent with such an interpretation. Also, it cannot be a limestone sink (there are no thick limestones in the underlying sedimentary section) and it cannot be volcanic (there are no volcanoes in the region, no volcanic products present and no evidence for any hydrothermal alteration). One archeologist has argued that the extreme sacredness of the lake is due to their having witnessed the meteorite impact. But the crater is physiographically too old to accept this possibility, and this high sacredness might easily be derived from the crater lake's uniqueness and beautiful setting.

It has been argued that an explanation of the upturned and overturned beds along the northeast side of the lake was a strike from the northwest by a meteorite. However, while overturned beds are suggestive of impact, established meteorite craters around the world show no such marked asymmetry and, instead, reveal almost symmetrical quaquaversal dips in regard to angle of impact. More likely possibilities are that this overturning is a result of salt-related slump or diapirism related to pre-cratering-event tectonism. Steep dips and overturned strata are common in this region. We could find no evidence of a localized quaquaversal dip, although such a dip superimposed on the complex faulting and folding of the region would be difficult to isolate. A fault apparently cut across the northern sector of the crater beyond which the overturned rocks are present.

Meteorite craters should have raised rims, and there are four elevated knolls which rise above the general rim level along the northeast quadrant. They are not ejecta piles, as would characterize a meteorite crater, but are outcrops of steeply dipping bedrock. Elsewhere there is neither sign of any raised rim, nor ejecta blocks, nor any base surge deposit or fallout blanket of debris. So the evidence favoring impact is found wanting once again.

No meteorite fragments have been reported from the area; neither did we find any. These probably are not to be expected because of high weathering rates in this wet region, as attested by the well developed soil

profile. For this reason we made a special, but unsuccessful, attempt to collect magnetic spherules along traverses inside, on the rim, and outside of the crater using a 3-kg alnico magnet. We reasoned that, within an impact explosion cloud, such spherules would form as are found at several modern meteorite craters (e.g., Barringer Crater) and in deep-sea red clays. Oxidized exteriors tend to preserve them from further weathering, so that they persist at an impact site.

We could find no evidence of shock fracturing or intense polymict injection brecciation. No shatter cones were found. Some brecciation is present within the upturned rock, but of the type that one would expect from the localized fracturing and breakup associated with tight folding and faulting. We observed no powdering or comminution (rock flour) of the sandstones. There is no evidence of high-temperature melt rocks (lechatelierite, vesiculated rock, pseudo-scoria, glass bombs or *Fladen*). Thin section studies of 11 rocks revealed no evidence of shock metamorphism (decorated planar features or shock lamellae in quartz, partial to complete isotropization of feldspar, or kink-banding in micas). The sandstone appears normal in all respects.

PROBABLE ORIGIN BY SALT COLLAPSE

Salt, as already noted, is at a moderate depth beneath the Guadalupe Formation in which the crater is developed. The salt of this region apparently is not diapiric salt derived from a deep "mother salt," but has migrated into anticlines with the folding of the beds while essentially maintaining its original stratigraphic level (Ujeuta, 1969; McLaughlin, in press). The famous Zipaquirá salt mine lies 25 km to the west and the Sesquilé abandoned mine (now the site of a *ruté* terrane or weathered outcrop of salt) lies only 8 km west. Both salt pockets are located in faulted anticlines such as at Guatavita. Due to the highly perched location of the crater and the "tectonic topography" (wherein the anticlines and synclines are clearly directly reflected in the ridges and valleys), a salt pocket formerly beneath the crater could have been readily sapped by ground water seepage aided by the broken rocks of a fault plane. This eventually could create a collapse crater. A former salt spring exiting as little as 1 km to the northeast – i.e., down the slope of the plunging anticline – could have flushed the salt away. As already noted, a tunnel only 400 m long was sufficient for draining the lake, attesting to the perched position of the crater. This unique position of the salt probably explains why there are no other similar collapses in the region. Sag lakes over salt diapirs are known in many other parts of the world, but we are aware of no other assumed salt collapse crater. This mode of origin is similar to that already offered by Beattie and Lowman (1965) and by McLaughlin (in press). Beattie and Lowman tested the water for chloride and sulphate with negative

results, but one should hardly expect to find it salty in view of the cessation of collapse, as already noted.

We believe that this investigation, while not finally proving a salt collapse origin, was sufficient to demonstrate that Guatavita Crater is not a meteorite crater.

ACKNOWLEDGEMENTS

We thank the Barringer Crater Company of Philadelphia for supporting this investigation. The crater was first brought to our attention by Henri Raasveldt who kindly provided his data and photos collected in 1954. We also thank Carlos Ulloa of INGEOMINAS for accompanying us in the field. Earl Irving (USAID program in Bogotá) provided us with much information and useful contacts as also did J. E. Ramirez, S. J., Paul Lowman and Donald McLaughlin. Minard Hall (University of Bogotá) provided us with thin sections of Laguna Guatavita rocks, and Robert Fudali (Smithsonian Institution) kindly examined them for any signs of shock metamorphism.

REFERENCES

Beattie, D., and Lowman, P., 1965. Origin of *Laguna de Guatavita*, Colombia: Geol. Soc. Meeting Program, p. 10 (abstract).

Freeburg, J., 1965. Terrestrial impact structures: *U.S. Geol. Survey Bull.* **1220** (and supplements).

McLaughlin, D. Evaporite deposits of Bogotá area, Cordillera Oriental, Colombia. In press.

Raasveldt, H., 1954. Los enigmas de la Laguna de Guatavita: misc. pub. Instituto Geológico Nacional, Bogotá, Colombia, 11 pp.

Ujueta, G., 1969. Salt in Eastern Cordillera of Colombia: *Geol. Soc. Amer. Bull.* **80**, 11, 2317-2320.

Weisswanger, K., 1911. *Am Lande der heiligen Seen:* (privately published), Nurenberg, 315 pp.

Manuscript received 8/3/72

Reprinted from Institute of Geological Sciences
Report No. 70/13, 143-151.

Overlaps and underlaps in the North America to Africa continental drift fit

R. S. Dietz and W. P. Sproll

Reprinted from ICSU/SCOR Working Party 31 Symposium, Cambridge 1970: The Geology of the East Atlantic Continental Margin. Edited by F. M. Delany, 1970. *Institute of Geological Sciences Report No.*70/13, pp. 143-151

CONTENTS

	Page
INTRODUCTION	147
POSSIBLE REASONS FOR MISFITS	147
IFNI GAP	149
CAP BLANC OVERLAP	149
BAHAMA PLATFORM OVERLAP	150
CONCLUSION	150
REFERENCES	150

ILLUSTRATION

Fig. 1. A computerised continental drift reconstruction fit between Africa and North America matching the 1000 fathom isobaths and based on the criterion of smallest average misfit. 148

SUMMARY

This article presents a reconstruction of pre-continental drift geography generated by a computer programmed to fit the bulge of Africa against the great bight of North America. Accepting the drift theory, it remains to explain three major areas of misfit: (1) the Ifni gap; (2) the Cap Blanc overlap; and, most importantly, (3) the Bahama platform overlap. The Ifni gap has probably been created by the tectonic displacement of the West Canaries block away from the African margin, as a sialic microcontinent. The Cap Blanc overlap is probably due to the post-drift accretion of a pile of sediments deposited on oceanic crust along the African margin off Cap Blanc. The Bahama platform appears to be a thick sedimentary clastic-carbonate accretionary 'layer cake' laid down on oceanic crust within a small ocean basin formed shortly after incipient rift opening of the Atlantic in the Triassic. In spite of the misfits, the complete closure of the North Atlantic Ocean prior to 200 m.y. ago (mid-Triassic) seems to be a valid continental drift reconstruction such that the universal landmass of Pangaea then existed.

SOMMAIRE

Cet article présente une refonte de la géographie d'avant la translation des continents, refonte générée par un calculateur programmé afin d'emboîter le bombement d'Afrique contre la grande baie d'Amérique du Nord. Si l'on accepte la théorie de translation, il reste à expliquer trois régions majeures qui ne s'accordent pas: (1) la breche d'Ifni; (2) le recouvrement de Cap Blanc; et surtout (3) le recouvrement de la plate-forme des Bahamas. La brèche d'Ifni à été probablement créée par le déplacement tectonique du bloc des Canaries de l'Ouest au loin du marge d'Afrique comme micro-continent sialique. Le recouvrement de Cap Blanc est probablement causé par la progression, après la translation, d'un tas de sédiment déposé sur la croûte océanique le long de la marge d'Afrique près de Cap Blanc. Le plate-forme des Bahamas semble être une progression épaisse de carbonate clastique (nommé 'layer cake') déposé sur la croûte océanique dans un petit bassin océanique formé peu après l'ouverture d'une fossé naissant de l'Atlantique pendant le Trias. Malgré les désaccords, la fermeture complète de l'Océan Atlantique du Nord il y a plus de 200 millions ans (Trias Moyen) semble être une refonte valide de la translation des continents, refonte qui est compatible avoc la théorie que le continent universal de Pangaea existait alors.

ZUSAMMENFASSUNG

Dieser Artikel bietet eine Wiederherstellung der Vorkontinentalverschiebungsgeographie. Diese Wiederherstellung wurde von einem Kalkulator erzeugt, dessen Programm die Ausbauchung von Afrika mit den grossen Bucht von Nord Amerika passend macht. Wenn man die Theorie der Kontinentalverschiebung annimmt, muss man drei wichtige, nichtpassende Gebiete erklären: (1) Die Ifni-Lücke; (2) die Cap Blanc-Überlappung; (3) und am wichtigsten die Überlappung von der Bahama-Terrasse. Die tektonische Verrückung des West Kanarien-Blockes weg vom afrikanischen Rand als sialischer Microkontinent hat wahrscheinlich die Ifni-Lücke geschafft. Die Cap Blanc-Überlappung ist wahrscheinlich die Folge der Nachverschiebungsschüttung von einem Sediments haufen, die auf die ozeanische Kruste den afrikanischen Rand entlang in der Nähe von Cap Blanc. Die Bahama-Terrasse scheint ein dicker sedimentarischer klastisch-carbonatischer Schüttung—'layer cake' (d.h. Schichttorte), der auf ozeanische Kruste in einem kleinen Ozeanbecken deponiert war. Dieser ozeanbecken wurde kurz nach dem beginnenden Lückenöffnen des Atlantischen Meeres während der triassischen Zeit gebildet. Trotz des Nichtpassens, scheint die ganze Verschliessung des Nordatlantischen Ozeans vor 200 Millionen Jahren (der Mitteltriassichen Zeit) eine gultige Kontinentalverschiebungsrekonstruktion, die mit der Theorie sich verträgt, dass die universale Landmasse Pangaea damals existierte.

Overlaps and underlaps in the North America to Africa continental drift fit

R. S. DIETZ and W. P. SPROLL

INTRODUCTION

In recent years the case for continental drift has been greatly strengthened and its validity can no longer be reasonably doubted. It remains, however, to determine how the continents broke up and dispersed in space and time. There is little question but that the continents around the Indian Ocean were once together and that the South Atlantic Ocean was also closed. But was the central North Atlantic also closed by the juxtaposition of the bulge of Africa against the bight of North America? The similar curvature of these two continental margins vaguely suggests that they were once together, but closer inspection reveals considerable misfit.

It is quite possible to accept the general thesis of continental drift but still to disbelieve the North America-to-Africa join. We were formerly inclined to accept the option that these two continents were never together forming the universal landmass of Pangaea, but, instead the continental cratons were formed into the two supercontinents of Gondwana (southern hemisphere group) and Laurasia (northern hemisphere group). The quality of the Africa-to-North America fit is critical in determining which version is correct. In this paper we attempt to make a case for the existence of Pangaea by attempting to account for the overlaps and underlaps of the misfit as post-rift additions to the continental cratons.

A computerised fit of Africa to North America is presented as Fig. 1. As explained elsewhere (Sproll and Dietz, 1969; Dietz and Sproll, 1970), it is based upon matching the 1000-fathom isobath using the smallest average misfit as the criterion. The map is shown as a stereographic projection projected about a common point at 14.0°N and 04.3°E. The fit thus obtained is somewhat 'looser' than the well known fit of Bullard and others (1965). By this we mean that the latitudinal fit is quite similar and so is the longitudinal fit in the northern portion. However, in the southern portion, Africa is rotated, or swung, about 200 km farther eastward than in the Bullard fit, where the point of Africa (the Guinea Nose) is shown to be nearly contiguous to Florida. In the Bullard fit, Africa overlaps the lower one quarter of Florida.

It can be seen that there are three major areas of misfit which may be termed (1) the Ifni gap (as it is located off the Spanish enclave of Ifni), (2) the Cap Blanc overlap, and (3) the Bahama platform overlap. These misfits need to be obviated by a satisfactory geologic explanation if the reconstruction is valid.

POSSIBLE REASONS FOR MISFITS

One can surmise many possible reasons for misfits in continental drift reconstructions. A few are indicated here and the list is not intended to be complete. It is remarkable that the continents did break apart rather cleanly as evidenced by the close congruency between Africa and South America. Both Wegener and Du Toit were satisfied with the mere semblance of a fit between these two continents and did not bother to test the fit precisely. They argued that the exigencies of geologic history were such that the margins did undergo major changes of outline. Wegener also supposed that the Mid-Atlantic Ridge and certain island groups such as the Cape Verde Islands were sialic and would need to be incorporated into the jigsaw-puzzle fit.

Studies of the Red Sea-Gulf of Aden region and the rift zone along the 'broken back' of high Africa should assist in understanding the incipient stages of continental rifting. In the Red Sea, for example, it appears that with rifting the marginal cratonic blocks are rotated along down-to-the-basin normal faults. This motion is in a prograde sense with respect to the direction of pull-apart, that is, the blocks rotate clockwise along the eastern margin of the Red Sea and counterclockwise along the western margin. In high Africa there is some geophysical evidence that the sialic craton is stretched by necking and thinned prior to complete rifting (Girdler, personal communication, 1969). While inducing some distortion into the jigsaw-fit puzzle and probably accounting for minor misfits, it seems unlikely that these effects would account for major overlaps or underlaps.

We should note in passing that special problems and complexities are associated with Y-junctions, or triple points. The development of the Afar triangle in the Red Sea at a Y-junction between three crustal plates is a case in point. A large area of new ground apparently has been created with a complex volcano-tectonic history. It seems likely that ancient equivalents of such regions are now preserved as marginal plateaus. The Naturaliste Plateau off the southwest point of Australia may be an example, and many others could be cited. The Y-junction problem need not concern us here as the misfits involved are associated with the North America-Africa join or 'suture' and not with either the North America-Europe-Africa Y-junction or the

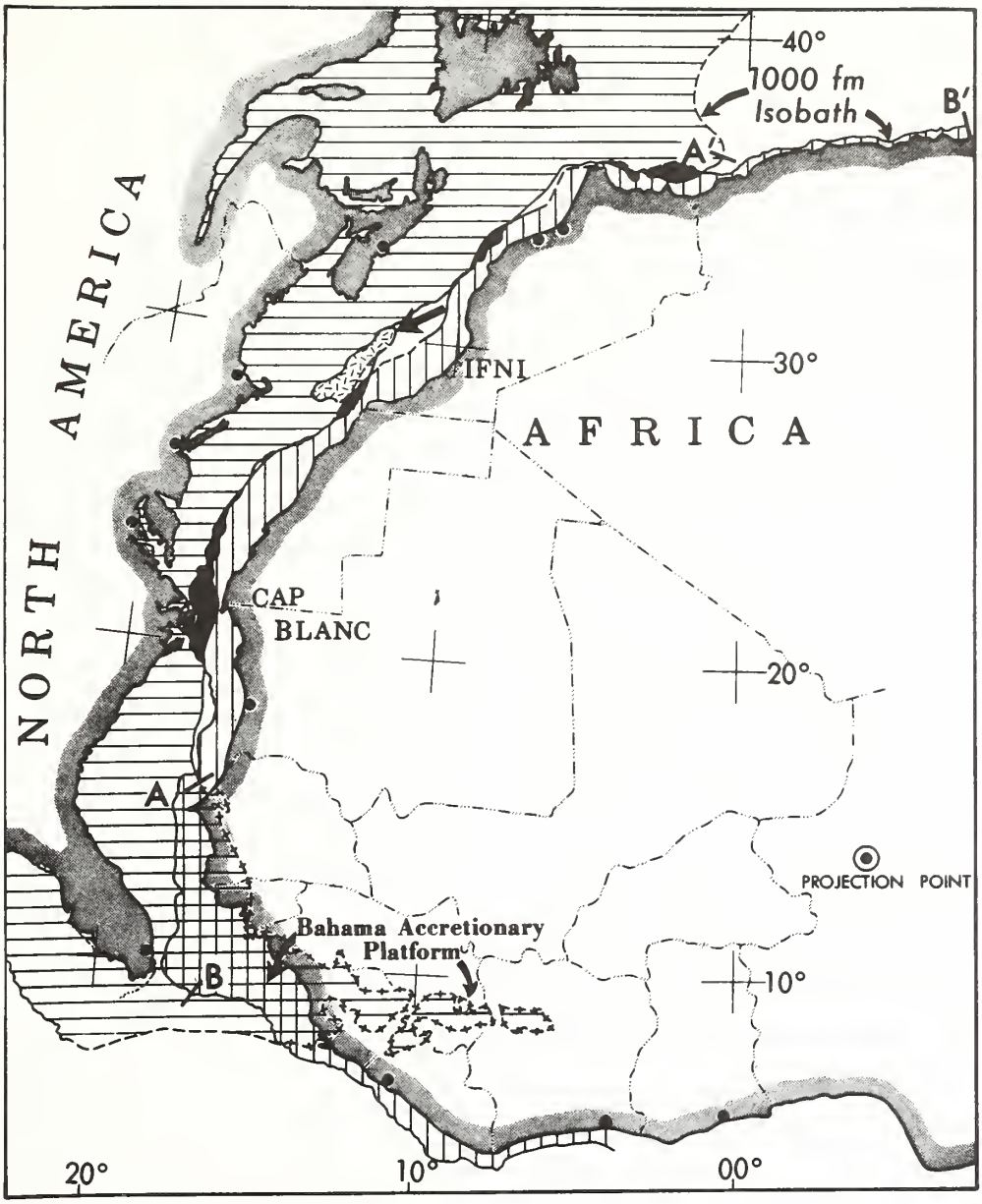

Fig. 1. A computerised continental drift reconstruction fit between Africa and North America matching the 1000 fathom isobaths and based on the criterion of smallest average misfit. The match was made by comparing the North American margin between points A to A' with the African margin between points B to B'. The North American shelf is shown by horizontally ruled lines and the African shelf by vertically ruled lines. The overlaps are shown as opaque areas except for the Bahama platform which is cross-hatched. The clear areas are gaps or underlaps in the fit. The West Canaries block, which may have fitted into the Ifni gap, is shown in random dash pattern.

North America-South America-Africa Y-junction. The Bahama platform overlap, however, occurring at the southern limit of the join, perhaps may be considered a Y-junction complexity.

Gaps or underlaps generally are more difficult to account for than overlaps. Possibly there is some logic for making computerised fits based on some criterion which minimises gaps at the expense of permitting considerable overlap. Basaltification or 'oceanisation', whereby the sialic craton is engulfed, foundered, and converted to sima, is a commonly offered explanation for such things as the disappearance of hypothetical Appalachia. While basins such as the North Sea basin and the Michigan basin commonly form within cratons, we doubt that the complete assimilation and disappearance of a craton is a real geologic process, so it will not be included here.

Tectonic translation by strike slip, but without detachment of the shifted block from the craton, may be one explanation for the gap. In this case, the gap should be compensated by an equal area of overlap nearby.

Tectonic detachment of a marginal sialic block through sea floor spreading associated with continental drift is another possible way of producing gaps. In this case, the micro-continental block should be preserved in the new ocean basin. The Seychelles Islands are presumably an example, and several others could be cited, as well.

So far as overlaps are concerned, sedimentation on the continental slope causing prograding over the adjacent ocean floor may cause a post-rift accretion. This is especially true if a delta pile is imposed. The Niger delta may be regarded as the type example, for it forms a large overlap in the fit between Africa and South America of Bullard and others (1965). The continental slope off Louisiana and Texas offers another example. There the continental margin has been extensively built outward by the emplacement of a series of depocenters creating a smeared deltaic pile which has migrated eastward along Texas to the present debouchement of the Mississippi River off Louisiana. Even in the absence of deltas some sediment may be carried across the shelf and prograde the margin over oceanic crust, but such accretionary elements must be of small scale causing only minor irregularities in the fit.

IFNI GAP

The principal gap revealed by Fig. 1 occurs off the Spanish enclave of Ifni and may be, therefore, named the Ifni gap. This underlap, however, may be largely removed if the East Canary Islands (Lanzarote-Fuerteventura-Concepcion Bank block) are a detached sialic fragment or microcontinent, originally a part of Africa, which is now displaced 190 km to the southwest. This suggestion is not gratuitous, as there are recent geologic and seismic studies which suggest that the East Canaries are continental, in contrast to the West Canaries which clearly are oceanic, volcanic seamounts (Rothe and Schmincke, 1968; Dash and Bosshard, 1968). This gap has an area of 25 600 square km, which is approximately matched by the 23 800 square km area of the East Canaries block. The probability of this transposition will be discussed in full detail elsewhere (Dietz and Sproll, in press).

The northern margin of Africa approximates the boundary of the African crustal plate which trends through the Mediterranean Sea, a zone of crustal resorption and also of dextral shear (Tethyan megashear). One might argue, therefore, that the African craton has been deformed in the Atlas orogenic region or even that portions of the northern margin of Africa were originally part of Europe. This would, in turn, make the fit as shown in Fig. 1 invalid and suggest that considerable latitudinal adjustments may be permissible. However, the fit we show on the basis of congruency is independently supported by extrapolating the strike of the transform fault-generated fracture zones which offset the Mid-Atlantic ridge. These are generally interpreted as marking the 'dead reckoning tracks' of the drifting continents. Although some extrapolation is necessary beneath the continental rises, their strike suggests, for example, that Cap Blanc should indeed be juxtaposed against Cape Hatteras as shown in Fig. 1.

CAP BLANC OVERLAP

The overlap of the African craton in the vicinity of Cap Blanc onto North America in the region of Cape Hatteras is a major zone of misfit which may be immediately termed the Cap Blanc overlap. We avoid the alternate term, Hatteras overlap, as this fit rather clearly could not be corrected on the American side. It is difficult to obviate this misfit, and it presents a major problem requiring resolution in terms of the tight closure of the North Atlantic Ocean by continental drift.

On the American margin it is well known that a homoclinal wedge of post-mid-Jurassic sediments caps the continental margin basement and underlies the coastal plain. This prism outcrops on the continental slope creating a series of deep terraces (Heezen and others, 1958; Rona, 1970). A 3000 m well on Cape Hatteras, only 30 km from the shelf break, has a crystalline basement of Palaeozoic age which is a portion of the basement complex of the North American craton (Denison and others, 1967). Hence, the North American craton in this region seems to have undergone no post-

rift accretion. It is possible to suppose that Triassic basins are inserted into the basement beneath the symmetry wedge which may have extended the continental margin seaward, but such an explanation is farfetched and would cause, at most, only a slight extension.

Rather clearly, the overlap must be obviated on the African margin by inferring the existence of a Cap Blanc overlap composed of a sedimentary pile laid down on oceanic crust off Cap Blanc. Such a possibility seems difficult at first sight, since not far inland from Cap Blanc there exists the Requibat Precambrian foldbelt striking toward this point of land. Flanking it to the north is the Aaiun basin and to the south the Senegal basin (Rona,1970, Fig. 1). It remains possible, however, that the Precambrian foldbelt after it disappears beneath the cover of coastal plain sediments abruptly terminates and is replaced by a thick post-rift sedimentary accumulation. In fact, the existence of such a sedimentary pile seems a distinct possibility.

Two deep offshore oil-test wells have recently been drilled in the vicinity of Cap Blanc, one to 3500 m and bottoming in Lower Cretaceous and the other to 4000 m and bottoming in Lower Jurassic. Since neither well encountered basement or sediments older than the time of initial rifting of this margin (mid-Triassic?), it seems possible that a thick sedimentary depocenter is present off Cap Blanc which may be a post-rift sedimentary excrescence to the African margin. If a Cap Blanc overlap cannot be obviated on the African margin, its presence remains a most puzzling aspect for continental drift reconstruction in the North Atlantic.

BAHAMA PLATFORM OVERLAP

The major region of misfit of Fig. 1 is the Bahama platform overlap, an enormous area half the size of Texas, which must be eliminated if the North America-Africa fit is valid. A thick section (greater than 5 km) of front-lying Cretaceous and younger carbonates capping the Bahama platform implies an unusual geotectonic history, characterised by great subsidence. We suggest that this platform was underlain neither by sial nor by a volcanic foundation, making it a 'mega-atoll'. Instead, it seems likely that a basement of oceanic crust now about 11 km deep has undergone slow subsidence. Jurassic rifting in the Atlantic probably initially created a small, closed ocean basin or mediterranean in the Bahama region. This was accomplished by a rotational movement of the North American plate away from the north African plate, accompanied by shearing across the South American plate, which remains stationary and attached to Africa. A wedge-shaped sphenochasm resulted which became a sediment trap within Pangaea and quickly filled to sea level with turbidites. With a renewal of continental drift, the Bahama platform became a subsiding marginal plateau attached to the North American craton. Upon this platform algal-coral growth flourished explosively under true oceanic conditions, causing sufficient upbuilding to offset subsidence and to maintain a sea-level freeboard.

This interpretation obviates the overlap of the Bahama platform onto Africa when the Atlantic Ocean was closed under continental drift reconstruction. It also accounts for the long history of subsidence without calling on 'oceanisation'. A full account of this interpretation is being presented elsewhere (Dietz and others, in press).

CONCLUSION

Fitting the bulge of Africa against North America is probably a valid continental drift reconstruction prior to the mid-Triassic, 200 m.y. ago. This means that all the continents were then fitted into the universal landmass of Pangaea. This fit is the crux of the problem: which is the initial configuration of the craton, Pangaea, or the two super-continents, Gondwana and Laurasia? Three major areas of misfit - the Ifni gap, the Bahama platform, and the Cap Blanc overlap - can probably all be adequately explained as post-rift modifications of the continental margins.

REFERENCES

BULLARD, E.C., EVERETT, J.E. and SMITH, A.G. 1965. The fit of the continents around the Atlantic. In Symposium on continental drift. Phil. Trans., R. Soc.A, Vol. 258 (1088), pp. 41-51.

DASH, B.P. and BOSSHARD, E. 1968. Crustal studies around the Canary Islands. Rep.23rd Int. Geol. Congr., Prague, Vol. 1, pp. 249-260.

DENISON, R.E., RAVELING, H.P. and ROUSE, J.T. 1967. Age and descriptions of subsurface basement rocks, Pamlico and Albemarle Sound areas, North Carolina. Bull. Am. Ass. Petrol. Geol., Vol. 51, pp. 268-272.

DIETZ, R.S., HOLDEN, J.C. and SPROLL, W.P. In press. Geotectonic evolution and subsidence of Bahama platform. Bull. geol. Soc. Am., July, 1970.

_____ and SPROLL, W.P. 1970. Fit between Africa and Antarctica: a continental drift reconstruction. Science, Vol. 167, pp. 1612-1614.

_____ _____ In press. East Canary Islands as a microcontinent within Africa-North America continental drift fit. Nature, Lond.

HEEZEN, B. C., THARP, M. and EWING, M. 1959. The floors of the oceans I. The North Atlantic. Spec. Pap. No. 65, geol. Soc. Am. 121 pp.

RONA, P. A. 1970. Comparison of continental margins of eastern North America at Cape Hatteras and north-western Africa at Cap Blanc. Bull. Am. Ass. Petrol. Geolog., Vol. 54, No. 1, pp. 129-157.

ROTHE, P. and SCHMINCKE, H.- U 1968. Contrasting origins of the eastern and western islands of the Canarian archipelago. Nature, Lond., Vol. 218, No. 5147, pp. 1152-1154.

SPROLL, W. P. and DIETZ, R. S. 1969. Morphological continental drift fit of Australia and Antarctica. Nature, Lond., Vol. 222, pp. 345-348.

ESSA, Atlantic Oceanographic &
Meteorological Labs.,
MIAMI,
Florida 33130.

Dd 500631 10/71

Printed in England for Her Majesty's Stationery Office by Commercial Colour Press

Reprinted from Proceedings SCAR/IUGS Symposium on Antarctic Geology and Solid Earth Geophysics, Oslo, Norway 1970, 837-842.

ANTARCTICA AND CONTINENTAL DRIFT

Robert S. Dietz,

John C. Holden and Walter P. Sproll

ESSA, Atlantic Oceanographic & Meteorological Labs,
901 South Miami Ave., Miami, Florida 33130

Contents:

Introduction
Africa/Antarctica Fit
Australia/Antarctica Fit
India/Antarctica Fit
Breakup and Dispersion of Continents from Antarctica
Pre-Mesozoic Ocean Crust
Circularity of East Antarctica
Concluding Note

Abstract

Continental drift reconstructions by computerized matching of the 1000-fm isobaths are presented for Africa/Antarctica, Australia/Antarctica, and India/Antarctica. Sufficiently good congruency is obtained for the first two to suggest that they are probably correct, but the India fit remains puzzling. A set of five maps is presented showing the original position of Antarctica within the framework of Gondwana and the subsequent continental drift breakup and dispersion through space and time. We suggest that while the Antarctica plate offers only modest prospect as the site of stranded areas of pre-Mesozoic ocean crust, the Wharton basin (defined as that sector of the Australian plate delimited by Ninetyeast ridge, Java trench, western Australia, and the Diamantina fracture zone) is underlain by old oceanic crust. We associate the circular outline of East Antarctica with the passive tensional scar left by fast-drifting plates moving northward from relatively fixed Antarctica.

INTRODUCTION

We propose in this paper to discuss the geometric position of Antarctica within Gondwana, especially with respect to Africa, India, and Australia. We will also discuss the breakup and continental drift dispersion of these continents northward from Antarctica--a Sudpolarfluchtkraft, to paraphrase Wegener's Polarfluchtkraft. Some comments are included about the circularity of East Antarctica and the possible location of old (pre-Mesozoic) ocean floor. This analysis is based upon the concept of sea floor spreading and plate tectonics. An interesting previous synthesis has been made by Heirtzler (in press).

AFRICA/ANTARCTICA FIT

A close morphologic fit (on the criterion of smallest average misfit) can be obtained by a computerized comparison of the 1000-fm isobath of Africa and Antarctica (Fig. 1). This reconstruction places the margin of southeastern Africa against the region of the Weddell Sea, Caird Coast, and Princess Martha Coast of East Antarctica. S-shaped portions of each continental margin then become congruent, with a total mismatch of only 60,000 km^2 (an area about the size of Denmark). The overlap is 36,000 km^2 and the underlap is 24,000 km^2. The average misfit along the join is 28 km (Dietz and Sproll, 1970).

This satisfying fit can only be obtained once the Antarctic Peninsula is omitted from consideration, on the rationale that the tip of this horn is a post-breakup accretionary foldbelt and/or a sector of considerable geotectonic displacement. Hence, in our reconstruction the outer portion of this horn is permitted to overlap, in ghost outline on Fig. 1, onto the Africa craton. We, of course, agree that this foldbelt is properly regarded as an extension of the Andean orogen, but we assume that it was developed subsequent to the initial continental drift breakup and probably during Antarctica's westward (counterclockwise) rotation and probable slight southward drift. Based on the radiometric age of the Stormberg lavas and related extrusions, this rifting commenced in mid-Triassic about 200 million years ago (McDougal, 1963; Manton, 1968). It is noteworthy that the South America/Africa continental drift reconstruction has an underlap at its southern end. This gap originally may have been occupied by a cratonic block which was later incorporated by drift into the modern Antarctic Peninsula, as it seems to be a mix of old and new rock.

Smith and Hallam (1970) proposed a fit almost identical to ours. However, they place Antarctica slightly westward, based upon the desire to close the Indian Ocean continents of Antarctica, India, and Madagascar against Africa, so as to eliminate a small

ocean basin within the framework of Gondwana. By using the 500-fm isobath for fitting, their fit still results in a mediterranean sea occupying much of the Weddell Sea region within Gondwana. This inland sea is totally eliminated in our reconstruction because we use 1000-fm isobath for fitting. This isobath, in fact, seems to better delimit the true margin of a continent (Carey, 1958).

ANTARCTICA/AUSTRALIA FIT

As Fig. 2 shows, a good fit can also be obtained along the 1000-fm isobath between the Great Bight of Australia and the margin of Antarctica extending from the Ross Sea to the Knox Coast (Sproll and Dietz, 1969). The total mismatch of this fit is 150,000 km^2, with an overlap of 95,000 km^2 and an underlap of 55,000 km^2.

Although this fit is a purely geometric solution, it is geologically permissible as well. The Adelaide Precambrian-Cambrian miogeosyncline, characterized by the pleosponge, Archeocyatha, becomes contiguous to a similar geosyncline in Antarctica. Dolorite dikes of Tasmania also become adjacent to dikes of similar age and orientation in Victoria Land. The intrusion of these dikes, which are about 160 million years old (Sunderland, 1956), probably seems, however, not to be related to the "lift off" of Australia from Antarctica, as the magnetic reversal anomalies suggest that this occurred as late as early Cenozoic (Le Pichon and Heirtzler, 1968). Their intrusion possibly could be synchronous with the breakaway of New Zealand from the Antarctica-Australia supercraton, as this event apparently occurred earlier.

A satisfying aspect of this join is that three marginal plateaus form toe ends which nicely box in and constrain the reconstruction. These are the Iselen and Bruce plateaus off Antarctica and the Naturaliste Plateau of southwestern Australia. These mid-depth salients were omitted from the fit solution shown in Fig. 2 on the basis that they might not be cratonic and because they would introduce too much bias in achieving the fit. In other words, the fit achieved would be virtually a foregone conclusion by simple inspection. The development of such marginal plateaus seems to be somehow related to former Y-junctions or triple-points (points of intersection between three crustal plates).

INDIA/ANTARCTICA FIT

Unlike the reconstructions described above, the fit of India against Antarctica finds no really satisfying morphologic solution, so it remains puzzling. Fig. 3 shows four possible pre-drift positions of India within Gondwana. The first of these versions (Fig. 3A) shows India as fitting against western Australia rather than Antarctica. This appears to be a reasonably good fit in that Ceylon is nicely accommodated into a bight within the Australian

margin. To achieve this fit, however, we eliminated the large Exmouth Plateau off northwestern Australia as being an integral part of the Australian craton. This assumption, however, is doubtful. More importantly, considerations of plate tectonics seem to void this reconstruction as there is no mid-ocean ridge (rift) between India and Australia. (It is conceivable that the Ninetyeast ridge is a fossil rift which once inserted new ocean crust between India and Australia. We prefer, however, to believe that this is a megashear boundary between the Indian and Australian plates which has conserved crust.) The fracture zones within the Indian Ocean, which provide useful "dead reckoning tracks" for continents, rather strongly suggest that the east coast of India was once juxtaposed against Antarctica (Dietz and Holden, in press).

Fig. 3B shows a second option but, aside from the fit being rather poor, this position is unlikely as India overlaps Africa once Africa is fitted against Antarctica as described above. Fig. 3C shows a third version in which Ceylon is accommodated against Gunnerus Bank, but in doing so a poor congruency results between the first-order curvature of both continents in that the convexity of Enderby Land does not fit into the concavity of the east margin of India.

Fig. 3D shows our preferred solution. In this fitting test, Ceylon is omitted from the computation, so that it is permitted to overlap the Gunnerus Bank. This, of course, is somewhat arbitrary, but perhaps the Gunnerus Bank is a post-rift excrescence on the margin of Antarctica. Smith and Hallam (1970) show a similar position for India against Antarctica and, in turn, have arbitrarily detached Ceylon from India and inserted it against the west side of Gunnerus Bank. This is an interesting optional solution, but so far as we are aware there is no geologic evidence that Ceylon was ever separated from India.

BREAKUP AND DISPERSION OF CONTINENTS FROM ANTARCTICA

The probable history of the breakup and dispersion of the continents once attached to Antarctica is depicted in Fig. 4. The positions of the continents are shown as of the end of each geologic period from the Triassic to the Present. The need for brevity prohibits any description of this dispersion here. Our basis for this map will be presented elsewhere (Dietz and Holden, 1970).

We emphasize here that Antarctica apparently is the most fixed of continents. The Antarctic plate is unique in that it is entirely margined by a rift system (the Panantarctic rift). There is no associated trench into which this plate is subducted. This rift system must have migrated outward from the margin of East Antarctica (Fig. 5). As rift system zones commonly accommodate shear, Antarctica probably has undergone some "tight" rotation

westward with the pole of rotation being within the antarctic continent. If Antarctica has drifted southward, as some paleomagnetic results suggest, the plate must have moved as a unit.

In some previous drift reconstructions, Africa has been considered as fixed as it is the heartland continent of Pangaea and is also largely surrounded by a rift. However, the African plate is bounded on the north by the Tethyan trench or subduction zone toward which this plate has moved.

PRE-MESOZOIC OCEAN CRUST

The sea floor spreading rates of from one to six cm/yr inferred from magnetic reversal anomalies suggest that about one half of the ocean floor has been "repaved" with new crust during the Cenozoic (Vine, 1968). By extrapolation, nearly all the remainder is probably younger than the -200 m.y. (mid-Triassic) commencement of the modern drift event associated with the breakup of Pangaea. The oldest sea floor known to date, of -160 m.y., was drilled on JOIDES Leg 11 just west of the Bahama platform (preliminary communication from J. Ewing and C. Hollister, chief scientists). The search for ancient oceanic crust (pre-Mesozoic) has become an interesting quest. The small ocean basins behind trenches, which could represent crustal sub-plates protected from subduction, offer a possibility. In fact, they appear to be neo-oceanic (e.g., Japan Sea, as this arc seems to have slowly migrated outward from Asia) or no older than Mesozoic (e.g., Caribbean).

At first thought, the Antarctic plate would seem to offer a bright prospect for preserving regions of ancient ocean floor, as this plate contains no subduction zones. If the Panantarctica rift has migrated only outward, as suggested above, then those marginal regions of Antarctica, which were not originally defined or blocked out as rift edges (where other continents formerly fitted under drift reconstruction), should contain stranded areas of pre-Mesozoic ocean floor. The Pacific sector of West Antarctica fits this description, but it is margined by a young foldbelt which suggests that a "fossil" sub-plate was consumed along this margin. So ancient sea floor is unlikely here.

Perhaps a more likely possibility is a marginal area about present-day lat. 90°E, as this is a region of gap in our proposed reconstruction between the former joins of India and Australia, as, in other words, a southern arm of Tethys. However, it may be that the margin of Antarctica along this sector is a rift scar, too, with the Broken Ridge microcontinent (Francis and Raitt, 1967) being the congruent jigsaw piece. (This region of ocean crust would also have been consumed if the Ninetyeast ridge is a fossil-spreading rift which originally opened up the longitudinal distance between India and Australia; but this prospect seems unlikely to us.)

The former Antarctica/Australia supercraton and crustal plate is, however, another matter. The Australian plate probably separated from Antarctica only in the early Cenozoic and has drifted northward, along with its associated rift, in a regime of fast spreading, as Le Pichon and Heirtzler (1968) have shown. Unlike these authors, we suppose that the Australia plate must have had a quite separated history and is independent of the India plate. In this context, the Wharton Sea basin (as bounded by Ninetyeast ridge, Java trench, western Australia, and Diamantina fracture zone) may be pre-Mesozoic ocean crust which has not as yet been subducted into the Java trench (Fig. 6). Here, then, is an extensive area of probably pre-Mesozoic ocean floor, perhaps the only large such region in the world.

CIRCULARITY OF EAST ANTARCTICA

East Antarctica is remarkably circular in outline; it is a margin that was established by rifting. We offer the following speculation to account for this circularity. By the usual version of the plate tectonics concept, the rifts are passive tensional breaks resulting from the active descent of the crustal plate into a subduction zone (Isacks et al., 1968). The shape of the leading edge of a plate is unknown as these are everywhere now subducted into trenches. We suggest, however, that they may tend to be convex outward or in opposition to the shape of island arcs which mark the surface trace of the subduction zone. In turn, the associated or paired rift may tend to parallel this curvature and so be convex into the active plate. When a plate is created and moves actively away from a relatively passive craton, a convex margin is impressed upon this craton. At least we seem to observe this result for the bight of North America which complements the bulge of Africa which may be regarded as the type example. The same relationship of an active plate moving away from a relatively fixed craton seems to apply for the margins of Antarctica-Australia and for India (western margin)-Antarctica. The resultant effect impressed a circular outline on East Antarctica.

CONCLUDING NOTE

To further investigate the main points raised in this paper, precise bathymetric and geophysical surveys are urgently needed along the margin of Antarctica by ice-reinforced survey ships equipped with satellite navigation. For example, is the Iselen Plateau really a marginal plateau or merely a group of seamounts? Is the Gunnerus salient really a cratonic projection which must be accommodated in a continental drift reconstruction or is it "new ground"? Paleomagnetic studies should help unravel any history of tectonic rotation of the Antarctic Peninsula. These and many other questions remain to be answered.

REFERENCES

Carey, S. W. (1958) A tectonic approach to continental drift: in S. W. Carey, ed., Continental Drift, a Symposium, Univ. of Tasmania Press, Hobart, 177-355.

Dietz, R. S., and J. C. Holden (1970) Reconstruction of Pangaea, its breakup and dispersion of continents--Permian to Present: J. Geophys. Res., 75, 26, Sept. 10.

Dietz, R. S., and W. P. Sproll (1970) Fit between Africa and Antarctica: a continental drift reconstruction: Science, 167, 1612-1614.

Francis, T., and R. Raitt (1967) Seismic refraction measurements in the southern Indian Ocean: J. Geophys. Res., 72, 12, 3015-3041.

Heirtzler, J. (in press) Evolution of the southern oceans: Amer. Assoc. Adv. Sci. Antarctica Symposium, Dallas, 1968.

Isacks, B., J. Oliver, and L. Sykes (1968) Seismology and the new global tectonics: J. Geophys. Res., 78, 18, 5855-5899.

Le Pichon, X., and J. Heirtzler (1968) Magnetic anomalies in the Indian Ocean and sea floor spreading: J. Geophys. Res., 73, 6, 2101-2117.

Manton, W. I. (1968) The origin of associated basic and acid rocks in the Lebombo-Nuanetsi igneous province, southern Africa, as implied by strontium isotopes: J. Petrol., 9, 23-39.

McDougall, I. (1963) Potassium-argon age measurements on dolerites from Antarctica and South Africa: J. Geophys. Res., 68, 1535-1545.

Smith, A., and A. Hallam (1970) The fit of the southern continents: Nature, 223, 139, 139-144.

Sproll, W., and R. Dietz (1969) Morphological continental drift fit of Australia and Antarctica: Nature, 222, 345-348.

Sunderland, F. L. (1966) Considerations on the emplacement of the Jurassic dolerites of Tasmania: Papers and Proc. Royal Soc. Tasmania, 100, 133-145.

Vine, F. (1968) Evidence from submarine geology: in Proc. Amer. Philos. Soc., 112, 5, 325-334 (symp. on Gondwanaland revisited: new evidence for continental drift).

Wilson, J. T. (1965) Submarine fracture zones, aseismic ridges, and the ICSU line: proposed western margin of the East Pacific Ridge: Nature, 207, 5000, 907-911.

Figure 1

The best fit position between Antarctica and Africa, a continental drift reconstruction in stereographic projection. Departures from congruency are shown as overlaps (opaque areas) or as underlaps (clear areas). The Antarctic Peninsula is shown in ghost outline on the presumption that it was non-existent (at least in its present position) prior to continental drift breakup.

Figure 2

The best fit position of Australia relative to Antarctica, a continental drift reconstruction. Ruled lines indicate shelf and upper continental slope areas to the 1000-fm isobath. Overlap areas are thus cross-ruled and underlap area is blank.

Figure 3

Possible continental drift reconstruction for India which places this continent either against Australia or Antarctica. None of the fits are regarded as good, but that shown in panel D is our preference. The apparently good fit of panel A is achieved by omitting the Exmouth Plateau as an integral part of Australia, a doubtful assumption.

Figure 4

Dispersion of the Gondwana continents from Antarctica by the opening up of the Atlantic and Indian rift oceans on an Aitoff projection. Antarctica remains relatively fixed while the other continents move north or west. Initial positions adjusted to fit magnetic paleolatitudes and orientations with the later dispersion fixed in geographic coordinates regarding the Walvis thermal center as fixed (Wilson, 1965). Explanation: Double lines are rifts and crossed lines are trenches. The stipple shows new ocean floor generated by sea floor spreading for each geologic period. Solid line is transform fault megashears. Open arrows are vectors showing the total drift rotation during each geologic period. The hatchered arc is the Scotia Arc to give the reader an arbitrary geographic fix. Circles with central dots are the Walvis and Maldive thermal centers from which nemataths (basaltic thread ridges) have developed.

Figure 5

A physiographic diagram showing the outward (northward) migration of the Panantarctic rift relative to Antarctica. New oceanic crust is emplaced along this northerly migrating axis of sea floor spreading while Antarctica has remained essentially fixed in position. Africa, India, and Australia have all drifted northward at twice the half-spreading rate as measured on the emplacement

of new oceanic crust on one limb of the mid-oceanic rift. The southern portion of the India plate is also depicted as bounded by a rift and two megashears.

Figure 6

The Wharton Sea basin offers a good prospect for being underlain by pre-Mesozoic ocean crust. The subduction of this western portion of the Australian crustal plate into the Java trench commenced only about 40 million years ago with the separation of Australia from Antarctica. Another small area of ancient ocean floor might be present near the Antarctica margin. Probably any old crust along West Antarctica has been subducted into a fossil trench with the development of the young West Antarctica foldbelt.

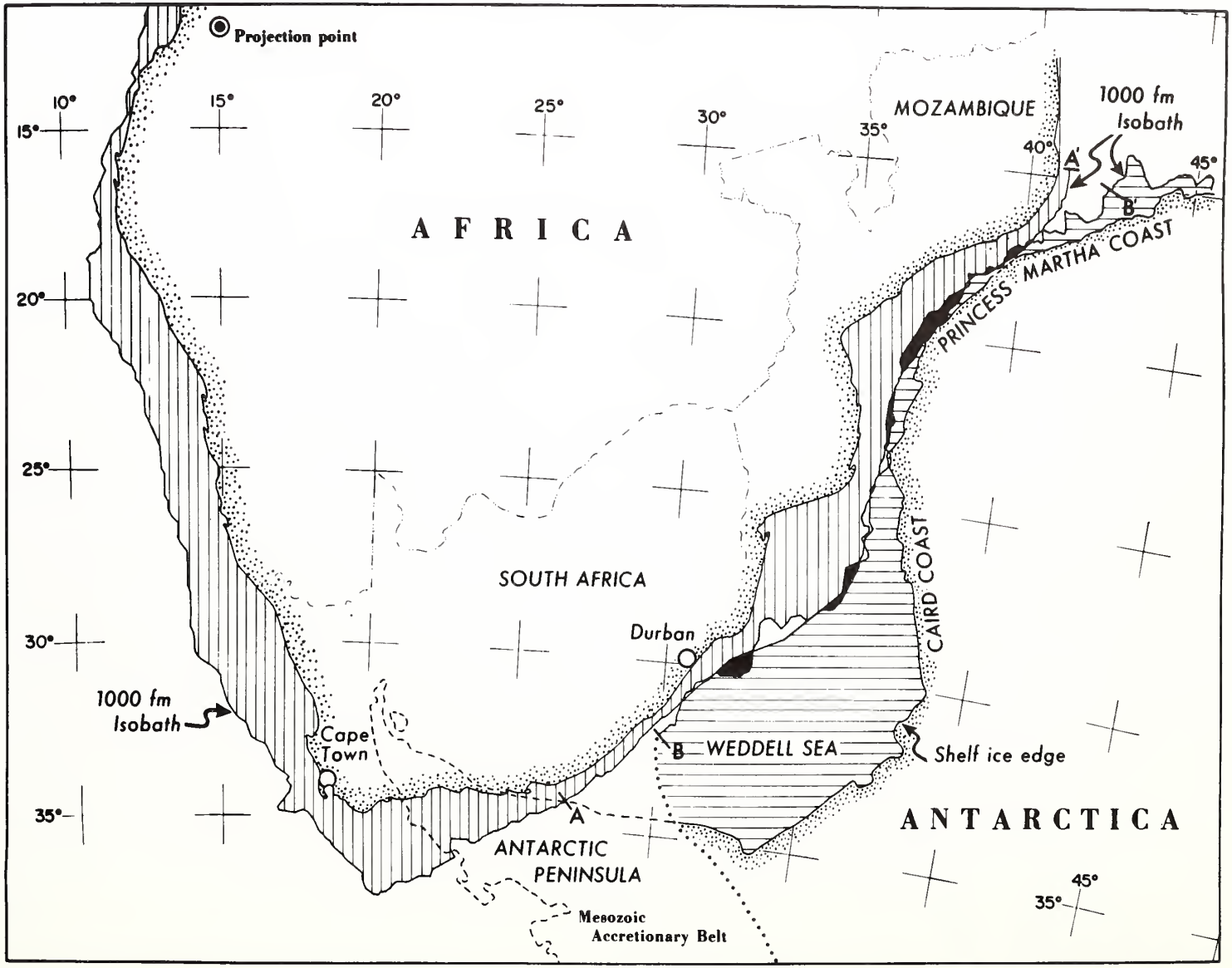
Projection point
10°
15°
20°
25°
30°
35°
40°
45°
MOZAMBIQUE
1000 fm Isobath
A'
B'
AFRICA
PRINCESS MARTHA COAST
SOUTH AFRICA
CAIRD COAST
Durban
1000 fm Isobath
Cape Town
B
WEDDELL SEA
Shelf ice edge
A
ANTARCTIC PENINSULA
ANTARCTICA
Mesozoic Accretionary Belt

DIETZ...FIG 1

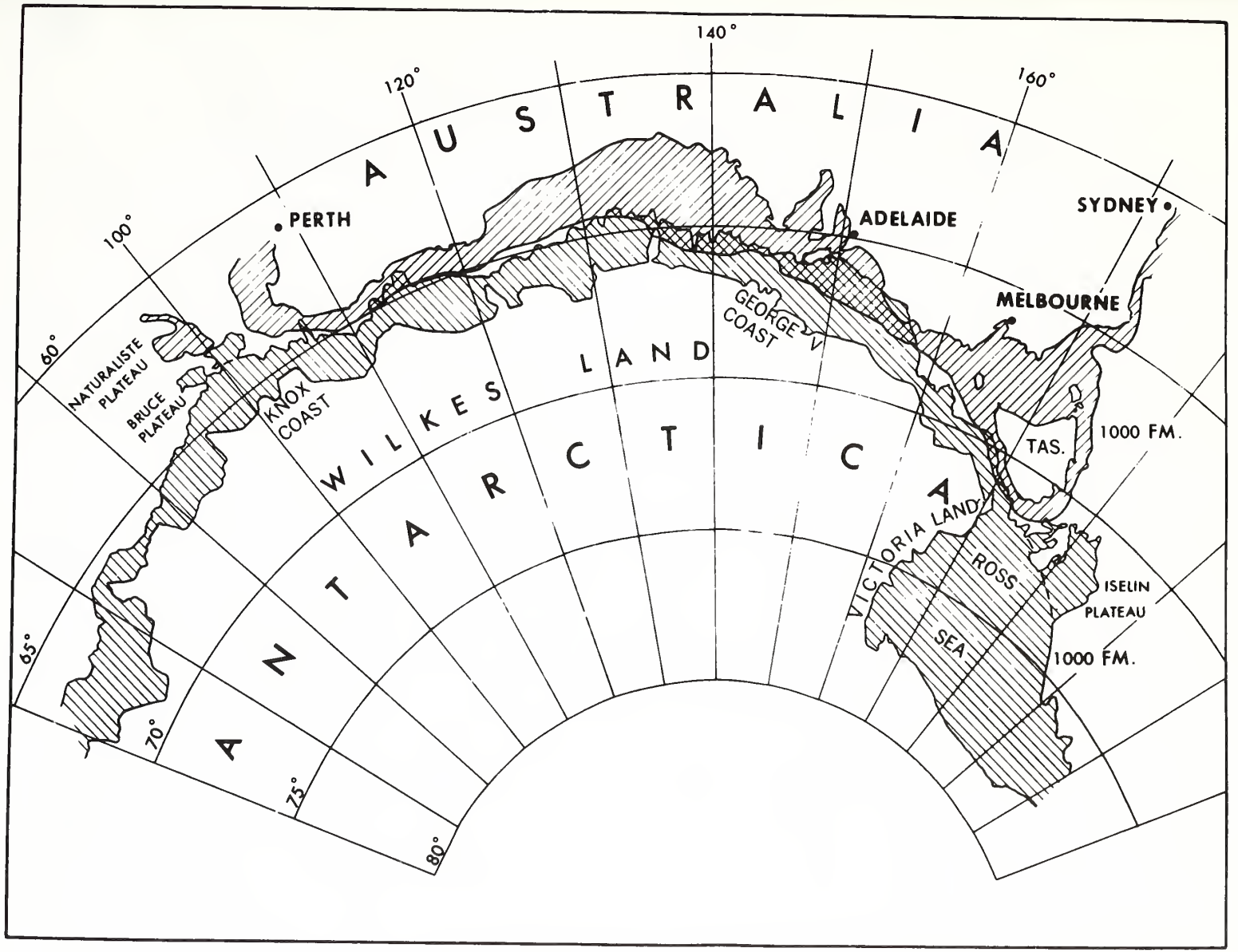
AUSTRALIA
ANTARCTICA
WILKES LAND
PERTH
ADELAIDE
SYDNEY
MELBOURNE
TAS.
1000 FM.
1000 FM.
GEORGE V COAST
KNOX COAST
NATURALISTE PLATEAU
BRUCE PLATEAU
VICTORIA LAND
ROSS SEA
ISELIN PLATEAU
140°
120°
160°
100°
60°
65°
70°
75°
80°

DIETZ .. FIG. 2

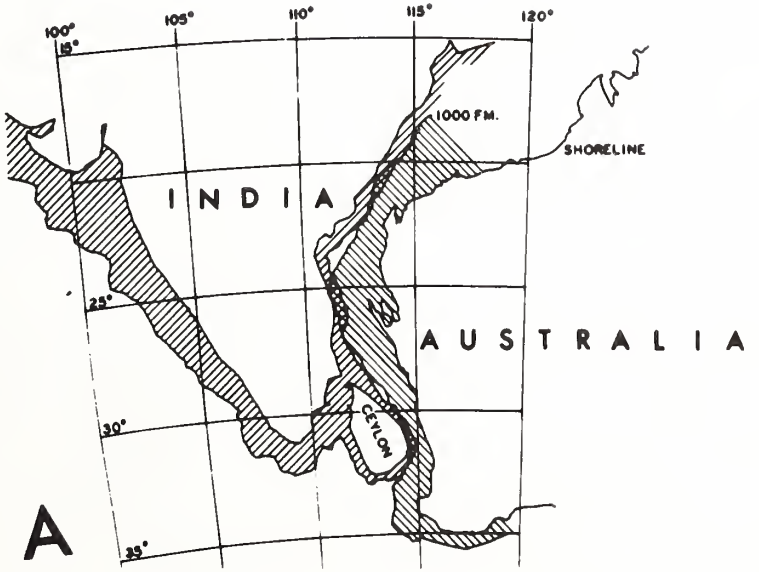
100°
105°
110°
115°
120°
15°
25°
30°
35°
1000 FM.
SHORELINE
INDIA
AUSTRALIA
CEYLON
A

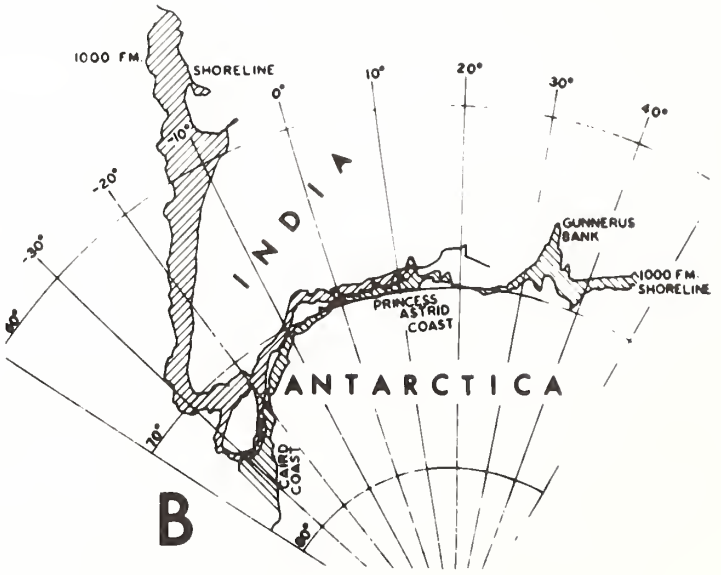
1000 FM.
SHORELINE
0°
10°
20°
30°
40°
-10°
-20°
-30°
60°
70°
80°
INDIA
GUNNERUS BANK
1000 FM.
SHORELINE
PRINCESS ASTRID COAST
ANTARCTICA
CAIRD COAST
B

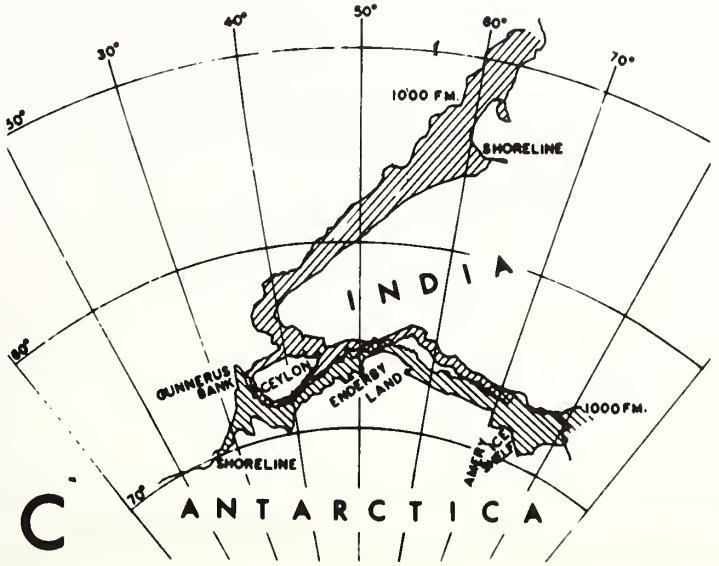
30°
40°
50°
60°
70°
50°
60°
70°
80°
1000 FM.
SHORELINE
INDIA
GUNNERUS BANK
CEYLON
ENDERBY LAND
1000 FM.
SHORELINE
AMERY ICE SHELF
ANTARCTICA
C

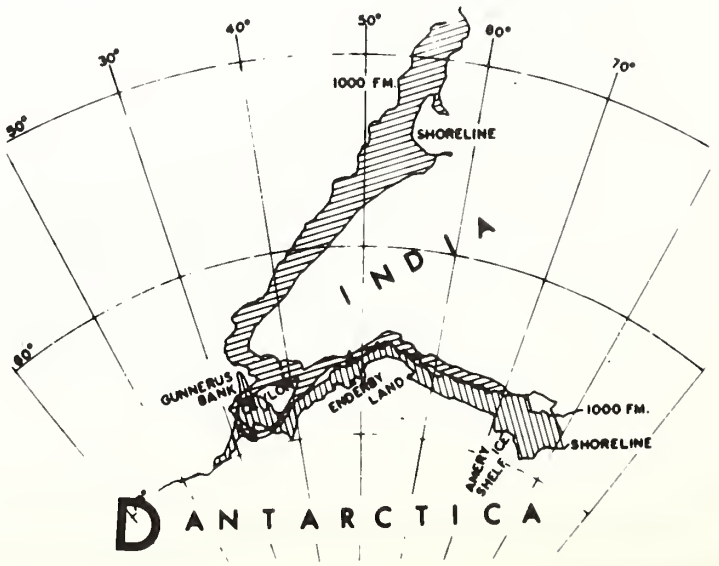
30°
40°
50°
60°
70°
50°
60°
70°
80°
1000 FM.
SHORELINE
INDIA
GUNNERUS BANK
ENDERBY LAND
1000 FM.
SHORELINE
AMERY ICE SHELF
ANTARCTICA
D

#3

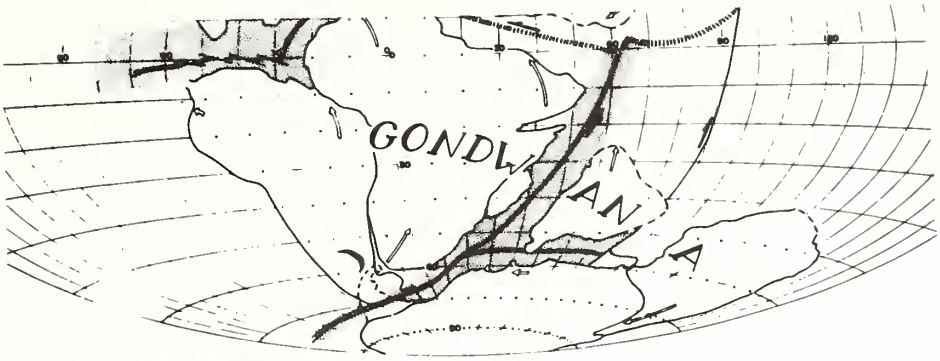

TRIASSIC -180 m.y.

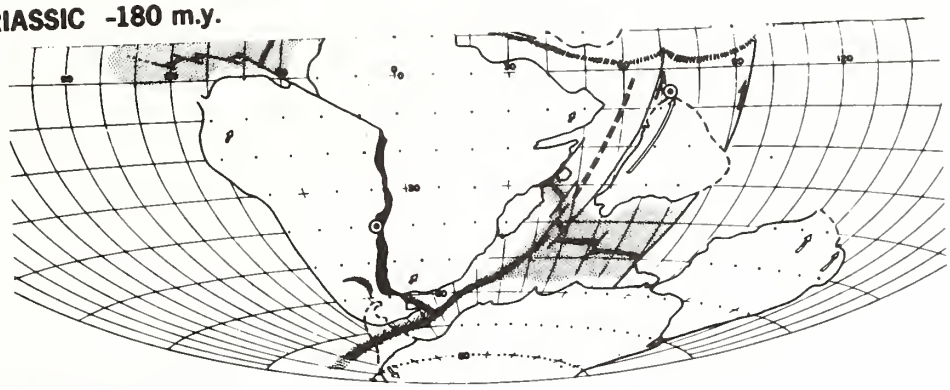

JURASSIC -135 m.y.

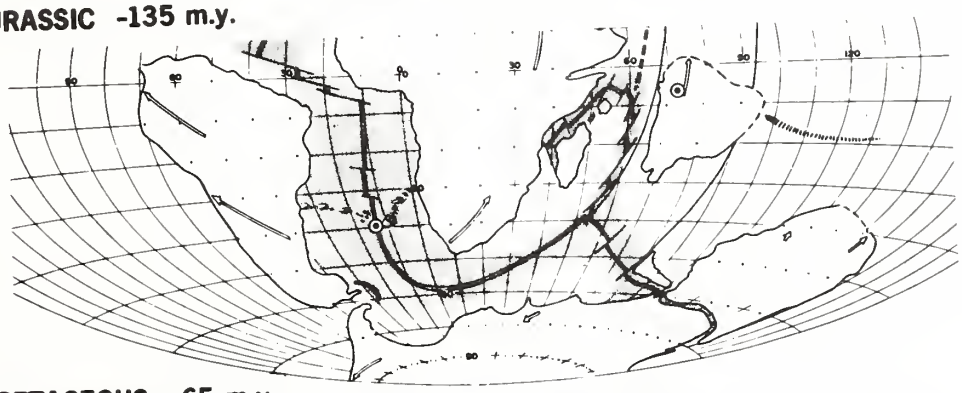

CRETACEOUS -65 m.y.

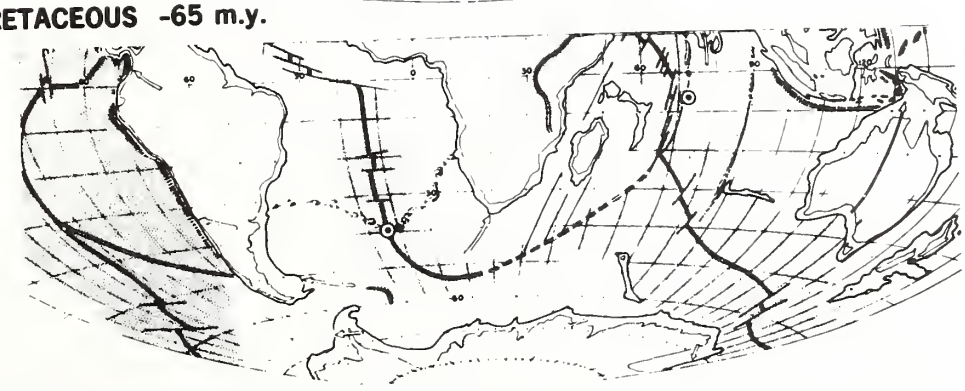

PRESENT

FIG 4

DIETZ et al.

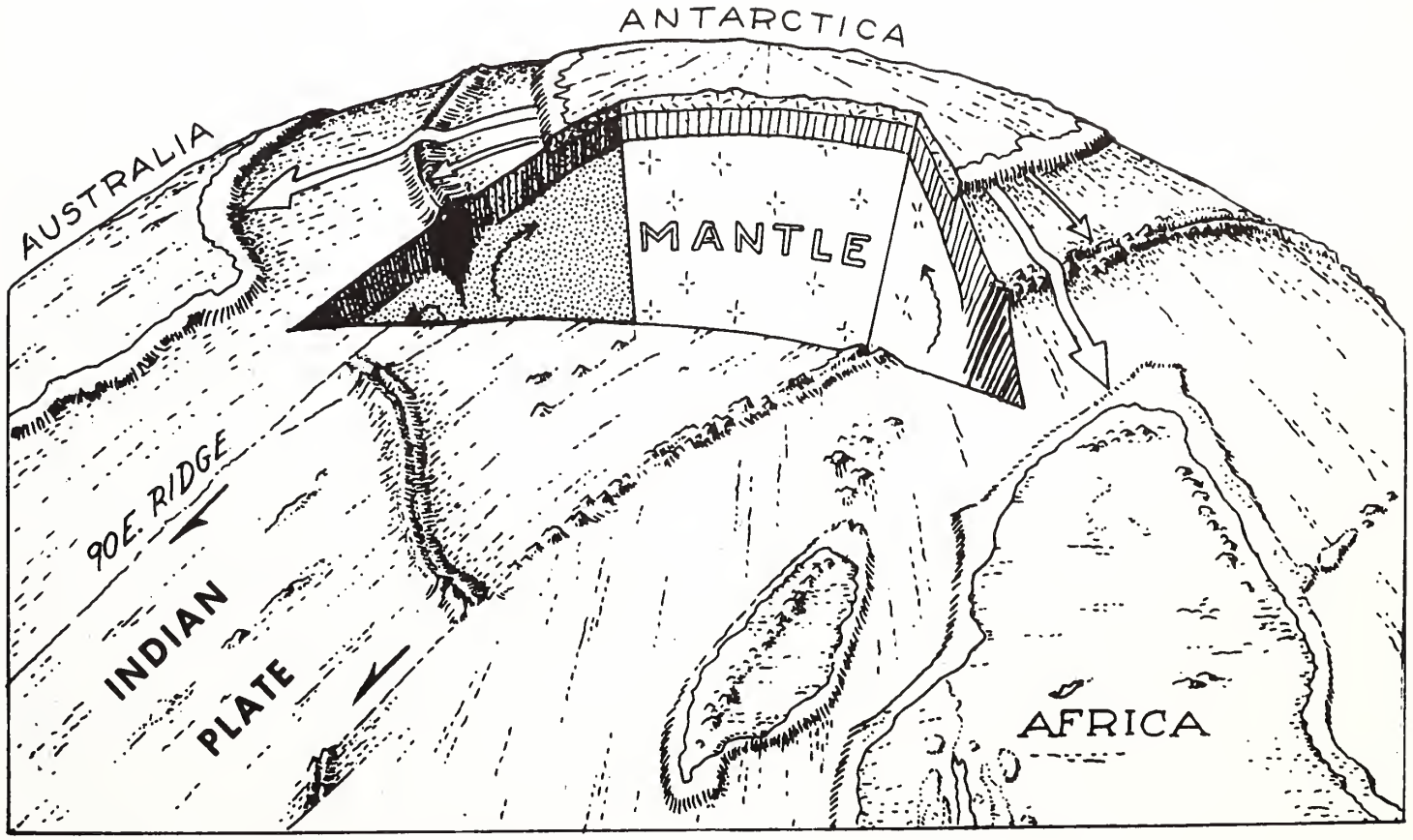

DIETZ et al. FIG. 5

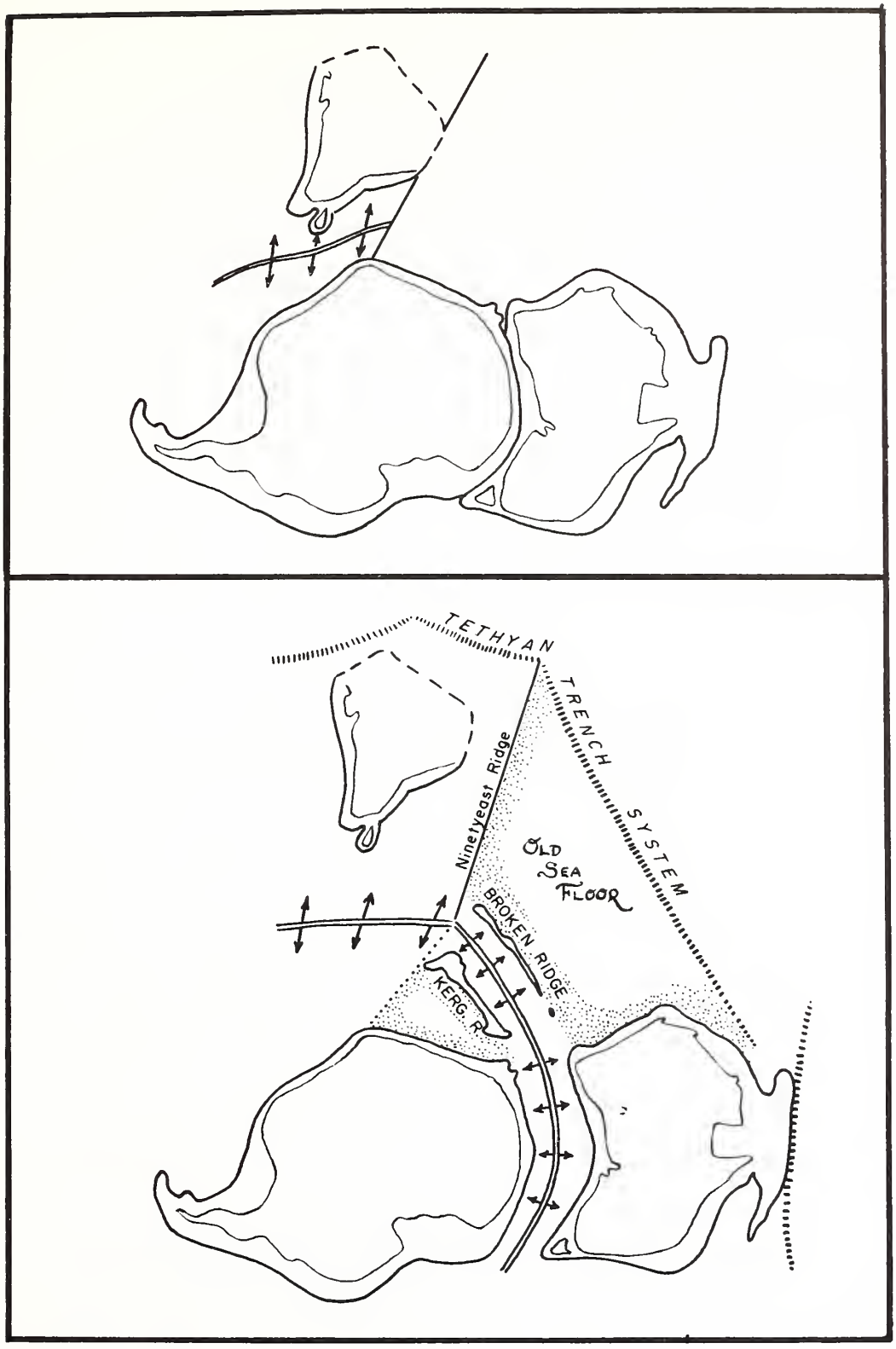

FIG 6 Dietz et al

Reprinted from SHELF SEDIMENT TRANSPORT, edited by Swift, Duane and Pilkey.

REPRINTED FOR U. S. ARMY, COASTAL ENGINEERING RESEARCH CENTER.

CHAPTER 22

Linear Shoals on the Atlantic Inner Continental Shelf, Florida to Long Island

David B. Duane,* Michael E. Field,* Edward P. Meisburger,* Donald J. P. Swift,†‡ and S. Jeffress Williams*

ABSTRACT

The inner Atlantic continental shelf from Long Island to Florida is characterized by fields of linear, northeast trending shoals. The shoals exhibit up to 30 ft of relief, have side slopes of a few degrees and extend for tens of miles. Clusters of linear shoals merge with the shoreface in water as shallow as 10 ft. Most of the shoals out to depths of 120 ft have been examined by means of seismic profiling, precision depth profiling, grab sampling, coring; current monitoring has been conducted on a few shoals. These inner-shelf sand bodies or shoals can be grouped as arcuate (inlet and cape-associated) and linear. Linear shoals may radiate from estuary mouths, as a second order structure on arcuate, inlet-associated shoals, or may occur on the open coast. Linear shoals on the open coast may be shoreface-connected or isolated. All linear shoals of the open coast form a small angle (most $< 35°$) with the coast line; most open northward regardless of presumed direction of net littoral drift. Seismic reflection profiles show the linear and arcuate cape-associated shoals to be plano-convex features, some exhibiting internal inclined bedding strcutures, resting upon a featureless, nearly horizontal stratum.

*Geology Branch, Coastal Engineering Research Center, Washington, D.C. 20016.

†Institute of Oceanography, Old Dominion University, Norfolk, Virginia 23508.

‡Present Address: Atlantic Oceanographic and Meteorological Laboratories, National Oceanic and Atmospheric Administration, 15 Rickenbacker Causeway, Miami, Florida 33149.

Marked differences exist between sediments of shoals and those of underlying acoustically defined strata, which also show local and regional changes in lithology. The underlying strata, which are occasionally exposed in troughs between ridges, range in age from 7,000 to 25,000 years old. These ages, obtained from radiocarbon analyses of shells, peat, and organic mud, indicate that formation of linear and cape-associated arcuate shoals post-dated the last transgression; hence they are all younger than at least 11,000 BP. Changes in mineralogy of the shoals parallel changes in the mineralogy of adjacent beaches. Shoreface-connected shoals have granulometric characteristics similar to the beach.

Shoreface-connected shoals appear to be presently forming in response to the interaction of south-trending, shore-parallel, wind set-up currents with wave-generated bottom currents during winter storms. In some areas sequences of shoreface-connected shoals seem to comprise effective evolutionary series whereby the process of shoal detachment by deepening and headward erosion of the landward trough is illustrated. Morphological and hydraulic evidence suggests that detached shoals continue to respond to the modern hyraulic regime of the inner shelf, with the helical flow that they induce in coast-parallel storm currents serving to aggrade their crests, and fair-weather wave surge serving to degrade them. Equilibrium shoal crest depth seems to be about 30 ft on the inner shelf; a second mode of crest depth at 50 ft may reflect a recent still-stand at that level.

INTRODUCTION

In the ultimate sense of Johnson's (1919) classic theory of marine planation, continental shelves of the world would be featureless. That the shelves are not simply a broad and gently sloping platform but are comprised of reefs, shoals, and deep channels was known to the earliest seafarers. However, it was not until the advent of acoustical hydrographic surveying techniques in the 1920s that those interested in the ocean and its bottom became fully aware of its ubiquitous irregular topography. Excellent reviews of early exploration of the shelf are provided by Schopf (1968) and by Emery (1966) who point out in particular the significance of early studies by Veatch and Smith (1939). The works of Emery (1965, 1966, 1967, 1968, 1969), and colleagues (Uchupi, 1968, 1970, Schlee and Pratt, 1972, Ross, 1970) are no less significant, for they represent the first integrated examination and interpretation of topography, surficial deposits, underlying bedrock, stream drainage, and Quaternary history.

In their pioneer analysis of the topography of the central Atlantic shelf, Veatch and Smith (1939) noted that it was traversed by channels normal to the shoreline which they interpreted as subaerial river channels. Their maps show between these channels a distinctive alternation of ridges and swales which tend to converge gradually with the shoreline toward the south. This ridge and swale topography is clearly evident in the series of bathymetric maps of the Atlantic shelf prepared by Uchupi (1968) (Figs. 171, 172, 173). Locations of these and other figures used in this paper are shown in Fig. 170. Although Uchupi's maps illustrate the dominance of the ridge and swale topography on the entire shelf (Figs. 171, 172, 173), the emphasis of this paper will be placed on the inner shelf as the zone of generation of this topography. Veatch and Smith (1939, P40) concluded that this topography "is due to wave planation, with terraces, succes-

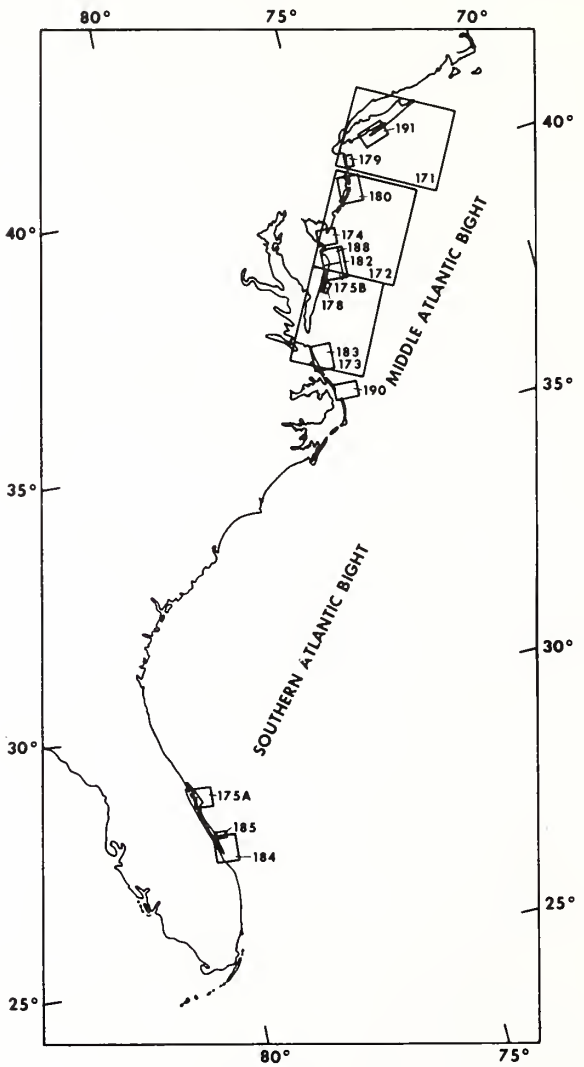

Figure 170.
Index of illustrations utilized in this paper.

sive barrier beaches and distinctive forms representing progressive steps of an advancing sea." This interpretation of the ridge and swale topography has been adhered to by many subsequent investigators, including Shepard (1963), Emery (1966), and Garrison and McMaster (1966).

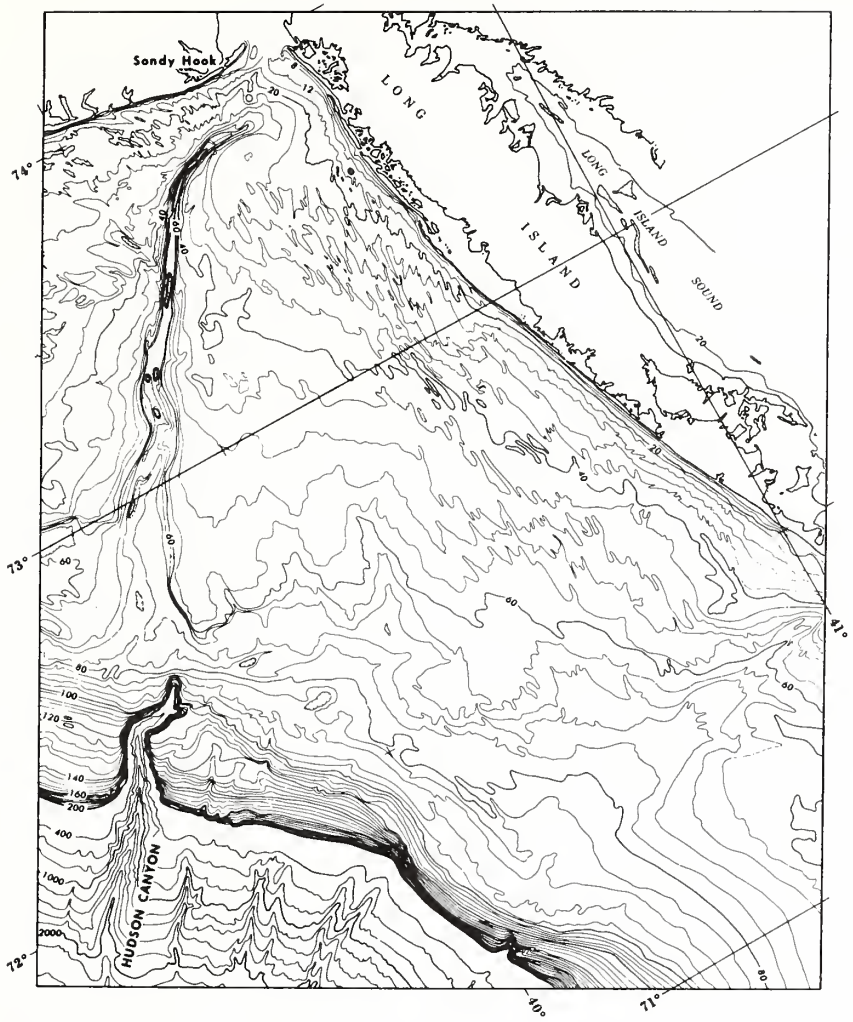

Figure 171.

Topography of the northern portion of the middle Atlantic Bight showing northeast trending bathymetric fabric off New Jersey and the southeast trending fabric south of Long Island. Contour interval is 4 m. From Uchupi (1968).

A variant hypothesis, concerned primarily with the inner-shelf ridges, correlates the ridges with subaerial beach ridges on the adjacent coast and interprets them as relict from a time of lower sea level earlier in the Pleistocene (Sanders, 1962; Kraft, 1971a, Fig. 6; Dietz, 1963, Fig. 13; Hyne and Goodell, 1967).

Another school of thought has suggested that the ridge topography of the

Figure 172.

Topography of the central portion of the Middle Atlantic Bight showing pervasive northeast bathymetric fabric. Contour interval is 4 m. From Uchupi (1968).

shelf is an assemblage of presently or recently active marine bedforms. Moody (1964) studied ridges on the shoreface of the Delaware coast and determined that they shifted position during the Ash Wednesday storm of 1962. He suggested that these ridges were of modern hydraulic origin, and that as the shoreface retreated, they were isolated and abandoned, to form the shelf ridge topography.

Uchupi (1968) commented in his study of both inner and outer shelf morphology that if the beach-ridge hypothesis was correct, then "there has been a drastic

Figure 173.

Topography of the southern portion of the Middle Atlantic Bight showing pervasive northeast bathymetric fabric irrespective to changes in shoreline orientation. Contour interval is 4 m. From Uchupi (1968).

reorientation of the shoreline in recent times," since ridge trends intersect the modern shoreline at an angle. He also suggested that the topography was a response to the modern hydraulic regime. However, Uchupi (1970) has more

recently returned to a tentative strand plain hypothesis. Schlee and Pratt (1972) refer to the "sets of sand ridges" (p. H33) and "systems of sand waves" (p. H36) and imply an hydraulic, post-transgression origin. McKinney and Friedman (1970), examining a portion of the Long Island shelf, concluded that since the majority of the ridges trended obliquely to the regional contours, they were instead stream interfluves.

It is clear from this brief review of pertinent studies that the physical characteristics, as well as relative age and mode of generation of these inner-shelf features are neither well defined nor agreed upon. Understanding the genesis and behavior of the ridge and swale topography is crucial to any hypothesis concerning the Holocene modification of the shelf surface and bedload transport. Effective planning for any use of the shelf surface also requires this understanding.

SCOPE AND TECHNIQUES

In 1964 the Inner Continental Shelf Sediment and Structure (ICONS) Program was initiated by the Coastal engineering Research Center (CERC) to survey subbottom structure and sediments of portions of the United States inner continental shelf. Objectives of the program are: delineation of sand bodies potentially available and suitable for beach nourishment; better understanding of sedimentation on the inner continental shelf as it pertains to supply of sand to beaches; changes in coastal and shelf morphology, longshore sediment transport, inlet migration-stabilization, and navigation; and better understanding of Quaternary shelf history. ICONS data pertinent to information contained in this paper are approximately 8000 mi of continuous seismic profiles and more than 800 10-30 ft cores from portions of the inner continental shelf of Long Island, New Jersey, Delaware, Maryland, Virginia, North Carolina, and eastern Florida. This coverage has permitted some examination of most linear sand bodies on the inner continental shelf of the eastern United States. Detailed study including measurement of water current velocity and direction along a portion of the Virginia Coast was carried out by one of the authors (Swift).

TYPES AND DEFINITION OF SHOALS

Our studies have been confined essentially to water depths of less than 130 ft (40 m). Within this depth range on the continental shelf there are numerous shoals, defined as "an elevation of the sea bottom comprised of any material except rock or coral . . ." (United States Army Corps of Engineers, 1966, p. A-31). We identify two broad classes: arcuate and linear. Two subgroups of each are also recognized: arcuate shoals we subdivide as inlet- and cape-associated (Fig. 174a, b), and linear shoals as shoreface-connected and isolated (Fig. 174c).

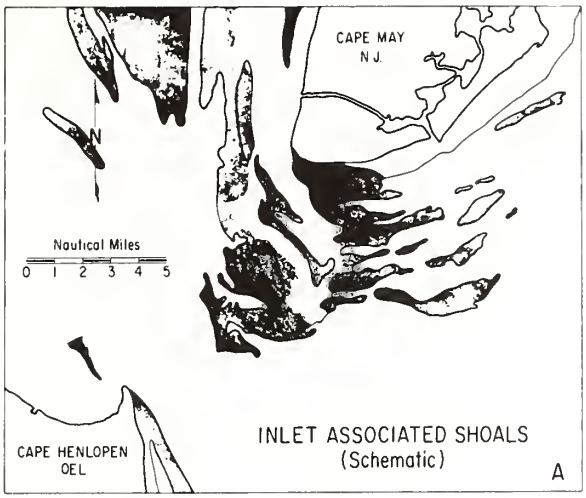

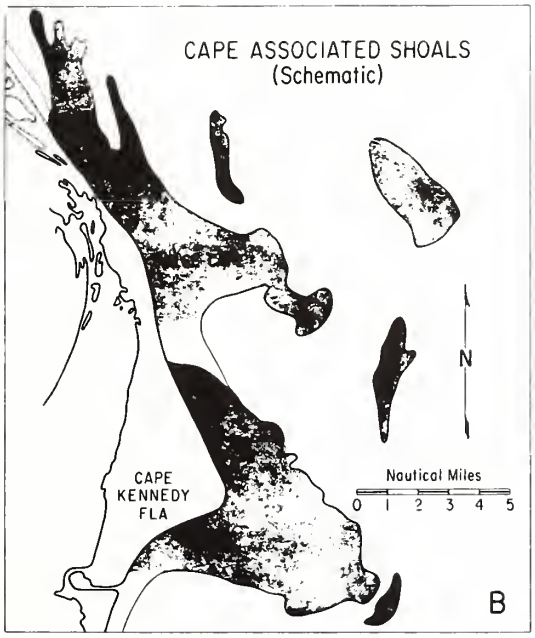

Figure 174.

Schematized plan view of major shoal types of the U.S. Atlantic coast. Types identified are : (a) inlet-associated shoals; (b) cape-associated shoals; and (c) linear shoals. The linear type occur as both shoreface-connected and isolated. (Shoal form enhanced by shading.)

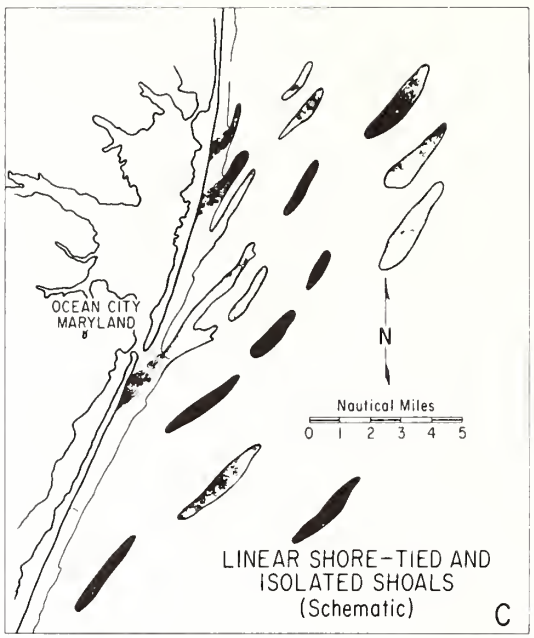

Arcuate inlet-associated shoals (Fig. 174a) are typified by those discussed by Ludwick (1972) and Oertel and Howard (1972). Arcuate cape-associated shoals are those such as Chester and southeast shoals at Cape Kennedy (Field and Duane, 1972) which have a hammerhead shape in plan view (Fig 174b). Linear shoals are defined as linear, positive features which exhibit at least 10 ft of relief between the crest and the surrounding surface. Shoreface tied shoals are those outlined by, but landward of, the isobath that defines the base of the shoreface (usually 30 ft). Isolated shoals are those lying on the inner continental shelf which display no topographic ties to the shoreface. Although linear shoals are known from other coasts, particularly the Gulf Coast, present discussion will be restricted to linear shoals on the United States east coast, south of Long Island. The distribution of linear and arcuate inlet and cape-associated shoals on the Atlantic Inner Continental Shelf is shown on Fig. 175.

CHARACTERISTICS OF LINEAR SHOALS: A SURVEY

General

At the present stage of our studies of linear shoals, we are concerned only with those shoals having a length of at least 3000 ft. Isolated shoals are those meeting the minimum length requirement and having a relief of at least 10 ft.

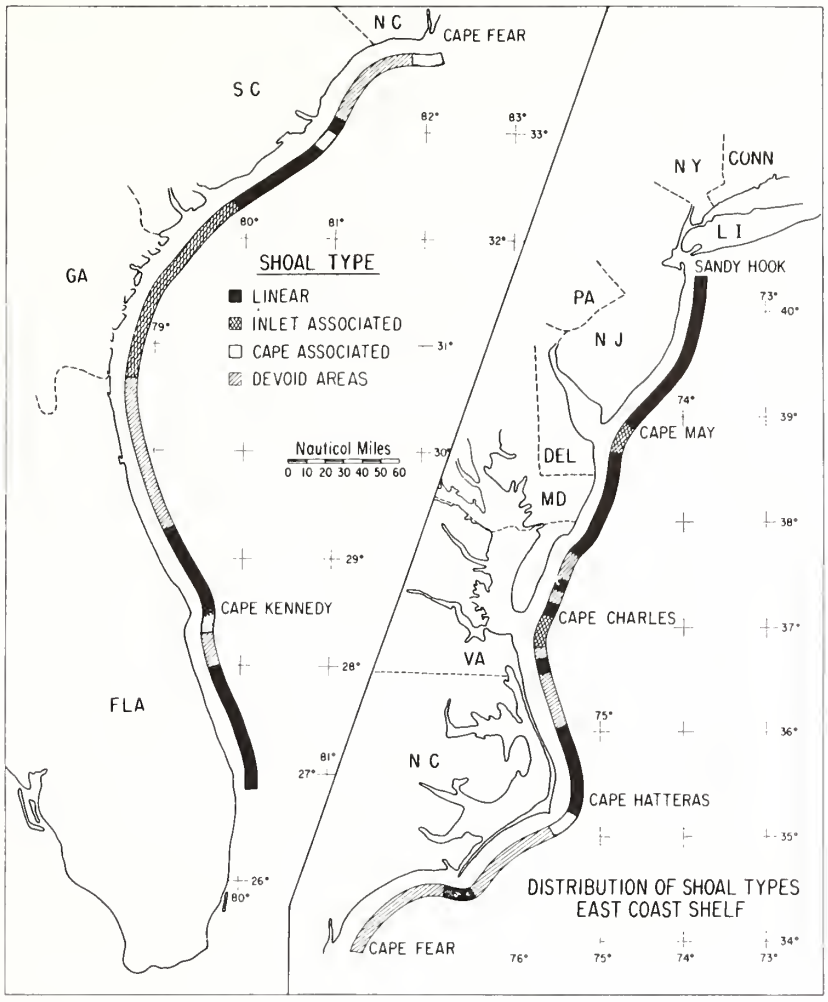

Figure 175.

Distribution of major shoal types on the United States Atlantic coast from Sandy Hook, New Jersey, to Palm Beach, Florida.

Shoals defined by a seaward excursion of the 30 ft depth contour of the shoreface are termed shoreface-connected.

All linear shoals in the area from northern New Jersey to Palm Beach, Florida form a small acute angle with the coastline. Nearly all shoals open northward regardless of presumed direction of net littoral drift. Seismic reflection profiles show that the linear cape-associated shoal complexes (such as those at Cape Kennedy, Florida and Cape Fear, North Carolina) to be plano-convex features

resting upon a virtually featureless, nearly horizontal stratum. Marked differences exist between sediments of the shoal and those of the underlying sonic reflector, which itself undergoes local and regional changes in lithology. Sediment of the shoals is nearly totally silicate sand, except those at and south of Cape Kennedy, Florida, where carbonate skeletal sand becomes an important constituent.

In order to obtain to obtain a quantitative picture, data on six geometric properties were gathered using USC&GS 1200 Series Charts as data base. Characteristics, keyed to the highest point on the shoal, were: (a) water depth; (b) shoal length [of the 10 ft relief contour]; (c) shoal width (end points of a line passing through highest point and terminating on the 10 ft relief contour); (d) distance latitudinally from shore; (e) azimuth; and (f) the angle of the shoal with the adjacent shore-line trend.

Approximately 200 shoals were analyzed. In the course of the analysis, it became apparent that some of the operational definitions were redundant, and for some of the criteria, not precise enough to provide good repeatability among the five operators involved. Therefore, only clearly unambiguous criteria are discussed; that is, water depth, azimuth, and angle (preceding items a, e, f).

A histogram of water depth over shoal peaks is depicted in Fig. 176a. Two modes, 20 to 30 ft, and 40 to 55 ft are clearly evident. A third is suggested in water deeper than 80 ft, near the depth limitations imposed in this study. That the shoals continue into greater depth is clearly indicated in the following study by Swift et al. (1972), as well as by earlier workers such as Veatch and Smith (1939), Shepard (1963), and Uchupi (1968).

Major axis of the shoals has a mean azimuth value of 32° with a standard deviation of 25° as depicted by the historgram in Fig. 176b. The histogram suggests two modes, at apprximately 5° and 35°, with a third mode possibly located at approximately −30°. The correlation between water depth and shoal azimuth is nearly zero indicating no apparent linear dependence. Histograms showing the deviation of the shoal axis from shoreline axis and the azimuth of shorelines adjacent to observed shoals, shown in Figs. 176c and 176d respectively, will be referred to later.

Semi-diurnal tide range over the study area measured at the coast varies somewhat but is generally 3 to 7 ft. In the classification of Davies (1964) the tidal range discussed above lies within the microtidal range (upper limit of 6.5 ft). With a tide range in the micro scale or near the lower limit of the meso scale, Davies (1964) suggests that tide-induced currents will be of negligible significance in sedimentation processes. Some calculations based on open coast tide values (United States Dept. of Commerce, 1970) for Maryland, North Carolina, and central Florida, and the progression of the tidal wave, indicate open coast tidal currents are insignificant. This tends to corroborate the conclusion of Davies (1964) and would allow extrapolation of Davies' statements to other portions of the study area.

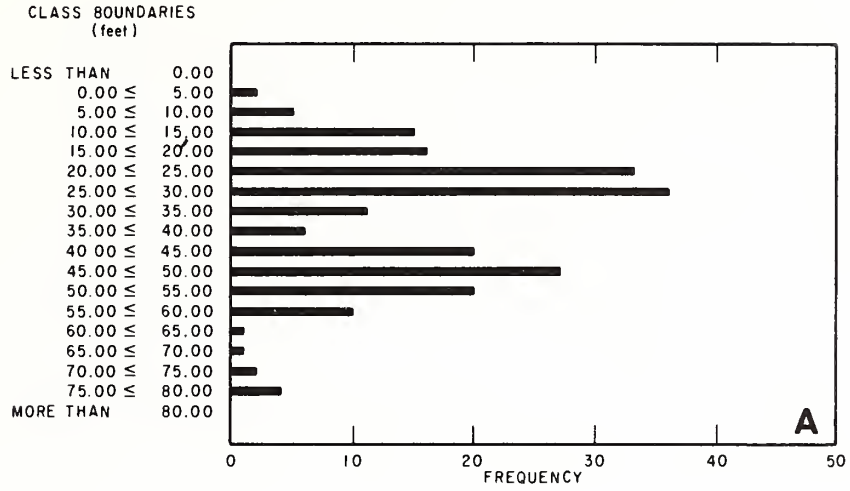

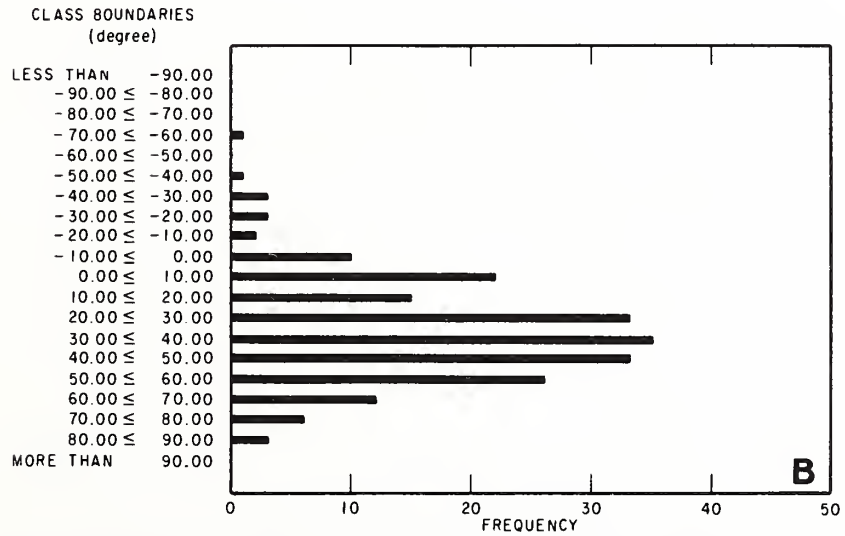

Figure 176.

Group characteristics of over 200 inner continental shelf linear shoals. Parameters plotted by frequency

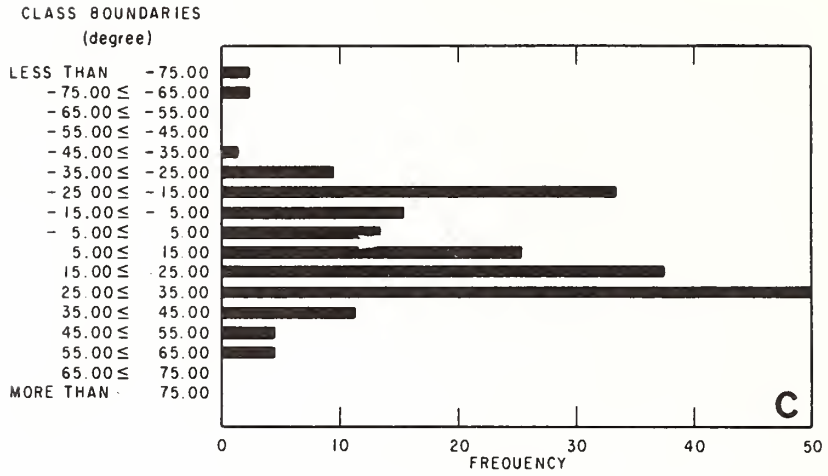

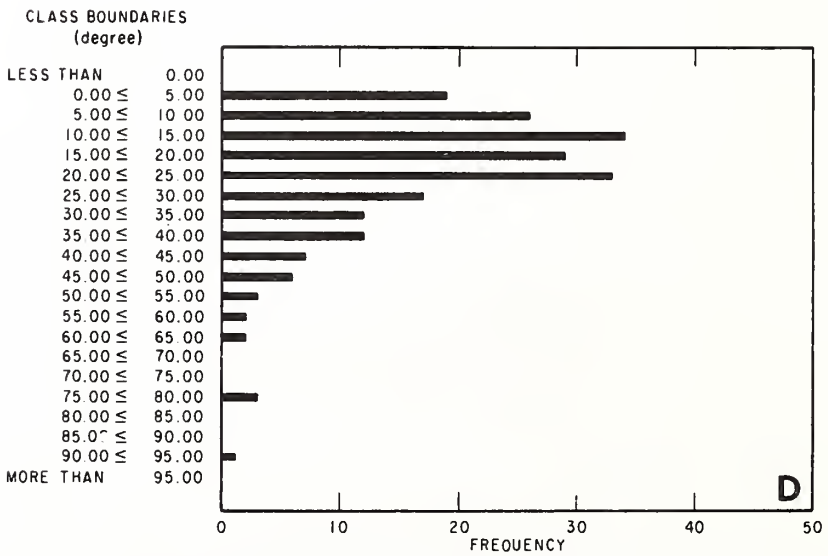

of occurrence are: (a) water depth over shoal crest; (b) azimuth of shoal axis; (c) azimuths of shorelines adjacent to shoals; and (d) angular deviation of shoal axis trend with coastline trend.

Surface drift currents in the study area vary seasonally in intensity and direction (Bumpus and Lauzier, 1965). Maximum velocity reported is 0.86 ft sec^{-1} (26.2 cm sec^{-1}).

Wave climate on the inner shelf of the study area is discussed by Harris (1972). From his data it can be seen that for most of the area, wave heights in excess of 5 ft occur only 10% of the time, and waves higher than 8 ft occur only 1% of the time.

We will follow this introduction to the dimensions and hydraulic environment of the linear shoals with a more detailed description of selected shoal areas. Regional patterns of shoals in the best known sector, the Middle Atlantic Bight, will be surveyed. Following will be a discussion detailing those areas for which we have the most data: the shoal fields of central New Jersey, Maryland, southern Virginia, and the south and central east Florida coast.

Inner Shelf Shoals and Coastal Compartments of the Middle Atlantic Bight

The portion of our study area for which the most bathymetric and geological data are available, from the literature and from our own efforts, is the Middle Atlantic Bight, between Cape Cod and Cape Hatteras. Within this sector it is useful to examine the related patterns of coastline and inner shelf morphology.

Shoreface-connected, isolated, cape-associated, and inlet-associated shoals occur in repeating patterns along four major coastal compartments of the Middle Atlantic Bight (Fig. 177). These compartments are delimited by the estuaries of Chesapeake Bay, Delaware Bay, New York Harbor, and Block Island Sound. Each compartment contains an eroding headland to the northeast. Because of the prevailing northeastern wave approach, recurved or cuspate barrier spits have grown on the north sides of the headlands. A seaward-convex barrier arc, consisting of a spit and successive barrier islands, has grown south from the headlands. Beyond the proximal barrier arc lies a less continuous distal barrier arc, generally seaward-concave, and separated from the proximal arc by a cuspate foreland, barrier-overlap inlet, or similar discontinuity.

Shoreface-connected shoals appear in this scheme as seaward extensions of the lower shoreface. The term shoreface is used herein as defined by Price (1954) as: "a relatively steep but short concave surface". Price's definition was made in reference to his idealized shelf equilibrium profile. Our usage of shoreface is geomorphic without necessarily implication as regards equilibrium. Despite local variation, a systematic scheme of distribution of shoreface ridge systems is discernable.

North-trending spits and cuspate forelands are associated with tide-dominated foreshores. An ebb tidal delta lies at the tip of Montauk Point (eastern end of Long Island Coastal Compartment). Sandy Hook and Cape Henlopen, the north-trending spits of the New Jersey and Delmarva Coastal Compartments, have linear, tide-built shoals extending southeast from their tips, between flood and ebb dominated channels. Hen and Chicken shoals, attached to Cape Henlopen

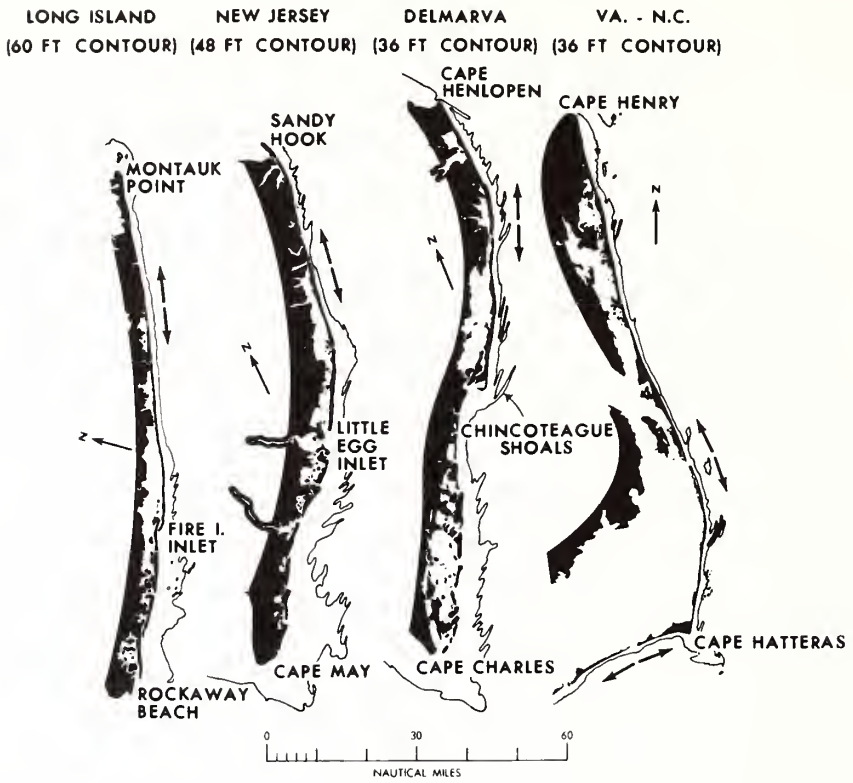

Figure 177.

Coastal compartments and shoreface-ridge systems of the Middle Atlantic Bight, as defined by the 60 ft contour off Long Island, the 48 ft contour off New Jersey, and 36 ft contour off the Delaware-Maryland-Virginia compartment and the Virginia-North Carolina compartment. Arrows indicate major littoral drift directions.

is large enough to appear in Fig. 177. A poorly defined "submarine tidal delta" extends east and south from Cape Henry (Payne, 1970).

The mainland beaches of the eroding headlands may be smooth (Long Island, North Carolina-Virginia coastal compartments), or may exhibit diffuse systems of wide angle (45° or greater) shore-connected shoals (New Jersey, Delmarva; Fig. 177). The proximal, seaward-convex barrier arcs tend to have shoreface-connected shoals grouped into more or less coherent fields. The fields tend to occur immediately south of gentle convexities in the shoreline (Fig. 177). Well-developed fields of shoreface-connected and isolated shoals generally occur adjacent to the barrier overlap, where inlet or cape-associated shoals separate the proximal from the distal barrier arcs (Figs. 177, 178). The shoal field corresponding to this category for the Virginia-North Carolina coastal compartment is Diamond Shoals, a classic cape-associated shoal system extending from Cape Lookout that will be discussed in the next chapter (Swift et al., 1972a).

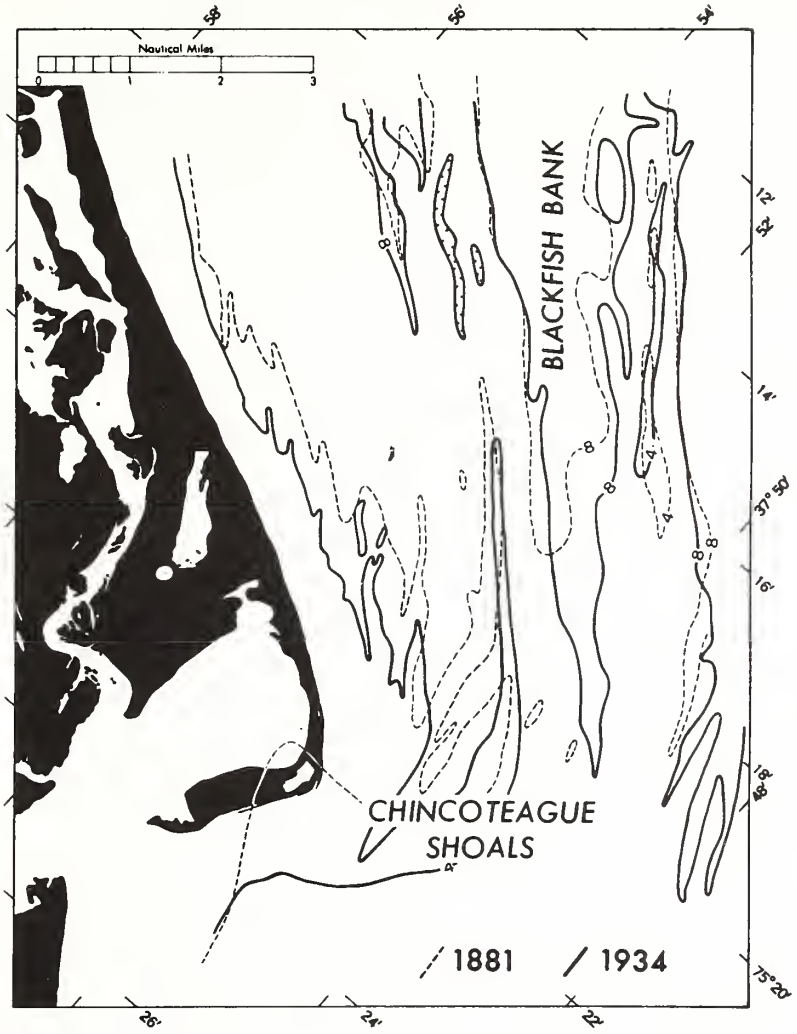

Figure 178.

Chincoteaque shoals off the southern end of Assateague, Md. Note the net southwestward movement as indicated by surveys in 1881 and 1934. Shoreline is from the 1934 survey. Isobaths are in fathoms.

The distal seaward-concave barrier arcs are characterized by a broad, gentle shoreface as indicated by the characteristic contour in Fig. 177. This is particularly true in the case of the look-alike New Jersey and Delaware-Maryland-Virginia (Delmarva) coastal compartments. The zig-zag nature of the contour indicates that linear shoals are present. However, they are so subdued (side slopes of

less than 2° and heights of 10 ft or less) and the slope of the sea floor is so gentle, that it becomes difficult to characterize them as either shoreface-connected or isolated. The broad extent and gentle slopes of the shoreface of the distal barrier arcs suggest that these portions of the sea floor are comprised of markedly finer sand than are the steep narrow shorefaces of the coastal compartments northern sectors. Textural data supporting such a coast-wise grain-size segregation are available for the New Jersey coast (McMaster, 1954), and the inner Virginia Carolina Shelf (Swift et al., 1971).

The Long Island, New Jersey, and Delmarva coastal compartments terminate with inlet associated shoals which radiate seaward from the north sides of estuary mouths. In Chesapeake Bay, this is the Bay-Mouth Shoal described by Ludwick (1972). In Delaware Bay, it is Overfall Shoal (Fig. 174a) and associated shoals (Jordan, 1962). Here the ridges are structured by tidal currents into intricate ebb and flood channel systems. A detailed map of lower New York Bay (Veatch and Smith, 1939; plate 10) shows that Long Island also has an inlet-associated shoal off its western end. The distal portions of these tide-built ridges swing northeast to merge with the inner shelf ridge and swale topography.

New Jersey Inner Shelf Shoals

The northern coastal region of New Jersey has a rather steep, strikingly regular, and narrow shoreface (Fig. 179) with an average width of 2100 ft. Linear shoals are isolated from the coast by approximately 2.5 n mi; Shrewsbury Rocks shoal is an exception. It can be traced from the shoreface out to about 6.5 n mi where it is truncated by the head of the Hudson Canyon (Fig. 171). The shoals vary in length from 1 to 3 n mi with the exception of Shrewsbury Rocks, and have a mean width of 1500 feet. Water depth above shoal crests approximates 30 to 60 ft with overall shoal relief of 10-35 ft. All of the shoals have their long axis oriented east northeast. They form an angle of 30° to the coastline in the Barnegat section and 30° to 85° in the Asbury Park-Long Branch sector (Figs. 179, 180). The shoals tend to be nearly symmetrical. Where asymmetry occurs, southern flanks are usually steeper, except where shoreface-connected shoals join the shoreface; here the northern, inshore flanks are steeper. Isolated shoals tend to exhibit a longitudinal asymmetry as well, with peaks occurring toward the southern ends of the crestlines.

High resolution seismic reflection records show that shoals off the Shark River Inlet are underlain by two shallow, gently southeast-dipping strata. Poor record quality prohibits resolution of acoustic reflections below 100 ft and shoal interiors appear opaque and featureless. However, coast morphology and bathymetric fabric of northern New Jersey suggest that coastal plain Cretaceous and Tertiary strata crop out on the sea floor and are covered by only a relatively thin overburden of sand and gravel (Williams and Duane, in prep.). In the Long Branch-Asbury Park sector, a reticulate pattern of ridges appears (Fig. 179). East-

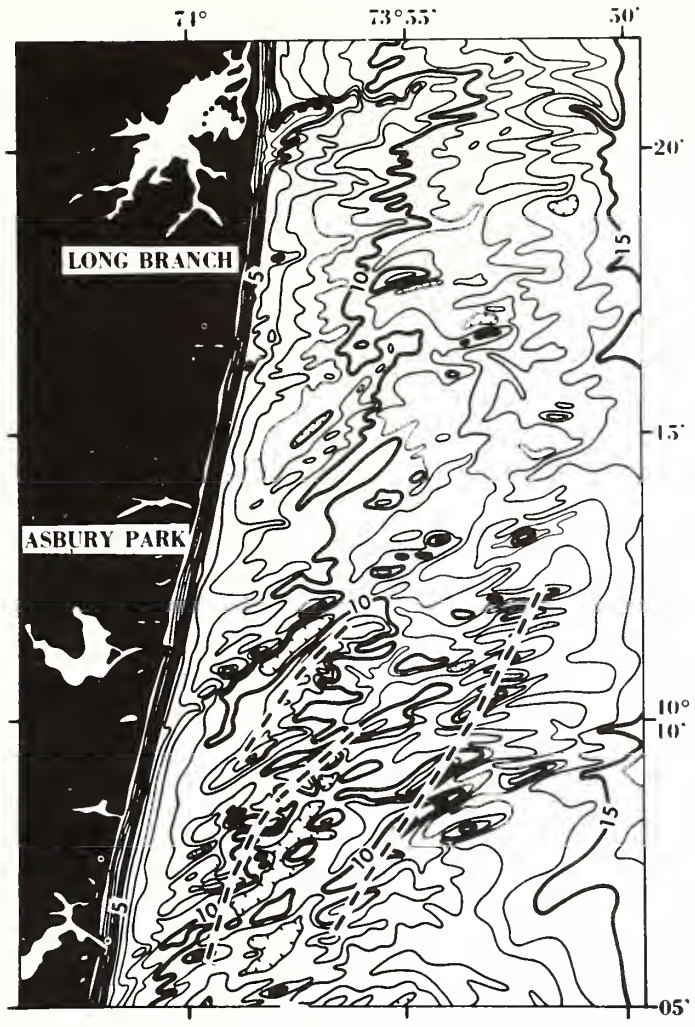

Figure 179.

Northern New Jersey shoreface region showing small linear ENE trending shoals superimposed on a NNE lineation (dashed lines) that reflect possible structural control. Contour interval is one fathom.

northeast trending ridges occur en echelon along at least two north-northeast axes. These axes are nearly parallel to the New Jersey coast and also to shelf-floor cuestas farther offshore (Swift, 1972). It seems probably that in this area, the ridges are at least in part attributable to an erosional origin. The erosion may have been marine, since the reticulate pattern bears no relationship to the adjacent subaerial drainage pattern (Fig. 171). Houbolt (1968) has described sand ridges of

this sort on the floor of the North Sea that are maintained by marine processes and form a continuum from wholly constructional forms to wholly erosional, tide-sculpted forms.

Study of northern New Jersey surface and subsurface shoal sediments from cores indicates that the shoals are composed of medium-grained, polished, well-sorted, quartzose sand. These shoals are superimposed on a thin veneer of coarse, poorly sorted, iron-stained and pitted quartz and glauconite, overlying a substrate of fine-grained sands, silts, and clays. This substrate change occurs at approximately the depth of the uppermost sonic reflector. The unconsolidated sediment cover of these northern New Jersey ridges has been shown to be a combination of Pleistocene outwash from the north and material derived from land erosion to the west (McMasters, 1954; Williams and Field, 1971).

In marked contrast to northern New Jersey the linear shoals from Barnegat Inlet south to Cape May are longer and more abundant (Fig. 180). The shoreface is broader and more irregular than to the north and a number of the shoals are shore tied with the 20 or 30 ft contour. Mean depths to shoal crests are 25 to 30 ft and except for shoreface-connected shoals, are fairly uniform over the entire shoal length. Shoreface-connected shoals have a broad base anchored to the shore and gradually taper seaward for an average length of 3.5 n mi. All the shoals form an angle of 20° to 60° with the coast and maintain a northeast and east-northeast orientation independent of the change in shoreline orientation; they show about 10 to 20 ft of relief with respect to the adjacent relatively featureless sea floor.

Geophysical coverage over the shoals offshore from Barnegat reveals the presence of an underlying, flat, featureless reflector dipping at a low angle to the southeast (Fig. 181). Selected cores on the shoal crests, flanks, and in the intervening troughs, show the shoals to be composed of clean, well-sorted, polished, medium-grained, quartz sand. Core penetration through the reflector shows it to be composed of a very coarse gravelly sand. The texture of the material and the presence of broken shell fragments suggest it is a lag deposit resulting from active marine reworking.

Field observations indicate that the Manasquan region is a littoral drift nodal area. South of Manasquan, longshore transport is southerly with an estimated volume of 50,000 yd^3 annually passing Barnegat Inlet (Fig. 180; Caldwell, 1966).

Maryland Inner Shelf Shoals

The coastal province of the Delaware-Maryland-Virginia (Delmarva) peninsula is a classic example of a headland-barrier island-spit complex that has developed through submergence, erosion, and extensive littoral transport (figs. 177, 182).

Natural borders to coastal Delmarva are the large Delaware and Chesapeake Bays to the north and south, respectively. Of the total 120 n mi of coastline, 20 mi belong to the low-lying headland-spit complex, which extends from

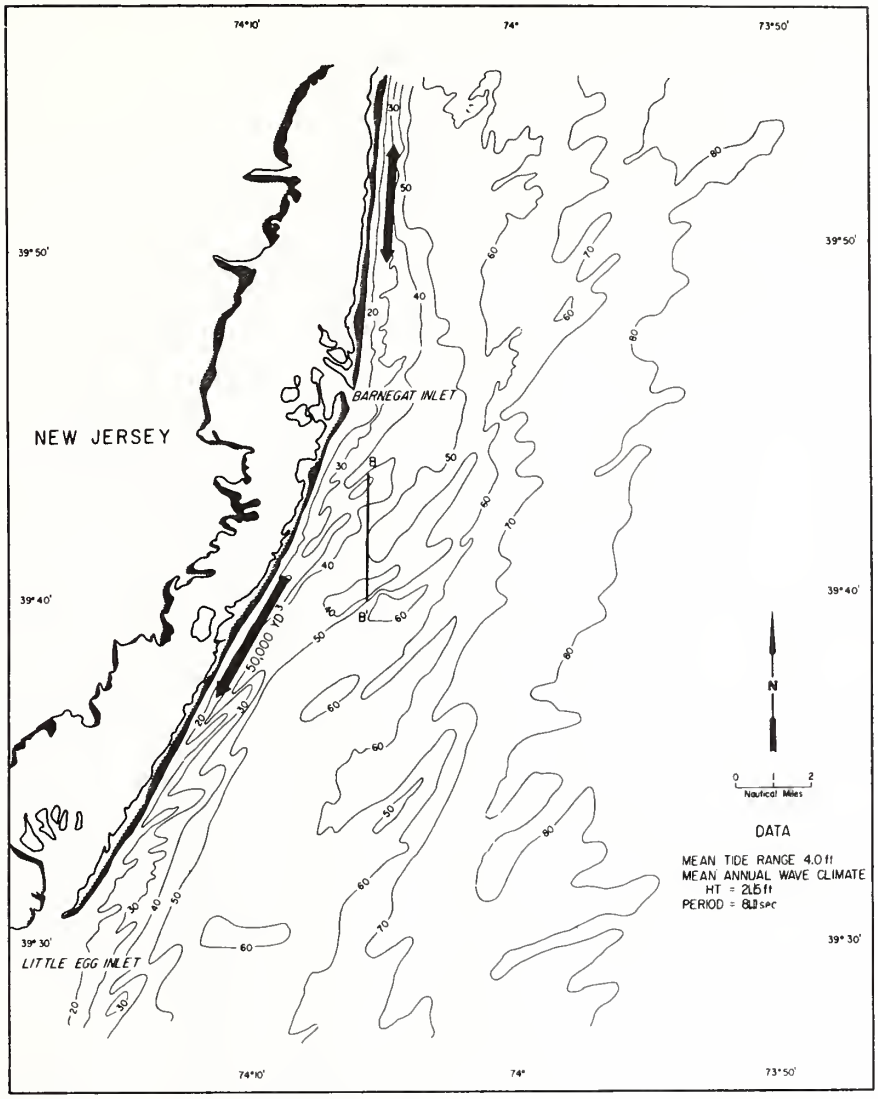

Figure 180.

Detailed bathymetry of the central New Jersey inner continental shelf at 10-ft contour interval. Direction and volume (yd^3) of littoral transport, tidal range, and mean wave characteristics are indicated. Double-headed arrow indicates nodal zone. Line BB′ is the trackline location of the Barnegat geophysical profile in Fig. 181.

Bethany Beach, just north of the Maryland-Delaware border, to the tip of Cape Henlopen and includes the bay-mouth or washover barriers that enclose Indian River Bay and Rehoboth Bay and are separated by Indian River Inlet. The

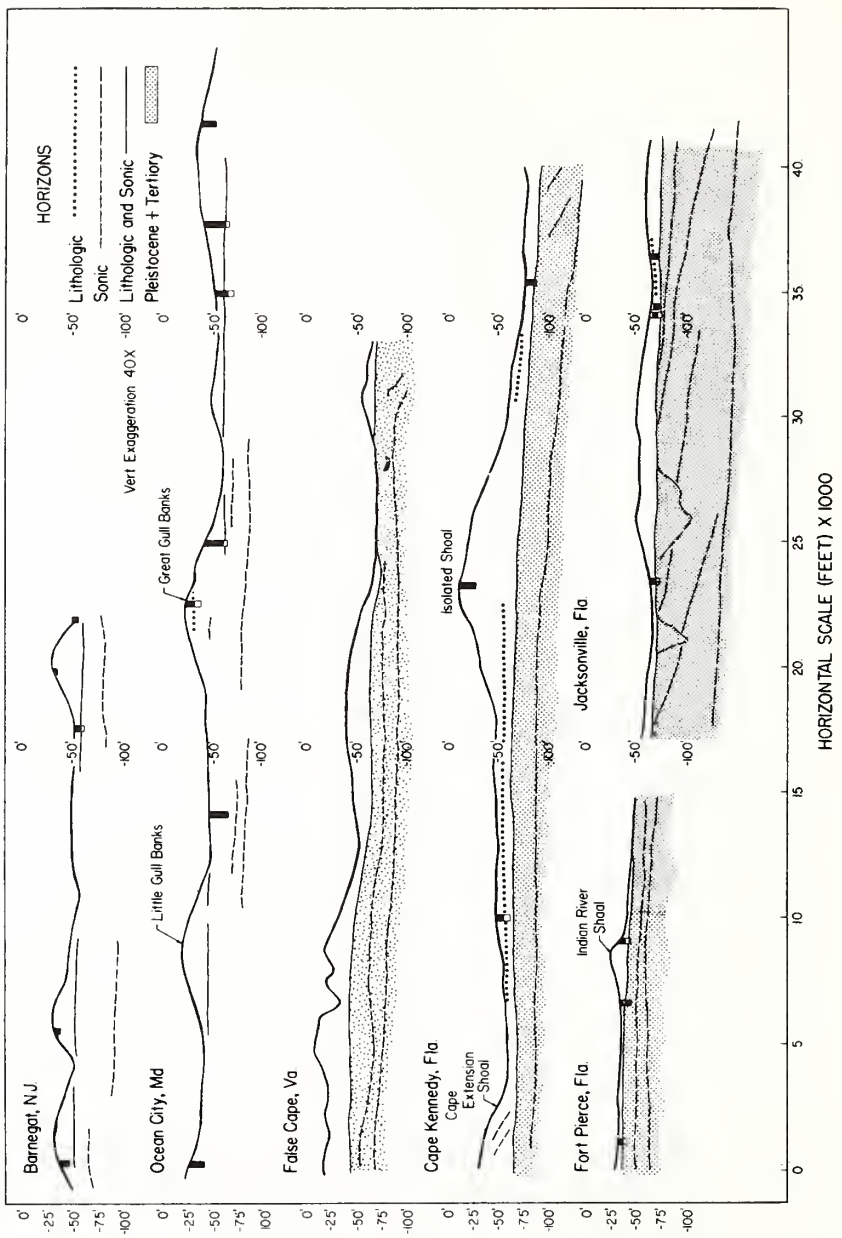

Figure 181.

Interpretative geophysical profiles across representative shoal areas of New Jersey, Maryland, Virginia, and Florida. Profile trackline locations are shown in Figs. 180, 182, 183, 184. Heavy vertical lines represent cores which define three indicated lithologic horizons.

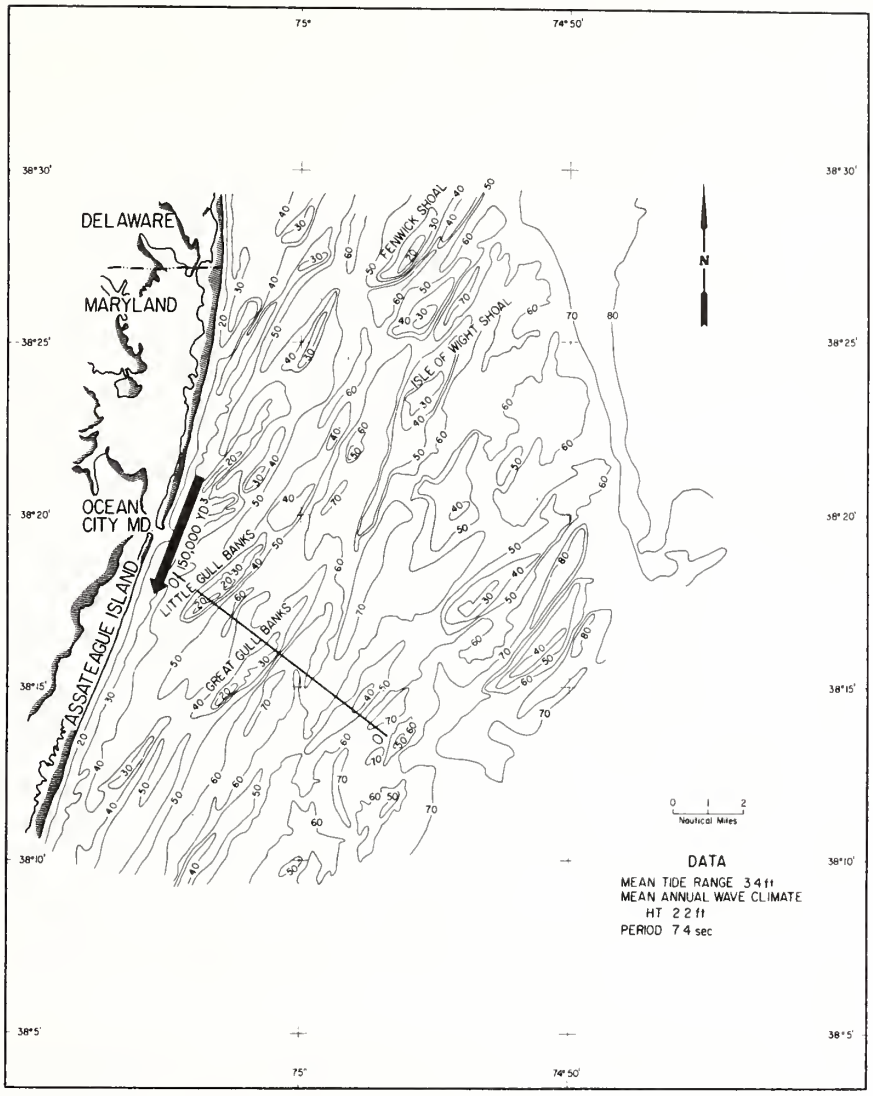

Figure 182.

Detailed bathymetry of the Maryland inner continental shelf at 10-ft contour interval. Direction and volume (yd^3) of littoral transport, tidal range, and mean wave characteristics are indicated. Line 00′ is the trackline location of the Ocean City, Md. geophysical profile in Fig. 181.

proximal barrier arc (Fenwick Island, Ocean City and Asseteague Island) is approximately 40 mi long and stretches south from Bethany Beach. At present there exists only one major inlet (Ocean City) though many such inlets have

existed within historical time. The 60 mi section of distal barrier arc south of Assateague to Chesapeake Bay entrance is dominated by numerous inlets and channels segregating small barrier islands and is similar in this regard to southern New Jersey and the sea island coast of Georgia (see Figs. 173, 177).

Littoral currents transport materials both southward and northward from the vicinity of Bethany Beach, Delaware. Going north toward Indian River Inlet, erosion has been occurring at a rate of 190,000 yd^3 annually; from the inlet north to Cape Henlopen the rate is five times as great. Littoral drift at Ocean City, Md. is estimated to be 150,000 yd^3 per annum in a southerly direction.

The central portion of the Delmarva Peninsula inner continental shelf is characterized by numerous long linear ridges or shoals trending northeast and opening at small acute angles with the shoreline (Fig. 172). From Ocean City to Indian River Inlet, the shoals become progressively smaller in scale, and become confined to the vicinity of the shoreface. Shore angles increase to 45° and greater in the Bethany Beach Shoals, while absolute orientation changes very little. A large ebb tidal shoal (Hen and Chicken Shoal) trends southeast from Cape Henlopen (Fig. 174a). South of the main Assateague Island barrier, inlet shoals are common; however the linear type under discussion in this paper are subdued and less abundant. Linear ridges between Fenwick Island and the southern end of Assateague Island display common characteristics in shape, depth, and orientation. Depths to crest range from slightly over 10 ft to nearly 50 ft; frequently shoals appear to be grouped en echelon (Fig. 181).

Transverse asymmetry (steeper southeastern sides) and longitudinal asymmetry (peaks toward the southwestern ends of crests) are better developed than on the New Jersey coast. The blunter southwestern ends of the ridges tend to curve toward the coast. The 46 shoreface-connected and isolated shoals in this region have a mean azimuth of 39° (standard deviation of 11.6°) and strike a mean angle of 18° (standard deviation of 8.9°) with the adjacent coast.

Typical subbottom structure and lithology of the shoals are demonstrated in the schematized cross section of the three well developed en echelon shoals (Little Gull Banks, Great Gull Banks and an unnamed shoal) shown in Fig. 181.

Continuous and discontinuous sonic reflectors are visible under the shoal region at shallow sediment depths (Fig. 181). At about −69 ft MLW near the shore face lies a nearly continuous reflector which dips very gently (5 ft mi^{-1} or 1/1000) seaward to about −90 ft MLW six miles offshore. Discontinuous sonic reflectors appear between the continuous horizon and the sediment-water interface. Frequently the upper horizons appear at or near the base of the shoals, suggesting a probable change in lithology. Cores penetrating to the depth of the upper horizon corroborate this lithologic change; sediments below the horizon are muds, while those above are comprised predominately of sand-sized material. Sediment distribution is related and attributable to local bottom morphology.

Inter-shoal flats and depressions contain silts and fine silty sands; shoals are composed of quartzose medium-grained sand in thicknesses up to 20 ft. Texture and composition of shoal sands are similar to adjacent beaches. Ocean City-Assateague beaches have a mean hydraulic (equivalent sphere) diameter of 0.440 mm or 1.18 phi (sieve diam. of 0.340 mm or 1.56 phi). Samples from the nearshore shoals are slightly finer, ranging in size from 0.203 mm to 0.400 mm (2.3 phi to 1.32 phi) in hydraulic diameter.

Age and environmental history of the surface and subsurface sediments are at present unknown; however, interpretation based on the literature and cursory examination of sediment data is possible. Based mainly on the sediment texture and to a lesser degree on indigenous fauna, the muds associated with the upper sonic reflector probably represent lagoonal-estuarine deposits. Lack of consolidation and desiccation in the fines suggest they represent deposition occurring landward of the barrier during the Holocene transgression. Supporting data are supplied by the radiocarbon dating of an organic mud deposit by Kraft (1971b). The sample was obtained offshore of Dewey Beach, Delaware, at a depth of −65 ft MLW and had a date of 7500 ± 135 yr BP. Depth of the sample correlates well with the depth range (−60 to −90 MLW) of the subsurface lithologic and sonic reflector from the Ocean City vicinity. We believe this strata may be a lagoonal deposit, and by correlation to Kraft's date, of Holocene age.

Detailed bathymetric mapping of the Ocean City area since 1850 has shown that the shoals have existed in their approximate location since that time. However, some migration to the south is apparent for most of the shoals. For instance, comparison of the 30 ft contour line of Little Gull Banks from surveys over the 80 yr period of 1850 to 1930 indicate the shoal center has shifted between 500 and 1500 ft to the southeast. At Chincoteaque (Fig. 178), north-south trending offshore shoals have extended themselves as much as 2 n mi to the south, while oblique, shoreface-connected shoals have migrated southeast.

False Cape, Virginia, Inner Shelf Shoals

The inner continental shelf off southeastern Virginia contains one of the best developed shoal fields between the south Florida field and Assateague Island, Maryland. Two large shore-connected shoals and one large isolated nearshore shoal off the False Cape, Virginia, area (Fig. 183) have been the subject of detailed study. North and east of these shoals the Virginia shelf as far north as Cape Henry contains many isolated shoals.

The False Cape shoals have a maximum relief of 20 ft with flank slopes of 2° or less. The main shoreface-connected shoals crest at around −20 and −30 ft MLW with the landward shoal being shallowest. The isolated shoal which lies farthest seaward crests at around −40 ft MLW. Shoal crests deepen and develop secondary crests toward the north. The long axes of the shoals are oriented on an azimuth of about 15° and form an angle with the adjacent

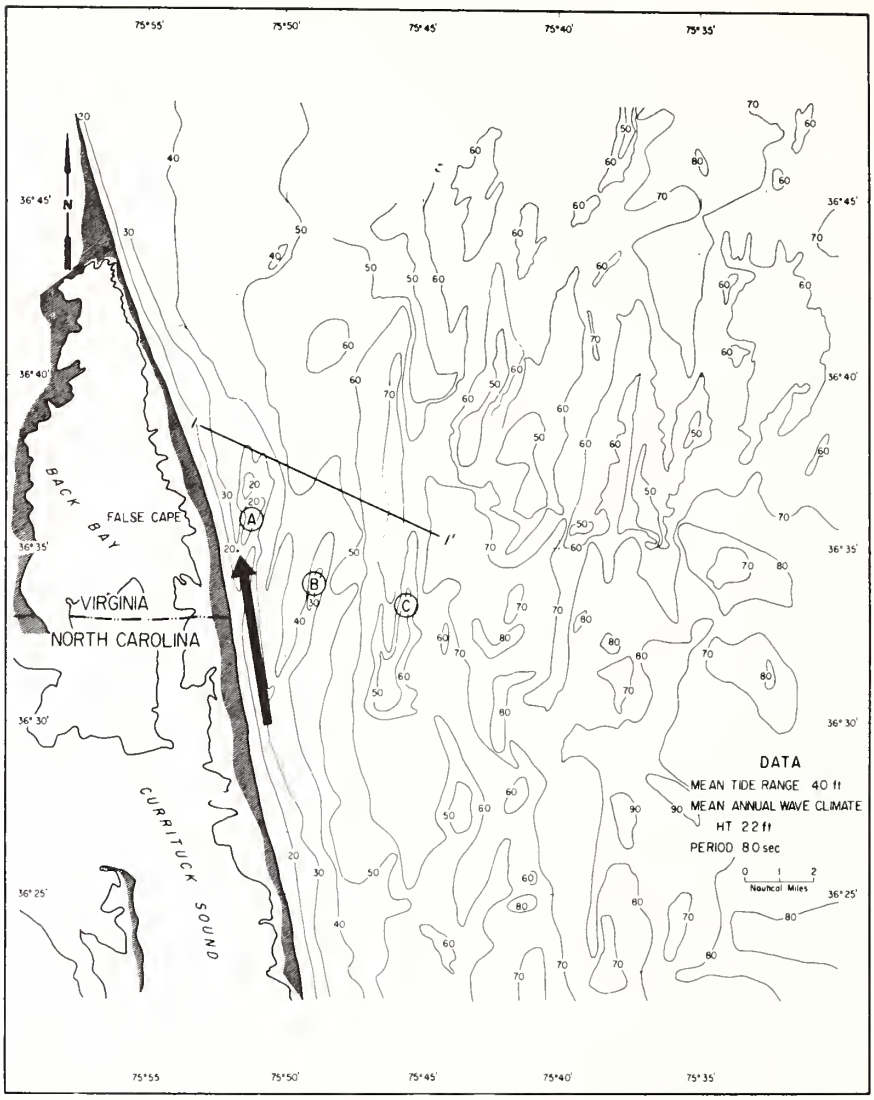

Figure 183.

Detailed bathymetry of the False Cape, Virginia, inner continental shelf at 10-ft contour interval. Direction of littoral transport, tidal range, and mean wave characteristics are indicated. Line 11' is the trackline location of the False Cape, Virginia geophysical profile in Fig. 181. Shoals A, B & C are shown in greater detail in Fig. 186.

shore of about 25°. A profile across the False Cape shoals (Fig. 181) shows typical topography and subbottom horizons delineated by seismic reflection profiles and cores. The lower horizon is underlain by a greenish-gray muddy

sand. A discontinuous layer of watery brown mud overlies the lower horizon and is in turn overlain by the surficial sand layer. Radiocarbon dates on carbonate material within the brown mud indicate that it is of mid-Wisconsin age. An articulated shell of *Mercenaria* sp recovered from a depth of 6 ft in the surficial sand unit was dated at 4220 ± 140 yr BP (Swift et al., 1972b).

Surficial sediment of the shoal crests is predominantly medium- to fine-grained quartz sand; shoal flanks, the adjacent shore face and margins of some intershoal troughs are characterized by fine- to very fine-grained sand. Along the central axis area of intershoal troughs a pebbly medium to coarse sand forms a thin and locally discontinuous layer covering compact greenish gray muddy sand and brown mud.

Florida Inner Shelf Shoals

General

The Florida inner continental shelf can be subdivided into three regions based on shoal morphology (Fig. 175). These regions are: South Florida which has a well developed shoal field similar to those of the Middle Atlantic Bight; Central Florida which is characterized by cape-associated and large linear shoals; and North Florida, which displays an anomalous morphology dominated by irregular banks of low-relief. Mean tide ranges and wave climate of the Ft. Pierce region are indicated in Fig. 184. Waves in the area come principally from the east and northeast giving rise to southerly littoral drift estimated to be 350,000 $yd^3\ yr^{-1}$ at Canaveral Harbor, 200,000 $yd^3\ yr^{-1}$ at Ft. Pierce Inlet, and 230,000 $yd^3\ yr^{-1}$ at St. Lucie Inlet (United States Army Corps of Engineers, 1967) (Fig. 184).

South Florida

The south Florida shoal field occupies the shelf off eastern Florida in the vicinity of Fort Pierce (Fig. 184). This field, the southernmost along the United States Atlantic Coast, contains well developed shoreface-connected, and isolated linear shoals with their long axes lying predominantly nearly north-south. Shoals in the south Florida field crest around −20 and −30 ft with some smaller shoals cresting at around −50 ft.

A definite and persistent acoustic reflector underlies the south Florida shoals at or near the elevation of shoal bases (Fig. 181). The sonic discontinuity is associated with marked changes in sediment characteristics.

Sediment comprising the shoals is characteristically well sorted biogenic medium- to coarse-grained sand with 15 to 30% quartz. Although the sand is occasionally fine or very coarse, poorly sorted, and varies in color from light brownish gray to medium gray, its constituents are similar. The biogenic fraction is composed mostly of barnacle plates, mollusk fragments and some

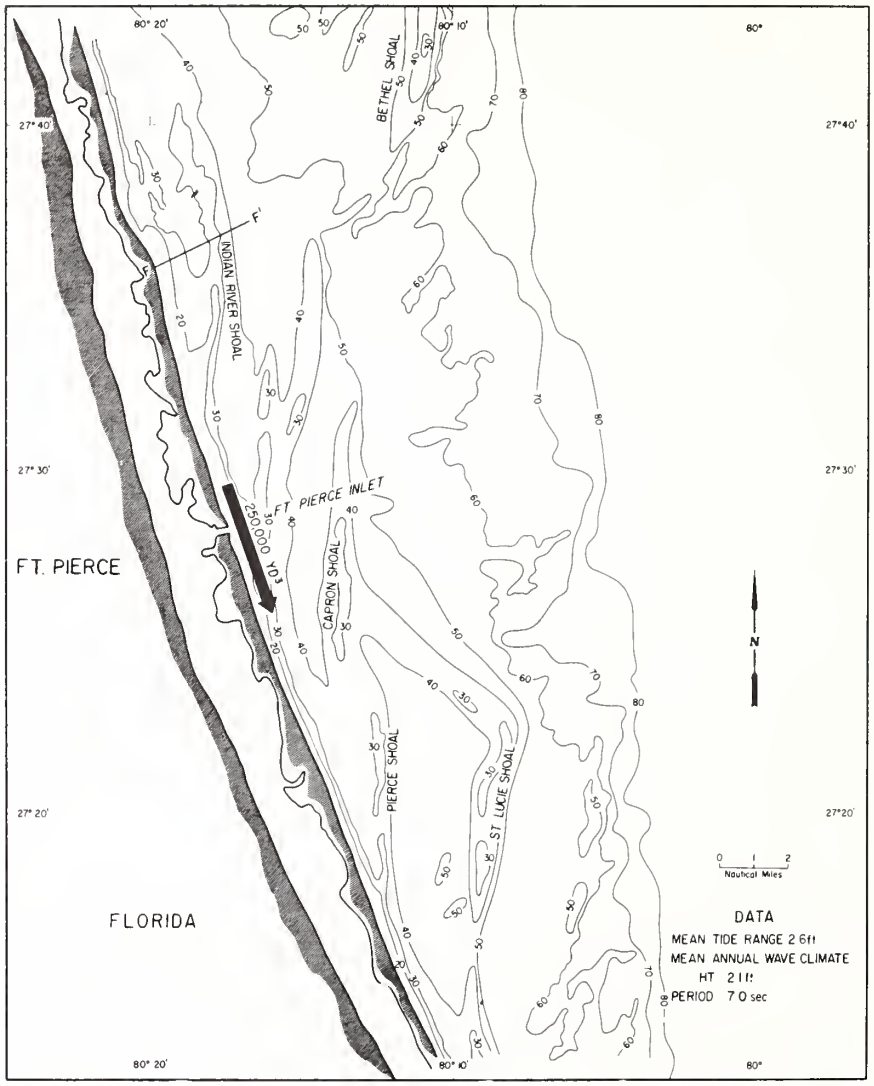

Figure 184.

Detailed bathymetry of the south Florida inner continental shelf at 10-ft contour interval. Direction and volume (yd^3) of littoral transport, tidal range, and mean wave characteristics are indicated. Line FF′ is the trackline location of the Ft. Pierce, Florida, geophysical profile in Fig. 181.

benthic foraminifera. The molluscan and foraminiferal assemblage is representative of one typical of a shallow water open marine environment similar to present conditions on the shoals. Meisburger and Duane (1971) present a more detailed description of sediment and geomorphology for this area.

Bethel Shoal situated near the seaward edge of the Fort Pierce shoal field is one of the largest shoals described in this study. It is also the only shoal of the Atlantic inner shelf area in which internal bedding can be delineated with the available seismic reflection profiles. Line profiles across Bethel Shoal showing internal acoustic reflectors are shown in Fig. 185. The internal bedding suggests a southeastward progradation of the shoal coupled with upward growth. The present surface configuration of the shoal seems to be roughly paralleled by the major internal reflector surfaces.

Between the shoals the bottom is nearly flat and covered by a layer of biogenic sand similar in character to that comprising the shoals. In contrast, however, the material in the intershoal layer tends to be more poorly sorted, coarser, and more angular and is highly bored and incrusted by organisms.

Sediment at or below the acoustic reflector at the base of the shoals in the Fort Pierce area, like that described later at Cape Kennedy, is a silty shell gravel and partly lithified calcarenite. A radiocarbon date of 8640 yr BP from peat overlying the surface suggests that the reflector marks the Holocene-Pleistocene surface.

Hurricanes passing within 150 n mi of the coast have occurred with an average frequency of one every 3 yr for the past 70 yr. Their effects have often been devastating but of short duration; tides generated by the storms often exceed 5 ft. Northeast storms have often resulted in more severe effects particularly with regard to erosion of the shore. Historical data do not indicate significant changes in the axial location of the shoals; however, the survey control is not precise. The well rounded and polished condition of sediment recovered from the shoal tops indicates reworking and movement of grains must occur, though this may not entail any overall displacement of the shoals themselves.

Beach sands on the adjacent Florida coast are similar in size, sorting and biogenic constituents to the characteristic shoal material. However, the quartz content is significantly higher in the beach sands, comprising approximately 60% of the beach material (Meisburger and Duane, 1971).

Central Florida

The inner continental shelf topography adjacent to Cape Kennedy is dominated by large, cape-associated shoals (Fig. 174b) trending southeast from the peninsula and large isolated linear shoals set immediately seaward of the cape-associated shoal tips. On the north side of Chester Shoal, extending from False Cape, small linear shoals trend north from the base of the shoal (Fig. 174b). Historical surveys of Chester Shoal and Southeast Shoal, extending from Cape Kennedy, indicate they are active depositional sites for fine and medium-grained sands transported in the littoral zone. Morphology, textural characteristics and proces-

Figure 185.

Interpretative geophysical profiles of Bethel shoal, Florida, area showing internal structure (inclined bedding) and relationship to underlying stratigraphy. Lines A,B,C are east-west; line 11 is north-south. Area location shown in Fig. 184. From Meisburger and Duane, 1971.

ses of formation and maintenance of these arcuate features will be topics of future studies.

Two large, linear isolated shoals, Ohio-Hetzel shoal and The Bull, lie adjacent of Cape Kennedy. They exhibit structural and lithologic characteristics common to linear shoals in south Florida and the middle Atlantic Bight; however, their morphology and association with the cape shoals suggests a genesis that may not be common to these other regions. The northeast trending Bull shoal is 27,000 ft long, 7,800 ft wide and rises from a base of −60 ft MLW to within −15 ft of MLW. Ohio and Hetzel Shoals are separated by a shallow narrow trough; combined they represent a northwest trending shoal complex that rises to −20 ft MLW and is slightly asymmetrical in cross section, with steeper slopes on the landward flank.

Shallow structure of the isolated shoals based in interpretation of core borings and seismic reflection records is depicted in Fig. 181. A continuous and mappable subbottom acoustic reflector lies at depths of −60 to −90 ft MLW throughout much of the area and as far south as Fort Pierce. Beneath the shoals the reflector is essentially flat lying; on the flanks and in the adjacent depressions the reflector correlates with a major change in sediment lithology. Beneath the reflector, sediments are partially recrystalized and cemented; above the reflector sediments are completely unconsolidated, but their composition indicates derivation in part from the underlying layer (Field and Duane, 1972). A radiocarbon date of 7,320 ±140 yr BP was obtained from a peat layer (probable fresh water origin) overlying the acoustic reflector at a depth of −55 ft MLW several miles south of the shoal area (Field and Duane, 1972). One mile seaward of the shoal, shells characteristic of the intertidal zone (*Donax variabilis*) were obtained from the subsurface depth of the major reflector. A ^{14}C date of 23,500 yr BP suggests a mid-Pleistocene age for the materials below the sonic and lithologic horizon (Field, 1972). Both sediment characteristics and age dates thus indicate that the sonic reflector represents a Pleistocene surface, and that the overlying shoals are no older than 7000 years. Internal structure in the shoals is not evident from seismic or sediment studies. Cores penetrating to depths of 12 ft on the shoal contain well sorted medium to coarse mixtures of biogenic (chiefly molluscan) and terrigenous (chiefly quartz) sand.

The highly polished nature of the sand at 12 ft below surface suggests recent tractive movement. Both grain size and composition of the shoal sands are similar to deposits on adjacent beaches and both show major contribution from erosion of older deposits. This seems to be true also for beaches from Fort Pierce north to Cape Kennedy (Field and Duane, 1972; Meisburger and Duane, 1971).

Historical profile data collected between 1898 and 1965 show that the shoals have become several feet higher and shifted over a thousand feet to the southeast. Twenty-five miles to the north of the Cape Kennedy shoal field a small group

of linear shoals occurs. These isolated linear bodies with the long axes oriented nearly parallel to shore are the most northerly shoals off the Florida coast which can be clearly related to the "accretional" linear and arcuate shoals occurring to the south.

North Florida

The typical shoal off north Florida is a broad nearly flat topped submerged bank which may be either roughly linear or totally irregular in outline. Predominant orientation of these shoal banks is northwest-southeast. Between many shoal banks there are deep northwest trending depressions which deepen progressively seaward.

Seismic reflection and sediment core data indicate that the nuclei of most large north Florida bank shoals may consist of pre-Holocene sediments (Meisburger and Field, 1972). The geometric pattern of the banks and intervening depressions suggests that the north Florida bank shoals are basically relict interfluves of a late Wisconsin subaereal erosion surface only slightly modified by the events of the Holocene. Thus, the north Florida "bank" shoals cannot be properly equated with the linear shelf shoals discussed elsewhere in this paper. Small linear shoals do exist, especially inshore, but these are generally ill defined on existing chart coverage and of insufficient relief to be included here.

LINEAR SHOALS AND COASTAL HYDRAULICS

Linear Shoals and the Wave Regime

The shoal fields of the inner Atlantic shelf lie at water depths which, during fair weather, are within the zone of wave surge. It seems reasonable, therefore, to consider experimental data pertaining to the generation of wavebuilt bars to determine the extent to which the shoals may be wavebuilt.

Kuelegan (1948), in a laboratory study of the formation of sand bars by waves impinging on a shoaling beach, developed dimensionless criteria relating the formation of bars to wave height and length and water depth to bar base. Concluding from his laboratory studies, Kuelegan (1948, p. 13) stated that: (a) "if water depth remains constant . . . the position of the bar, formed by a single system of waves, is a function of wave height and steepness; (b) if the water depth and wave steepness are held constant, an increase in the wave height will move the bar seaward; (c) if the water depth and wave height are held constant, an increase in wave steepness (shorter period) will move the bar shoreward; and (d) if the wave height and wave length are held constant, the depth of bar base below water will likewise remain constant, and any increase in the depth of water moves the bar shoreward."

Extrapolation of laboratory findings to field conditions is not always easy, nor direct. However, several aspects of Kuelegan's experiments have been confirmed in the field: Ratio of water depth over trough to depth over crest, approximately 1.9 in the lab, is 1.5 for Lake Michigan (Saylor and Hands, 1971) and 1.5 for Pacific Coast beaches (Shepard, 1950). Further, in the case of the Geat Lakes (where, wave climate can be considered constant, or nearly so) increase in water depth (rise of lake levels) is associated with shoreward bar movement (Saylor and Hands, 1971) and increased erosion (Berg and Duane, 1968).

We have examined the bars in the four areas discussed in detail in the previous section, using water depth over bar base and wave characteristics. Ratios obtained from Atlantic inner shelf shoals show significant variation in the ratio of trough depth to crest depth. Range values for each of the major regions are as follows: Central New Jersey, 1.13 to 1.70; Maryland, 1.45 to 4.2; False Cape, Virginia, 1.3 to 1.7; and south Florida, 1.47 to 2.1. Although many of these values are within the limits established by Kuelegan (1948) and corroborated by field studies, the range of values indicates that it is unlikely that all the features described are wave-generated. The offshore bars from Lake Michigan and the Pacific Coast are nearly an order of magnitude smaller than the shoals under discussion here. Also, those Lake Michigan and Pacific Coast features display a remarkable linear continuity: they parallel the coast for distances in excess of tens of miles, unlike the relatively short, discontinuous, acute-angle shoals of the East Coast. Furthermore, using Kuelegan's data, we have calculated the theoretical parameters of waves required to form the shoals. Shoals lying at $-40'$ MLW and deeper would require waves having heights (H_0) ranging from 18′ to 40′ and periods (T) greater than 20 sec. The frequency of occurrence of waves having these heights is shown by Harris (1972) to be extremely low; also in shoaling water a wave will break when d/H is in the range of 0.78 to 1.0 (d is water depth). Hence, particular combinations of H_0, T required are unrealistic or theoretically impossible.

For shoaler features ($-25'$ MSL) certain combinations of H_0, T could conceivably occur and, therefore, result in bar construction. However, the vast majority of shoals require for their formation theoretical wave height and period combinations that are unrealistic for the United States Atlantic coast.

Linear Shoals and Storm-Generated Coastal Currents

The hydraulic regime of the inner shelf during storms offers more promise as a generative agent for the inner shelf shoal fields. Harrison et al. (1967) have summarized what is known concerning the effect of storms on the circulation of the Middle Atlantic Bight. During the winter, successive mid-latitude lows passing up the Alantic seaboard generate intense northeast winds. Repeated

intense wind stress combined with falling temperatures serves to destroy the stratification of the shelf water during this period. Harrison et al. (1967, p. 72) note of individual storms that: "as the onshore component of the wind increases over the shelf and slope water zones of the northern part of the Middle Atlantic Bight, it may produce or augment a net southerly drift (permanent flow) owing to the effect of set-up on the southwesterly trending coast line, or to southward barotropic flow where the wind drift extends to the sea floor." They also note that such a southward flow would overcome the Ekman component of the drift. Wind-drift currents tend to develop speeds of one twentieth to one fiftieth that of surface and wind speeds (Weigel, 1964), and a northeaster blowing at 40 knots could generate a surface current of one or two knots (1.7 to 3.4 ft sec^{-1}) which, during several days of downward momentum transfer, might extend some portion of that velocity to the inner shelf floor

In two of the most carefully studied systems of shoreface-connected linear shoals, a variety of textural and bathymetric data have been compared with direct hydraulic data. The combined data suggest that such storm currents and the wave trains associated with them are the dominant forces shaping the shoals. These systems occur at False Cape, Virginia (Swift et al., 1972b), and at Bethany Beach (Moody, 1964).

Process and Response in the False Cape System

Substrate Characteristics

Significant features of the linear shoals at False Cape which yield circumstantial evidence concerning the character of the hydraulic regime are the distribution of grain sizes and the geometry and orientation of the ridges themselves. Grain-size gradients at False Cape, Virginia, vary regularly with the topography (Fig. 186a, b). Crests consist of well-sorted medium- to fine-grained sand. Flanks are covered with fine- to very fine-grained sand. Stiff, pre-Holocene substrate is exposed intermittently in the troughs; locally it is covered with a few centimeters of coarse, pebbly sand which includes clay balls from the underlying substrate. A longitudinal gradient is superimposed on this transverse variation in grain size, in that toward the south the fine and very fine flank sands become more extensive and finally bridge over the coarse trough sands.

A comparison of graphic mean diameter with graphic inclusive standard deviation shows that trough and crest sands become better sorted with increasing grain size (Fig. 186b). This is interpreted as lag behavior in zones of higher energy; with time, more and more fines are removed, increasing the mean diameter and decreasing the size range. Flank sands, showing the reverse trend, are interpreted as the winnowed-out fractionates which, as they move intermittently away from the high-energy areas, lose successive coarsest fractions, thus decreasing the mean diameter while decreasing the size range.

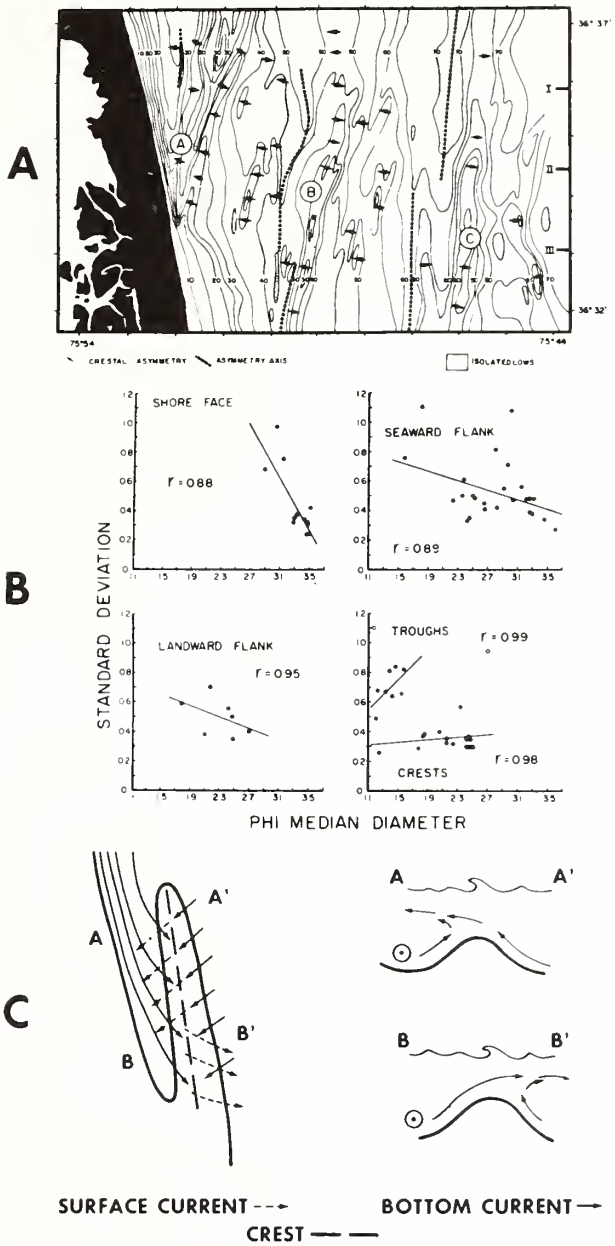

Figure 186.

Substrate response and hydraulic process for a narrow-angle, shore-connected shoal, False Cape, Virginia. (A) bathymetry, from precision navigation survey (Swift et al., 1972); (B) graphic mean diameter versus inclusive graphic standard deviation for False Cape sediment types (Swift et al., 1972); and (C) plan view (left) and cross-section (right) model for hydraulic regime over "A" ridge during a major storm.

The coarse trough sands are interpreted as a primary lag, generated by periodic storm currents which erode the troughs and sweep the sand up on the crests. Similar coarse lags have been noted in troughs of the tide-maintained ridge systems of the southern bight of the North Sea (Houbolt, 1968). In the North Sea the gain size continues to fine all the way to the ridge crests. The crestal grain-size reversal at False Cape suggests that in this area the operative currents are far more infrequent and that shoal crests are strongly modified by fair weather wave surge. Thus, a secondary lag is generated on the crests by swells whose surge winnows out fine to very fine sand and deposits it on the flanks.

The intermittent generating currents would appear to be south-trending. Crest and trough axes climb to the south. As each of the shoals joins the shoreface, its seaward flank becomes heavily mantled with fine sand—apparently swept out of the adjacent (landward) trough. There is an indication that the south-trending currents are structured into helical flow cells, as are the currents which form the shoals of the southern bight of the North Sea (Houbolt, 1968). The False Cape shoals bear asymmetrical, second-order ridges on their flanks, whose steeper sides face toward shoal crests and away from the "asymmetry axes" of major troughs (Fig. 187a). This geometry is compatible with the concept that, during the storms, the south-trending currents tend to descend in the troughs and sweep obliquely up the sides of the ridges to converge over the crests. To the extent that such helical flow may be a generating mechanism of water movement, analogies may be made to the helical flow patterns attributed by Dzulynski (1965) to experimental formation of bedforms; and to helical movements in the boundary layer of the air mass flowing over desert seif dunes (Folk, 1971). The most widely described helical flow phenomenon is Langmuir circulation observed above the thermocline at sea (Langmuir, 1938; Faller, 1969; Assaf et al., 1971). However differences exist between these examples and the linear shoals under discussion herein. For instance, seif dunes attain the angle of repose at least locally, and are generally of smaller wavelength. Langmuir cells tend to have a wavelength no greater than equal to the depth of the mixed layer (Assaf et al., 1971) and thus are nearly equant in cross section; the False Cape shoals are separated by distances of miles, but lie in 66 ft or less of water.

Hydraulic Data

Five direct observations of bottom currents have been made at False Cape with a Bendix Q-18 Orthogonal Current Meter (Holliday et al., in press). All but one were obtained during periods of calm weather. Weak north-trending currents generally less than 0.3 ft sec^{-1} (10 cm sec^{-1}) were measured for durations of 12 to 24 hr by 6 inch impellers; units were mounted on the sea floor. Currents observed may have been caused by the indraft of saline bottom water to Chesapeake Bay to the north. The currents were too weak to affect the troughs, but in combination with wave surge visibly affected shoal crests. Scuba dives

to the station on the crest of "C" ridge (Fig. 186a) revealed sand ripples 4 to 6 inches (10 to 15 cm) high whose crests were activated by each wave surge and which slowly migrated to the northwest. The residual current for the 26-hr station was 0.12 ft sec^{-1} (3.6 cm sec^{-1}) to the north. However, when only the highest 10% of velocities were considered, the direction of the residual current swung to the northwest. This station apparently recorded the fair-weather situation that is interpreted to winnow and degrade the shoal and to create a secondary lag on their crests.

One of the current-meter stations in the most landward trough may have observed the sort of current that builds the shoals. Monitoring began under relatively calm conditions. Initially, currents of varying orientation and speeds less than 5 cm sec^{-1} were observed. After the passage of a cold front, a wind from the northeast built rapidly to 25 knots. A steady, south-trending bottom current with peak velocities in excess of 0.7 ft sec^{-1} (20 cm sec^{-1}) developed and persisted through the turn of the tide.

Wave-refraction studies at the False Cape area (Weinman, 1971) indicate that northeast and east-northeast waves (and to a lesser extent, east-southeast and southeast waves) concentrate energy on the False Cape area. During this particular station seas from the northeast at 4 to 6 ft began to break on the ridge; water pumped by surf over the crest of the ridge must have intensified the shore parallel current. The hydraulic head generated in the trough by the combination of this wave set-up and the wind drift current resulted in a large rip current which began to flow diagonally seaward across the head of the ridge, marked by flocks of terns hunting fish swept over the crest.

The pattern of bottom and surface currents at this time must have resembled that of Fig. 186c. Landward bottom currents associated with wave transport over the northern end and seaward flank of the ridge would become landward surface currents as the waves break on the crest and become bores. Indeed, the smooth, convex-up profile of the seaward flank of the shoal is nearly identical to the profile of the shoreface landward of the shoal. Bathymetric and grain-size profiles suggest that during a storm the shoal's seaward flank is an environment hydraulically analogous to zone of shoaling waves that shape the shore face (Swift et al., 1972b) and that its crest is an environment hydraulically analogous to the surf zone. With 9 to 11 second waves 4 to 6 ft high, a crest at 8 ft below sea level and a base at 15 ft below sea level, the shoal near its junction with the shore face would, by Keulegan's criteria, marginally have the response characteristics of a wavebuilt bar.

Southerly-trending wind set-up currents in the trough, amplified by water pumped over the crest of the shoal by mass transport effect of breaking waves, would become seaward surface currents as they pass over the base of the ridge

(Fig. 186c). Thus, during strong northeast winds, southerly bottom currents appear to converge over the ridge, maintaining it, and scouring out the trough.

As indicated in the cross-sections of Fig. 186c, the convergence generates helical flow half-cells on either side of the shoal. The two major shoals to the seaward may have had a similar genesis; if so, the most seaward shoal has broken contact with the shore face and is presumably maintained only by helical flow, which now is probably as much a consequence as a cause of the linear shoal's presence.

Process and Response in the Bethany Beach System

The distribution of grain sizes and the geometry of the ridges is rather different in the case of the Bethany Beach, Delaware, ridge system (Fig. 187a, b). Moody (1964) has shown that the Bethany Beach troughs are, like False Cape troughs, floored by pebbly, coarse-grained sand. The coarse sand becomes better sorted toward the next crest to the seaward and also finer, grading to medium-grained sand (Fig. 187c). The grain size decrease continues down the south slope, accompanied by a decrease in sorting, then increases abruptly to coarse sand when the next trough is reached. Thus, at Bethany Beach, the grain size distribution is more asymmetrical than at False Cape and more nearly resembles the distribution associated with a simple sand wave built by a unidirectional current, although slope angles are far below the angle of repose. The geometry of the shoals likewise more nearly approaches that of a transverse bedform than do the False Cape shoals; the shore angle is higher, ranging from 30° to 80° and averaging 45°, versus an average 25° for False Cape. Thus, the shoals are more nearly normal to coast-parallel currents. Relief, crestal continuity, and southward asymmetry increase to the south, which Moody, on the basis of his own and other surveys, shows to be the direction of migration (Table XXIX). Moody's migration figures show that, for a 42-yr period, rates were about 10 ft per year. However, the ridges moved up to 250 ft to the southeast between surveys of 1961 and 1963 which bracket the great Ash Wednesday Storm of 1962. Thus, as at False Cape, a dominant driving force appears to be the intense south-trending currents generated by major storms.

Also, as at False Cape, the wave regime appears to be a controlling force, although here in a rather different way. The mean trend of the ridges appears to be precisely that of the dominant northeast direction of wave approach. Moody (1964) prepared a series of wave-refraction diagrams which show that orthogonals tend to converge over crests. This by itself would tend to maintain the ridges, as near-bottom residual wave currents would converge obliquely shoreward toward the crests. Moody suggests that, in addition, they are generating mechan-

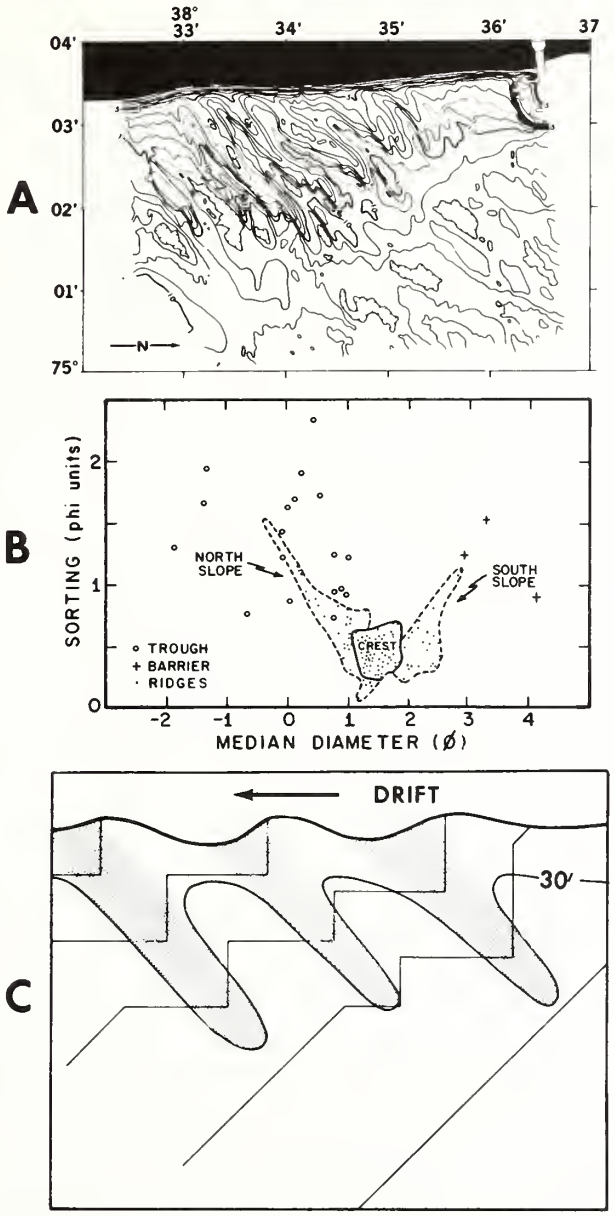

Figure 187.

Substrate response and hydraulic process for a wide-angle, shoreface-connected ridge, Bethany Beach, Delaware. (A) bathymetry, from Moody (1964); (B) median diameter versus inclusive graphic standard deviation for Bethany Beach sediment types [from Moody (1964)]; and (C) schematic model for the maintenance and generation of wide-angle ridges by wave refraction. Refracted waves converge toward ridge crests. Wave energy is concentrated at heads of troughs. Modified from Goldsmith and Colonell (1970).

Table XXIX
Rates of Crest Movement Offshore between Indian River Inlet and Bethany Beach[a]

Ridge	Rate of movement 1919-1961	Amount and direction of movement (m)			
	(m yr^{-1})	1919-1961		1961-1963	
D	0.0	0	–	55	SE
E	3.8	160	SE	30	NW
F	3.8	160	SE	10	SE
H	2.4 (NE end)	100	SE	25	SE
	2.6 (SW end)	110	NW	80	SE
J	3.9 (NE end)	165	SE	75	SE
	5.0	210	SE	40	SE
	2.9	120	SE	90	NW
	6.0 (SW end)	250	SE	50	NW
K	3.6	150	SE	55	SE
M	2.4 (NE end)	100	SE	54	SE
	–	0	–	30	SE
	3.7 (SW end)	155	SE	14	NW
N	1.4 (NE end)	60	SE	15	SE
	5.7	240	SE	20	SE
O	2.1	90	SE	20	SE

[a]From Moody, 1964, his Table 9.

ism for the shoal topography. The ridges, oriented parallel to the prevailing direction of wave approach, would serve (Fig. 187c) to focus wave energy rhythmically along the beach. Moody (1964, p. 113) notes that,

> "although the pattern of crossed orthogonals and the amount of wave convergence differs according to wave direction, the wave-divergence zones on the shoreline remain about the same, slightly north of points where ridges meet the barrier. These areas should undergo greater amounts of erosion than adjacent sections of the shore."

Therefore, the ridges would tend to perpetuate themselves during coastal retreat by a sort of feedback mechanism. Goldsmith and Colonell (1970) documented this process on Monomoy Barrier Island, Cape Cod. While more work needs to be done before the situation at Bethany Beach is clarified, the parallelism of the ridges with the dominant direction of wave approach would require this or a similar pattern of process and response.

Thus, the False Cape and Bethany Beach systems of linear shore-connected shoals are interpreted to comprise two related, yet distinct, responses of the inner shelf substrate to a storm-dominated hydraulic regime. Storm-generated coast-parallel currents interact with waves in two different ways, and yet other modes of interaction may be represented in the spectrum of inner shelf shoals described in this paper. In both of the cases discussed above, the bottom topography appears to be a resultant response between the storm hydraulic regime,

Figure 188.

Detail of Delaware-Maryland inner shelf bathymetry, showing shoreface-connected shoals in different stages of detachment. Stepped crestlines (dashed lines) of offshore shoal sequences record successive detachments of that series. Contoured at 2 fathom interval. See USC&GS 0807N-57 for one fathom resolution.

which tends to aggrade the ridges, and a fair-weather hydraulic regime of northwest-trending swells which tends to degrade the ridges.

SHOREFACE-CONNECTED TO ISOLATED SHOALS: SHOAL DETACHMENT AND EVOLUTION

Continuity between Shoreface-Connected and Shelf Shoal Fields

The apparently gradational transition between shoreface-connected and isolated shoals of the Atlantic shelf suggests that a genetic relationship exists between the two categories. The patterns of inner shelf shoals can be traced

for up to 36 n mi across the continental shelves of Long Island, New Jersey, and Delaware (Figs. 171, 172, 173) to terminate in shoreface-connected shoals of apparently hydraulic origin. Brigantine Shoals off Atlantic City, New Jersey, and Chincoteague Shoals, south of Ocean City, Maryland, are located at the point of separation of the proximal and distal barrier arcs of their respective headlands. At these points, the arcuate trend of the innermost shoals is initiated by shoals as far seaward as the 120 ft isobath.

Significance of Shoal Orientation

Our shoal orientation statistics are useful in assessing the relation of shore face to inner shelf shoals. Generally speaking, the shoals maintain a constant angular relationship with the shoreline of about 20°, regardless of the shoreline orientation. Note that the histograms of azimuth of shoal axis (Fig. 176b) and azimuth of shoreline adjacent to shoals (Fig. 176c) are very similar, suggesting strongly that the orientation of the shoals follows that of the shoreline. However, it is significant that the shoals are not parallel to the shoreline (Fig. 167d). The mean angle (measured clockwise) of shoal with shoreline trend is 22°; standard deviation is 16°; and there are almost no negative values (> 90°).

This relationship breaks down for the wide angle-shoals of the northern New Jersey and northern Delaware coasts. In these two areas, the angle between the dominant northeast to east wave trend and the due north shoreline is apparently so large as to lead to development of shoals transverse to, rather than nearly parallel to, coastal storm currents. Additionally, morphological development in both areas may be influenced by subbottom structure and preexisting morphology (this paper, Fig. 179; Kraft, 1971a, Fig. 3). Both Delaware and northern New Jersey exhibit a northward transition in shoal orientation and symmetry. South of the transition zone shoals are symmetrical and open at approximately 20° with the coast, such as those at Ocean City, Md. and Barnegat, N.J. To the north of these areas shoals become progressively asymmetrical; shoal azimuths remain constant but the shoreline trend is more northerly.

From this it is possible to conclude that the characteristic 20° shore angle of the shoals is a consequence of the dynamics of shoal formation. As described in the previous section, shoreface-connected shoals appear to align themselves at this angle to the current which excavates their landward troughs and sweeps obliquely over their crests. Only when the angle between wave approach and shoreline is greater than 40° do the shoals apparently tend to orient themselves with the absolute direction of wave approach.

Shoreface-connected shoals seem to have been generated by nearshore processes. For isolated shoals though it means that they are now "relict" having been abandoned as the shore retreated in response to sea-level rise. The orientation of the shoals and correlation to the shoreline suggests also that during the retreat,

the shoreline has retained essentially the same orientation it now has. The distribution of minerals on the shelf and beaches described by Pilkey and Field (1972) might be interpreted to record such a retreat.

It should be emphasized here that these shoreface-connected shoals are very large features and our data do not indicate these shoals ever move large distances. In this regard, the shoreface-connected shoals should not be construed to be the same as shallow water or swash bars which are usually described as 1-3 ft high, laterally continuous, and which through relatively short periods of time move landward, become welded to the beach, and in effect, prograde i (Bajorunas and Duane, 1967); Hayes and Boothroyd, 1969; Saylor and Hands 1970). We judge, therefore, the formative processes for the "swash bars" and the linear shoals are also distinctly different.

Evolutionary Shoal Series

The relationship between shoreface-connected and isolated shoals is more explicitly inferred from an examination of four shoal fields whose constituent members appear to form evolutionary series. Moody (1964) had called attention to the apparent sequential relationship of the Bethany Beach ridges. As noted, his bathymetric time series indicates that these wide-angle shoals are migrating to the southeast, maintaining contact with the shore face and extending their crest lines as they do so. Height and asymmetry also increase to the southeast. Moody suggested that, as the shore face retreated and the water deepened over the ridges, faster ridges overtook slower ones, with the result that large shoals were isolated and left behind on the sea floor. He called attention to Fenwick shoal (Figs. 182, 188) as a possible example.

The Bethany Beach shoal system appears to be acceptable as an evolutionary series of wide-angle, shoreface-connected shoals, but shoreface-connected and isolated shoals to the south off Ocean City (Fig. 182) appear instead to be narrow-angle shoals of the False Cape type. Here the shoreface-connected shoals appear to form a typological or apparent evolutionary sequence of their own, from a wholly shoreface-connected, unnamed ridge in the north through ridges with saddles and various degrees of isolation to the wholly isolated Great Gull Bank to the south (Figs. 182, 188).

The westward hook of the base of Fenwick shoal and the shoal immediately to the south of it is reflected by the westward-skewed orientation of the saddles that connect some of the shoals to the shoreface and may relate to the manner in which the saddles are deepened and cut through during the isolation process. The en echelon nature of shoal peaks, and the stepwise trend of crestlines (Figs. 182, 188) suggest that a shoreface-connected ridge developed by headward erosion and continued deepening of its landward trough, with concomitant crestal aggradation, until a critical threshold is reached. The base of the ridge is then

severed, and a new ridge begins to form inshore and down current from the initial segment. This sequence is schematized in Fig. 189.

The False Cape shoal system may also be envisioned as an evolutionary sequence (Fig. 183, 186a), with "A" shoal undergoing active accretion and "A" trough undergoing enlargement by headward and trough-floor erosion. Recent bathymetric observations of this sector indicate that a shallow trough separates "A" shoal from the shoreface, where during the northeaster a large-scale rip current was observed, and that the position of this saddle shifts from month to month. South of the saddle fine sand swept out of "A" trough has built up the shoreface 5 to 15 ft since 1922 (Swift et al., 1971). The shoreline south of the junction of the ridge with the shoreface has prograded up to 180 feet since 1922, while the shoreline north of the ridge junction has retreated 90 ft during this same period (Grafton, unpublished manuscript, Norfolk District, United States Army Corps of Engineers). Back barrier peat and clay in the floor of "A" trough is alternately covered with a few feet of coarse sand, then laid bare. In view of these systematic changes, it seems reasonable to surmise that, with time, first "B" shoal, then "A" shoal will sever their connections with

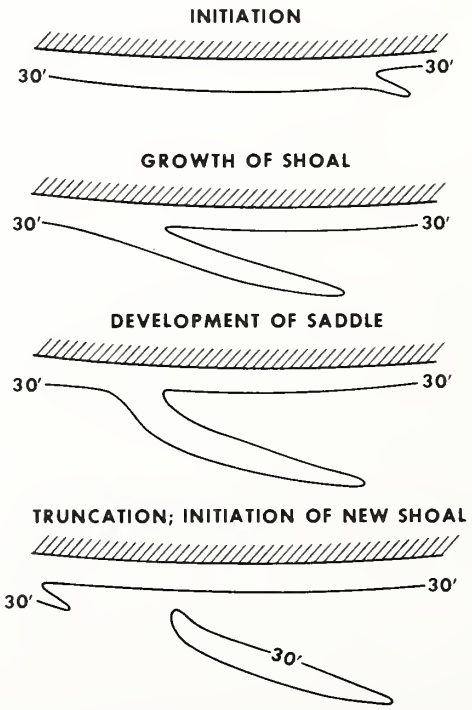

Figure 189.
Schematic of shoal detachment sequence.

the shore face, and that "C" shoal was once a shoreface-connected ridge like the other two.

A final morphological sequence with genetic implications occurs in the Platt shoals sector of the North Carolina coast adjacent to Oregon Inlet (see Fig. 190). A low, broad, linear shoal is attached to the shoreface north of Oregon Inlet. To the south lies the Platt shoals complex. Inner Platt shoals, cresting at 30 ft, is separated from the shore face by a trough over 60 ft deep. Unpublished vibracore data indicate that the trough is floored by a few feet of grav-

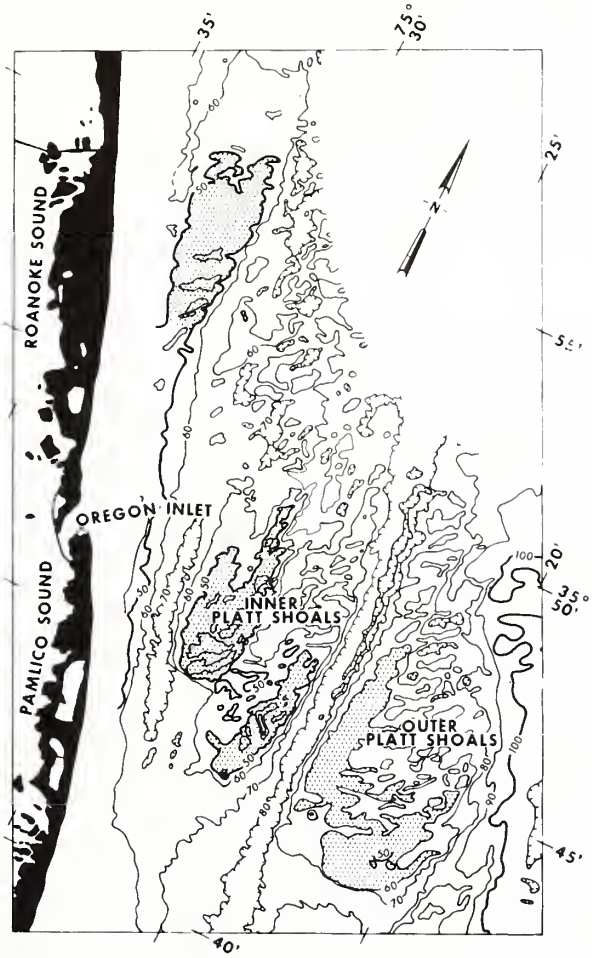

Figure 190.

Platt shoals sector of the North Carolina coast. Outer Platt shoals are interpreted as having undergone shoreface detachment. Contour interval is 10 ft.

el, with worn fragments of *Mercenaria* sp. as a prominent clast. The gravel overlies clean, well-sorted sand and is presumed to be a lag generated during the development of the trough.

Inner Platt shoals are still connected to the shore face by a low saddle; outer Platt shoals to the south and seaward may once have been similarly connected, but at present are entirely isolated. The linear, north-south-trending shoals in this area have superimposed upon them small-scale, short-crested ridges up to 10 ft high. They trend northeast, are nearly normal to the shoreline, and are asymmetrical with steeper southeast flanks. Side slopes are much less than the angle of repose. These features appear to be large transverse sand waves that are activated during storms and, in this respect, are similar to the wide-angle shoals of Bethany Beach.

Clearly, there is much to be learned from continued study and observation of the sectors described. However, the shoal sequence of these sectors suggest that the creation of isolated linear shoals from shoreface-connected shoals by deepening and headward erosion of inner troughs is a presently occurring process and one which in the past is judged to have occurred in concert with shoreline retreat.

DISCUSSION

Past investigations of the morphology of the inner continental shelf have resulted in a variety of genetic interpretations. Garrison and McMaster (1966) attributed the ridge and swale topography of the shelf east of Long Island and south of Rhode Island as primarily fluvial in origin. Knott and Hoskins (1962) inferred that this shelf sector was shaped by fluvial and glacial processes. Mckinney and Friedman (1970) concluded that the topography of a corridor across the continental shelf south of Long Island comprised a modified fluvial surface.

The nature of the central and outer shelf of the southern New England shelf is beyond the scope of this paper and will be considered in future publications. The Long Island shore face has not been examined in detail in this paper, because our data on this sector are only partially processed. However, we note that the linear, shoreface-connected shoals of the Fire Island sector (Fig. 191) are similar in all important respects to the narrow-angle systems that we examined farther south. In particular, the shoals exhibit the southward asymmetry which we attribute to the action of coast-parallel, southeasterly storm-generated currents. Consequently, we suspect that the shoreface-connected shoals of the Long Island shelf are of modern hydraulic origin as well. However, the influence of Pleistocene glacial outwash from Long Island in forming the existing surface or in controlling subsurface morphology is not well known at this time. Certainly the proximity and magnitude of the source are factors to be taken into consideration.

Sanders (1962) and Payne (1970) have pointed out that the False Cape, Virginia,

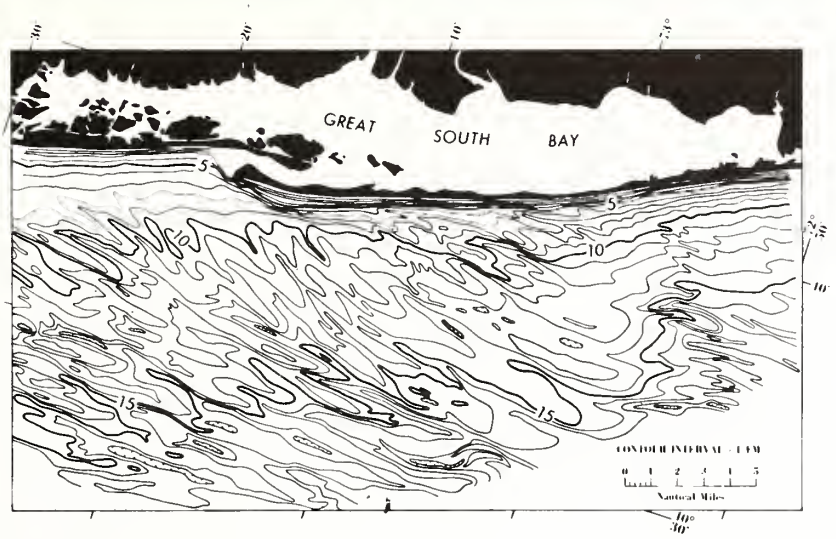

Figure 191.
Fire Island shoreface ridge system, south shore of Long Island, New York.

shoreface-connected shoals are on the same trend as the Late Sangamon raised beach ridges on the adjacent land and suggest that the shoals are relict Pleistocene features. Kraft (1971a, p. 21-35) notes that the Bethany Beach ridges are parallel to raised Pleistocene beach ridges on the adjacent shore. He suggests that "at least the loci of formation of the parallel offshore ridges must be related to pre-existing topography."

However, it is difficult to see how even this relationship between shoreface-connected shoals and raised Pleistocene beach ridges could exist. For one thing, these features occur at two different levels. The latter lie on a sub-horizontal, sub-aerial surface that is over 30 ft higher than the sub-horizontal inner shelf surface on which the shoals rest. These two "steps" are separated by the "riser" of the shoreface. If the shoals are remnants of seaward extensions of the subaerial beach ridges, then these seaward extensions must once have had a relief of 50 ft. No existing linear shoals and none of the classic barriers of the present United States coast have such relief. We are also doubtful of the stability of relict barriers in the high-energy zone of shoaling waves. The equilibrium profile of the shore face is typically that of a smooth, exponentially curved surface. This surface continually adjusts so as to absorb wave energy with maximum efficiency, and response time is extremely short, geologically speaking. Beaches may be stripped back 150 ft by a single storm, but most of the sand is returned during several weeks of fair weather as the beach adjusts to the reduced energy level. As noted by Fischer (1961), this profile must translate landward and upward during a marine transgression, and the result must be erosion of the

shore face and destruction of its internal stratigraphy. Consequently, it is very difficult to accept the concept that large linear mounds of unconsolidated sand could exist on the shore face out of equilibrium with its hydraulic regime. We conclude that in the light of our studies and data, the alignment of raised subaerial Pleistocene beach ridges and nearby submarine shoreface-connected shoals is fortuitous and is not *a priori* evidence for either the age or origin of the shoals. Where hard data in the form of radiometric ages are available. the ridges prove to be younger than 11,000 yr.

A second hypothesis, first advanced by Veatch and Smith (1939) interprets the shelf surface as a relict strand plain, with ridges marking stillstands of the advancing Holocene sea. On close examination, however, it is difficult to fit the extensive inner shelf shoal field of the Atlantic shelf into this pattern. Subaerial barrier systems on the Atlantic coastal plain mark culminations of transgressions (Hails and Hoyt, 1969) or were formed during regressions (Colquhoun, 1969; Oaks and Coch, 1963). Only in the latter case does the spacing approach anything like the 1 to 2 mi of the inner shelf ridge fields. Furthermore, the shoal fields do not satisfy the stairstep criterion, first advanced by Gilbert (1899). Gilbert pointed out that, if a barrier is overstepped, the base of the next barrier to be built farther inland must lie at the same elevation as the head of the first. The shoal fields of Delmarva and New Jersey lie on a gently sloping surface which is parallel to a second gently sloping surface, defined by the nearly accordant summits of the closely spaced ridges. Instead of forming a sequence of steps and risers, the profile approximates a gently inclined sine wave. Each ridge has a shoreward trough nearly as deep as its seaward trough. Hence, any hypothesis interpreting these inner shelf ridges as overstepped barriers must acknowledge extreme modification of original morphology by modern hydraulic processes.

A third major hypothesis for the generation of linear, shelf-floor shoals has been proposed by Moody (1964). Basis of the hypothesis is that the ridges form in response to the modern hydraulic regime at the foot of the shore face and that they are isolated by the retreat of shoreline. Our survey of the central and southern inner Atlantic shelf is compatible with this hypothesis and adds supporting detail. Shoreface-connected ridges are seen as generated by the interaction of wind- and wave-generated currents with the substrate on the shore face during storms. Two major categories of response are envisaged; wide-angle (over 30°) and narrow-angle (less than 30°), depending on the angle made by the ridges to the shoreface. Narrow-angle ridges form normal to wave-generated bottom currents and nearly parallel to shore-parallel wind set-up currents, and during these initial stages have some of the response characteristics of wave-built bars. Wide-angle ridges with the reverse relationship appear to be more nearly large-scale, low-angle, intermittently active transverse bedforms with respect to coast parallel storm currents; with respect to wave generated currents they are viewed as longitudinal structures.

Our scattered hydraulic observations serve to provide only the most rudimentary and qualitative picture and have raised as many questions as they have answered. Clearly, the greater part of linear shoal dynamics is yet to be learned. We conclude that shoreface-connected shoals are generated by nearshore processes. For isolated shoals though it means that they are now "relict" having been abandoned as the shore retreated in response to sea level rise. Shoal sequences which appear to demonstrate various stages of the detachment process are present on all sections of the U.S. Atlantic coast. However, further detailed investigations of petrography, shallow stratigraphy and bathymetric time series of shoal system are required before this process will be completely understood. Nevertheless, it seems reasonable to state at this time that the linear shoal systems do record Holocene barrier retreat across the shelf surface, but in a manner more complex than originally envisaged by that hypothesis' proponents. The shoals represent neither the subaerial superstructure nor the submarine foundation of barriers. They are instead independent and distinct daughter forms, adjusted to the deeper water environment in which they are now located. The orientation of the shoals and correlation to the shoreline suggests furthermore that during the Holocene coastal retreat the shoreline has retained essentially the same orientation it now has.

CONCLUSIONS

The surface of the United States Atlantic continental shelf is characterized by numerous arcuate and northeast trending linear shoals and ridges which rise 10 to 40 ft above the surrounding sea floor and measure from hundreds to thousands of feet in length. The two broad shoal classes are further divisible as arcuate shoals: inlet-associated and cape-associated; and linear shoals: shoreface-connected and isolated. Regional patterns in shoal distribution parallel regional trends in coastline morphology. Thus inlet-associated shoals exist only at estuaries and other large inlets, and cape-associated shoals only at cuspate forelands and major barrier overlaps. Shoreface-connected linear shoals are present off headland areas; both shoreface-connected and isolated linear shoals are present adjacent to main barriers.

Marked similarities in external morphology of over 200 linear shoals on the Atlantic inner continental shelf between Long Island and Florida strongly suggest similar genesis of all linear shoals. All of the shoals open to the northeast forming small acute angles with the coastline (most less than 35°). Depth to shoal crests is strongly bimodal with modes existing at 20 to 30 ft and 40 to 55 ft; a third mode possibly exists in water deeper than 80 ft.

High resolution seismic reflection profiles and sediment cores from most shoals show them to be planoconvex bodies of sand resting upon a mappable, essentially featureless, acoustic horizon. The stratum associated with the acoustic reflector,

which in some areas is exposed, varies from coarse unconsolidated sands to compacted muds to semiindurated calcarenites.

Samples of organic rich muds, peat, or shells lying at or just above the depth of the acoustic reflector upon which the shoals lie have radio-carbon ages of early to mid Holocene. Extrapolation of this information to other shoals which are morphologically and stratigraphically similar indicates that these other linear shoals are also of Holocene age. No evidence to support Pleistocene origin of these features was found.

Shoal sands are generally well-sorted, medium-grained sands that are similar in lithology to adjacent beaches and bear evidence of recent current and wave activity. Textural grading, historical records of shoal movement, and selected field hydraulic studies all show inner shelf shoals, particularly shoreface-connected ones, to be presently undergoing modification by storm currents and shoaling waves.

Available data indicate the mode of formation only in a general way. It seems clear, however, that the shoals are formed by nearshore processes. The consistency of shoal angle with the shoreline, internal structure (inclined bedding) and similarity in cross-sectional profile of shoals from Long Island to Florida, are judged proof that all shoals are genetically related by hydrodynamic processes that are operative on a regional scale.

In the area of study, shoreface-connected shoals exist which are believed to be in various stages of elongation, separation and isolation from the shore face as a result of coastal retreat. Therefore, isolated shoals on the shelf are judged to have been formerly shoreface-connected and subsequently detached during landward coastal retreat. If, as proposed, the linear shoals originate nearshore, then the similarity in orientation of both shoreface-connected and isolated shoals with respect to the shoreline indicates that shoreline orientation probably remained essentially constant as the Holocene sea transgressed the entire inner continental shelf. Presence of similar appearing shoal features on the outer shelf may indicate unchanging conditions for an even longer time period.

ACKNOWLEDGMENTS

The ideas discussed in this paper have benefited from discussions with so many of our colleagues that it is impossible to list them all. However, for particular help and provocative discussion, special thanks are extended to Dr. Wm. R. James of the Coastal Engineering Research Center, Dr. Ole S. Madsen of Massachusetts Institute of Technology, Dr. Robert Byrne of the Virginia Institute of Marine Science, and Dr. J. C. Ludwick of Old Dominion University.

Data obtained for this study, unless otherwise noted, resulted from the general research program of the Corps of Engineers' Coastal Engineering Research Center. Permission was granted by the Chief of Engineers to publish this information. Work on the Virginia coast was carried out under contract DACW 72-69-C-0016 between CERC and Old Dominion University. Additional funding of the Virginia coast work was provided by NSF grants GA-13831 and GA-27305 and by the United States Geological Survey. Portions of the field work were conducted aboard the Duke

research vessel Eastward, supported by NSF grant GB-17545. The contribution by Swift to this paper is part of the COMSED project of NOAA-AOML, an investigation of sedimentation on the Atlantic continental margin of the United States.

REFERENCES

Assaf, G., Gerard, R., and Gordon, A. L. (1971). Some mechanisms of ocean mixing revealed in aerial photographs. *J. of Geophysical Res.* **76**, 6550-6572.

Bajorunas, L., and Duane, D. B. (1967). Shifting offshore bars and harbor shoaling. *J. of Geophysical Res.* **72**, 6195-6205.

Berg, D. W., and Duane, D. B. (1968). Effect of particle size and distribution on stability of artificially filled beach, Presque Isle Peninsula, Pa. *In* "Proc. 11th Conf. Great Lakes Res.," pp. 161-178. Internatl. Assoc. for Great Lakes Res., Ann Arbor, Michigan.

Bumpus, D. F., and Lauzier, L. M. (1965). Surface circulation on the continental shelf of eastern North America between Newfoundland and Florida. *In* "Serial Atlas of the Marine Environment." Folio 7, Am. Geographical Soc., New York.

Caldwell, Joseph M. (1966). Coastal processes and beach erosion. *J. Sc. Civil Eng.* **53**, 142-157.

Colquhoun, D. J. (1969). Coastal plain terraces in the Carolinas and Georgia, USA. *In* "Quaternary Geology and Climate." pp. 150-162. National Academy of Science, Washington, D.C.

Davies, J. L. (1964). A morphogenic approach to world shorelines. *Zeit. für Geomorphologie* **8**, 127-142.

Dietz, R. S. (1963). Wave-base, marine profile of equilibrium and wave built terraces: a critical appraisal. *Bull. Geol. Soc. Am.* **74**, 971-990.

Dzulynski, S. (1965). New data on experimental production of sedimentary structures. *J. Sed. Petrology* **35**, 196-212.

Emery, K. O. (1965). Characteristics of continental shelves and slopes. *Am. Assoc. Petrol. Geol.* **49**, 1379-1384.

Emery, K. O. (1966). Atlantic continental shelf and slope of the United States, geologic background. *U.S. Geol. Survey Prof. Paper* **529-A**, 1-23.

Emery, K. O. (1967). The Atlantic continental margin of the United States during the past 70 million years. *Geol. Assoc. Canada, Spec. Paper* **4**, 53-70.

Emery, K. O. (1968). Relict sediments on continental shelves of the world. *Am. Assoc. Petrol. Geol.* **52**, 445-464.

Emery, K. O. (1969). The contiental shelves. *Scientific Am.* **221**, 106-121.

Faller, A. J. 1969). The generation of Langmuir circulations by the eddy pressure of surface waves. *Limnology and Oceanography* **14**, 504-513.

Field, M. E. (1972). Buried strandline deposits on the central Florida inner continental shelf, 74 pp. Abstr. with Program, Geol. Soc. Amer. Southeastern Sect. Annual Mtg., **6**, 74.

Field, M. E., and Duane, D. B. (1972). Geomorphology and sediments of the inner continental shelf, Cape Kennedy, Florida. *U.S. Army Coastal Engr. Res. Ctr.*, Technical Memo.

Fischer, A. G. (1961). Stratigraphic record of transgressing seas in light of sedimentation on Atlantic coast of New Jersey. *Bull. Am. Assoc. of Pet. Geologists* **45**, 1656-1666.

Folk, R. L. (1971). Longitudinal dunes of the northwestern edge of the Simpson desert, Northern Territory, Australia. *Sedimentology* **16**, 5-54.

Garrison, L. E., and McMaster, R. C. (1966). Sediments and geomorphology of the continental shelf off southern New England. *Mar. Geol.* **4**, 273-289.

Gilbert, G. K. (1890). Lake Bonneville. *U.S. Geol. Surv. Monograph 1*, 438 pp.

Goldsmith, V., and Colonell, J. M. (1970). Effects of nonuniform wave energy in the littoral zone. *Proc. 12th Coastal Engineering Conf. Amer. Soc. of Civil Engineers, New York* **2**, 767-785.

Hails, J. R., and Hoyt, J. H. (1969). An appraisal of the evolution of the lower Atlantic coastal plain of Georgia, USA. *Tran. Papers Inst. Brit. Geog.* **46**, 53-68.

Harris, D. L. (1972). Wave estimates for coastal regions. *In* "Shelf Sediment Transport: Process and Pattern" (D. J. P. Swift, D. B. Duane, and O. H. Pilkey, eds.). Dowden, Hutchinson & Ross, Stroudsburg, Pennsylvania.

Harrison, W., Norcross, J. J., Pore, N. A., and Stanly, E. M. (1967). Shelf waters off the Chesapeake Bight. *Environmental Sciences Services Administration, Prof. Paper* **3**, 1-82.

Hayes, M. O., and Bothroyd, J. C. (1969). Storms as modifying agents in the coastal environment. *In* Coastal Environments, NE Mass. and N.H.," 245-265. Coastal Res. Group, Univ. Mass., Amherst.

Hjulstrom, F. (1939). Transportation of detritus by moving water. *In* "Recent Marine Sediments," (P. D. Trask, ed.), AAPG, Tulsa, Oklahoma.

Holliday, B. W., McHone, J., Shielder, G., and Swift, D. J. P. (in preparation). Evolution of an inner shelf ridge system, Virginia Beach, Virginia.

Houbolt, J. H. C. (1968). Recent sediments in the southern bight of the North Sea. *Geol. Mijnbouw* **47**, 245-273.

Hyne, N. J., and Goodell, H. G. (1967). Origin of sediments and submarine geology of the inner continental shelf off Choctawatchee Bay, Florida. *Marine Geol.* **5**, 1125-1136.

Johnson, D. W. (1919). "Shore Processes and Shoreline Development." 584 pp. Hafner, New York.

Jordan, G. F. (1962). Large submarine sand waves. *Science* **136**, 839-848.

Knott, S. T., and Hoskins, H. (1968). Evidence of Pleistocene events in the structure of the continental shelf off the northeastern U.S. *Marine Geol.* **6**, 5-43.

Kraft, J. C. (1971a). Sedimentary facies patterns and geologic history of a Holocene marine transgression. *Bull. Geol. Soc. Am.* **82**, 2131-2158.

Kraft, J. C. (1971b). A guide to the geology of Delaware's coastal environments. Publ. 2GL039, 220 pp. College of Marine Studies, Univ. of Delaware, Newark, Delaware.

Kuelegan, G. H. (1948). An experimental study of submarine sand bars. *Beach Erosion Board, U.S. Army Corps of Engineers Tech. Rept* **3**, 40 pp.

Langmuir, I. (1938). Surface motion of water induced by wind. *Science* **87**, 119-123.

Ludwick, J. C. (1972). Migration of tidal sand waves in Chesapeake Bay entrance. *In* "Shelf Sediment Transport: Process and Pattern" (D. J. P. Swift, D. B. Duane, and O. H. Pilkey, eds.). Dowden, Hutchinson & Ross, Stroudsburg, Pennsylvania.

McKinney, T. F., and Friedman, G. M. (1970). Continental shelf sediments of Long Island, New York. *Jour. Sed. Petrol.* **40**, 213-248.

McMaster, R. L. (1954). Petrography and genesis of the New Jersey beach sands. *State of N.J., Dept. of Conserv. and Econ. Devel., Bull.* **63**, 239 pp.

Meisburger, E. P., and Field, M. E. (1972). Neogene sediments of the North Florida Atlantic inner shelf. Abstr. with Program, Geol. Soc. Am. Annual Mtg., **85**, 593.

Meisburger, E. P., and Duane, D. B. (1971). Geomorphology and sediments of the inner continental shelf Palm Beach to Cape Kennedy, Florida. *U.S. Army Coastal Engineering Center, Technical Memo.* **34**, 111 pp.

Moody, D. W. (1964). Coastal morphology and processes in relation to the development of submarine sand ridges off Bethany Beach, Delaware. 160 pp. Ph.D. thesis, The Johns Hopkins University, Baltimore, unpublished.

Oaks, R. Q., Jr., and Coch, K. (1963). Pleistocene sea levels, southeastern Virginia. *Science*

Oertel, G. F., and Howard, J. D. (1972). Water circulation and sedimentation at estuary entrances on the Georgia coast. *In* "Shelf Sediment Transport: Process and Pattern" (D. J. P. Swift, D. B. Duane, and O. H. Pilkey, eds.). Dowden, Hutchinson & Ross, Stroudsburg, Pennsylvania.

Payne, L. H. (1970). Sediments and morphology of the continental shelf off southeastern Virginia. 70 pp. Thesis, Columbia University, New York, unpublished.

Pilkey, O. H., and Field, M. E. (1972). Onshore transportation of continental shelf sediment: Atlantic southeastern United States. *In* "Shelf Sediment Transport: Process and Pattern" (D. J. P.

Swift, D. B. Duane, and O. H. Pilkey, eds.). Dowden, Hutchinson and Ross, Stroudsburg, Pennsylvania.

Price, W. A. (1954). Dynamic environments: reconnaissance mapping, geologic and geomorphic, of continental shelf of Gulf of Mexico. *Transactions Gulf Coast Assoc. of Geologic Societies, Houston, Texas,* **IV**, 78-107.

Ross, D. A. (1970). Atlantic continental shelf and slope of the United States - heavy minerals of the continental margin from southern Nova Scotia to northern New Jersey. *U.S. Geol. Survey Prof. Paper* **529-G**, 40 pp.

Sanders, J. F. (1962). North-south trending submarine ridge composed of coarse sand off False Cape, Virginia (Abstr.). *Bull. Amer. Assoc. Petrol. Geologists* **46**, 278.

Saylor, J. H., and Hands, E. B. (1970). Properties of longshore bars in the Great Lakes. *Proc. 12th Conf. on Coastal Engineering, Amer. Soc. Civil Engineers, New York* **2**, 838-853.

Schlee, J., and Pratt, R. (1972). Atlantic continental shelf and slope of the United States. *U.S. Geol. Survey Prof. Paper* **529-H**.

Schopf, T. J. M. (1968). Atlantic continental shelf and slope of the United States - Nineteenth Century exploration. *U.S. Geol. Survey Prof. Paper* **529-F**.

Shepard, F. P. (1950). Longshore-bars and longshore-troughs. *Beach Erosion Board, Corps of Engineers,* Washington, D.C., *Tech. Memo.* **15**, 32 pp.

Shepard, F P. (1963). "Submarine Geology." 2nd Ed., 557 pp., Harper and Row, New York.

Swift, D. J. P., Sanford, R. B., Dill, C. E., Jr., and Avignone, N. F. (1971). Textural differentiation on the shore face during erosional retreat of an unconsolidated coast, Cape Henry to Cape Hatteras, western North Atlantic shelf. *Sedimentology* **16**, 221-250.

Swift, D. J. P., Holliday, B., Avignone, N., and Schideler, G. (1972a). Anatomy of a shore face ridge system, False Cape, Virginia. *Marine Geol.* **12**, 59-84.

Swift, D. J. P., Kofoed, J. W., Saulsbury, F. P., Sears, P. (1972). Holocene evolution of the shelf surface, central and southern Atlantic coast of North America. *In* "Shelf Sediment Transport: Process and Pattern" (D. J. P. Swift, D. B. Duane, and O. H. Pilkey, eds.). Dowden, Hutchinson & Ross, Stroudsburg, Pennsylvania.

Uchupi, E. (1968). The Atlantic continental shelf and slope of the United States (Physiography). *U.S. Geol. Survey, Prof. Paper* **529-C**, 30 pp.

Uchupi, E. (1970). Atlantic continental shelf and slope of the United States—shallow structure. *U.S. Geol. Survey Prof. Paper* **529-I**, 44 pp.

Veatch, A. C., and Smith, P. A. (1939). Atlantic submarine valleys of the United States and the Congo submarine valleys. *Geol. Soc. Am., Spec. Papers* **7**, 101 pp.

U.S. Army Corps of Engineers (1966). Shore Protection, Planning and Design. *Tech. Rept* **4** (3rd Ed.), 400 pp.

U.S. Army Corps of Engineers, Jacksonville District (1967). "Beach Erosion Control Study on Brevard Co., Florida." Jacksonville, Florida, 42 pp.

U.S. Army Corps of Engineers, Baltimore District (1970). "Beach Erosion Control Study Atlantic Coast of Maryland and Assateague Island, Virginia." Baltimore, Maryland, unpublished.

U.S. Dept. of Commerce (1970). *Tide Tables for 1971, East Coast of North and South America, Including Greenland.* Environmental Sciences Service Administration.

Weigel, R. L. (1964). "Oceanographical Engineering." 532 pp. Prentice-Hall, Englewood Cliffs, New Jersey.

Weinman, Z. H. (1971). "Analysis of Littoral Transport by Wave Energy: Cape Henry, Virginia to the Virginia, North Carolina border." Ph D Thesis, Old Dominion Univ., Norfolk, Virginia, unpublished.

Williams, S. J., and Field, M. E. (1971). Sediments and shallow structures of the inner continental shelf off Sandy Hook, New Jersey. *Abstr. with Program, Geol. Soc. Amer., Northeastern Sect. Mtg.*, **3**, 62.

Williams, S. J., and D. B. Duane (in prep.). Geomorphology and sediments of the inner New York Bight continental shelf. U.S. Army Coastal Engineering Center, Technical Memo.

Reprinted from Nature 235, 156-157.

Plate Tectonics in the Caribbean

Freeland and Dietz[1] have presented a speculative geological history of the Caribbean using plate tectonic theory, and simultaneously Dickinson[2] suggested that two types of plate convergence may be distinguished by examining sedimentary and tectonic evidence. Geological data from the Caribbean support much of the proposed geological history but differ in significant details. On the other hand, the Caribbean seems to fit rather well the Dickinson distinction between plate convergence types.

Freeland and Dietz suggest that the pre-Jurassic Middle America areas of Yucatan and Nicaragua were nestled within the Gulf of Mexico, and that the Caribbean did not exist until Triassic times. During the Triassic the area fragmented into plates which rotated and moved into their present positions. Little can be criticized in the pre-Jurassic history presented, as no dated pre-Jurassic rocks have been mapped in the West Indies. Rocks as old as Middle Jurassic are exposed in Cuba[3], but the oldest dated sedimentary rocks are Albian elsewhere in the West Indies. Metamorphic rocks and ultramafic rocks are pre-Albian in the Greater Antilles[4] except in Cuba where they may be pre-Jurassic[5]. Ocean floor sampling in the Caribbean and Gulf of Mexico has revealed no rocks older than Jurassic and Cretaceous[6]. This perhaps suggests that no basins existed before that time, but it is equally possible that older oceanic rocks underlie the sampled horizons. Dengo[7] and others[8,9] have presented an interpretation of the geological history of the Yucatan–Guatamala and Nicaragua blocks which is internally consistent and which suggests that the two blocks were on opposite sides of a converging plate junction during pre-Mesozoic times. It would be quite a coincidence if these two plates split apart, moved several hundred miles, and re-united in the same relative positions. Moreover, to move the blocks from the Gulf of Mexico into their present positions requires a peculiar spiral spreading motion[1] with northwestern Yucatan pivoting on its north-west corner impelled by a spreading centre in the form of a circular arc stretching along the base of the continental shelf from Florida to southern Mexico near Vera Cruz. Perhaps a more successful history would follow Dengo and treat Middle America as a tectonic unit formed in the Palaeozoic as a convergent plate junction, and moved into its present location as a unit but not necessarily from the present Gulf of Mexico. The southern edge of the Palaeozoic North American continent was not necessarily at the present edge of the continental shelf in the Gulf of Mexico; it may have been further north next to the Appalachian orogenic belt. Palaeomagnetic data from Middle America should be a prerequisite for further speculation about large rotations of the one or more plates that can be defined.

The post-Triassic history of the Caribbean as suggested by Freeland and Dietz is more plausible. It is possible that the Cuban area began as a shelf between Yucatan and Nicaragua and moved northwards from a spreading axis along the northern Nicaraguan coast[1]. Jurassic rocks in Cuba thicken and become more quartz-rich to the south[3] indicating a southward source area. The Isle of Pines and the Trinidad Mountains, exposures of pre-Jurassic metamorphic rocks near to and in southern Cuba, could provide such a source without invoking the Middle American plates, however. Alternatively the Cuban metamorphics could be fragments of the Nicaragua plate moved to the north.

A more serious objection is the differing characters of the Yucatan basin and the Nicaragua rise. Freeland and Dietz suggest that these had the same origin: proto-Cuba and proto-Hispaniola split off from Middle America and moved northeastward across the Caribbean, making volcanoes and islands as they went. But the Yucatan basin is oceanic with the closest resemblance to oceanic crust of any part of the Caribbean, while the Nicaragua rise is a shallow bank with a thicker crust and the moderate sized island of Jamaica. Why are they different? Moreover, the Greater Antilles are suggested to achieve their present position by small conveniently located spreading centres between each island pair: at least four separate spreading centres. This ignores the Cretaceous and early Tertiary tectonic pattern in the Greater Antilles which seems to show the results of a uniform force applied over a large area forming a complex but almost continuous ridge whose upper portions form islands, not a series of fault troughs and horsts oriented normal to the ridge as required by the Ptolemaic modifications to the plate tectonic hypothesis under discussion.

Dickinson's idea of activation and collision types of plate convergence at continental margins[2] offers a partial solution to the differing development of the Yucatan–Cuba and the Nicaragua–Hispaniola areas. The activation type of junction has oceanic lithosphere underthrusting the adjacent continental lithosphere, the normal type of plate convergence at a continental margin. This idea can be applied to intra-oceanic junctions if one lithospheric plate is less dense than the other; the less dense plate forms the overriding unit and a volcanic island arc is formed. The eastern Greater Antilles is an example, with a volcanic arc forming from Albian to Middle Eocene times.

The collision type of junction occurs when continental lithosphere is on the underthrusting side of a converging plate junction. It is less dense, and its buoyancy prevents it from descending into the Benioff Zone to any great distance. The convergence either stops, or in exceptional cases continues as continental lithosphere underthrusting the other plate as in the Himalayas, or there is a "readjustment of plate boundaries" (ref. 2). The third possibility can be applied to the tectonic history of the Caribbean.

In a general way, the tectonic history of the Caribbean can be viewed as the interaction of two lithosphere plates which changes its character progressively from west to east, from a converging junction to a lateral junction. Convergence began in the Antilles in Cretaceous, perhaps Albian time, with a less dense Caribbean plate overriding a more dense Atlantic plate along the Cuba–Virgin Islands trend. Perhaps the western end of the overriding plate moved north-eastward along the eastern edge of the Yucatan Peninsula[1]. This movement and its volcanism continued until Turonian or Campanian time, when the Bahamas area of continental lithosphere entered the Benioff Zone north of Cuba and choked it, effectively welding the Cuban end of the Caribbean plate to the North America–Atlantic Plate. This is the collision type of convergence of Dickinson[2]. The eastern part of the northward moving Caribbean plate continued to move, however, and a lateral junction began to develop in the Cayman Trench area, perhaps forming the Nicaragua rise and the Early Tertiary volcanism in easternmost Cuba, Jamaica, and the eastern Greater Antilles. Then, in mid-Eocene times, convergence and volcanism ceased in the Jamaica–Virgin Islands segment, but lateral movement continued. At roughly that time convergence and volcanism began in the Lesser Antilles. Thus the orogeny shifted eastward in the Caribbean, being progressively replaced by lateral motion at the plate boundary. This analysis could perhaps be expanded to Middle America, where convergence may have changed to lateral movement in the Jurassic[1]. It is possible that the submarine Beata and Aves Ridges represent early zones of convergence related to the western Caribbean convergences, but those ridges are as yet almost unknown.

This work was carried out at the Department of Earth Sciences, University of Leeds.

PETER H. MATTSON

Department of Earth and Environmental Sciences,
Queens College,
City University of New York,
Flushing, New York 11367

Received August 31, 1971.

[1] Freeland, G. L., and Dietz, R. S., *Nature*, **232**, 20 (1971).
[2] Dickinson, W. R., *Nature*, **232**, 41 (1971).
[3] Furrazola-Bermudez, G., Judoley, C. M., Mijailovskaya, M. S., Miroliubov, Y. S., Novojatsky, I. P., Nuñez-Jiminez, A., and Solsona, J. B., *Geologia de Cuba*, 239 (Inst. Cubano Recursos Minerales, Habana, 1964).
[4] Mattson, P. H., in *Data for Orogenic Studies* (Geol. Soc. London, Special Publ. 4, in the press).
[5] Ewing, M., Worzel, J. L., Beall, A. O., Berggren, W. A., Bukry, D., Burk, C. A., Fischer, A., and Pessagno, jun., E. A., *Initial Reports of the Deep Sea Drilling Project*, **1**, 672 (US Government Printing Office, Washington DC, 1969).
[6] JOIDES, *Geotimes*, **16**, 12 (1971).
[7] Dengo, G., *Trans. Gulf Coast Assoc. Geol. Soc.*, 311 (1969).
[8] Dengo, G., and Bohnenberger, O., in *Tectonic Relations of North Central America and the Western Caribbean*, 203 (AAPG Mem. 11, 1969).
[9] McBirney, A. R., and Bass, M. N., in *Tectonic Relations of North Central America and the Western Caribbean*, 203 (AAPG Mem. 11, 1969).

Plate Tectonics in the Caribbean: a Reply

MATTSON's critique is in accord with most of our views[1]. Here we answer most of his points by mentioning details omitted from the original paper because of space limitations.

(1) The region was essentially a landmass, part of Pangaea, before the end of the Triassic (190 m.y. BP, revised time scale)[2]. The only pre-Jurassic movement was initiation of tension causing the Triassic grabens revealed by drilling in the subsurface along the northern and western edges of the Gulf Coastal Plain. The initial split was along the edge of the basin, not at the present coastline. Palaeozoic metamorphic rocks on both the Yucatan and Nicaragua blocks, where they are not affected by subsequent compression and increased metamorphism in the Guatemalan foldbelt, are low grade, with affinities to rocks of Mexico[3] and the Ouachita belt in Texas and Arkansas[4]. The major deformational episodes were synchronous with those of the Appalachians[3]. Accepting the Bullard reconstruction[5], the Yucatan-Nicaraguan block must have fit either in the Gulf of Mexico or the Pacific Ocean if one is to avoid extensive overlaps on the South American continent. A fit within the Gulf seems most plausible. No continental areas created during the Mesozoic or Cainozoic were included in our reconstruction of Pangaea. Some Palaeozoic continental crust may, however, have been present in the gap to the south-west of the Bahamas. If so, this material has now been incorporated in the metamorphic-volcanic melange of the oldest parts of the Greater Antilles and is not at present recognizable.

(2) The Yucatan-Nicaragua blocks rotated to their present positions during the early and middle Jurassic, forming the proto-Gulf (the northern half of which is now filled with prograded Mesozoic and Cainozoic sediments); the proto-Gulf of Honduras; and the Guatemalan foldbelt.

(3) The Caribbean did not form until South America drifted away from Africa about 135 m.y. BP. By our interpretation, it was a spreading centre as the North and South American plates moved in separate directions, North America rotating anticlockwise relative to South America (see Fig. 6 of ref. 1). While the Caribbean opened, the Lesser Antilles subduction zone became active as the Atlantic, to the east, underrode the new seafloor.

(4) The early motion of South America was nearly due west with respect to Africa, but towards the end of the Lower Cretaceous it became more northerly. The later motion initiated compression and subduction along the Venezuela-Colombia coast. Initially larger than it is today, the Caribbean underwent closure during the Upper Cretaceous and early Tertiary.

An alternative hypothesis for the origin of the Jamaica-Hispaniola-Puerto Rico blocks would be orogenic construction along a single line of compression along the entire northern margin of the Caribbean. As closure progressed, subduction with attendant volcanism and metamorphism might have built these islands in their present locations instead of drifting them away from Nicaragua. Cuba, however, would still be formed by a spreading centre in the Gulf of Honduras, because Cuba is north of the Puerto Rico-Cayman trench and therefore outside of the Caribbean plate. The Yucatan Basin would be the result of this movement. The marginal basins thus produced are similar to others in crustal structure[6]. Although they attain nearly oceanic depths, they are usually generated by spreading characterized by the absence of a central ridge. In the Caribbean, however, certain rises may be fossil spreading centres.

(5) The Caribbean continued to close slowly. The climax of movement was during the middle Eocene when there was major tectonism on the northern and southern margins. The islands of the Greater Antilles then attained their present proportions.

(6) From the Eocene to the Present, the plate comprising the Caribbean Sea and the Nicaraguan block has been essentially welded to the northern margin of South America. Field evidence indicates no movement between them[7], although there is some seismic activity[8]. The major present movement between the North and South American plates is a sinistral shear along the Puerto Rico-Cayman trench[8]. The lack of apparent offset between the Yucatan and Nicaragua blocks indicates limited movement.

Mattson's comments concerning plate boundaries seem to confuse the issue. The nomenclature of the convergences is not as important as the results of the motions. The western, northern, and eastern boundaries of the Caribbean during the Upper Cretaceous-Early Tertiary closing stage were inward-dipping Benioff zones. It does not seem to matter whether the overriding portion of the plate was continental or oceanic; the results are similar. Part of the Caribbean plate was underthrust beneath South America. In turn, the Caribbean consumed ocean floor south of the Bahamas, east of the Antilles, and west of Nicaragua, Costa Rica, and Panama. During the last half of the Cainozoic, overthrusting ceased along the northern margin and a vertical shear zone took its place. To the west the Mexican trench is still active, although partially blocked by the Cocos ridge. The Lesser Antilles zone is still active, although it has probably migrated eastward.

GEORGE L. FREELAND
ROBERT S. DIETZ

NOAA, Atlantic Oceanographic and
Meteorological Laboratories,
901 *South Miami Avenue,*
Miami, Florida 33130

Received November 2, 1971.

[1] Freeland, G. L., and Dietz, R. S., *Nature*, **232**, 20 (1971).
[2] *Geol. Soc. Phanerozoic Time Scale: Quart. J. Geol. Soc. London*, **120S**, 260 (1964).
[3] Dengo, G., *Trans. Gulf. Coast Geol. Soc.*, **19**, 311 (1969).
[4] Flawn, P., *The Ouachita System* (University of Texas Publ., 6120, 1961).
[5] Bullard, E., *et al.*, in *A Symposium on Continental Drift*, 41 (*Phil. Trans. Roy. Soc.*, 1965).
[6] Karig, D. E., *Geol. Soc. Amer. Bull.*, **82**, 323 (1971).
[7] Hess, H. H., in *Caribbean Geological Investigations*, 1 (Geol. Soc. Amer. Mem. 98, 1966).
[8] Molnar, P., and Sykes, L. R., *Geol. Soc. Amer. Bull.*, **80**, 1639 (1969).

Reprinted from International Hydrographic Review *XLIX*, No. 1, 81-94.

COMPUTER PRODUCED PROFILES OF MICROTOPOGRAPHY AS A SUPPLEMENT TO CONTOUR MAPS

by Paul J. Grim (*), George H. Keller,
and Robert J. Barday (**)
Atlantic Oceanographic and Meteorological Laboratories
Miami, Florida

ABSTRACT

The principal products of deep sea bathymetric surveys are contour maps depicting the relatively larger features of the floor. Unfortunately, however, these maps cannot display most of the small scale features (microtopography) that are recorded on fathograms. Knowledge of this microtopography and some means of displaying it are increasingly important as man develops a greater need for utilization of the sea floor. Since future surveys are likely to be automated for data reduction, an economical and quickly produced supplement to contour maps can be computer produced profiles that clearly display the details of the bottom topography. Illustrations based on a recent narrow-beam echo sounder survey clearly point out the benefit from presenting bathymetric data in other than map form.

INTRODUCTION

Man is rapidly developing his technology to the point where exploitation of the sea floor will be a common occurrence in all depths of the oceans. One of the tools most needed for this will be an accurate knowledge of the undersea topography. This must be known if man is to lay pipelines and cables, construct bottom mounted structures or conduct sea floor mining activities. However, bathymetric contour maps of large portions of the deep ocean do not show the exact nature of the sea floor because these areas are often characterized by small scale features (here referred to as microtopography) having lateral dimensions much less than the separation of the survey tracklines. A knowledge of the nature of

(*) Currently at the National Geophysical Data Center of NOAA's Environmental Data Service.

(**) Currently at the Department of Oceanography, Oregon State University, Corvallis, Oregon.

this microtopography is the very information that will be most valuable for some aspects of man's utilization of the sea floor.

The purpose of this paper is to point out that in many oceanic areas, bathymetric profiles showing the microtopography are valuable supplements to contour maps. With the use of computers and automatic X-Y plotters, these profiles can be produced rapidly and economically since it is likely that most deep sea soundings collected in the future will be digitized for computer processing.

The profile presentation of bathymetry is particularly meaningful if, when conducting the survey, a narrow beam echo sounder is used. Such a sounding system obtains a much greater degree of detail than is normally possible with a conventional wide beam sounder (see, for example, KRAUSE and KANAEV, 1970) thus providing a very close approximation of the sea floor relief even in the roughest terrains.

EXAMPLES FROM A SURVEY SOUTH OF PANAMA AND COSTA RICA

To develop the argument presented in this paper, bathymetric data selected from a recent deep-sea survey are used. These data serve to illustrate: (1) the character of typical microtopography as shown by narrow beam echo sounder fathograms, (2) the difficulty or near impossibility of showing in a meaningful manner the nature of the sea floor in certain areas with contour maps based on the trackline spacing that will likely be used in future deep sea surveys of significantly large regions of the ocean floor and (3) how the microtopography can be shown with computer-produced profiles quickly and economically if digital methods are used for reducing the survey data.

The survey was conducted in the equatorial Pacific Ocean (figure 1) in August 1969 by the National Ocean Survey ship *Oceanographer*. Approximately 11 200 kilometres (6 000 nautical miles) of trackline data were obtained with satellite navigational control centered on the Panama fracture zone, a seismically active fault zone trending north-south between 82° and 83°W (MOLNAR and SYKES, 1969). The basic survey pattern was a grid with tracklines oriented north-south and east-west at one quarter degree intervals (about every 28 kilometres, or 15 nautical miles). Bathymetric and magnetic results of this survey, including data reduction techniques, have been discussed by GRIM (1970a). All depths have been corrected for variations of sound velocity using Matthews' tables (1939).

The trackline density of this survey is about the same as that which has been used in the past, and proposed for future systematic surveys in the deep ocean. See, for example, the coverage of NOAA's north Pacific SEAMAP survey given by RYAN and GRIM (1968).

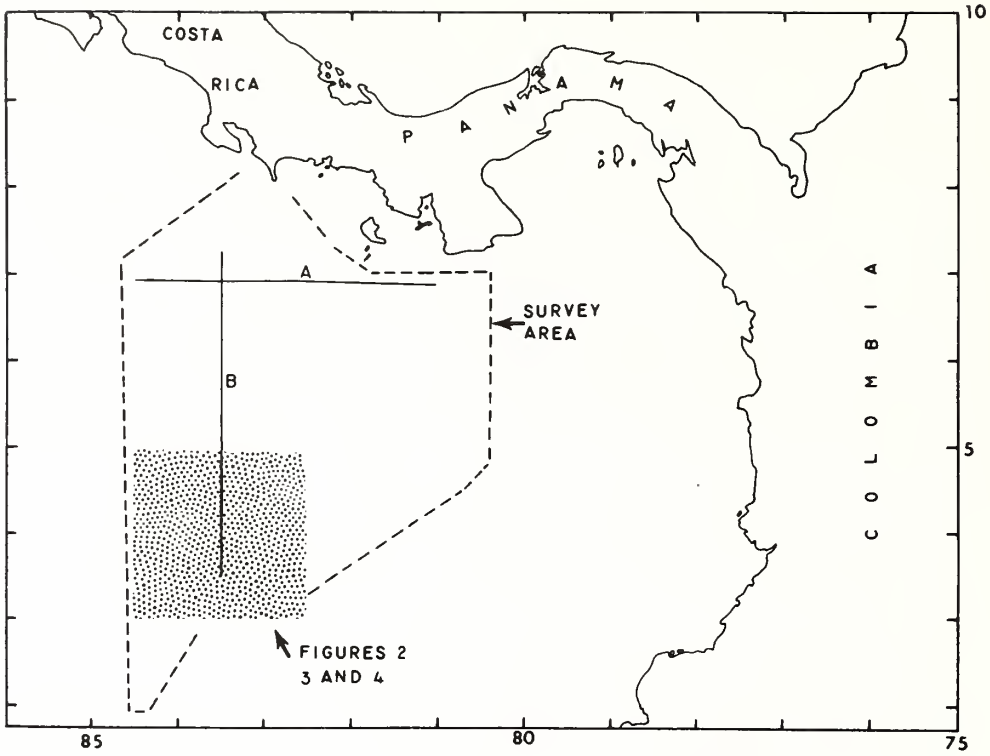

FIG. 1. — Survey area. The stippled part of the area is characterized by extremely rugged topography. Computer produced bathymetric profiles are given for tracklines A and B in figures 5 and 6.

NARROW BEAM ECHO SOUNDER FATHOGRAMS

Depth measurements were obtained with a gyro-stabilized narrow beam echo sounder (20 000 hertz with a 3° beam width between −3 dB points and 6° between −15 dB points) and recorded on a precision bathymetric recorder. The records were digitized at 5-minute intervals (about every 2.3 km, or 1.25 n. miles) and at additional times (peaks, deeps, and slope changes) judged necessary to show the details of the sea floor on the subsequently produced computer plots. Plates 1 and 2 display portions of the survey fathograms which reveal areas of highly irregular relief. These fathograms clearly show that the very abrupt changes in the topography are faithfully recorded with a narrow-beam sounder. With conventional wide-beam echo sounding equipment the straightness of the scarps and the existence of the narrow deeps would not be seen. Discussions of directional echo sounding and how these results compare with those of wide beam sounders can be found in COHEN (1959) and KRAUSE and KANAEV (1970).

PROFILE A

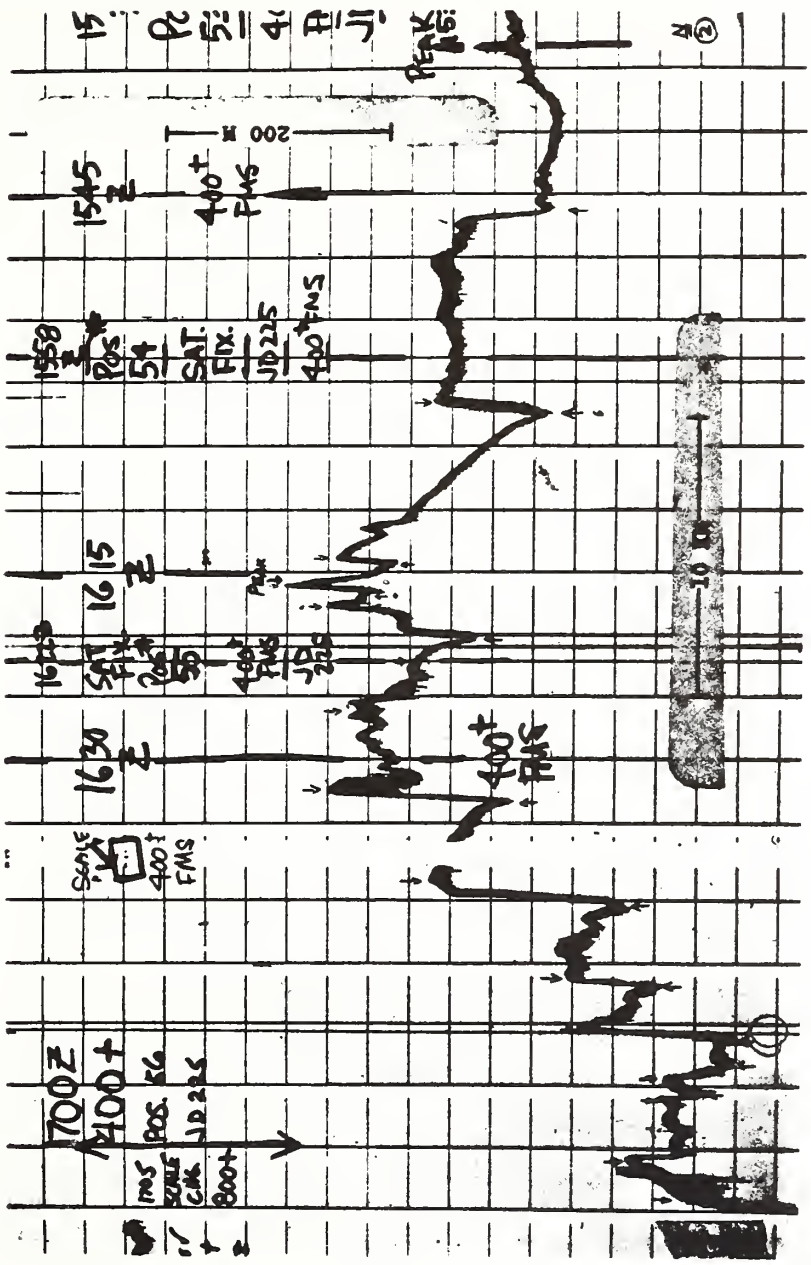
200 M
1545 Z
400+ FMS
1558 Z
POS 54
SAT. FIX.
JD 225
400+ FMS
1615 Z
SAT FIX
JD 225
400+ FMS
1630 Z
400+ FMS
SCALE 1:5
400+ FMS
1700 Z
400+
POS. 56
JD 225
800+
10 KM

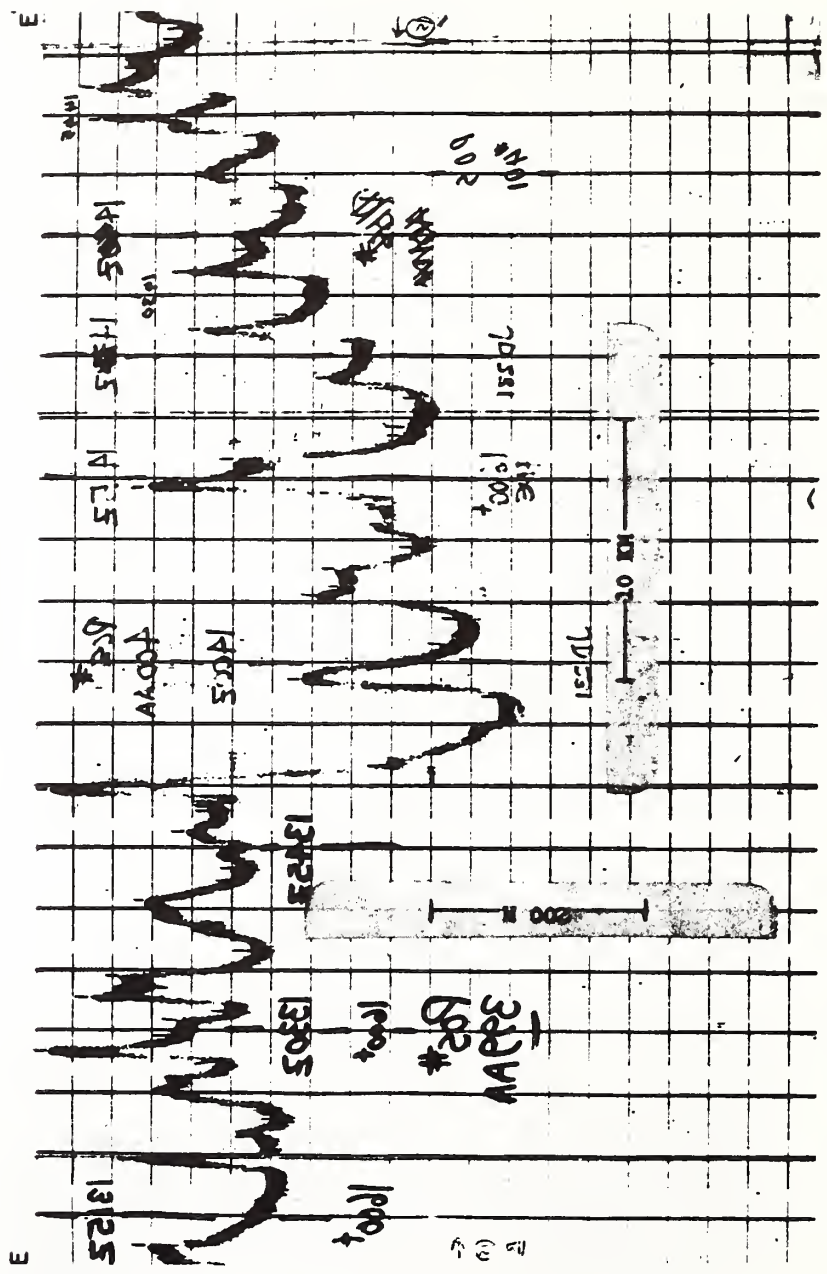

PLATES 1 and 2

Portions of narrow beam echo sounder fathogram records corresponding to parts of profiles A and B in figures 5 and 6 respectively. Vertical exaggeration about 35/1. Vertical black lines were made automatically every 5 minutes and at fix times and other events. The fathogram in plate 2 is printed in reverse so that its orientation is the same as profile B in figure 6.

LOSS OF TOPOGRAPHIC DETAIL ON A CONTOUR MAP

In portions of the survey area it is difficult or impossible to contour accurately the sea floor because of the microtopography. Such a terrain is located in the southern part of the survey area. The complicated nature of the bathymetry owing to such microtopography is clearly shown by the series of profiles in figure 2. Each trackline plot represents the average depth of the soundings obtained along that particular segment. With one exception these averages lie between about 2 900 metres and 3 300 metres (the exception being the short east-west segment at 3.5°N between 83.5°W

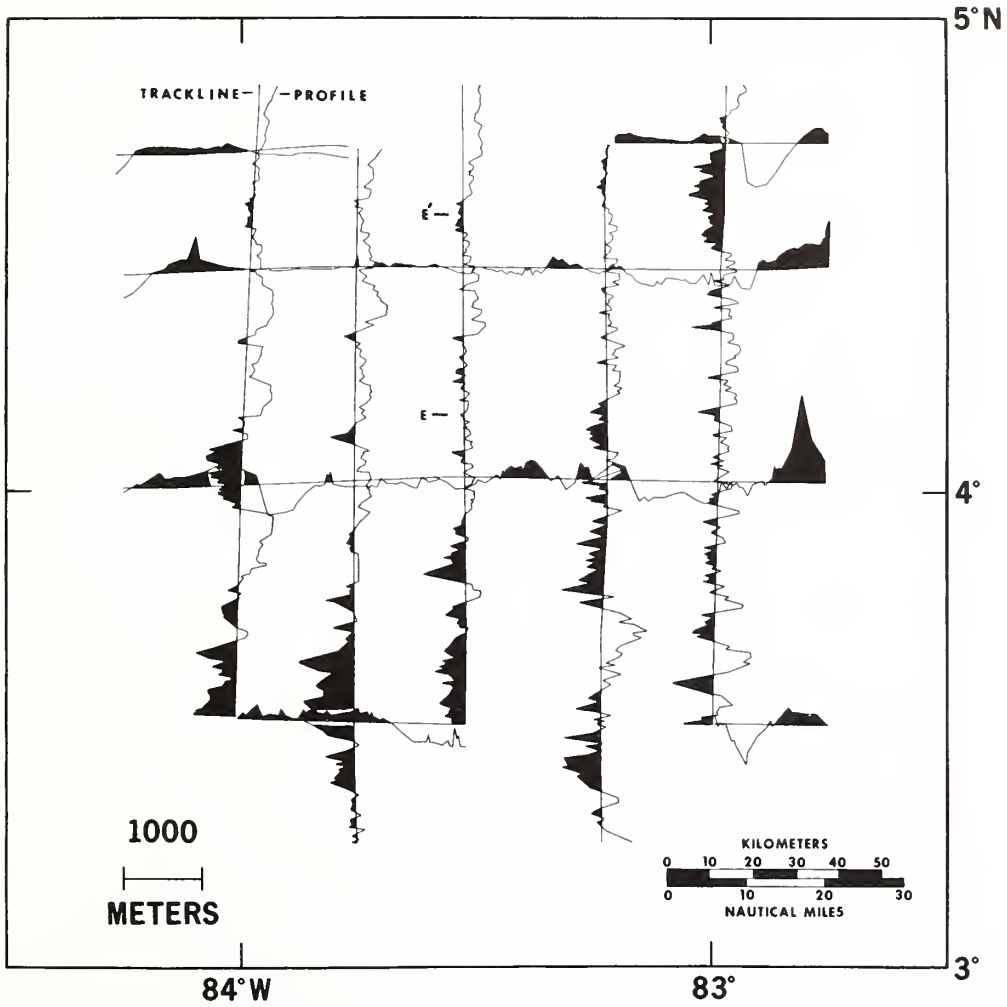

FIG. 2. — Bathymetric profiles from southern part of survey area presented along tracklines (see figure 1). The blackened portions of the profiles represent depths shoaler than the average depth along each trackline segment. Vertical exaggeration for each profile is about 20/1. Relief of the microtopography is given by the 1 000-metre scale. The fathogram record between E and E′ is shown in plate 2.

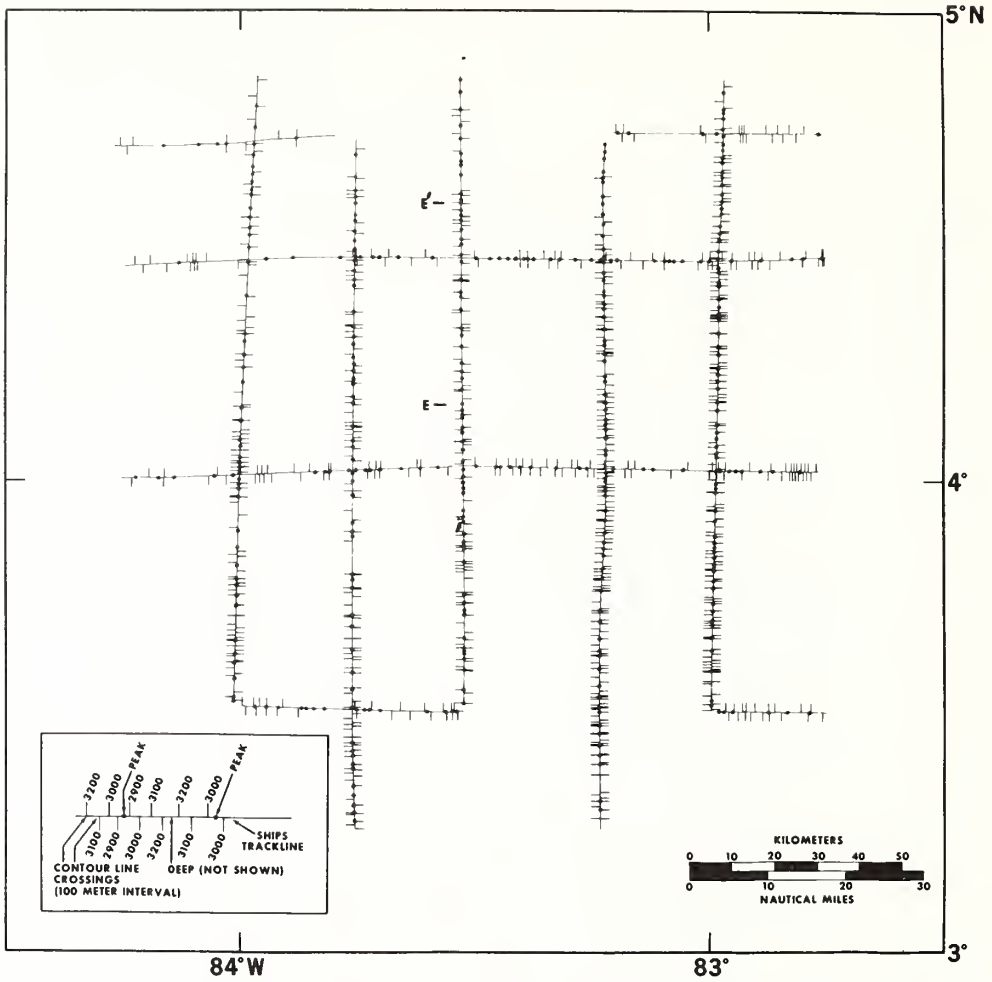

FIG. 3. — Alternating ticks normal to the tracklines indicate locations of 100-metre contour lines. Dots show locations of bathymetric peaks. Deeps are not indicated (see inset and text for explanation).

and 84°W which has an average depth of about 2 700 metres). The portions of each profile shoaler than the average depth are blackened.

Most of the depths within the area of figure 2 are between 2 600 and 3 800 metres. West of 83°W the grain of the topography (i.e. the trend of the ridges and troughs) is east-west as seen by the correlation of some of the larger features across several north-south traverses. This is consistent with the observation that the topography along the north-south tracklines shows more peaks and deeps than that along east-west lines (i.e. the north-south lines have a shorter topographic "wavelength"). However, most of the smaller peaks and deeps cannot be correlated across the north-south lines showing that they lose their identity (for example, by bifurcating or merging with other ridges and troughs) over the spacing of the tracklines.

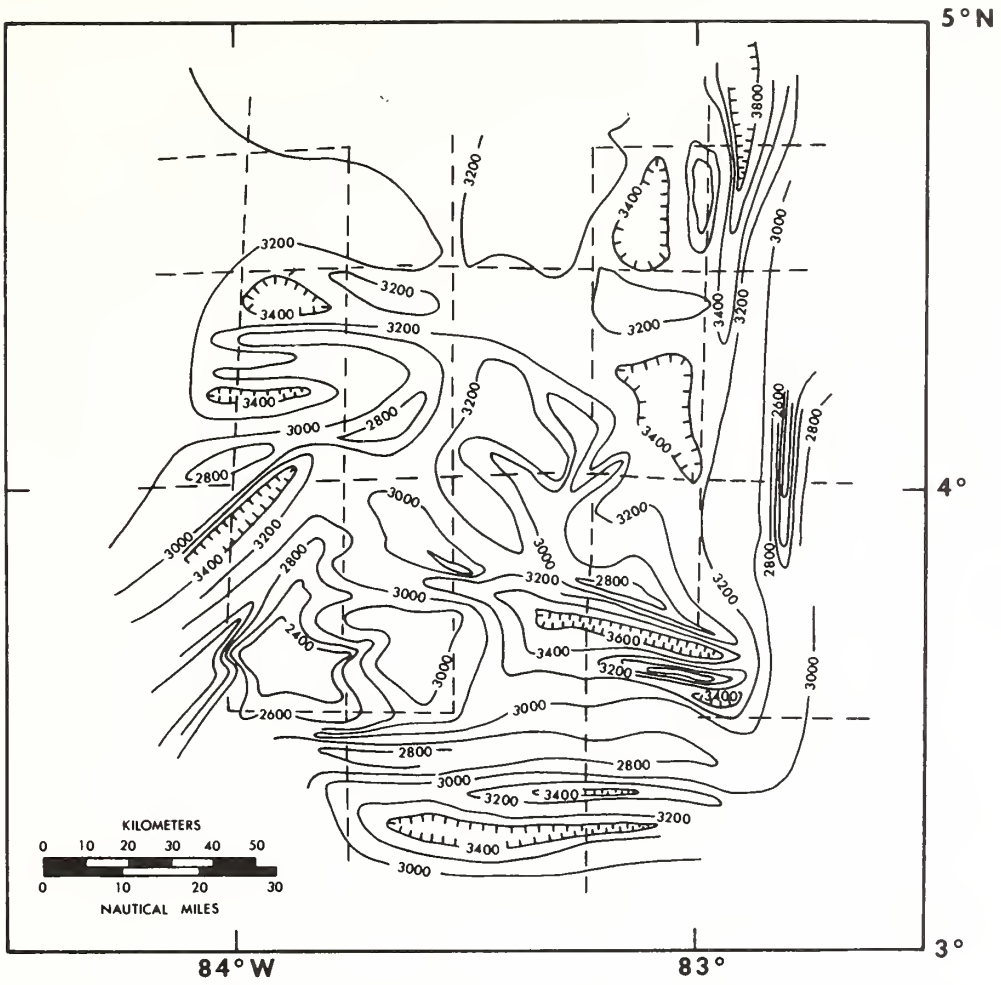

Fig. 4. — Generalized contour map (200-metre interval) of area shown in figures 2 and 3. Contours are also based on a single northeasterly trending trackline which is not shown here or in figures 2 and 3 for clarity of presentation.

The most noticeable aspect of figure 2 is the ruggedness of the sea floor although it has about the same general depth throughout the area. Abrupt changes in depths of hundreds of metres with slopes of 15° to 20° or more are common.

It is difficult to evaluate the problems in contouring such an area on the basis of the profiles. Figure 3 shows in map form how complex the area is for one attempting to contour it with a 100-metre contour interval. This figure was made by using all of the depths digitized from the sounding profiles. The intersections of the tracklines with the 100-metre isolines (i.e., where 100-metre contour lines would cross) are indicated by alternating tick marks normal to the track (this does not necessarily imply that the contours trend normal to the trackline). Minimum depths (peaks seen on the fathograms) are indicated by dots along the trackline. For clarity of presentation the values of the individual contour crossings at each tick are not given and the deeps that exist between the peaks are not shown.

This figure demonstrates the problems in showing the actual sea floor relief in this area with a contour map. If such deep sea areas are to be contoured, the tracklines will have to be spaced much closer than those of this survey and an appropriate map scale used. In spite of these difficulties, bathymetric contour maps in area similar to this are essential to provide some indication of the general depths. Such a map is given in figure 4. The contours of this map were drawn after subjectively smoothing the depth profiles. By comparing this figure with the profiles in figure 2, some of the larger features are seen to be clearly shown by the contours, although there is no indication of the great amount of microtopography present in this area. It should be emphasized that if this area were contoured by other workers using the same data, it is likely that the contour lines in much of the area would be drawn quite differently from the presentation given here.

COMPUTER PRODUCED PROFILES

In figures 5 and 6 computer-produced profiles from the survey are given as examples of how the profiles might be presented (although it is probably desirable to publish the profiles at a larger scale than given in the pages of this review). These profiles were made by an offline X-Y plotter using a computer program (GRIM, 1970b) which accepts reduced bathymetric data as input and produces annotated plots of bathymetry at any scale and vertical exaggeration desired. The profiles were made on the plotter in ink and are suitable for publication with very little additional labeling.

In the future one of the steps in producing contour maps will probably be obtaining reduced data such as those used as input to the above plotting program. Thus, the profiles can be considered as an economically produced "spin off" in the process leading to the production of the final map.

Although most of the microtopography seen on the fathograms can be displayed with computer-produced profiles, some of the very smallest features (those with relief on the order of metres and lateral dimensions on the order of tens of metres) are difficult to show. If these features are deemed important enough to present on the profiles, then care must be taken, not only in scaling the depths at very short intervals on the fathograms but in the vertical exaggeration and physical size of the resulting plots

DISCUSSION

Small scale bottom features are becoming increasingly important as technological advances enable man to utilize greater and greater depths in

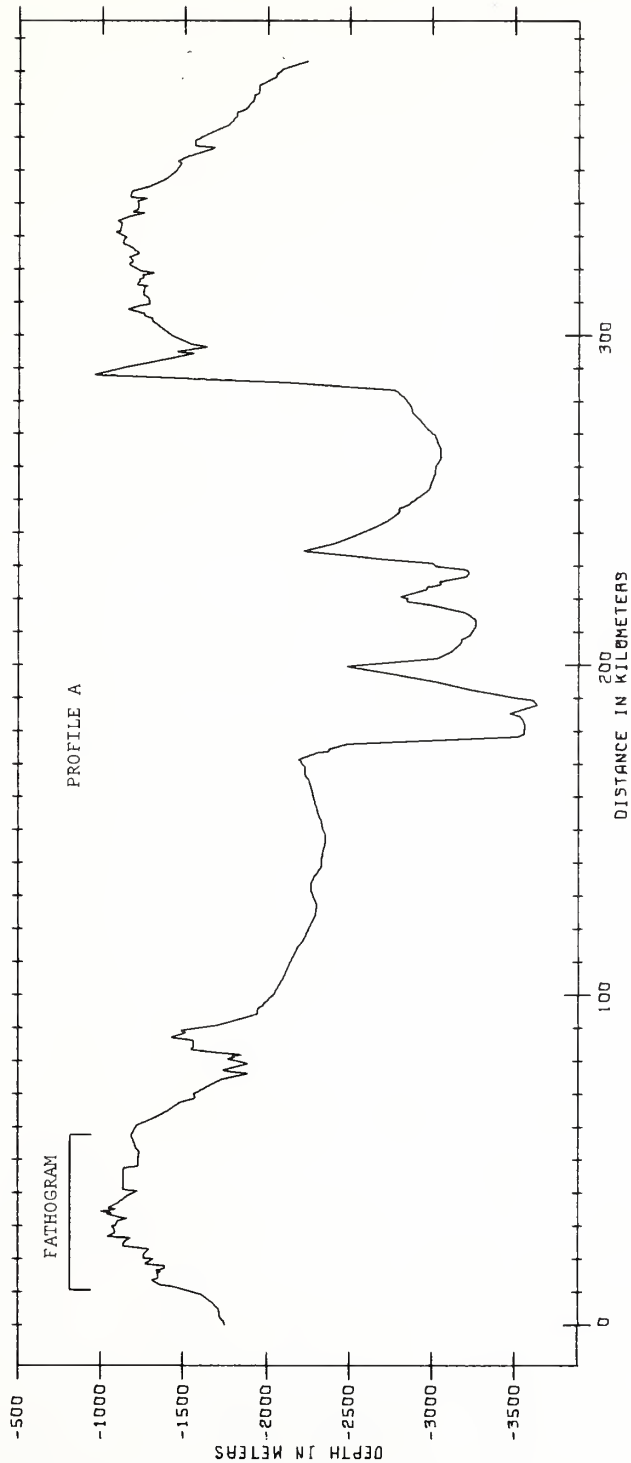

FIG. 5. — Computer produced bathymetric profile. See figure 1 for location. Vertical exaggeration 50/1. Plate 1 shows the fathogram record corresponding to bracketed part of the profile.

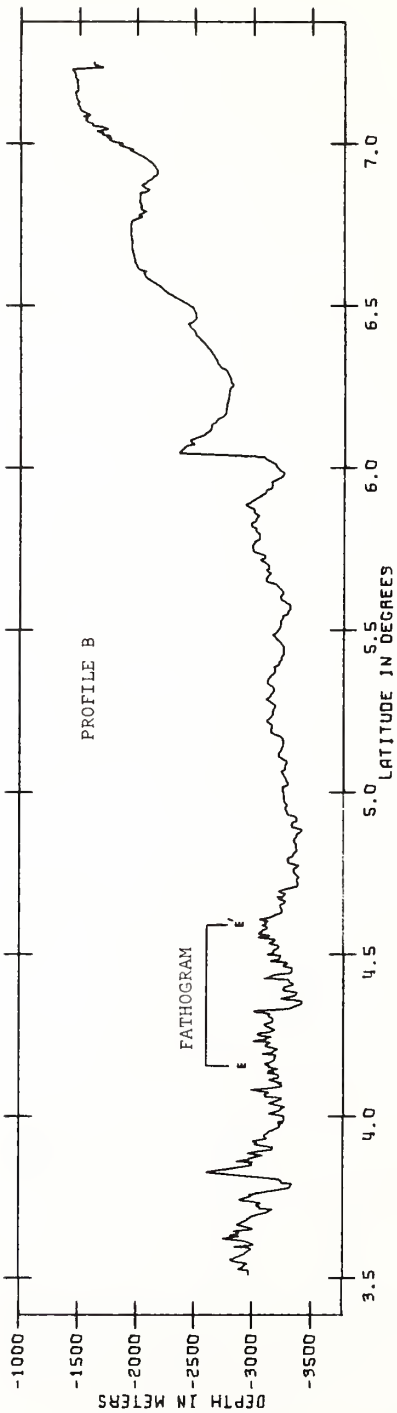

FIG. 6. — Computer produced bathymetric profile. See figure 1 for location. Vertical exaggeration 40/1. Fathogram record for E-E′ given in Plate 2.

his exploitation of the sea floor. Properly annotated and presented bathymetric profiles are essential in locating sites for various ocean engineering projects and for planning such operations as the mining of manganese nodules or other mineral resources. The detail provided by such profiles is also required for search and rescue operations as well as various salvage programs.

In addition to the probability that such information will be of great practical use in the near future, these same data are of significant interest to the marine geologist in studying geologic processes that have affected the sea floor. Various features resulting from sedimentary processes show up very clearly on profiles. For example, the detail associated with submarine canyons, fan valleys, and deep sea channels that exist on continental margins and their adjacent abyssal plains can only be shown in such profiles. The nature of small lineations on the sea floor such as sand waves might be determined by comparing profiles based on results obtained from systematic survey tracklines. Other bottom features seen on profiles would include block faulting, the smoothing effect of sediment as a function of distance from a sediment source, and evidence for craters on seamounts or the flattening of their summits.

The idea of producing bathymetric profiles from deep sea tracklines is not new. This has been a standard technique for presenting bathymetric information in scientific journals for years but at scales which often omit the detail needed to evaluate the microtopography. More recently, data reports from bathymetric and geophysical studies based on profiles produced by automatic X-Y plotters have been published (e.g., Hayes *et al.*, 1969; Lowrie and Escowitz, 1969). However, almost all the tracklines of such scientifically oriented studies are not spaced closely enough to allow contouring of the data. This paper has shown that even when surveys are systematic and detailed enough to generate bathymetric contour maps, properly produced profiles are a valuable supplement to the maps because only with such profiles can the microtopography be delineated. It is especially important that the idea of publishing profiles be brought to the attention of survey organizations such as hydrographic offices that may not be research oriented but will probably conduct many of the deep sea surveys in the future. The traditional single product of a bathymetric survey made by such organizations is a contour map and the routine publishing of deep sea bathymetric profiles, such as suggested here, may be a novel concept.

Thus far only deep sea surveys have been considered. However, the ideas developed here can also be applied to surveys conducted on continental shelf and slope areas. Although such surveys are likely to have a trackline density sufficient to permit the construction of relatively accurate contour maps, the nature of features with scales of tens or hundreds of metres will still be difficult to show meaningfully on these maps.

Computer produced profiles could essentially be published as data reports (including trackline location charts) at the same time or at an earlier time than the contour map. These reports could be available months or even years before the maps since the profiles are simply a straightforward method of showing the basic data and would require none

of the interpretation needed in contouring the depths. The physical size of the profile plots would depend on the roughness of the sea floor in the area surveyed, the accuracy of the navigational control, and the type and quality of the fathogram records. For example, the size of profiles from a survey conducted with a wide beam echo sounder with relatively poor control might be much smaller than the size of profiles based on a survey conducted with good control and a narrow-beam echo sounder. In general, both the profiles and the trackline location chart should be presented at a scale that allows the positions of individual features to be determined with an accuracy consistent with that of the navigational control.

In the future an increasing number of bathymetric surveys will use advanced echo sounders and will be automated for data reduction. The resulting contour maps of many oceanic areas can be supplemented by computer produced profiles quickly and economically by using the reduced bathymetric data. Such profiles will display much of the sea floor microtopography which cannot be shown adequately on contour maps but a knowledge of which may be very important as man acquires the ability to utilize the sea floor more fully.

ACKNOWLEDGEMENTS

We wish to thank Dr. D.C. KRAUSE for his comments on this paper.

REFERENCES

COHEN, P.M. : Directional echo sounding on hydrographic surveys, *International Hydrographic Review*, Vol. 36 (1), p. 29-42, 1959.

GRIM, P.J. : Bathymetric and magnetic anomaly profiles from a survey south of Panama and Costa Rica (USC&GSS *Oceanographer*, August 1969), ESSA Technical Memorandum, ERLTM-AOML 9, 87 p., 1970a.

GRIM, P.J. : Computer program for automatic plotting of bathymetric and magnetic anomaly profiles, ESSA Technical Memorandum, ERLTM-AOML, 8, 31 p., 1970b.

HAYES, D.E., J.R. HEIRTZLER, E.M. HERRON and W.C. PITMAN III : Preliminary report of Volume 21 USNS *Eltanin* cruises 22-27 January, 1966 - February, 1967, Lamont Doherty Surveys of the World Ocean (General Editor, Maurice Ewing), Tech. Rep. No. 2-CU-2-69, 130 p., 1969.

KRAUSE, D.C. and V.F. KANAEV : Narrow-beam echo sounding in marine geomorphology, *International Hydrographic Review*, Vol. 47 (1), p. 23-33, 1970.

LOWRIE, A. and E. ESCOWITZ, editors : U.S. Naval Oceanographic Office global ocean floor analysis and research data series, Vol. 1, *Kane* cruise 9, 971 p., 1969.

MATTHEWS, D.J. : Tables of the velocity of sound in pure water and sea water for use in echo sounding and sound ranging, British Admiralty Hydrographic Department No. 282, 1939 (second edition).

MOLNAR, P. and L.R. SYKES : Tectonics of the Caribbean and Middle America regions from focal mechanisms and seismicity, *Geological Soc. of America Bulletin*, Vol. 80 (9), pp. 1639-1684, 1969.

RYAN, T.V. and P.J. GRIM : A new technique for echo sounding corrections, *International Hydrographic Review,* Vol. 45, (2), p. 41-58, 1968.

Reprinted from Nature 235, 266-269.

Galapagos Gore, NazCoPac Triple Junction and Carnegie/Cocos Ridges

JOHN C. HOLDEN & ROBERT S. DIETZ

National Oceanic and Atmospheric Administration, Atlantic Oceanographic and Meteorological Laboratories, 901 South Miami Avenue, Miami, Florida 33130

In this article a solution is offered to the problem of the Galapagos "gore", a triangular region in the equatorial eastern Pacific which includes within its boundaries the Galapagos Islands.

THE Galapagos gore (Fig. 1) has its apex at the intersection of the Nazca, Cocos and Pacific rigid lithospheric plates, called in this article the NazCoPac triple junction. Extending eastward from this apex, the gore is apparent as a region of anomalous structure and topography which is excellently displayed, for example, on the new Scripps Institution of Oceanography bathymetric charts of the North Pacific[1]. The base of the gore is defined by the Panama fracture zone (a transform fault), which begins at the Middle America trench and then forms the northern half of the base of the gore triangle. The southern half of the base is formed by its extension as a seismically dead fracture zone.

The gore has an apical angle of 36° which is asymmetrically bisected by the Galapagos rift. These rift zones have only been partially surveyed, but parallel magnetic anomaly patterns have been identified back to anomaly 3 on the scale of Heirtzler *et al.*[2], indicating active seafloor spreading and emplacement of new oceanic crust. The higher ground of the gore as compared with the surrounding Pacific we infer as due to slow spreading within the gore (which produces high, rugged

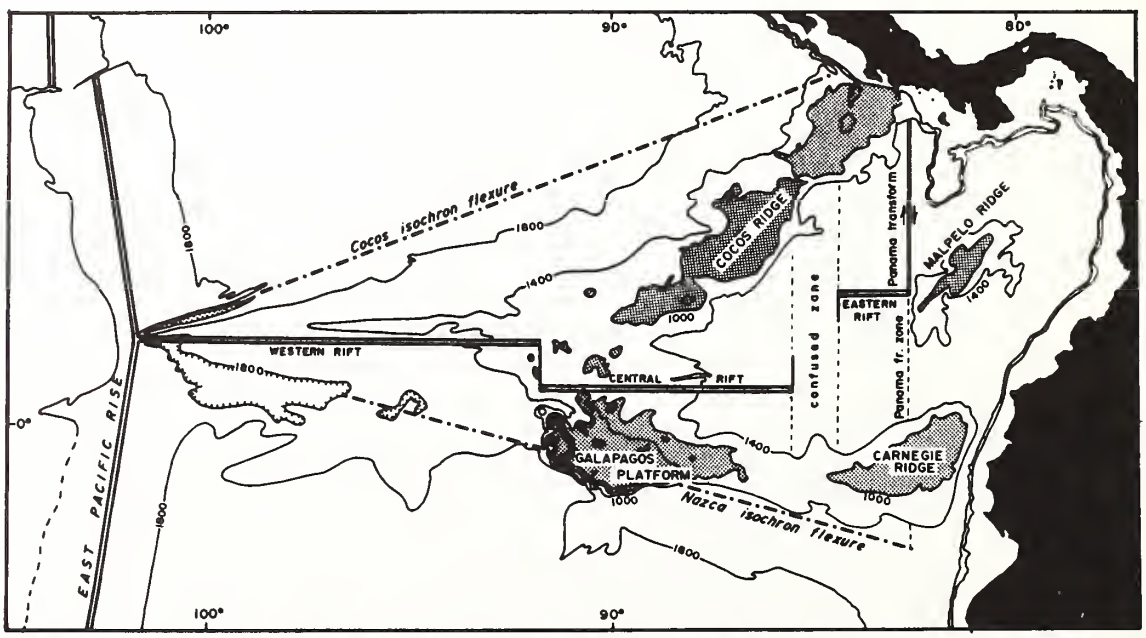

Fig. 1 Bathymetry of the Galapagos gore with prominent topography above 1,000 fm shaded. The gore, delimited by the Carnegie and Cocos isochron flexures, is defined by high relief and linear basins near the NazCoPac triple junction. Modified from Chase *et al.*[1] and Chase[16].

topography) and fast spreading on the limbs of the Pacific Rise rift (which produces a low, smooth rise). The overall dimensions of the gore are: length of wings, 2,200 km; length of base, 1,200 km; total area, 1.3×10^6 km^2.

The gore encloses two large ridges which bifurcate from the Galapagos Islands. These are the Cocos Ridge and the Carnegie Ridge (the latter may be actually construed to include the Galapagos Islands). We believe that these ridges form a binematath—that is, two thread ridges of mostly alkaline basalt which have been laid down as the moving lithospheric crust drifted over a fixed, or almost fixed, hot spot—the Galapagos hot spot. This involves the belief that a plume of magma is rising from the deep upper mantle (175 km or more), or below the zone of shear of the moving crustal plates. As this region seems not to be in motion, the resultant nematath spilled on the ocean floor provides an absolute measure of the drift of a crustal plate. In addition, we infer that the central Galapagos rift has remained near the hot spot so that lava extruded has been alternately spilled on both the Cocos and Nazca plates. We have already suggested that the Walvis and Rio Grande ridges emanating from the Tristan da Cunha hot spot are another example of a binematath[3].

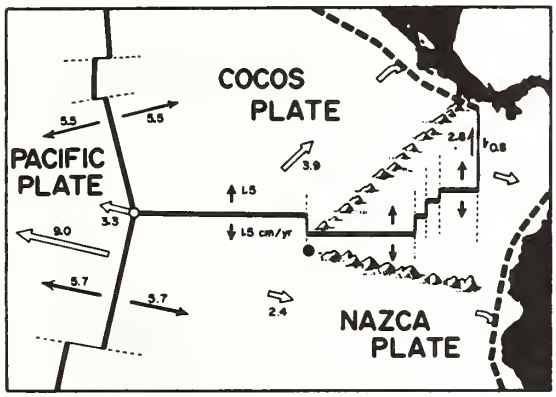

Fig. 2 Schematic representation of the Cocos and Carnegie ridges as nemataths emanating from the Galapagos fixed hot spot near the Cocos and Nazca plate boundary. Open arrows indicate absolute magnitudes and directions of plates and NazCoPac triple junction in cm/yr. Solid arrows indicate relative magnitudes and directions of plate boundaries.

Although the map of Chase *et al.*[1] referred to the Galapagos rift as a fracture zone, seafloor surveys by Raff[4], Herron and Heirtzler[5] and Grim[6] clearly show it to be a region of rifting and seafloor spreading. In fact, three rifts have been mapped which we can term the Western Galapagos Rift, the Central Galapagos Rift, and the Eastern Galapagos Rift. These rifts are separated by transform faults, with the area between the central and eastern rifts being a zone of confusion (a stepladder of faults and rifts).

Relative and Absolute Plate Motions

The relative and absolute plate motions are presented in Fig. 2.

The spreading rate at the NazCoPac triple junction is not known from magnetic surveys. But this rate should be about 5.7 cm/yr based on a rate of 6.0 cm/yr reported 20° further south along the same rift[2], which is at essentially the equator for the Pacific/Nazca relative pole of rotation, at latitude 53° N, longitude 47° W (south of Greenland)[7]. Under the premise of rigid plate rotation, the spreading rate varies as the cosine of the latitude with respect to the pole of rotation. Geometrical considerations then require the spreading rate to be 5.5 cm/yr to the north of the triple junction. There is no need to infer a zone of compression in the Pacific plate to the west of the triple junction as suggested by Raff[4] and by Herron and Heirtzler[5] which would be in violation of rigid plate tectonics. At triple junctions, seafloor spreading cannot be perpendicular to all three of the rifts. Two or possibly three of the rifts must insert dikes of new crust oblique both to the rifts and to the magnetic anomaly patterns. This avoids compression.

By using these spreading rates, we have erected 10 m.y. isochrons (lines of equal age of oceanic basement) for the seafloor outside the gore (Fig. 3). The seafloor thus grows progressively older to the east, finally attaining an age of 40 m.y. at the zone of subduction. Seafloor spreading theory requires that these isochrons be parallel to rifts. So within the gore we have erected isochrons parallel to the Galapagos rifts. Their spacing is fixed by the apical angle of the gore, because these interior isochrons must abut the exterior isochrons. The isochrons thus turn through an angle of 75° at the gore margin and their trend creates an isochron flexure. This geometry imposes a seafloor spreading rate within the gore of about 1.6 cm/yr (or a plate separation rate of 3.2 cm/yr). It should be noted that our rate of seafloor spreading is less than that inferred from earlier surveys[4,6]; for example, Heinrichs (in Van Andel *et al.*[8]) infers a spreading rate of 2.5–2.8 cm/yr for the eastern rift. But these surveys go back only to anomaly 3 (5 m.y. BP). Accepting such a high spreading rate would be to increase considerably the apical angle of the Galapagos gore, which would violate the bathymetric data.

Using the nematath concept of fixed hot spots, we can determine the absolute vectors for the Pacific, Nazca and Cocos plates in the Galapagos region. The Hawaiian nematath increases in age from zero at Hawaii to 26 m.y. BP at Midway[9] and to 40 m.y. BP at the junction with the Emperor Seamounts[10]. This gives the Pacific plate along the trend of the Hawaiian Chain a velocity of 9 cm/yr. This same velocity applies for the Pacific plate at the NazCoPac triple junction, because it lies along the same line of latitude relative to Morgan's[10] absolute pole of rotation for the Pacific plate at latitude 67° N, longitude 73° W. The East Pacific rift is opening at a rate of 11.4 cm/yr, so the NazCoPac junction must be moving north-west at 2.4 cm/yr bearing 277°. This is also the bearing of the isochron flexure within the Nazca plate, suggesting that the triple point has migrated along this flexure in the past. By similar vector subtraction the Nazca plate appears to have an absolute drift of 2.4 cm/yr bearing 095° (based on trend of the Carnegie ridge), or essentially in the opposite direction; and the Cocos plate a drift of 3.3 cm/yr bearing 045°.

The absolute drift rate of the Pacific plate of 9 cm/yr at the Galapagos triple junction is critical to our argument for the age of the Galapagos gore. For example, an increase of the spreading rate to 7.0 cm/yr (instead of 5.7 cm/yr) along the East Pacific Rise would then give a separation rate (twice the spreading rate) of 14 cm/yr. Subtracting 9 cm/yr (the absolute drift rate of the Pacific plate) from the 14 cm/yr separation rate with respect to the East Pacific rift results in a 5 cm/yr absolute drift rate for the Nazca plate. This is a doubling of the velocity of the Nazca plate which in turn would make the Galapagos gore only 20 m.y. old instead of 40 m.y. old. Thus, a higher rate of spreading along the East Pacific Rise profoundly affects our seafloor isochrons and timing. The principles involved in our interpretation would, however, remain valid.

The Galapagos rifts within the gore do not exactly bisect the gore as they should if seafloor spreading were strictly symmetrical, with the same amount of seafloor being added on both limbs. But the western and eastern Galapagos rifts are essentially central, and it appears that there has been only slight asymmetry in spreading, with greater spreading to the north than to the south. In contrast, the Central Galapagos rift requires highly asymmetrical seafloor spreading or, alternatively, the rift taking successive small jumps to re-position itself southward. The Galapagos hot spot probably imposes a weakness on the lithosphere, which tends to keep the rift

over the hot spot. To show the effect of such a jump on the seafloor isochrons, we have arbitrarily assumed a jump at 10 m.y. BP of the central rift (Fig. 3). The tendency for a hot spot to force the relocation of a spreading rift can also be observed at Iceland. This hot spot apparently causes a 175 km eastward offset of the Mid-Atlantic rift relative to an extrapolated trend connecting the Reykjanes rift directly to the Jan Mayen rift.

Five "basement ages" in the region have been reported by the Deep Sea Drilling Project (JOIDES)[11,12]. These are: for leg 9, cores No. 83 and 84; and for leg 16, cores No. 155, 157 and 158. Ages of the lowermost sediments from these cores are: 11 m.y. BP at core 83; 10 m.y. BP at core 84; 15–20 m.y. BP at core 155; 10 m.y. BP at core 157; 15–20 m.y. BP at core 158. Although core 83 agrees rather closely with our isochron, all "basement dates" are somewhat younger than the basement indicated on our isochron map (Fig. 3). These data possibly suggest that the Galapagos gore is younger than we have surmised. Considering the uncertainties involved in the JOIDES dates (later effusions of lava onto the seafloor; lava from nemataths which were emplaced later than the basalt injected into spreading rifts and so on), we believe that our construction is constrained only to the extent that our seafloor age dates always must be older (and they are) than the JOIDES dates.

Cocos nemataths are appropriately reduced in length and they both mark the absolute drift vectors of the plates on which they are imposed. Since the Nazca plate is moving parallel to the southern isochron flexure, the opening of the gore is due entirely to the drift of the Cocos plate along a bearing of 045°. The Galapagos rifts migrate northward attempting to maintain a central position with the gore. This is not achieved by the Central Galapagos rift because it tends to hug the hot spot.

Fig. 5 depicts the gore 30 m.y. BP, or 10 m.y. after its birth. The gore was then very small, and the triple junction was near the hot spot. A long transform fault connected the new rift to the Middle America subduction zone (off the diagram). In this construction, the close fit of the Carnegie and Cocos ridges along their 1,000-fm isobath is intriguing. Even earlier (40 m.y. BP), the hot spot and the triple junction would be joined and the gore would vanish to zero. This would mark

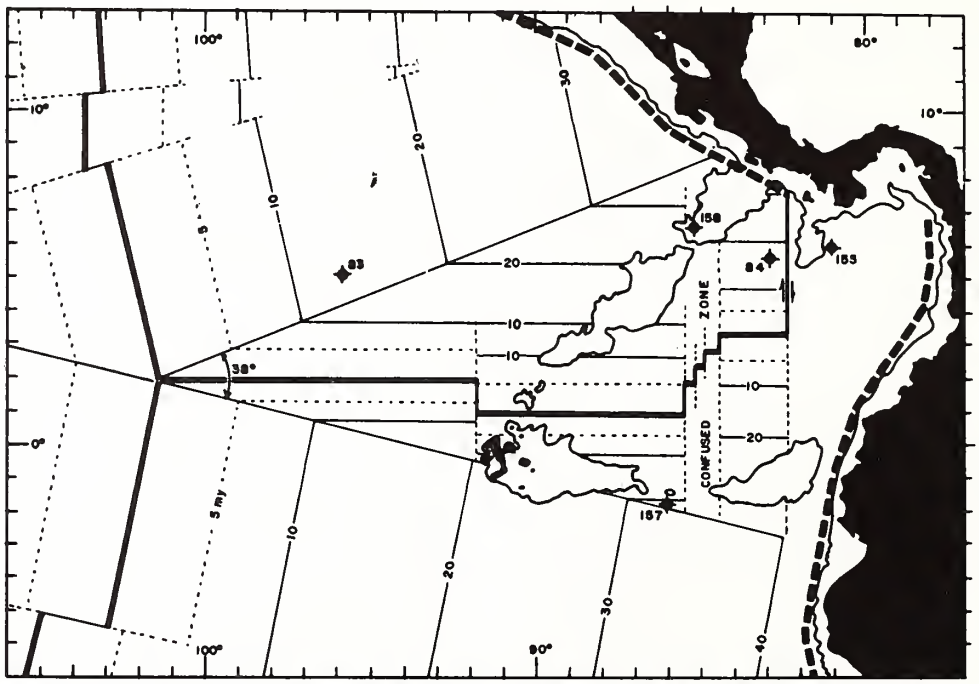

Fig. 3 Isochron map based on seafloor spreading. Glomar Challenger stations at which basement ages are available or inferred denoted by spiked circles. Mid part of Galapagos rift isochrons constructed to show a southward rift jump of about one degree 10 m.y. BP.

Evolution of the Galapagos Gore

Fig. 4 shows the gore at 10 m.y. BP. This is obtained by projecting the NazCoPac triple junction backwards along the Nazca isochron flexure (a reversal of its modern migration vector) while holding the Galapagos hot spot fixed. We have assumed constant spreading and drift rates. The gore consequently shrinks in all dimensions. Both the Carnegie and the birth of the gore, the triple junction, and the hot spot. Presumably the hot spot came first and initiated the new plate boundaries.

We can rule out the possibility of any large change in the angular geometry of the triple junction, a stable type of triple junction[13]. Such an effect would be to flare or constrict the isochron flexure, which is not observed. The Galapagos gore instead has straight wings, approximating an isosceles triangle.

We can also demonstrate that the triple point has migrated. If this were not so, the strike of the Cocos ridge as a nematath would be parallel to the trend of the isochron flexure marking the north limb of the gore (Fig. 3). The isochron flexure trend is actually less steep than the Cocos ridge, which can only mean that the triple point has migrated toward the west. In addition, the fact that the Cocos ridge strikes into the northeast corner of the gore demonstrates that the triple point and the hot spot were once at the same position when this far end

of the Cocos ridge was extruded. We offer the solution, therefore, that the angular geometry of the triple point has remained geometrically stable while it has migrated north-westward.

If it were possible to show that the Cocos ridge, in its entirety, is constrained within the limits of the gore, this would mean that the triple point was born at the Galapagos hot spot 40 m.y. BP. We suppose that this is probably true, but it cannot be demonstrated because an unknown amount of north-westward extension of the Cocos ridge may have been subducted into the Middle America trench and thus not exist today. The Malpelo ridge just to the east of the Panama fracture zone might possibly be such a remnant of the Cocos ridge. Such an interpretation would necessitate an earlier extension of the Galapagos rift zone into that region that had become inactive, leaving this part of the ridge frozen on the Nazca plate. If this were the case then the early gore would have extended further east of the hot spot than west. The hot spot would then predate the triple junction. On the other hand, if the hot spot existed prior to the creation of the triple junction, an ancient and now isolated nematath should be present on the Pacific plate, on a bearing of 277° from the triple point and commencing where the Pacific is older than 40 m.y. We can find no evidence for such a nematath. This suggests that the hot spot and the triple point were born at the same time.

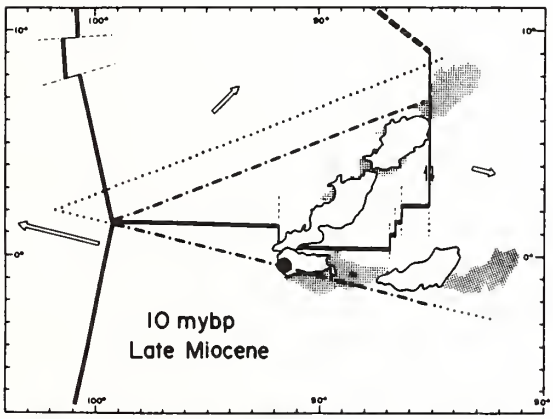

Fig. 4 Development of Galapagos gore 10 m.y. BP. Dash–dot line represents Cocos and Nazca isochron flexures at that time; dotted line represents the Recent position of the flexures. Recent positions of Cocos and Carnegie ridges shaded. Arrows as in Fig. 2.

Models Compared

Van Andel *et al.*[8] have offered an alternative explanation for a portion of the Galapagos gore. They suggest that the Cocos and Carnegie ridges were once juxtaposed and then were split apart by the insertion of spreading rifts associated with a jumping transform fault. This infers that these two ridges are old (in that they pre-existed the creation of the Galapagos rift as the Nazca–Cocos plate boundary) and that the ridges are of equal age along their strike. Clearly, the volcanically active Galapagos Islands are youthful and they appear to grow older to the east[14], a trend which we suppose can be extrapolated along the Carnegie ridge. It also implies that fast spreading occurred to the east and that this spreading decreased essentially to zero at the Galapagos where the two ridges converge. We question this model because it seems to violate some of the basic rules of plate tectonics. Their scheme would seem plausible if the triple point was fixed at the hot spot, but this is not the case.

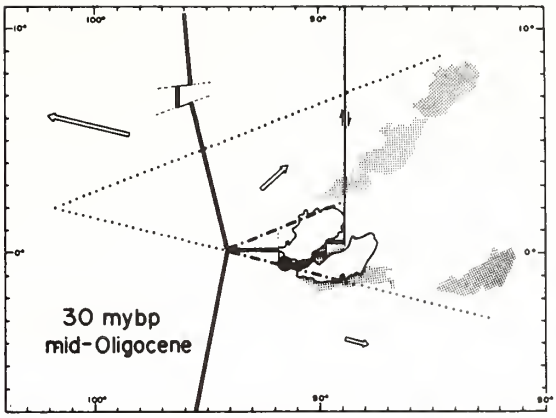

Fig. 5 Development of Galapagos gore 30 m.y. BP. See Fig. 4 for explanations.

The Galapagos Islands contain many endemic birds and bizarre animals which have required millions of years for their evolution in isolation. By our model, the modern Galapagos Islands may have inherited faunas from a whole series of ancestral "Galapagos islands" which existed over a span of 40 m.y. Presumably the animals would have little difficulty negotiating the short span of water to a new volcanic island as an older extinct volcanic island drifted eastward and subsided beneath the sea (a subsiding "stepping stone"), adding itself to the end of the Cocos and Carnegie ridges. To date, no guyots have been reported from either the Carnegie or Cocos chains, but this still is not conclusive evidence that these ridges were not subareal at some time in their history[15].

In summary, we conclude the following. (1) The gore and the creation of the Galapagos rift (which in turn created the Cocos plate) is about 40 m.y. old; but possibly much younger if relative spreading rates along either the Galapagos or East Pacific Rise can be shown to be faster than those inferred here. (2) The NazCoPac RRR triple junction has maintained a stable angular configuration but has migrated away from the Galapagos hot spot along a bearing of 277° and a velocity of 3.3 cm/yr since its inception. (3) The Cocos and Nazca ridges form a binematath emanating from the fixed Galapagos hot spot, the bearing of each indicating the absolute vector of the two plates they surmount. (4) The opening of the gore, as a zone of extension, is new ocean floor resulting from the absolute drift motion of the Cocos plate to the north-east.

Received November 8, 1971.

1 Chase, T., Menard, H., and Mammerickx, J., *Bathymetry of the North Pacific: Scripps Inst. Oceanog.—Inst. Marine Resources* (map No. 10) (1971).
2 Heirtzler, J. R., Dickson, G. O., Herron, E. M., Pitman, W. C., III, and Le Pichon, X., *J. Geophys. Res.*, 73, 2130 (1968).
3 Dietz, R. S., and Holden, J. C., *J. Geophys. Res.*, 75, 4948 (1970).
4 Raff, A. D., *J. Geophys. Res.*, 73 (1968).
5 Herron, E., and Heirtzler, J., *Science*, 158, 775 (1968).
6 Grim, P. J., *Marine Geophys. Res.*, 1, 85 (1970).
7 LePichon, X., *J. Geophys. Res.*, 73, 3665 (1968).
8 Van Andel, T., Heath, G. R., Malfail, B. T., Heinrichs, D. F., and Ewing, J. I., *Geol. Soc. Amer. Bull.*, 82, 1489 (1971).
9 Ladd, H., Tracey, J., and Gross, M., *US Geol. Surv. Prof. Paper 680-A*, 21 (1970).
10 Morgan, J., *Nature*, 230, 42 (1971).
11 JOIDES Deep Sea Drilling Project: leg 9, *Geotimes*, 11 (1970).
12 JOIDES Deep Sea Drilling Project: leg 16, *Geotimes*, 14 (1971).
13 McKenzie, D. P., and Morgan, W. J., *Nature*, 224, 125 (1969).
14 Cox, A., and Dalrymple, G. B., *Nature*, 209, 776 (1966).
15 McBirney, A. R., and Williams, H., *Geol. Soc. Amer., Mem. 118*, 110 (1969).
16 Chase, T. E., *US Dept Interior, Bur. Commercial Fisheries, Circular 291* (1968).

Reprinted from Proceedings First International Conference on Port and Ocean Engineering under Arctic Conditions *11*, 1285-1311.

Reprinted without change of pagination from the Proceedings from the First International Conference on Port and Ocean Engineering under Arctic Conditions, Volume II, pp. 1285—1311, 1971.

PORT AND OCEAN ENGINEERING UNDER ARCTIC CONDITIONS

TECHNICAL UNIVERSITY OF NORWAY

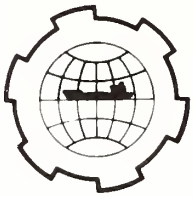

ENGINEERING PROPERTIES OF GREENLAND AND NORWEGIAN BASIN SEDIMENTS

George H. Keller
Director,
Marine Geology and Geophysics Laboratory

National Oceanic and Atmospheric Administration
Atlantic Oceanographic and Meteorological Laboratories

901 S. Miami Avenue
Miami, Florida 33130
U.S.A.

Engineering and foundational characteristics of sea-floor deposits are relatively unknown except in certain areas of the coastal zone where man has built structures such as wharves, bridges, tunnels and various pile supported platforms. Although the number of investigations pertaining to the engineering properties of the outer coastal zone and deep-sea deposits has increased significantly during the past decade, the quantity of available information is yet very limited. The scarcity of such data is even more pronounced in Arctic regions where approximately 140 to 150 sediment cores have been collected for engineering (geotechnique) studies.

Sediments of the Greenland-Norwegian basin display considerable variation of such properties as shear strength, water content, and porosity, both laterally and with depth. These deposits tend to exhibit higher average unit weight (bulk density) and shear strength, but lower water content, porosity, sensitivity, grain specific gravity, and Atterberg Limits than those sediments blanketing most of the North Atlantic basin. The Greenland-Norwegian basin sediments are characterized by inorganic clays of medium to high plasticity, sand clays, and slightly plastic inorganic silts. The process of ice-rafting, which is unique to higher latitudes, strongly influences the engineering properties of Arctic submarine deposits by transporting and later depositing coarse material, e.g., coarse sand and gravel, in oceanic areas which otherwise would only receive fine sand, silt and clay. Fine silt and clay of relatively low strength appear to blanket much of the Greenland-Norwegian basin resulting in relatively low ultimate bearing capacities of the surface deposits.

INTRODUCTION

The foundational characteristics of sea-floor deposits are yet relatively little known except in coastal areas where man has long been involved in the construction of such facilities as wharves, bridges, and breakwaters. It was only about 20 years ago, when offshore petroleum exploration began to receive serious attention, that sincere investigations began on the engineering properties of submarine sediments beyond the breaker zone.

As yet, most of the engineering studies carried out on deep-sea sediments have been by marine geologists who have utilized various aspects of soil mechanics (geotechnique) in their attempt to understand the sedimentological characteristics and depositional history of the ocean floor. One of the earliest studies was that of Arrhenius (2) who determined relative strengths on sediment cores collected during the Swedish Deep-Sea Expedition 1947-1948. Although a number of investigators were concerned with the geotechnical properties of submarine sediments prior to 1960, e.g., Hamilton (9, 10), Hamilton and Menard (11), Fisk and McClelland (8), and Moore and Shumway (30); Richards (33, 34) was the first to report on the overall engineering aspects of deep-sea deposits based on a limited number of locations in the Atlantic, Mediterranean, and Pacific basins. During the last decade an increasing number of investigators entered this field of study and have looked into such relationships as sound velocity versus certain engineering properties (5), unit weight variations with depth (17), consolidation characteristics of various deposits (4, 35), or have defined the engineering properties of some local area such as the Chesapeake Bay (13), Gulf of Bothnian (18), or the Mississippi Delta region (28, 29). The first regional study of the distribution of various geotechnical properties was presented by Keller (23) in his report on approximately 500 sediment cores from the North Atlantic and North Pacific basins. A similar study has recently been completed by Keller and Lambert (27) for the Mediterranean basin.

With the advent of the U. S. Deep Sea Drilling Project in 1968, it became possible to extend geotechnical studies to much greater depths below the sea floor. Thus far, this program has obtained sediment cores from depths as great as 1070 m below the sea floor on which tests have been made for unit weight, water

content, porosity, grain size and relative strength, (31). Although these samples are disturbed, they have provided some degree of insight into the properties of sediments never before sampled in the deep sea.

To date, it is estimated that on the order of 1000 to 1300 sediment cores have been collected from all the ocean basins (beyond the continental shelf) for the purpose of geotechnical studies. In the Arctic, only about 140 deep-sea cores have been obtained for such studies. Many of these samples have been collected from icebreakers which were only equipped to handle small core samplers. As a result of this limitation, approximately 60 percent of these samples are of limited value.

This study is based on a total of 67 sediment cores, 42 of which were only suitable for Atterberg Limits, grain specific gravity, and grain size determinations. The data used herein were obtained from analyses carried out by the U. S. Naval Oceanographic Office and from project reports contracted for by the U. S. Naval Oceanographic Office (37, 39). In addition to presenting the areal distribution of selected geotechnical properties in the Greenland-Norwegian basin, the ultimate bearing capacity of surface deposits in the area is also discussed. Local variability in deep-sea deposits may not be as severe as those found in the coastal zone, nevertheless both lateral and vertical changes in these deposits are found to be significant.

Regional Setting

The regional morphology of the Greenland-Norwegian basin is not that of two simple adjacent basins but consists of a number of ridges and fracture zones which transect the area (Fig. 1). The northern extension of the mid-Atlantic ridge trends northeast from Iceland to about 72°30'N where it is intersected by the Jan Mayen fracture zone. Here the ridge has been offset to the east on the order of 200 km. The ridge then trends east-northeast, approximately midway between Greenland and Norway, to 74°N where it assumes a north-south trend as a result of its displacement by the Greenland fracture zone. A second major ridge, the Jan Mayen ridge, extends southeast from Jan Mayen Island serving as the eastern border of the Icelandic plateau. It is readily apparent from figure 1 that the continental

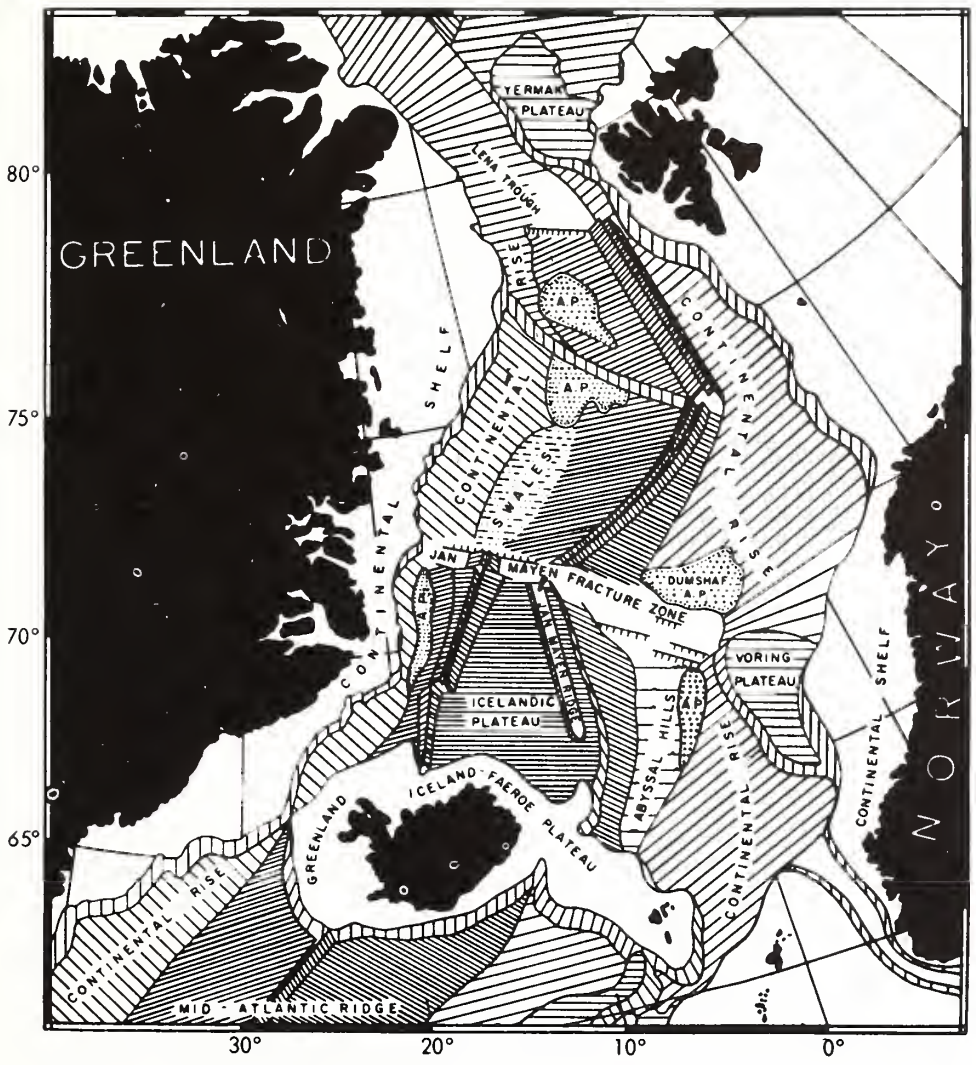
GREENLAND
NORWAY
TERMAK PLATEAU
LENA TROUGH
SVALBARD
A.P.
A.P.
CONTINENTAL SHELF
CONTINENTAL RISE
JAN MAYEN FRACTURE ZONE
DUMSHAF A.P.
VORING PLATEAU
ICELANDIC PLATEAU
ABYSSAL HILLS
A.P.
ICELAND-FAEROE PLATEAU
GREENLAND
CONTINENTAL RISE
MID-ATLANTIC RIDGE
CONTINENTAL SHELF
80°
75°
70°
65°
30°
20°
10°
0°

FIG. 1

rise is much more extensive off Norway than along the Greenland margin. This may be attributed to a higher rate of sedimentation as geophysical observations indicate that large volumes of sediment are prograding out from the Norwegian shelf onto the continental rise (21). Tectonism and the resulting crustal features have contributed to a complex bottom topography and the absence of any large abyssal plain. For a more detailed discussion of the morphology and structural history of the Greenland-Norwegian basin, the reader is referred to the studies of Johnson and Eckhoff (19) and Johnson and Heezen (20).

Regional Aspects of Geotechnical Properties

Surface Sediment Types.-Sediments found in the Greenland-Norwegian basin are largely the product of glacial activity, with varying amounts of material contributed by ice-rafting as well as slumping from nearby submarine ridges. Aside from the 67 sediment samples discussed here (Fig. 2), the majority of the samples collected in this area date back to the Norwgian Vöringen cruise (36), the Danish Ingolf-Expedition (3) and the studies of Holtedahl (14, 15, 16). Only a very general distribution of surface deposits in the Greenland-Norwegian basin can be presented from the available data. Excluding those areas of considerable topographic relief, the basin is primarily blanketed with fine silts and clays which probably have been derived from the streams and rivers of Norway and Greenland. Seismic reflection observations (39) indicate that most of the sediment east of the mid-Oceanic ridge has been derived from Norway. Local areas of coarser grained material result from slumping and small scale turbidity currents associated with seismic ridges such as Jan Mayen ridge (39). West of the mid-Oceanic ridge fine pelagic sediments cover much of the area with local variations in sediment type owing to slump and turbidity current activity from the steep flanks of the adjacent ridge (39). Bottom photographs from various parts of the Norwegian Sea (continental slope, abyssal plain, abyssal hills, and Icelandic plateau) all revealed a bottom composed of silty and sandy clay and occasional ice-rafted pebbles (39). None of the photographs showed any indication of active bottom currents.

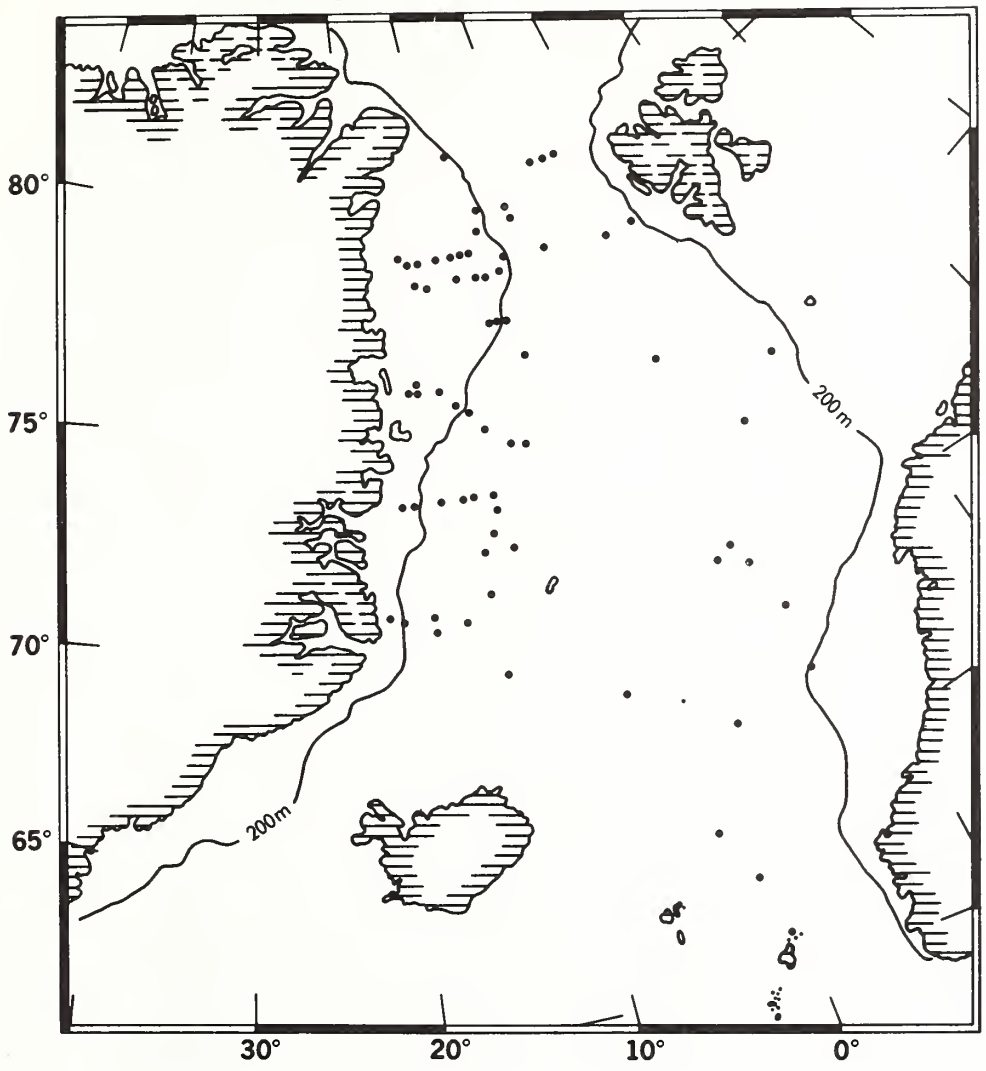

FIG. 2

As a generalization, it appears that surface deposits on the margins of the basins consist of relatively coarse grained (sandy silt) glacial-fluvial-sediments grading seaward into silty clay and finally at the greater depths to a calcareous ooze (23). In his study of the southeastern part of the Norwegian Sea, Holtedahl (16) described a series of sediment cores from the continental slope out onto the continental rise. He reported surface deposits of gray sandy clay to water depths of approximately 800 m and gray silty clay from depths of 800 m to at least 1000 m. Beyond depths of 1500 m he found a brown sandy clay with a very high concentraion of Foraminifera. For this deep-water surface deposit, which is on the order of 15 cm thick, Holtedahl reported a calcium carbonate content of 45 percent. The detailed work of Holtedahl tends to substantiate the generalization made above.

In contrast to the mid-Oceanic ridge which has little or no sediment cover, the Jan Mayen ridge is blanketed by 100 to 300 m of sediment (20). Sedimentation in the Greenland-Norwegian basin is typical of the Arctic area, but atypical of most deep-sea basins in that ice-rafting plays a significant role in Arctic deposition. The occurrence of coarse material (pebbles and cobbles) has been frequently noted both on the Arctic sea-floor and in cored samples (Fig. 3). Such ice-rafted material obviously influences the engineering properties of basin deposits to a considerable degree, especially if the debris should comprise a sizeable proportion of the deposits. Engineering tests performed on the cored samples avoided zones of ice-rafted material and, therefore, provided biased results which only approximate the general characteristics of these particular sediments.

Shear Strength.-Shear strength measurements were made on samples comprised primarily of fine grained cohesive sediment (silty clay) with minor occurrences of fine sand stringers. Zones with pebbles were not tested. Shear strength of cohesive material is dependent on the cohesion (c), angle of internal friction (ϕ) of the sediment, and the effective stress normal to the shear plane ($\bar{\sigma}$) simply expressed as:

$$\tau_f = c + \bar{\sigma} \tan \phi$$

Saturated, silty clays, stressed without drainage (loss of pore water) respond with respect to the applied load as if they have no angle of internal friction (ϕ=o). Under these conditions, shear strength then is equal to the cohesion (τ_f=c).

FIG. 3

A more detailed discussion of shear strength can be found in a basic soil mechanics text book.

Measurements of shear strength were made by either a laboratory vane shear apparatus or the fall cone. Both methods provide a simple yet suitable test for these relatively soft submarine sediments. All fall cone measurements were taken from Texas Instruments, Inc. (39) and were based on the conversion graphs of Hansbo (12). The vane shear method follows that described by Evans and Sherratt (7) and more specifically as applied to deep-sea deposits using the procedure outlined by Richards (33).

Both piston and gravity corers were used during the sampling program of this area. The cores varied from 2.6 to 6.0 cm in diameter and from 0.35 to 10 m in length. An average length for the 67 cores studies is on the order of 2.0 m. The smaller diameter cores were only used for grain size, Atterberg Limits and grain specific gravity measurements. Considering the areal extent of the Greenland-Norwegian basin and the relatively shallow depths to which sampling was possible it was decided, for the purpose of displaying the areal distribution of the geotechnical properties, to average the measured values of the respective parameters over the entire length of each core. This averaged value is that which is displayed at each core location noted in later figures. It is realized that the limited number of sediment cores available for this study precludes any detail discussion of the engineering properties of the deposits occurring in the Greenland-Norwegian basin, however, these data do provide an insight into the general sedimentological characteristics of the basin. Sediments blanketing the sea floor underlying the Greenland Sea appear to possess distinctly lower shear strengths than those of the Norwegian Sea (Fig. 4). A general boundary between the two areas appears to approximate the location of the Jan Mayen fracture zone. To the north, average shear strengths in the upper meter or two of the sea floor seldom reach 60 g/cm^2 (0.8 psi), and more commonly range from 30 to 40 g/cm^2 (0.4 to 0.6 psi). South of the Jan Mayen fracture zone shear strengths are much higher and vary from 74 to 142 g/cm^2 (1.2 to 2.0 psi). A distinct area of relatively high strength material is noted along the Jan Mayen ridge. Studies elsewhere have also observed higher shear strengths associated with topographic "highs" (24). This

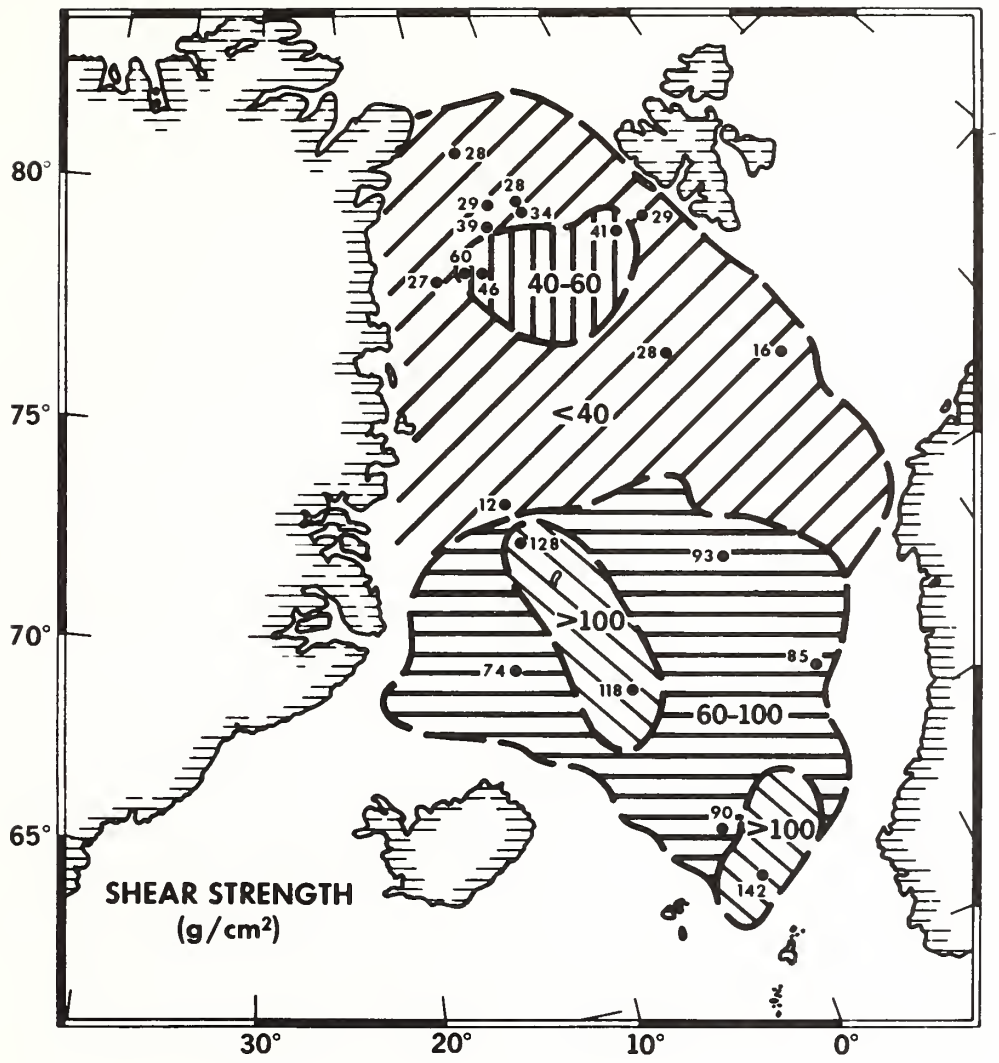
80°
75°
70°
65°
30°
20°
10°
0°
28
28
29
34
39
41
29
60
27
46
40-60
28
16
<40
12
128
93
>100
85
74
118
60-100
90
>100
142
SHEAR STRENGTH
(g/cm²)

FIG. 4

phenomenon may be possibly attributed to the winnowing action of water movement over "highs" which then results in a slightly denser, stronger sediment occurring in such areas. This cannot, however, be taken as a generalization since this relationship is not always found to be true. Another area of high average shear strength is located just northeast of the Shetland Islands at the foot of the continental slope.

The higher shear strengths found south of the Jan Mayen fracture zone may be, in part, attributed to the influx of slightly coarser material from nearby submarine ridges, the Faeroe and Shetland Islands, the margin of Iceland, as well as from Greenland and Norway. On the other hand, source areas for the northern portion of the basin are few and more distant. As an overall comparison, shear strengths are commonly found to be lower than those reported for the North Atlantic basin (23). Based on the limited data presented here, it is not possible to characterize the various physiographic provinces of the study area by their strength properties. For example, little distinction can be found between the shear strength values reported for the Dumshaf abyssal plain, Voring plateau, or Icelandic plateau.

Water Content.-Water content (w) is used here as a ratio, expressed as a percent, of the weight of water to the weight of oven-dried solids in a specific sediment mass. Laboratory determination of water content is based on the standard procedure outlined by the American Society for Testing Materials (1).

Average water contents for the Greenland-Norwegian basin range from 30 to 89 percent, but more frequently vary between 40 and 60 percent (Fig. 5). The Jan Mayen fracture zone appears to separate the relatively higher water content sediments to the north from the slightly lower water content deposits south of this prominent feature. In comparing figures 1 and 5, little correlation can be seen between the water content distribution and the presence of major bottom features. Continental shelf sediments off the northeast coast of Greenland display water contents of 40 to 50 percent reflecting the relative increase in sediment grain size found in that area. Similar low values in the southern portion of the basin may also be influenced by the presence of coarse sediments eroded from topographic

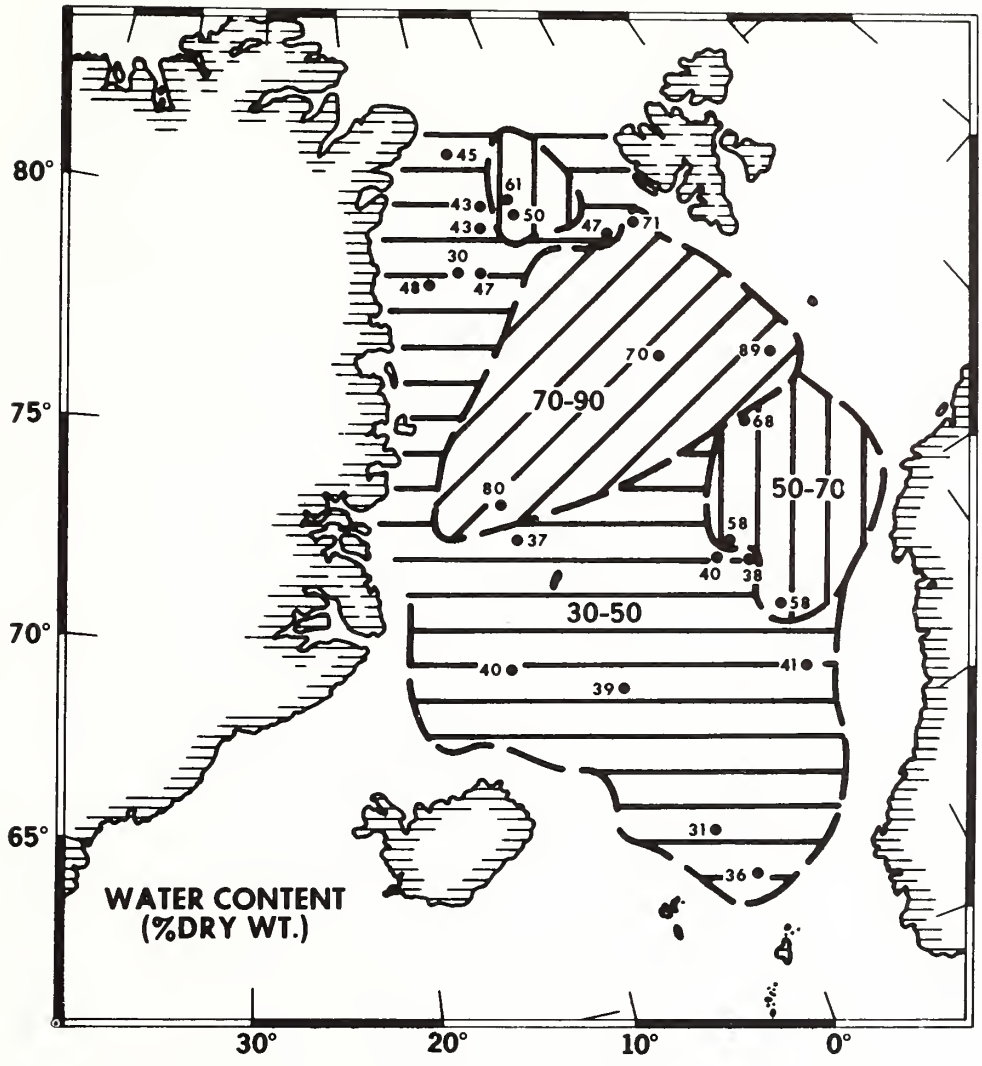
80°
75°
70°
65°
30°
20°
10°
0°
45
61
43
43
50
47
71
30
48
47
70
89
70-90
68
50-70
80
58
37
40
38
58
30-50
40
41
39
31
36
WATER CONTENT
(%DRY WT.)

FIG. 5

features in the general area. Most of the Greenland-Norwegian Sea basin deposits possess water contents well below those commonly found in the North Atlantic and North Pacific basins (23).

Unit Weight.-Unit weight or bulk density (γ) is the weight per unit of total volume of a given sediment mass. Deep-sea sediments are sufficiently close to being 100 percent saturated that the term saturated unit weight can also be applied here.

Variation in the areal distribution of average unit weights in the Greenland-Norwegian basin is remarkably small. Values range from 1.51 to 1.97 g/cm^3 (94.2 to 122.9 pcf), but more commonly vary between 1.60 and 1.75 g/cm^3 (99.8 and 109.2 pcf) (Fig. 6). A zone of relatively high unit weights [1.72 to 1.97 g/cm^3 (107.3 to 122.9 pcf)] extends across the northern part of the study area between Greenland and Vestspitsbergen. This band of high density sediment may be a phenomenon resulting from a combination of relatively nearby sources of heavy minerals (Greenland and Vestspitsbergen) and the general current pattern in this portion of the Greenland Sea. The presence of similar high density sediment in the southeast sector of the basin could possibly be attributed to bottom topography and bottom currents. Indications are that bottom water flows out of the Norwegian Sea between the Faeroe and Shetland Islands (22). It has also been found that considerable sediment has been deposited on the north slope of the Faeroe-Iceland ridge indicating a relatively quiet bottom energy condition just prior to the passage of the water mass out of the basin and over the ridge. Such a current regime might tend to selectively deposit heavier grains and result in the distribution pattern shown in figure 6.

Average unit weights throughout the Greenland-Norwegian basin are generally somewhat higher than those reported for much of the North Pacific and North Atlantic basins (23).

Porosity.-Porosity (n) as used here, is the ratio of the volume of voids in a given sediment mass to the total volume of the mass and is calculated based on the measured water content, unit weight and grain specific gravity. A more detailed discussion of porosity determination or that of any of the other engineering properties discussed above is commonly found in texts dealing with soil mechanics.

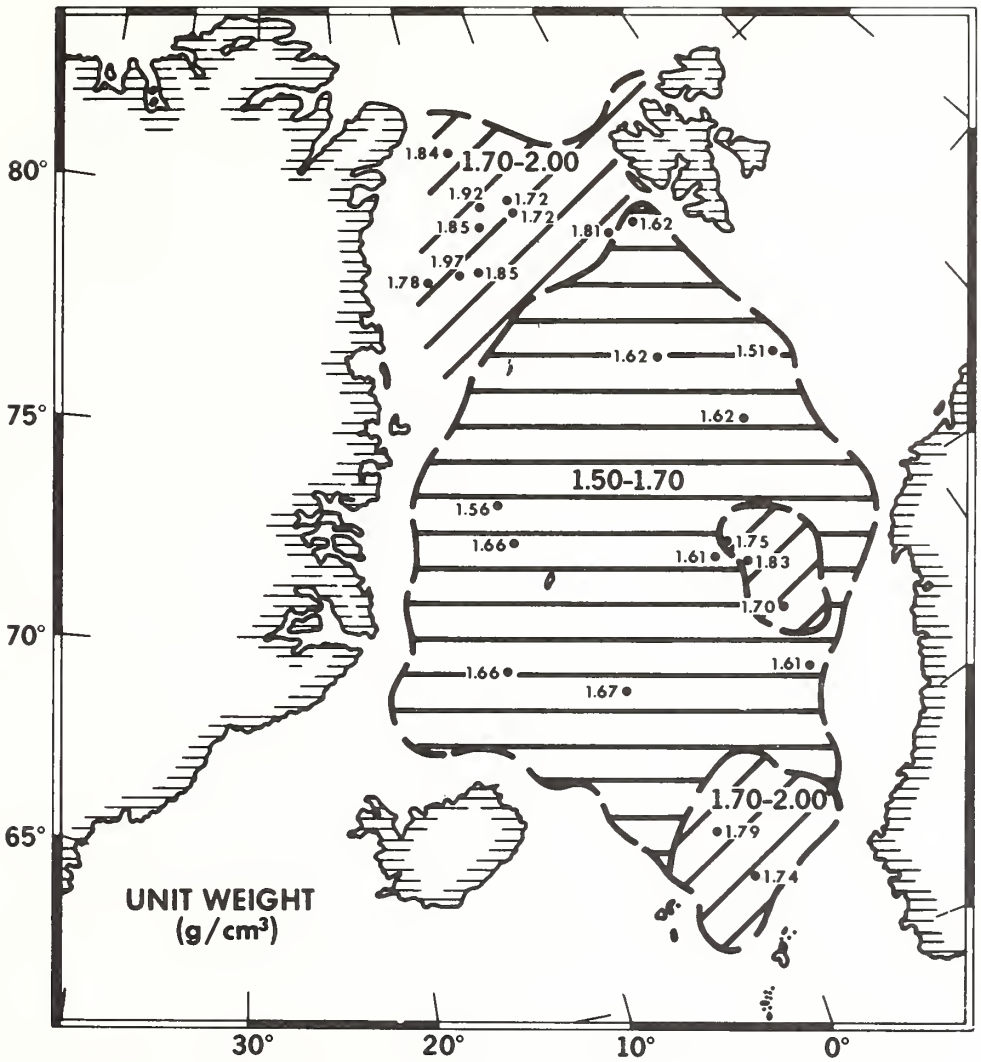
80°
75°
70°
65°
30°
20°
10°
0°
1.84
1.70-2.00
1.92
1.72
1.72
1.85
1.81
1.62
1.97
1.78
1.85
1.62
1.51
1.62
1.50-1.70
1.56
1.66
1.75
1.61
1.83
1.70
1.66
1.61
1.67
1.70-2.00
1.79
1.74
UNIT WEIGHT
(g/cm³)

FIG. 6

Some of the lowest porosities yet observed in submarine sediments (43 to 50 percent) occur on the northeast continental shelf of Greenland. Porosities in the study area vary from 43 to 69 percent, but more frequently are in the range of 55 to 65 percent (Fig. 7). As might be anticipated, the areal distribution of porosity in the basin has taken on much the same pattern as that noted for unit weight. In comparison, porosities for the Greenland-Norwegian basin appear to be only slightly lower than those commonly found over much of the North Atlantic (25).

Ultimate Bearing Capacity.—Most installations on the deep-sea floor to date, have been relatively light weight (e.g., pipelines, cables, and various pieces of mining equipment). For the engineer concerned with the placement of such structures or hardware on the sea floor, bearing capacity of the bottom material must be ascertained in order to determine the depth to which such an installation will penetrate the sediment during its initial placement. Because bearing capacity rather than consolidation characteristics of deep-sea sediments is of greater significance to the engineer in such a situation, a short discussion of the ultimate bearing capacity of surficial deposits in the Greenland-Norwegian basin has been included here.

Ultimate bearing capacity is the average load per unit of area needed to produce failure by rupture of a supporting sediment mass. This property is a function of the product of the shear strength and one or more factors, which depend on the size and shape of the load as well as the depth of loading. For the purpose of this discussion, a strip load at the sediment surface serves as the basis for ultimate bearing capacity determinations shown in figure 8. The commonly used bearing capacity equation for a shallow strip footing developed by Prandtl (32) and modified by Terzaghi (38) is:

$$Qc = cNc + \gamma DN_q + \frac{\gamma B}{2} N\gamma \qquad (1)$$

Where Qc is the ultimate bearing capacity, c the cohesion, γ sediment unit weight, D the depth of the load below the surface, B width of the footing, and Nc, N_q, and $N\gamma$ are bearing capacity factors which are dependent on the angle of internal friction, depth and shape of the footing and roughness of its base. In the case of a surface loading and assumed zero angle of internal friction, the factors N_q

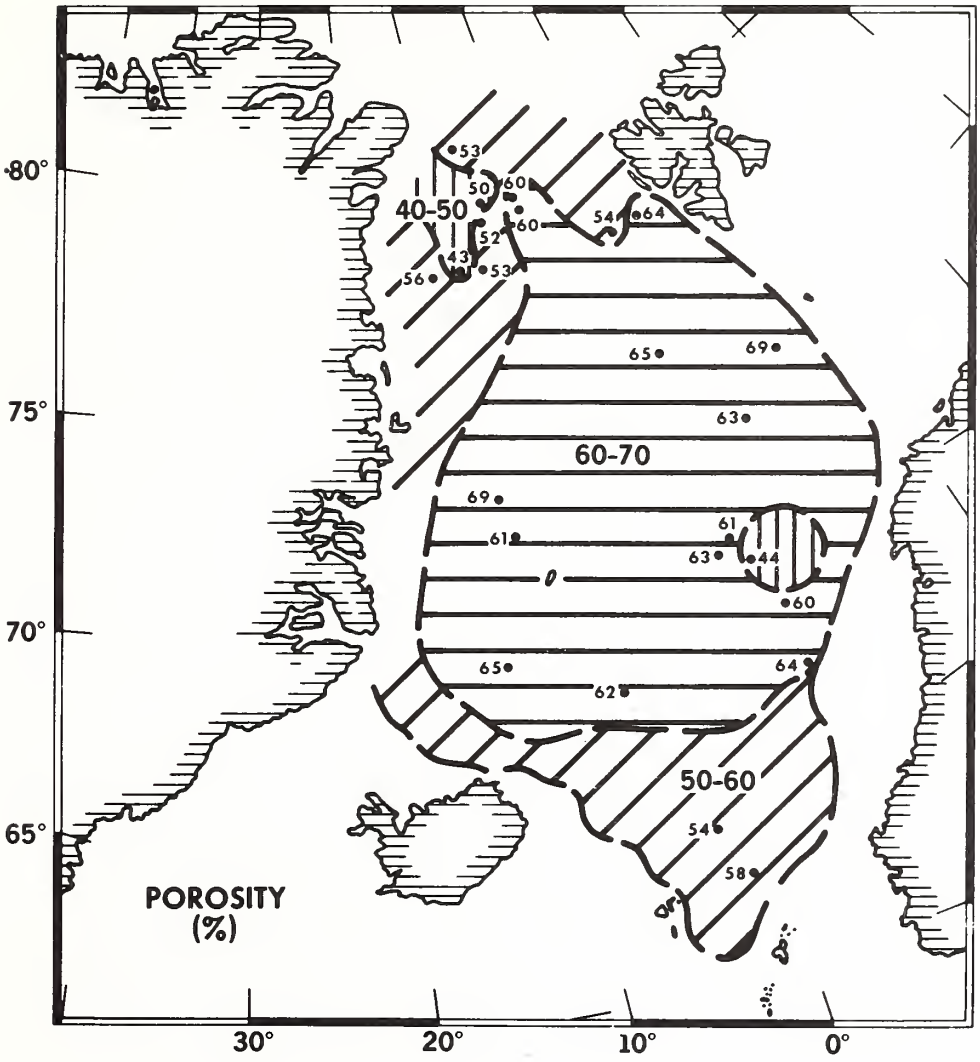
80°
75°
70°
65°
30°
20°
10°
0°
40-50
53
50
60
52
60
54
64
43
56
53
65
69
63
60-70
69
61
61
63
44
60
65
64
62
50-60
54
58
POROSITY
(%)

FIG. 7

16 1300

and $N\gamma$ become unity and zero respectively and equation (1) is reduced to:

$$Qc=cNc \qquad (2)$$

Although several values have been suggested and used for Nc, 5.14 has been selected for the purpose of this discussion. Based on equation (2) and a few selected surface (0 to 5 cm) shear strength values, ultimate bearing capacity was determined for the study area (Fig. 8). Bearing capacity values range from a low of 31 g/cm^2 (0.4 psi) to a high of 350 g/cm^2 (4.9 psi), but within the few samples in which surface shear strength data exist values of 100 to 200 g/cm^2 (1.4 to 2.9 psi) are more common.

As a result of the sampling procedure, the upper few centimeters of a sediment core are frequently disturbed to a greater degree than the lower portion of the sample. This then would lead to lower shear strengths and thus to lower bearing capacities than would be found had the shear tests been made in situ. The values shown in figure 8 are, therefore, conservative, but just how conservative cannot be determined from the available data. A study in the Gulf of Maine dealing with the variation between in place versus laboratory tests found shear strength in surficial sediments to vary from as little as 1 or 2 percent to as much as 85 percent. Such variations are dependent on the design of the sampling device, sediment type, and handling of the samples prior to laboratory testing.

Sediment Plasticity.—Based on sediment plasticity properties, Casagrande (6) developed a rather simple method for classifying fine-grained deposits. This classification utilizes a plasticity chart, the ordinate being the plasticity index and the abscissa the liquid limit. An A-line drawn across the chart serves as an empirical boundary between inorganic clays above with organic clays and inorganic silts falling below. Based on relatively simple liquid and plastic limit determinations, sediments can be roughtly classed as to their textural and organic characteristics. In some instances it has been found that the plasticity chart also serves to indicate similar and dissimilar source areas of the deposits as was reported by Keller and Lambert (27) in their study of the Mediterranean Sea. The samples studied here do not reveal any such distinction between the deposits of the Norwegian and Greenland Seas (Fig. 9).

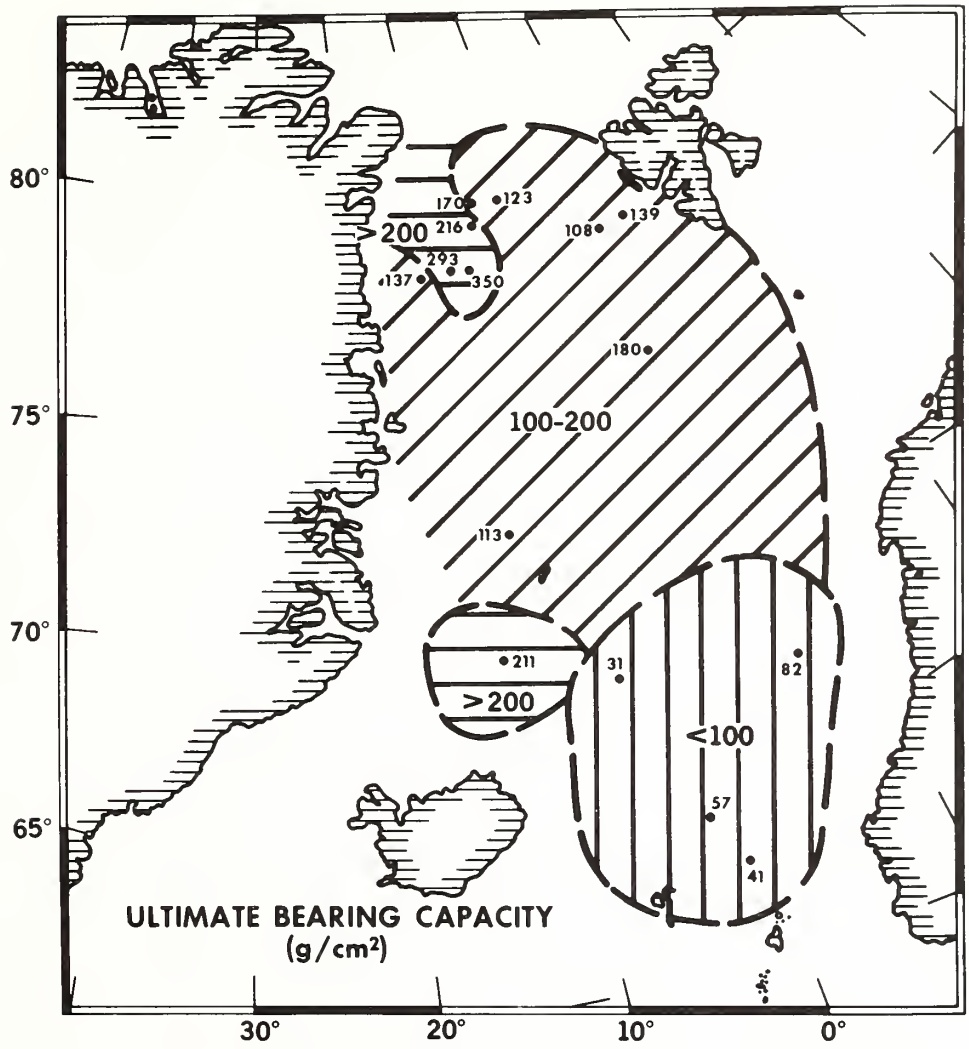
80°
75°
70°
65°
30°
20°
10°
0°
170
123
200
216
108
139
293
137
350
180
100-200
113
211
>200
31
82
<100
57
41
ULTIMATE BEARING CAPACITY
(g/cm²)

FIG. 8

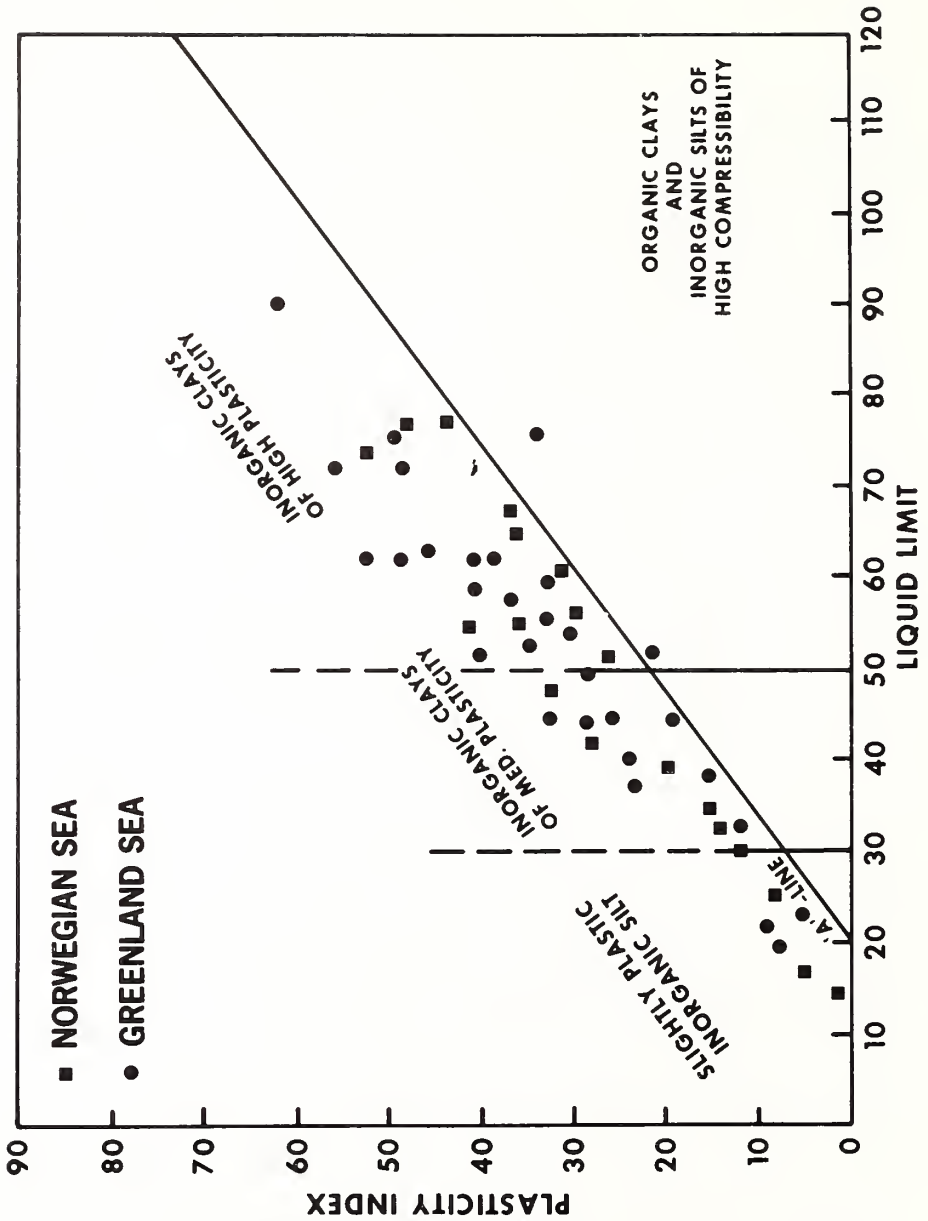
NORWEGIAN SEA
GREENLAND SEA
INORGANIC CLAYS OF HIGH PLASTICITY
INORGANIC CLAYS OF MED. PLASTICITY
SLIGHTLY PLASTIC INORGANIC SILT
A-LINE
ORGANIC CLAYS AND INORGANIC SILTS OF HIGH COMPRESSIBILITY
PLASTICITY INDEX
LIQUID LIMIT
0
10
20
30
40
50
60
70
80
90
100
110
120

FIG. 9

As has been found in the case of all the engineering properties discussed above, the plasticity charactistics of the Greenland-Norwegian basin sediments are also noticably distinct from those of the North Atlantic basin. The Greenland-Norwegian basin deposits are found to be largely inorganic clays of medium to high plasticity, sandy clays, and slightly plastic inorganic silts (Fig. 9). Inorganic clays of high to medium plasticity predominate in the North Atlantic basin (34), but are considerably less significant in the area of this study.

Variation of Engineering Properties with Depth.-The previous discussion has dealt with averaged values of various geotechnical parameters which is a practical way in which to display the areal distribution of such properties over a large area. There is, however, obviously considerable variation of these properties with depth owing to a number of different environmental conditions influencing deposition in the basin, e.g., turbidity currents, ice-rafting, and "normal" sedimentation. As shown in Table 1, the "extremes" observed in the Greenland-Norwegian basin are substantial in many instances.

The occurrence of ice-rafted material throughout the basin can be significant and may well prove to be very deceiving when attempting to determine the engineering properties of a deposit to a relatively shallow depth. The significance of turbidity currents and their influence on a depositional environment may not be quite so obvious. Turbidity current deposits (turbidites), which occur in the study area, are decidedly distinct when observed in a cored sample and greatly influence the overall engineering properties of the sedimentary deposit (Fig. 10).

SUMMARY

Sixty-seven sediment cores from throughout the Greenland-Norwegian basin were examined for their engineering properties. Although these relatively few cores cannot be considered as representive of the entire basin, some generalizations are feasible regarding the regional distribution of certain engineering properties and the range of the respective parameters for the surficial layers within the basin deposits.

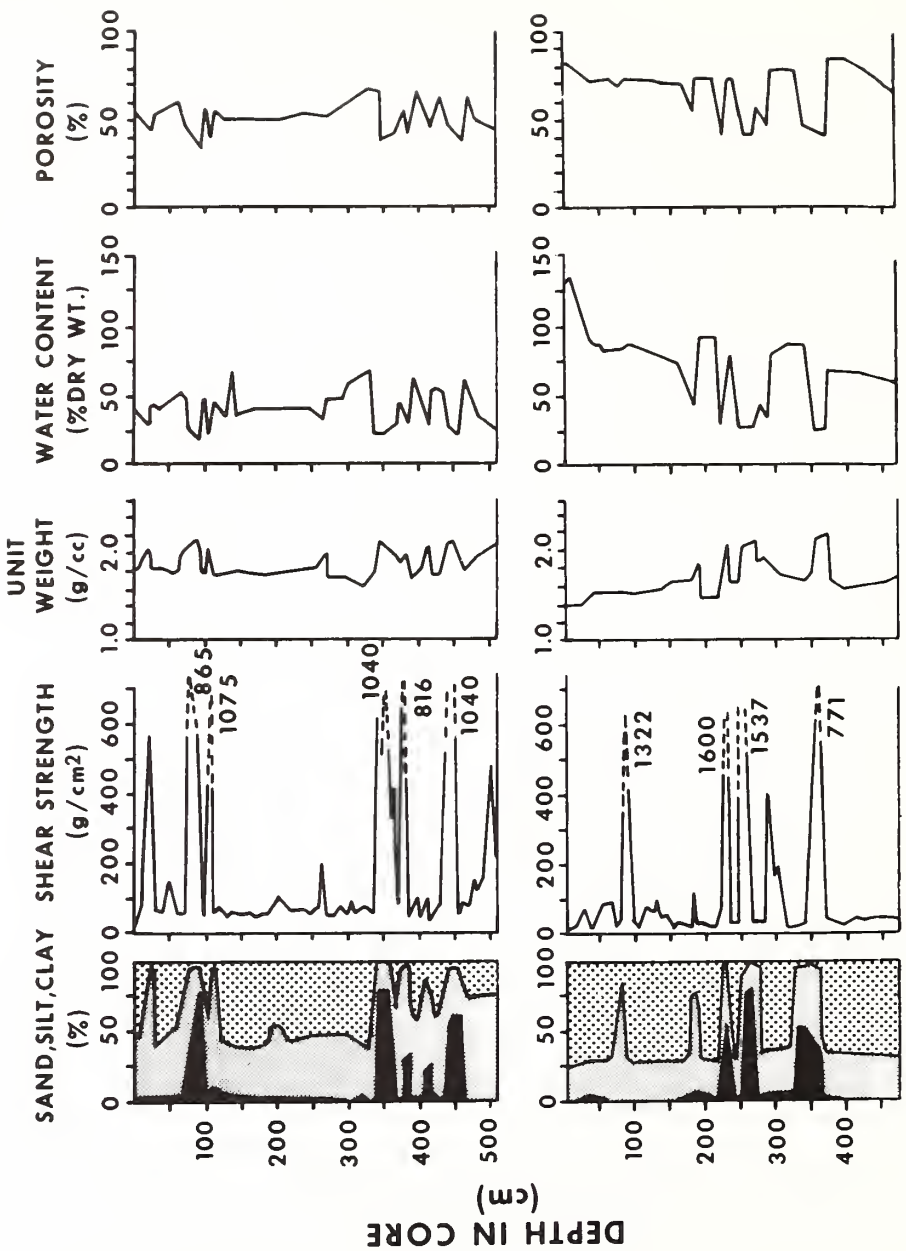
POROSITY (%)
WATER CONTENT (%DRY WT.)
UNIT WEIGHT (g/cc)
SHEAR STRENGTH (g/cm²)
SAND,SILT,CLAY (%)
865
1075
1040
816
1040
1322
1600
1537
771
DEPTH IN CORE (cm)

FIG. 10

Sediments blanketing the Greenland-Norwegian basin are primarily of glacial-fluvial origin, entering the basin from nearby land masses. The deposits consist mainly of silty and sandy clays interlayered with silt and fine sand turbidite sequences. Pelagic clays comprise a large portion of the deposits occurring in the southwest sector of the basin, whereas a foraminiferal ooze constitutes much of the surface deposit in the center of the basin. Ice-rafted pebbles and cobbles occur randomly both laterally and vertically throughout the area.

Average shear strengths range from 27 to 142 g/cm^2 (0.4 to 2.0 psi), with the higher values commonly found in association with the sediments overlying the Jan Mayen ridge. As a general observation it is noted that the sediments south of the Jan Mayen fracture zone possess a higher shear strength than those to the north.

Water content within the basin deposits varies from 31 to 89 percent, but is normally within the range of 40 to 70 percent over much of the area. Water contents are generally lower in the southern part of the basin increasing northward beyond the Jan Mayen fracture zone. In the northern sector of the basin low water contents are also encountered on the northeast continental shelf of Greenland.

Average unit weights are relatively high in comparison to other deep-sea deposits and are found to range from 1.51 to 1.97 g/cm^3 (94.2 to 122.9 pcf) in the Greenland-Norwegian basin. Much of the basin, however, is found to be covered with sediments possessing unit weights between 1.60 and 1.75 g/cm^3 (99.8 to 109.2 pcf). Areas of relatively high density material are found in the northern and southern most parts of the basin. This distribution may reflect the influence of bottom current transport.

Porosity of the Greenland-Norwegian basin deposits varies from 43 to 69 percent, but more commonly ranges from 55 to 65 percent over much of the area. Relatively low porosities occur in the northern and southern parts of the study area.

Using the classification system developed by Casagrande (6) which is based on the plastic characteristics of a sediment, it is found that the Greenland-Norwegian basin deposits are largely classed as inorganic clays of medium to high plasticity, sand clays, and slightly plastic inorganic silts. Based on plasticity

indices no basic distinction can be made among the sediments found in various parts of the basin as to their source.

An overall examination of the distribution of engineering properties in the Greenland-Norwegian basin indicates that those deposits underlying the Greenland Sea possess relatively higher unit weight and water content, but lower porosity and shear strength than those sediments of the Norwegian Sea. In comparison to the North Atlantic, the Greenland-Norwegian basin sediments display distinctly different engineering properties (Table 1). Unit weights are considerably higher than those in the Atlantic as are shear strengths and grain specific gravities, but to a somewhat lesser extent. Such properties as water content, porosity, sensitivity, liquid limit, and plastic limit are all lower than those reported by Keller and Bennett (26) for the North Atlantic basin.

ACKNOWLEDGMENTS

I gratefully acknowledge the assistance of Joseph Kravitz of the U. S. Naval Oceanographic Office for providing the photograph shown in figure 3 and of G. Leonard Johnson from the same office for permission to use his physiographic diagram.

TABLE I

VARIATION OF ENGINEERING PROPERTIES

GREENLAND-NORWEGIAN BASIN

	γ (g/cm^3)	w (%)	n (%)	τ_f (g/cm^2)	S_t	G	w_L	w_p
MAX.	2.21	187	84	300	9	2.98	96	40
MIN.	1.32	20	35	5	1	2.56	17	12
AVE.	1.72	51	59	57	3	2.74	51	23
				NORTH ATLANTIC BASIN				
MAX.	2.56	207	85	925	88	2.86	104	38
MIN.	1.25	15	32	1	1	2.45	47	20
AVE.	1.52	86	66	52	4	2.73	65	27

S_t = Sensitivity
G = Grain specific gravity
w_L = Liquid limit
w_p = Plastic limit
see text for other symbols

REFERENCES

(1) American Society for Testing Materials (1958): 1958 Book of ASTM Standards including tentatives, Part 4. Philadelphia, Pa., 1426 p.

(2) Arrhenius, G. (1952): Sediment cores from the East Pacific: Reports of the Swedish Deep-Sea Expedition, 1947-1948, v. 5, no. 1, 277 p.

(3) Böggild, O. B. (1899): Habvundens afleiringer: Den Danske Ingolf-Expedition, v. 1, no. 3.

(4) Bryant, W. R., P. Cernock, and J. Morelock, Jr. (1967): Shear Strength and consolidation characteristics of marine sediments from the western Gulf of Mexico. pp. 41-62, in Richards, A. F., (ed.) Marine Geotechnique, Univ. Ill. Press, Urbana, Ill., 327 p.

(5) Buchan, S., F. C. D. Dewes, D. M. McCann and D. Taylor Smith (1967): Measurements of the acoustic and geotechnical properties of marine sediment cores. pp. 67-92, in Richards, A. F., (ed.) Marine Geotechnique, Univ. Ill. Press, Urbana, Ill., 327 p.

(6) Casagrande, A. (1948): Classification and identification of soils. American Society Civil Engineers, Trans. v. 113, pp. 901-931.

(7) Evans, I., and G. G. Sherratt (1948): A simple and convenient instrument for measuring the shear resistance of clay soils. Jour. Scientific Instruments and Physics in Industry, v. 25, pp. 411-414.

(8) Fisk, H. N., and B. McClelland (1959): Geology of continental shelf off Louisiana: its influence on offshore foundation design. Geological Society America, Bulletin, v. 70, pp. 1369-1394.

(9) Hamilton, E. L. (1956): Low sound velocities in high porosity sediments. Jour. Acoustical Society America, v. 28, pp. 16-19.

(10) Hamilton, E. L. (1959): Thickness and consolidation of deep-sea sediments. Geological Society America, Bulletin, v. 70, pp. 1399-1424.

(11) Hamilton, E. L., and H. W. Menard (1956): Density and porosity of sea-floor surface sediments off San Diego, California. American Association Petroleum Geologists, v. 40, pp. 754-761.

(12) Hansbo, S. (1957): A new approach to the determination of the shear strength of clay by the fall-cone test. Royal Swedish Geotechnical Institute Proc., No. 14, 47 p.

(13) Harrison, W., M. P. Lynch, and A. G. Altschaeffl (1964): Sediments of lower Chesapeake Bay, with emphasis on mass properties. Jour. Sedimentary Petrology, v. 34, pp. 727-755.

(14) Holtedahl, H. (1950): A study of the topography and the sediments of the continental slope west of Möre, W. Norway. Univ. Bergen Årbok, Naturv. r. 5.

(15) Holtedahl, H. (1955): On the Norwegian continental terrace, primarily outside Möre-Romsdal, its geomorphology and sediments. With contributions on the Quaternary geology of the adjacent land and on the bottom deposits of the Norwegian sea. Univ. Bergen Årbok, Naturv. r. 14.

(16) Holtedahl, H (1959): Geology and paleontology of Norwegian Sea bottom cores. Jour. Sedimentary Petrology, v. 29, pp. 16-29.

(17) Igelman, K. R., and E. L. Hamilton (1963): Bulk densities of mineral grains from Mohole samples (Guadalupe site). Jour. Sedimentary Petrology, v. 33, pp. 474-478.

(18) Jerbo, A. (1967): Geochemical and strength aspects of Bothnian clay sediments. pp. 177-186, in Richards, A. F. (ed.) Marine Geotechnique, Univ. Ill. Press, Urbana, Ill., 327 p.

(19) Johnson, G. L., and O. B. Eckhoff (1966): Bathymetry of the North Greenland sea. Deep-Sea Research, v. 13, pp. 1161-1173.

(20) Johnson, G. L., and B. C. Heezen (1967): Morphology and evolution of the Norwegian-Greenland Sea. Deep-Sea Research, v. 14, pp. 755-771.

(21) Johnson, G. L., J. A. Ballard, and J. A. Watson (1968): Seismic studies of the Norwegian continental margin. Norsk Polarinstitut-Årbok 1966, pp. 112-119.

(22) Jones, E. J. W., M. Ewing, J. I. Ewing, and S. L. Eittreim (1970): Influences of Norwegian Sea overflow water on sedimentation in the northern North Atlantic and Labrador Sea. Jour. Geophysical Research, v. 75, pp. 1655-1680.

(23) Keller, G. H. (1968): Shear strength and other physical properties of sediments from some ocean basins. pp. 391-417, in Proc. Civil Engineering in the Oceans. American Society of Civil Engineers, 926 p.

(24) Keller, G. H. (1969): Mass properties of the sea floor in a selected depositional environment. pp. 857-877, in Proc. Civil Engineering in the Oceans - II. American Society of Civil Engineers, 1265 p.

(25) Keller, G. H., and R. H. Bennett (1968): Mass physical properties of submarine sediments in the Atlantic and Pacific basins. pp. 33-50, in Proc. XXIII International Geological Congress, Section 8, 321 p.

(26) Keller, G. H., and R. H. Bennett (1970): Variations in the mass physical properties of selected submarine sediments. Marine Geology, v. 9, pp. 215-223.

(27) Keller, G. H., and D. Lambert (1971): Geotechnical properties of submarine sediments, Mediterranean Sea. in Proc. Mediterranean Symposium, VIII International Sedimentological Congress (in press).

(28) Kolb, C. R., and R. I. Kaufman (1967): Prodelta clays of southeast Louisiana. pp. 3-21, in Richards, A. F., (ed.) Marine Geotechnique, Univ. Ill. Press, Urbana, Ill., 327 p.

(29) McClelland, B. (1967): Progress of consolidation in delta front and prodelta clays of the Mississippi River. pp. 22-40, in Richards, A. F. (ed.) Marine Geotechnique, Univ. Ill. Press, Urbana, Ill., 327 p.

(30) Moore, D. G., and G. Shumway (1959): Sediment thickness and physical properties: Pigeon Point Shelf, California. Jour. Geophysical Research, v. 64, pp. 367-374.

(31) Peterson, M. N. A., N. T. Edgar, M. Cita, S. Gartner, Jr., R. Goll, C. Nigrini, C. von der Borch (1970): Initial reports of the Deep-Sea Drilling Project, v. II, Washington, D. C., 501 p.

(32) Prandtl, L. (1920): Über die Härte plastischer Körper. Koniglichen Gesellschaft der Wissenschaften zu Göttingen, Matematisch - physikalische Klasse, p. 74-85.

(33) Richards, A. F. (1961): Investigations of deep-sea sediment cores, I. Shear strength, bearing capacity, and consolidation. U. S. Navy Hydrographic Office, Tech. Rept. 63, 70 p.

(34) Richards, A. F. (1962): Investigation of deep-sea sediment cores, II. Mass physical properties. U. S. Navy Hydrographic Office, Tech. Rept. 106, 146 p.

(35) Richards, A. F., and E. L. Hamilton (1967): Investigations of deep-sea sediment cores, III. Consolidation. pp. 93-117, in Richards, A. F., (ed.) Marine Geotechnique, Univ. Ill. Press, Urbana, Ill., 327 p.

(36) Schmelck, L. (1882): On oceanic deposits: The Norwegian North-Atlantic expedition 1876-1878, v. 9, no. 2.

(37) Schreiber, B. C. (1967): Marine Geophysical Survey Program 65-67, Western North Atlantic and Eastern and Central North Pacific Oceans - core, sound velocometer, hydrographic and bottom photographic stations. Alpine Geophysical Associates, Inc., SP-96-SF-8, Area SF, v. 8, 19 p. 26 fig.

(38) Terzaghi, K. (1943): Theoretical soil mechanics. John Wiley & Sons, Inc., New York, 510 p.

(39) Texas Instruments, Inc. (1967): U. S. Naval Oceanographic Office Marine Geophysical Survey Program 1965-1967, North Atlantic Ocean, Norwegian Sea and Mediterranean Sea. Area 1, v. 5, Geology and Geophysics, 39 p.

FIGURE CAPTIONS

Fig. 1 Physiographic provinces of the Greenland-Norwegian basin. After Johnson and Heezen (1967).

Fig. 2 Location of core samples used in this study.

Fig. 3 Radiograph of a sediment core showing the presence of ice-rafted material. (Photo courtesy of Joseph Kravitz).

Fig. 4 Areal distribution of average shear strength.

Fig. 5 Areal distribution of average water content.

Fig. 6 Areal distribution of average unit weight.

Fig. 7 Areal distribution of average porosity.

Fig. 8 Ultimate bearing capacity values for a strip load placed on the sea-floor surface.

Fig. 9 Plasticity chart.

Fig. 10 Variation of geotechnical properties with depth in two sediment cores collected in an area of turbidites.

Reprinted from VI Conferencia Geologica del Caribe, Margarita, Venezuela, Memorias - 405-408.

VI CONFERENCIA GEOLOGICA DEE CARIBE – MARGARITA, VENEZUELA
MEMORIAS 1972

MASS PHYSICAL PROPERTIES OF TOBAGO TROUGH SEDIMENTS

by:

George H. Keller [1], Douglas N. Lambert [1]
Richard H. Bennett [1], and James B. Rucker [2]

The Tobago Trough is a basinal feature located in the southeastern Caribbean (Fig. 1). Morphologically, it is a relatively simple basin bordered to the west by the Lesser Antilles island arc, by the Venezuelan margin to the south, the submarine Barbados Ridge to the east and to the north, by a ridge extending from St. Lucia Island eastward to the Barbados Ridge. The eastern and northern portions of the Tobago Trough display a simple topography, with subbottom strata dipping very gently towards the center of the basin. The western part of the basin is characterized by numerous slump deposits and bottom irregularities. To the south, the relatively smooth bottom is interrupted by a number of submarine valleys extending into the basin from the Venezuelan margin.

Earlier studies have indicated two primary sources for the sediments blanketing this sector of the Caribbean. The Amazon and Orinoco rivers contribute much of the clay and fine silt-size fraction to the Tobago Trough, whereas there is also a strong indication that much material enters the basin from the south and southwest from along the northern Venezuelan margin.

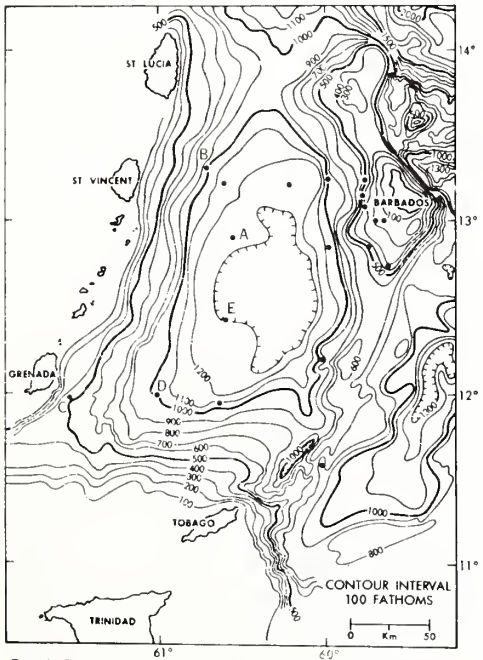

Fig. 1. Bathymetric map of the Tobago Trough with core station, locations. Lettered core stations refer to figures 3,4 &5.

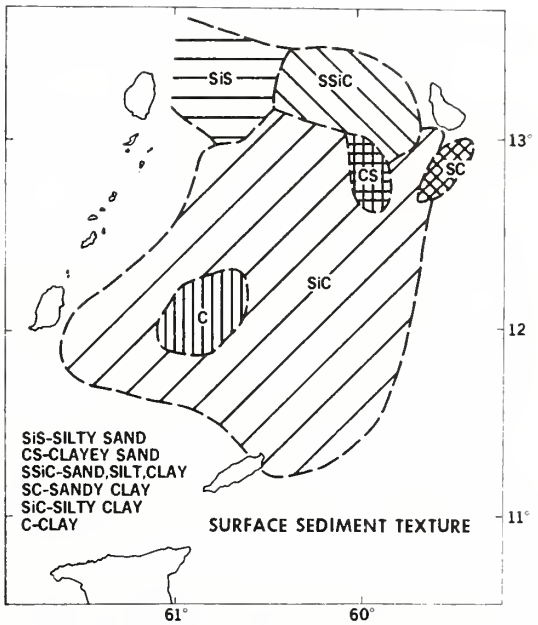

Fig. 2. Textural characteristics of surface deposits based on the classification of Shepard (1954).

(1) NOAA Atlantic Oceanographic and Meteorological Laboratories, Miami, Florida.
(2) U. S. Naval Oceanographic Office, Washington, D. C.

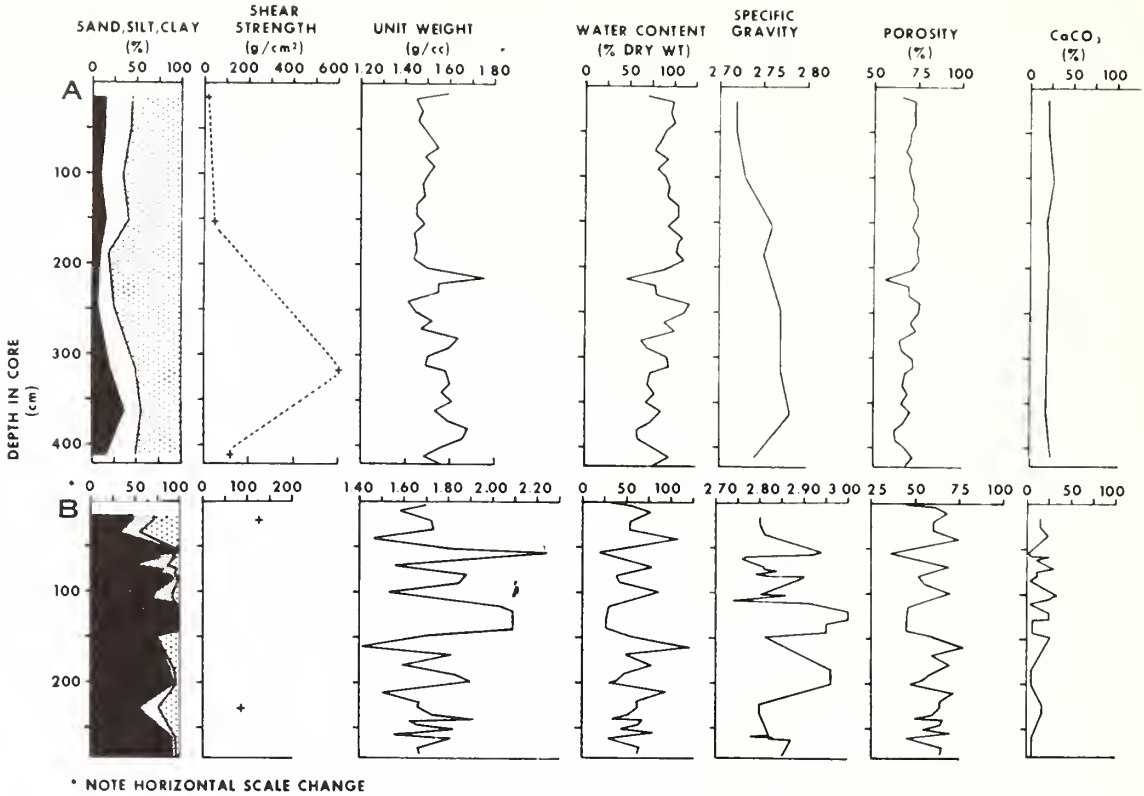

Fig. 3. Variation of selected properties with depth in cores A and B (See Fig. 1 for core location)

A series of 32 sediment cores collected at 19 sites in the Tobago Trough and analyzed for their mass physical properties serve as the basis for this study. Surface sediments are primarily silty clays except along the western and northern portions of the trough where sand comprises a large percentage of the bottom deposits (Fig. 2). Between the islands of St. Vincent and Barbados, sand content within the sampled interval ranges from 75 to 21 percent (Fig. 3B), decreasing in an easterly direction. East of Grenada Island, sand constitutes as much as 88 percent of the sediment to a depth of 100 cm (Fig. 4). There appears to be little doubt that the Lesser Antilles islands serve as a source for much of the coarse material entering the trough. Sediment cores from the central portion of the trough consist primarily of silt and clay-size material and are relatively homogeneous with depth (few graded beds are observed) (Figs. 3A, and 5). Most of the trough deposits are classified as fluvial-marine, owing to the relatively low calcium carbonate content (12 to 28 percent) and their presumed source.

The high concentrations of calcium carbonate found east of Grenada Island are attributed to the slumping and transport of coral, shell and reef debris from the reefs adjacent to the Grenadine Islands (Fig. 6).

Average sediment shear strength (average of a series of tests per core) varies considerably (38 to 260 g/cm²) throughout the trough. Lower values occur in the central portion of the basin and southwest of Barbados. Higher strengths are commonly associated with coarser sediments and those processing higher percentages of calcium carbonate. Sensitivity (measure of the loss of strength when the material strength of the sediment is destroyed by remolding; natural/remolded ratio) of these deposits is relatively high (4 to 7), indicating a loss of 75 to 87 percent of the original strength when severely disturbed.

Water contents (weight of water to the weight of dried solids in a given sediment mass) are generally lower (52 to 85 percent) in the coarser northern deposits and off the island of Grenada, increasing to slightly more than 100 percent in the finer sediments of the central portion of the basin (Fig. 7). Unit weight or more commonly, bulk density, clearly reveals the contrast between the majority of the basin deposits and those found along the northern margin (Fig. 8). Those to the north are considerably more dense, owing to the greater concentration of heavy *vs.* light minerals (25 to 75 percent) than elsewhere in the basin (5 to 95 percent) (Fig. 9). As might be expected the highest observed values of grain specific gravity (2.87) occur just east of St. Vincent Island where both bulk densities and heavy mineral concentrations are the highest.

With the exception of the samples collected just east of St. Vincent Island, the sediments of the Tobago Trough exhibit a high degree of plasticity, closely resembling the properties of North Atlantic deposits. Although much of the sediment entering the Tobago Trough is derived from the Venezuelan margin as well as the Orinoco and Amazon rivers, the volcanic islands of the Lesser Antilles, along with their associated reefs, are major contributors of the coarse grained constituents found in the trough.

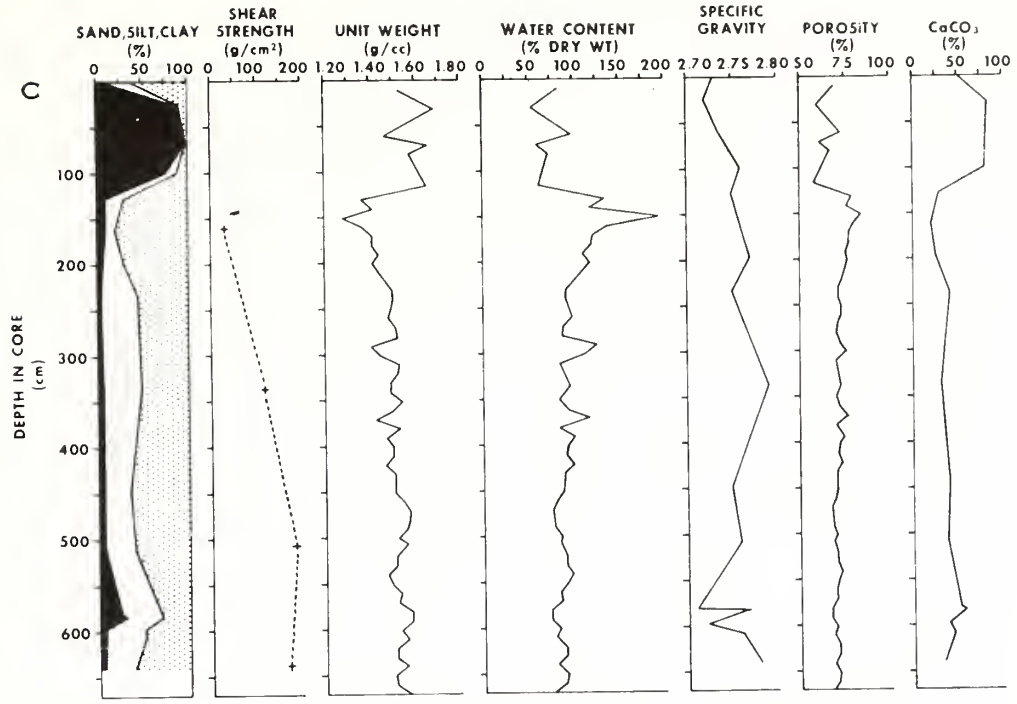

Fig. 4. Variation of selected properties with depth in core C. (See Figure 1 for core location).

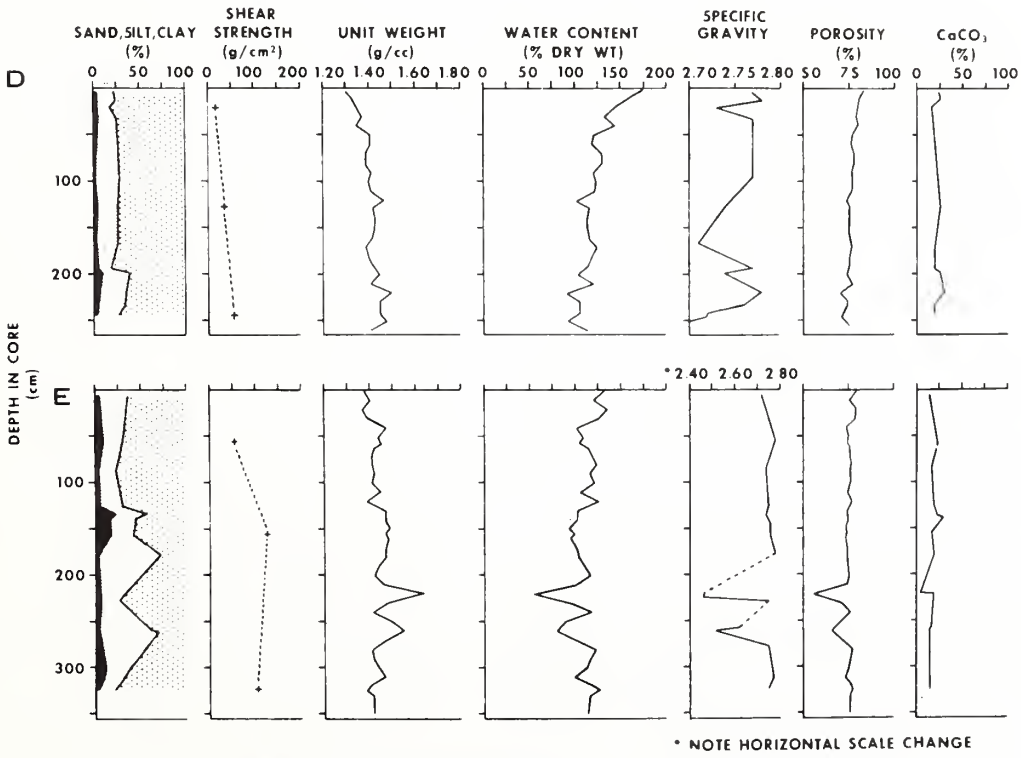

Fig. 5. Variation of selected properties with depth in cores D and E.(See Fig. 1 for core locations).

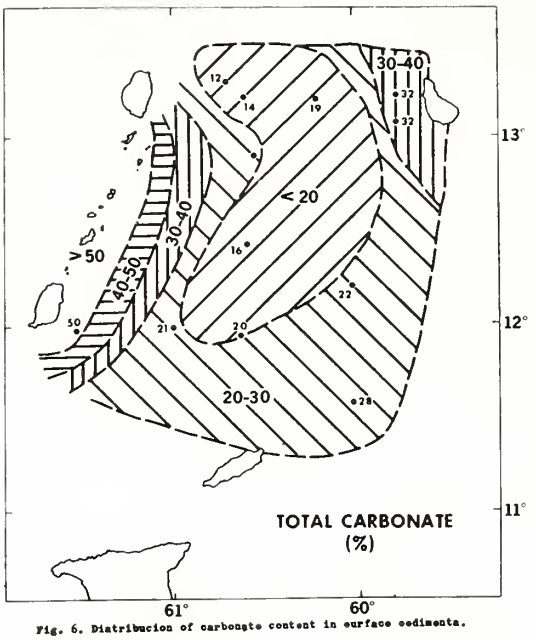

Fig. 6. Distribucion of carbonate content in surface sediments.

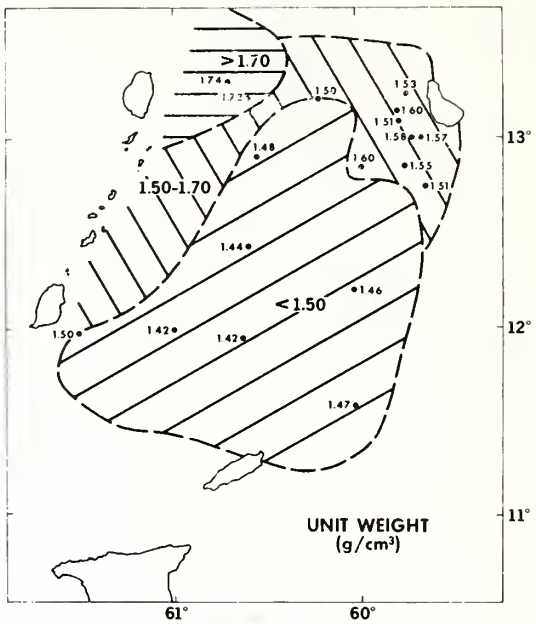

Fig. 8. Unit weight distribution based on averaging all the measurements made in each core. Average core length 3 meters.

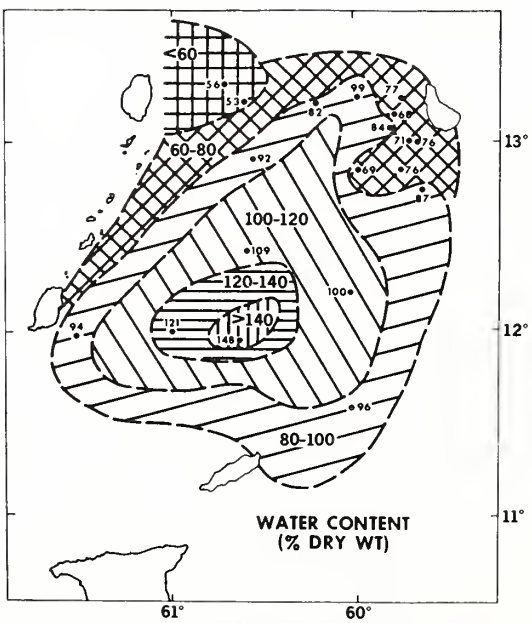

Fig. 7. Water content distribution based on averaging all the measurements made in each core. Average core length 3 meters.

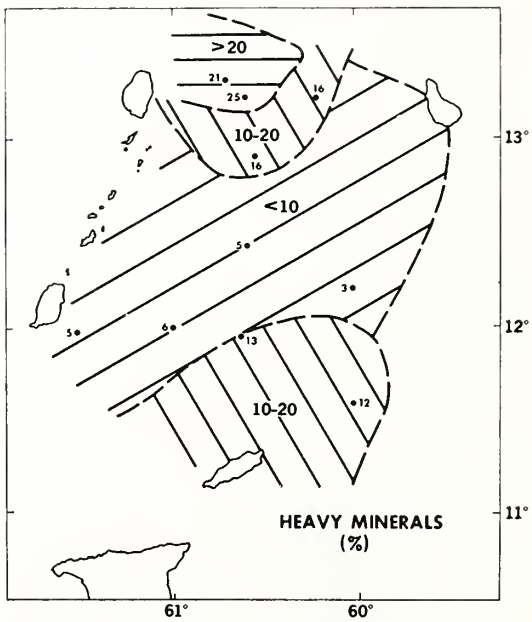

Fig. 9. Distribution of heavy mineral concentration in the surface sediments.

The clay mineral assemblage throughout the Tobago Trough is dominated by mixed layer clays and illite with lesser amounts of montmorillonite, kaolinite and chlorite. Indications are that much of the illite is derived from the Amazon River. Feldspar/quartz ratios of the less than 2 size fraction are commonly higher (2.2 to 7.1) in the northern sector of the basin than in the central and southern portion. These observed ratios appear to be higher in the trough than those reported for much of the Caribbean, owing to the strong influence of the nearby Lesser Antilles islands.

BIBLIOGRAPHY

SHEPARD, F. D. (1954).—*Nomenclature based on sand-silt-clay ratios:* Jour. Sedimentary Petrology, Vol. 24, p. 151-158.

U.S. DEPARTMENT OF COMMERCE
National Oceanic and Atmospheric Administration
Environmental Research Laboratories

NOAA Technical Memorandum ERL AOML-17

TABLES FOR DETERMINING POROSITY OF DEEP-SEA SEDIMENTS FROM WATER CONTENT AND AVERAGE GRAIN DENSITY MEASUREMENTS

Douglas N. Lambert
Richard H. Bennett

Marine Geology and Geophysics Laboratory

Atlantic Oceanographic and Meteorological Laboratories
Miami, Florida
November 1972

TABLE OF CONTENTS

	Page
ABSTRACT	1
1. INTRODUCTION	1
2. MEASUREMENTS AND PROCEDURES	2
3. TABULAR RESULTS	2
4. SUMMARY AND CONCLUSIONS	2
5. REFERENCES	3
APPENDIX Porosity as a Function of Average Grain Density and Water Content	5

TABLES FOR DETERMINING POROSITY OF DEEP-SEA SEDIMENTS FROM WATER CONTENT AND AVERAGE GRAIN DENSITY MEASUREMENTS

Douglas N. Lambert and Richard H. Bennett

An expedient and reliable method is shown for determining porosity of deep-sea sediment using water content and average grain density measurements. Tables with water contents ranging from 25 percent to 600 percent and average grain densities from 1.70 to 3.19 g/cc are presented.

1. INTRODUCTION

Porosity, defined as the ratio (usually expressed in percent) of the volume of voids of a given soil mass to the total volume of the soil mass (ASTM, 1967), is normally computed from unit weight, average grain density, water content, and an assumed interstitial water density. Bennett and Lambert, (1971) presented a rapid and reliable technique to determine porosity (n) from laboratory measurements of water content (W_w/W_d x 100, the weight ratio of water to dried solids) and average grain density of saturated marine sediments. This relationship is expressed in c.g.s. units as

$$n = \frac{V_v}{V_t} = \frac{W_w + V_{ss}}{\frac{W_d}{DG} + W_w} \times 100 \qquad (1)$$

where in a saturated sediment the volume of the voids (V_v) is approximately equal to the weight of water (W_w) plus the volume of the salts in solution (Vss). The total volume (V_t) of the sediment sample is equal to the volume of the dry solids (W_d/DG) plus the volume of the water (W_w), where the volume of the dry solids is the weight of the dry solids, including salts, (W_d) divided by the average grain density (DG). V_{ss} is very close to 1.2 percent of the volume of water for disolved salt concentrations of 35 parts per thousand. V_{ss} is therefore considered negligible. Equation 1 then becomes

$$n = \frac{W_w}{\frac{W_d}{DG} + W_w} \times 100 \qquad (2)$$

2. MEASUREMENTS AND PROCEDURES

As a measure of the reliability of the above technique, 77 porosity measurements were determined using equation 2. These results were compared to porosities calculated from unit weight measurements determined by the tube method (weight per unit volume), average grain density, and water content values with no corrections for salt content. A linear correlation coefficient of +0.998 was found between the two porosity methods with 67 percent of all measured values falling within $\pm$ 0.42 percent of each other. These data show, for all practical purposes, correlation between the two techniques is nearly perfect and that either method of determining porosity is equally reliable.

3. TABULAR RESULTS

The bulk of this report consists of tables for determining porosity using equation 2. These tables include the range of values for water content and average grain density commonly found in submarine sediments (Keller and Bennett, 1970); and are established for water content at one-percent intervals from 25 to 100 percent, five-percent intervals from 100 to 200 percent and at ten-percent intervals from 200 to 600 percent. Water content (percent dry weight) is given at the heading of each table, and the left-hand column (DB) shows the range of average grain densities (1.70 to 3.10) in 0.01 g/cc increments. See Appendix.

To determine the porosity, select the table which approximates or equals the water content for that sample and then locate the average grain density of the sample to the first decimal place in the left-hand column. Move across the row to the appropriate column (numbered zero through nine at the top of each column) for the second decimal place of the average grain density. The number given in the column is the percent porosity to the first decimal place. However, in all practicality, porosity values from these tables should be reported only to the nearest whole number.

Assuming a salinity of 35 parts per thousand for the interstitial water, porosity values which have been corrected for salt content will be up to one percent higher than the data given in the tables.

4. SUMMARY AND CONCLUSIONS

Water content and average grain density are particularly useful for determining porosity of deep-sea sediment not amenable to other techniques. Data show that for all practical

purposes, correlation between this technique and the standard volumetric method is nearly perfect. The tables provide a quick and reliable procedure for determining the porosity of submarine sediments.

5. REFERENCES

American Society for Testing Materials, 1967, 1967 Book of ASTM Standards, Part II. Philadelphia, Pa., p. 285-302.

Bennett, Richard H. and Lambert, Douglas N., 1971, Rapid and reliable technique for determining unit weight and porosity of deep-sea sediments. Marine Geology, 11: p. 201-207.

Keller, George H. and Bennett, Richard H., 1970, Variations in the mass physical properties of selected submarine sediments, Marine Geology, 9: p. 215-223.

Reprinted from Geological Survey of Georgia,
State of Georgia Department of Natural Resources.

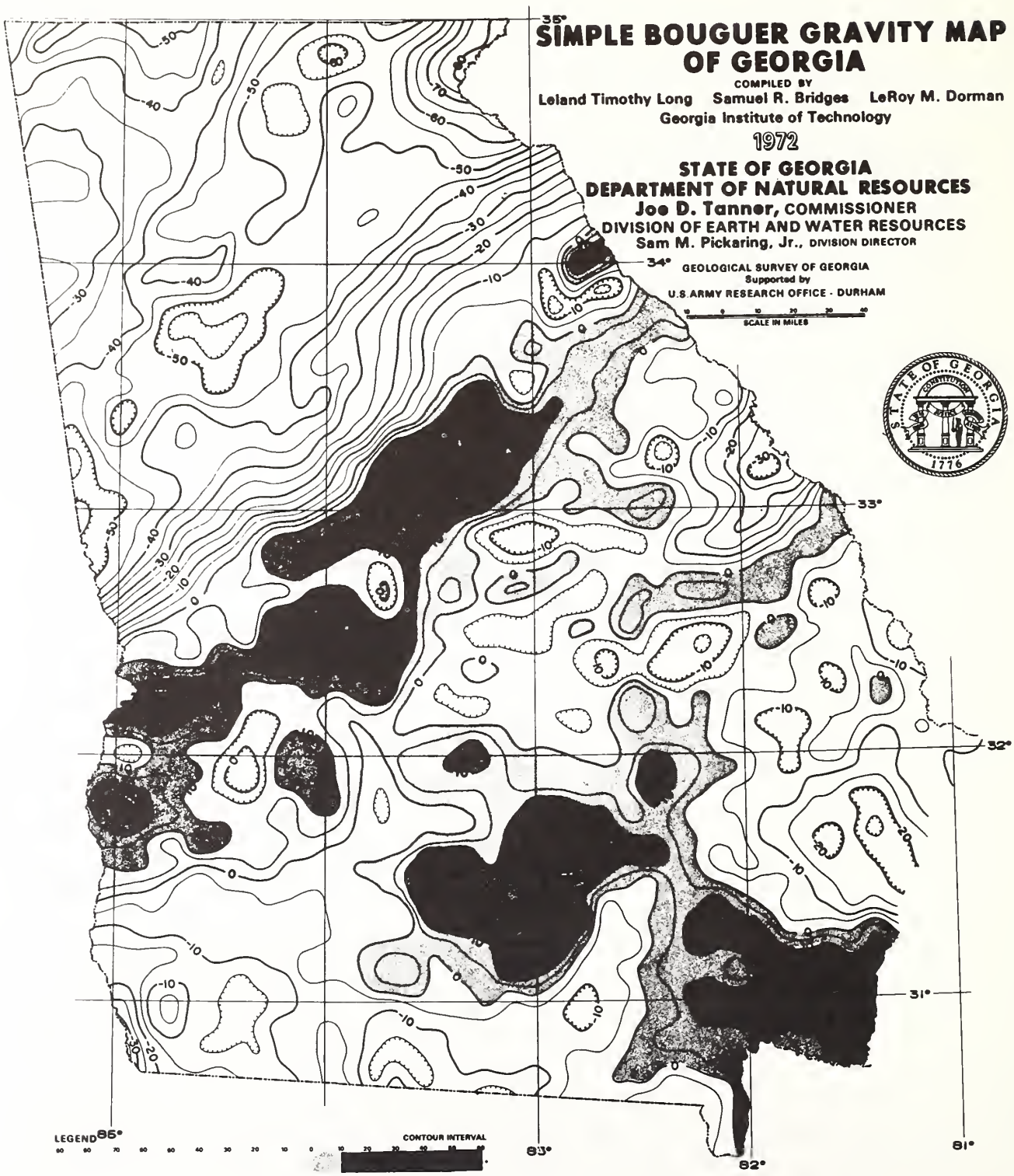

EXPLANATION

Interpretation of Bouguer Anomalies

Bouguer gravity anomalies are measures of the influence of local geology and crustal structure on the earth's gravitational field. The character of these anomalies is determined by the distribution of the variations of the density in the earth's crust which in turn is due to changes in rock type or structure. Positive and negative Bouguer anomalies indicate an excess or deficiency, respectively, of mass near the point of observation. Shallow density variations usually will cause anomalies of short length whereas density variations deep in the earth's crust will cause anomalies which will vary gradually over a distance comparable to their depth. The gravity map shown here is a representation of the Bouguer gravity anomalies (see section on computation for theoretical details) in the form of a contour map. The contour lines connect points of equal strength in the anomalous portion of the earth's gravity field in the same manner that topographic contours connect points of equal elevation. The scale of this map is best suited for illustrating the regional trends of the gravity surface, but it provides valuable information for more detailed future studies. Such studies will help solve geologic and mineral exploration problems by locating rock bodies and structures which are not exposed at the surface, and to give information on the 3-dimensional geometry of known rock bodies.

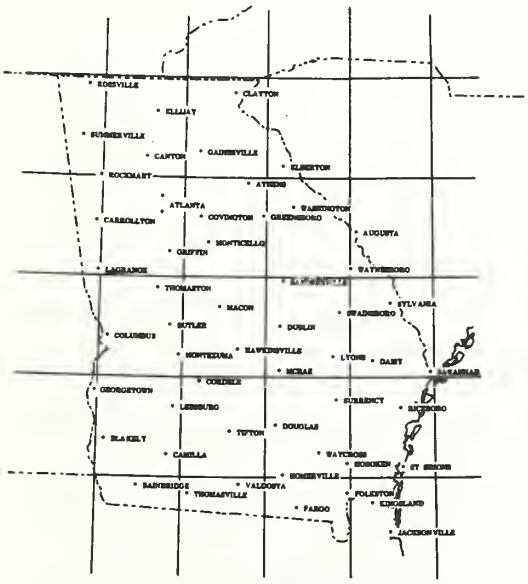

GRAVIMETRIC REFERENCE BASE NET
STATE OF GEORGIA

On a broad scale, the Bouguer gravity anomaly map shows regional patterns which correlate with the major geologic subdivisions in Georgia. The folded, unmetamorphosed Paleozoic rocks of the Valley and Ridge Province of northwest Georgia are characterized by -20 to -40 milligal anomalies with only moderate variation. Southeast of this zone the Brevard Fault Zone, which extends northeastward across Georgia through the northwestern portion of Atlanta, follows a region of broad gravity lows. These lows extend north of the Brevard Fault Zone into the northeast Georgia mountains where on the South Carolina border they attain the lowest value (-80 milligals) found in the State. The boundary of the zone of broad lows to the northwest generally corresponds to the Murphy Marble Belt. Continuing southward from the Brevard Fault Zone, the gravity increases smoothly until this trend culminates in a sharp northeast-trending "ridge" just north of the Fall Line. The negative anomalies north of the Fall Line can be accounted for almost entirely by the existence of low density roots for the crust which are required to support mountainous and elevated areas like north Georgia in isostatic equilibrium.

South of the Fall Line, the Bouguer anomalies average about zero but show a wide range of from -30 milligals to +50 milligals. The positive anomalies occur in the form of irregularly spaced knobs on ridges. The negative anomalies are the smoother intervening depressions which tend to be aligned along the northeasterly trend. One particularly prominent set of knobs and ridges occurs just south of the southwestern portion of the Fall Line. Another set of three prominent knobs, divided from the first by a series of irregular depressions, occurs further to the southeast. The Bouguer anomaly on one of those exceeds +50 milligals, the highest positive anomaly in the state. The positive Bouguer anomalies of the knobs and ridges are most likely due to the occurrence of dense basic rock types (like diabase or gabbro). The knobs show strong magnetic anomalies typical of basic rocks and furthermore basic rocks have been encountered in some deep wells. These rocks were either intruded into the crustal rocks now below a sedimentary blanket, intruded as sills (between the sedimentary strata), or extruded as flows on the former surface. Most of the prominent knobs show steeper anomalies on the northwest flank than to the southeast indicating a possible dip of the structures to the southeast. The gravity lows are related to increased thicknesses of sedimentary rock of pre-Cretaceous age. The younger rocks exposed at the surface do not significantly affect the gravity anomalies since they have uniform or only gradually varying thicknesses.

Computation of Bouguer Anomalies

The attraction of gravity at the earth's surface shows both regular and irregular variation. The regular variations are a consequence of the earth's shape and rotation. The irregular variations of primary interest to the geologist (see previous section) are a result of the distribution of mass in the earth's crust. In the Bouguer reduction of gravity data, the regular variations of the earth's gravity field are removed to allow the comparison of gravity anomalies with the densities of geologic structures.

Reprinted from Ocean 72, IEEE International Conference on Engineering in the Ocean Environment, 474-479.

MEASUREMENT AND CONTROL SYSTEM FOR DEEP SEA VANE-SHEAR DEVICE

V. J. McDonald, Roy E. Olson,[1] Adrian F. Richards,[2] George H. Keller[3]

Associate Professor of Civil Engineering and Research Engineer
University of Illinois at Urbana-Champaign
Urbana, Illinois 61801

Abstract

A vane shear device was developed for in-place measurement of the undrained strength of clays in the marine environment. This device required a measurement of torque applied to a vane as the soil in which the vane was embedded failed in shear and was remolded. The system was designed to operate at depths of 4.5 km and to conduct measurements at depths up to nearly 3 m below the mudline. Control signals to and data from the apparatus were telemetered over a single wire with ground return and the tower was self-powered. Torque measurements required successful use of electrical stain gages and leads exposed to high hydrostatic pressures. The apparatus has been successfully operated at several sites in the Atlantic Ocean and in the Gulf of Mexico at depths of 3635 m.

Acknowledgments

We are appreciative of the many unnamed men who contributed greatly to the success of the project. The officers and men of the various ships used in the investigation and the technical support group of the Department of Civil Engineering at the University of Illinois deserve particular thanks. Special mention must be given Mr. J. N. Sterner, who maintained and operated this equipment at sea during the tests reported here. This project was jointly sponsored at the University of Illinois by the U. S. Navy Bureau of Yards and Docks and the Office of Naval Research under Contract NONR 3985(09), NR 083-248 until 1969. This paper was partly written under the sponsorship of ONR Contract N00014-67-A-0370-0005, NR 083-248 to Lehigh University.

Introduction

The apparatus described in this paper resulted from a 1965 invitation by the Office of Naval Research to initiate research on the geotechnical properties of deep-sea soils. At that time, the knowledge of soil properties for water depths greater than approximately 3 km was obtained from samples which had been physically removed from the sea floor and studied on the surface. It was highly probable that data obtained in such a manner was in significant error. The next step was to conduct in-place measurements on undisturbed soils on the sea floor. Although both structural and soils engineers were interested in tests that extended to depths of at least 15 m below the mudline, practical dictates of time, ship sizes, and particularly budgetary matters, limited this prototype apparatus to studies of depths of 3 m or less. This was a reasonable depth in that it coincided with the depths required for most structures placed on the deep sea floor at the time the project was initiated. The design water depth was set at 4.6 km.

The apparatus described herein has also been used as a vehicle in other studies,[1,2] but it was primarily designed to do measurements of soil shear strength by the vane shear test. In this test, a vane is embedded in the soil and a torque is applied to it. Torque magnitude for soil shearing failure and the torque required for remolding the soil or motion of the vane in the soil are the measurements of interest to soils engineers.[3]

The logic and engineering compromises which resulted in the adoption of the vane shear test experiment parameters and which, as a result, largely determine the mechanical configuration of the apparatus have been detailed in another paper.[4] This paper is a description of the electrical and electronic measurement and control sections of the apparatus.

[1] Professor of Civil Engineering, Engineering-Science Building, University of Texas, Austin Texas 78712.

[2] Professor of Oceanography and Ocean Engineering and Director, Marine Geotechnical Laboratory, Lehigh University, Bethlehem, Pa. 18015.

[3] Director of the Marine Geology and Geophysics Laboratory, NOAA, Atlantic Oceanographic and Meteorological Laboratories, Miami, Florida 33130.

General Design Considerations

The design of the measurement and control system involved consideration of certain factors above the purely technical problems related to task accomplishment. The primary factor was low cost. In addition, the system and its components were to be physically rugged, simple to operate and troubleshoot, and the elements were to be, as far as possible, off-the-shelf units available at the nearest electronic supply house.

The same philosophy controlled the mechanical design of the structure which carried the vane shear measuring apparatus to the bottom (Fig. 1); its height was sufficient to accommodate

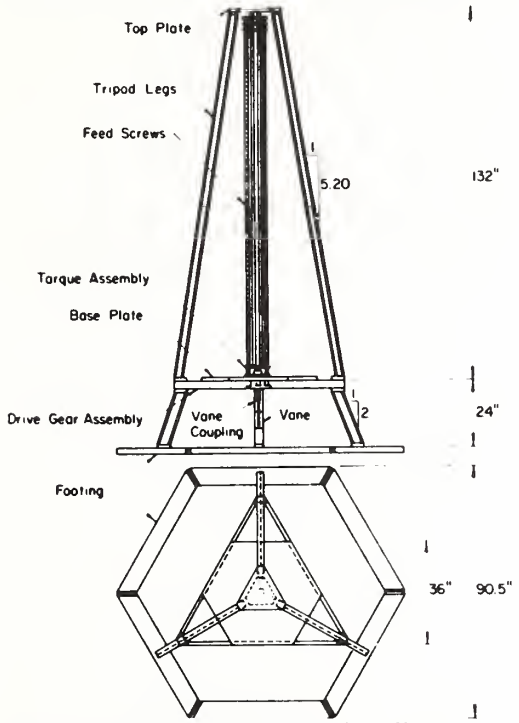

Fig. 1 Simplified Drawing of Vane Shear Strength Equipment

the 3 m vane rod when retracted and it was also short enough to permit handling by cranes aboard relatively small ships. In addition, the base was made as broad as average small-ship capabilities would permit to provide the maximum stability against overturning while on the bottom. The tower was mainly fabricated of 6061-T651 aluminum with minor amounts of 316.L stainless steel. All components of the tower, with the exception of three long threaded drive rods, could be fabricated or repaired in any normally equipped machine shop.

The mechanical system was constructed in such a way that a shaft rotation would produce penetration of a vane and vane rod into the sea-bed upon which the tower rested. Reverse rotation of the same shaft would retract the vane. Similarly, rotation of the second shaft would produce rotation of the vane.

The task of the electrical control and measurement system was to produce controlled motions of these shafts and to measure the torque developed by the resistance of the soil on the vane.

Electrical System Design Selections

The system required two-way communication between the surface vessel and the vane shear apparatus. Commands from the ship to the bottom to produce, reverse, or stop rotation or penetration of the vane were required. Data from the bottom apparatus describing vane position, degree of rotation, amount of torque, and power plant condition had to be transmitted to the surface vessel. A single, relatively high resistance conductor with ground return was available for these tasks. The cable resistance precluded any significant power transmission from the surface to the tower and therefore the tower was battery powered. Direct current commands from surface to tower and alternating current, multiplexed, frequency modulated, carrier signals from the vane shear device to the surface were the general methods of transmission selected because they could easily be separated and could operate simultaneously in both directions.

Other units of equipment were selected because of both their characteristics and availability. These included magnetically activated proximity switches for limiting travel and indicating position; torque measurements using strain gages mounted on a dynamometer section; dc operated relay logic for control purposes; and stepping motors to serve as the prime movers.

The special characteristics of stepping motors made them particularly suited to the application. These motors produce a relatively large forward and holding torque that is essentially independent of average shaft speed. The shaft advances a known and fixed amount per cycle of input power and, if stalled, the motor does not draw excessive current. Commercially available motors of this type produce adequate torque for this job and have shaft speeds of the order of 72 RPM and which, additionally, may be cased and pressure equalized for undersea use.

The components described above were combined to form the system described below.

Command System

Control of the penetration and rotational motors required a minimum of four separate commands: vane penetrate; vane rotate; reverse; and stop. In addition to these, the torque measurement required an electrical calibration

that could be commanded manually and automatically. Tower orientation along either of two horizontal axis and power supply condition were also to be measured. Since only two channels of measurement telemetry were available, additional measurement selection commands were required. One channel was dedicated to the primary measurement of torque and the second channel was selected on shipboard to measure any of the remaining three parameters. A two level bidirectional command signal was used between the surface vessel and the tower. The five possible states of this current were used as commands. The number of possible control actions was augmented by nonexecution of some commands until the command current was terminated. As an example, the torque measuring system was electrically calibrated during the time the "penetrate" command existed, but penetration did not begin until after release of the command current and removal of the calibration.

The circuit of a logic system of ten, DPDT, 6 volt dc relays is shown in Fig. 2. Diodes

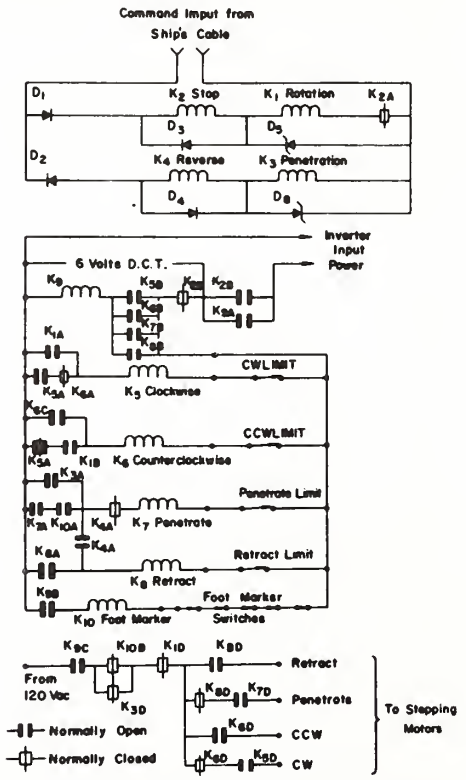

Fig. 2 Command Decode and Logic

D_1 and D_2 are steering diodes to separate two command current directions. Relays K_1 and K_3 coils were rewound with approximately ten times the number of turns as were K_2 and K_4 so that these two respond to lower current levels. Diodes D_3, D_4, D_5, and D_6 suppress inductive surges while D_5 and D_6 also act as voltage limiters across K_1 and K_3. The contact closures of any command relay circuit supply 6 vdc to an inverter for conversion to 115 volts 60 HZ power to power measurement devices and to drive the step motors. Power is not applied to the motors until the command relay is released except when penetration has stopped at a foot marker switch. The foot marker switches are placed at penetration intervals of one foot; thus, when penetration occurs, it proceeds until one foot has passed. When any marker switch is activated, the system is halted. If another penetration command is given, the system will restart and penetration will proceed while the command is in effect or until the system clears the foot marker switch, where it will halt until the penetration command is released. The foot marker switches do not halt retraction. All motor overtravel is prohibited by the action of limit switches. Contacts of relays K_1, K_3, K_4, K_8, and K_{10} are used to calibrate the torque measuring channel and to shift telemetry channel B to its various input signals. These contacts are shown in Figs. 3 and 4 and detailed discussion of their action is reserved for later.

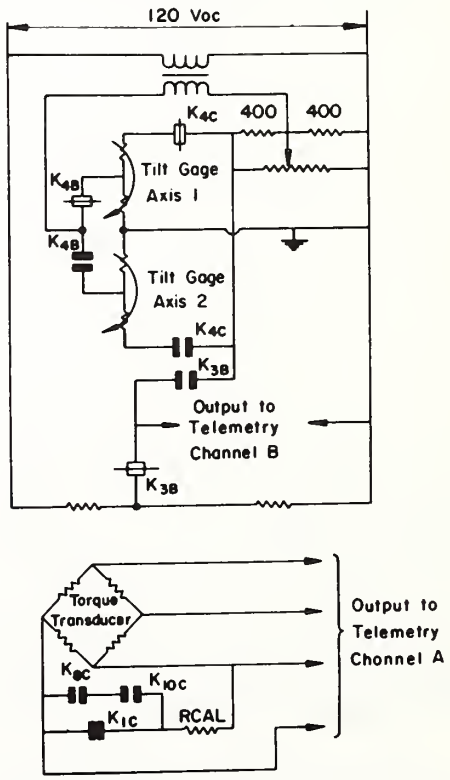

Fig. 3 Tilt Gage and Calibration Circuits

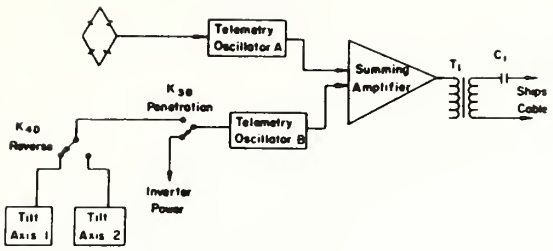

Fig. 4 Measurement and Telemetry System

It may be noted that this system is conservative in that power is only taken during penetration, retraction, and rotation of the vane or while a command is sent to the tower, and that during periods of torque measurements, no command currents exist on the ship to tower cable.

Measurement and Telemetry System

Torque Gage

In its final version, the torque gage consists of a reduced section of the vane drive rod which is gaged with bonded electrical resistance strain gages. This section is located just above the vane attachment point. Four gages are located to measure the tensile and compressive strains in the cylindrical element which resulted from applied torsion. The gages are connected to cancel strains due to both bending moments and axial loads. Gages were carefully applied to avoid entrapped air or other bubbles under the gage. Waterproofing consisted of layers of wax, RTV silastic, and a commercial sealant called "Petrolostic." Lead wires were stripped of all insulation and directly embedded in the waterproofing to seal the gage. Lead cable was located in a 7 mm slot cut in the square vane rod to the upper end of the rod where the cable festooned to the instrument housing. The cable was placed in this slot to protect it from the force of the soil during rotation and to permit passage through a square-holed rotary drive plate which turns the vane. The gaged and waterproofed section also preserved the same drive rod geometry to protect the gaging during penetration and retraction. Waterproofing of electrical strain gages is always a problem and the hydrostatic pressures encountered at design depths made the excellence of waterproofing of prime importance. Electrical strain gages produce only a small resistance change from elongation of its conductors. Because full scale output can be generated by leakage resistance across any gage of the order of 60,000 ohms or less, excellence of waterproofing is mandatory. Tank pressure tests of cable arrays and gaged sections were run at 10,000 psi to verify the waterproofing techniques in the laboratory. At sea, the validity of the installation was shown because of no apparent torque noted as the system was lowered to the depths.

The vane was attached to the vane rod just below the gaged section. The attachment was in the form of a slip coupling which permitted a rod rotation of the order of $\pi/6$ rad before the vane was engaged. This insured that torque due to the vane rod rotation could be separated from that due to the vane. It also provides a free vane at the start of rotation.

Because of the possibility of gage zero shifts and/or sensitivity changes due to water leakage into the gages and to prove the system operational while on the bottom, an electrically equivalent calibration was made available. The principle is that since the strain gages change resistance and produce an output signal when under tension or compression, another technique to artificially produce a similar resistance change can be used to check the operation of the electrical part of the measuring system. Thus, a resistor connected in shunt with one of the gages will increase the total current that flows through the gage and shunt resistor combination; this is the same electrical effect as a compressive strain of known magnitude applied to that gage.

This technique is used in the system as shown in Figs. 3 and 4. Relay K_1 or relays K_8 and K_{10} together will complete the circuit to the calibration resistor. Thus, when the penetration command is given, the system will energize and the torque measuring system will receive an equivalent electrical calibration. In like manner, the calibration is applied during retraction of the vane as each foot marker is passed. This is a check on the total vane penetration. The exact equivalent of the electrical calibration was established on deck by application of a known mechanical torque to the vane rod.

Tilt Gage

The tile measurement was desired primarily to prove that the tower was erect on the seafloor. The gage was a commercial product which has gaging elements for two perpendicular horizontal axes. Each measuring element consists of two arms of a bridge circuit. The bridge is balanced in the level condition and unbalanced as the angle from the horizontal is increased. The gage used was nonlinear in response, but adequate to establish relatively small angles of tower tilt. As shown in Figs. 3 and 4, the measurement along axis one was obtained when the penetration command existed and the second axis was measured when the reverse and penetration commands simultaneously existed. These data were transmitted to the surface on channel B.

The telemetry equipment on the tower consists of one module for each channel, a summing

amplifier module and a line isolation transformer. These are commercially available units and occupy a total volume of only a few cubic inches. Carrier frequencies are 3900 HZ and 1700 Hz, deviation is 20 percent. The telemetry was powered by a 115 vac 60 Hz to 9 vdc supply.

Power System

The tower system was powered by a lead-acid storage battery which was pressure equalized by an acid-oil-saltwater interface. The battery had a 180 amp-hour capacity. This voltage directly powered the logic relay bank and was also converted to 115 volts 60 Hz by a vibrator supply. This was done to provide the needed alternating current to power the stepping motors, the telemetry equipment, and the electrolytic measuring cells of the tilt gage. Except during tilt measurements, this ac voltage was fed to channel B of the telemetry as a signal to be sent to the surface. The uses of this power signal are discussed in another section.

Shipboard Equipment

The shipboard measuring equipment used with this apparatus is shown in Fig. 5. The

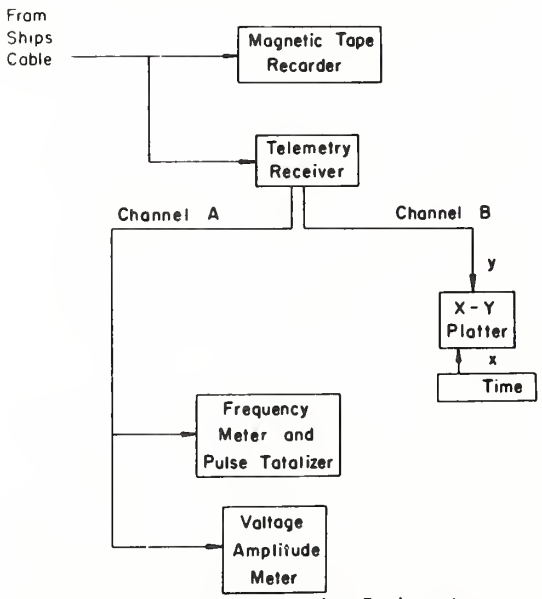

Fig. 5 Ship-Board Measuring Equipment

raw telemetry signal is recorded on magnetic tape directly from the cable to the tower. This serves as an emergency backup in case of gross equipment failure aboard ship, but more importantly, provides a method of reproducing the test data in real time. The same signal is delivered to the telemetry receiver where it is separated into its original analogs. The torque signal drives one axis of a recorder and the other axis, driven by time, is equivalent to vane rotation. The output of channel B may be tilt in either direction or the power signal. It is measured on a pointer instrument and fed to a counter-frequency meter. The pointer meter scale is calibrated in degrees tilt and RMS voltage. Thus, the amplitude, frequency, and total number of cycles of the 115 volt ac power can be determined.

System Operation

After the tower has been placed on the bottom, the first check is made on the two tilt gages, and the power system. This proves the tower to be erect, and the correct voltage and frequency available. The torque system checked by first applying the electrically equivalent torque calibration signal by using the penetrate command. Telemetry carrier deviation and the dc output of telemetry channel A was observed and compared to the correct values. Upon release of the penetration command, the rotation command was energized. Alternate application of these two commands allowed both the zero torque and full scale torque values to be checked. As a last step, the vane was permitted to rotate its limit while in the retracted position. Thus, the telemetry noise level and stability under sea-floor conditions can be verified. The above procedure also insures a known starting point for the next rotation of the vane. If preliminary checks are satisfactory, the vane rod is commanded to penetrate 0.3 m. Penetration commences upon release of the command and is halted after one foot of penetration by the action of the foot marker proximity switches. As soon as the halt occurs, the system de-energizes. This can be observed on the surface by loss of the 115 vac power signal, and by the total accumulated count of applied frequency cycles. (The number of cycles that are necessary for one foot penetration has been established earlier.) Rotation command release starts vane rod rotation. Upon start of rotation, the time axis of the plotter is energized. If the vane is in the soil, the plotter will display the torque developed as a function of time. The initial value will be that produced by the rod rotation prior to engagement of the vane slip coupling. This, in effect, establishes the vane measurement base line. Completion of the rotation can be verified by the total cycles applied to the step motor and by loss of 115 vac power when the limit is reached. The rotation drive system is mechanically stiff so that applied power cycles to the motor can be taken as a measure of vane rotation angle. This is shown in an on-deck test where the vane is locked so that it cannot rotate. The results obtained under such conditions show an almost immediate change in the measured torque at the end of slip--i.e., the torque changes from zero to full scale within a few cycles of motor rotation compared to the approximately 4000 cycles necessary to produce full vane travel. Thus, the positional measurement was accurate to at least 1 percent. In the event a very stiff soil was encountered and

the vane rotation drive motor stalled, the torque-time curve had a distinctive distortion that made this clearly evident. During penetration, stalling could only be determined from the surface if the vane penetration power had not been removed after the proper number of cycles had been applied to the motor (approximately 7000) to produce a foot of penetration. The positional stop.

The same general procedure was repeated for tests at each foot level to the final depth. During vane retraction as the vane passed each foot level, the calibration was applied to the torque system. Thus, the shipboard plotter provided a log verification of the final penetration position.

History

The apparatus described here was first operated in the Cape Cod Bay. Later tests included the Wilkinson Basin off Massachusetts, Exuma Sound in the Bahamas, the Continental Shelf off Galveston, and the Mississippi Delta and the Abyssal Plain in the Gulf of Mexico. These various trips were productive of data describing the soil and were used to debug and prove the practicality of this system.

Conclusions

An apparatus has been described which has successfully operated a vane shear device at depths of 3.64 km. The device has the merit of low cost, simplicity, and relative completeness. A design has been made which makes maximum use of a minimum number of components and surface to bottom command communications. The device fulfilled its designer's intentions.

References

1. K. Preiss, "*In Situ* Measurement of Marine Sediment Density by Gamma Radiation," Deep-Sea Research, Vol. 15, pp. 637-41, 1968.

2. K. Preiss, "*In Situ* Measurement of the Density of Sea Floor Sediment by Gamma Ray Transmission," Radiation and Isotope Technology in Latin American Development, Proceedings of the American Nuclear Society Topical Meeting, San Juan, Puerto Rico, May 4-6, 1969, Puerto Rico Nuclear Center - 135 (TID-4500), pp. 483-93, 1969.

3. J. O. Osterberg, "Introduction," in Symposium on Vane Shear Testing of Soils, ASTM Special Publication, Vol. 193, pp. 1-7, 1957.

4. A. F. Richards, V. J. McDonald, R. E. Olson and G. H. Keller, "In-Place Measurement of Deep-Sea Soil Shear Strength," Underwater Soil Sampling, Testing and Construction Control, ASTM, STP 501, 1972.

U.S. DEPARTMENT OF COMMERCE
Peter G. Peterson, Secretary

NATIONAL OCEANIC AND ATMOSPHERIC ADMINISTRATION
Robert M. White, Administrator
ENVIRONMENTAL RESEARCH LABORATORIES
Wilmot N. Hess, Director

NOAA TECHNICAL REPORT ERL 226-AOML

Geology and Geophysics of the Venezuelan Continental Margin Between Blanquilla and Orchilla Islands

GEORGE PETER

BOULDER, COLO.
February 1972

TABLE OF CONTENTS

	Page
ABSTRACT	vi
1. INTRODUCTION	1
1.1 Location and planning	1
1.2 Field and laboratory methods	2
1.2.1 Navigation	2
1.2.2 Depth survey	3
1.2.3 Gravity survey	3
1.2.4 Magnetic survey	5
1.2.5 Seismic reflection survey	5
1.2.6 Rock sampling	6
1.3 Previous marine work	6
2. PHYSIOGRAPHY AND SUBMARINE GEOMORPHOLOGY	7
2.1 Caribbean physiography	7
2.2 Geomorphology of the Venezuelan margin	8
2.3 Coastal physiography	11
3. GEOPHYSICAL OBSERVATIONS	12
3.1 Seismic reflection profiles	12
3.1.1 The continental shelf	13
3.1.2 Island platforms - Los Roques Canyon	19
3.1.3 Venezuelan Basin - Curacao Ridge	27
3.1.4 Venezuelan Basin - Aves Ridge	28
3.2 Geomagnetic measurements	31
3.3 Gravity measurements	31
4. GEOLOGICAL INTERPRETATION AND DISCUSSION	35
4.1 The continental shelf	35
4.1.1 Regional geology	35
4.1.2 Discussion	41
4.2 Island platforms - Los Roques Canyon	46
4.2.1 Regional geology	46
4.2.2 Discussion	48
4.3 Southeast margin of the Venezuelan Basin	50
4.3.1 Regional geology	50
4.3.2 Discussion	51
4.4 Crustal structure of the Venezuelan continental margin	52
4.4.1 Evidence from seismic refraction data	52
4.4.2 Crustal thickness of the Venezuelan continental margin	53
4.5 Tectonic elements of the island arc	55
4.6 Regional history and development	57
4.6.1 Origin of the Caribbean Sea	57
4.6.2 Paleozoic	58
4.6.3 Mesozoic	58
4.6.4 Cenozoic	59

Page

5. SUMMARY 59

6. ACKNOWLEDGEMENTS 61

7. REFERENCES 62

APPENDIX I 67

APPENDIX II 75

APPENDIX III 79

LIST OF FIGURES

Figure Page

1. Location chart of study area 2
2. Survey tracklines 4
3. Physiography of the Caribbean area 7
4. Physiographic features of the north-central Venezuelan margin 9
5. Bathymetric chart of survey area 9
6. Slopes at 10:1 and 5:1 vertical exaggerations 13
7. Location of north-south profiles 14
8. Line drawing of seismic reflection profiles across continental shelf 15
9. Original seismic section of Cubagua high (Profile 7) 16
10. Original seismic section of buried terraces southwest of Margarita (Profile 5) 17
11. Copy of original seismic section of the southern part of the sill between the two deeps of the Cariaco Basin (Profile 3) 18
12. Copy of seismic section showing the central part of the western deep of the Cariaco Basin (Profile 2) 19
13. Location of east-west profiles 21
14. Line drawing of seismic reflection Profile 2 between the Los Roques Canyon and the Tortuga-Margarita Bank 21
15. Line drawing of seismic reflection Profiles 3 and 14 between the Blanquilla platform and the Tortuga-Margarita Bank 22
16. Line drawing of seismic reflection Profile 13 23
17. Copy of original seismic section showing the two different types of basements on Orchilla platform (Profile 13) 24
18. Line drawing of seismic reflection Profiles 1 and 11 24
19. Copy of original seismic section along 65°45'W, made by R/V CONRAD-9 (See fig. 2 for location) 25
20. Line drawing of profile 3 across the Blanquilla platform 25

Page

21. Copy of original seismic section normal to the trends of the Blanquilla platform (See fig. 2 for location) 27
22. Line drawing of seismic reflection Profiles 12 and 10 28
23. Copy of original seismic section over the northwestern part of the Los Roques Canyon (Profile 10) 29
24. Line drawing of seismic reflection Profiles 1,2, and 3, over the southern margin of the Venezuelan Basin 29
25. Original seismic section of Profile 1, southern margin, Venezuelan Basin 30
26. Line drawings of seismic reflection Profile 8 30
27. Magnetic total intensity contour chart of the study area 32
28. Determination of the dipole field from the values of the total intensity chart along 65°00'W and 65°30'W 33
29. Magnetic total intensity anomaly map of the continental shelf off north-central Venezuela 33
30. Free-air gravity anomaly map of the study area 34
31. Bouguer gravity anomaly map of the study area 34
32. Location of two-dimensional Bouguer anomaly profiles and the regional Bouguer anomaly map 36
33. Comparison of "simple" and "two-dimensional" Bouguer corrections 36
34. Tectonic belts of the Caribbean mountains west of the Bay of Barcelona 37
35. Structural elements in northeastern Venezuela 39
36. Geologic map of the Araya Peninsula 40
37. Comparison of gravity anomalies across the eastern and western halves of the Cariaco Basin 42
38. Principal faults of the Venezuelan continental margin in the study area 44
39. Geologic map of Orchilla Island 47
40. Geologic map of Blanquilla Island 49
41. Residual Bouguer anomaly map 49
42. Composite seismic refraction section across the Venezuelan continental margin 52
43. Crustal thickness profile of the Venezuelan continental margin 54
44. Contour map of the depth below sea level to the top of the mantle 56
45. Reconstruction of Pangea at the end of Permian 225 m.y. ago 57

ABSTRACT

A study of the geology of the continental margin of northeast Venezuela was conducted by marine magnetic, gravity, seismic reflection, and bathymetric investigations, and by a program of dredging of submarine rock outcrops.

Previous surveys have established that geophysical anomalies associated with discrete tectonic elements of the Lesser Antilles Island Arc continue southwestward onto the continental shelf of Trinidad and Venezuela. This study demonstrates the extension of these tectonic elements westward to 65°W, where they either truncated or are interrupted by a major northwest-southeast trending fault system. The bordering faults of the Los Roques Canyon and the Urica and possibly the San Francisco faults form a continuous, northwest-southeast trending discontinuity, whose existence since Cretaceous time mitigates against large east-west displacements along the northeast Venezuelan margin during the Cenozoic.

Geophysical measurements indicate that west of the Urica fault the Bay of Barcelona is underlain by rocks that probably belong to the seaward extension of the tectonic belts of the western Serrania del Interior mountains. Over the island platforms these measurements indicate the presence of igneous rocks. Sampling of basement outcrops on Blanquilla platform yielded granites, granodiorites, quartz monzonites, and metabasalts. A potassium-argon age of 81 m.y. was obtained from the biotites of one granite sample, which is consistent with the ages of similar rocks dated on Curacao, Aruba, and the southern part of the Aves Ridge.

The major fault systems and the numerous minor faults offsetting the sea floor along the continental margin attest to Late Tertiary to Holocene tectonic activity, that most likely was responsible for the subsidence of several basins on the continental shelf.

GEOLOGY AND GEOPHYSICS OF THE VENEZUELAN CONTINENTAL MARGIN BETWEEN BLANQUILLA AND ORCHILLA ISLANDS

George Peter

1. INTRODUCTION

This paper presents the results of one of a series of research projects that were initiated in 1968 by the Marine Geology and Geophysics Laboratory of the NOAA Atlantic Oceanographic and Meteorological Laboratories. The general purpose of these projects is to study the marine geology in key areas of the Caribbean through the use of systematic geophysical surveys.

One of the most important geologic problems in the Caribbean is the nature of junction between the Lesser Antilles Island Arc and the South American continent. The acceptance of the new global tectonics hypothesis (Morgan, 1968; Le Pichon, 1968; Isacks et al., 1968) as well as current studies of the Lesser Antilles Island Arc (Chase and Bunce, 1969) seem to give strength to an earlier hypothesis of Hess and Maxwell (1953) that a major east-west strike-slip (or transform) fault must exist between the island arc and the continent.

On the other hand, geophysical studies of the area of junction between the island arc and the continent (Talwani, 1966; Weeks et al., 1969, 1971; Bassinger et al., 1971; Lattimore et al., 1971) indicate that the major tectonic elements of the arc, such as the Barbados anticlinorium, the Tobago Trough, and the volcanic arc of the Lesser Antilles extend into the continental shelves of northeast Venezuela and Trinidad without noticeable interruption.

Tracing the structural elements of the Lesser Antilles Island Arc farther westward and establishing the relationship of these structures to the Cordillera de la Costa of Venezuela comprise the major part of the present study. In addition, the boundary of the Venezuelan Basin with the Curacao and Aves ridges, the structure of the Los Roques Canyon, the extend of the plutonic basement rock complex around the Aruba-Orchilla-Blanquilla island chain, and the extension of the major faults of the continent into the offshore area are investigated.

1.1 Location and Planning

The area selected for this study lies north of the Gulf of Barcelona, off north-central Venezuela (fig. 1). The approximate eastern and western limits are along 64°W and 66°W longitudes respectively; to the north the 13°N parallel is the approximate border.

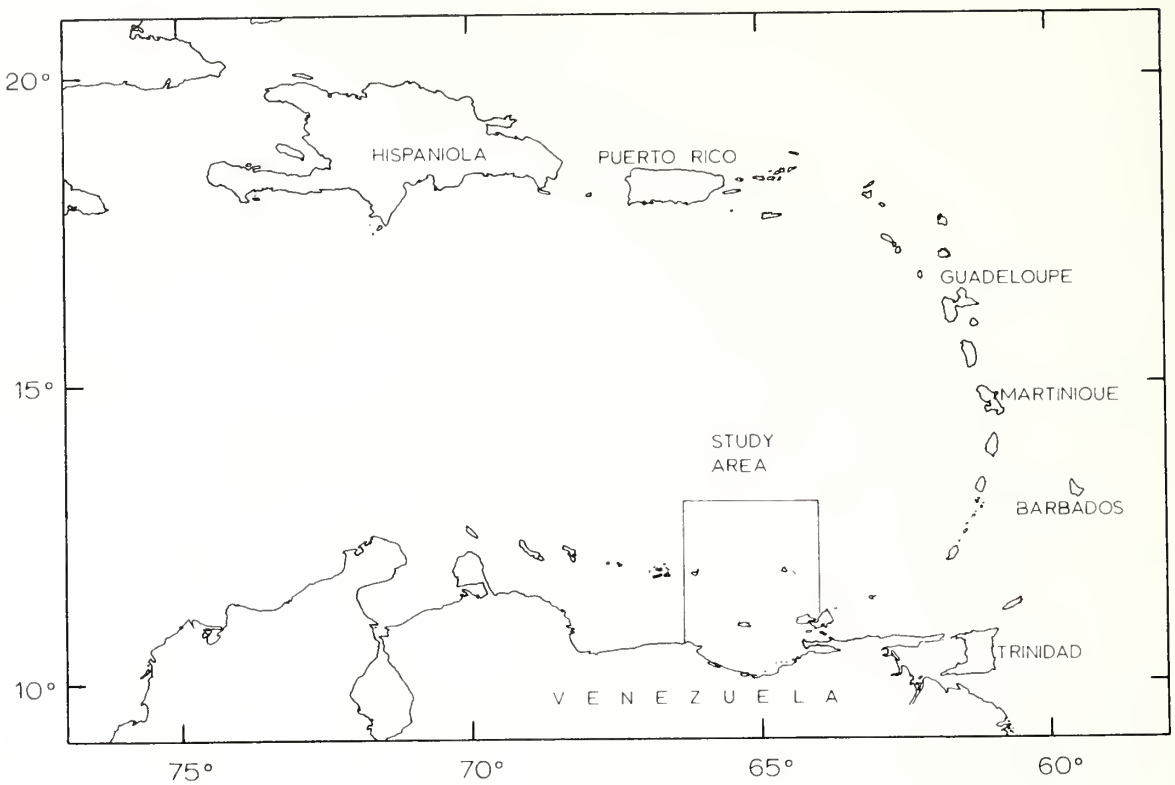

Figure 1. Location chart of study area.

Six north-south geophysical lines were laid out to cover the essentially east-west geologic trends in the southern half of the area; four north-south and four east-west lines were chosen to cover the geologic trends in the northern half.

The geological sampling program was concentrated on six potential sites, which looked promising for dredging or coring operations according to the available bathymetric information.

1.2 Field and Laboratory Methods

1.2.1 Navigation

The position of the U.S.C. & G.S. Ship *DISCOVERER* when near the islands was controlled by visual bearings during daylight and by radar range and bearings during the nights. OMEGA and star fixes were utilized when the ship was outside radar range of the islands.

The effect of surface currents was very pronounced during seismic profiling because the speed of the ship was only 5 to 7 knots (9 to 13 km/hr). Because the strongest currents were felt in the northern half of the survey area where navigational control was marginal, the planned east-west and north-south tracklines in that area could not be followed.

The navigation was rechecked in the laboratory, and the tracklines were adjusted on the basis of the original navigation information and the repeated geophysical measurements at trackline crossings. It is estimated that the corrected position of the tracklines in the southern half of the survey is better than ± 3 km, in the northern half ± 5 km. The track between Julian Day 222, 0700 hour and Julian Day 223, 0300 hour may be in error by as much as ± 10 km (fig. 2).

1.2.2 Depth Survey

Depth soundings were taken continuously along all the tracklines with a "narrow beam echo-sounding system" that utilizes an electronically stabilized beam with an effective cone-width of approximately 3°.

The sounding records were read to the nearest fathom (1 fm = 1.83 m) at even 5 min intervals and at intermediate points where peaks, troughs, or inflection points occurred. These data were digitized, merged with the magnetic and gravity information, and were plotted by an electronic computer using the program developed by Grim (1970). The soundings are based on an assumed sound velocity of 800 fm/sec. Corrections for sea water density variations were not applied to facilitate the comparison of these profiles with the seismic sections and to make data compatible with sounding lines run by other ships.

As the sounding coverage obtained during the field survey is clearly insufficient to describe the bottom physiography, the bathymetric chart of Maloney (1966) was adopted as a base map for the area. Corrections, additions, and reinterpretations to this map were made on the basis of HO charts 6572, 6573, and 2319, BC chart 0703N, unpublished U.S. Navy charts (USOC), and the sounding data of the present survey.

1.2.3 Gravity Survey

Gravity measurements were made continuously along most of the survey lines by an Askania-Graf seagravimeter mounted on an Anschütz gyro-stabilized platform.

The gravity analog records were read to the nearest dial unit at even 5 min intervals. These data were digitized and then reduced to free-air anomalies with the aid of an electronic computer. This involved the multiplication of dial units with the instrument constant to obtain the gravity variation in milligals (mgals), the addition of the Base Gravity value (Barbados Seawell Airport $\bar{g}$ = 978.2997 Gals), the correction for instrument drift (3.2 mgals in 20 days) and for the speed and heading of the ship (Eötvös correction). From the corrected data, the theoretical gravity values were subtracted to obtain the free-air anomalies. The free-air anomalies were merged with magnetic and bathymetric data and plotted in a profile form, as described previously.

The survey has twelve trackline crossings with gravity data. At five crossings the discrepancy is ± 2 mgals or less; eight are within ± 3 mgals. The other four crossings (± 11 mgals, ± 12 mgals, ± 14 mgals, and ± 17 mgals) are over areas of large gravity gradient or directly

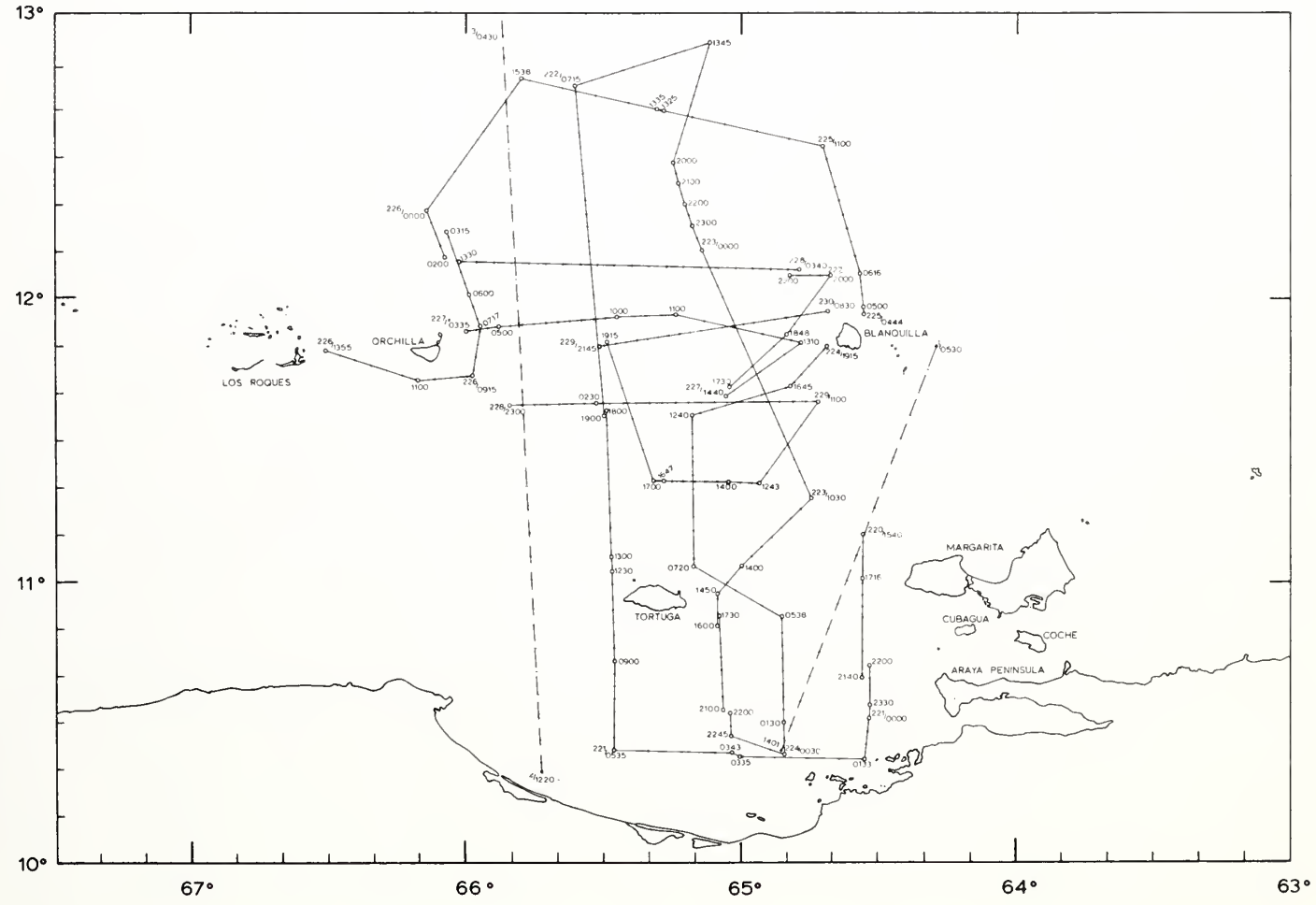

Figure 2 Survey tracklines. Solid line = ship DISCOVERER , dashed line = ship CONRAD - 9.Julian Day, hour, and minutes indicated at points of major course and speed changes. Cross-dashes are at every half-hour intervals.

involve tracklines with uncertain navigation or both. On this basis the accuracy of the gravity data is estimated to be better than ± 3 mgals. A similar estimate is indicated from comparisons with previous data obtained by Ewing et al. (1957), Wollard and Rose (1963), and Ball et al. (1971).

1.2.4 Magnetic Survey

Continuous measurements of the Earth's total magnetic field were obtained along all the tracklines with a Varian direct-reading proton precession magnetometer, whose sensor was towed approximately 150 m behind the ship.

The total field values were read from the analog records to the nearest gamma (10^{-5} Oe.) at 5 min intervals and at intermediate points where peaks, troughs, or abrupt changes in slope occurred.

The data were digitized with the aid of an electronic computer, and the core field was removed using the International Geomagnetic Reference Field (IGRF) with a constant correction (-160 gammas) added to it. The anomalies were plotted together with the bathymetric and gravity data.

It was assumed that the magnetic influence of the survey ship on the sensor is negligible when compared to the error caused by the diurnal variation of the Earth's magnetic field. As the survey was not detailed enough to warrant it, corrections were not made for the diurnal variations. From repeated observations at trackline crossings, it is estimated that the accuracy of the magnetic data is better than ± 25 gammas.

1.2.5 Seismic Reflection Survey

Continuous seismic reflection profiling data were obtained along the majority of the tracklines with a 40 cubic inch (656 cm^3) Bolt air gun as a sound source. An array of 10 variable-reluctance hydrophones towed approximately 30 m behind the ship served as the sensor. The gun was fired at variable intervals between 2 and 5 sec and the return signal filtered through a 20 - 320 Hz variable filter that was adjusted periodically to obtain optimum signal-to-noise ratio. The filtered signal was recorded on an Alpine wet-paper recorder at either 2 sec or 5 sec full scale.

To present a clear picture of the subbottom structures, without the inherent noise and multiple reflections, an interpretive line drawing of the seismic sections was prepared. Although it is impossible to present the true quality of the original records of these compressed scale drawings, care was taken to imitate the original records through emphasizing the reflective characteristics of the various strata. In this manner, double continuous lines represent the strongest continuous reflectors that can be traced usually for several tens of kilometers; single continuous lines, weaker but continuous reflectors; and dashed and dotted lines, either weak or discontinuous reflecting horizons. Short unoriented dashes were used for chaotic, indescernable reflections.

The seismic reflection sections were plotted against latitude or longitude, depending on the ship's heading. The vertical scale is two-way reflection time in seconds. The records are readily comparable to the other geophysical profiles in which the depths are plotted in fathoms (each interval of 400 fathoms is approximately equal to 1-sec two-way reflection time in the water column).

The capability of the seismic equipment may be judged by the fact that approximately 2 sec of subbottom penetration was obtained in 2000 fathoms of water.

1.2.6 Rock Sampling

Twelve attempts were made to retrieve bottom samples in the study area. It was considered first priority to obtain samples from outcrops of the basement (believed to be part of the plutonic rock complex known from the islands). After two successful chain bag dredge samples were obtained on the Blanquilla Island platform, six chain bag and one pipe dredge attempts on the Orchilla Island platform were unsuccessful. Similarly no rocks were recovered off the southeast tip of Los Roques Islands during another chain bag dredging attempt.

One chain bag dredge in the Blanquilla canyon brought up only hard clay. A boomerang core aimed at the outcrop of a major reflector at the eastern wall of Los Roques canyon returned empty, suggesting that the material penetrated may have been too coarse and washed out during the ascent of the sampling tube. Another boomerang core from the floor of the Los Roques canyon returned with dark layered clay.

A large unaltered sample of granitic rock from the second dredge haul west of Blanquilla canyon was dated (see Appendix III).*

The two sediment samples obtained are not described because of their locations are too far apart, and the samples lack pertinent information. A cursory examination of the hard clay sample from the chain bag dredge from Blanquilla canyon (where it was hoped to recover older sediments) indicates only shallow water reworked Foraminifera and Brachiopoda assemblages of Pleistocene and Recent age (J. Holden, personal communication).

1.3 Previous Marine Work

The geomorphology of the Venezuelan coast and margin has been studied by Maloney (1965, 1966). Heezen *et al.* (1959) and Lidz *et al.* (1969) described the regional bathymetry and sediment pattern in the Cariaco Basin and vicinity.

---

*Ten thin sections were prepared from the representative rock samples by the University of Miami, Rosenstiel School of Marine and Atmospheric Sciences, through the courtesy of Dr. E. Bonatti. A general identification of the rock specimens and the thin sections were made by the writer; detailed description of the thin sections were made by Mr. P. Kirch of the University of Miami, Rosenstiel School of Marine and Atmospheric Sciences (Appendix III).

The first gravity measurements were made by submarines in 1936-1937 (Ewing et al., 1957). More recent gravity data were summarized by Talwani (1966), and Bush and Bush (1969).

Results of combined geophysical studies over the southern part of of the study area are published by Lidz et al. (1968) and Ball et al. (1971). Magnetic data presented by these latter authors were incorporated with those obtained during this study. Two unpublished seismic reflection profiles received through the courtesy of J. I. Ewing, Lamont-Doherty Geological Observatory, were also utilized in the interpretation.

The first seismic refraction studies of the area were made by Officer et al. (1957); summary of more recent seismic refraction and reflection results in the Caribbean is given in Edgar (1968). The seismicity of the area is described by Sykes and Ewing (1965) and Molnar and Sykes (1969).

2. PHYSIOGRAPHY AND SUBMARINE GEOMORPHOLOGY

2.1 Caribbean Physiography

The Caribbean Sea consists of three major basins; from west to east, these are the Yucatan Basin, the Colombian Basin, and the Venezuelan Basin (fig. 3). The Yucatan Basin lies between the island of Cuba

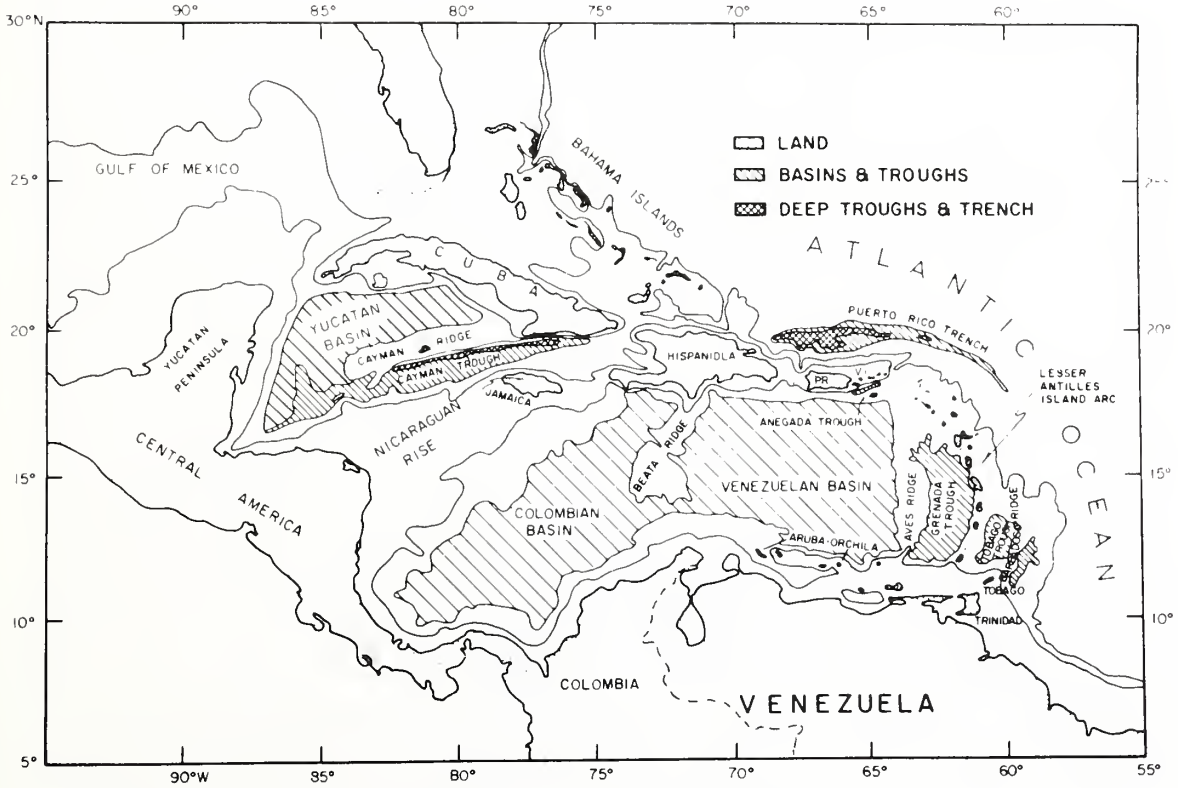

Figure 3. Physiography of the Caribbean area (after Fink, 1968).

on the north and the Yucatan Peninsula on the west; its southern margin is formed by the Cayman Ridge and the Cayman Trough complex, which is considered to be the trace of a major fault zone (Hess and Maxwell, 1953)

South of the Cayman Trough lies the broad Nicaraguan Rise, which connects Central America with the islands of Jamaica and Hispaniola. East of this rise, the Colombian Basin extends between Panama and Hispaniola. Its eastern margin is formed by the South American continent (Colombia) and a narrow submarine ridge, the Beata Ridge.

The Venezuelan Basin is bounded by the Beata Ridge on the west and the Aves Ridge on the east; the Aves Ridge is separated from the Lesser Antilles Island Arc by the Grenada Trough.

The study area includes only the southeastern corner of the Venezuelan Basin, where the floor of the basin is essentially flat at a depth of 2630 fm. The sea floor rises gently toward the east to about 1500 fm, where an abrupt increase in gradient marks the physiographic border of the Aves Ridge.

2.2 Geomorphology of the Venezuelan Margin

The area between the shore line of the South American continent and the Venezuelan Basin is occupied by a complex system of ridges, basins, canyons, and island platforms (fig. 4).

Starting on the north, the Venezuelan Basin has a sharp southern border against the Curacao Ridge and its narrow eastward extension. This ridge is much more pronounced west of 67°W; in the study area it is only about 35 km wide and rises some 460 m over the Venezuelan Basin. Toward the east it merges with a spur of the Blanquilla Island platform (fig. 5).

The Los Roques Trench and the Los Roques Canyon lie to the south of the Curacao Ridge. The Los Roques Canyon has a flat base of 2180 fm that joins the Los Roques Trench just north of Orchilla (fig. 5). On its southern part the canyon bifurcates into narrow "V" shaped valleys that suggest active erosional processes in this area. The canyon head is not connected to any river or drainage pattern; it terminates against the Tortuga-Margarita Bank.

West of the Los Roques Canyon and south of the Los Roques Trench lie the islands of the Aruba-Orchilla chain. The southern half of Orchilla Island is flat and covered with limestone. On the northern side of the island the mountains consist of the more resistant rocks of the igneous-metamorphic complex (Schubert, 1969b). There is a north-south trending shoal east of Orchilla (Burgana Bank); between the shoal and Orchilla a northeast-southwest trending canyon parallels the trend of the northern islands.

Depth contours of the Orchilla platform are tentative; data available were inadequate to show the intricate details, especially on the eastern and southern parts of the platform where there may be other isolated highs.

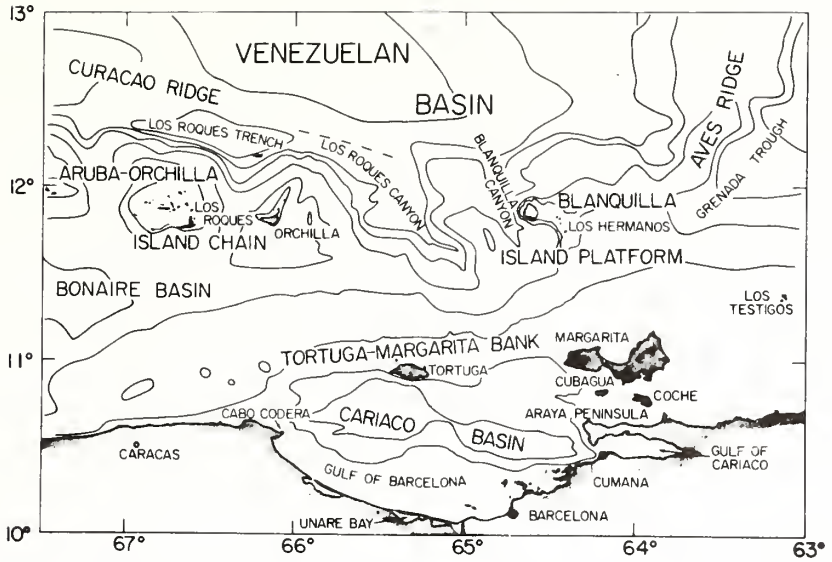

Figure 4. Physiographic features of the north-central Venezuelan margin (after Lidz et al., 1969; Maloney 1966).

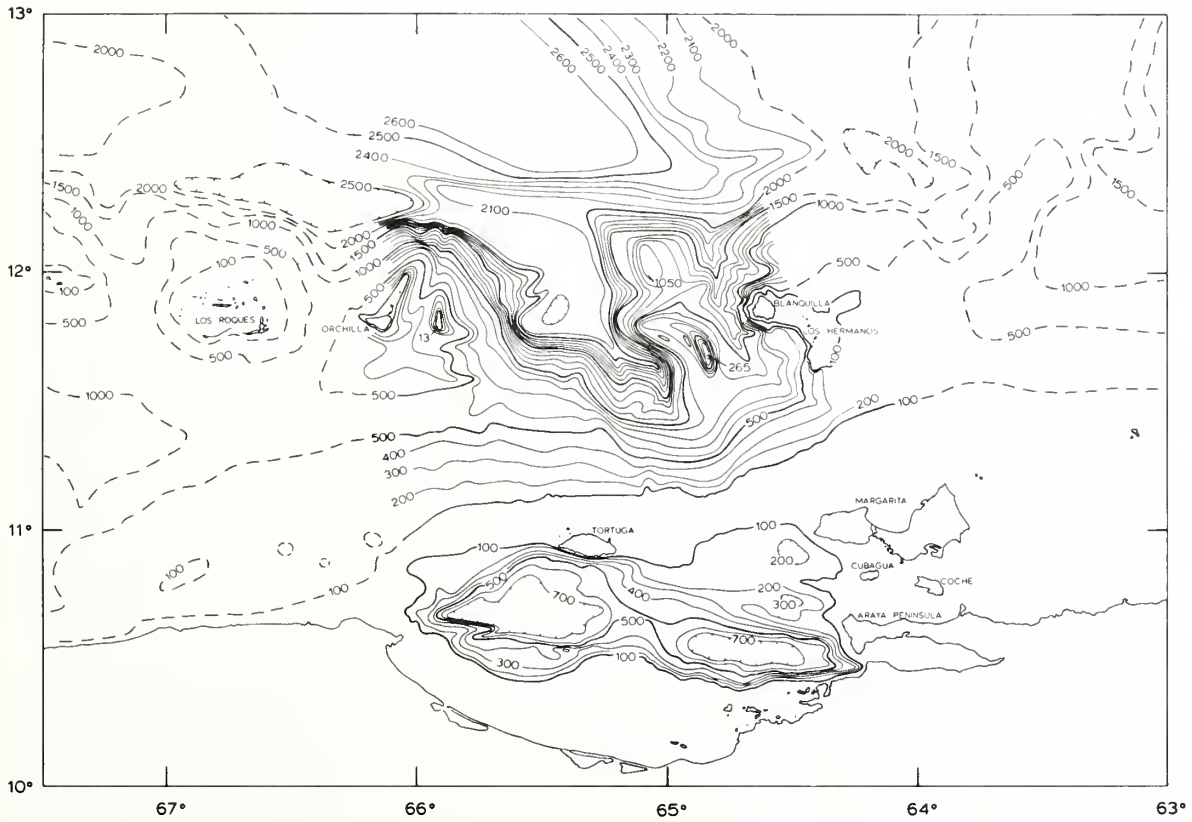

Figure 5. Bathymetric chart of survey area (revised after Maloney, 1966). Dashed contours outside of the immediate area of interest are only approximate. Contour interval 100 fm.

East of Los Roques Canyon lies the Blanquilla Island platform. The Venezuelan Basin and the west flank of the Aves Ridge form its northern border; toward the northeast it merges with the Aves Ridge. East of the Blanquilla platform the Grenada Trough extends southwestward and separates the platform from the Venezuelan shelf.

The Blanquilla platform is divided by a northwest-southeast trending canyon, here named the Blanquilla Canyon. In the western half of the platform the highest elevation is a northwest-southeast trending ridge that rises to 265 fm (fig. 5). It has a west-northwest trending spur that projects into the wall of the Los Roques Trench. A gentle depression separates this ridge from a broad topographic high on the north that reaches only to 1050 fm.

The northern half of Blanquilla Canyon is "V" shaped suggesting erosion, while the center part has a basin-like appearance (Maloney, 1966); farther south the head of the canyon is once again narrow and "V" shaped. It gently curves southeast into the depression between the Venezuelan shelf and the Blanquilla platform.

The major island on the platform is Blanquilla, which is a flat island covered mostly by limestone (Maloney, 1968). A string of islands southeast of Blanquilla, called the Los Hermanos, are sharp peaks of protruding basement rocks (Schubert, 1969a).

The 100-fm line representing the edge of the Venezuelan shelf is 95 km north of the Araya Peninsula (fig. 5). The shelf break has an overall west-southwest trend and comes within 5 km of the shore line west of Cabo Cordera (see fig. 4). West of Cabo Codera to 68°20'W, the shore line of Venezuela reflects the same west-southwest trend. As the Aruba-Orchilla island chain trends west-northwest, the distance between the shore and the island chain increases westward. The space created by the diverging trends of these two topographic elements is occupied by the Bonaire Basin.

Southwest of Margarita, the broad shelf is depressed into a major, deep basin, the Cariaco Basin. It is divided by a sill into two deeps of almost equal length and depth (fig. 4). The width of the western deep is nearly twice that of the eastern deep; however, with two smaller basins to the north, the eastern deep matches the width of the western deep. One of the small basins is located northwest of the Araya Peninsula, and the other is southwest of Margarita. The two basins are separated by a small ridge that appears to be in alignment with the Island of Cubagua. To the south, another ridge that appears to be in alignment with the Araya Peninsula separates these basins from the eastern deep (fig. 5).

An 100 fm line encloses the three basins and forms the southern boundary of a flat-topped ridge between Cabo Codera and Margarita. Following the definition of Ball et al. (1971), this ridge is referred to as the Tortuga-Margarita Bank (see fig. 4).

Shepard and Emery (1941), Maloney (1966), and Lidz et al. (1969) described the Venezuelan shelf between Margarita and Curacao as a continental borderland. The writer believes that the Los Roques Trench and the Aruba-Orchilla island chain are independent of the structural

framework of Venezuela and should not be termed a part of a continental borderland.

As the present study suggests, the geologic trends of the continent extend into the area south of the Tortuga-Margarita Bank which, therefore, may be termed a borderland; however, the Tortuga-Margarita Bank is a simple feature and forms an uninterrupted part of the shelf both to the east of Margarita and to the west of Cabo Codera. For these reasons the writer prefers to call the northern border of the Tortuga-Margarita Bank a "shelf edge" and the Cariaco and other basins of the area "depressions" within the continental shelf.

The area south of the Cariaco Basin is occupied by the Gulf of Barcelona (fig. 4). Between the two deeps of the Cariaco Basin this part of the shelf is approximately 40 km wide and has a gentle northward gradient with water depths ranging between 20 and 50 fm.

To the west, the distance between the shore line and the basin narrows to 20 km; to the east, the basin nearly merges with the shore line at Cumana (Maloney, 1966).

2.3 Coastal Physiography

Following the description of Maloney (1965), the Venezuelan coast in the study area can be divided into mountain front, lagoonal, and ria coasts. The best example of the mountain front coast lies west of Cabo Codera, where the Cordillera de la Costa mountain range reaches a height of 2765 m north of Caracas (fig. 4). Elevations are much more subdued along the Cordillera de la Costa Oriental on the Araya-Paria Peninsula, where at the western end of the peninsula mountains reach only 300 m. Toward the east along the peninsula the mountains rise as high as 600 m, and exposures of the more resistant rocks of the Carupano Formation are present (Schubert, 1971).

The coastline along the Cordillera de la Costa is quite straight and probably controlled by a system of normal faults (Dengo, 1953; Morgan, 1967; Lattimore et al., 1971). There are numerous raised terraces and beaches that suggest Holocene tectonic activity of these regions (Maloney, 1965).

A lagoonal coast exists between Cabo Codera and Barcelona and around Cumana (fig. 4). In both areas large rivers enter the Caribbean Sea, transporting sediments to the coast. There are sand beaches, lagoons, and mangrove swamps along the coast with occasional sand bars and tombolos.

The ria coast lies between Barcelona and Cumana (fig. 4). In this area numerous offshore islands lie along east-west structural trends that are traceable onshore (Von der Osten, 1955, 1957). Steeply dipping Lower Cretaceous limestones form sharp cliffs on several of the islands (Rod and Maync, 1954). The drowning of the ria coast was mainly the result of the Holocene rise of sea level, but Recent tectonic uplift and subsidence could also have played an important role in forming the topography (Von der Osten, 1955).

East of Cumana, between the mainland and the Araya Peninsula, lies the Gulf of Cariaco. It is another structural depression lying at the eastern extension of the Cariaco Basin. According to Maloney (1965), the coastal landforms of the gulf are mostly of the drowned river type.

3. GEOPHYSICAL OBSERVATIONS

3.1 Seismic Reflection Profiles

Seismic reflections indicate a change in the acoustic impedance of the rocks caused by variations of lithology, density, porosity, and other factors. The depth of penetration and the resolution of individual horizons are functions of the output energy and frequency of the sound source and the acoustic impedance of the underlying rocks.

The seismic equipment used for this survey can distinguish only those impedance changes, which involve strata that are at least 10 to 20 m thick. Portions of the seismic records that are characterized by numerous conformable reflectors, therefore, are interpreted as "well stratified" or "massively stratified" sediments. Those parts of the seismic record that are devoid of discernible reflectors are interpreted as "acoustically transparent" sediments and may possess fine scale stratification.

The major faults are indicated on the line tracings with solid lines. The direction of motion along the faults can be inferred from the attitude of the displaced beds, the dip changes, and the direction of offsets of the sea floor.

As the effective speed of the ship varied along each seismic reflection line, the vertical exaggeration of each tracing is different. On the average it is between 10:1 and 5:1. This gives a false impression of the actual relief, angle of slopes, and subbottom penetration (fig. 6).

The vertical exaggeration of the topographic relief which is given on the tracings of the seismic records is based on the assumption that the velocity of sound in sea water is 800 fm/sec (1460 m/sec). The vertical exaggeration for subbottom slopes is approximately 30% less, because of the higher velocity of the sound in the sediments. As a first approximation, each second of penetration can be equated with 1 km of depth below the sea floor, based on the range of 1.9 km/sec to 3.0 km/sec velocities measured in the sediments of this area (Officer *et al.*, 1957; Edgar, 1968).

Dip of reflectors always means "apparent dip", that is dip related to the plane of the seismic section discussed. The true dip of the sedimentary beds cannot be determined without additional control lines, which in most cases are not available.

Side echoes commonly occur when flat parts of the sea floor join steep slopes. The reflector that in this case may extend the slope below the flat surface may not be real, because the reflection could be from the side instead of the buried part of the slope. Cross-over reflections and parabolic echoes are good indicators of side echoes, but

these are not always present. Reflections from features on either side of the seismic line often appear as if these were directly under the profile; these also rarely can be identified without additional information.

The seismic records are discussed in relation to four key morphologic areas: (1) the continental shelf; (2) the island platforms and the Los Roques Canyon; (3) the Venezuelan Basin and the Curacao Ridge; and (4) the Venezuelan Basin and the Aves Ridge. A brief description of the salient features of the line tracings is given for each area.

3.1.1 The Continental Shelf

Seismic reflection records discussed in this section cover the area between the Tortuga-Margarita Bank and the Gulf of Barcelona: Profiles 7 and 5 cross the eastern deep of the Cariaco Basin and the adjacent basins to the north; Profile 3 is across the sill that separates the eastern and western Cariaco Basin deeps, and Profile 2 is across the western deep (fig. 7).

Profile 7 is located near the islands of Margarita and Cubagua and the Araya Peninsula (fig. 8). The westward extension of these features is clearly visible on this record. South of Margarita, sediments on the flank of a buried anticline (at 10°55'N), the Punta Arenas High (Ball et al., 1971), dip toward the north. These are overlain unconformably by younger, southward dipping sediments derived from the Tortuga-Margarita Bank.

The westward extension of Cubagua at 10°50'N appears as an anticline on Profile 7, although the north dipping normal faults separating it from the Punta Arenas High might indicate a fault origin of this

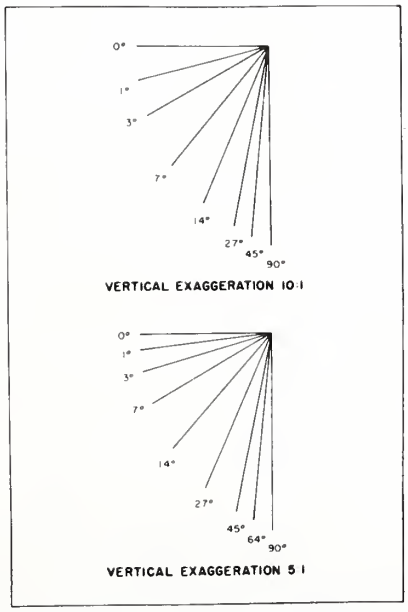

Figure 6. Slopes at 10:1 and 5:1 vertical exaggerations.

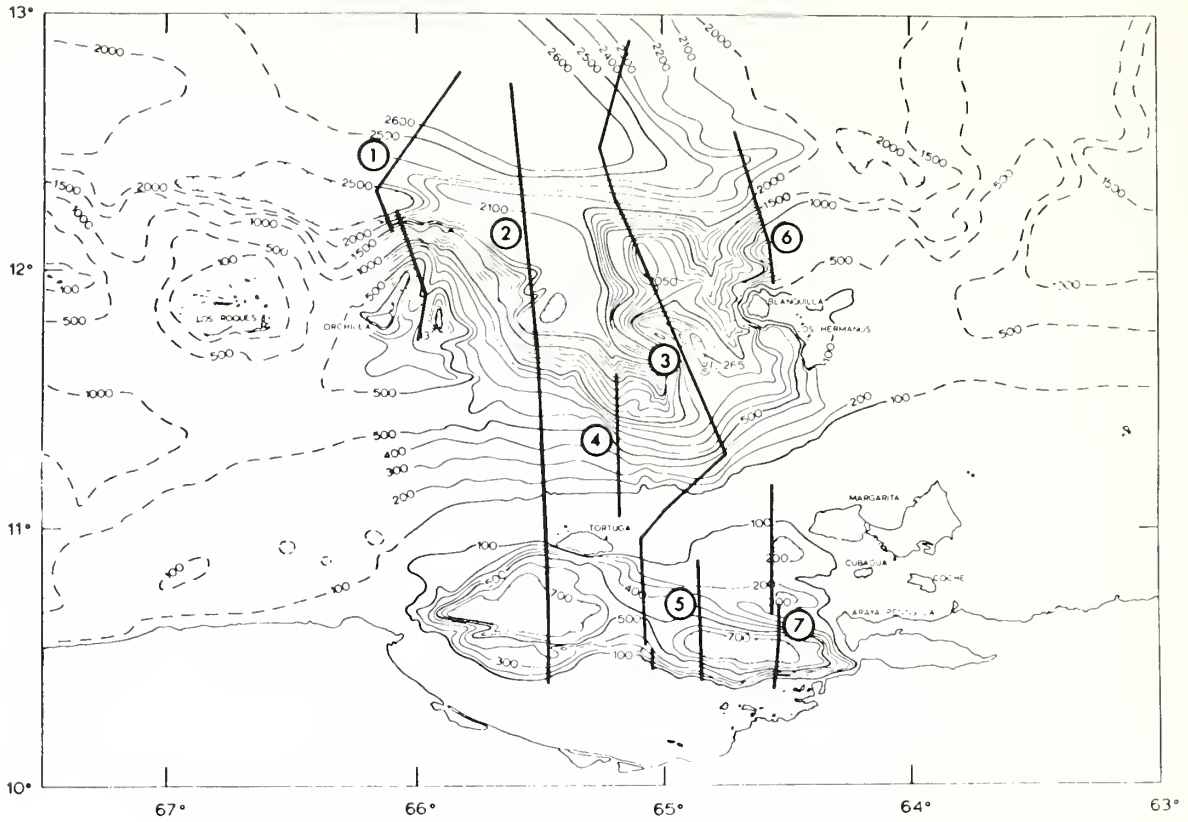

Figure 7. Location of north-south profiles.

feature (Ball et al., 1971). Some of the beds near the crest of the Cubagua anticline are tightly folded and possibly thrust-faulted (fig. 9). These beds can be traced southward into a basin, and then up and across several faults on the northern flank of a horst block (10°40'N), here named the Araya block.

Beds dip southward on the top of the Araya block, but down on its southern flank reflections become chaotic with no indication of bedding until the base of the block is reached. A major fault contact may be traced beneath the sediments of the southern flank.

The Cariaco Basin south of the Araya block can be divided into a northern half that is underlain by the downfaulted sediments (or metamorphics) of the Araya block and a southern half, which is a deep trough, filled with at least 700 m of sediments. The sediments of the southern half thicken northward and are ponded against a fault contact that separates the two halves indicating that subsidence has been greater along this fault than along the southern border of the basin.

The seaward extension of the El Pilar fault coincides with the southern wall of the Cariaco Basin (Ball et al., 1971). On this seismic section (Profile 7) the El Pilar fault appears as a steep slope (near 30°). The lack of penetration may suggest that this slope is underlain by dense rocks, although some of the energy could have been dissipated because of the steepness of the slope.

Profile 5 is located 35 km west of Profile 7. On the north it terminates on a broad terrace that lies at the westward extension of the basin southwest of Margarita. Below the sediments of the terrace, several nearly horizontal reflectors mark prograded scarps, the deepest of which is located 300 m below the sea floor. If these at one time were at surf-base, they suggest a 600 m subsidence of the area (fig. 10).

The terrace terminates at a normal fault, that with the other faults immediately to the south suggest recent tectonic activity. The beds of the downthrown blocks dip into the fault plane and thicken with depth, indicating that sediment deposition was concurrent with the motion along the faults.

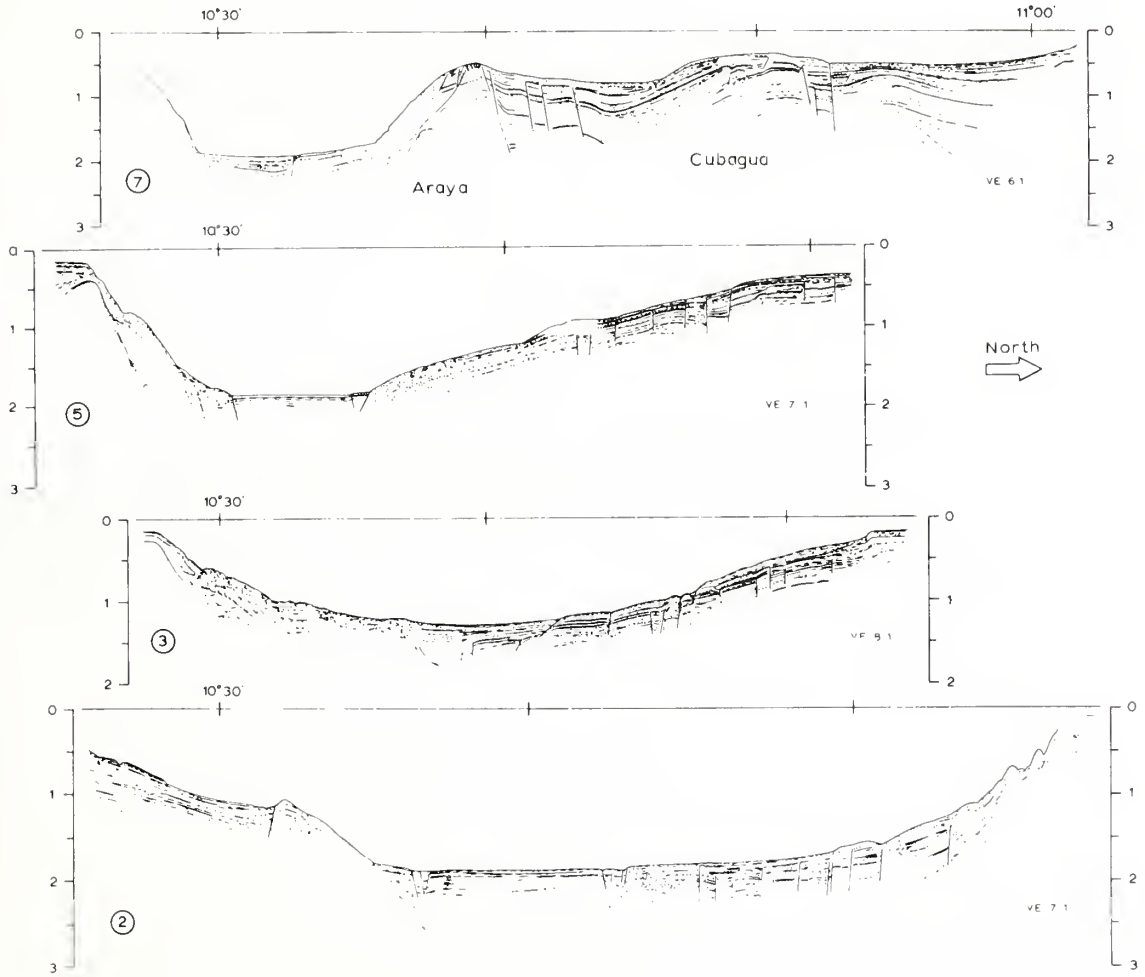

Figure 8. Line drawings of seismic reflection profiles across the continental shelf.

At 10°42'N the upper part of the record is missing, but 200 m below the sea floor two faults are seen that border a zone of incoherent reflections. Based on the extension of trends from Profile 7, this fault zone may mark a near-surface expression of the faults associated with the northern border of the Araya Block; the fault contact between the Cariaco Basin sediments and the incoherent reflectors at 10°36'N (Profile 5) may represent its southern margin.

In Profile 5, only about 150 m of well stratified sediments are detected in the Cariaco Basin; below these the sediments are acoustically transparent. There is a small reverse fault at the northern edge of the basin, and the sediments, instead of forming a pond (as to the east in Profile 7), are arched upward in the middle of the basin. This could be caused by compression, or the sediments may be thickening into the boundary faults and form a broad fault anticline, as suggested by Ball et al. (1971).

Beyond the southern boundary fault there is a gentle rise underlain by at least 300 m of sediments. There is some indication of stratification within these sediments, but it is discontinuous and suggestive of slumping. The slope becomes steeper at another fault contact, and the sediments that lie below this part of the slope (at least 200 m) also appear to be broken up by slumping. Just below the shelf break

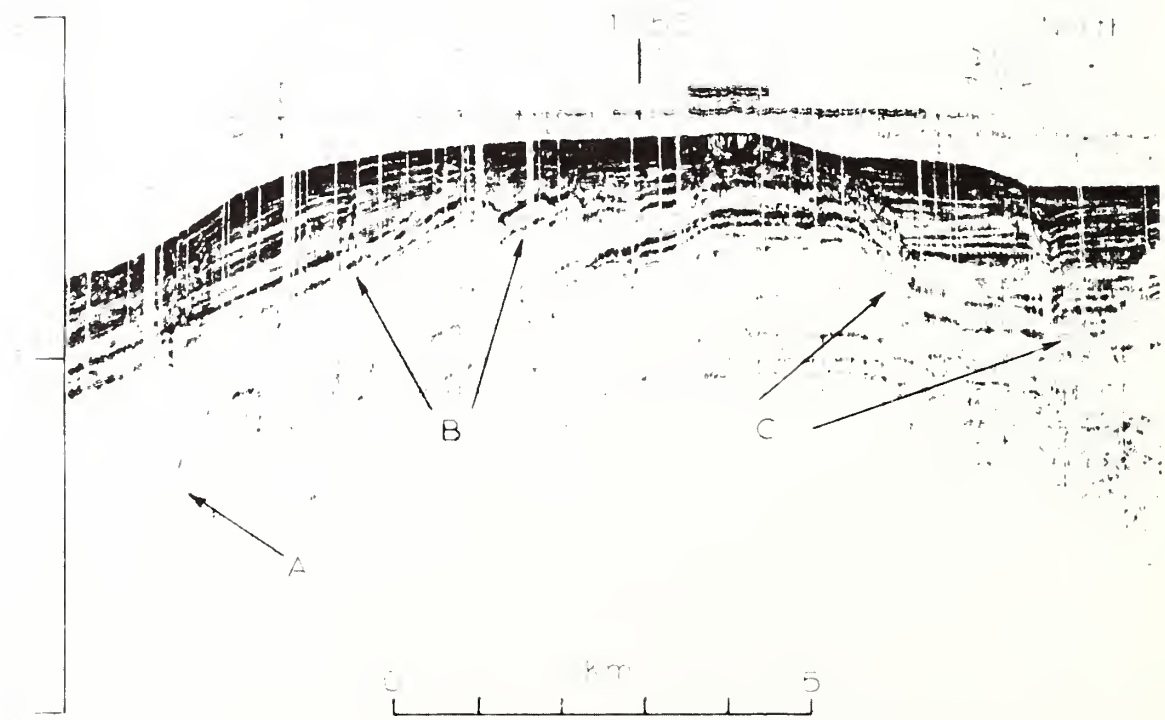

Figure 9. Copy of original seismic section of the Cubagua anticline (Profile 7). Arrows: A, multiples; B, thrust faulted (?) and folded strata; C, major normal faults.

there is a strong reflector that parallels the slope, but at the shelf break it dips to the south under the flat shelf. It is covered conformably with layered sediments to about 150 m below the shelf. At this depth there is an unconformity, followed by a sequence of horizontally bedded sediments.

Profile 3 (fig. 8) is across the sill that separates the eastern and western deeps of the Cariaco Basin. On the northern half of the profile approximately 350 m well-stratified sediments were penetrated, with major disconformities at 70 m and 150 m. Below 350 m there is a possible unconformity, beneath which steeper, southward dipping reflectors are seen. The upper 150 m of the sediments south of the shelf break show foreset bedding; below 150 m, there are several faults with small vertical displacements. At 10°47'N there is a major fault along which the sediments of the slope are downfaulted by 150 m. Minor folding or slumping is associated with this fault.

At 10°37'N the well stratified sediments of the northern slope abut against broad folded rocks that are characterized by mostly incoherent internal reflectors (fig. 11). South of the folded rocks, the

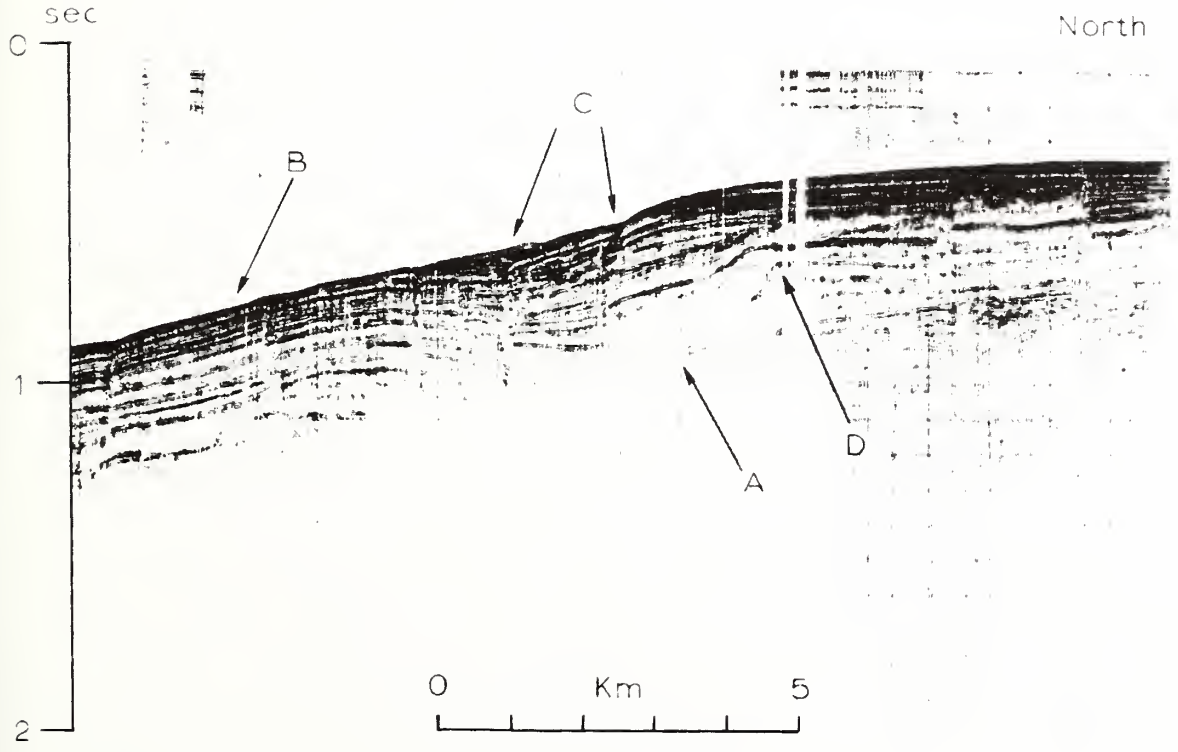

Figure 10. Copy of original seismic section of buried terraces southwest of Margarita (Profile 5). Arrows: A, multiples; B, stratified sediments; C, faults related to the Cubagua high (?); D, prograded scarps.

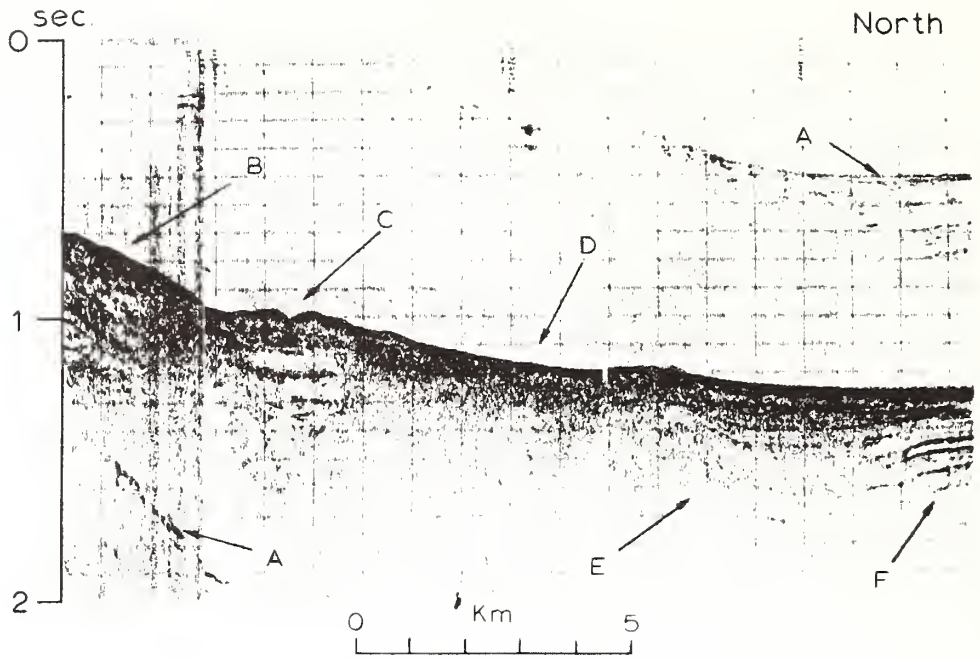

Figure 11. Copy of original seismic section of the southern part of the sill between the two deeps of the Cariaco Basin (Profile 3). Arrows: A, multiplies; B, stratified slope sediments; C, buried canyon with small channel on top; D, competent rocks; E, arch; F, stratified sediments.

southern slope of the sill is underlain by the rocks with similar reflective characteristics. At 10°33'N there may be a 600 m deep filled-in canyon. Its top is occupied by either sediment slumps, or a small leveed channel.

The southern slope is underlain by approximately 300 m of well stratified sediments with large slumps at 10°30'N. About 600 m below the surface of the slope in this area a horizontal reflector indicates a major unconformity. To the south, sediments on the slope return only incoherent reflections that may also be the result of slumping. There is a major acoustic basement type reflector 150-200 m below these sediments.

Profile 2 crosses the western deep of the Cariaco Basin. South of the sharp shelf break of the Tortuga-Margarita Bank, the hummocky bottom and the incoherent reflections may indicate large slump blocks, although it is equally possible that these reflections represent more competent rocks that plunge below the softer sediments to the south.

From near the base of the slope to approximately 10°45'N, several normal faults of small displacement offset the well stratified sediments. The faults at 10°45'N appear to be related to a broad arch, centered at 10°43'N (fig. 12), which divides the western deep of the Cariaco Basin into two halves. The northern half of the western deep is characterized by a sequence of well stratified and faulted sediments. Recent uplift of the arch is suggested by the approximately 40 m higher elevation of

the sea floor over the arch and by a graben located directly to the south of it. The elevation is obscured, because the fault scarp north of the arch (also 40 m high) is buried by sediments that ponded behind it.

In the southern half of the western deep the sediments are not as well stratified and are devoid of internal faults. The only faults in this half of the deep are near 10°37'N, where they form a small graben and a fault anticline near the southern wall of the deep. Below 500 fm, reflections under the southern wall are incoherent, most likely because of the reflective characteristic of the rocks, and not because of slumping. Above 500 fm the slope is underlain by well stratified sediments with numerous large slump blocks at 10°28'N. The promontory at 10°32'N is the result of faulting and relative uplift of the more competent rocks of the lower slope.

3.1.2 Island Platforms - Los Roques Canyon

Seismic reflection profiles of this area are discussed in relation to the major physiographic provinces. For the identification and location of the seismic sections figure 7 and figure 13 are used.

Profile 14 and segments of Profile 2 and Profile 3 illustrate the subbottom structure between the Tortuga-Margarita Bank and the island platforms.

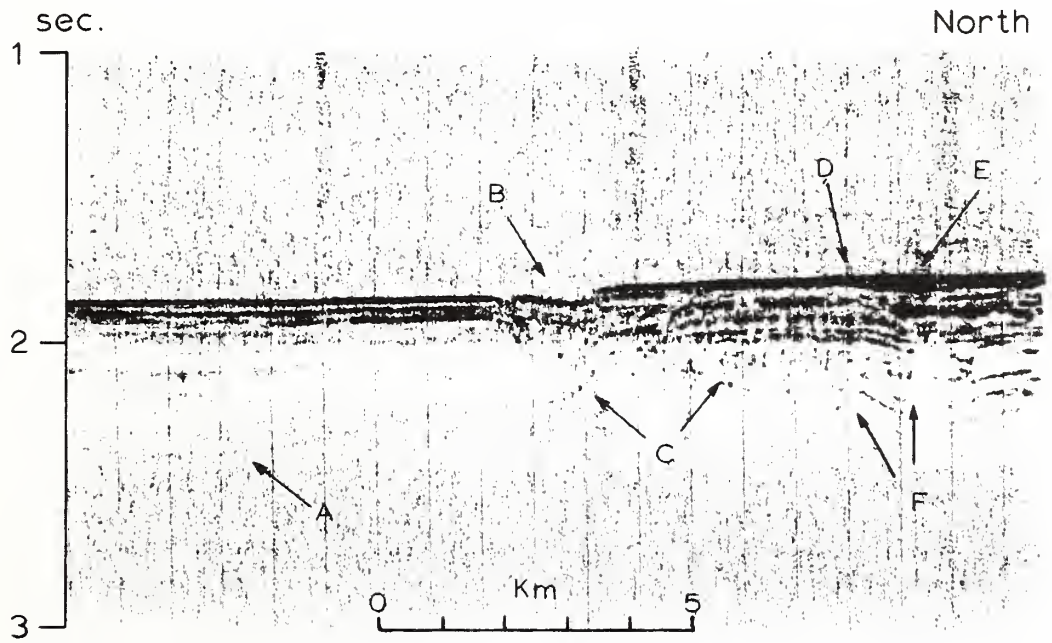

Figure 12. Copy of seismic section showing the central part of the western deep of the Cariaco Basin (Profile 2). Arrows: A, southern half of basin; B, graben; C, arch; D, buried northern scarp; E, sediment pond; F, faults north of the arch.

The sediments on the northern slope of the Tortuga-Margarita Bank are well-stratified (Profile 2) and are virtually undisturbed by faults (fig. 14). The only faulting in the section is related to a buried ridge at 11°13'N that arched the lower half of the stratified sediments. The upper 300 m of the well-stratified sequence in the middle of the shelf appears to pinch out near this ridge on the south, and near to another high at 11°36'N, next to the southern wall of the Los Roques Canyon. Reflectors that characterize this second high have crescent-shaped side echoes and incoherent internal reflections. For convenience of presentation these reflectors are described as "acoustic basement", because of their wide distribution throughout the area of the platforms and the canyon. These can be distinguished from the smooth, coherent basement reflectors that usually form dome-shaped structures and are referred to as "granitic" basement.

In the southern end of Profile 3 (fig. 15) there are several sequences of foreset bedding near the shelf break of the Tortuga-Margarita Bank. These overlie a gently northward dipping unconformity 200 m below the sea floor. Below the unconformity the dip of the beds is steeper and increases northward to 11°15'N, where a major fault uplifted the section to the north. Although the deeper beds are not seen in the immediate area of the major fault, the sense of displacement is clearly indicated by the offsets of the sea floor and by the sense of displacement and drag of the upper 300 m sediments along some of the auxiliary faults. These faults lie along the extension of the eastern wall of the Los Roques Canyon and strongly suggest that recent motions took place along this wall.

Approximately 400 m of well stratified sediments cover an unconformity directly north of the major fault and continue down-slope and over the Blanquilla platform. The numerous small faults within the well stratified sequence seem to be related to basement highs, indicated by the arched sediments below the well stratified group.

Profile 14 (fig. 15) is oriented east-west, parallel to the slope of the Tortuga-Margarita Bank. The eastern half of the section shows a 700 m thick, well stratified sequence that becomes gently folded west of 65°02'W, and faulted at 65°06'W. The fault contact lies at the extension of the western branch of the Los Roques Canyon, suggesting again recent motions and tectonic control for the formation of the canyon.

Profile 13 crosses the southern part of the Los Roques Canyon and the Orchilla and Blanquilla platforms (fig. 16). West of the canyon on the Orchilla platform two "granitic" basement domes are shown: One is at 65°53'W, the other at 65°38'W. This section crossed only the northern flank of the first dome; it appears as a prominent feature, forming an 80 fm high outcrop on the sea floor on a north-south seismic reflection line. The second dome is flanked on the east by the rough acoustic basement (fig. 17) that was noted in this area also on the north-south crossing of Profile 2. Between the two domes approximately 600 m of well stratified sediments overlay acoustically transparent sediments that are at least that thick.

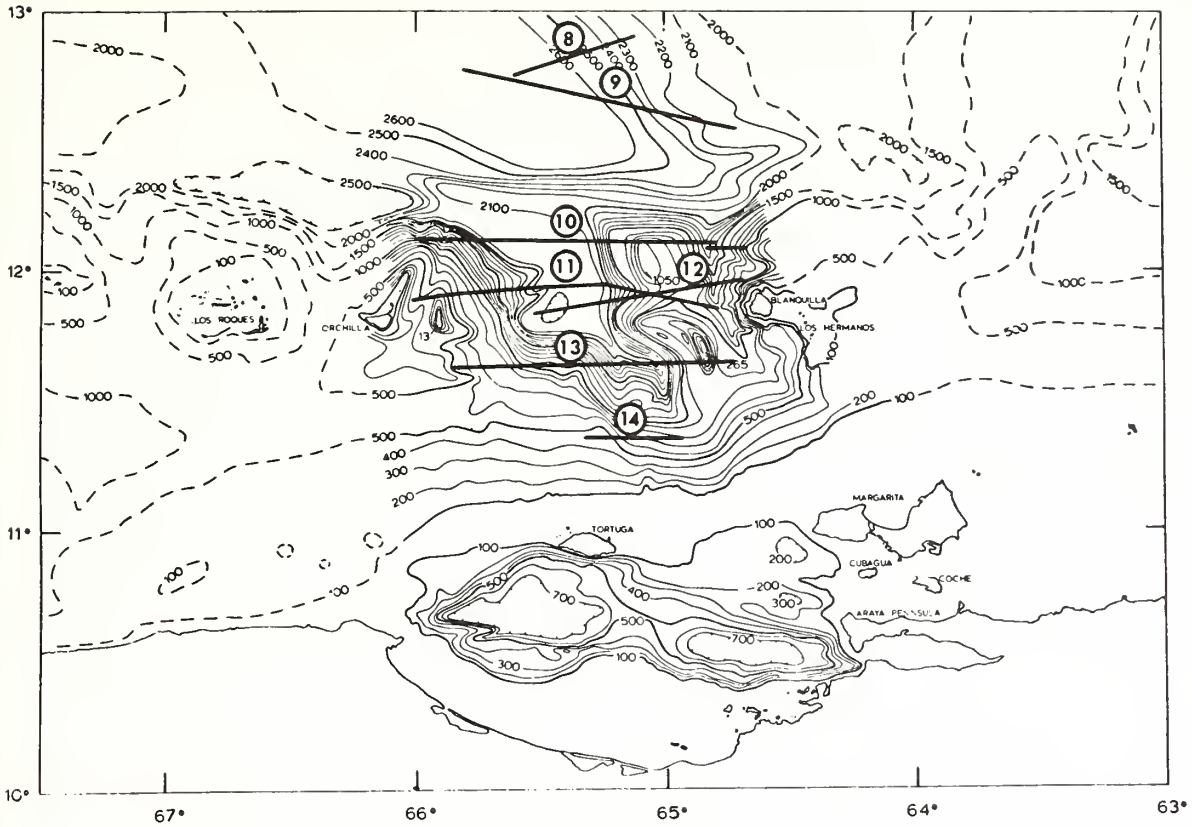

Figure 13. Location of east-west profiles.

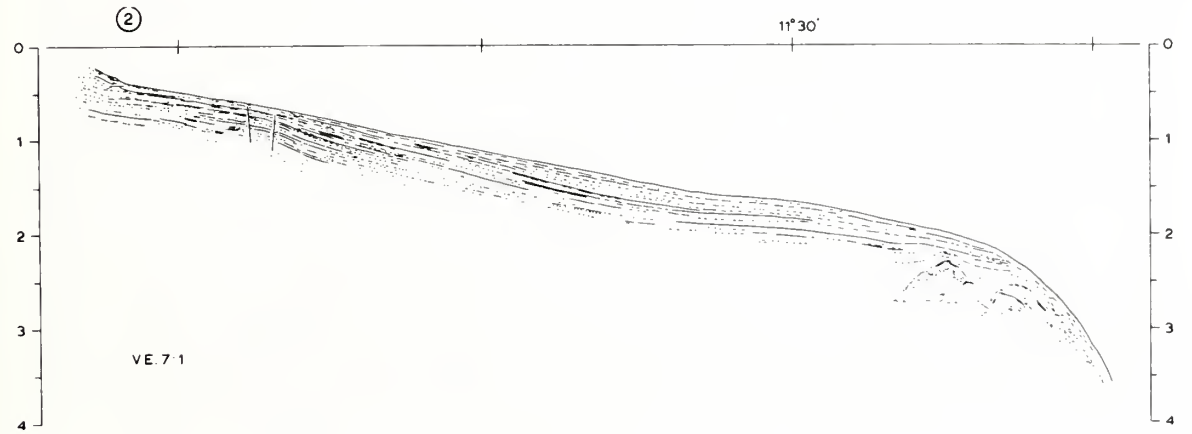

Figure 14. Line drawing of seismic reflection Profile 2 between the Los Roques Canyon and the Tortuga-Margarita Bank.

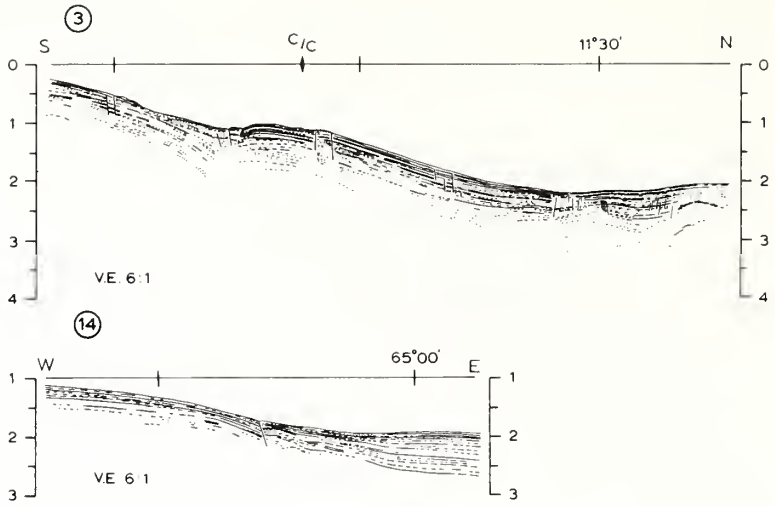

Figure 15. Line drawing of seismic reflection Profiles 3 and 14 between the Blanquilla platform and the Tortuga-Margarita Bank.

To the east at 65°30'W the acoustic basement is only 150 m below the sea floor, and the stratified sequence is missing. East of 65°25'W approximately 250 m of acoustically transparent sediments cover the basement that outcrops in the wall of the Los Roques Canyon.

Both branches of the Los Roques Canyon are carved into the unit that comprises the rough acoustic basement; on the eastern wall of the canyon these rocks outcrop at depths greater than 1,100 fm. Between 1,100 fm and 800 fm the well stratified sequence of the Blanquilla platform is truncated at the canyon wall. At 64°50'W the granitic basement rises above the surrounding sea floor and forms a major ridge.

The topography of the sea floor is closely controlled by the basement west of the canyon. Although clear fault contacts are not seen, on one may infer that the step-like changes of the sea floor at 65°35'W and at 65°25'W, and the western branch of the canyon may represent faulting.

Profile 11 and Profile 1 illustrate the subbottom structure of the Orchilla platform (fig. 18). The western end of Profile 11 is over a depression east of Orchilla Island, where more than 600 m of acoustically transparent sediments and 300 m of well stratified sediments cover the "granitic" basement. This basement outcrops at 65°55'W along the northern extension of the Burgana Bank. Basement type reflectors underlie the entire platform. The eastern limit of the "granitic" type

basement is 65°46'W; farther to the east the character of the reflectors suggest the presence of the acoustic basement. The scarps at 65°40'W and 65°35'W and the sediment-basement contact at 65°30' most likely represent the fault borders of the Los Roques Canyon.

Another seismic reflection line over the eastern Orchilla platform was made by the R/V CONRAD-9 (fig. 19). Some of the features that were discussed in connection with Profile 2, Profile 13, and Profile 11 are shown better on that north-south crossing (see also p. and fig. 14 and fig. 16).

The structure of the central and northern parts of the Orchilla platform is shown on Profile 1. A major "granitic" basement outcrop dominates this section at 12°00'N, at the extension of the trend of the islands north of Orchilla. The basement high directly to the south of this outcrop is probably another "granitic" dome, but further south the acoustic basement type reflectors probably represent lower density rocks.

At 11°45'N the broad subbottom arch exhibits internal stratification suggestive of sedimentary rocks. To the north, the acoustic basement outcrops at 12°07'N and apparently forms the northern slope of the Orchilla platform.

A part of Profile 3 crosses the western half of the Blanquilla platform (fig. 20). The dominant feature here is the "granitic" basement ridge whose western spur is crossed by this section. Approximately 600 m of stratified sediments are present on both sides of the "granitic" ridge; rough, acoustic basement-type reflectors are seen at the edges of the broad high to the north. On the top of the high, about 300 m of stratified sediments are present that seem to pinch out farther to the north as the rocks of the acoustic basement approach the northern slope.

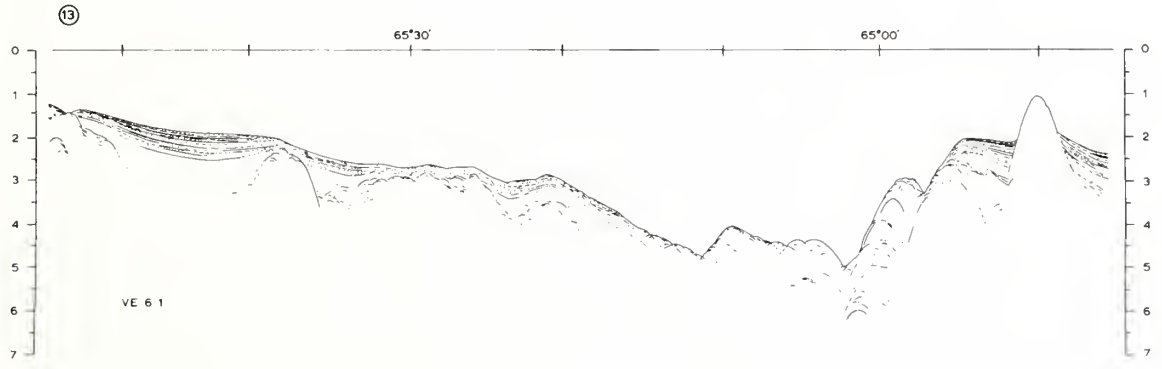

Figure 16. Line drawing of seismic reflection Profile 13.

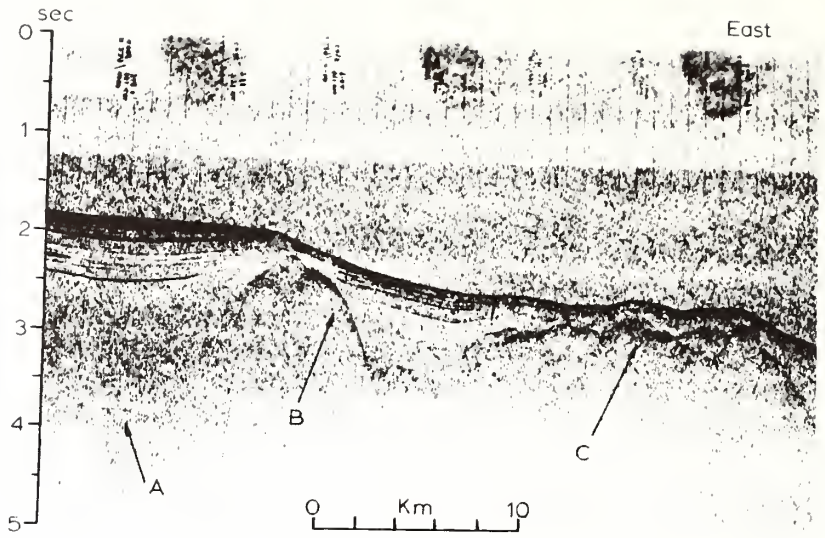

Figure 17. Copy of original seismic section showing the two different type of basements on Orchilla platform (Profile 13). Arrows: A, multiples; B, "granitic" basement; C, rough, acoustic basement.

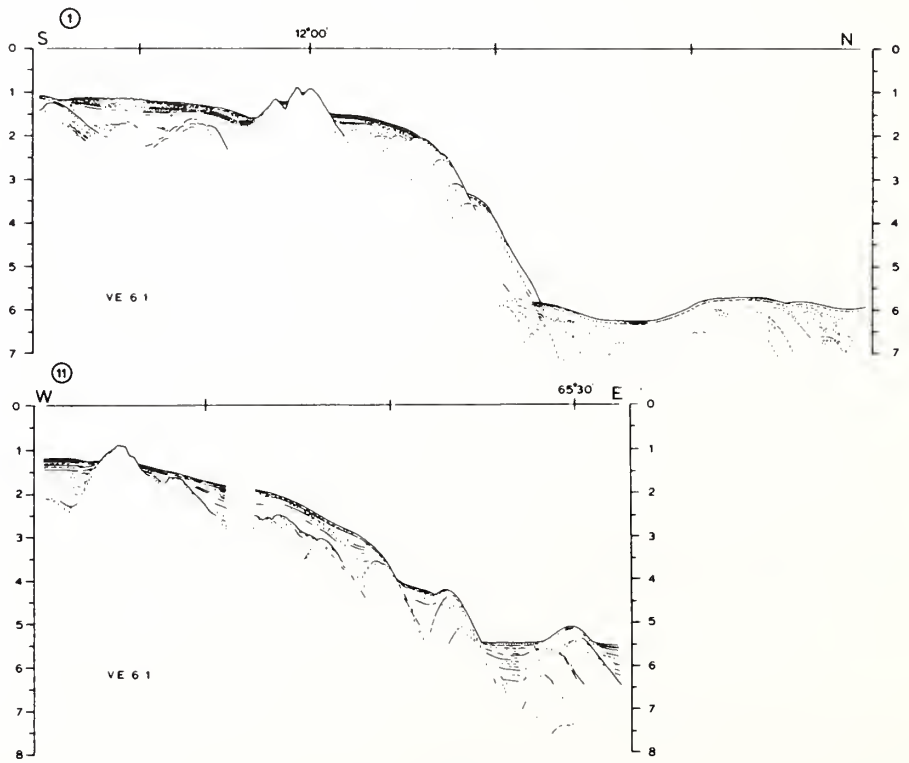

Figure 18. Line drawing of seismic reflection Profiles 1 and 11.

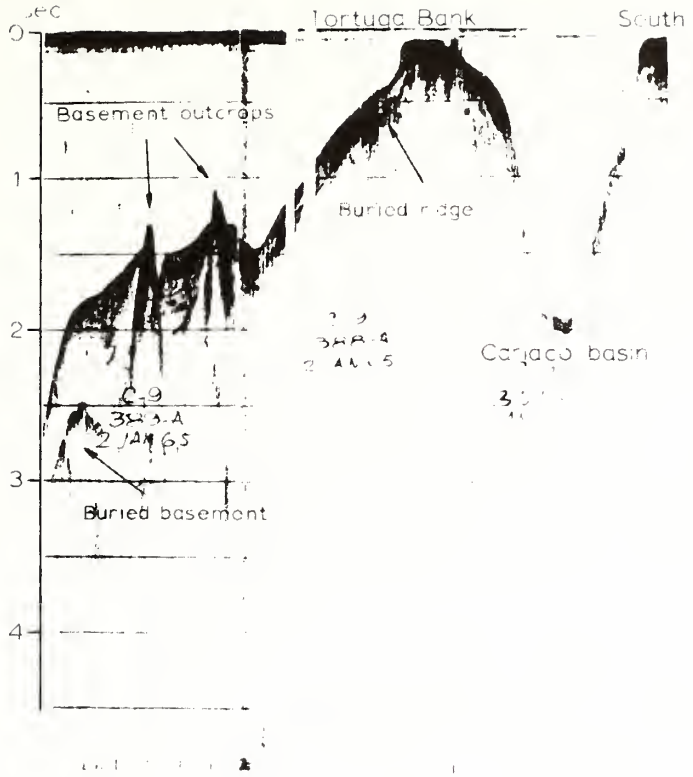

Figure 19. R/V CONRAD-9 seismic section along 65°45'W. For location see figure 2.

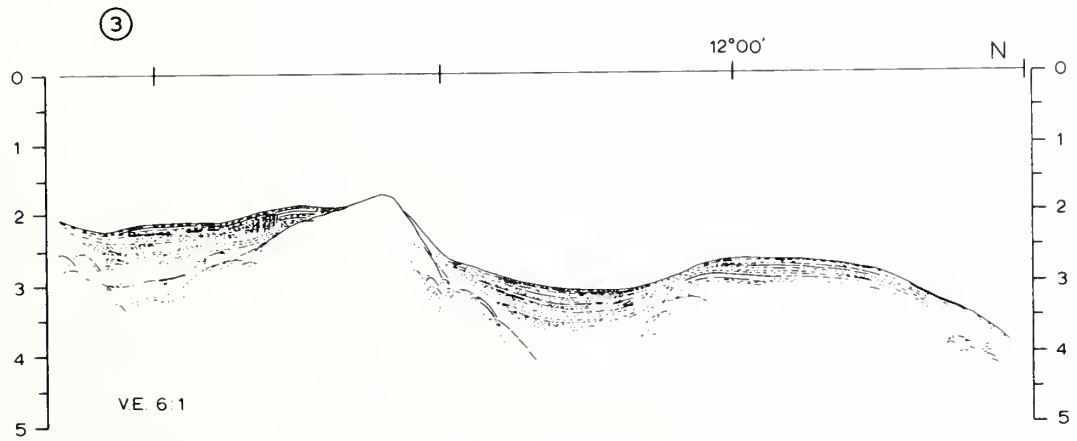

Figure 20. Line drawing of Profile 3 across the Blanquilla platform.

A short seismic section crosses the eastern half of Profile 13 and presents the structure of the southwestern part of the Blanquilla platform (fig. 21). The section is essentially the same as Profile 13 west of the "granitic" ridge (D). To the east it shows 600 m of stratified sediments covering the ridge becoming disturbed as they mix with the talus of the island and other sediments in the Blanquilla Canyon (E). A nonconformity or fault contact is indicated (F) at the base of Blanquilla Island and below the eastern wall of the Los Roques Canyon.

Profile 12 and Profile 10 cross the northwestern part of the Blanquilla platform and the Los Roques Canyon (fig. 22). In Profile 12 over 700 m of well stratified sediments cover the western part of the Blanquilla platform. Blanquilla Canyon at 64°48'W has been cut into this strata, but its eastern wall in this profile appears to be a slump block. The canyon is underlain by westward dipping reflectors, probably related to the island on the east. Farther north in Profile 10 the canyon walls are apparently cut into more competent rocks of the platform that show no stratification. Some incoherent reflectors underlying the western wall represent either rocks derived by slumping or the acoustic basement.

At 64°56'W (Profile 10) stratified sediments may indicate a former channel of the canyon, which is now filled. In this profile acoustic basement type reflectors are present between 64°56'W and 65°10'W. At 65°10'W, a fault contact probably represents one of the two faults bordering the Los Roques Canyon on the east. The eastern wall of the canyon itself represents the other fault.

The acoustic basement is seen only under the western part of the platform in Profile 12 where it outcrops at the wall of the Los Roques Canyon at 65°10'W. This wall represents one of the faults associated with the eastern edge of the canyon; the other fault contact is seen at 65°13'W where the more than 1000 m of well stratified sediments covering the floor of the Los Roques Canyon abut the acoustic basement rocks. The sediments thicken against this contact, suggesting relatively greater subsidence of the canyon floor on the east. Sediments on the west are in fault contact with the downfaulted acoustic basement rocks of the Orchilla platform at 65°30'W. This buried basement apparently extends northward from Profile 12 and forms the topographic high in Profile 11 (fig. 18). It becomes buried again farther north but appears below the stratified sediments at 65°31'W in Profile 10 (fig. 23). In Profile 10 the division of the canyon floor into two halves is well illustrated; the western half is underlain by the buried acoustic basement; the eastern half, similar to Profile 12, contains well stratified sediments that thicken to the east.

Profile 10 crossed the northern tip of the Orchilla platform, where the lack of subbottom penetration suggests the presence of competent basement-type rocks. The steep western wall of the canyon probably represents its major fault border.

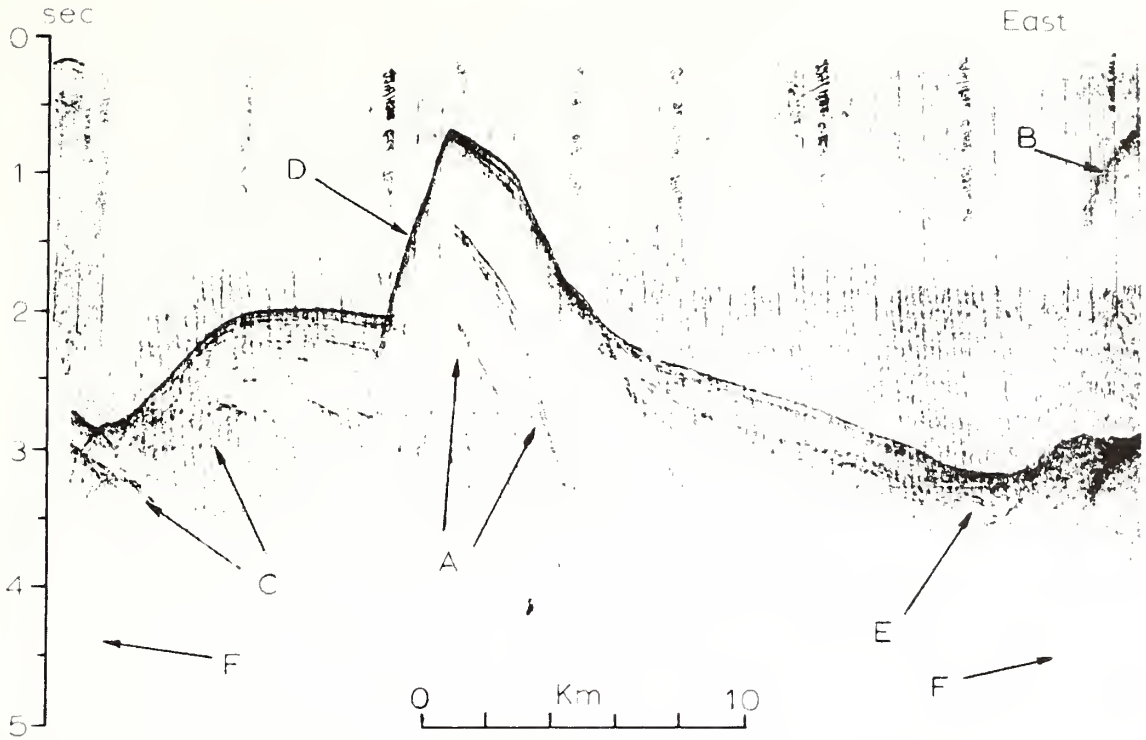

Figure 21. Copy of original seismic section normal to the trends of the Blanquilla platform. Illustration covers part of the track line made between 11°40'N, 46°56'W and 11°49'N, 64°42'W, southwest of Blanquilla Island (fig. 2). Arrows: A, multiples; B, side echo from the slope of Blanquilla; C, acoustic basement; D, "granitic" ridge; E, Blanquilla Canyon; F, fault contact (?)

3.1.3 Venezuelan Basin - Curacao Ridge

Segments of Profile 1, Profile 2, and Profile 3 cross the southern margin of the Venezuelan Basin (fig. 24). Each profile shows approximately 900 m of well stratified sediments that abut the Curacao Ridge along a possible fault contact. These sediments are essentially horizontal and contain several reflectors that can be identified on each profile (e.g. the reflectors 350 m below the sea floor). The large number of the reflecting horizons that dominate the upper part of the sediment column decrease with depth; the deepest reflectors coming from about 1800 m below the sea floor are separated from the well stratified near-surface sequence by a 600-700 m thick acoustically transparent layer. In Profiles 1 and 2 the lowest reflector has a definite upward curve near its contact with the Curacao Ridge that may suggest drag as a result of relative uplift of the ridge.

The Curacao Ridge in Profile 1 has a rough surface topography that is conformable with the folded subsurface sediments. The strong parabolic reflectors (fig. 25) most likely represent side echoes from the

large buried arches, characteristic of this part of the ridge. In Profile 2 the extension of the Curacao Ridge has a much smoother surface, and it is covered by 250 m of well stratified sediments. Folded sediments similar to those observed in Profile 1 appear approximately 600 m below the northern slope of the ridge.

South of 12°10'N Profile 2 crosses the northwestern part of the Los Roques Canyon. It shows the stratified sediments, ponded between the Curacao Ridge and the Orchilla platform and the acoustic basement near the southern edge of the profile.

Profile 3 shows the contact between the well stratified sediment sequence of the Venezuelan Basin and the competent acoustic basement-type rocks of the Blanquilla platform. On the northern end of this section the sea floor gently rises as the profile crosses the flank of the Aves Ridge. Numerous layers of the well stratified sequence pinch out at the beginning of the rise until only 300 m remains over the flank. Beneath the well stratified sequence on the flank of the Aves Ridge, there is a 500 m thick, acoustically transparent layer, which terminates at the bottom at a 150-200 m wide reflector, characterized by incoherent returns on the original records.

3.1.4 Venezuelan Basin - Aves Ridge

Profile 8 (fig. 26) crosses the transition area from the Venezuelan Basin to the western flank of the Aves Ridge. Most of the well stratified sediments that cover the southern margin of the Venezuelan Basin pinch out near the edge of the flank of the Aves Ridge (65°29'W) until only about 300 m of the sequence remains. There are two down-to-basin normal faults near 65°29'W; another similar fault is at 65°21'W. The well stratified sequence is underlain by a 600 m thick acoustically transparent layer that ends at a 150-200 m thick incoherent reflector, noted also in this area on Profile 3. There are two other reflectors

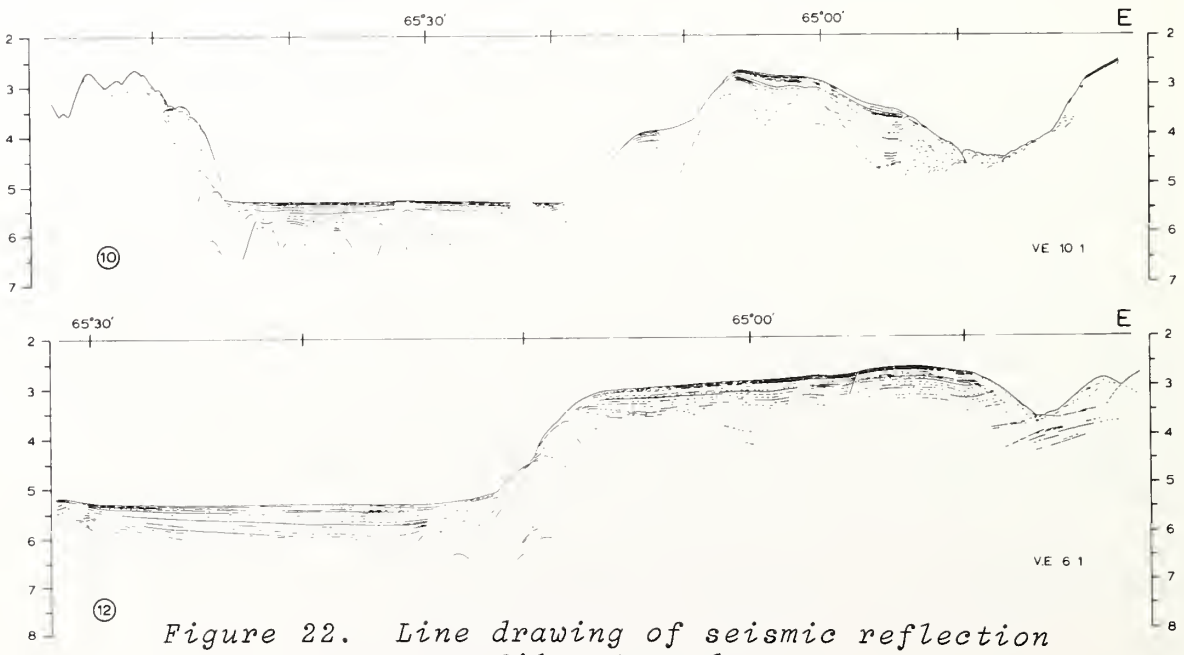

Figure 22. Line drawing of seismic reflection Profiles 12 and 10.

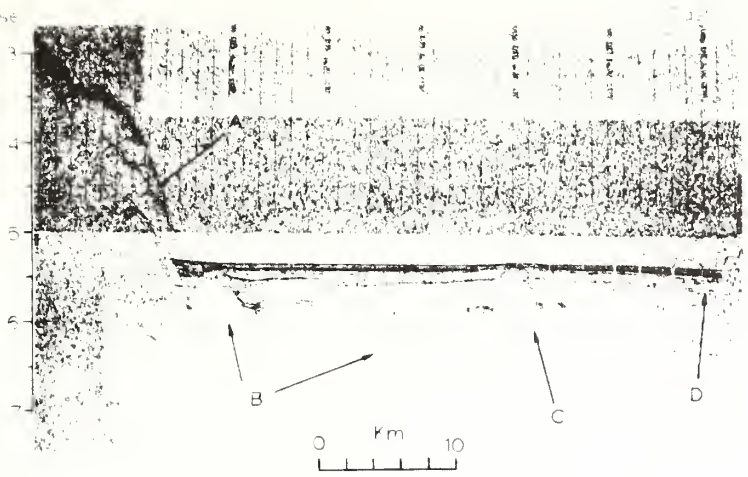

Figure 23. Copy of original seismic section over the northwestern part of the Los Roques Canyon (Profile 10). Arrows: A, western wall of canyon; B, acoustic basement; C, buried basement ridge; D, thickening strata toward the east.

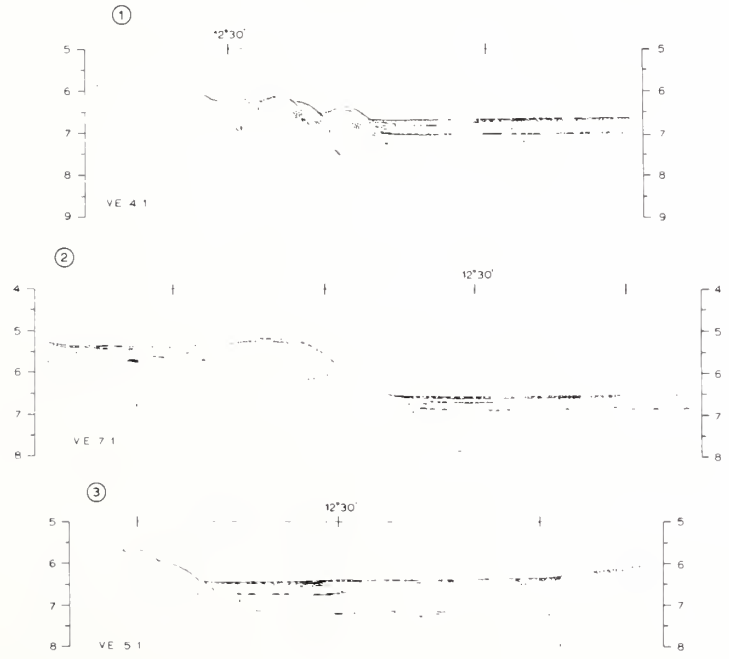

Figure 24. Line drawing of seismic reflection Profiles 1, 2, and 3 over the southern margin of the Venezuelan Basin.

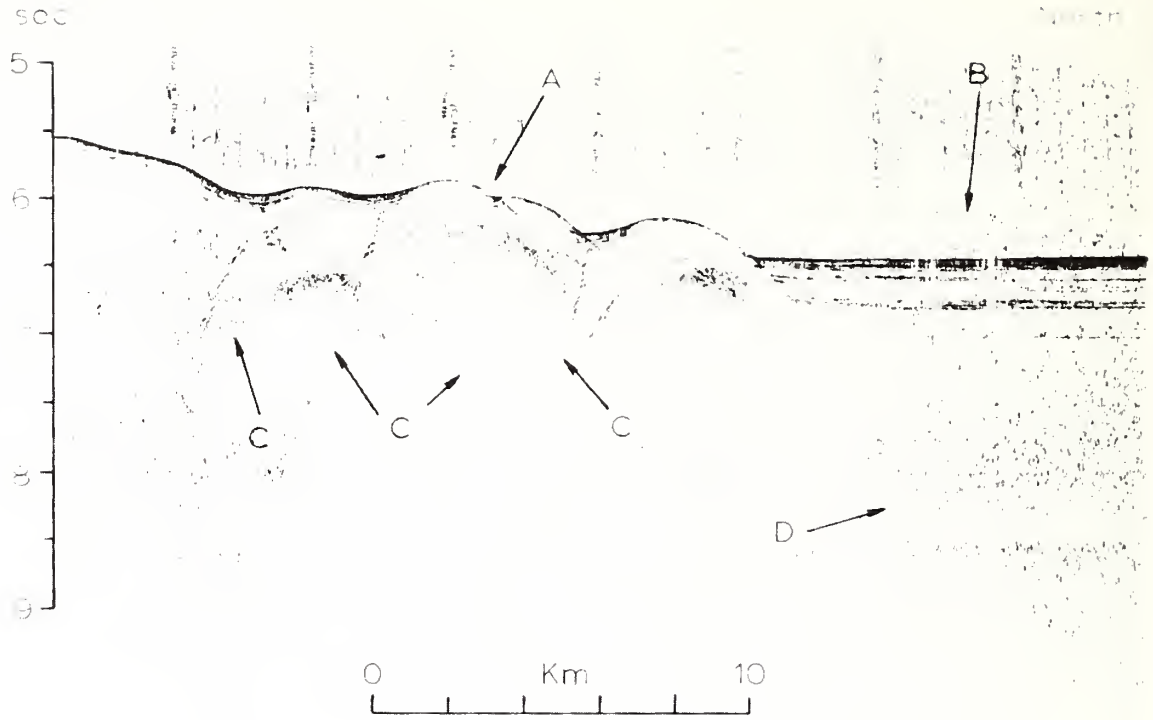

Figure 25. Copy of original seismic section of Profile 1 over the southern margin of the Venezuelan Basin. Arrows: A, eastward extension of Curaçao Ridge; B, Venezuelan Basin turbidite sequence; C, parabolic reflectors; D, deepest reflector.

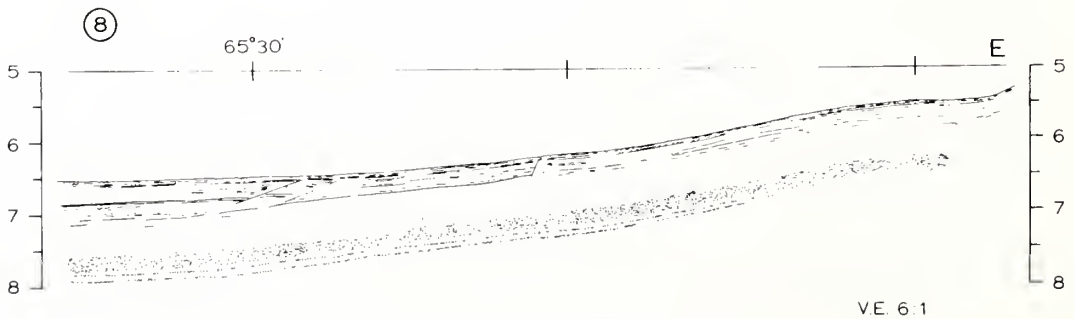

Figure 26. Line drawing of seismic reflection Profile 8.

approximately 100 m apart that underlie the band of incoherent returns and with it extend to the west toward the Venezuelan Basin.

3.2 Geomagnetic Measurements

Geomagnetic data obtained during this investigation are presented in the form of a magnetic total intensity contour chart (fig. 27) and as a series of magnetic total intensity anomaly profiles, plotted together with the profiles of the bottom topography and the free-air gravity anomaly (see Appendix I). Data collected along all the tracklines were utilized in the preparation of the total intensity contour map, but Appendix I contains only the key sections shown in figures 7 and 13.

Additional geomagnetic data obtained along north-south tracklines in the area south of 11°C0'N by Ball et al. (1971) were also incorporated in the total intensity contour map. A correction of -150 γ was added to these data to eliminate the effect of the secular variation that occurred during the two-year interval separating the two sets of measurements.

An essentially smooth magnetic field characterizes the northern part of the study area which overlies the Venezuelan Basin, the northern slope of the Tortuga-Margarita Bank, and, in the south, the Bay of Barcelona. Anomalies up to ± 300 γ were observed over the Orchilla and Blanquilla platforms, where the tracklines were too widely spaced for the accurate presentation of the magnetic field variations. The magnetic data in these areas serve only to indicate the presence of igneous rocks in various parts of the platform.

Over the continental shelf south of 11°00'N the density of the trackline coverage permits a much more accurate presentation of the magnetic field. In order to see the magnetic anomalies of this area more clearly, the earth's main magnetic field was removed by using a grid, constructed from the values of the total intensity chart along 65°00'W and 65°30'W (fig. 28). The magnetic anomaly map (fig. 29) reveals two 600-γ (peak-to-trough) anomalies off the Araya Peninsula, and a number of smaller, short-wavelength (<10 km) anomalies southwest of Margarita. The Bay of Barcelona and large parts of the Cariaco Basin are essentially free of short-wavelength magnetic anomalies, although a 300-γ positive anomaly off Cabo Codera extends into the western deep of the Cariaco Basin, and a small minimum seems to follow the southern margin of the Tortuga-Margarita Bank west of 65°00'W.

3.3 Gravity Measurements

Gravity free-air anomaly values are presented in the form of a contour map (fig. 30) and as a series of profiles, plotted together with the magnetic anomalies and the bottom topography (Appendix I).

The largest free-air anomalies are associated with the area of the island platforms and the extension of the Curacao Ridge. A -194 mgal minimum is associated with the Curacao Ridge at 66°00'W, which diminishes eastward to about -120 mgals at the point where the ridge merges

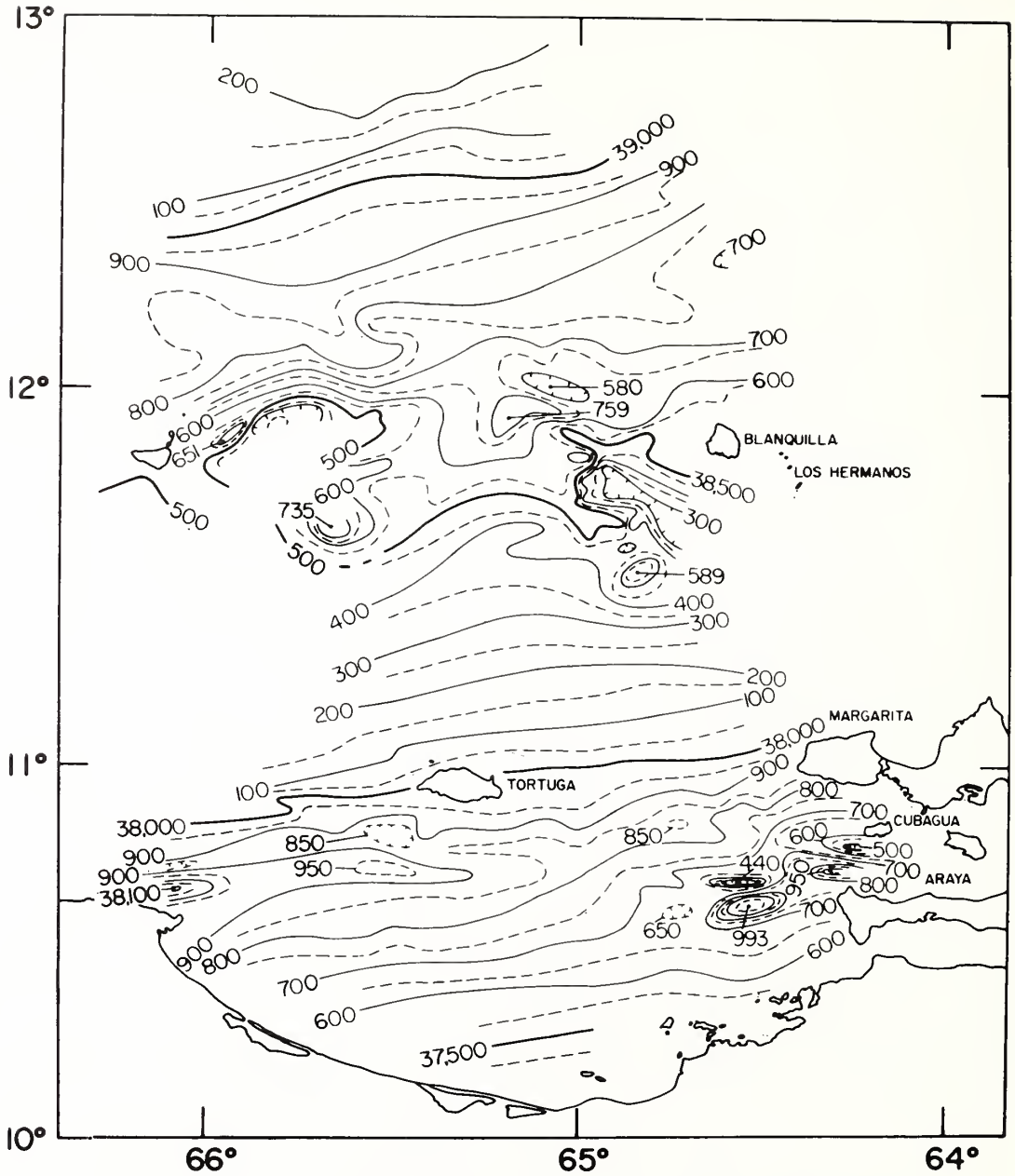

Figure 27. Magnetic total intensity chart of the study area. Contour interval 50 γ (10^{-5} Oe).

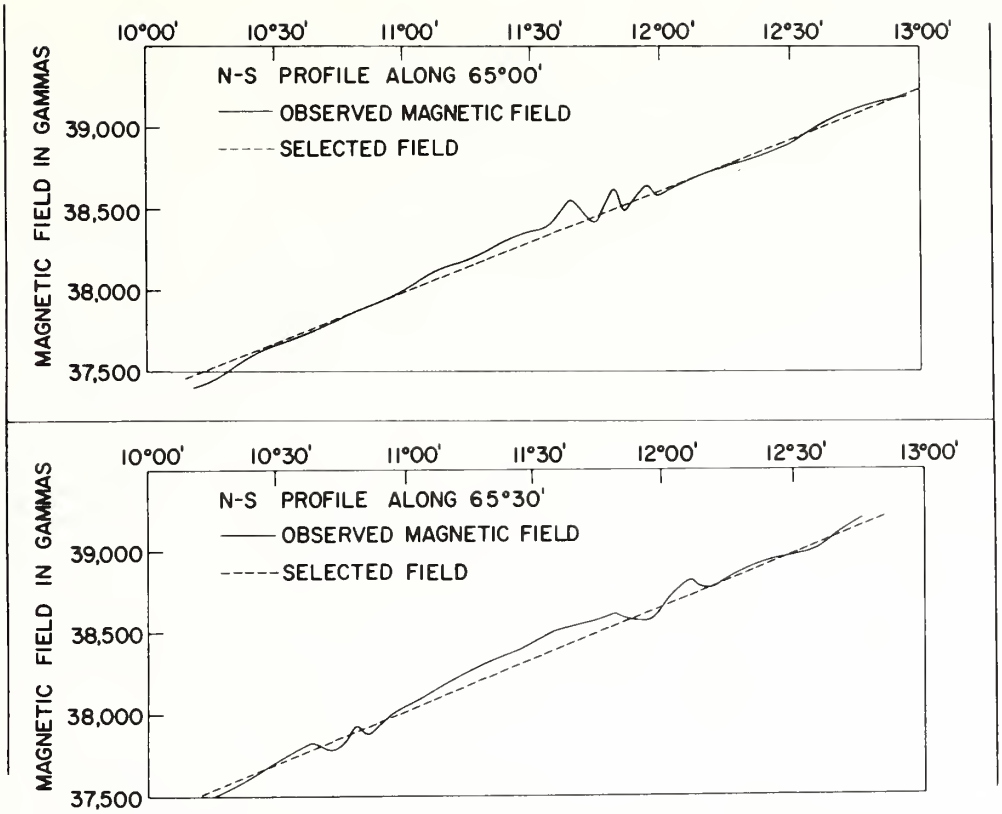

Figure 28. Determination of the regional magnetic field from the values of the total intensity chart along 65°00'W and 65°35'W.

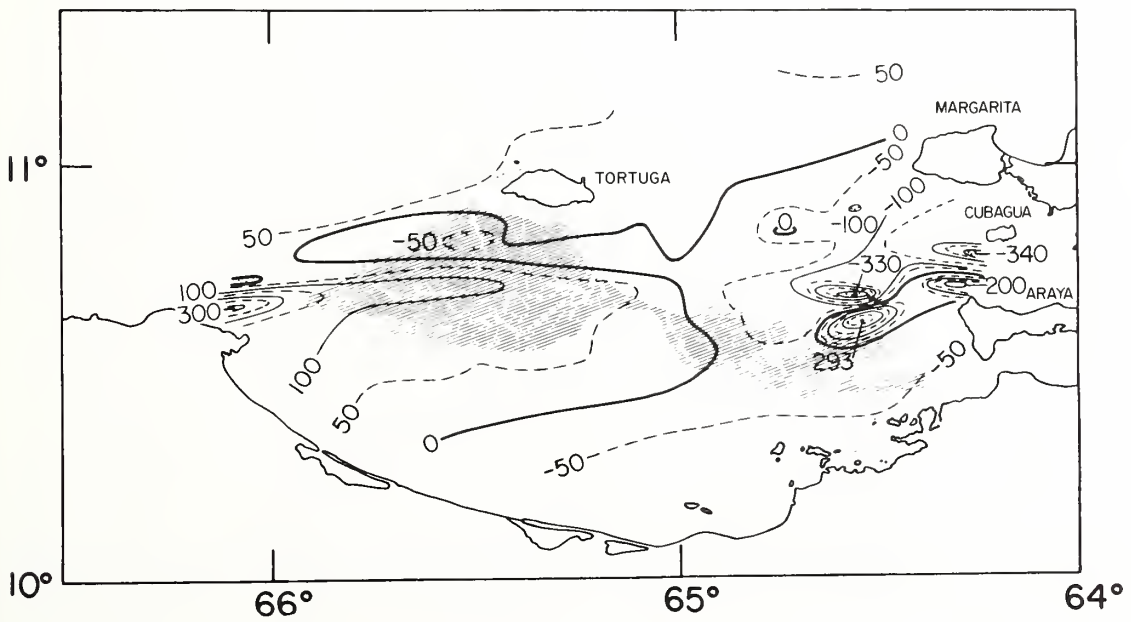

Figure 29. Magnetic total intensity anomaly map of the continental shelf off north-central Venezuela. Shaded area: Cariaco Basin below 500 fm.

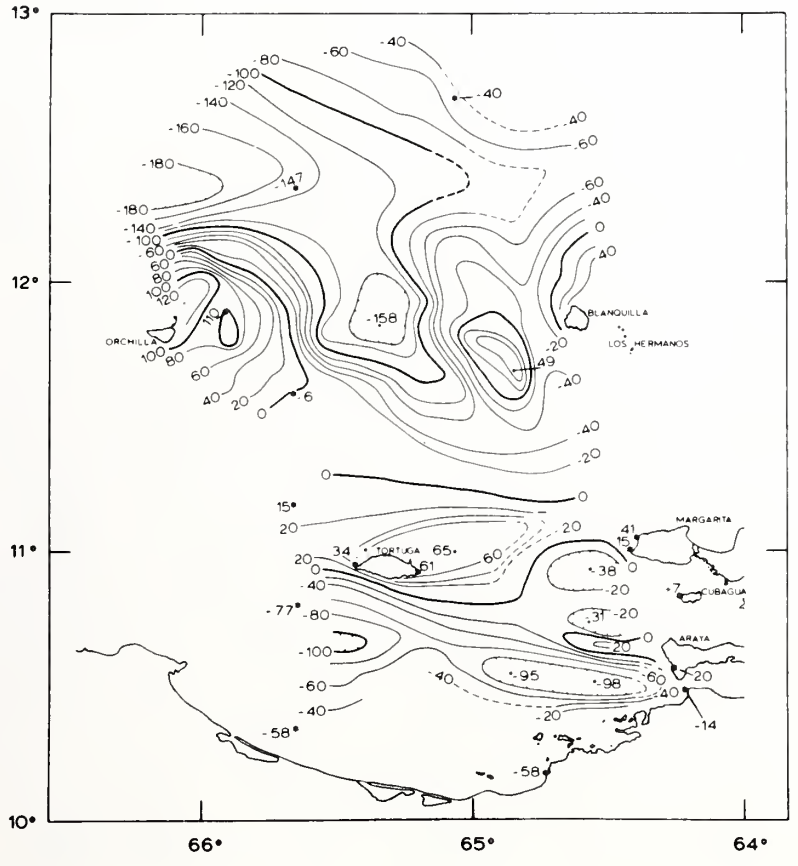

Figure 30. Free-air gravity anomaly map of the study area. Contour interval 20 mgals. Values with stars: Marine measurements, Ewing et al., 1957; Land measurements, Ball et al., 1971.

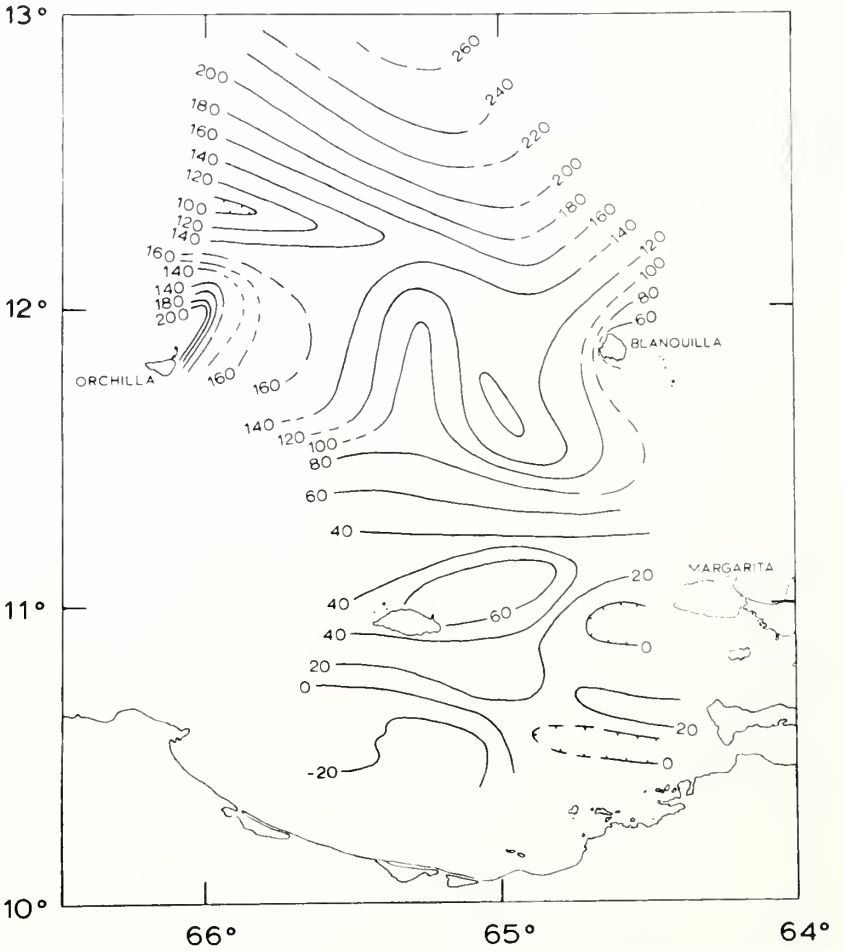

Figure 31. Bouguer gravity anomaly map of the study area. Contour interval 20 mgals.

with the Blanquilla platform. Farther to the east the axis of this minimum shifts northward, and follows the topographic depression north of the platform.

There is a -158 mgal minimum in the Los Roques Canyon, and positive anomalies of 125 mgals and 49 mgals were observed over the Orchilla and Blanquilla platforms, respectively.

The Tortuga-Margarita Bank is characterized by small amplitude positive free-air anomalies that range up to 65 mgals in the area immediately east of Tortuga. Farther south, over the depressions of the shelf negative anomalies predominate, with approximately -100 mgal values in the Cariaco Basin. Positive anomalies are associated with the westward extension of Cubagua Island and the Araya Peninsula.

In order to eliminate the effect of the topography on the gravity anomalies and to study the subbottom density distribution, a Bouguer anomaly map was prepared (fig. 31). Instead of computing the commonly used "simple Bouguer anomaly" (Free-air anomaly + depth x constant x density difference between sea water and underlying rocks), "two-dimensional Bouguer anomaly" computations (Talwani et al., 1959) were performed along eight profiles (fig. 32) that were selected in areas where the sea floor had no appreciable variations transverse to the section (see Appendix II). A comparison of the "simple Bouguer" correction and the "two-dimensional Bouguer" correction (fig. 33) shows that the latter in essence contains a terrain correction also that can amount to 40 mgals in areas of rough topography. The Bouguer anomaly map was prepared on the basis of the eight two-dimensional Bouguer anomaly profiles (Appendix II) that were computed with an assumed subbottom density of 2.67 g/cm^3. The density value chosen is representative of granitic rocks that were sampled through dredging and described in the literature as outcrops on several islands.

The Bouguer anomaly map is dominated by a strong regional gradient reflecting the dip of the mantle beneath the continental margin. There are positive Bouguer anomalies over the Tortuga-Margarita Bank, but the large negative free-air anomalies over the Cariaco Basin have been eliminated. A local low of approximately 40 mgals characterizes the Los Roques Canyon, and a 100 mgal local low identifies with the Curacao Ridge north of Orchilla.

4. GEOLOGICAL INTERPRETATION AND DISCUSSION

4.1 The Continental Shelf

4.1.1 Regional Geology

Northern Venezuela is dominated by a complexly folded and faulted mountain system, the Caribbean ranges. These mountains trend in a general east-west (N75°E) direction and are separated into an eastern and western region by the Bay of Barcelona. The topographic lows associated with the Gulf of Cariaco on the east and the Tuy River - Valencia Lake depression on the west further divide the mountains into the

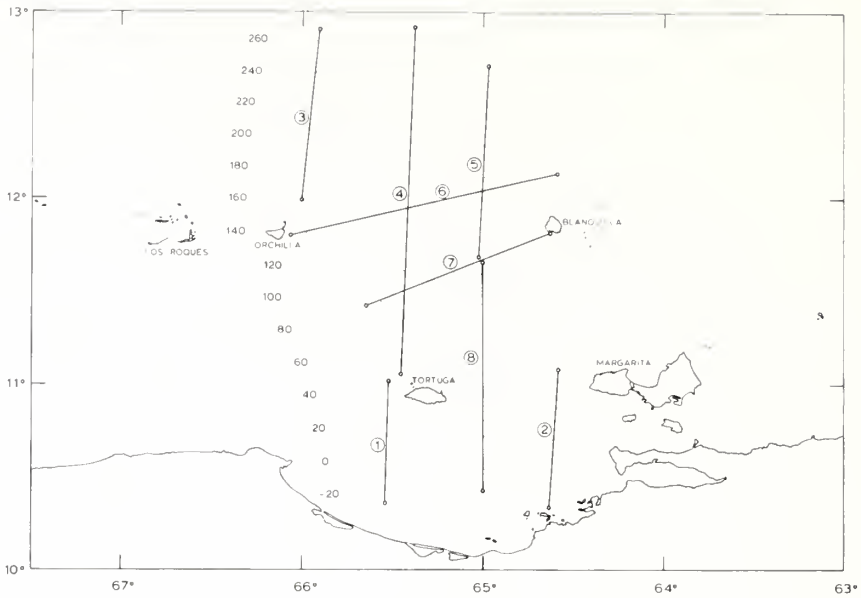

Figure 32. Location of two-dimensional Bouguer anomaly profiles, and the regional Bouguer anomaly map. Contour interval 20 mgals.

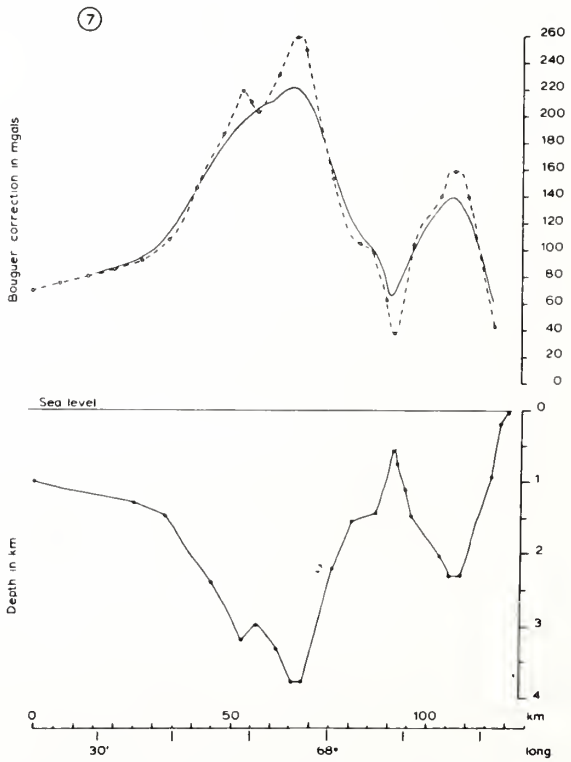

Figure 33. Comparison of "simple" (dashed line) and "two-dimensional" (solid line) Bouguer corrections.

Cordillera de la Costa on the north and the Serrania del Interior on the South.

Summaries of the geology of the area west of Barcelona Bay are contained in the works of Bell (1967), Dengo (1953), Menendez (1962, 1967), Morgan (1967), and Oxburgh (1966). Sources used for the geology of the eastern region are Mencher et al. (1953), Metz (1968a, 1968b), Rod (1956, 1959), Rod and Maync (1954), Salvador and Stainforth (1968), Schubert (1971), and Von der Osten (1955, 1957). The geology of Cubagua, Margarita, and Tortuga is from Kugler (1957), Taylor (1960), and Maloney and Macsotay (1967), respectively.

Bell (1967) distinguished eight tectonic belts in the Caribbean mountains west of the Bay of Barcelona (fig. 34). Although their ages are subject to debate, the basement rocks are considered pre-Mesozoic, and represented by the Sebastopol granitic gneiss complex and the Peña de Mora gneiss in the Cordillera de la Costa belt. These are overlain unconformably by the quartz-mica schists of the Las Brisas and Las Mercedes formations, generally believed to be Upper Jurassic to Lower Cretaceous in age (Menendez, 1967; Salvador and Stainforth, 1968). There are several amphibolite layers in the Las Mercedes formation which probably were emplaced originally as basic igneous intrusions; serpentinites occur along the contact of the two formations in the northern part of the belt (Dengo, 1953).

The El Tinaco gneisses and schists represent the pre-Mesozoic (?) basement complex in the Caucagua-El Tinaco belt. This basement is overlain by varied groups of sedimentary and metasedimentary units, ranging in age from Lower to Upper Cretaceous (Menendez, 1962, 1967).

These two tectonic belts form the Cordillera de la Costa mountains west of the Bay of Barcelona. They contain the oldest rocks exposed and a complex sequence of metasedimentary rocks that generally are called

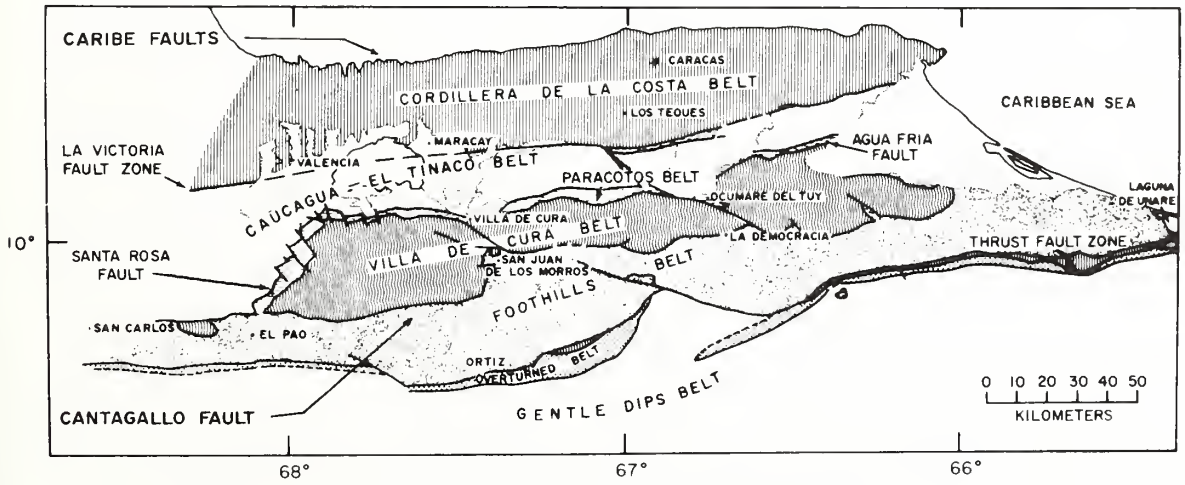

TECTONIC BELTS IN THE VENEZUELAN COAST RANGES

Figure 34. Tectonic belts of the Caribbean mountains west of the Bay of Barcelona (from Bell, 1967).

the Caracas group (Aguerrevere and Zuloaga, 1937). The Caracas group is believed to represent a thick, largely clastic sequence of marine shelf deposits that were metamorphosed in the Upper Cretaceous (Dengo, 1953; Oxburgh, 1966). The regional metamorphism of the Caracas group increases from south to north: In the southern part of the Cordillera de la Costa it is in the greenschist facies, while in the northern part the metamorphism of the Caracas group is in the epidote-amphibolite facies.

Major longitudinal fault systems border the two tectonic belts just described. These are the Caribe fault systems that terminate the Cordillera de la Costa on the north; the La Victoria fault zone that separates the two tectonic belts; and the Santa Rosa fault that borders the Caucagua-El Tinaco belt on the south. Based on the prominence and length of the linear fault traces, these have been considered primarily strike-slip faults (Smith, 1953; Rod, 1956; Alberding, 1957), but more recent interpretations emphasize that the dominant motions along these faults were vertical, and continued from the Upper Cretaceous to Holocene time (Menendez, 1967; Morgan, 1967). Cross-faults along northwest-southeast trends cut the longitudinal faults in many places. Morgan (1967) suggests that the persistence of formations along the strike direction, despite the consistent 5° to 25° plunge of fold axes, is caused by uplift along a series of repetitive high-angle cross faults.

The two major tectonic elements of the Serrania del Interior to the south of this area are the Villa de Cura belt and the Foothills belt (fig. 34). The Villa de Cura belt is a 3 to 6 km thick sequence of low grade metavolcanic rocks, that are believed to represent former submarine volcanic deposits (Bell, 1967; Menende , 1967). The sequence consists of quartz-albite-chlorite-epidote schists, quartz-albite-granulites with smaller amounts of volcanic conglomerates, metatuffs, metalavas, and metacherts (Bell, 1967). Along its southern margin it is overlain by the weakly metamorphosed basalts and gabbroes of the Tiara volcanic formation.

Menendez (1962, 1967) and Bell (1967) suggest that the Villa de Cura belt is an allochthon block, deposited in the Lower Cretaceous over the Caracas group, metamorphosed, and then moved southward during the Maestrichtian and Paleocene time across the narrow Paracotos belt, located now on its northern border. The Agua Fria and the Cantagallo faults dip under the Villa de Cura belt and represent the solethrust of the block.

The Foothills belt south of the Villa de Cura belt contains Middle Cretaceous conglomerates, lithic wackes, siltstones and shales, with pyroxene-breccia sills and serpentinites (Garrapata formation). The major part of the belt is occupied by the Paleocene sandstones, siltstones, and shales of the Guarico formation.

The Foothills belt, in essence, consists of a series of "tectonic slices", separated by north-sipping thrust faults, that were formed as the result of renewed southward gravity sliding of the Villa de Cura block in Late Tertiary time (Bell, 1967). Cross-faulting with both horizontal and vertical movements is common along northwest-southeast trends, just as it was noted in the Cordillera de la Costa.

The western part of the Eastern Venezuelan Basin, known as the Guarico sub-basin, lies south of the frontal thrust zone of the western Serrania del Interior. It contains Late Tertiary shales, mudstones, and sandstones that reach 6000 m in thickness. That the basin was overridden on the north by the southward thrusts of the Foothills belt is suggested by the numerous outcrops of the Late Eocene Roblecito formation within the Foothills belt and within the Overturned belt and thrust fault zone (Bell, 1967).

The Tertiary basin ends abruptly to the northeast at the Urica Fault (fig. 35). East of this fault extend the eastern Caribbean ranges: The eastern Serrania del Interior lies between the El Pilar fault on the north and the frontal thrust faults on the south; to the north of the El Pilar fault the eastern Cordillera de la Costa occupies the narrow coastal region.

The eastern Serrania del Interior and the small offshore islands between Barcelona and the mouth of the Gulf of Cariaco are dominated by Lower Cretaceous quartzose sandstones (Barranquin formation), massive biostromal limestones (El Cantil formation), and alternating sandstones,

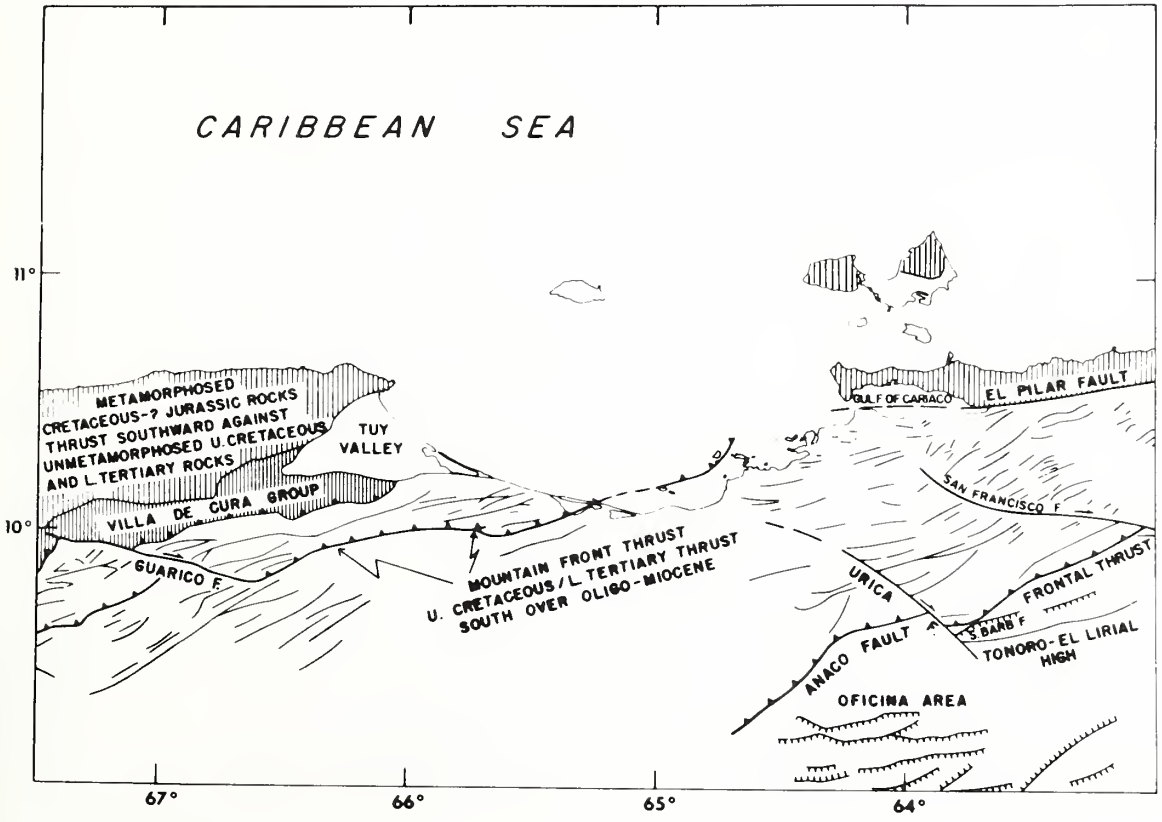

Figure 35. Structural elements in northeastern Venezuela (from Salvador and Stainforth, 1968).

limestones, and shales (Chimana formation) (Metz, 1968b). Early Upper Cretaceous limestones and cherts (Querecual formation) were almost entirely stripped during an intra-Senonian folding and erosion. Maestrichtian and Paleocene massive sandstones (San Juan formation) and shales and marls (Vidoño formation) were subjected to erosion together with the earlier Cretaceous rocks since Late Eocene or Early Oligocene time (Metz, 1968b).

The eastern Cordillera de la Costa is an anticlinorium which consists of Lower Cretaceous garnet-epidote schists, quartz-mica schists, and calcareous schists that are similar in many respects to the Caracas group of the western Cordillera de la Costa (Christensen, 1961; Schubert, 1971). In the Araya Peninsula the Guamache formation (fig. 36) represents the oldest and most metamorphosed rocks (epidote-amphibolite facies; Schubert, 1971); the Carupano and Tunapui formations represent greenschist facies metamorphism and were compared to the Las Mercedes and the Las Brisas formations by Christensen (1961). Serpentinites and serpentinized periodotites are found in numerous localities near the contact of the Laguna Chica and Carupano formations (Schubert, 1971).

The regional strike of the folding is east-northeast in both the Cordillera de la Costa and the Serrania del Interior, suggesting compression and thrusts from the north-northwest. While the motion along the longitudinal fault system that separates the metamorphic formations of the Araya Peninsula was essentially vertical (Schubert, 1971), Christensen (1961), Salvador and Stainforth (1968), and Metz (1968a) believe that a large southward thrust placed the metamorphic rocks of the Araya and Paria Peninsula in contact with the Cretaceous sedimentary rocks of the Serrania del Interior in Late Eocene time.

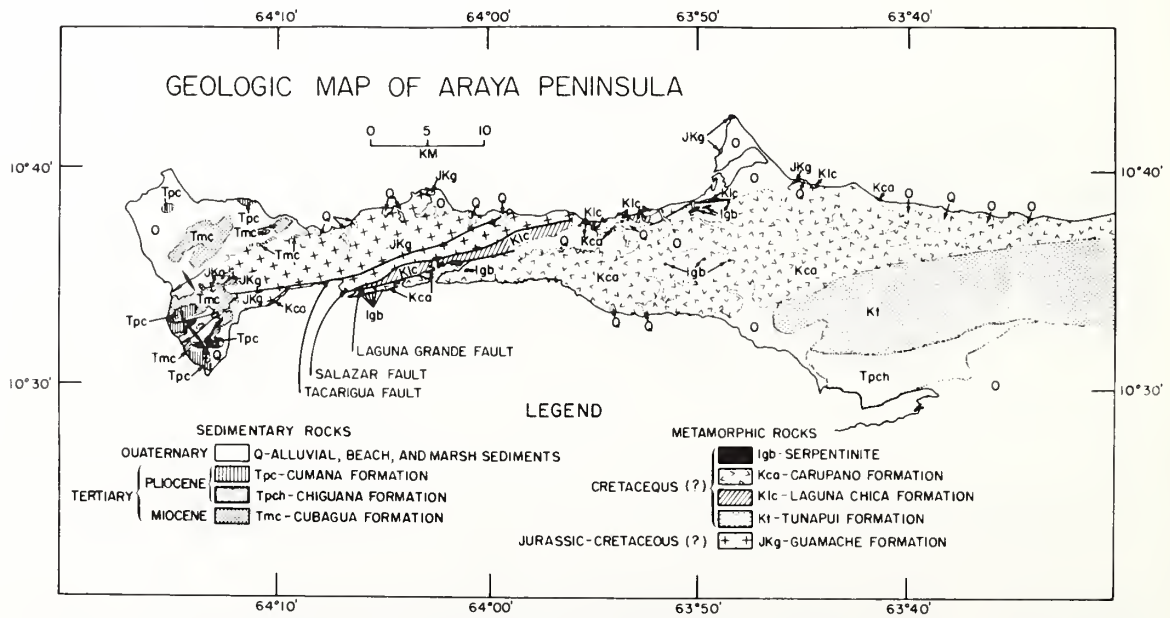

Figure 36. Geologic map of the Araya Peninsula (from Schubert, 1971).

Contrary to earlier interpretations suggesting large right-lateral motions along the El Pilar fault system (Liddle, 1946; Rod, 1956; Alberding, 1957), it may have originated as part of the southward thrust (Salvador and Stainforth, 1968). According to Metz (1968a), however, the motions were essentially vertical along the El Pilar fault system (less than 15 km right-lateral component) and related to Late Tertiary orogenic processes.

Crossfaulting along a northwest-southeast trend is common also in the eastern Caribbean ranges. Motion along the two major cross-faults of the area, the Urica and San Francisco faults, has been dominantly right-lateral, and related to the orogenic episodes (folding and uplift) between the Cretaceous and Miocene times (Rod, 1959). Salvador and Stainforth (1968) report that significant right lateral motions took place along the Urica fault during the Late Miocene and Pliocene, while no post-Eocene motions are noted along the San Francisco fault.

North of the Araya Peninsula the island of Cubagua represents the exposed part of an anticline composed of several thousand meters of Tertiary sediments (Kugler, 1957).

North of Cubagua, the northern part of the eastern island of Margarita and most of the western island (also called Macanao) are underlain by a metasedimentary and metavolcanic sequence that was intruded by both granitic and ultramafic rocks (Taylor, 1960). The oldest rocks belong to the presumably Upper Jurassic to Lower Cretaceous Juan Griego group that, although more metamorphosed than the Caracas group of the western Cordillera de la Costa, may represent its equivalent on Margarita. Major orogenic deformation, metamorphism, and the intrusion of the ultramafic rocks occurred in mid-Upper Cretaceous (?), followed in mid-Maestrichtian time by another deformation and milder metamorphism (Los Robles group). Paleocene and Lower Eocene sediments were mostly eroded during a Middle Eocene uplift that was followed by rapid subsidence and the accumulation of at least 2000 m of Upper Eocene limestones, conglomerates, and shales (Punta Carnero formation). A milder deformation folded these rocks during mid-Miocene, but sediment accumulation continued throughout the remainder of the Tertiary. Uplift and faulting reoccurred during the Pleistocene and Holocene times (Taylor, 1960).

The trend of the fold axes in Margarita is generally southwest-northeast. Northwest-southeast trending faults are commonly normal faults, whereas many of the east-west faults are high angle reverse faults (Kugler, 1957; Taylor, 1960).

West of Margarita, on the island of Tortuga only Pliocene marls and Pleistocene coral reefs and associated clastic limestones are exposed. The available structural data suggest a possible northward tilting of the island during Late Pleistocene time (Maloney and Macsotay, 1967).

4.1.2 Discussion

Geologic units of the continental shelf are tentatively identified on the basis of the relationship of their apparent physical characteristics to those of the known rock formations exposed on the adjacent land

areas. Where possible, a more direct correlation is made through the extension of the exposed geologic units along trends of topography or structure or both.

The best examples for the extension of the land geology to the shelf are seen east of 65°W. The El Pilar fault, located near the contact of the metamorphic rocks of the Araya Peninsula and the more competent rocks of the eastern Serrania del Interior (Metz, 1968a), extends westward from Cumana and forms the southern boundary of the eastern deep of the Cariaco Basin. The offshore portion of the El Pilar fault resembles a north dipping normal fault (Profiles 5 and 7, fig. 8), as suggested by Ball et al. (1971). The presence of the competent Lower Cretaceous sedimentary rocks (Barranquin and El Cantil formations) south of the El Pilar fault is indicated by the lack of reflectors below the southern wall of the Cariaco Basin on Profile 7, the presence of a strong "basement type" reflector on Profile 5, the absence of magnetic anomalies, and by the small positive Bouguer anomalies (figs. 29, 31, and 37).

The writer believes that the metamorphic rocks of the Araya Peninsula, like the Caracas and Juan Griego groups, have igneous intrusives associated with them. These underlie the northern edge of the peninsula and are responsible for its westward topographic extension on the shelf.

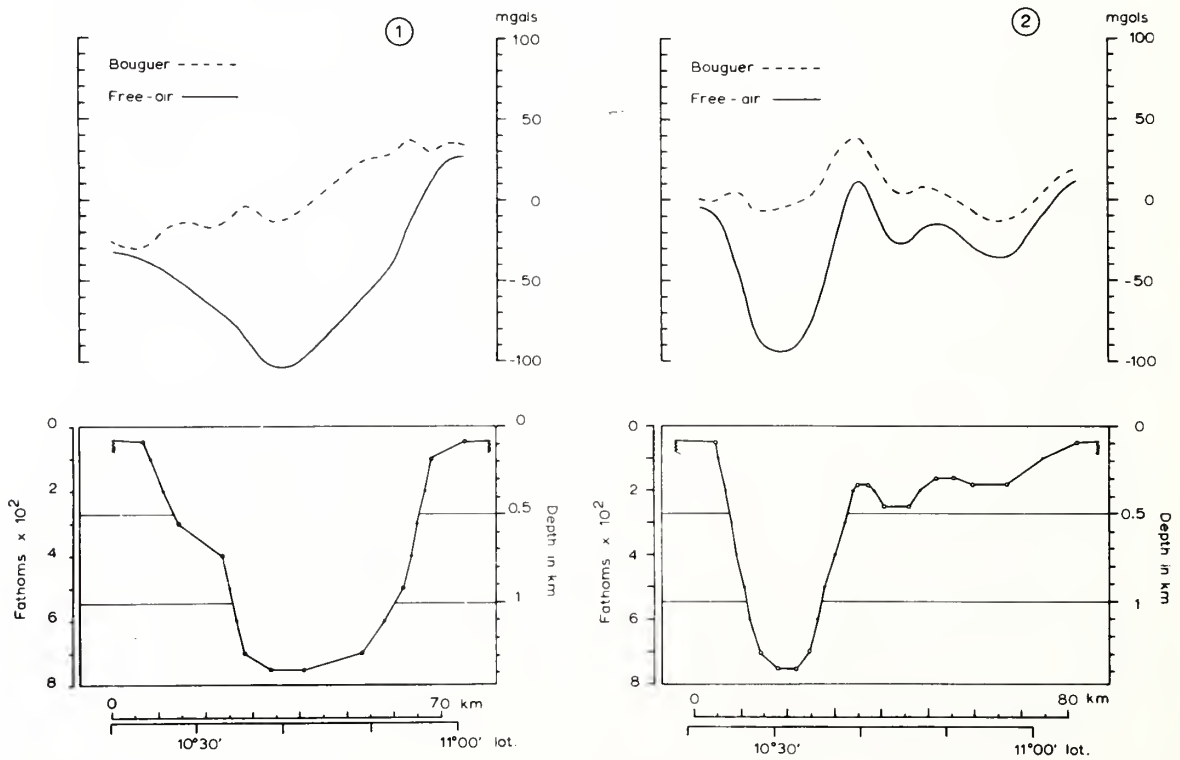

Figure 37. Comparison of gravity anomalies across the eastern and western deeps of the Cariaco Basin (see fig. 32 for location).

This conclusion is supported by the fact that a topographic high extending from the northern edge of the peninsula (fig. 5) is associated with a +38 mgal Bouguer anomaly and two of the largest magnetic anomalies (one approximately 600 γ, the other 550 γ) observed in the area of the shelf (fig. 29).

From model studies of the magnetic anomaly west of the Araya Peninsula, Ball et al. (1971) concluded that the magnetic effect of a 5 km wide, 15 km long igneous body located 2 km below the surface gives the best fit of the observed anomalies. The close similarity of this anomaly to the one directly north of the tip of the Araya Peninsula (fig. 29) suggests a similar interpretation for that area. Ball et al. (1971) suggest that the two structures responsible for the magnetic anomalies might have been offset by a left-lateral fault. The relatively low magnetic values between the two major anomalies may suggest, however, that the anomalies belong to two separate intrusions, emplaced along a same east-northeast structural trend that characterizes the peninsula.

The igneous basement cannot be detected on Profile 7 because of inadequate penetration. The massive well-bedded strata overlying the Araya block most likely represent the Tertiary and Quarternary sediment cover. The 300 m thick layer on the southern slope of the Araya block characterized by mostly incoherent internal reflectors may represent the westward extension of the metamorphic schists of the Guamache formation (fig. 36). The fault contact between the inferred metamorphic rocks and the younger sediments in the eastern deep of the Cariaco Basin could be the extension of the Salazar or Laguna Grande faults. The Carupano formation, which is located south of this fault contact on the Araya Peninsula, has been apparently downfaulted along a cross-fault between Profile 7 and the eastern slope of the basin (location of this fault must be west of Line 2, fig. 6 of Ball et al., 1971, where the entire metamorphic {?} sequence of the Araya Peninsula abuts the El Pilar fault).

Another cross-fault is suggested between Profile 7 and Profile 5 (fig. 8). On Profile 7 the seismic reflectors indicate a sinking basin with over 700 m of well stratified sediments south of the inferred Salazar fault, whereas on Profile 5 there is no indication of the "Salazar fault", and the reflectors show gently arched sediments below the floor of the basin, with no reflectors below 150 m. A cross-fault with a down-to-west displacement could explain the different tectonic conditions in the two halves of the eastern deep as well as the disappearance of the metamorphic rocks under the basin floor, and the elimination of the Araya block as a topographic high. The faults at the northern margin of the basin floor (10°35'N) and at 10°43'N on Profile 5, however, are probably still related to the Araya block.

Profile 3 (fig. 8) across the saddle between the two deeps of the Cariaco Basin shows no indication of either the El Pilar fault or the faults that were seen associated with the edges of the Araya block in Profile 5. The Bouguer anomaly is -38 mgal near the southern end of this profile (Line 8, Appendix II), as opposed to the small but positive values measured to the east.

This fact suggests that the relatively dense, competent Lower Cretaceous rocks do not extend this far west. The writer suggests that the Urica fault that forms the border between the eastern Serrania del Interior and the Eastern Venezuelan Basin southwest of Cumana extends northwestward from the area of Cumana and forms the western limit of the El Pilar fault and the Araya block. The Urica fault also cuts the Cariaco Basin into two halves, and may be responsible for the relative right lateral offset of the eastern and western deeps (fig. 38).

The series of north-dipping normal faults north of the Araya block (Profile 7, fig. 8) are probably part of the "coastline fault system", noted farther to the east by Lattimore et al. (1971). To the north of these faults the Cubagua and Punta Arenas highs appear to have a complex structure: Profile 7 and the seismic reflection work of Ball et al. (1971) suggest that either the Tertiary sediments of Cubagua were uplifted by a basement fault block, or these sediments were draped over the basement horst. A westward plunge of the Cubagua basement block with greater uplift along its northern bordering faults (southward tilting) could explain the more faulted appearance of the Cubagua high to the east (on Line 2, Ball et al., 1971), and the existence of the faults between the Cubagua and Punta Arenas highs on Profile 7. Southward tilt-

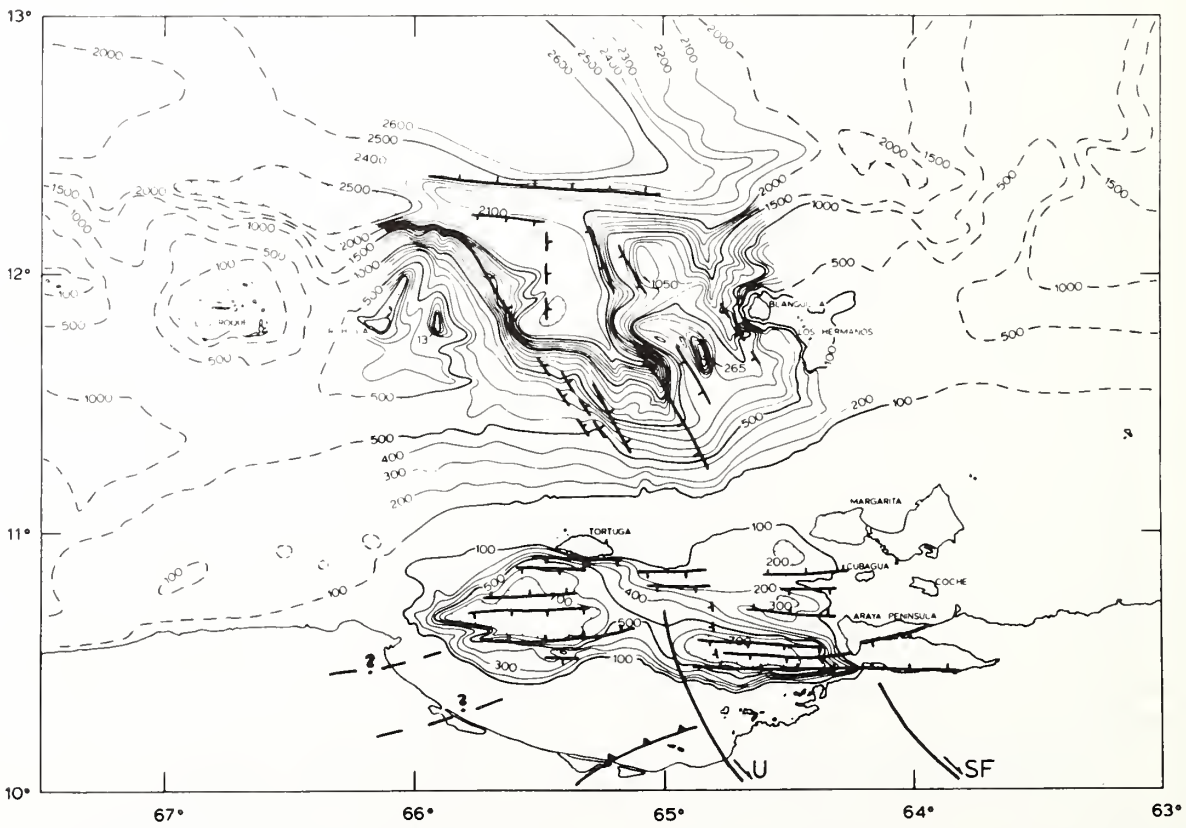

Figure 38. Principal faults of the Venezuelan continental margin in the study area.

ing was suggested not only for the Cubagua high but also for the Araya block because of the apparent southward dip of the overlying sediments (Ball et al., 1971).

The 80 γ magnetic anomaly associated with the Cubagua high may be related to this proposed basement fault block. The wavelength of this anomaly is similar to that of the Araya block, suggesting same depth to source, but its smaller amplitude indicates a much weaker magnetic material, possibly one that consists of metamorphic rather than basic igneous rocks.

Although numerous faults occur on the shelf directly south of the Tortuga-Margarita Bank, none of those in Profile 5 can be correlated with certainty with faults on Profile 7 (fig. 8). Also, with the exception of the faults at 10°47'N and 10°50'N, the faults on Profile 5 cannot be correlated with those on Profile 3; however, the character of the reflectors is very similar in each profile in this area of the shelf and closely resemble the reflectors around the Cubagua high. It is suggested, therefore, that these massive stratified sediments represent a Late Tertiary sequence, similar to that drilled on Cubagua Island (Kugler, 1957).

The resemblance of the reflective characteristics and faulting of the sediments on the gentle slope south of the Tortuga-Margarita Bank (Profile 3, fig. 8) and in the northern half of the western deep of the Cariaco Basin (Profile 2, fig. 8) is also striking. The writer concurs with the interpretation of Maloney and Macsotay (1967) that the relatively steep submarine slope south and southwest of Tortuga is a faultscarp and proposes that along this fault part of the former shelf of this area has been subsided. This former shelf now underlies the northern half of the western deep of the Cariaco Basin and is responsible for its anomalous width.

The southern edge of the down-faulted shelf is underlain by a basement ridge at 10°43'N that extends westward from Profile 2 (fig. 8) to just north of Cabo Codera. This ridge probably consists of igneous rocks and is outlined by the +100 γ isogama line over the western deep and a +300 γ magnetic anomaly north of Cabo Codera (fig. 29). The suggested down-faulting of the shelf is supported by the reduced amplitude and broadened wavelength of the magnetic anomalies associated with the igneous ridge.

South of the subsided shelf lies the main graben of the western deep of the Cariaco Basin (Profile 2, fig. 8). The rocks that form the southern slope of the western deep between 10°32'N and its boundary fault (10°37'N), characterized by incoherent internal reflectors, may represent the eastward extension of more competent sedimentary or metamorphic rocks, possibly associated with the Villa de Cura belt. These rocks probably extend farther eastward to Profile 3 (fig. 8), where they abut the massive stratified sediments of the slope of the Tortuga-Margarita Bank at 10°37'N.

Direct interpretation of the seismic reflection data in terms of the geology of the western Caribbean mountains is difficult because the most useful aides in correlation, the known fault trends separating the major tectonic elements, cannot be traced from the continent into the shelf. With the aid of gravity and magnetic data, however, it is pos-

sible to suggest that certain elements of the major tectonic belts (Bell, 1967, fig. 34) do extend eastward into the Bay of Barcelona.

The best example is a -38 mgal Bouguer anomaly minimum (outlined by the -20 mgal isogal in fig. 31) southwest of the central sill of the Cariaco Basin. As this gravity minimum coincides with the projected trend of the Foothills belt (Bell, 1967, fig. 34), the writer suggests that it represents the extension of the thick Tertiary sedimentary sequence of the Foothills belt into the Bay of Barcelona. The lack of magnetic anomalies in this area also supports such an interpretation.

North of the Foothills belt the metavolcanic sequence of the Villa de Cura belt contains rocks with higher magnetization and susceptibility. The gentle northward increase of the regional magnetic anomaly west of 65°W could be related to this magnetic property of the underlying rocks. The magnetic data, and the small negative Bouguer anomaly values are consistent with an interpretation suggesting the seaward extension of the Villa de Cura belt. Short-wavelength magnetic anomalies that might be expected over the small flows and intrusions associated with the Villa de Cura sequence are probably not seen because of the burial of these rocks below the sea floor (rocks tentatively identified on the seismic profiles as metamorphics outcrop on the southern wall of the sill and the western deep below 750 m), although the small undulations of the 50 γ isogamma line could be related to them.

4.2 Island Platforms - Los Roques Canyon

4.2.1 Regional Geology

The Orchilla and the Blanquilla platforms, separated by the Los Roques Canyon, are the two eastern members of a series of island platforms located north of Venezuela between the continental shelf and the Venezuelan Basin. The geologic framework of the islands is similar in many respects: The oldest rocks dated are Cretaceous intrusives of intermediate composition which are associated with volcanic or metamorphic rocks, and overlain commonly by limestones of Quarternary age (Lagaay, 1969; Rutten, 1939, 1940).

The variety of igneous intrusive rocks which comprise these offshore platforms is illustrated by the reconnaissance of Orchilla by Schubert (1970), who found quartz-diorites associated with quartz-mica schists and diabase on the extreme northwestern edge of the island of Orchilla (fig. 39) and amphibole-schists, intruded by granite-gneiss, on the eastern part. In the central part of Orchilla an ultrabasic complex consisting of serpentinized gabbroes and possibly peridotites was mapped. This igneous-metamorphic complex is covered by Quaternary sediments, among them numerous reefs elevated to 3-4 m (Schubert, 1970).

The oldest known rocks on the Blanquilla Island are the hornblende-quartz-diorites and biotite granodiorites of the Garanton Stock (Maloney, 1968), exposed near the western and southern margin of the island (fig. 40). Rutten (1931), Zuloaga (1953), Maloney (1968), and Schubert (1969a) described hornblende dioritic-gabbro, granitic pegmatite, diorite-hornblendite, amphibole-gneiss, schists and quartzites on the island of the Los Hermanos.

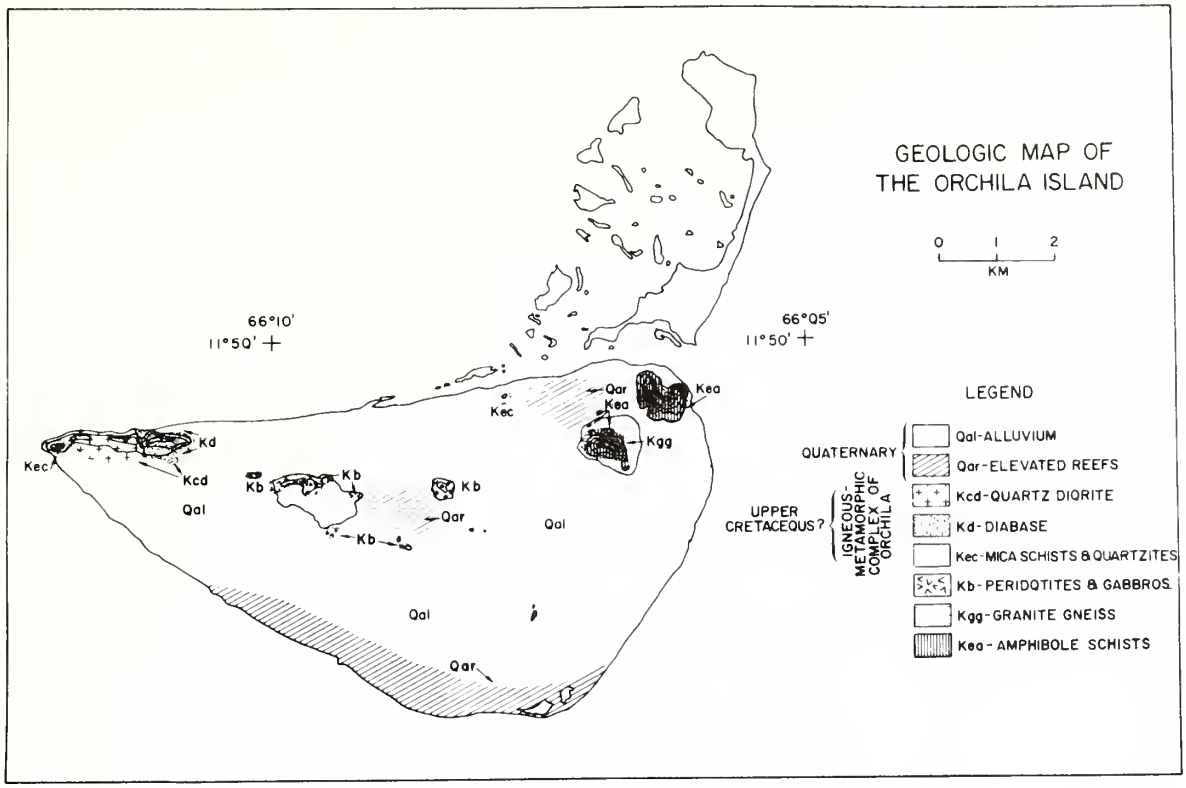

Figure 39. Geologic map of Orchilla Island (from Schubert, 1970).

On the basis of the similarity of the Garanton Stock and the quartz-diorites of Aruba, Rutten (1931) suggested that they are probably of the same age. Isotopic age determinations (Rb-Sr and K-Ar) made on the biotites of the quartz-diorites of Aruba gave 73±3 m.y. for the formation of these rocks (Priem, et al., 1966). Whole-rock K-Ar age determinations on similar rocks in Curacao gave 72±7 m.y. (Priem, 1967).

The central and eastern part of Blanquilla Island is covered by coralline limestones of Pleistocene and Recent age (Maloney, 1968). Based on the elevations of terraces in the southwestern part of Blanquilla Island and on their dip towards the northeast, Maloney (1968) suggested that the island was tilted to the northeast in the Pleistocene.

Although faults or folds were not reported from Blanquilla Island, there are numerous east-west and northwest-southeast trending faults on Los Hermanos islands (Maloney, 1968; Schubert, 1969a).

The writer dredged the talus material off the southwest tip of Blanquilla Island and recovered quartz-diorite, quartz-monzonite, metabasalt, and marble. Another dredge haul from the western slope of the seamount southwest of Blanquilla Island (11°41'N, 64°54'W) yielded graphic granite, amphibole-biotite granite, quartz-diorite, and granodiorite. An age of 81 m.y. was determined by K-Ar measurements on the

biotite of the granite (see Appendix III), which is in close agreement with the age of the other batholitic rocks of the island chain.

4.2.2 Discussion

An acoustic basement and a "granitic" basement have been tentatively identified in the presentation of the seismic reflection profiles of the Orchilla and Blanquilla platforms. Reflectors that characterize the acoustic basement were observed in many places on the island platforms below the well stratified and the acoustically transparent sediments. These reflectors appear to crop out also on the northern slope of the platforms and on the walls of the Los Roques Canyon. On the other hand, reflectors that were interpreted to represent the "granitic" basement appear to be restricted to individual dome-shaped structures on both platforms.

The identification of the dome-shaped structures as "granitic" basement is supported by the following data: (1) The outcrop of one such structure sampled on the Blanquilla platform yielded granitic rocks; (2) "granitic" plutons are known to exist on the adjacent islands; and (3) magnetic anomalies are generally restricted to those parts of the platforms where these structures are present (fig. 27).

The writer, therefore, suggests that not only the islands but also the submerged parts of the Orchilla and Blanquilla platforms are underlain by "granitic" intrusives of Upper Cretaceous age. The irregular acoustic basement probably represents the older, more competent sedimentary rocks that were affected by the emplacement of the igneous intrusions. The subdued surface of the acoustic basement and the plutonic rocks penetrating through it suggest that a major uplift and subaerial erosion followed the emplacement of the plutons. The massive stratified sediment overlying the acoustic basement and the plutonic rocks probably represent Late Tertiary sediments deposited after the subsidence of the platforms.

It has been shown on the seismic reflection profiles that the Los Roques Canyon, which separates the Orchilla and Blanquilla platforms, is a major graben whose bordering faults are still active. These faults strike northwest-southeast (fig. 38), the same as the principal cross-faults of the Caribbean mountain system to the south. The canyon is the only major structure that intersects the Aruba-Orchilla-Blanquilla island chain; that it is also located at the seaward extension of the most significant discontinuity of the Caribbean mountain system, the abrupt termination of the eastern Serrania del Interior along the Urica fault, suggests that its formation may be genetically related to this discontinuity.

Seismic Profiles 10 and 12 (fig. 22) and the residual Bouguer anomalies (fig. 41) indicate that the main graben of the canyon lies east of 65°30'W. The smooth floor of the canyon west of 65°30'W is underlain by the downfaulted acoustic basement of the Orchilla platform.

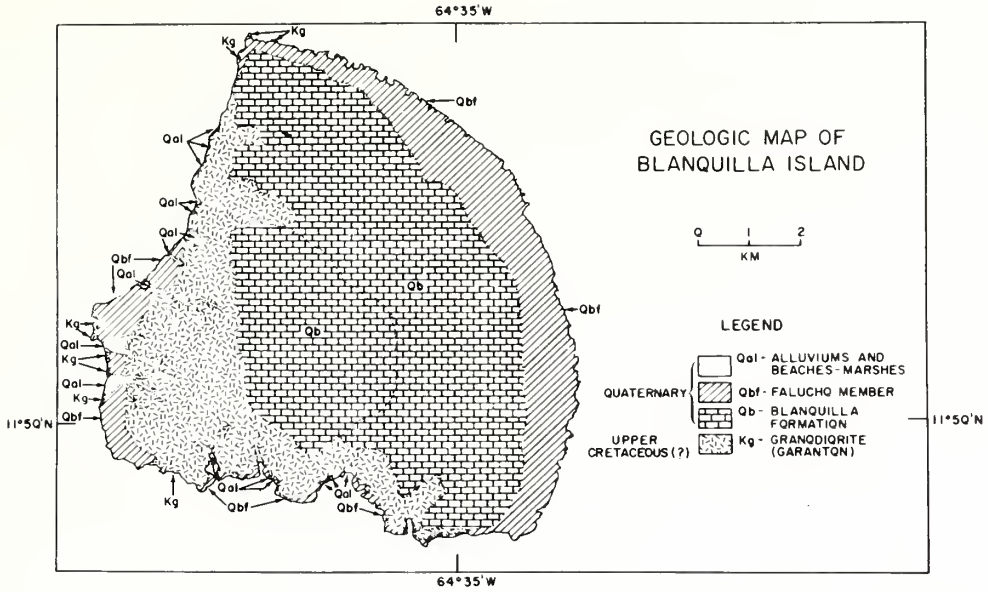

Figure 40. Geologic map of Blanquilla Island (after Maloney, 1968, and Schubert, 1969b).

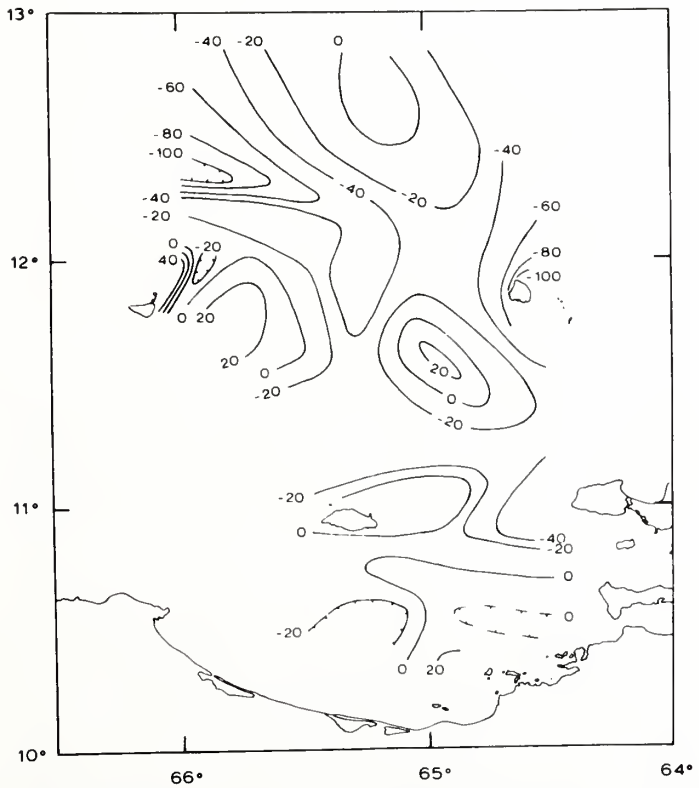

Figure 41. Residual Bouguer anomaly map of study area. Contour interval 20 mgals. Regional field removed from the Bouguer anomaly map (fig. 31) is shown on figure 32.

In the southern part of the Los Roques Canyon there are two narrow "V" shaped valleys within the main depression of the canyon. The lack of the well stratified Late Tertiary to Recent (?) sediments in this area suggests that erosional processes are currently active here. To the north, the floor of the canyon is flat because of sediment fill. The eastward extension of the Curacao Ridge apparently forms a dam against which the sediments carried down the canyon are ponded and restricted from flowing into the Venezuelan basin. Profile 1 (fig. 18) suggests that the downfaulted base of the Orchilla platform and the extension of the Curacao Ridge merge north of the platform and form a sill between the Los Roques Canyon and Los Roques Trench. This prevented also the sediment flow from the canyon into the trench, until the sediments filled the canyon floor and spilled over the sill.

Erosion and slumping are indicated in the northern part of Blanquilla Canyon (fig. 22), whereas the center part is being filled with sediments (fig. 21) derived from the Blanquilla platform as well as from the area of the head of the canyon.

4.3 Southeast Margin of the Venezuelan Basin

4.3.1 Regional Geology

The general structure and distribution of the sediments in the Caribbean Sea and the identification of the major reflecting horizons have been established through an extensive program of seismic reflection and refraction measurements (Ewing et al., 1967; Edgar, 1968). Ewing et al. (1967) identified two prominent reflecting horizons that can be traced throughout most of the Caribbean Sea. The upper horizon was called A", the lower horizon B" because of their similarity to the prominent reflectors of A and B in the Atlantic (J. Ewing et al., 1966), A' and B' in the Pacific Ocean (M. Ewing et al., 1966).

Edgar (1968) noted that on the seismic system used during his survey, horizon A" in the Venezuelan Basin appears as the top reflector of a sequence of two or three closely spaced horizons, and horizon B" as a reflector with coherent, smooth surface, which was the deepest recorded in the basin. An approximately 500 m thick acoustically transparent layer is present above A", which together with a similar layer (approximately 400 m thick) between A" and B" are termed the Carib beds (Ewing et al., 1967; Edgar, 1968).

From coring (Ewing et al., 1967; Edgar, 1968) and deep sea drilling (JOIDES, 1969) A" has been identified as a chert or cherty limestone layer, overlain by Lower Eocene radiolarian ooze. Ewing et al. (1967) suggested that A" may represent the Mesozoic-Cenozoic boundary, and extrapolating the sedimentation rate established above A", they inferred that B" could represent the Paleozoic-Mesozoic boundary. The Carib beds were interpreted as pelagic sediments or very fine-layered turbidites, that would appear as acoustically transparent layers on the seismic reflection records.

The Carib beds and A" and B" were observed to dip under a thick sequence of well stratified turbidites on the northern and southern margin of the Venezuelan Basin; to the east these layers conformably overlap the lower flank of Aves Ridge (Ewing et al., 1967).

4.3.2 Discussion

The three seismic reflection profiles (fig. 24) across the southeast margin of the Venezuelan Basin indicate an approximately 700 to 900 m thick sequence of massively stratified, horizontally bedded sediments that are similar to those identified as turbidites on a profile made by Ewing et al. (1967) to the west of this area. The turbidite sequence abuts sharply the Curacao Ridge to the south, while to the east it onlaps the lower flank of the Aves Ridge (see Profile 3, fig. 24; Profile 8, fig. 26).

Profile 8 and the northern portion of Profile 3 clearly show that below the turbidites there is an acoustically transparent layer, approximately 600 m (0.6 sec) thick, which is underlain by a prominent sequence of reflectors. The latter consists of a thick (150-200 m), irregular band, characterized by incoherent reflections, underlain by two sharp horizons, approximately 100 m apart. Based on the description of the character and general occurrence of the Carib beds and A" (Ewing et al., 1967; Edgar, 1968), the writer suggests that the acoustically transparent layer below the well stratified sequence corresponds to the upper Carib bed, and the underlying prominent group of reflectors represent A".

Because the western end of Profile 8 joins the northern end of Profile 2 (see figs. 2, 7, and 14), the upper Carib bed and A" can be correlated and extended southward despite an apparent change in character of the seismic record, which is due mostly to the different noise conditions brought about by the new heading of the ship. The broad incoherent upper reflector of A" cannot be distinguished on the profiles of figure 23 because of the background noise of the record; but the acoustically transparent layer and the two sharp lower horizons of A" can be distinguished on Profile 2. The acoustically transparent layer is also evident on Profile 1 and Profile 3, and the reflectors that resemble the lower horizons of A" are present near the contact of the sedimentary sequence with the base of the Curacao Ridge and the Blanquilla platform.

Both Profile 1 and Profile 2 indicate that the eastward extension of the Curacao Ridge contains strongly folded sediments (fig. 24). The well stratified sediments on the top of the Curacao Ridge in Profile 2 suggest that the sediments have been carried directly to the Venezuelan Basin from the Los Roques Canyon before an uplift of the ridge took place. An apparent fault contact between the Curacao Ridge and the sediments of the Los Roques Canyon (Profile 2, fig. 24) and upward arching of A" and the upper Carib bed support the proposed uplift of the ridge.

Both the free-air (fig. 30) and the residual Bouguer (fig. 41) anomaly maps indicate that the major bulk of the sediments of the Curacao Ridge (Edgar, 1968) lies west of 65°30'W. The northward swing of the Bouguer anomaly isogal lines (fig. 31) northwest of Blanquilla may be attributed to the eastward plunge of the mantle under the flank of the Aves Ridge.

4.4 Crustal Structure of the Venezuelan Continental Margin

4.4.1 Evidence from Seismic Refraction Data

Refraction data in the area of the Venezuelan continental margin exhibit a large variation of seismic velocities (Edgar, 1968). Measurements in the Venezuelan Basin indicate a 1.9 km/sec velocity for the sediments above A" and 2.7 km/sec velocity for the sediments between A" and B". The velocity of the turbidites in the Bonaire Basin and elsewhere on the continental margin falls in the 1.9 - 2.1 km/sec range. A layer of sediments with a velocity range of 3.9 - 4.2 km/sec underlies the low velocity sediments of the Venezuelan Basin and forms the bulk of the sediments under the Curacao Ridge (fig. 42). The large negative gravity anomalies could, in large part, be attributed to these sediments on the Curacao Ridge. The presence of 5 km thick, combined low and high velocity sediments north of the Blanquilla platform (Edgar, 1968) can explain the gravity minimum in that area.

In the area of the island platforms the seismic velocities of the rocks underlying the surface sediments range between 5.1 - 5.8 km/sec, which is expected for the "granitic" rocks that were dredged on the Blanquilla platform, and were indicated under the platforms by the magnetic, gravity, and seismic reflection data.

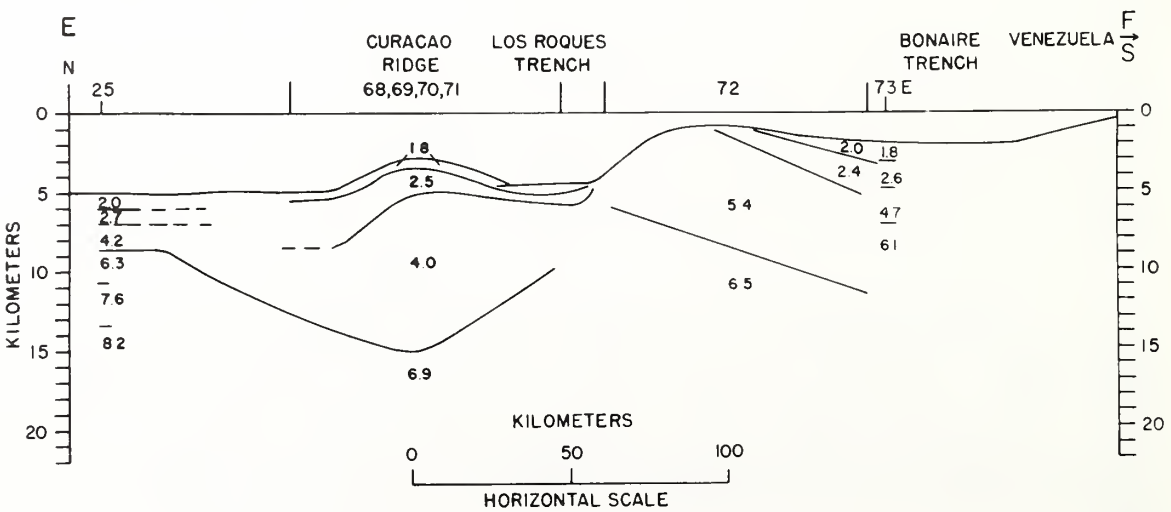

Figure 42. Composite seismic refraction section across the Venezuelan continental margin (from Edgar, 1968).

A velocity of 5.8 km/sec was recorded 1 km below the surface sediments on a refraction profile run directly east of Tortuga Island (Officer et al., 1957). The absence of a major magnetic anomaly over the Tortuga-Margarita Bank does not allow an interpretation that would assign an igneous basement to this seismic velocity 1 km below the surface of the bank. The reflector may indicate a small acidic igneous intrusion, a very competent limestone, or metamorphic rocks.

The crustal velocities under the continental margin range from 6.1 to 6.9 km/sec (fig. 42), while under the Venezuelan Basin there is a two layered crust: The upper crustal layer has an average velocity of 6.3 km/sec, the lower crustal layer, of 7.6 km/sec (Edgar, 1968). A mantle velocity of 8.2 km/sec was measured on a refraction profile run in the southeastern Venezuelan Basin; under the continental margin mantle arrivals were not recorded (Edgar, 1968).

4.4.2 Crustal Thickness of the Venezuelan Continental Margin

A first approximation of the thickness of the crust was made along a section normal to the shoreline by matching a Bouguer anomaly profile with a crust-mantle interface, determined at one end of the section by a seismic refraction line located approximately 170 km northwest of the study area (station 25; fig. 42). The technique follows that of Woollard (1959) and Talwani et al. (1959).

For the computation of the crustal section (fig. 43) a two-dimensional Bouguer anomaly profile was used (combined from Profile 1 and Profile 4; fig. 32 and Appendix II). For the area of the seismic section a simple Bouguer anomaly was computed (ρ crust = 2.67 g/cm^3) by using an assumed free air anomaly value of -20 mgal (reported as an average for the Venezuelan Basin: Edgar, 1968). The regional Bouguer anomaly was determined by inspection (see dashed line in fig. 43), and was extrapolated along the same gradient northward until it matched the Bouguer anomaly computed for the area of the seismic refraction profile. It is assumed that the crust-mantle interface at the continental margin is a simple dipping surface whose angle of dip can be determined, if the crust-mantle density contrast is known, by computing the gravitational attraction of various mantle surfaces until a match with the regional Bouguer anomaly is obtained. A key assumption of this technique is that no lateral density variations exist either within the crust or the mantle.

The densities used for the computation were determined on the basis of the crustal and mantle velocities determined at the seismic section (Nafe and Drake, 1963), and are shown in figure 43. Alternates are given there also to illustrate the change in mantle depth in response to different crust-mantle density contrasts.

The results indicate that if the assumptions used in the computation are valid then the mantle is at a depth of 28 km under the Tortuga-Margarita Bank and at 37 km under the shoreline (fig. 43).

If it is assumed that the Bouguer anomalies, with the exception of the short-wavelength variations ($<$ 10 km), reflect only the depths of

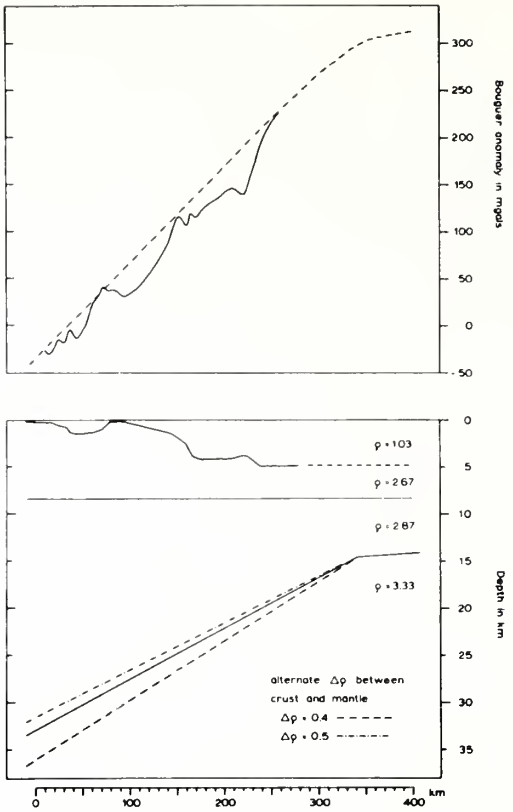

Figure 43. Crustal thickness profile of the Venezuelan continental margin. Upper half: solid line = two-dimensional Bouguer anomaly profile; dashed line = regional Bouguer anomaly profile. Lower half: bathymetric profile and crust-mantle interfaces, as computed using three different density-contrast values.

the mantle without any contribution from crustal and mantle density variations, a contour map can be prepared showing the depth below sea level to the top of the mantle (fig. 44).

Based on the crustal section (fig. 43), the deviation of the Bouguer anomalies (fig. 31) from the regional Bouguer anomalies (fig. 32) can be expressed in terms of depth differences (from fig. 43, a 50 mgal change of the regional Bouguer anomaly equals to a 3 km change in depth).

The mantle surface contours (fig. 44) north of 12°30'N are in close agreement with those made by Edgar (1968) on the basis of refraction profiles. The sharp northward curve of the depth contours north of Blanquilla Island probably reflects the eastward plunge of the mantle under the flank of the Aves Ridge. The mantle depth below the Blanquilla platform is in agreement with the bathymetric data in that both suggest that the Blanquilla platform is a southwestern extension of the Aves Ridge.

The 2 km depression indicated over the Curacao Ridge (fig. 44), the isolated high east of Tortuga Island, and the low in the western half of the Bay of Barcelona are probably not real, since geophysical measurements suggest that density changes within the crust cause the

Bouguer anomaly variations in these areas. The depression below the Los Roques Trench, on the other hand, is most likely real because the seismic measurements in this area do not indicate low crustal densities that could account for the Bouguer anomalies (Edgar, 1968).

4.5 Tectonic Elements of the Island Arc

The major tectonic elements associated with the southern half of the Lesser Antilles Island Arc are: (1) The Barbados Ridge; (2) the Tobago Trough; (3) the volcanic island arc; (4) the Grenada Trough; and (5) the Aves Ridge (Bunce et al., 1970; Weeks et al., 1971). As each of these features approach the shelf of the South American continent, they become indistinguishable and can be followed only through the geophysical anomalies associated with them.

The Barbados Ridge, the easternmost element of the island arc (see fig. 3), is characterized by a major negative free-air anomaly belt that has been traced southwestward into Trinidad and then into the Eastern Venezuelan Basin (Talwani, 1966; Bush and Bush, 1969; Bassinger et al., 1971).

The southwestward extension of the Tobago Trough is manifested in a shallow depression of the Trinidad-Venezuela shelf and a second belt of negative free-air anomalies. This belt is separated from the negative gravity anomalies of the Barbados Ridge by a weak positive trend associated with the North Tobago anticline (Bassinger et al., 1971; Lattimore et al., 1971).

Lattimore et al. (1971) suggest that the Tobago Trough is a graben bounded on the south by the coast-line fault system, that extends westward to at least 63°W. If the depression between the islands of Margarita and Los Testigos, the Carupano Sea Valley (Maloney, 1967), is the westward continuation of this same trend, then the depressions and negative free-air anomalies southwest of Margarita Island and north of the Araya block could represent its westward extension into the study area. The trend ends at 64°40'W where the presence of a cross-fault was suggested on the basis of seismic reflection results.

The volcanic arc of the Lesser Antilles has been traced southwestward from Grenada Island into Los Testigos and Margarita islands through a zone of short-wavelength magnetic anomalies and a positive free-air gravity anomaly belt (Talwani, 1966; Lattimore et al., 1971). The Tortuga-Margarita Bank, characterized by positive free-air and Bouguer gravity anomalies, could represent the westward continuation of this tectonic element across the study area; however, there is a major distinction in that the short-wavelength, high-amplitude magnetic anomalies that seem to characterize this tectonic belt to the east are completely missing from this area.

The lack of the magnetic anomalies may be caused by gradual petrologic changes that might be expected as the island arc crosses from the oceanic crust into the continental crust and becomes an alpine-type mountain system (Hess, 1960a). Such petrologic changes along this

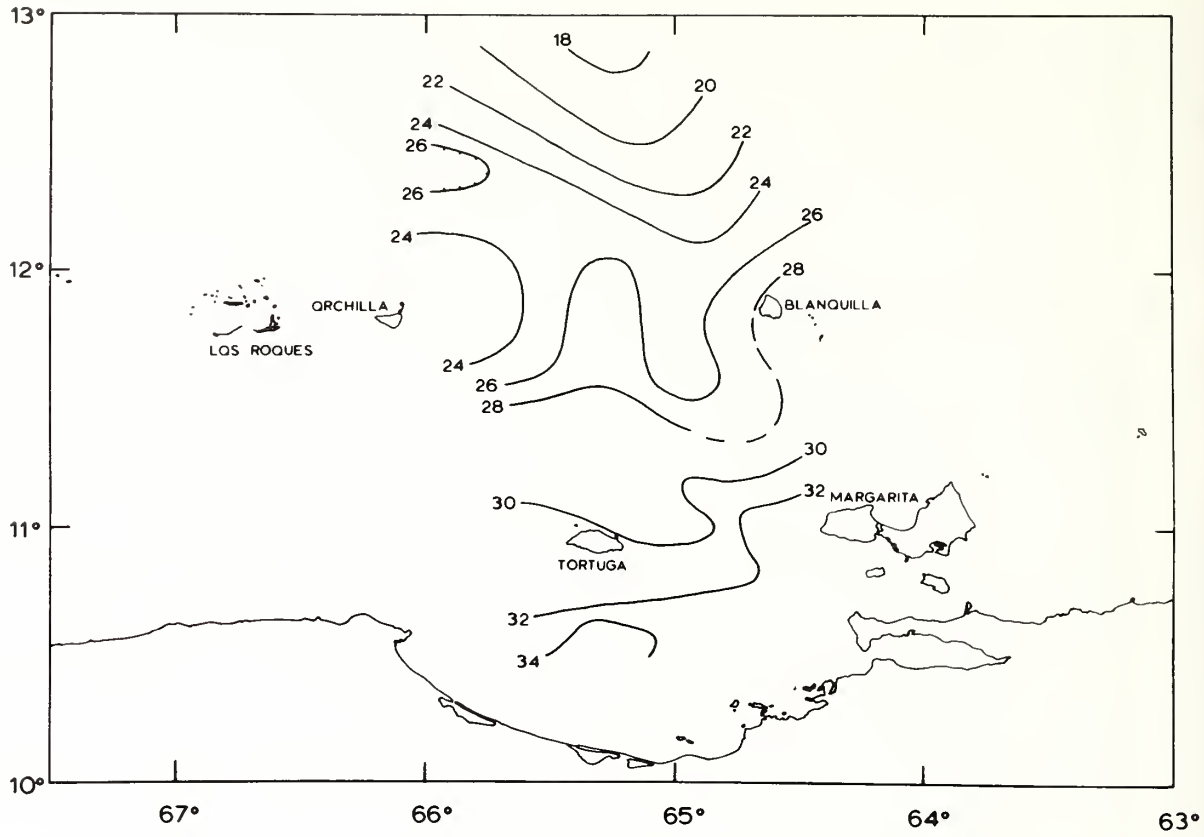

Figure 44. Contour map of the depth below sea level to the top of the mantle. Contour interval 2 km.

tectonic element were noted by Nagle (1971), who, in fact, questions the southwest extension of the volcanic arc on the basis of dissimilarity between the rock types of Grenada (unmetamorphosed Tertiary sediments, basalts, and andesites) and Margarita (highly metamorphosed Jurassic-Cretaceous sediments and intrusives.

Another explanation for the absence of the magnetic anomalies is that the igneous rocks associated with this tectonic belt may have been downfaulted along the numerous northwest-southeast trending cross-faults of the area. The writer proposes that petrologic changes and cross-faulting are both responsible for the different character of this tectonic belt along the Tortuga-Margarita Bank.

The Grenada Trough is characterized by a negative free-air anomaly belt that extends southwestward to the shelf north of Margarita Island. Talwani (1966) extends this belt farther to the southwest and joins it with the -38 mgal low southwest of Margarita. The writer believes that the positive free-air anomalies (up to 40 mgals) measured along the western coastline of Margarita (Ball et al., 1971) suggest an alternative interpretation (fig. 30), namely that the positive free-air anomaly band is uninterrupted between Tortuga and Margarita, although largely reduced in width and amplitude as a result of structural collapses along cross-faults.

The positive free-air anomaly belt of the Aves Ridge extends into the Blanquilla platform where it joins the positive values associated with the Tortuga-Margarita Bank (Talwani, 1966). East of the Blanquilla platform, the large negative free-air anomaly values of the Los Roques Canyon interrupt this belt, but west of the canyon the same belt appears to follow the islands of the Aruba-Orchilla chain (Talwani, 1966; Lagaay, 1969).

4.6 Regional History and Development

4.6.1 Origin of the Caribbean Sea

Any interpretation of the geologic development of the recent continental margin of Venezuela is dependent on the interpretation adopted for the evolution of the entire Caribbean region. Before the advent of the sea floor spreading hypothesis (Hess, 1960b, 1962; Dietz, 1961, 1962) the Caribbean Sea generally was considered to be either a subsided former continental area (Eardley, 1954), or an ancient, relict ocean basin (Schuchert, 1935). Menard (1967) thinks that the development of the Caribbean Sea is typical of small ocean basins in which the oceanic crust is modified as a result of the accumulation of a thick sequence of sediments.

Dietz and Holden (1970) suggest that the Caribbean Sea was formed during the Triassic and Jurassic periods by a mid-oceanic rift system that broke up the universal continent of Pangaea (fig. 45), and carried North America away from Africa and South America.

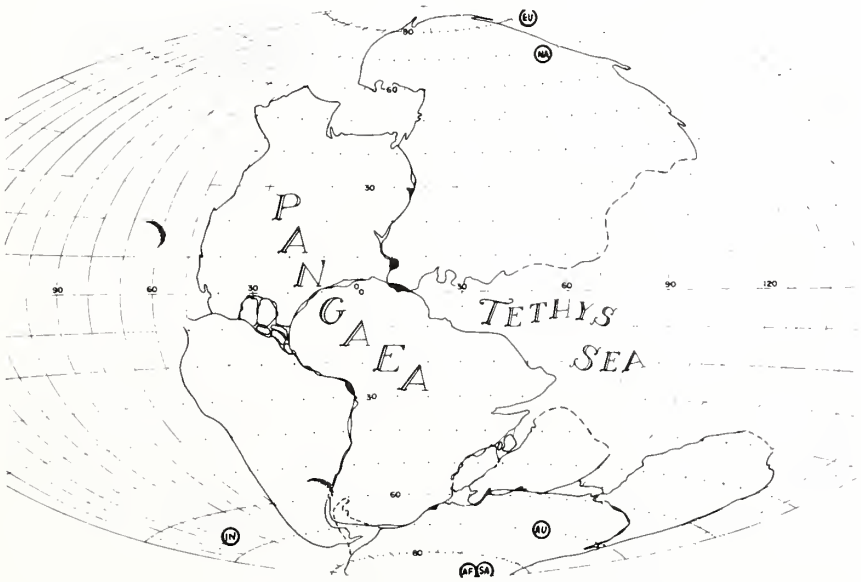

Figure 45. Reconstruction of the universal landmass of Pangaea at the end of Permian, 225 m.y. ago. Cross-hachures indicate the present position of the Lesser Antilles Island Arc at 15°N, 60°W (from Dietz and Holden, 1970).

Carey (1958), Funnel and Smith (1968), and Ball and Harrison (1969) describe the Gulf of Mexico and the Caribbean Sea as an area formed by north-south extension accompanied by east-west shearing.

Based on the wide distribution of the undisturbed B" seismic reflector, which is tentatively dated as Upper Jurassic, Edgar (1968) proposed that the Caribbean Sea must have existed prior to the earliest sea floor spreading episodes. As he believed that sea floor spreading did not commence in the Atlantic until the mid-Mesozoic, he suggested that the Caribbean crust is either a relict primitive oceanic crust or a continental crust that subsided very early in geologic time.

The writer accepts Edgar's (1968) interpretation that the basins of the Caribbean Sea must have formed prior to mid-Mesozoic, but prefers Carey's (1958) explanation that the basins developed between the small continental fragments that were left behind as North America drifted northwestward away from South America in Early Mesozoic time.

Utilizing these concepts of continental drift, knowledge of regional geology, and the results of this investigation, the following brief history is proposed for the development of the continental margin of northeastern Venezuela.

4.6.2 Paleozoic

The reconstruction of the continents into an universal Paleozoic landmass (fig. 45) (Carey, 1958; Bullard et al., 1965; Dietz and Holden, 1970) appears to support the contention of Eardley (1954) and Carey (1958) that the Paleozoic tectonic belt of eastern North America may be continuous with a similar belt in western South America. The oldest known rocks in north-central Venezuela, the Tinaco, Sebastopol, and Peña de Mora gneiss complexes, may represent the easternmost vestiges of this belt, or they may be continuous with the Guayana shield.

In northeastern Venezuela the end of the Paleozoic and the beginning of the Mesozoic was essentially a period of erosion (Bucher, 1952; Mencher, 1963). The initial breakup of the continents probably started in the Permian with the development of depressions and grabens, along which the continents fragmented as the separation intensified.

4.6.3 Mesozoic

The separation of North America from South America, and the breaking off, rotation, and shearing of continental fragments probably continued throughout the Triassic and Lower Jurassic periods (Carey, 1958; Dietz and Holden, 1970). According to the sediment record (Edgar, 1968), the separation of the individual continental fragments must have ceased, allowing the development of uniform conditions for sedimentation within the Caribbean basins by Upper Jurassic.

During Middle and Upper Jurassic times a volcanic island arc developed on the eastern margin of the primordial Caribbean Sea (Fink, 1968), and this ancestral Lesser Antilles Arc probably extended southwestward and westward into the area north of Venezuela. Volcanics and

sediments filled a geosyncline that developed between the South American craton and the volcanic arc during Upper Jurassic and Lower Cretaceous; metamorphism, emplacement of batholiths, and uplift of these rocks occurred during the Upper Cretaceous and Paleocene.

Large scale east-west shearing probably accompanied the separation of the continents along the El Pilar and the coast line fault systems, but the dominant shearing motion most likely stopped during the Upper Cretaceous when the welding of the Caribbean and South American crustal plates took place. This conclusion appears to be supported by the studies of Metz (1968a) along the El Pilar fault by the extension of the tectonic elements of the Lesser Antilles Island Arc into the Venezuelan shelf and by the alignment of the Urica and San Francisco faults with the faults bordering the Los Roques Canyon.

4.6.4 Cenozoic

The Cenozoic was essentially an era of vertical adjustments, which caused folding, thrusting, and large scale erosion and sediment deposition in the area of the continental margin of Venezuela. The elements of the former volcanic arc off the Venezuelan shelf underwent considerable uplift and erosion,and their plutonic core became exposed. Probably in Late Cenozoic, the island platforms started to subside, and to the north the Curacao Ridge was uplifted. Vertical adjustments on the shelf caused the formation of the basins in which there are indications of Recent normal faulting.

The writer does not believe that a major transform fault boundary was active along the southern margin of the Caribbean Sea in the Cenozoic. The relatively few earthquakes along the southern border of the Caribbean Sea with right-lateral motion (Molnar and Sykes, 1969) in comparison to the northern margin may be related to comparatively minor tectonic adjustments; however, if the seismicity gap is only apparent and strike-slip motions are indeed predominate, then one may assume that the South American-Caribbean weld is weakening and may be in the process of breaking up.

5. SUMMARY

(1) The east-west trending tectonic elements of the Venezuelan continental margin are interrupted by a series of northwest-southeast trending faults bordering the Los Roques Canyon and by the seaward extension of the Urica fault.

(2) On the continental shelf, the Urica fault forms the western limit of the competent Lower Cretaceous rocks of the eastern Serrania del Interior, the El Pilar fault, the Araya horst block, and the basins that extend north of the coast line fault system of the eastern Cordillera de la Costa.

(3) Geophysical measurements indicate that west of the Urica fault the Bay of Barcelona is underlain by rocks that probably belong to the seaward extension of the tectonic belts of the western Serrania del Interior.

(4) The Tortuga-Margarita Bank lies along the westward continuation of a positive gravity anomaly belt that is associated with the volcanic island chain of the Lesser Antilles Island Arc. Where the southward extension of the faults along the eastern wall of the Los Roques Canyon intersect the Tortuga-Margarita Bank, the amplitude and the width of the gravity anomalies are reduced, suggesting that the igneous basement rocks are probably down-faulted. The absence of high-amplitude, short-wavelength anomalies over the Tortuga-Margarita Bank also support the proposed down-faulting of the basement, although petrologic changes along this belt could also equally account for the lack of significant magnetic anomalies.

(5) Magnetic and seismic reflection data suggest that the island platforms are underlain by igneous basement rocks. On the basis of the known geology of the islands and the sampling of a basement outcrop, it is suggested that these basement rocks are mostly Upper Cretaceous "granitic" plutons. The K-Ar age determinations on the biotites of one "granitic" sample gave 81 m.y. for the formation of the plutons on the Blanquilla platform.

(6) The Los Roques Canyon appears to be a graben, which is in alignment with two major northwest-southeast trending faults of northeastern Venezuela, the Urica and the San Francisco faults. The northwest-southeast alignment of these faults suggests that they may be related, and that no major strike-slip displacement has occurred along the east-west trending fault systems since Cretaceous time.

(7) The similarity of the reflectors on the southern slope of the Tortuga-Margarita Bank and in the western deep of the Cariaco Basin, together with the numerous faults that appear to offset the sea floor on the continental margin, suggest that Late Tertiary to Recent tectonic activity is responsible for the subsidence of the basins on the shelf, and for the formation of the present topography.

(8) Recent tectonic activity is indicated not only in the area of the shelf but also along the faults of the Los Roques Canyon and the Curacao Ridge. The presence of well-stratified sediments that cover the Curacao Ridge north of the Los Roques Canyon suggest that these may have been carried directly from the canyon into the Venezuelan Basin prior to the uplift of the ridge.

(9) Bouguer anomalies northwest to the Blanquilla platform indicate that the mantle plunges eastward beneath the Aves Ridge. A mantle depth of 32 km is indicated west of Margarita Island and south of

Tortuga Island; a 28 km depth-to-mantle below the Blanquilla platform most likely reflects the influence of the Aves Ridge.

(10) The major tectonic elements of the continental margin of northeast Venezuela were established by the Upper Cretaceous; during the Cenozoic mainly vertical adjustments occurred, which were responsible for folding, thrusting, large scale erosion, and periodic readjustment of the sedimentation pattern.

6. ACKNOWLEDGEMENTS

This publication is based on work done in partial fulfillment of the Doctor of Philosophy degree at The George Washington University, Washington, D.C. I wish to thank my dissertation advisors, Drs. J. W. Pierce and M. M. Ball, for their untiring interest, advice, criticism and encouragement during this investigation.

Special thanks go to Drs. M. M. Ball, F. Nagle, E. Bonatti, and P. Kirch of the Rosenstiel School of Marine and Atmospheric Sciences, University of Miami, for their help in the preparation and identification of the thin sections, and for making available to the author their extensive bibliography on Caribbean geology, among them several yet unpublished manuscripts.

Unpublished maps and manuscripts were received also from Dr. C. Schubert of the Instituto Venezolano de Investigaciones Cientificas, which are hereby gratefully acknowledged.

The author is indebted to I. Zietz for providing guidance during part of this investigation, and to G. H. Keller, R. K. Lattimore, H. B. Stewart, and his dissertation advisors for their suggestions and critical review of this manuscript.

The author also wishes to express his gratitude to J. I. Ewing of the Lamont-Doherty Geological Observatory, Columbia University, for providing unpublished seismic reflection data, and to G. Pardo of the Gulf Oil Company for many useful discussions during the field work and for arranging the K-Ar dating of one of the rock samples.

I also wish to thank Drs. G. Teleki and H. B. Stewart for providing the inspiration and encouragement during the past several years, that resulted in this dissertation.

This research was carried out as part of the Caribbean research project of the Marine Geology and Geophysics Laboratory of the NOAA Atlantic Oceanographic and Meteorological Laboratories. The field work was performed on the NOS Ship DISCOVERER, whose officers and crew are gratefully acknowledged for their help and cooperation.

7. REFERENCES

Aguerrevere, S. E., and G. Zuloago (1937), Observaciones geologicas en la parte central de la Cordillera de la Costa, Venezuela, Bol. de Geol. y Min., 1, p. 3-22.

Alberding, H. (1957), Application of principles of wrench-fault tectonics of Moody and Hill to northern South America, Geol. Soc. America Bull., 68, p. 785-790.

Ball, M. M., and C. G. A. Harrison (1969), Origin of the Gulf and Caribbean and implications regarding ocean ridge extension, migration, and shear, Gulf Coast Assoc. Geol. Soc. Trans., 19, p. 287-294.

Ball, M. M., C. G. A. Harrison, P. R. Supko, W. D. Bock, and N. J. Maloney (1971), Marine geophysical measurements on the southern boundary of the Caribbean Sea, Geol. Soc. America. Mem. (in press).

Bassinger, B. G., R. N. Harbison, and L. A. Weeks (1971), Marine geophysical study northeast of Trinidad-Tobago, Am. Assoc. Petroleum Geologists Bull., 55, p. 1730-1740.

Bell, J. S. (1967), Geology of the Camatagua area Estado Aragua, Venezuela: unpublished PhD Thesis, Princeton University.

Bucher, W. H. (1952), Geologic structure and orogenic history of Venezuela, Geol. Soc. America Mem. 49, 113 p.

Bunce, T. E., J. D. Phillips, R. L. Chase, and C. O. Bowin (1970), The Lesser Antilles Arc and the eastern margin of the Caribbean Sea, in Maxwell A., Editor, The Sea, 4, (in press).

Bullard, E. C., J. E. Everett, and A. G. Smith (1965), The fit of the continents around the Atlantic, Phil. Royal Soc. Trans., 258, p. 41-51.

Bush, S. A., and P. A. Bush (1969), Isostatic gravity map of the Eastern Caribbean region, Gulf Coast Assoc. Geol. Soc. Trans., 19, p. 281-285.

Carey, S. W. (1958), The tectonic approach to continental drift, in Carey, S. W., Editor, Continental Drift, A Symposium, Dept. Geology, Univ. Tasmania, Hobart, Tasmania, Australia, p. 177-355.

Chase, R. L., and E. T. Bunce (1969), Underthrusting of the eastern margin of the Antilles by the floor of the western Atlantic Ocean and origin of the Barbados Ridge, Jour. Geophys. Research, 74, p. 1413-1420.

Christensen, R. M. (1961), Geology of the Paria-Araya Peninsula, Northeastern Venezuela, unpublished PhD Thesis, University of Nebraska.

Dengo, G. (1953), Geology of the Caracas region, Venezuela, Geol. Soc. America Bull., 64, p. 7-40.

Dietz, R. S. (1961), Continent and ocean basin evolution by spreading of the sea floor, Nature, 190, p. 854-857.

_____ (1962), Ocean basin evolution by sea floor spreading, in MacDonald, G. A. and H. Kuno, Editors, The crust of the Pacific Basin, Amer. Geophys. Union, Mon. 6, p. 11-12.

Dietz, R. S., and J. C. Holden (1970), Reconstruction of Pangea: Breakup and dispersion of continents, Permian to Present, Jour. Geophys. Research, 75, p. 4939-4956.
Eardley, A. J. (1954), Tectonic relations of North and South America, Am. Assoc. Petroleum Geologists Bull., 38, p. 107-773.
Edgar, N. T. (1968), Seismic refraction and reflection in the Caribbean Sea, unpublished PhD Thesis, Columbia University.
Ewing, J., J. L. Worzel, M. Ewing, and C. Windisch (1966), Ages of Horizon A and the oldest Atlantic sediments, Science, 154, p. 1125-1132.
Ewing, J., M. Talwani, M. Ewing, and T. Edgar (1967), Sediments of the Caribbean, Stud. Trop. Oceanography, University of Miami, 5, p. 88-102.
Ewing, M. J. L. Worzel, and G. L. Shurbet (1957), Gravity observations at sea in U. S. submarines Barracuda, Tusk, Conger, Argonaut and Medregal, Kon. Nederlandsch Geo.-Mijn. Genootschap Ver., Geol. Ser., 18, p. 49-116.
Ewing, M., T. Saito, J. Ewing, and L. Burckle (1966), Lower Cretaceous sediments from the northwestern Pacific Ocean, Science, 152, p. 751-755.
Fink, K. L. (1968), Geology of the Guadeloupe region, Lesser Antilles Island Arc, unpublished PhD Thesis, University of Miami.
Funnel, B. M., and A. G. Smith (1968), Opening of the Atlantic Ocean, Nature, 219, p. 1328-1333.
Grim, P. J. (1970), Computer program for automatic plotting of bathymetric and magnetic anomaly profiles, ESSA Technical Memorandum, ERLTM-AOML 8, 31 p.
Hess, H. H. (1960a), Caribbean research project - a progress report, Geol. Soc. America Bull., 71, p. 235-240.
_____ (1960b), Evolution of ocean basins, unpublished manuscript, ONR contract 1858(10), 38 p.
_____ (1962), History of ocean basins, in A. E. Engel et al., Editors, Petrologic studies: A volume in honor of A. F. Buddington, Geol. Soc. America, p. 599-620.
Hess, H. H., and J. C. Maxwell (1953), Caribbean research project, Geol. Soc. America Bull., 64, p. 1-6.
Heezen, B. C., R. J. Menzies, W. S. Broecker, and M. Ewing (1959), Date of Stagnation of the Cariaco Trench, southeast Caribbean (abs.), Geol. Soc. America Bull., 69, p. 1579.
Isacks, B., J. Oliver, and L. R. Sykes (1968), Seismology and the New Global Tectonics, Jour. Geophys. Research, 73, p. 5855-5900.
JOIDES Deep Sea Drilling Project, Leg 3 and Leg 4 (1969), Geotimes, 14, p. 13-16.
Kugler, H. G. (1957), Contribution to the geology of the islands of Margarita and Cubagua, Venezuela, Geol. Soc. America Bull., 68, p. 555-566.
Lagaay, R. A. (1969), Geophysical investigations of the Netherlands Leeward Antilles, Verh. Kon. Ned. Akad. Wetensch., Amsterdam, 25, 86 p.

Lattimore, R. K., L. A. Weeks, and L. W. Mordock (1971), Marine geophysical reconnaissance of the Paria shelf, Am. Assoc. Petroleum Geologists Bull., 55, p. 1719-1729.

Le Pichon, X. (1968), Sea floor spreading and continental drift, Jour. Geophys. Research, 73, p. 3661-3697.

Liddle, R. A. (1946), The geology of Venezuela and Trinidad: 2nd Ed. Paleon. Research Inst., Ithaca, N. Y., 890 p.

Lidz, L., M. Ball, and W. Charm (1968), Geophysical measurements bearing on the problem of the El Pilar fault in the Northern Venezuelan offshore: Marine Science Bull., 18, p. 545-560.

Lidz, L., W. B. Charm, M. M. Ball, and S. Valdes (1969), Marine basins off the coast of Venezuela: Marine Science Bull., 19, p. 1-17.

Maloney, N. J. (1965), Geomorphology of the central coast of Venezuela: Bol. Inst. Oceanog., Univ. Oriente, 4, p. 246-265.

_____ (1966), Geomorphology of continental margin of Venezuela Part I Cariaco Basin, Bol. Inst. Oceanog., Univ. Oriente, 5, p. 38-53.

_____ (1967), Geomorphology of the continental margin of Venezuela Part II Continental terrace off Carupano, Bol. Inst. Oceanog., Univ. Oriente, 6, p. 147-155.

_____ (1968), Geology of La Blanquilla Island with notes on Los Hermanos islands, Preprint, Fifth Carib. Geol. Conf., St. Thomas, 12 p.

Maloney, N. J., and O. Macsotay (1967), Geology of La Tortuga Island, Venezuela, Assoc. Ven. Geol. Min. y Petroleo, Bol. Inform., 10, p. 265-285.

Menard, H. W., (1967), Transitional types of crust under small ocean basins, Jour. Geophys. Research, 72, p. 3061-3073.

Mencher, E., H. J. Fichter, H. H. Renz, W. E. Wallis, H. H. Renz, J. M. Patterson, and R. E. Robie (1953), Geology of Venezuela and its oil fields, Am. Assoc. Petroleum Geologists Bull., 37, p. 690-777.

Mencher, E. (1963), Tectonic history of Venezuela, in Childs, O. E., and B. W. Beebe, Editors, Backbone of the Americas, Am. Assoc. Petroleum Geologists Mem. 2, p. 73-87.

Menendez, A. (1962), Geology of the Tinaco area, northcentral Cojedes Venezuela, unpublished PhD Thesis, Princeton University.

_____ (1967), Tectonics of the central part of the Western Caribbean Mountains, Venezuela, Stud. Trop. Oceanography, University of Miami, 5, p. 103-130.

Metz, H. L. (1968a), Geology of the El Pilar fault zone States of Sucre, Venezuela: in Saunders, J. B. Editor, Fourth Carib. Geol. Conf. Trans., Caribbean Printers, Arina, Trinidad and Tobago, p. 293-298.

_____ (1968b), Stratigraphic and geologic history of extreme northeastern Serrania del Interior, State of Sucre, Venezuela: ibid., p. 275-292.

Morgan, B. A. (1967), Geology of the Valencia area Carabobo, Venezuela, unpublished PhD Thesis, Princeton University.

Morgan, J. W. (1968), Rises, trenches, great faults, and crustal blocks, Jour. Geophys. Research, 73, p. 1959-1982.

Molnar, P., and L. R. Sykes (1969), Tectonics of the Caribbean and Middle America regions from focal mechanisms and seismicity, Geol. Soc. America Bull., 80, p. 1639-1684.

Nafe, J. E., and C. L. Drake (1963), Physical properties of sediments, Chapter 29, p. 794-815, in Hill, M. N., Goldbert, E. D., Iselin, C. O'D., and Munk, W. H., Editors, The Sea, 3 - The earth beneath the sea: New York, John Wiley and Sons, Inc., 963 p.

Nagle, F. (1971), Caribbean geology, 1970: Marine Science Bull., 20, (in press).

Officer, C. B., J. I. Ewing, R. S. Edwards, and H. R. Johnson (1957), Geophysical investigations in the eastern Caribbean: Venezuelan Basin, Antilles island arc, and Puerto Rico Trench: Geol. Soc. America Bull., 68, p. 359-378.

Oxburgh, E. R. (1966), Geology and metamorphism of Cretaceous rocks in eastern Carabobo State, Venezuelan Coast Ranges: in Hess, H. H., Editor, Caribbean Geological Investigations, Geol. Soc. America Mem. 98, p. 241-310.

Piburn, M. D. (1967), Metamorphism and structure of the Villa de Cura group, Northeastern Venezuela, unpublished PhD Thesis, Princeton University.

Priem, H. N. A., N. A. I. M. Boelrijk, R. H. Verschure, E. H. Hebeda, and R. A. Lagaay (1966), Isotopic age of the quartz-diorite batholith on the island of Aruba, Netherlands Antilles, Geol. en Mijnb., 45, p. 188-190.

Priem, H. N. A. (1967), Beknopt verslag over de werkzaamheden in het jaar van september 1966 tot september 1967: Z. W. O. Laboratorium voor isotopgeologie, Amsterdam.

Rod, E. (1956), Strike-slip faults of northern Venezuela, Am. Assoc. Petroleum Geologists Bull., 40, p. 457-476.

_____ (1959), West end of Serrania del Interior, Eastern Venezuela, Am. Assoc. Petroleum Geologists Bull., 43, p. 772-789.

Rod, E., and W. Maync (1954), Revision of Lower Cretaceous stratigraphy of Venezuela, Am. Assoc. Petroleum Geologists Bull., 38, p. 193-260.

Rutten, L. M. R. (1931), On the rocks from the Venezuelan islands between Bonaire and Trinidad, and on some rocks from northwestern Venezuela, Proc. Kon. Ned. Akad. Wetensch., Amsterdam, 34, p. 1101-1110.

_____ (1939), The age of the quartz-diorite and granodioritic rocks of the West Indies, Geol. en Mijnb., 1, p. 128-133.

_____ (1940), New data on the smaller islands North of Venezuela, Proc. Kon. Ned. Akad. Wetensch., Amsterdam, 43, p. 828-841.

Salvador, A., and R. M. Stainforth (1968), Clues in Venezuela to the geology of Trinidad, and vice versa, in Saunders, J. B., Editor, Fourth Carib. Geol. Conf. Trans. Caribbean Printers, Arina, Trinidad and Tobago, p. 31-40.

Schubert, C. (1969a), Mapa geologico del Archipielago de Los Hermanos, Dependencias Federales, (map), Minist. de Min. e Hidrocarburos, Caracas.

_____ (1969b), Mapa geologico de la isla La Blanquilla, Dependencias Federales, (map), Minist. de Min. e Hibdrocarburos, Caracas.
_____ (1970), Geologia de la Isla la Orchilla, Dependencias Federales: (abs.), Acta Cient. Venezolana, 21, p. 55.
_____ (1971), Geologia de la Peninsula de Araya, Estado, Sucre: Memorias IV Congreso Geologico Venezolano, Caracas, (in press).
Schuchert, C. (1935), Historical geology of the Antillean - Caribbean region, John Wiley and Sons, Inc., New York, 84 p.
Shepard, F. P., and K. O. Emery (1941), Submarine topography of the California coast: canyons and tectonic interpretation, Geol. Soc. America, Special Paper 37, 171 p.
Smith, R. J. (1953), Geology of the Los Teques-Cua region, Venezuela, Geol. Soc. America Bull., 64, p. 41-64.
Sykes, L. R., and M. Ewing (1965), The seismicity of the Caribbean region, Jour. Geophys. Research, 70, p. 5065-5074.
Talwani, M. (1966), Gravity anomaly belts in the Caribbean, p. 177, in Poole, W. H., Editor, Continental margins and island arcs, Geol. Sur. Can. Paper 66-15, 486 p.
Talwani, M., G. H. Sutton, and J. L. Worzel (1959), A crustal section across the Puerto Rico Trench, Jour. Geophys. Research, 64, p. 1545-1555.
Taylor, G. C. (1960), Geology of the island of Margarita, unpublished PhD Thesis, Princeton University.
Von der Osten, E. (1955), Geologia de la Bahia Santa Fe (Estado Sucre), Bol. de Geol., Caracas, 3, p. 123-201.
_____ (1957), Lower Cretaceous Barranquin Formation of northeastern Venezuela, Am. Assoc. Petroleum Geologist Bull., 41, p. 679-708.
Weeks, L. A., R. K. Lattimore, R. N. Harbison, B. G. Bassinger, and G. F. Merrill (1969), Structural relationships between Lesser Antilles, Venezuela, and Trinidad-Tobago, Gulf Coast Assoc. Geol. Soc. Trans., 19, p. 321
_____ (1971), Structural relationships between Lesser Antilles, Venezuela, and Trinidad-Tobago, Am. Assoc. Petroleum Geologists Bull., 54, (in press).
Woollard, G. P. (1959), Crustal structure from gravity and seismic measurements, Jour. Geophys. Research, 64, p. 1521-1544.
Woollard, G. P., and J. C. Rose (1963), International gravity measurements, George Bantha Co., Inc., Menasha, Wisconsin, 518 p.
Zuloaga, G. (1953), La Blanquilla y Los Hermanos, Bol. Acad. Cient. Venezolana, 49, p. 1-46.

APPENDIX I

The following pages contain the combined computer plotted profiles of the bathymetry, magnetic anomaly, and gravity free-air anomaly.

These profiles represent the key geophysical survey crossings of the study area. Locations of these profiles are shown in figure 7 and figure 13; these figures are also included here for quick reference. Profile 8 was too short to include as an independent illustration.

Description of the data and methods used to obtain these profiles are discussed in the Introduction (Bathymetric Survey, Magnetic Survey, Gravity Survey).

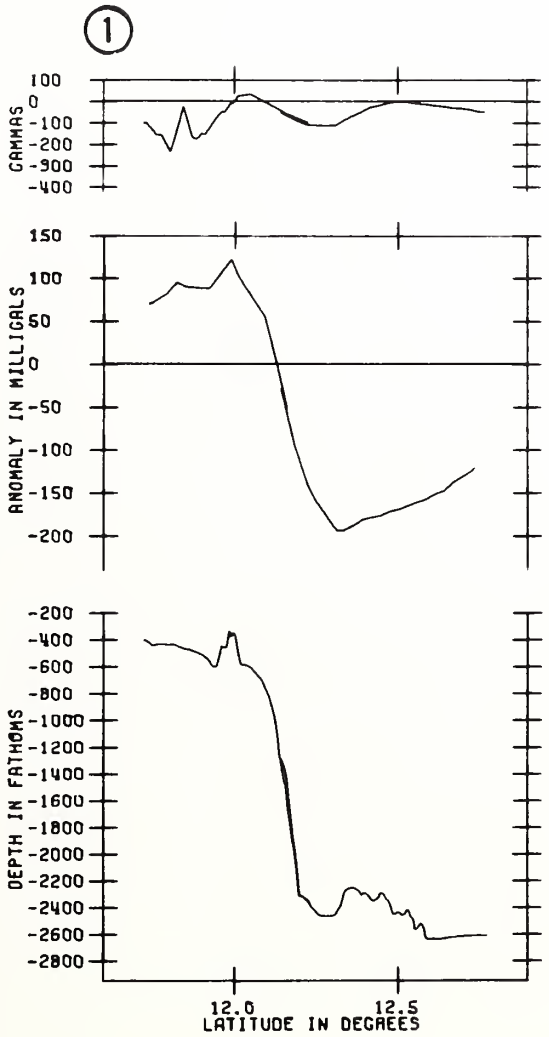
1
100
0
-100
-200
-900
-400
GAMMAS
150
100
50
0
-50
-100
-150
-200
ANOMALY IN MILLIGALS
-200
-400
-600
-800
-1000
-1200
-1400
-1600
-1800
-2000
-2200
-2400
-2600
-2800
DEPTH IN FATHOMS
12.0
12.5
LATITUDE IN DEGREES

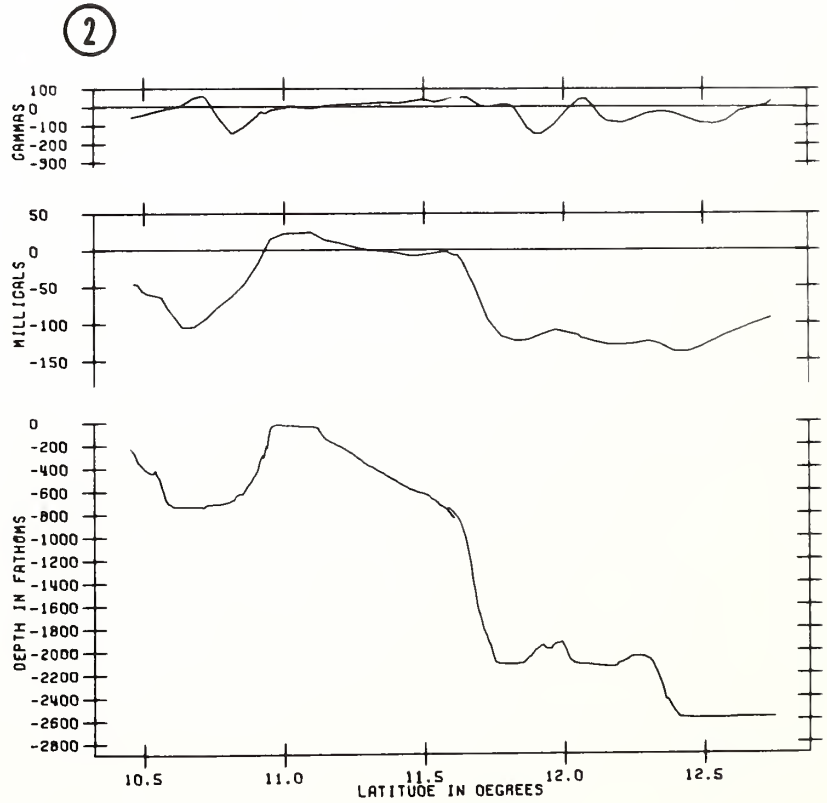
2
100
0
-100
-200
-900
GAMMAS
50
0
-50
-100
-150
MILLIGALS
0
-200
-400
-600
-800
-1000
-1200
-1400
-1600
-1800
-2000
-2200
-2400
-2600
-2800
DEPTH IN FATHOMS
10.5
11.0
11.5
12.0
12.5
LATITUDE IN DEGREES

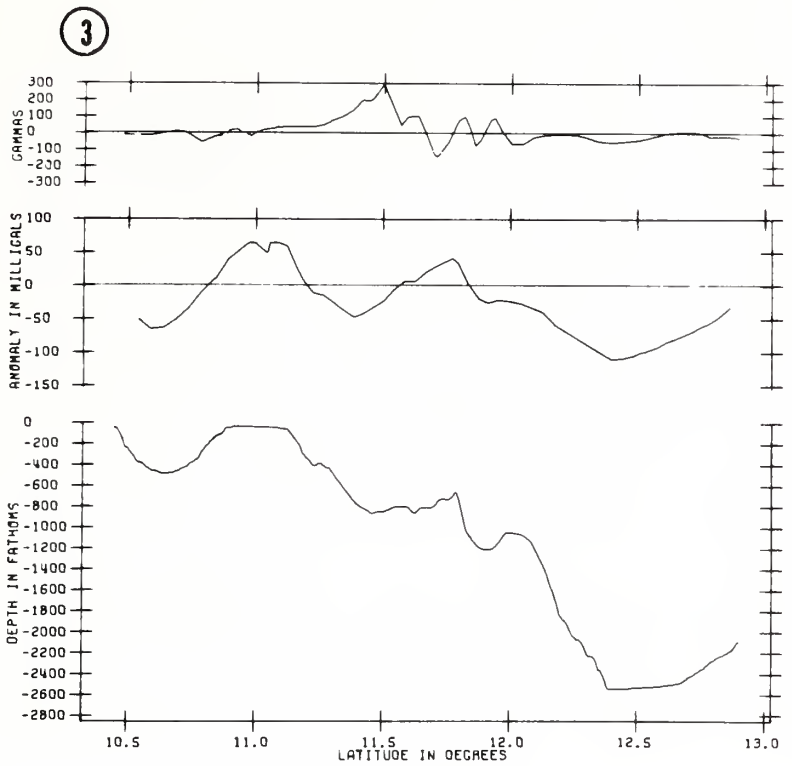
3
GAMMAS
300
200
100
0
-100
-200
-300
ANOMALY IN MILLIGALS
100
50
0
-50
-100
-150
DEPTH IN FATHOMS
0
-200
-400
-600
-800
-1000
-1200
-1400
-1600
-1800
-2000
-2200
-2400
-2600
-2800
10.5
11.0
11.5
12.0
12.5
13.0
LATITUDE IN DEGREES

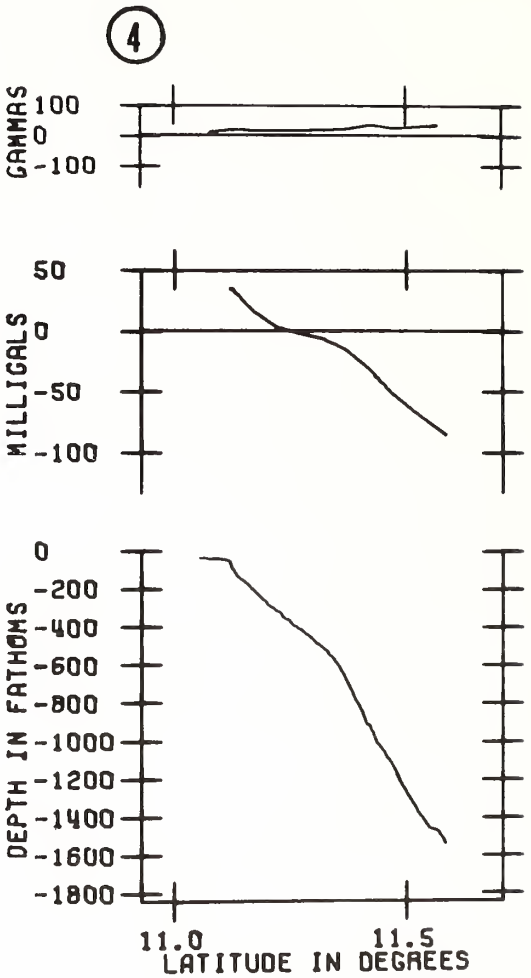
4
GAMMAS
100
0
-100
MILLIGALS
50
0
-50
-100
DEPTH IN FATHOMS
0
-200
-400
-600
-800
-1000
-1200
-1400
-1600
-1800
11.0
11.5
LATITUDE IN DEGREES

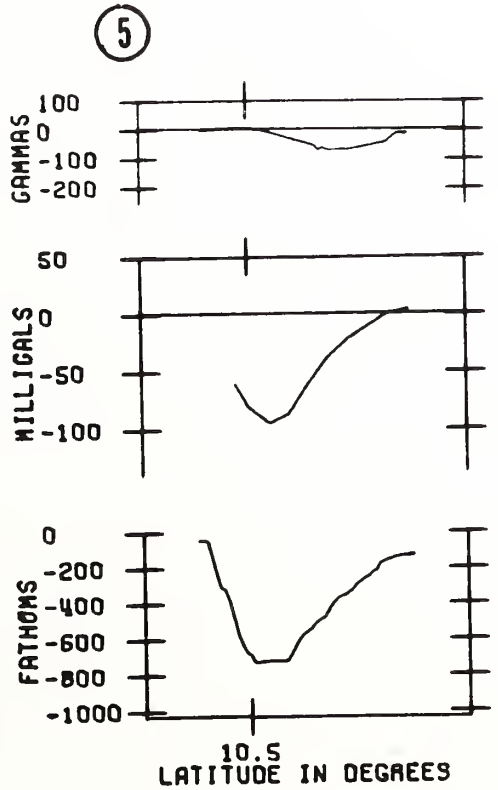
5
100
0
-100
-200
GAMMAS
50
0
-50
-100
MILLIGALS
0
-200
-400
-600
-800
-1000
FATHOMS
10.5
LATITUDE IN DEGREES

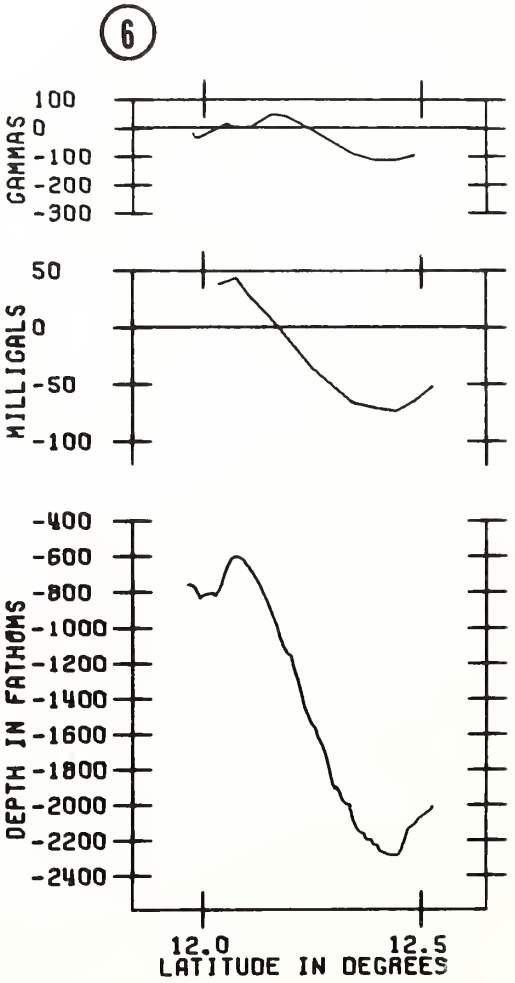
6
100
0
-100
-200
-300
GAMMAS
50
0
-50
-100
MILLIGALS
-400
-600
-800
-1000
-1200
-1400
-1600
-1800
-2000
-2200
-2400
DEPTH IN FATHOMS
12.0
12.5
LATITUDE IN DEGREES

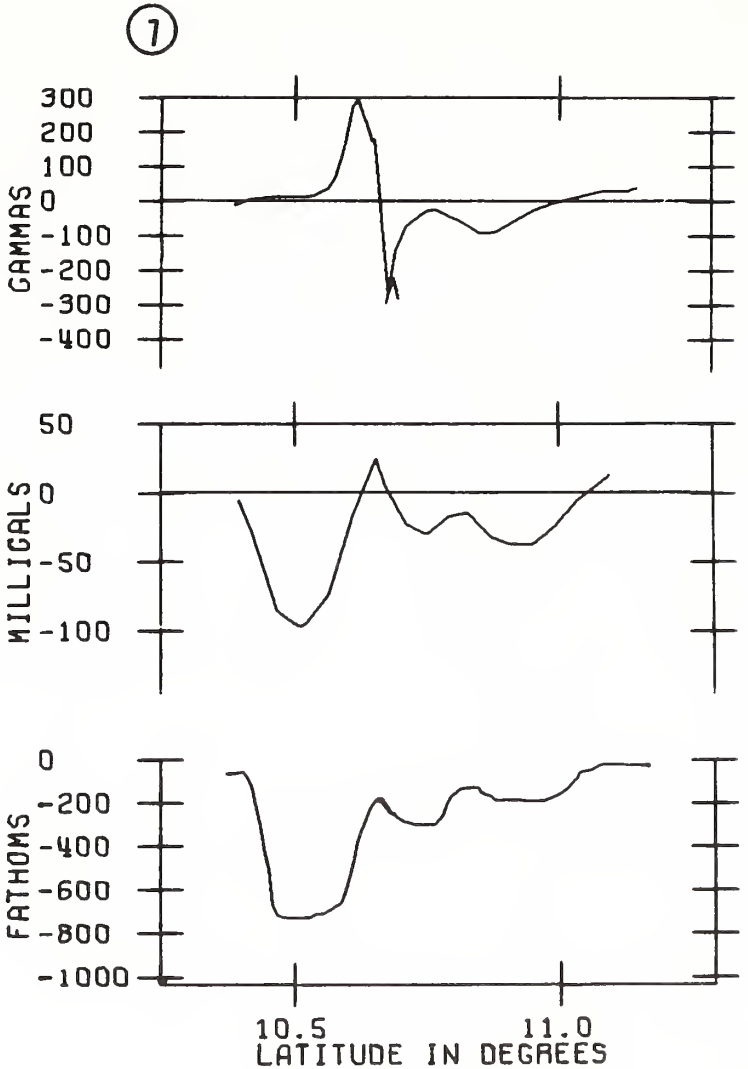
7
300
200
100
0
-100
-200
-300
-400
GAMMAS
50
0
-50
-100
MILLIGALS
0
-200
-400
-600
-800
-1000
FATHOMS
10.5
11.0
LATITUDE IN DEGREES

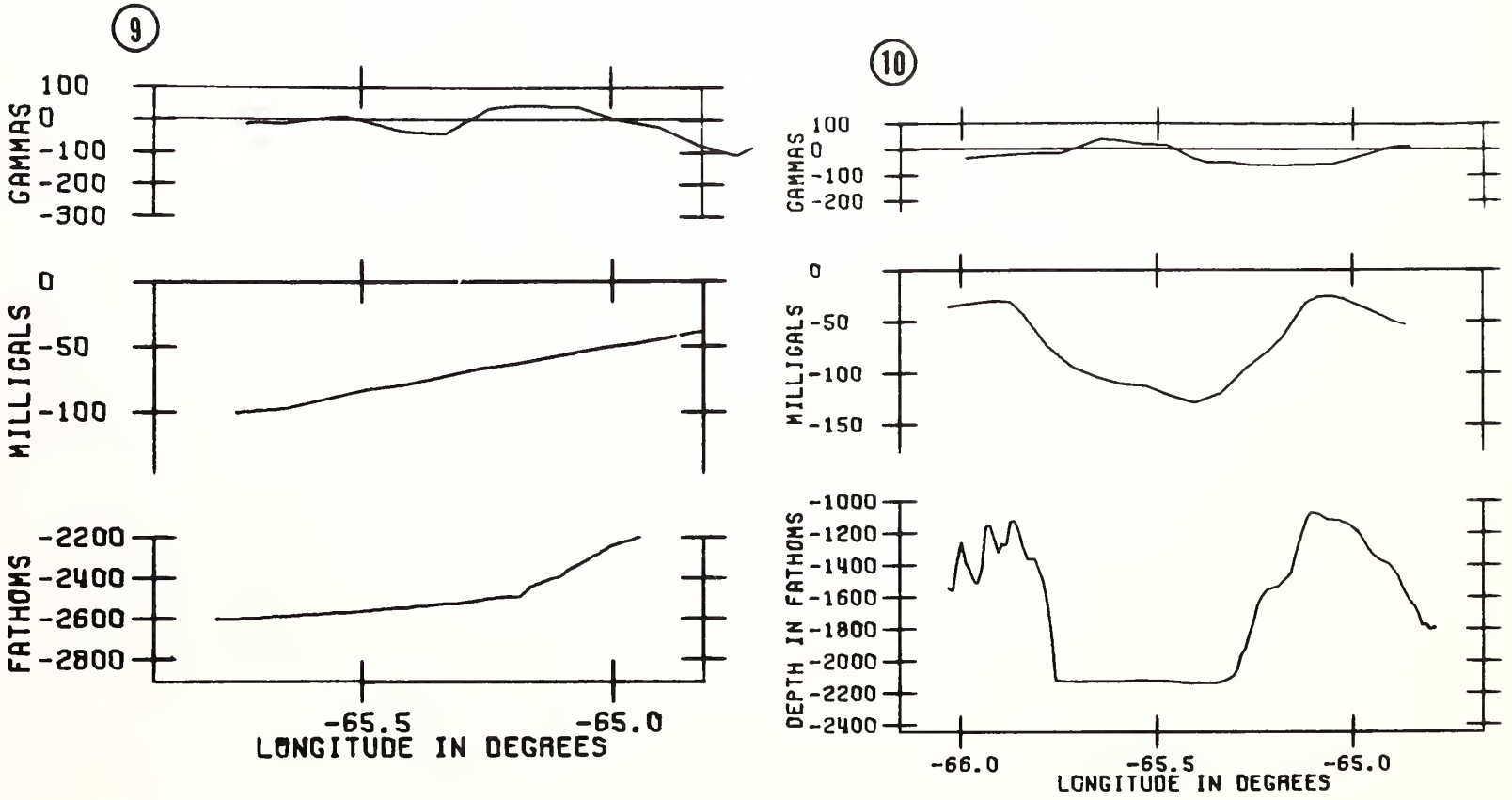
9
GAMMAS
100
0
-100
-200
-300
MILLIGALS
0
-50
-100
FATHOMS
-2200
-2400
-2600
-2800
-65.5
-65.0
LONGITUDE IN DEGREES
10
GAMMAS
100
0
-100
-200
MILLIGALS
0
-50
-100
-150
DEPTH IN FATHOMS
-1000
-1200
-1400
-1600
-1800
-2000
-2200
-2400
-66.0
-65.5
-65.0
LONGITUDE IN DEGREES

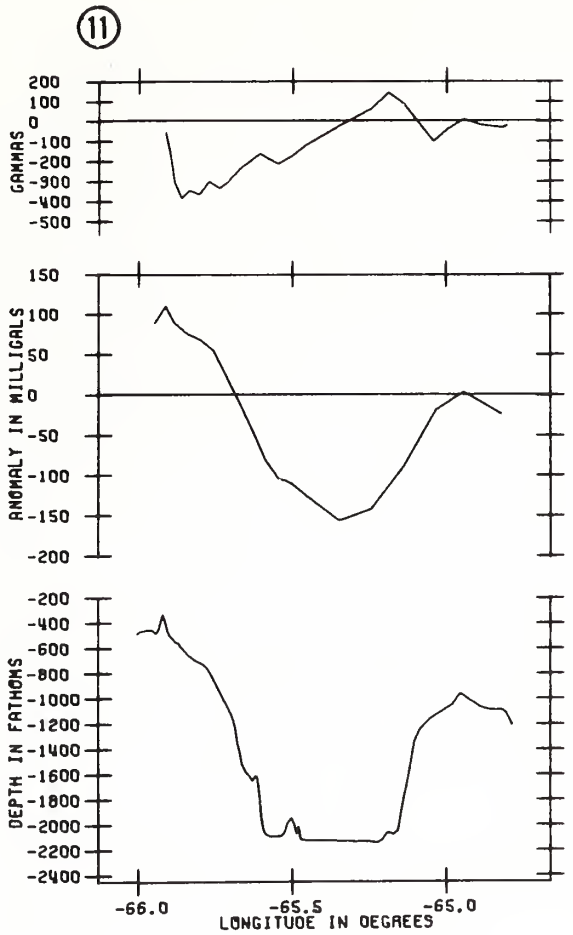
11
GAMMAS
200
100
0
-100
-200
-900
-400
-500
ANOMALY IN MILLIGALS
150
100
50
0
-50
-100
-150
-200
DEPTH IN FATHOMS
-200
-400
-600
-800
-1000
-1200
-1400
-1600
-1800
-2000
-2200
-2400
-66.0
-65.5
-65.0
LONGITUDE IN DEGREES

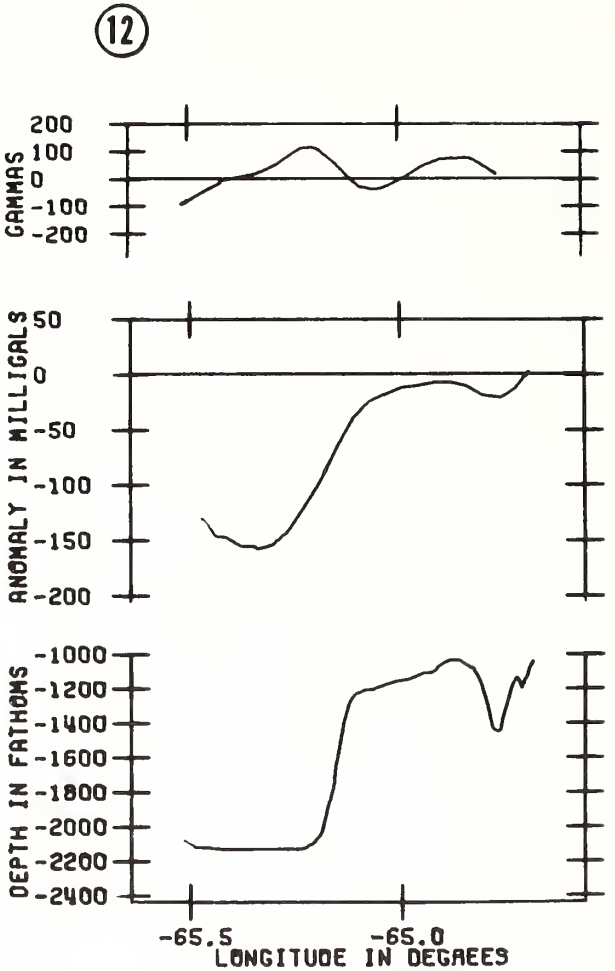
12
GAMMAS
200
100
0
-100
-200
ANOMALY IN MILLIGALS
50
0
-50
-100
-150
-200
DEPTH IN FATHOMS
-1000
-1200
-1400
-1600
-1800
-2000
-2200
-2400
-65.5
-65.0
LONGITUDE IN DEGREES

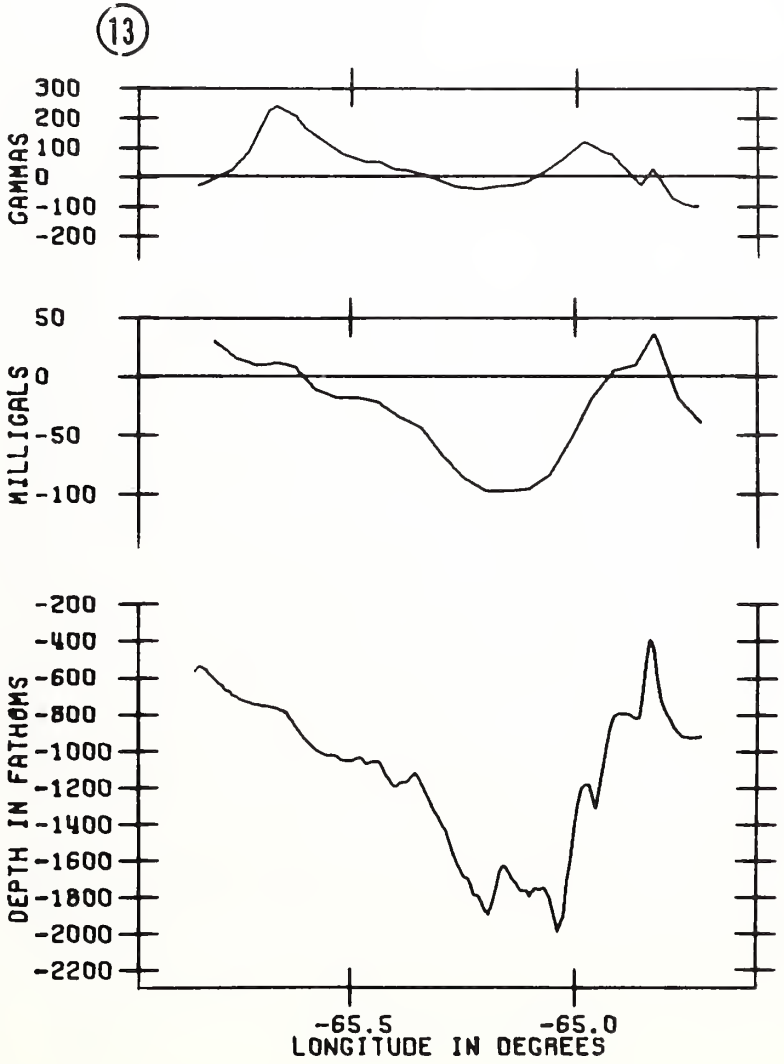
13
300
200
100
0
-100
-200
GAMMAS
50
0
-50
-100
MILLIGALS
-200
-400
-600
-800
-1000
-1200
-1400
-1600
-1800
-2000
-2200
DEPTH IN FATHOMS
-65.5
-65.0
LONGITUDE IN DEGREES

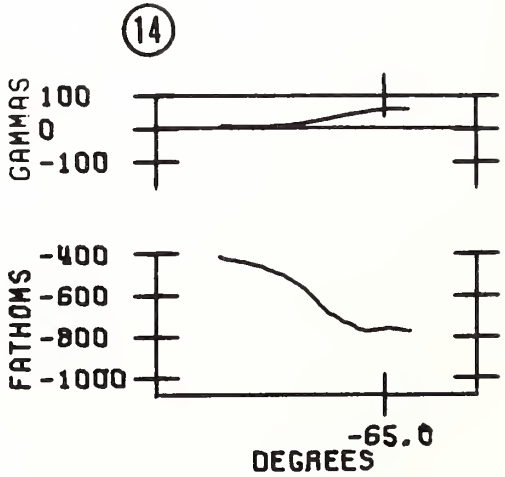
14
100
0
-100
GAMMAS
-400
-600
-800
-1000
FATHOMS
-65.0
DEGREES

APPENDIX II

The following pages contain eight two-dimensional Bouguer anomaly profiles used to construct the Bouguer anomaly map, figure 31 in the main part of the text.

The free-air anomalies are also shown together with Bouguer anomaly profiles to illustrate that the selection of density for the Bouguer correction (2.67 g/cm) is essentially correct.

In the lower half of each profile a simplified bottom topography is shown. The large circles represent the major gradient changes in the topography, which were used in the computation of the two-dimensional Bouguer correction.

Locations of the profiles are shown in figure 32, but included here also for quick reference. The discussion of the methods used is contained in the section: GEOPHYSICAL OBSERVATIONS, Gravity measurements.

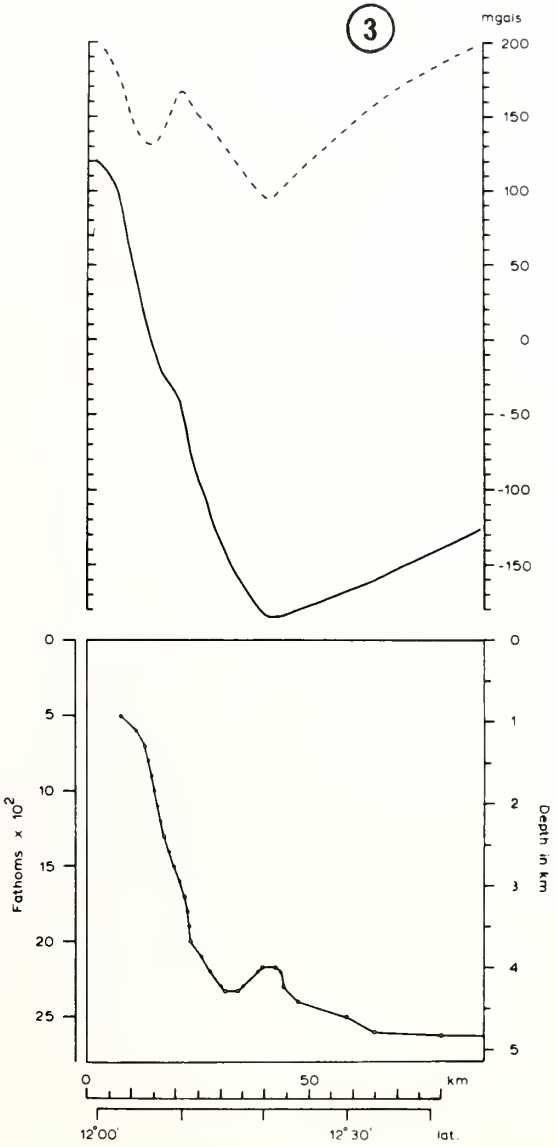
3
mgals
200
150
100
50
0
-50
-100
-150
Fathoms x 10^2
Depth in km
0
5
10
15
20
25
1
2
3
4
km
50
12°00'
12°30'
lat.

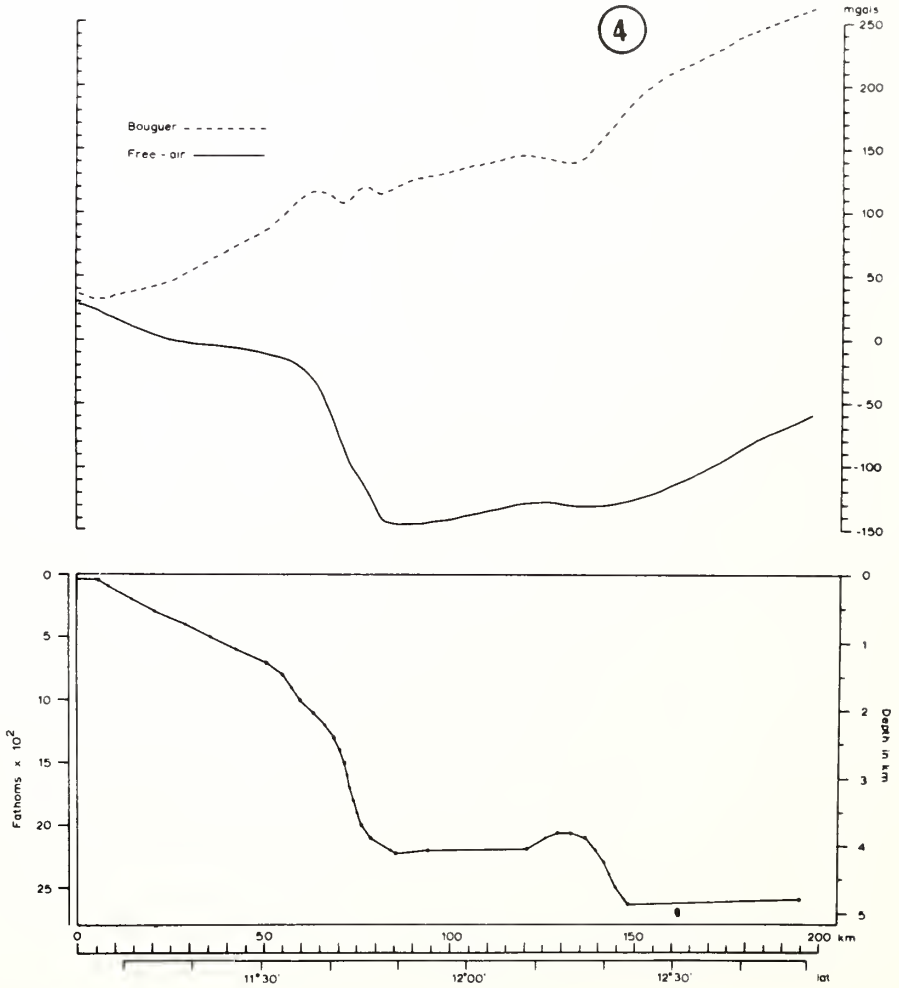
4
mgals
Bouguer
Free - air
250
200
150
100
50
0
-50
-100
-150
Fathoms x 10^2
Depth in km
0
5
10
15
20
25
1
2
3
4
km
50
100
150
200
11°30'
12°00'
12°30'
lat.

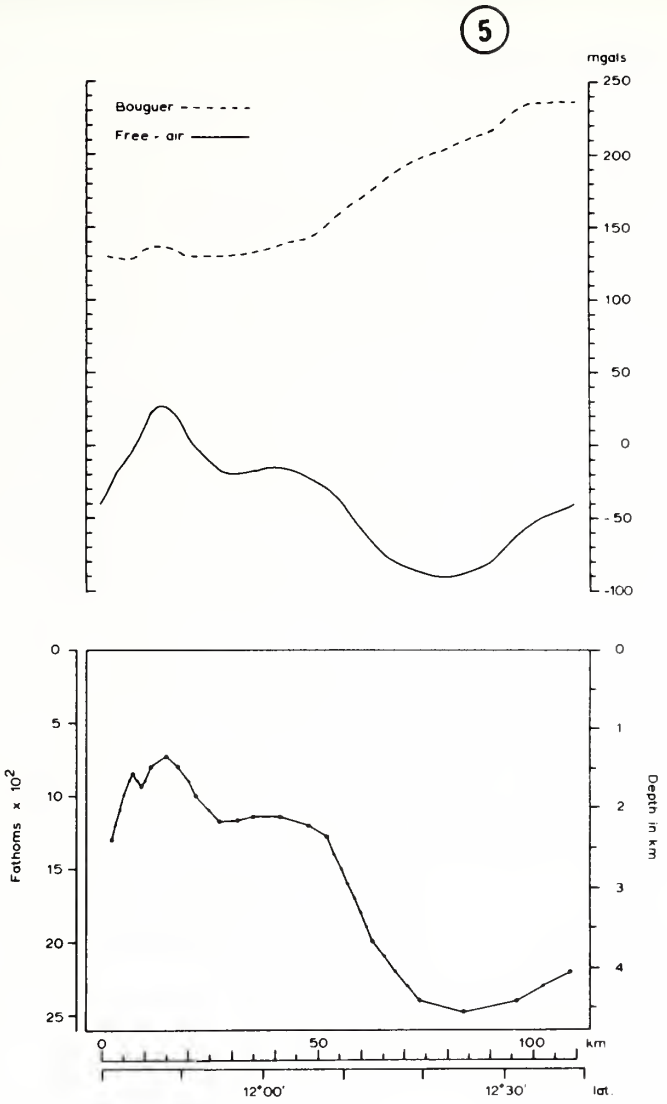
5
mgals
Bouguer
Free - air
250
200
150
100
50
0
-50
-100
Fathoms x 10²
Depth in km
0
5
10
15
20
25
1
2
3
4
0
50
100
km
12°00'
12°30'
lat.

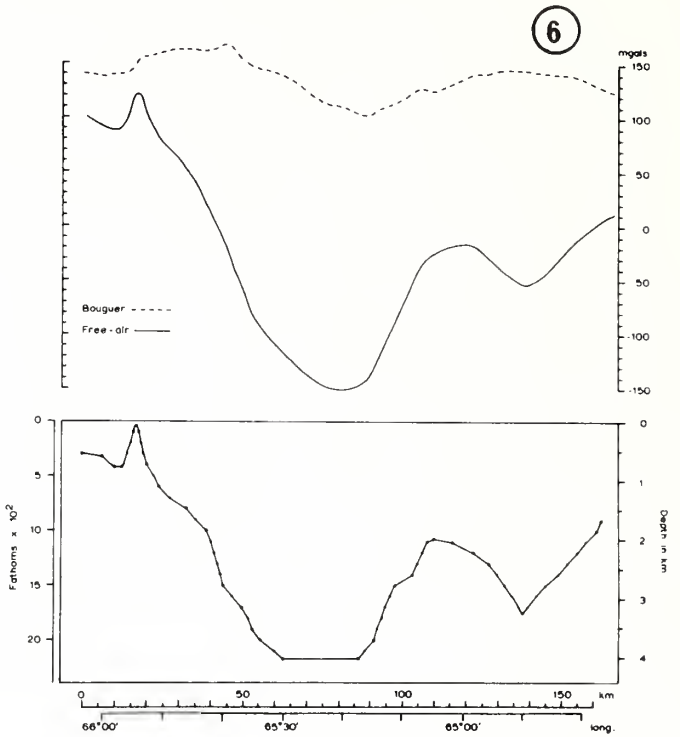
6
mgals
Bouguer
Free - air
150
100
50
0
-50
-100
-150
Fathoms x 10²
Depth in km
0
5
10
15
20
1
2
3
4
0
50
100
150
km
66°00'
65°30'
65°00'
long.

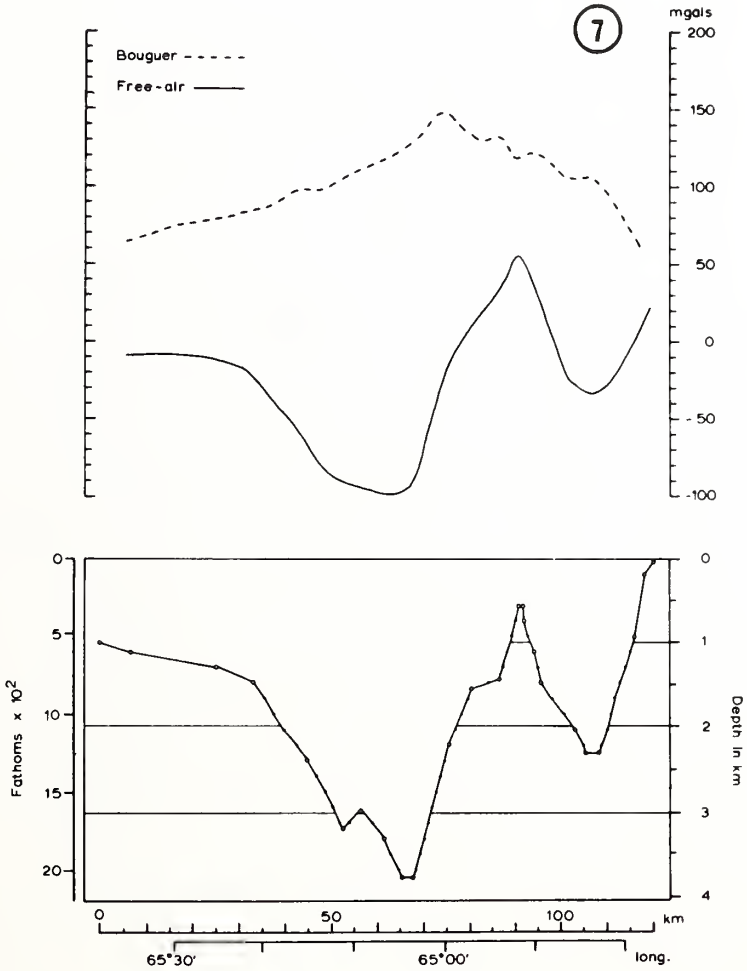
7
mgals
Bouguer
Free-air
200
150
100
50
0
-50
-100
Fathoms x 10²
Depth in km
0
5
10
15
20
1
2
3
4
0
50
100
km
65°30'
65°00'
long.

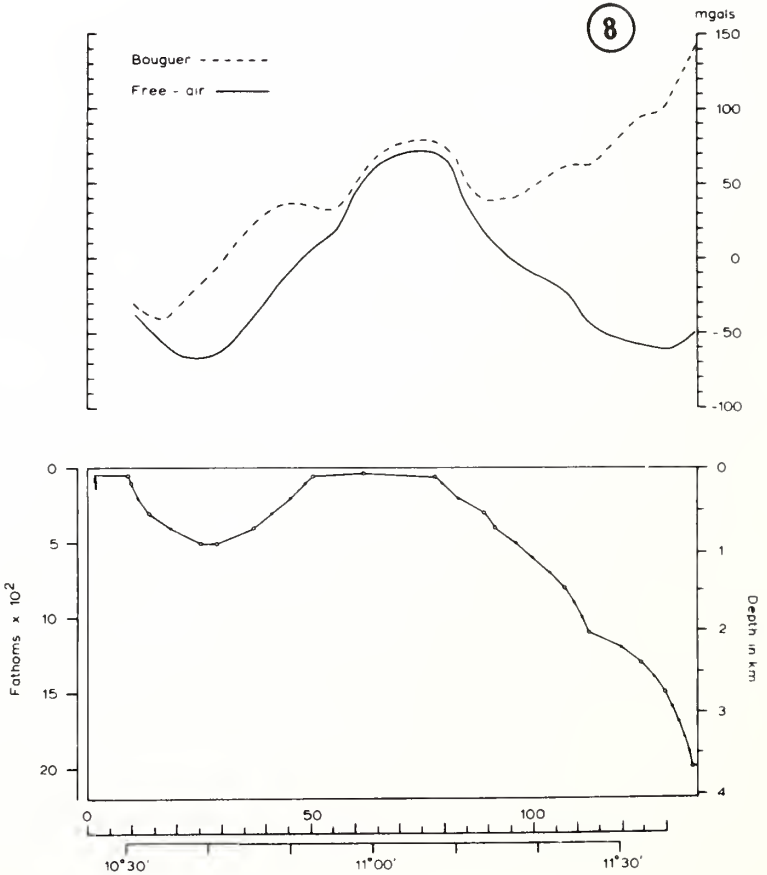
8
mgals
Bouguer
Free-air
150
100
50
0
-50
-100
Fathoms x 10²
Depth in km
0
5
10
15
20
1
2
3
4
0
50
100
10°30'
11°00'
11°30'

APPENDIX III

The location and description of the rocks recovered in the two successful dredge-hauls on the Blanquilla platform follow (Microscopic description is summarized from P. Kirch):

Dredge No. 1

Location: 11°00.7'N, 64°41.6'W, of the southwest tip of Blanquilla Island. The rocks were recovered from the lower slope of the island.

Depth: Approximate depth between 700 and 500 fm.

Field description: The dredge brought up about 10 lbs of mostly cobble-size (15 cm x 10 cm x 5 cm) rocks, apparently from the talus material covering the slope. Most of the rocks we were deeply weathered, but the larger pieces had fresh interiors.

The samples were divided into four types of rocks:
1) medium to fine grained, light grey, intrusive rock, with some indication of parallelism among the mafic minerals;
2) medium grained, dark grey intrusive rocks;
3) fine grained, dark grey, massive effusive or metamorphic rock; some samples porphyritic, and contain light green alteration (?) zones;
4) Microcrystalline limestone or marble.

Microscopic description:

Dredge # 1/1

Quartz diorite

Quartz, 2-5 mm, 10%,
undulatory extinction in most grains;
K-spar, .5-2 mm, 30%,
poorly defined zoning, minor sericitization along fractures;
Plagioclase, An(variable), .5-2 mm, 55%(?),
zoned xls perhaps as high as $An_{85?}$ in centers and An_{30-45} on rims;
Hornblende, 1-3 mm, 1/2 - 1%,
random distribution;
Biotite, 1-3 mm, 2%,
sub-parallel alignment, contains small inclusions of apatite;

Opague, 1/2-2 mm, 1/2-1%,
contains small inclusions of apatite.

Dredge # 1/2

Quartz monzonite

Quartz, 1-2 mm, 5% or less;
K-spar, 1-3 mm, 45%,
untwinned, partially sericitized;
Plagioclase, An , 1-2 mm, 45%,
continuous, normal zoning, interiors (calcic) are more altered than rims, extensive alteration along cleavages and fractures.
Hornblend, 1-4 mm, 4-5%;
Biotite, 1-3 mm, 1%,
abundant apatite inclusions;
Sphene, .5-1 mm, <1%,
associated with mafics in clots;
Opague, .5-1 mm, 1%;
Chlorite, .5-1 mm, <1%,
as alteration along fractures in hornblende, and alteration from biotite.

Dredge # 1/3

Meta-basalt

Plagioclase, An $_{(?)}$, 40-45%,
normally zoned, centers almost completely altered to clays, Epidotized in places;
Amphibole (?), 40%,
intermediate birefringence, fibrous, pleuchroism green - colorless;
Epidote, in aggregates, varies in samples 3-20%,
occurs in veins, no relict mineral is seen to produce the Epidote;
Opaque, variable up to 10%.

Dredge # 1/4

Marble

Calcite, .1-.5 mm, 99.5%,
irregular shape, random orientation, complete lack of twinning, possible serpentine inclusions.

Dredge No. 2

Location: 11°41.5'N, 64°53.8'W, from the western slope of a ridge southwest of Blanquilla Island.

Depth: Approximate depth between 600 and 400 fm.

Field description: The dredge brought up approximately 150 lbs of rock. Most of the rocks were of large cobble size (30 cm x 20 cm x 15 cm), with one boulder size rock (90 xm x 40 cm x 25 cm). Many of the smaller rocks were weathered talus material, but the boulder was freshly broken off the slope.

The samples were divided into three types of rocks:
1) very coarse grained (pegmatitic), light brown intrusive rock;
2) medium grained, orange yellow, intrusive rock;
3) medium grained, light grey, intrusive rock.

Microscopic description:

Dredge # 2/1

Graphic granite

Quartz, 1/2-3 mm, 25%,
random distribution, local patches of quartz intergrown with microcline;
Microcline, 5-30 mm, 74%;
Opaque, .5 mm, 1%,
Chlorite, trace;
Muscovite, trace.

Dredge # 2/2

Quartz diorite (highly altered)

Quartz, 1-3 mm, 15%,
random, highly fractured;
K-spar, 3-4 mm, 10%(?),
highly sericitized and fractured;
Plagioclase, $An_{30(?)}$, 1-6 mm, 60-70%,
deformed (curved) twin planes, highly fractured, very intense sausseritization, extensively epidotized;
Epidote, 1-2 mm, 4%,
in vein fillings and cross-cutting through plagioclase;

Chlorite (?), 1-2 mm, 1-2%;
Apatite, .5-1 mm, <1%,
associated with mafics;
Opaque, 2-3 mm, 1%,
fractured and altered to chlorite (?);
Sphene, .5 mm, trace,
associated with mafics.

Dredge # 2/3

Granodiorite

Quartz, 1-3 mm, 20-30%;
K-spar, 1-3 mm, 20-30%,
untwinned, undulatory extinction;
Plagioclase, $An_{(30-40)}$, 1-4 mm, 40-50%,
multiple normal zoning;
Hornblende, 1-4 mm, 1-2%,
small apatite inclusions;
Biotite, .5-2 mm, 1-2%,
small apatite inclusions;
Sphene, .5-1 mm, <1%;
Magnetite, .2 mm, <1/2%.

Dredge No. 2, Sample 2/3 was sent for age determination (courtesy of G. Pardo).

Petrographic description:

The rock sample is a medium grained, unaltered granite, with a following mineral composition:

Plagioclase, fresh crystals to 3 mm dia.; 40%;
Orthoclase, irregular fresh crystals to 3 mm dia.;
some zoning; 30%;
Quartz, very irregular patches to 3 mm dia.; 20%;
Hornblende, elongate crystals to 3 mm in length; partly altered to chlorite; 5%;
Biotite, associated with hornblende; to 3 mm dia.; 5%.

Tabulation of data pertinent to geochronometry:

A 30 - 50 mesh biotite separate was used for the K-Ar age determinations.
Potassium content = 7.29%;
Radiogenic Argon content = 3.981×10^{-8} g/gram biotite;
Radiogenic character of extracted argon gas = 69.4%;
$Ar^{40}/K^{40} = 4.45 \times 10^{3}$; Age = 81×10^{6} years.

Reprinted from Journal of Geophysical Research 77, No. 27, 5255-5265.

Vertical and Areal Distribution of Saharan Dust over the Western Equatorial North Atlantic Ocean

JOSEPH M. PROSPERO

Rosenstiel School of Marine and Atmospheric Science
University of Miami, Miami, Florida 33149

TOBY N. CARLSON

Atlantic Oceanographic and Meteorological Laboratories
Environmental Research Laboratories
National Oceanic and Atmospheric Administration, Miami, Florida 33124

Aerosol measurements were made as a part of the Barbados Oceanographic and Meteorological Experiment (Bomex) during May, June, and July 1969. Maximum dust concentrations occurred between the altitudes of 1.5 km and 3.7 km, a region which we call the Saharan air layer. The average concentration of mineral aerosol within this layer was 61 $\mu g\ m^{-3}$; in contrast, the average concentration in the low-level air was 22 $\mu g\ m^{-3}$. These dust concentrations are comparable to those found in continental surface air. Because of the presence of a strong inversion at the base of the Saharan layer, sea salt was confined to te lower altitudes where the average concentration was 10 $\mu g\ m^{-3}$. Thus, sea salt appears to be a relatively minor constituent of the trade wind aerosol during much of the year. On the basis of these measurements and of a model describing the movement of Saharan air outbreaks, we estimate that 25 to 37 million tons of dust are transported through the longitude of Barbados each year. This quantity of dust is sufficient to supply all the material required to maintain the present rate of pelagic sedimentation across the entire northern equatorial Atlantic Ocean.

The mineral aerosol concentration in sea-level, trade wind air at Barbados, West Indies (13°N, 59°W), has been measured from the fall of 1965 to the present [*Delany et al.*, 1967; *Prospero*, 1968; *Prospero et al.*, 1970; *Carlson and Prospero*, 1972]. During the first four years of this program, the air sampling was essentially continuous. These measurements have shown that large quantities of dust are transported across the northern equatorial Atlantic from the deserts of North Africa during the late spring, summer, and early fall. The average surface air concentration of mineral aerosol at Barbados during the dusty season varies from year to year but generally is of the order of 10 $\mu g\ m^{-3}$ of air; the concentration during the rest of the year is more than an order of magnitude less [*Prospero*, 1968; *Carlson and Prospero*, 1972].

During the Barbados Oceanographic and Meteorological Experiment (Bomex), we made an extensive investigation of the vertical distribution of mineral aerosols over the western equatorial North Atlantic and of the relationship of the aerosol distribution to meteorological parameters. The meteorological aspects of this work, a study of the large-scale movement of Saharan air outbreaks over the northern equatorial Atlantic, are presented by us elsewhere [*Carlson and Prospero*, 1972]. Briefly, we found that the characteristics of dusty air parcels appearing in the Barbados area are determined by events occurring over North Africa more than a week earlier. The transport process begins with the movement of air in a westerly direction over the Sahara; in the journey of several days across the desert, the air is subjected to intense heating at the desert surface. The heating produces strong convective activity, and eventually a mixed layer is generated that extends upward to 4.6–6.1 km (15–20 kft). As this hot, dry air emerges from the west coast of Africa, it is undercut by the relatively cool and moist trade winds that confine the Saharan air to altitudes above 1.2–1.8 km (4–6 kft). Because the base of the Saharan air parcel is 5–6°C warmer than the normal tropical

atmosphere, there is a very strong suppressive inversion above the moist trade wind air, a condition that persists during the 5 to 7 days usually required for air parcels to cross the Atlantic. The arrival of Saharan air over the Caribbean can be detected from soundings on the basis of the presence of such an inversion above which lies air having a low water vapor mixing ratio (2–4 g kg^{-1}) and an essentially constant potential temperature. The Saharan air generally extends upward to about 3.7 km (12 kft), where it is topped by a second inversion. In effect, then, the Saharan air is confined to a layer between two inversions.

Our aerosol studies show that the Saharan air layer is characterized by dust concentrations that are markedly higher than those found in the air above the layer or in the 'normal' maritime air below. In this paper, we present a summary of all the aerosol data obtained by us in Bomex and, on the basis of these data, estimate the total mass transport.

Experimental Procedure

The air sampling program was carried out aboard two DC-6 aircraft of the Research Flight Facility (NOAA, Miami, Florida). Aerosols were collected with IPC 1478 filters (Institute for Paper Chemistry, Appleton, Wisconsin) by means of the I2A foil (ram air) sampling system aboard each aircraft. The flow rate through the filter is determined by aircraft speed and altitude; under the flight conditions encountered in our work, sampling times of 7 to 15 min yielded 20 to 60 m^3 of standard air through a filter area of 45 cm^2. In all, 1360 filters were exposed continuously on each of 32 flights (281 hours flying time).

Aerosol weight on the filter was determined by first extracting the water-soluble component from the filter using three 4-ml aliquots of air-equilibrated distilled and deionized water; the extract was passed through a 0.45-μ membrane filter and was analyzed for sodium, magnesium, potassium, and calcium by means of standard atomic absorption spectroscopy techniques. Chloride ion was determined by a photometric technique [*Iwasaki et al.*, 1956]. The insoluble aerosol component was then measured by dry-ashing the water-extracted filter at 500°C and weighing the residue.

The processing of all 1360 filters in the manner outlined would have been exceedingly tedious and time consuming. Therefore, in an effort to obtain a semi-quantitative estimate of dust loads during Bomex, we first graded all the filters according to color density. This could be readily done because a large percentage of the exposed filters had a pronounced red-brown coloration. The fact that this hue was quite constant all summer long greatly facilitated the color grading; a change in color occurred only once on a mission in which the aircraft penetrated the inter-tropical convergence zone (ITCZ) and entered the southern hemisphere trade winds, at which time the filter became grey.

A color density scale was established by the visual examination of the filters from several flights made under atmospheric conditions ranging from exceptionally clear (dust-free) to extremely hazy (dusty). These filters, 200 in all, were placed on a white background, and from these we chose a series of eight reference filters whose colors encompassed the entire color density range. These were numbered from zero, represented by an unused filter, to 7, the most densely colored filter. All the Bomex filters were then graded by comparison with the reference filters. Filters that could not be definitely assigned to either of two adjacent density groups were given an intermediate classification (for example, 6.5 for a filter color falling between 6 and 7). Henceforth, we will refer to the numerical classification of filter color density as the filter color index (FCI).

The correlation of ashed filter residue (i.e., insoluble aerosol) with FCI is shown in Figure 1. The large scatter in the data for FCI values below 1.5 is attributable to a number of factors. First, the amount of material on the filter, of the order of a few micrograms per square centimeter, is barely visible. Consequently, variations in filter texture could easily lead to an erroneous index assignment; because of the loose construction of the filter matrix, surface texture was affected by sample duration and, especially, by passage through cloud. This exposure effect probably explains why no filter ever warranted a zero FCI, for which the reference standard was an unexposed filter. Also, the filters employed during Bomex were obtained in sealed lots of 20, which apparently were derived from at least several different production runs, each

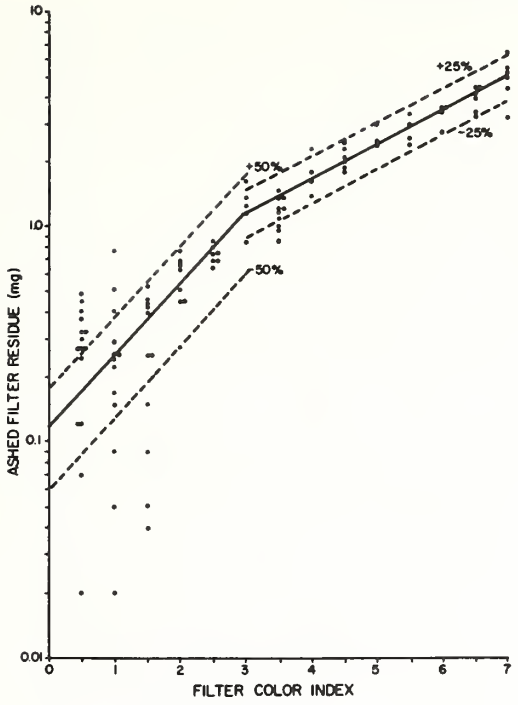

Fig. 1. Filter color index as a function of ashed filter residue. Residue weights have been corrected for an average filter blank of 0.15 mg. The dashed lines have no statistical significance but are drawn to delineate a range of values about the best fit line.

of which produced filters of somewhat different texture and weight. The variation in filter weight introduced a second source of error because we were obliged to use an average blank of 0.15 mg for the ashed filter matrix, although individual values ranged from 0.10 to 0.24 mg. Above FCI 1.5, the agreement is good enough to warrant the use of the FCI as a semiquantitative measure of filter dust load and, subsequently, the atmospheric dust concentration. The aerosol data presented here consist of concentrations based on 107 ashed filter determinations and 1253 FCI values; these data supersede the few dust load estimates based on a preliminary color scale presented earlier [*Carlson and Prospero*, 1972].

The measured efficiency of the IPC filter for monodisperse test aerosols in the size range 0.30- to 1.17-μ diameter at the speeds and altitudes used in our flights ranged in the extreme from 70% to 95% [*Stern et al.*, 1960]. Under typical flight conditions, the efficiency was about 80%. However, in the data presented here, we have simply assumed a filter collection efficiency of 100% unless otherwise indicated.

Results

Bomex was divided into four study periods; (1) May 3–15; (2) May 24 to June 10; (3) June 19 to July 2; (4) July 11–28. During the first three periods, all activity was confined to the area encompassed by the square, the Bomex 'box,' shown in Figure 2. The fourth period was designated as a tropical exploration program in which experiments were defined from day to day on the basis of the synoptic situation; there were no fixed research areas or flight plans.

Our sampling program was unbiased as far as sample selection was concerned in the sense that aerosol sampling was never a primary objective in the flights; consequently, we did not actively participate in flight planning. Once the mission was assigned, the flight parameters were strictly fixed and sampling was carried out continuously from take-off until touchdown. In addition, we further avoided sampling bias by participating in all but one mission assigned to our aircraft (RFF 40C).

Insoluble Aerosols

A summary of all the Bomex aerosol data is presented in Figure 3. Included are data ob-

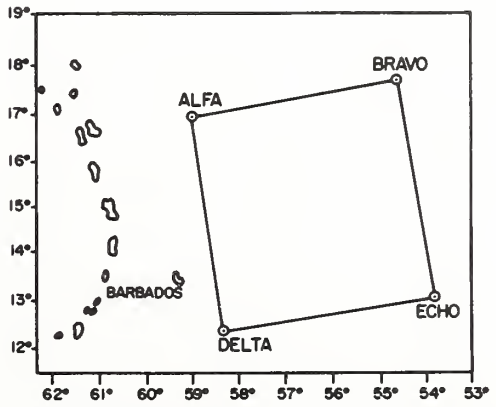

Fig. 2. The Bomex investigational area during the first three periods of the program. Each side of the box is 500 km long.

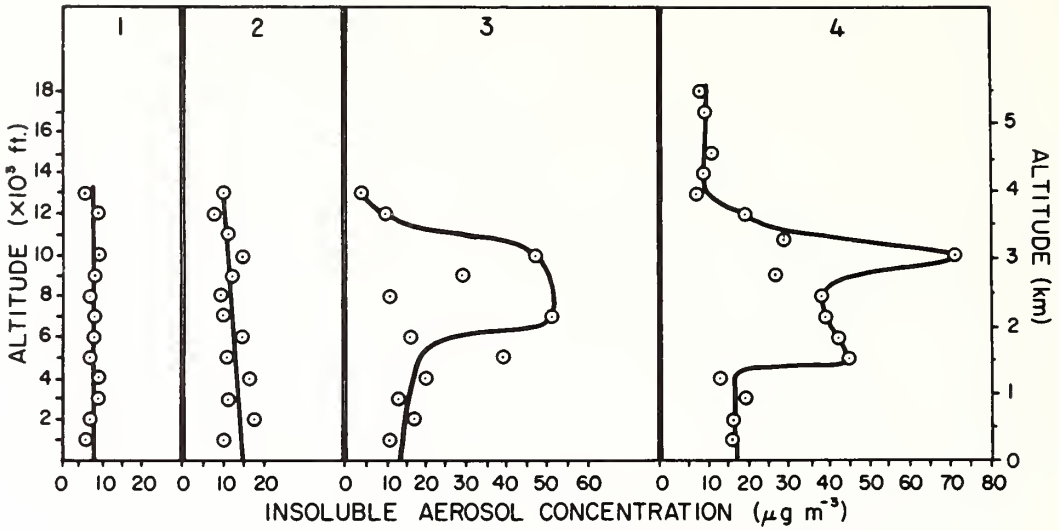

Fig. 3. The vertical distribution of insoluble aerosol during each of the four Bomex periods. Each point represents the arithmetic average of all measurements made within 305-meter (1-kft) altitude intervals. The points lying off the smoothed distribution drawn for periods 3 and 4 are averages of only one or two measurements, whereas the adjacent points through which the line is drawn are averages of at least 21 measurements. The total number of measurements in each period were 180, 411, 221, and 552, respectively. The data in this figure and those following have not been corrected for filter efficiency or for the loss of volatile aerosol material during ashing.

tained on shuttle flights between Barbados and Miami and a flight to Recife, Brazil; however, only data points between 10°N and 25°N were used from these flights.

The average trade wind aerosol concentration during each of the four Bomex periods calculated on the basis of the smoothed vertical distributions shown in Figure 3 is: (1) 8 μg m^{-3}; (2) 13 μg m^{-3}; (3) 26 μg m^{-3}; (4) 25 μg m^{-3}. If we correct these data for a filter efficiency of 80% and a volatile aerosol weight loss of 10% at ignition, these averages become 11, 18, 36, and 35 μg m^{-3}, respectively.

The increase in the insoluble aerosol concentration as the summer progresses is consistent with our long-term surface-air measurements, which show that the dust transport generally attains its maximum late in the summer [*Prospero*, 1968; *Carlson and Prospero*, 1972]. The increase is most dramatic between the altitudes of 1.5 and 3.7 km, the region that we identify as the Saharan air layer on the basis of its meteorological characteristics.

The variation of aerosol concentration with altitude and geographical position is best seen from the data of individual flights such as those discussed below.

June 22. The aircraft departed from Barbados on June 22 and climbed eastward until it intersected the western side of the Bomex box at a point about 100 km north of delta (Figure 4). The aircraft then turned to the north and flew around the box at 3.0 km in a clockwise fashion (alpha, beta, echo, delta). At delta, the aircraft climbed to 4.6 km and retraced the flight path counterclockwise back to Barbados. The dust loads at 3.0 km were consistently in the range of 75–100 μg m^{-3} on the west, north, and east sides of the box (see reference points in Figure 2) but decreased toward the west on the south side. At delta, the dust concentration decreased to a few μg m^{-3} air between 3.0 and 4.6 km. At 4.6 km, the maximum concentrations, 55–60 μg m^{-3}, were obtained along the north side of the box. The only dust load data below 3.0 km were obtained on climb-out and descent near Barbados. It is evident from the relatively high dust load of the first sample, collected between 1.0 and 2.5 km, that the base of the dust layer extended considerably below

the 3.0-km flight level. The samples from the descent made at the same point some 10 hours later show only a few $\mu g\ m^{-3}$ of dust from 4.6 km to the surface.

We can visualize the dust distribution on this day as being a rather uniform layer covering all but the southernmost side of the Bomex box, an area of 2.5 by 10^5 km^2 (10^5 mi^2); the upper surface of the layer apparently rises to the north, extending above 4.6 km along 17°N. On the basis of the data from the descent near Barbados, as contrasted with the ascent, we conclude that the southernmost edge of the dusty area, and presumably the entire layer itself, had moved to the north during the 10-hour interval; this conclusion is consistent with wind data, which showed ESE and SE winds over the entire region.

June 23. The aircraft departed from Barbados on June 23 and flew ESE to Point Kilo, midway between delta and echo on the southern side of the Bomex box (Figure 2). The aircraft then returned to delta and proceeded to make a series of runs at 0.3, 1.2, and 2.1 km (1, 4, and 7 kft) between alpha and delta on the west side of the box. The data in Figure 5 reveal that the dust loads increased markedly with altitude; however, at any one altitude, the loads were very uniform along the entire 500 km length of the run, except for the occurrence of a sharp decrease in dust load about midway between alpha and delta in both the 1.2-km and 2.1-km runs. The dust loads at 0.3 km were unchanged from the time of departure until the return more than 10 hours later. Taking into account the data from the initial eastward runs of 400 km to Kilo and the advective effect of the 24 to 32 km hr^{-1} easterly winds during this time interval, we conclude that the entire Bomex area was covered by this dust layer.

June 29. The experimental flight pattern on June 29 was similar to that of June 23, except that the runs were performed on the eastern side of the box between bravo and echo. At

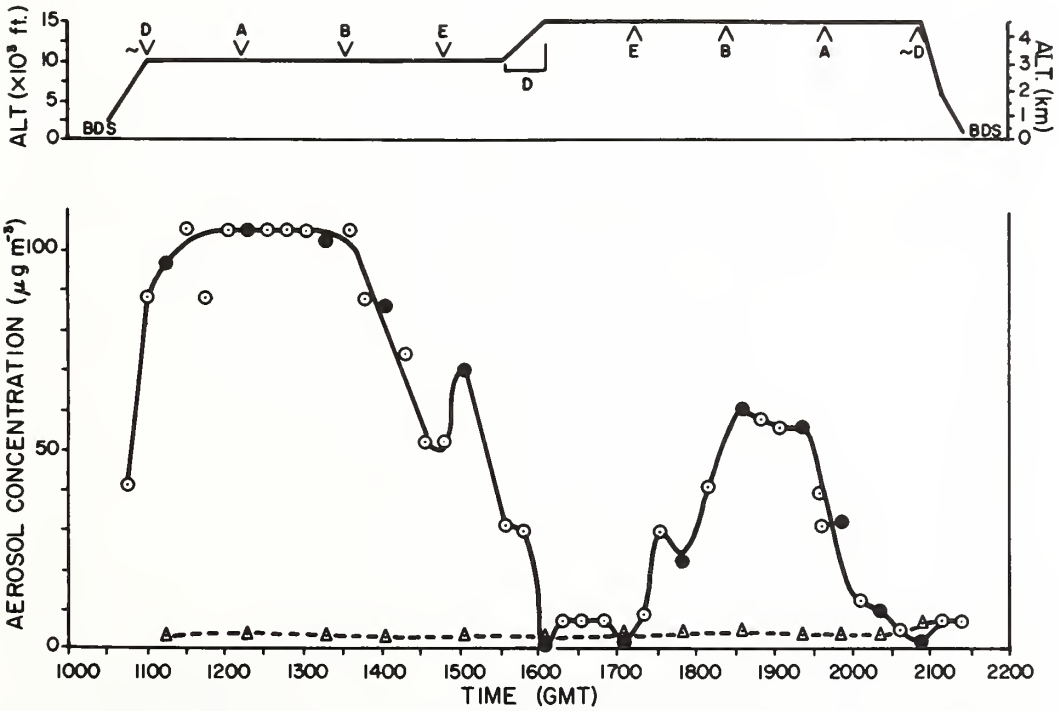

Fig. 4. Aerosol concentration and aircraft altitude in Bomex on June 22, 1969. The data points represented by filled circles are calculated on the basis of the net ashed filter residue; the open circles are based on the filter color index (FCI). The triangles represent sea salt aerosol concentrations. The letters *A*, *B*, *D*, and *E* refer to the points alpha, bravo, delta, and echo in Figure 2; BDS represents Barbados.

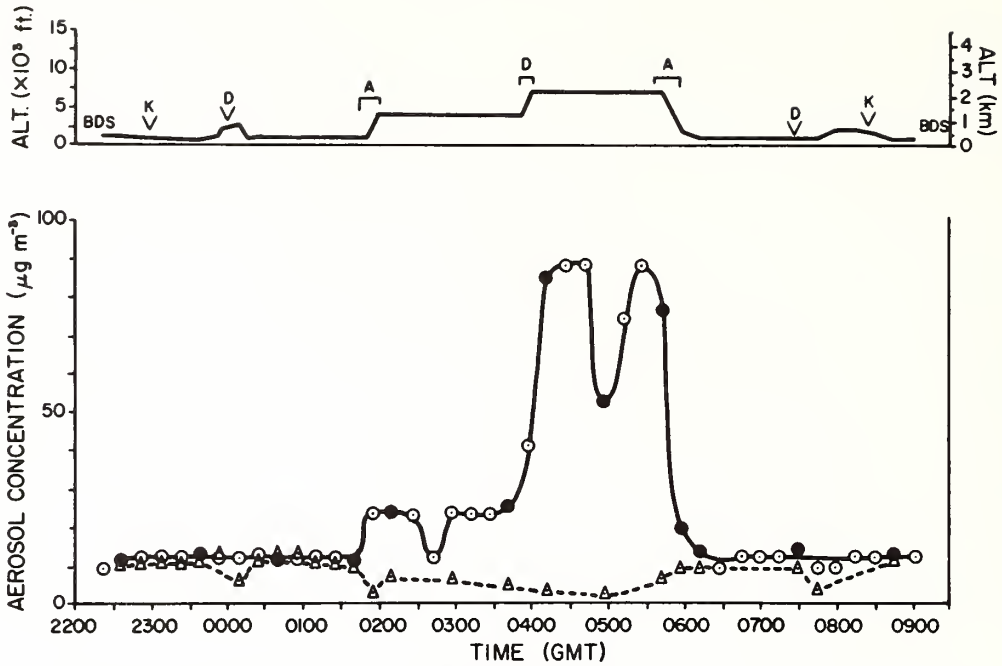

Fig. 5. Aerosol concentration and aircraft altitude in Bomex on June 23, 1969. Point *K* is midway between points delta and echo in Figure 2. Symbols same as in Figure 4.

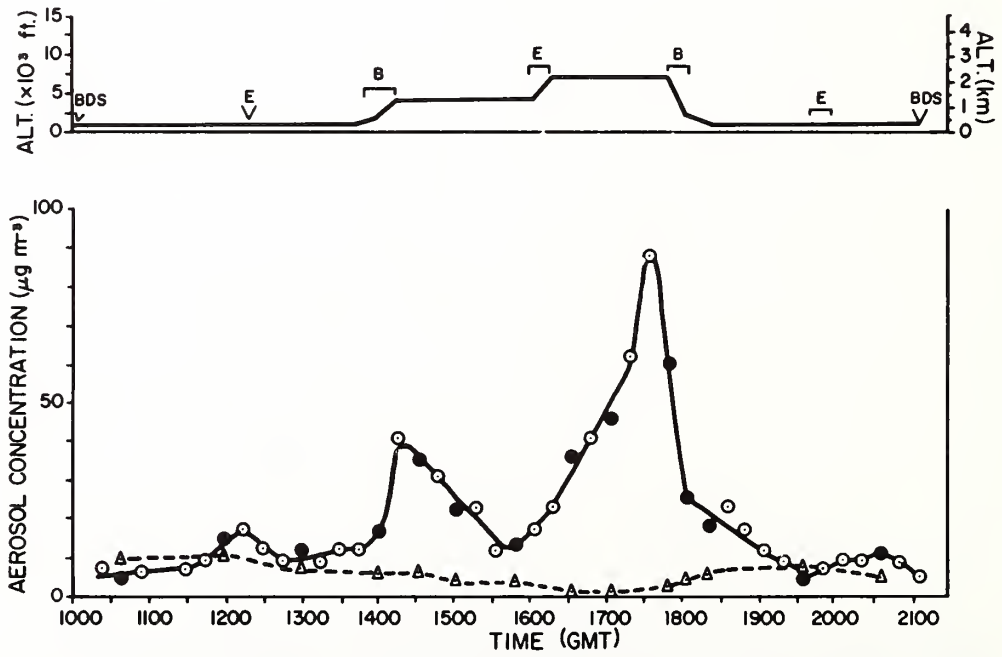

Fig. 6. Aerosol concentration and aircraft altitude in Bomex on June 29, 1969. Symbols same as in Figure 4.

the 0.3-km level from Barbados to echo to bravo, the dust loads were fairly uniform, ranging from 5 to 15 $\mu g\ m^{-3}$ (Figure 6). In the climb to 1.2 km at bravo, the load increased sharply to 40 $\mu g\ m^{-3}$ but then decreased on the flight southward to echo. There was no significant increase in the climb from 1.2 km to 2.1 km at echo, but during the flight to bravo the dust loads increased markedly; the maximum at 2.1 km, 90 $\mu g\ m^{-3}$, occurred at the same geographical location as the maximum observed at 1.2 km. On the descent to 0.3 km, the concentration dropped sharply. It appears from these data that the Saharan dust layer penetrated the Bomex area only on the northernmost side of the box.

July 14. The purpose of the mission on July 14 was the investigation of a tropical disturbance whose axis was east of Barbados near 57°W. The flight pattern was essentially an isosceles triangle with the apex at Barbados and the base between 17°N, 47°W, and 23°N, 50°W. The dust loads were low as the aircraft climbed through the disturbance at 14°N, 57°W but increased dramatically above 2.7 km and remained high (50–120 $\mu g\ m^{-3}$) for the duration of the flight at 3.0 km (Figure 7). The sharp horizontal definition between the base of the Saharan layer and the mixed layer below is shown by the data obtained during the rapid descent from 3.0 to 0.4 km at about 1900 GMT; the dust load from 2.2 to 1.6 km was 95 $\mu g\ m^{-3}$, whereas that from 1.5 to 0.4 km was sharply lower, 6 $\mu g\ m^{-3}$, a value that was maintained for the rest of the flight. On the basis of these and other observational data [*Carlson and Prospero*, 1972], we conclude that the African dust layer was confined to a region behind the disturbance axis (57°W) between 24°N and the edge of the ITCZ, about 10°N; the layer extended eastward beyond 45°W, the limit of the observational area.

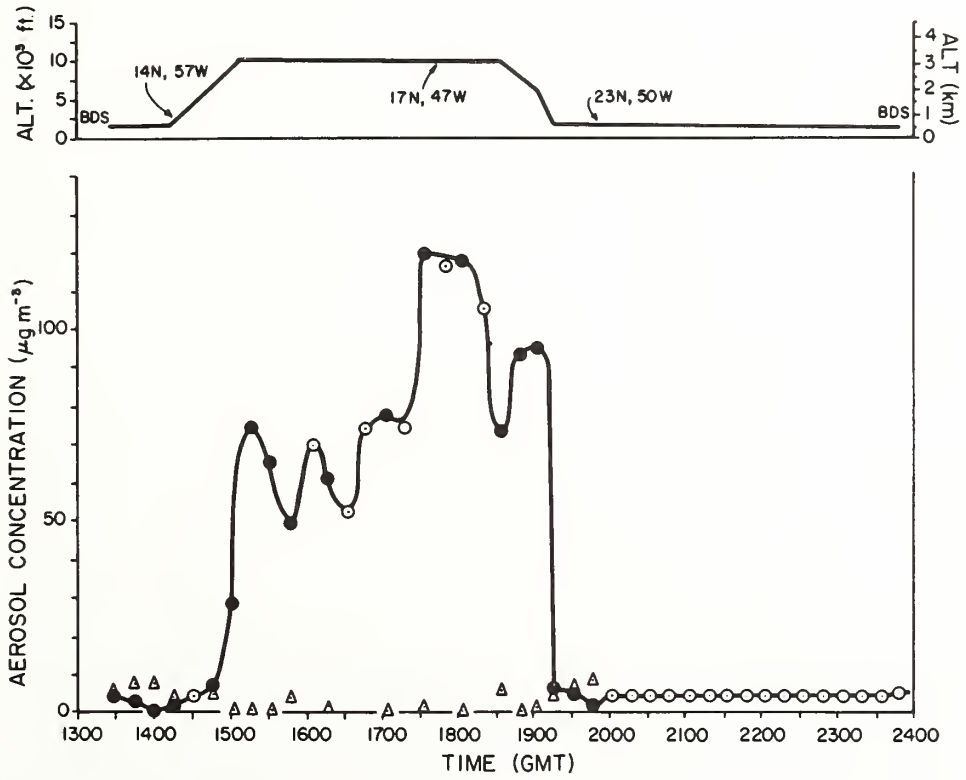

Fig. 7. Aerosol concentration and aircraft altitude in Bomex on July 14, 1969. The positions indicated on the altitude plot are explained in the text. Symbols same as in Figure 4.

July 18. The missions on July 18 followed a triangular track to the east of Barbados: NE to 16°N, 51°W; SW to 9°N, 54°W; NW to Barbados. In this case (Figure 8), the dust load increased by more than an order of magnitude over the distance of a few miles during horizontal flight. The maximum dust load of the flight and of the entire Bomex experiment, 160 μg m^{-3}, occurred about 300 km behind the dust 'front.' Dust loads were high as the aircraft turned south and remained high even after the plane had descended to 0.3 km; we attribute the presence of a large concentration of dust at lower levels to the effects of the widespread convective activity associated with the northern edge of the ITCZ. On the rest of the flight, dust loads were low except for a short period when the aircraft briefly re-entered the dust 'front' east of Barbados. We surmise from these measurements, corrected for advective transport, that the leading edge of the dust layer extended from the ITCZ at 11°N, 52°W to 15°N, 60°W and beyond.

On this day, aerosol measurements were also being made aboard a second aircraft, RFF 39C, using identical equipment and procedures; the aircraft followed a course similar to that of our aircraft, but at an altitude of 5.5 km (18 kft). The average dust load was 4 μg m^{-3}, more than an order of magnitude lower than the value obtained at 3.0 km in the region of the Saharan air layer.

Soluble Aerosols

The only data that we will present on this aspect of our study are sea salt aerosol concentrations calculated on the basis of the chloride content (28 samples) or the sodium content (38 samples) of our aqueous filter extract; we assume that all the chloride or sodium was derived from sea water and that the relative concentrations of the sea water constituents in the

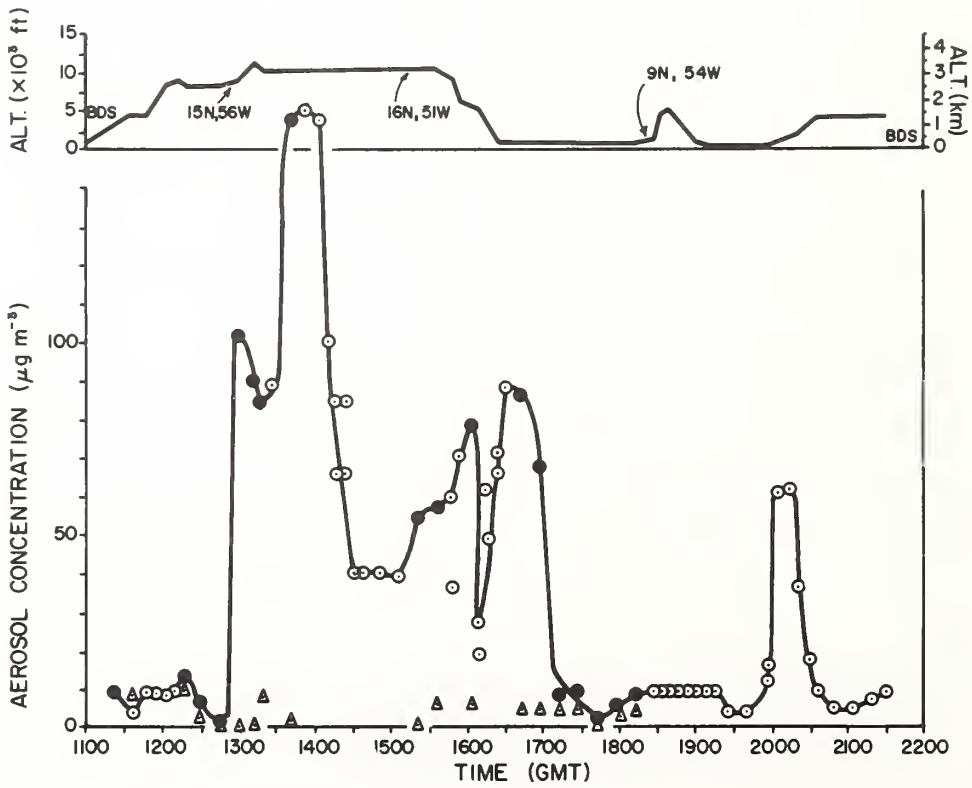

Fig. 8. Aerosol concentration and aircraft altitude in Bomex on July 18, 1969. Symbols same as in Figure 4.

aerosol were the same as those in sea water. This assumption is not strictly valid, because we did indeed observe substantial deviations from sea water ratios for some of the aerosol constituents; specifically, the average ratio Cl/Na was about 20% less than that of sea water, whereas that of Mg/Na was about 15% greater. However, the ratios obtained for these major ions were sufficiently close to that of sea water to warrant the use of sea water ratios for our calculations.

The sea salt aerosol concentrations are presented in Figures 4–8. It is evident that the sea salt aerosol concentration decreases rapidly with altitude (see in particular Figures 5–8). Whereas the average concentration below the Saharan layer was 10 $\mu g\ m^{-3}$, deep within the dust layer it was less than 2 $\mu g\ m^{-3}$; the latter values are probably high because of the contribution from the soluble components in the dust, whose concentration in some cases is more than a hundred times greater. The concentration of sea salt aerosol as a function of altitude agrees well with the data of *Woodcock* [1953, 1962] obtained under similar wind conditions. The few cases where relatively high sea salt concentrations were measured in regions of high dust load are directly attributable to the effects of strong convective mixing at the base of the Saharan layer; this is true for the measurements made between 1530 and 1730 GMT on July 18 (Figure 8) in a region on the northern edge of the ITCZ.

DISCUSSION

The average concentration of mineral aerosol within the Saharan air layer over the western Atlantic during Bomex periods 3 and 4 was 44 $\mu g\ m^{-3}$; if we correct this value for the filter efficiency of 80% and a 10% weight loss of volatiles that occurs upon ignition, we obtain an average value of 61 $\mu g\ m^{-3}$. The average adjusted dust load below the layer was 22 $\mu g\ m^{-3}$.

In view of the results of our sea salt measurements, we conclude that, during the dusty season, sea salt is a relatively minor component of the so-called marine aerosol in this region. Indeed, the dust loads are comparable to continental values; for example, the average surface air concentration of suspended particulates, both soluble and insoluble, as measured in the United States by the National Air Surveillance Network [*National Air Pollution Control Administration*, 1968] was 21 $\mu g\ m^{-3}$ for remote sites, 40 $\mu g\ m^{-3}$ for nonurban sites, and 102 $\mu g\ m^{-3}$ for urban sites.

The areal extent of the Saharan layer can often be determined from satellite photographs; the dusty areas have a grey smudged appearance and are relatively cloud-free. The lack of significant cloud build-up is due to the presence of the strong inversion. However, the inversion gradually weakens because of radiational cooling within the layer and, after several days over the ocean, convective penetration occurs with increasing frequency, making identification of the parcel difficult. Consequently, over the western Atlantic, the presence of the layer is best ascertained by searching radiosonde data for the appearance of a layer of relatively warm and dry air having a uniform lapse of potential temperature and mixing ratio.

Carlson and Prospero [1972] present a number of examples in which the history of Saharan air outbreaks is determined through the combined use of conventional radiosonde data and satellite photographs; they also present a schematic model that depicts the generation and movement of these outbreaks. Utilizing this model, we can calculate the quantity of mineral aerosol transported through the longitude of Barbados. We will assume:

1. An average transport velocity of 25 km hr^{-1}.
2. A transport belt extending from 10°N to 25°N.
3. A transport depth of 5.5 km.

Using the average adjusted dust load obtained during all of Bomex, 25 $\mu g\ m^{-3}$, we obtain a mass transport of 0.14 Mt day^{-1} (1 Mt = 10^{12} grams). If we use the average dust load of 35 $\mu g\ m^{-3}$ obtained for periods 3 and 4, when conditions existed that we feel are more representative, the calculated transport is 0.2 Mt day^{-1} or 37 Mt during a dust transport period of 6 months.

Obviously, the quantity of dust moving across the west coast of Africa is larger. During the summer months, 15–25% of the meteorological reports from the region between the Cape Verde Islands and the coast of Africa cite haze, assumed to be indicative of dust, whereas in the western Atlantic the frequency is only a few

per cent [*MacDonald*, 1938]. The haze distribution also suggests that heavy dust transport occurs all year long; however, the winter dusts are carried principally in the latitudes below 10°N, which explains why high dust concentrations are not observed at Barbados at this time of year. Although there have been a few surface-air measurements of dust loads off the coast of Africa [*Chester et al.*, 1971; *Chester and Johnson*, 1971; *Folger*, 1970; *Junge and Jaenicke*, 1971; *Parkin et al.*, 1970], they are of doubtful utility for estimating transport, because the principal transport takes place at higher levels. The dust collected in surface air may be material that has settled out of the Saharan layer; alternatively, the dust may be material raised by the low-level northerly winds of oceanic origin that sweep inland along the coast of Spanish Sahara, Mauritania, and Senegal. They are the very winds that undercut the hot, dry, dust-laden air emerging from the Sahara and thereby produce the layered structure that we observe [*Carlson and Prospero*, 1972].

It is difficult to make a good estimate of dust deposition across the width of the Atlantic because of our lack of knowledge of the concentration and size distribution of the dust emerging from Africa in the Saharan air layer. As far as removal mechanisms are concerned, it appears that, initially, the principal mode of deposition must be by dry removal; the strong inversion at the base of the Saharan layer severely limits convective activity and, consequently, precludes the possibility of wet removal except in disturbances. The inhibition of wet removal, the mechanism by which 80–90% of the aerosol mass is normally deposited [*Junge*, 1963], may in part explain the persistence of the dust layer.

Wet removal probably becomes significant over the western Atlantic, the Caribbean, and the Gulf of Mexico. Deposition in this region can be estimated by applying the concept of a deposition velocity, which for radioactive fallout is generally about 1 cm sec^{-1} [*Peterson and Crawford*, 1970]. For an average aerosol concentration of 25 $\mu g\ m^{-3}$, the deposition calculated on a 6-month transport basis is 0.4 g cm^{-2} per thousand years. This quantity of dust on the ocean floor would yield 5–6 mm of sediments, assuming a typical in situ density of 0.65–0.85 g cm^{-3} for dry, uncompressed pelagic material [*Richards*, 1962]. This sedimentation rate is consistent with the measured $CaCO_3$-free rates that in this region are generally in the range of 2 to 10 mm per thousand years [*Ku et al.*, 1968]. If the deposition rate of 0.4 g cm^{-2} per thousand years is applied to the entire equatorial Atlantic from Barbados to Africa between 10°N and 25°N (i.e., the dust transport belt), the annual mass deposition would be 30 Mt, a quantity comparable to the annual mass transported through the longitude of Barbados. Thus, it is conceivable that airborne Saharan dust may be a major source of material for equatorial North Atlantic oceanic sediments.

A number of estimates have been made of the wind transport on a worldwide basis. *Judson* [1968] calculates that 60 to 360 Mt are delivered to the oceans annually. *Inadvertent Climate Modification: Report of the Study of Man's Impact on Climate* [1971] reviews the work of several groups who obtained estimates ranging from 200 Mt yr^{-1} to 100–500 Mt yr^{-1}. On the basis of the extremes of this range of estimates, the mass transported through the longitude of Barbados constitutes at a minimum 5% of the world transport and at a maximum 62%.

Acknowledgments. We thank the Research Flight Facility, NOAA, particularly the crews of aircraft 39C and 40C, for their generous cooperation. We are especially grateful to Ann R. Prospero, who participated in many of the flights and gathered much of the data presented here. We are indebted to Judge G. L. Taylor, Barbados, for the continued use of his land and residence for our operations and to R. Nees for technical assistance.

Part of this research was supported by National Science Foundation grants GA-25916 and GA-31104 and Office of Naval Research contract Nonr 4008(02).

Contribution 1537 from the Rosenstiel School of Marine and Atmospheric Science, University of Miami, Miami, Florida 33149.

REFERENCES

Carlson, T. N., and J. M. Prospero, The large-scale movement of Saharan air outbreaks over the equatorial North Atlantic, *J. Appl. Meteorol.*, *11*, 283, 1972.

Chester, R., and L. R. Johnson, Atmospheric dusts collected off the Atlantic coasts of North Africa and the Iberian Peninsula, *Marine Geol.*, *11*, 251, 1971.

Chester, R., H. Elderfield, and J. J. Griffin, Dust transported in the north-east and south-east trade winds in the Atlantic Ocean, *Nature, 233,* 474, 1971.

Delany, A. C., A. C. Delany, D. W. Parkin, J. J. Griffin, E. D. Goldberg, and B. E. F. Reimann, Airborne dust collected at Barbados, *Geochim. Cosmochim. Acta, 31,* 885, 1967.

Folger, D. W., Wind transport of land-derived mineral, biogenic and industrial matter over the North Atlantic, *Deep Sea Res., 17,* 337, 1970.

Inadvertent Climate Modification: Report of the Study of Man's Impact on Climate, MIT Press, Cambridge, Mass., 1971.

Iwasaki, I., S. Utsumi, K. Hagino, and T. Ozawa, A new spectrophotometer method for the determination of small amounts of chloride using the mercuric thiocyanate method, *Bull. Chem. Soc. Jap., 29,* 860, 1956.

Judson, S., Erosion of the land, *Amer. Sci., 56,* 356, 1968.

Junge, C. E., *Air Chemistry and Radioactivity,* Academic, New York, 1963.

Junge, C., and R. Jaenicke, New results in background aerosols studied from the Atlantic expedition of the RV *Meteor,* Spring 1969, *J. Aerosol Sci., 2,* 305, 1971.

Ku, T. L., W. S. Broecker, and N. Opdyke, Comparison of sedimentation rates measured by paleomagnetic and ionium methods of age determination, *Earth Planet. Sci. Lett., 4,* 1, 1968.

MacDonald, W. F., *Atlas of Climatic Charts of the Oceans, Publ. 1247,* U.S. Dept. Agr., Weather Bureau, Washington, D.C., 1938.

National Air Pollution Control Administration, Air Quality Data from the National Air Sampling Networks and Contributing State and Local Networks, 1966 Edition, *NAPCA Publ. APTD 68-9,* U.S. Dept. of Health, Education and Welfare, Washington, D.C., 1968.

Parkin, D. W., D. R. Phillips, R. A. L. Sullivan, and L. Johnson, Airborne dust collections over the North Atlantic, *J. Geophys. Res., 75,* 1782, 1970.

Peterson, K. R., and T. V. Crawford, Precipitation scavenging in a large-cloud diffusion code, in *Precipitation Scavenging (1970),* edited by R. J. Engelmann and W. G. N. Slinn, p. 425, U.S. Atomic Energy Comm., Washington, D.C., 1970.

Prospero, J. M., Atmospheric dust studies on Barbados, *Bull. Amer. Meteorol. Soc., 49,* 645, 1968.

Prospero, J. M., and T. N. Carlson, Radon-222 in the North Atlantic trade winds: Its relationship to dust transport from Africa, *Science, 167,* 974, 1970.

Prospero, J. M., E. Bonatti, C. Schubert, and T. N. Carlson, Dust in the Caribbean atmosphere traced to an African dust storm, *Earth. Planet. Sci. Lett., 9,* 287, 1970.

Richards, A. F., *Investigations of Deep-Sea Sediment Cores, 2, Mass Physical Properties, Publ. TR-106,* U.S. Navy Hydrographic Office, Washington, D.C., 1962.

Stern, S. C., H. W. Zeller, and A. I. Schekman, The aerosol efficiency and pressure drop of a fibrous filter at reduced pressures, *J. Colloid Sci., 15,* 546, 1960.

Woodcock, A. H., Salt nuclei in marine air as a function of altitude and wind force, *J. Meteorol., 10,* 362, 1953.

Woodcock, A. H., Solubles, in *The Sea,* vol. 1, edited by M. N. Hill, Interscience, New York, 1962.

(Received March 20, 1972;
revised May 23, 1972.)

U.S. DEPARTMENT OF COMMERCE
Peter G. Peterson, Secretary

NATIONAL OCEANIC AND ATMOSPHERIC ADMINISTRATION
Robert M. White, Administrator
ENVIRONMENTAL RESEARCH LABORATORIES
Wilmot N. Hess, Director

NOAA TECHNICAL REPORT ERL 238-AOML 8

Exploration Methods for the Continental Shelf: Geology, Geophysics, Geochemistry

PETER A. RONA

BOULDER, COLO.
June 1972

TABLE OF CONTENTS

		Page
1.	INTRODUCTION	1
2.	OCCURRENCE OF CONTINENTAL SHELF MINERAL DEPOSITS	3
3.	GEOLOGICAL METHODS	5
	3.1 Bathymetry and Side-looking Sonar	5
	3.2 Photography	9
	3.3 Bottom Sampling	10
4.	GEOPHYSICAL METHODS	15
	4.1 Seismic Reflection	16
	4.2 Seismic Refraction	20
	4.3 Magnetic Method	22
	4.4 Gravity	27
	4.5 Electrical Methods	30
	4.6 Heat Flow	33
	4.7 Radioactive Methods	36
5.	GEOCHEMICAL METHODS	37
6.	THE MARINE ENVIRONMENT	38
7.	NAVIGATION	40
8.	COMPOSITE EXPLORATION METHODS	41
9.	BIBLIOGRAPHY	42
	9.1 General	42
	9.2 Occurrence of Continental Shelf Mineral Deposits	42
	9.3 Geological Methods	43
	9.4 Geophysical Methods	43
	9.5 Geochemical Methods	46
	9.6 Navigation	46

EXPLORATION METHODS FOR THE CONTINENTAL SHELF: GEOLOGY, GEOPHYSICS, GEOCHEMISTRY*

Peter A. Rona

The continental shelf is an extension of the continent into the ocean. This fact determines both the occurrence of mineral deposits and methods used to seek these deposits.

1. INTRODUCTION

The problem of mineral exploration is the proverbial one of searching for a needle in a haystack. Just as the needle is a small object in the large haystack, economic concentrations of mineral deposits, including oil, occupy a minute fraction of the earth's crust. Exploration methods aim to delineate anomalous quantities, that is, abnormal concentrations of the mineral being sought. Just as the needle is different from the hay, the mineral deposits are different from the surrounding crust. Their presence must be detected by measuring the distinctive physical properties such as size, shape, density, sound velocity, magnetism, electrical and heat conductivity, or the chemical properties such as composition, that reside in or are associated with the deposits. In the case of the needle, a method might be employed to detect its magnetic properties; likewise, exploration methods are matched to detect the distinctive properties of different types of mineral deposits.

The exploration method employed must have adequate resolution and penetration to detect the size and depth of burial of the deposit being sought. By "resolution" is meant the minimum size deposit that the particular method is capable of detecting. "Penetration" refers to the maximum vertical distance beneath the sea bottom that a particular method can detect a deposit. The resolution of a particular method decreases as its penetration increases so that deeply buried deposits may be unresolvable. For example, the magnetic method used to search for the needle must be capable of penetrating through the haystack and resolving the tiny needle.

In addition to resolution and penetration, the capability of discriminating the deposit sought from its surroundings depends on the ratio of signal-to-noise of the method employed, which specifies the clarity with which the measured properties of the deposit stand out from extraneous effects. The results may be so noisy that the detecting signal is obscured. Techniques of amplifying, filtering, and signal processing are designed to enhance the signal and suppress the noise.

---

*Adapted from a paper presented in 1971 at the United Nations Interregional Seminar on the Development of Mineral Resources of the Continental Shelf.

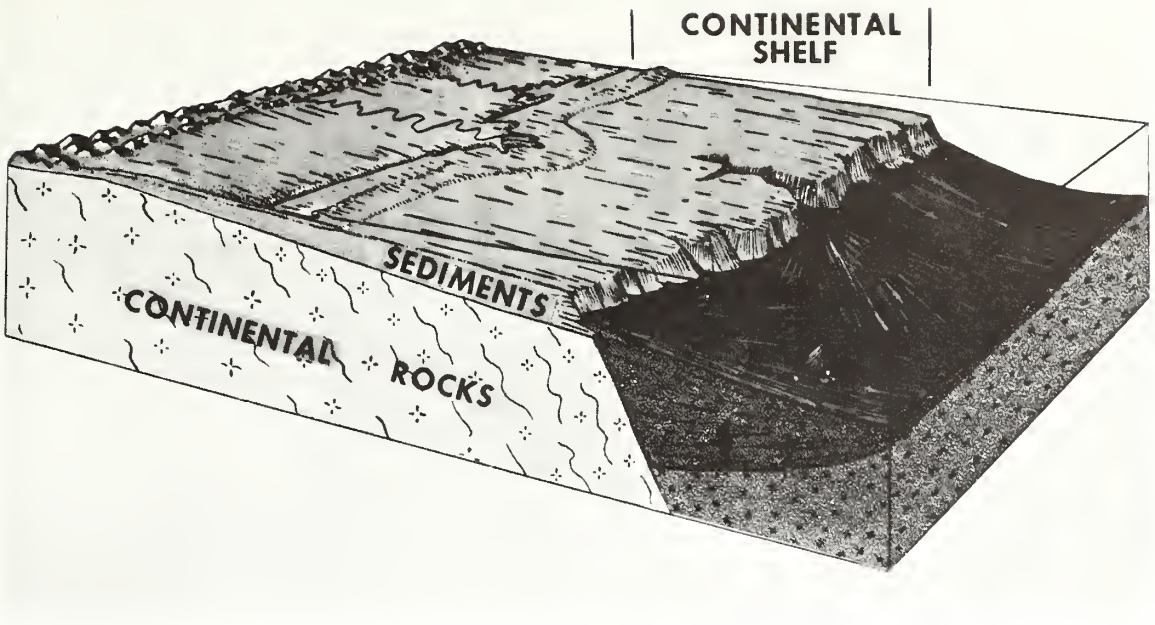

Figure 1. The continental shelf is an extension of the continent into the ocean. Rocks of the continent extend beneath the continental shelf where they may be covered by sediment several kilometers thick (Courtesy of Robert S. Dietz and John C. Holden).

Exploration methods usually obtain a two-dimensional profile of the quantity being measured along a line run across a region where the mineral deposits are thought to occur. A pattern of profiles along straight lines both parallel and perpendicular to the known or presumed orientation of the deposit being sought provides measurements to construct a three-dimensional picture. The measurements are conveniently presented on a contour map which joins points of equal values and thereby outlines areas of high and low values. The distance between profiles will determine the minimum lateral dimensions of a deposit that can be detected, just as the size of openings in a fishing net will determine the smallest fish that can be caught. An optimum line spacing must be chosen for the type of mineral occurrence being sought.

The interpretation of the information obtained from mineral exploration begins with a geological understanding of the mineral occurrence. The method selected and the measurements made must be thoughtfully tailored to obtain the information critical to detecting a particular type of deposit. The measurements obtained must be interpreted by competent geologists and geophysicists. An important discovery can be overlooked for lack of good interpretation.

2. OCCURRENCE OF CONTINENTAL SHELF MINERAL DEPOSITS

The occurrence of the mineral deposit being sought must be considered in advance of the actual exploration because the method employed must be selected for the specific occurrence anticipated. Rocks of the continent underlie the continental shelf so that mineral deposits of the continental shelf would be expected to be similar to those of the adjacent portion of the continent with the addition of certain deposits peculiar to the marine environment (fig. 1). For purposes of exploration, mineral deposits of the continental shelf can be divided into consolidated and unconsolidated, depending on whether hard or soft, as well as bottom and sub-bottom, depending on whether they lie on or beneath the sea floor (table 1). Consolidated mineral deposits include coal, limestone, common salt, sulphur, certain iron ores, and metal-bearing hardrock deposits. Unconsolidated deposits include diamond-bearing gravels, barite, glauconite sands, manganese and phosphorite nodules, sea shells, and petroleum. The unconsolidated deposits may occur either as bottom or sub-bottom deposits. The consolidated deposits may be buried beneath thicknesses up to several kilometers of unconsolidated materials. Rocks are consolidated materials, and sediments like sand, silt, and clay, are unconsolidated materials. In addition to sea-floor deposits, a number of useful minerals may be extracted from seawater including borax, bromine, magnesium, potash, common salt, sulphur, and fresh water. The methods used to explore the continental shelf are adapted from methods developed to explore the continent (table 2).

*Table 1. Occurrence of Continental Shelf Mineral Deposits**

Unconsolidated		Consolidated		Dissolved
Bottom	Sub-bottom	Bottom	Sub-bottom	Seawater
Shallow beach or offshore placers:	Buried beach and river placers:	Exposed stratified deposits:	Disseminated massive, vein or tabular deposits:	Metals and salts:
Heavy mineral sands	Diamonds	Ironstone	Coal	Magnesium
Iron sands	Gold	Limestone	Iron	Sodium
Silica sands	Platinum		Tin	Calcium
Lime sands	Tin	Chemical deposits:	Gold	Bromine
Sand and gravel		Manganese oxide	Sulphur	Potassium
	Heavy minerals:	Associated Co, Ni, Cu	Metallic sulfides	Sulphur
Chemical deposits:	Magnetite	Phosphorite	Metallic salts	Strontium
Manganese nodules (Co, Ni, Cu, Mn)	Ilmenite			Boron
	Rutile	Hydrocarbons:		Uranium
Phosphorite nodules	Zircon	Coal		Fresh water
Phosphorite sands	Leucoxene			
Glauconite sands	Monazite			
	Chromite			
	Scheelite			
	Wolframite			
	Hydrocarbons:			
	Oil			
	Gas			

Modified from Cruickshank, 1970

Table 2. Application of Marine Geological, Geophysical, and Geochemical Exploration Methods

	GEOLOGICAL METHODS			GEOPHYSICAL METHODS			
	BATHYMETRY AND SIDE-LOOKING SONAR	BOTTOM PHOTOGRAPHY		BOTTOM SAMPLING	SEISMIC REFLECTION	SEISMIC REFRACTION	MAGNETIC
INSTRUMENTS	Vertical echo-sounder Horizontal echo-sounder	Underwater still and television cameras	Satellite camera	Core, dredge, drill	Hydrophone, amplifier, recorder	Hydrophone, amplifier, recorder	Magnetometer
MOVING OR STATIONARY	Moving	Stationary	Moving	Stationary	Moving	Moving	Moving
RECONNAISSANCE OR DETAIL	Either	Detail	Reconnaissance	Detail	Either	Either	Reconnaissance
QUANTITY DIRECTLY MEASURED	Travel time of reflected sound wave between ocean surface and bottom	Picture of small area (tens of square meters) of ocean bottom	Picture of large area (thousands of square kilometers) of ocean bottom	Sample of bottom material	Travel time of reflected sound wave between ocean surface and sub-bottom reflecting interfaces	Travel time of refracted sound wave between ocean surface and sub-bottom refracting layers.	Variations in intensity of magnetic field
QUANTITY INDIRECTLY DETERMINED FROM MEASUREMENTS	Depth and shape of ocean bottom	Shape and texture of ocean bottom	Overall shape, dimensions, and inhomogeneities	Detailed composition and engineering properties	Dip of beds Depth to distinct reflecting interfaces	Depth to refracting horizons, horizontal speeds of seismic waves	Depth or susceptibility of rocks with magnetic properties or magnetic ore bodies
TYPES OF STRUCTURES MOST OFTEN LOCATED	Submerged features such as beaches, channels, and exposures of bedrock	Small scale features such as ripple marks, shells, nodules, and exposures of bedrock	Large features such as channels, bars, and deltas	Chemical, placer, massive vein, and tabular deposits	Faults, anticlines, synclines, monoclines, unconformities, ore deposits buried in sediments	Faults, salt domes, basement configuration, anticlines	Anticlines, synclines, faults, igneous intrusive rocks, iron bearing deposits

	GEOPHYSICAL METHODS (continued)				GEOCHEMICAL METHODS
	GRAVITY	ELECTRICAL	HEAT FLOW	RADIOACTIVE	CHEMICAL ANALYSIS
INSTRUMENTS	Gravimeter	Electrodes, milliammeter, potentiometer	Thermograd	Geiger counter Scintillation counter	Emission and flame spectrometer, x-ray spectrometer, radiometer, wet laboratory
MOVING OR STATIONARY	Moving and stationary	Moving and stationary	Stationary	Moving	Moving and stationary
RECONNAISSANCE OR DETAIL	Reconnaissance	Either	Detail	Either	Either
QUANTITY DIRECTLY MEASURED	Variations in force of gravity	Current transmitted through earth between electrodes and resulting potential	Temperature gradient beneath ocean bottom	Natural and artificially induced gamma radiation	Composition of rock and water samples, identity and amounts of elements present
QUANTITY INDIRECTLY DETERMINED FROM MEASUREMENTS	Density of rocks and depths to anomalous rock bodies	Depth to interfaces, resistivities of rock bodies	Amount of heat flowing through the ocean bottom	Presence of radioactive elements	Proximity to mineral concentrations
TYPES OF STRUCTURES MOST OFTEN LOCATED	Buried mountains, salt domes, faults	Metallic ore bodies	Salt domes and metallic ore bodies	The presence of radioactive minerals and certain rock types	Chemical, hydrocarbon, placer, massive, vein or tabular ore deposits

3. GEOLOGICAL METHODS

Geological methods provide the most direct, unambiguous information about depth below sea level, shape, and composition of the continental shelf.

3.1 Bathymetry and Side-looking Sonar

Bathymetry is the measurement of ocean depth and is the single most routine and useful measurement made at sea. Sound travels much better through water than air and so is extensively applied in bathymetric and seismic methods. Bathymetric techniques are based on the principle of acoustic reflection, according to which a pulse of high frequency sound will be reflected by the ocean bottom at an angle equal to its angle of incidence, like a ball bouncing off the ground or a ray of light reflected from a mirror.

Depth is measured with an echo-sounding system which comprises a combined sound-source/receiver (high frequency piezo-electric transducer), usually mounted on the hull of a ship, and a graphic recorder (fig. 2) (Shepard, 1963). As the ship moves along, short pulses of sound are repeatedly projected at the bottom and the round-trip travel time of the bottom-reflected pulse is continuously displayed as depth below sea level on the graphic recorder which is calibrated for the known speed of sound through seawater. Each record provides a profile of the ocean bottom along the ship's track (fig. 3). When many profiles have been obtained over an area they are compiled into a bottom contour map which depicts the shape of the ocean bottom by drawing lines to join points of equal depth (isobaths) (fig. 4) (Johnson and Jugel, 1968).

Side-looking sonar systems are similar to standard echo-sounders, except that the sound transducer is mounted to give a side-looking instead of vertical beam, in order to obtain a sonar display of the sea floor analogous to an oblique aerial photograph on land (fig. 5). Fan-shaped beams of sound that are narrow in a horizontal plane and wide in a vertical plane are projected to either side of the moving ship's track. The geographical location and shape of ocean bottom features are determined along a swath bisected by the ship's track. The minimum size bottom feature that the system can resolve is limited by the horizontal beam width, the dynamic range, and the number of reflected sound pulses received from that feature. In short-range side-looking sonar, the sound transducer is towed some tens of meters above the ocean bottom and ensonifies a swath about one kilometer wide with a resolution of about 5 meters (Chesterman et al., 1958; Clay et al., 1964). In long-range side-looking sonar, the sound transducer is towed near the sea surface and projects sound to a lateral distance of about 20 km with resolution of about 1 km (Rusby, 1970). Many overlapping side-looking sonar records may be combined into a mosaid of the ocean bottom comparable to an air photo-mosaic on land.

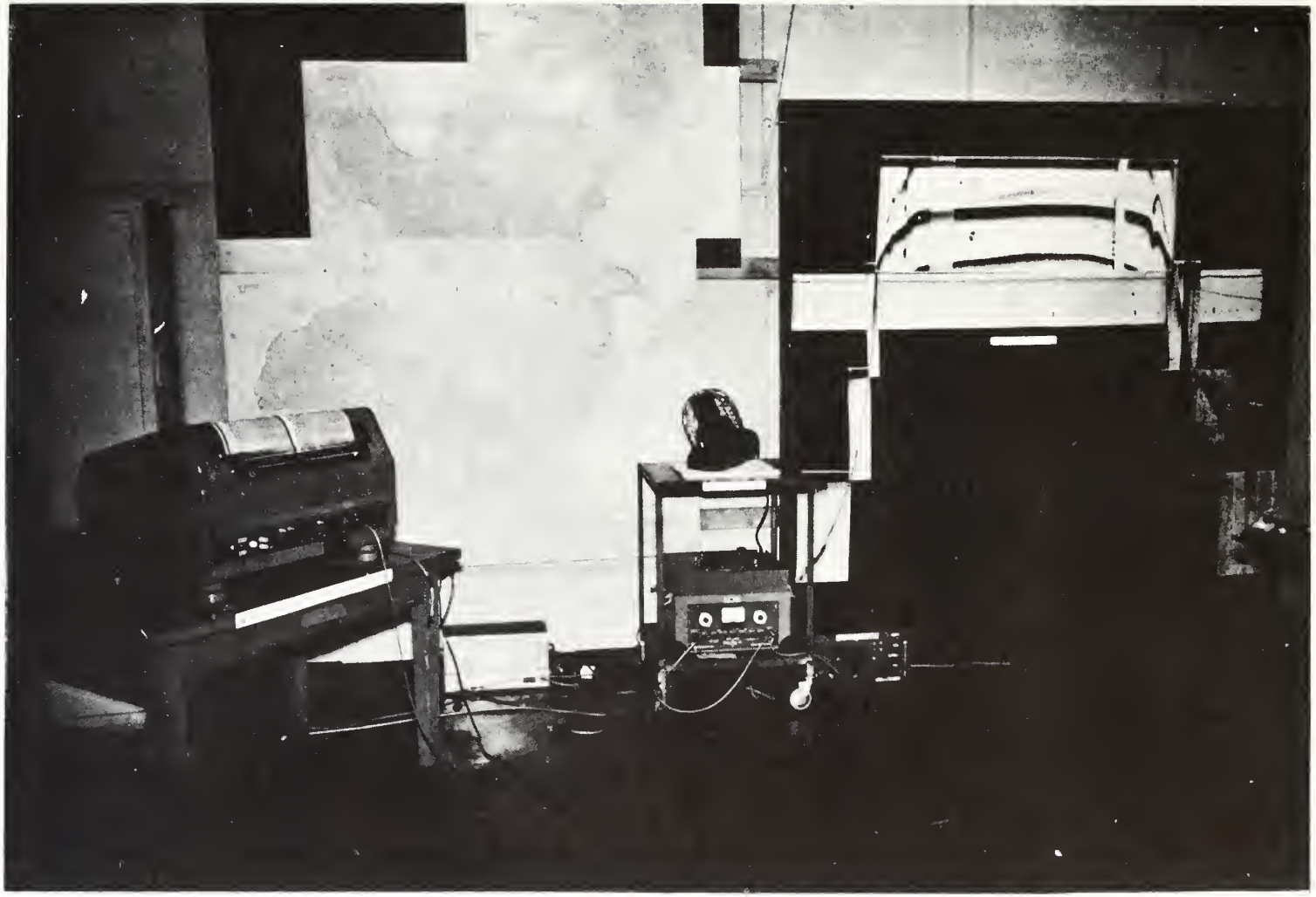

Figure 2. The components of a bathymetric system comprise a combined sound source-receiver (center) mounted either on a ship's hull or towed, and a graphic recorder (left). Bathymetric profiles (right) are compiled to construct bathymetric charts (on wall at left of center).

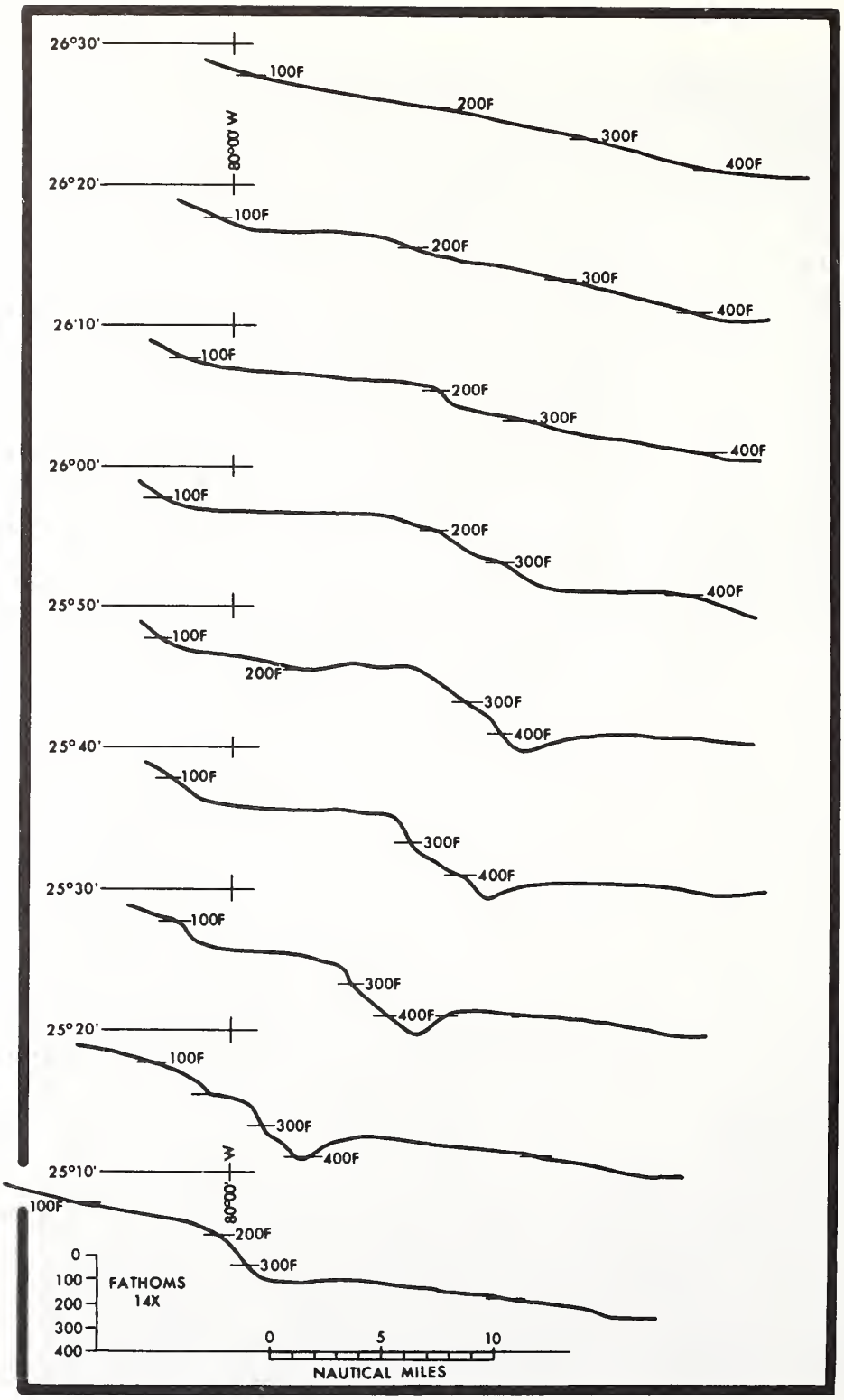

Figure 3. Bathymetric profiles across the continental shelf off Miami, Florida, (from Kofoed and Malloy, 1965, fig.2).

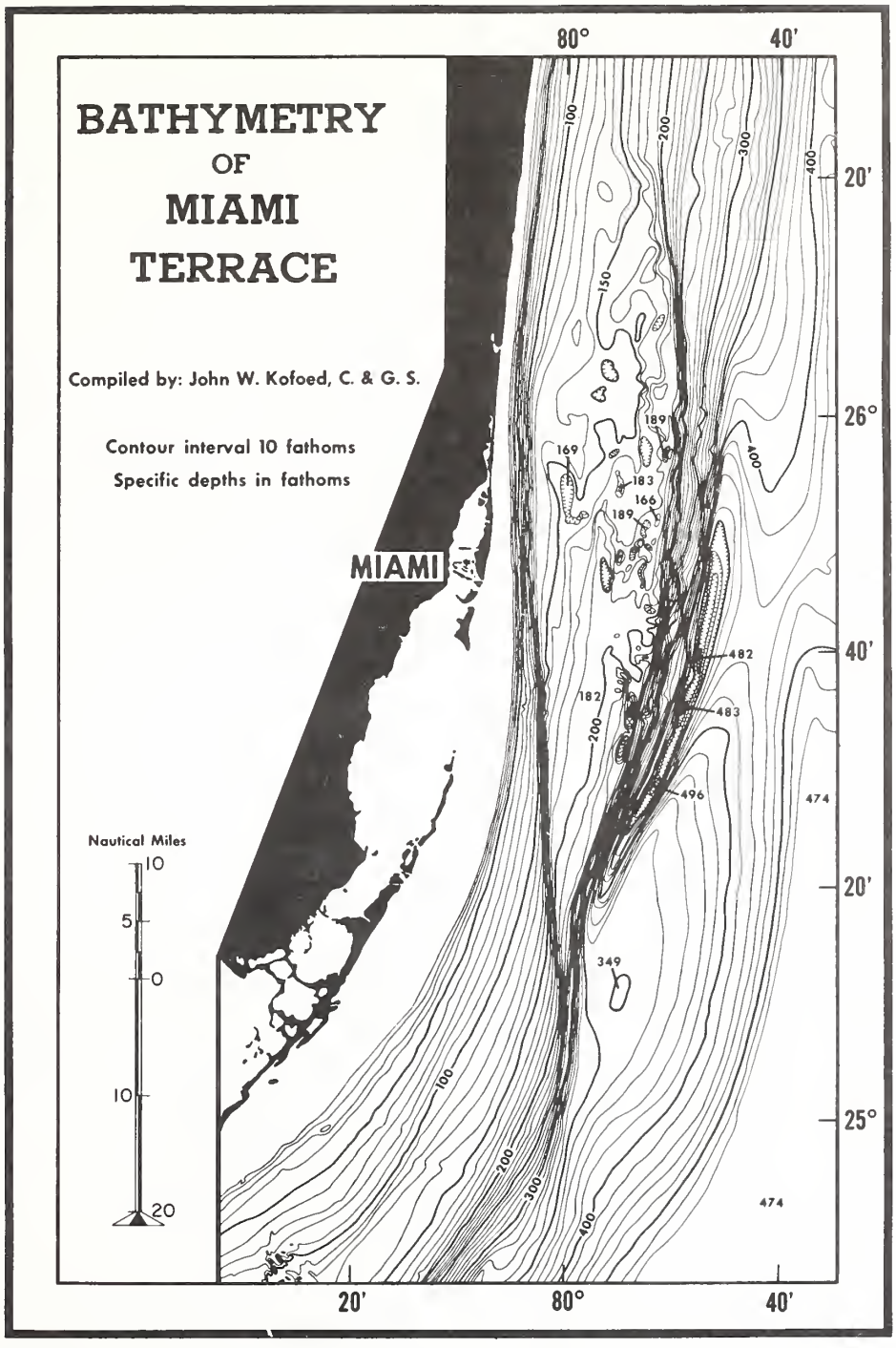

Figure 4. A bathymetric map depicting the depth and shape of the continental shelf off Miami, Florida, constructed from many individual bathymetric profiles, such as those shown in figure 3, by connecting points of equal depth with contour lines (isobaths). From Kofoed and Malloy, 1965, fig. 1.

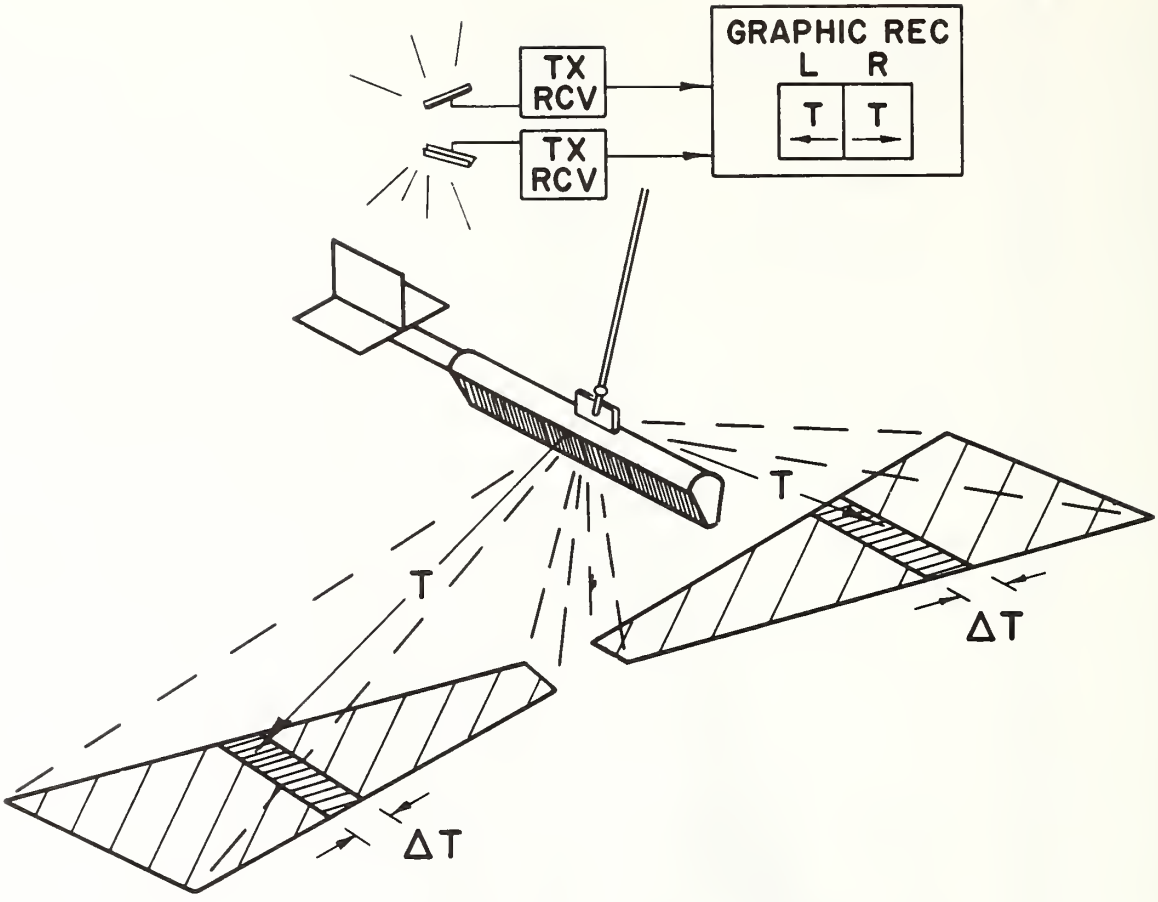

Figure 5. A side-looking sonar system in which sound sources are mounted to project sound laterally from a vehicle towed by a ship to obtain a sonar display of the ocean bottom analogous to an oblique aerial photograph (From Clay et al., 1964, fig. 1).

3.2 Photography

The ocean constitutes an effective cover over the continental shelf because light is rapidly attenuated by passage through water and scattered by suspended matter. The amount of light at 100 meters below sea level is a small fraction of that at the sea surface. The continental shelf can be photographed either at extremely close or far ranges but not at intermediate range. Deep-sea cameras operate by illuminating small areas from two to ten square meters of the ocean bottom and sequentially taking pictures as they are towed within about 5 meters of

the bottom (figs. 6 and 7) (Hersey, 1967). Cameras mounted in airplanes and satellites flying at elevations of hundreds of meters to hundreds of kilometers above sea level photograph areas encompassing thousands of square kilometers revealing major features of continental shelves such as submerged river deltas, islands, channels, and sand bars. Films sensitive to different portions of light spectrum reveal different features such as color variations and areas of abnormal heat on the continental shelf and in the overlying seawater.

3.3 Bottom Sampling

The only exploration method that proves the presence of a particular mineral deposit is sampling. Information obtained by sampling is limited to the precise spot sampled. For sampling to be effective, the sampling location must be closely delineated by the exploration methods or a sampling pattern employed suited to the anticipated size and subbottom depth of the deposit being sought.

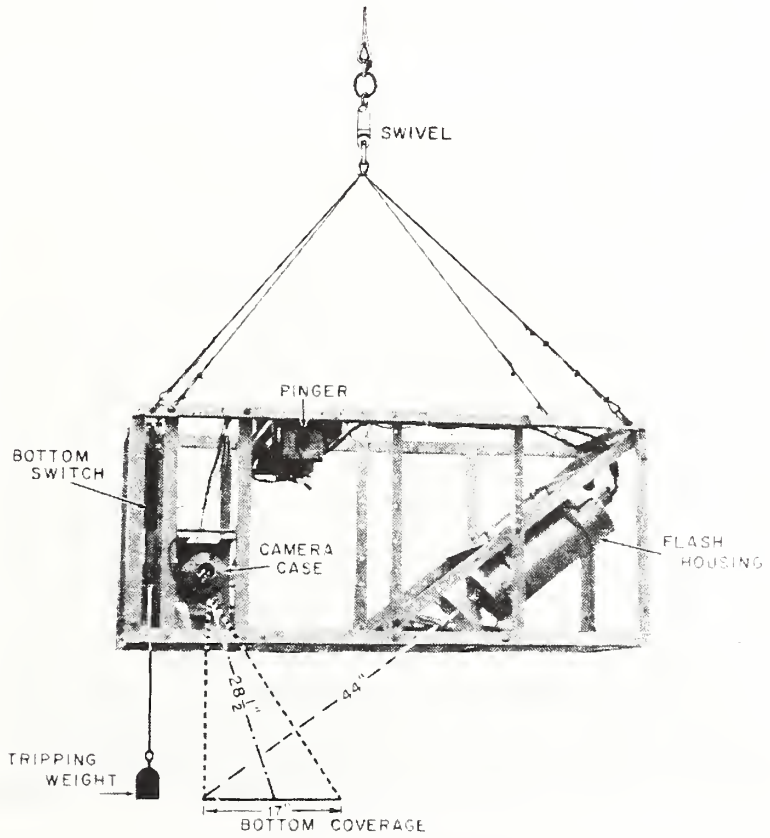

Figure 6. A deep-sea camera system consisting of a camera, stroboscopic flash, and triggering device designed to take photographs of small areas of the ocean bottom (From Owen, 1967, figs. 8-4).

In the technique of coring, a core barrel consisting of a tube several centimeters in diameter up to about 20 meters in length penetrates into the sediments of the ocean bottom either by gravitational impact or mechanical vibration (fig. 8). The core barrel recovers a sample in the form of a vertical column through the ocean bottom (Shepard, 1963). Several cores can be collected in an hour on the continental shelf using a power operated winch to lower and retrieve the coring device on a cable. Standard coring devices are not suitable for penetrating rocks.

Dredging is a technique to gather fragments of rocks exposed on the sea floor that are too hard and large to recover by coring. A chain basket or pipe suspended from the ship on a cable is dragged along the bottom in areas where echo sounding records and bottom photographs indicate rock ledges or loose nodules and rock fragments (fig. 9). Information from coring and dredging may be portrayed as a map of the distribution of sediment and rock types (fig. 10).

Drilling techniques are employed to recover samples of rock or of sediments beyond the penetration of conventional coring techniques. Ship mounted rotary, percussive, and vibratory drills of various sizes are capable of different penetrations. Drilling for oil is done by rotary drills mounted on floating barges or on fixed platforms capable

Figure 7. A deep-sea photograph showing about one square meter of the ocean bottom covered with manganese nodules. The individual manganese nodules are about the size of tennis balls (7 to 10 cm in diameter). (Photograph by R. M. Pratt and Woods Hole Oceanographic Institution).

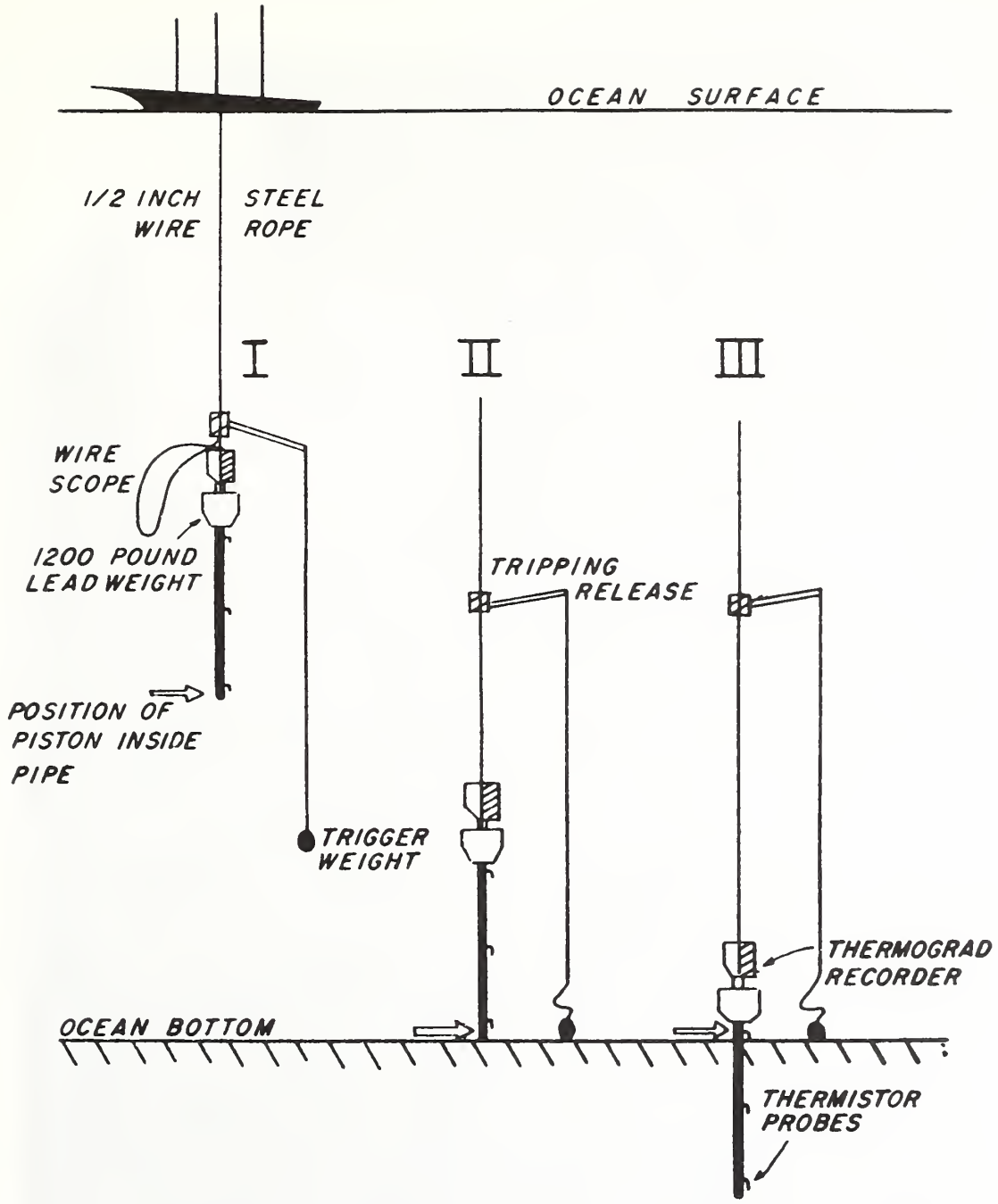

OPERATION OF PISTON CORING DEVICE AND THERMOGRAD

Figure 8. A coring device shown while being lowered, at the instant of the hit, and while in the sediment (from Talwani, 1964, fig. 9a). Thermister probes mounted along the core barrel measure the temperature gradient in the ocean bottom to determine heat flow (Gerard et al., 1962).

Figure 9. A dredge which is dragged along the bottom on a cable from a ship to recover loose rocks.

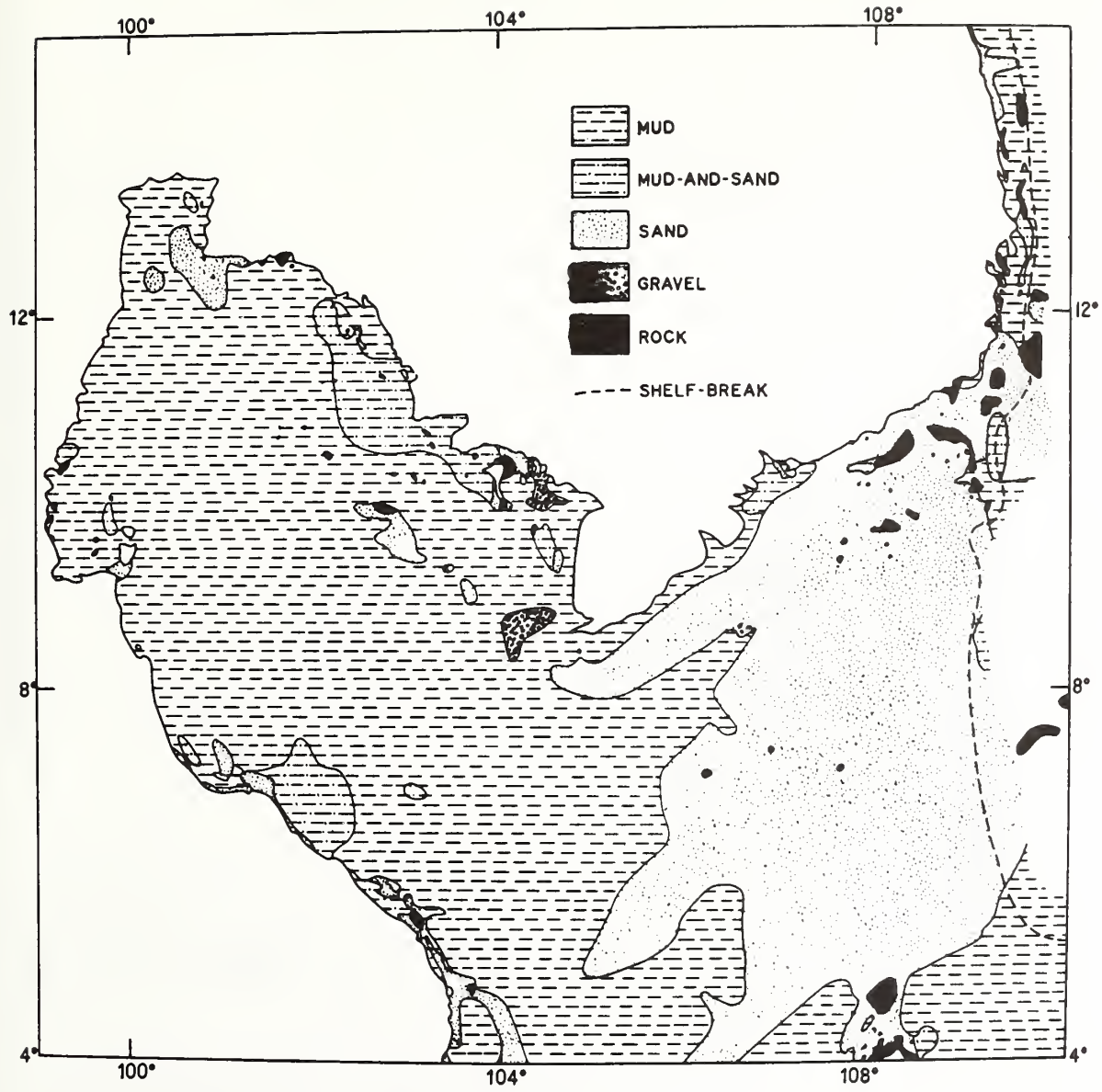

Figure 10. A map of the distribution of sediment types and rock in the Gulf of Thailand compiled from bottom samples (Shepard et al., 1949).

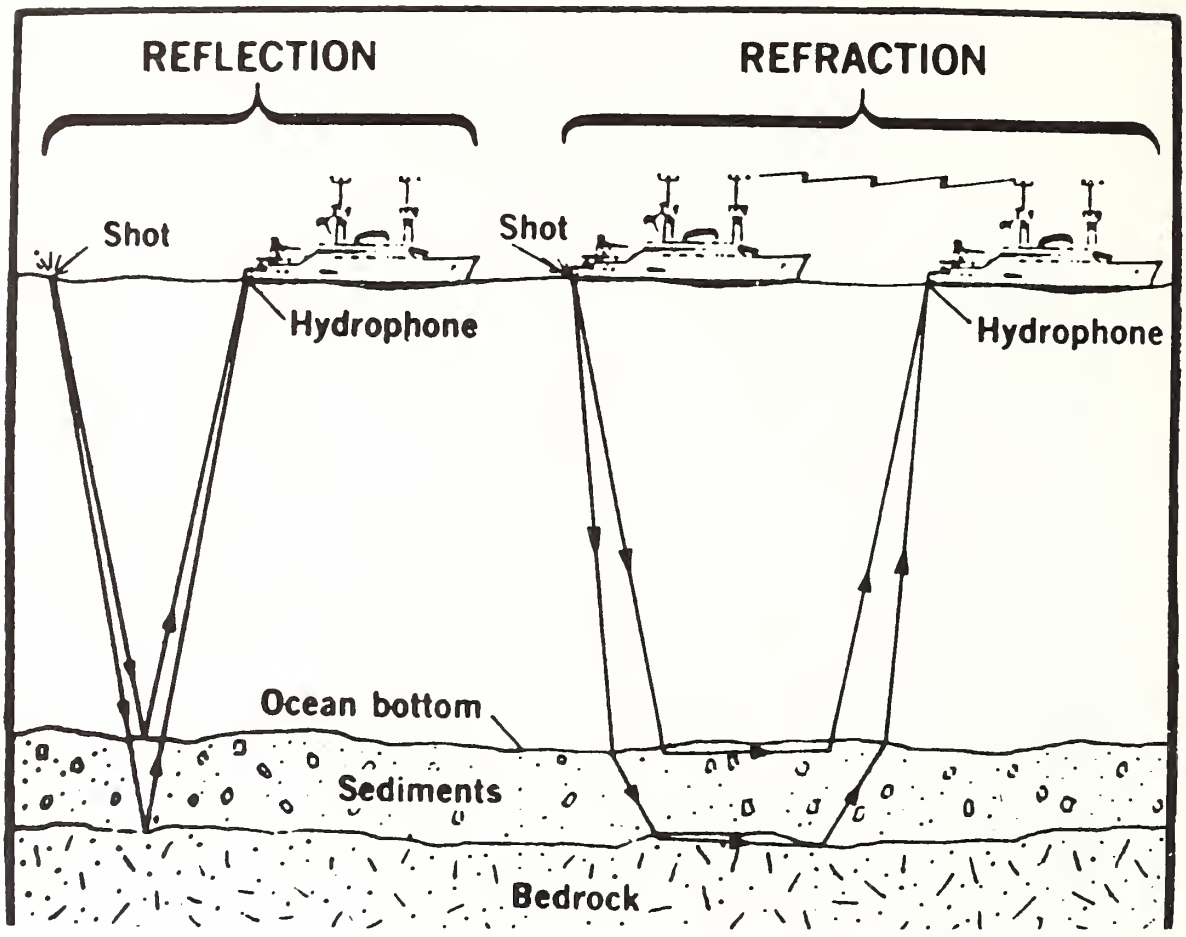

Figure 11. In the seismic reflection technique sound waves from a source at a ship bounce directly back to the ship from sediment and rock layers. In the seismic refraction technique the sound waves from a "shooting" ship travel along the sediment and rock layers before propagating back to a "receiving" ship.

of penetrating over 5 kilometers through sediments (Petroleum Engineer Publishing Co.). Drilling in moderate water depths is so expensive that it is generally limited to targets identified by other methods rather than as an exploration tool.

4. GEOPHYSICAL METHODS

Geophysical methods provide indirect quantitative measurements of physical properties of sediments and rocks and are subject to varying degrees of ambiguity in their interpretation.

4.1 Seismic Reflection

Seismic reflection is the most useful method to delineate structures favorable to the occurrence of oil and other mineral deposits buried in or beneath the sediments which cover most continental shelves. Seismic methods utilize the fact that sound waves travel with different velocities (expressed as kilometers per second) in different materials. The principle is to initiate sound waves at a point and determine at another point the time of arrival of the energy that is reflected by discontinuities between different materials (fig. 11). The discontinuities result from differences in the density of the materials and the velocity with which sound waves travel in the materials. The seismic reflection method unambiguously determines the relative positions of such discontinuities.

The basic components of a seismic reflection system comprise a sound source, receiver, amplifier, filters, and recorder (fig. 12).

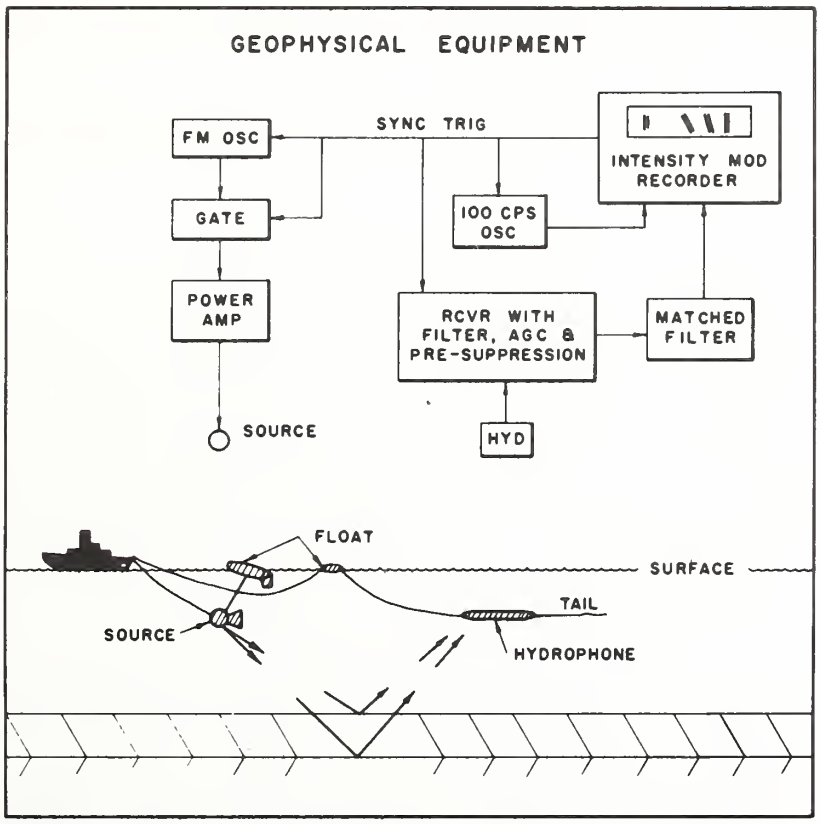

Figure 12. A seismic reflection profiling system including a repeating sound source, hydrophones to receive the sound reflected from sediment and rock layers, and amplifiers, filters, and a graphic recorder to display the reflection (From Clay and Liang, 1962, fig. 1).

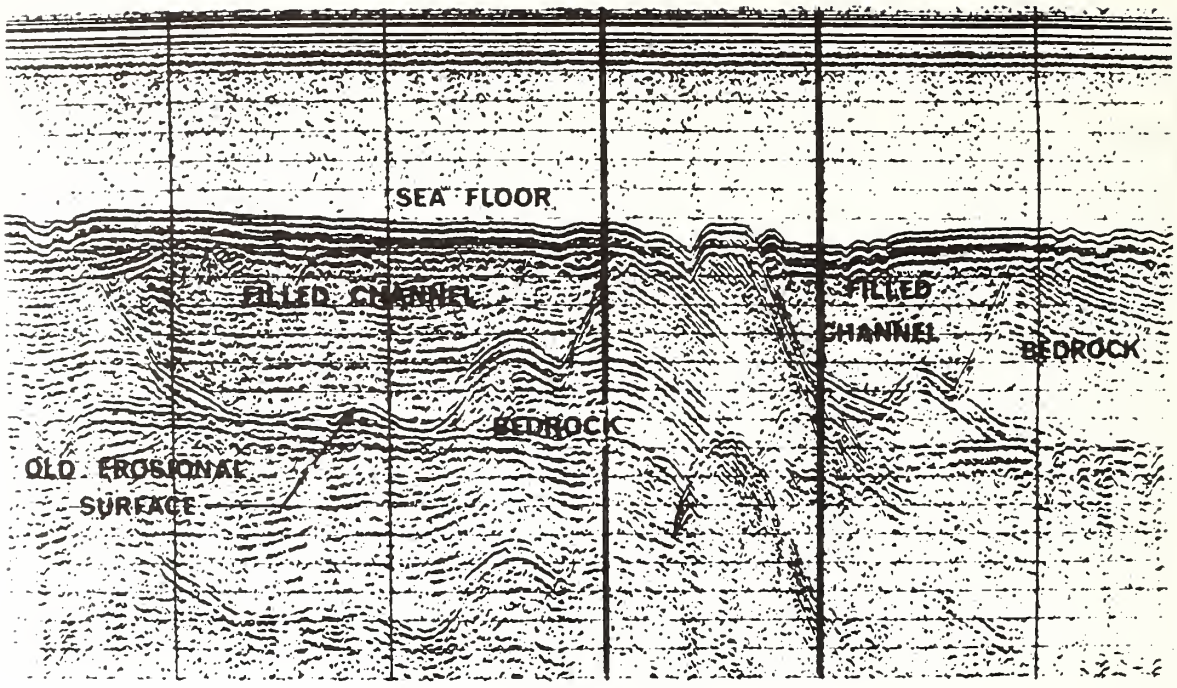

Figure 13. A high resolution, shallow penetration (0.5 kilometers) seismic reflection profile shows sediment-filled river channels cut in bedrock beneath the surface of a continental shelf.

Penetration by different systems varies between about 1 meter and 10 kilometers beneath the ocean bottom. Penetration is primarily determined by the amount of energy transmitted by the sound source in the low frequency range (less than 100 Hertz, i.e., cycles per second) because low frequencies of sound undergo less absorption in travel through sediment and rock layers than higher frequencies. The resolution of different seismic reflection systems varies between about one meter and hundreds of meters. Resolution is related to the duration, peak frequency, and frequency content (bandwidth) of the acoustic signal transmitted. In general, the shorter the duration, or the higher the peak frequency, or the wider the bandwidth, the thinner the layer that can be resolved (Brillouin, 1956). Shortening of the signal duration limits the amount of energy transmitted resulting in decreased penetration. Raising the peak frequency (greater than 100 Hertz) also limits the penetration by increasing absorption losses. Widening the signal bandwidth does not restrict the amount of energy that can be transmitted and is being developed as the most promising direction to achieve relatively deep penetration with high resolution.

The state-of-the-art forces the user to choose between systems which achieve either high resolution or deep penetration. The choice depends on whether the objective is to find a relatively thin deposit in the upper several hundred meters sub-bottom (fig. 13) or a more

deeply buried thick deposit (fig. 14). Thin deposits that are deeply buried cannot be resolved by present systems. In either case, the deposit sought must be associated with density and sound velocity discontinuities in order to be detected by seismic reflection.

A variety of sound sources exists differing in their acoustic characteristics (Kramer et al., 1968; Ocean Industry, 1968). The low frequency energy component of explosive sources such as TNT, Nitromon, and Geofex (du Pont Blasters Handbook) can achieve penetration of several tens of kilometers at the expense of resolution. Explosive charges from about 250 grams up to thousands of kilograms are generally prepared and thrown over-the-side manually, which limits the repetition rate. Other types of sources repeat automatically at faster repetition rates providing more sampling points to delineate reflecting interfaces which can change markedly over distances of one kilometer. Gas mixture sources generate explosions within long rubber hoses producing low peak frequency (less than 10 Hertz), broad bandwidth signals with intermediate resolution up to about 6 kilometers penetration in unconsolidated rocks. The Vibroseis source hydraulically drives metal plates to produce low frequency (less than 100 Hertz), broad bandwidth signals which can be shaped and programmed to yield deep penetration with fair resolution. The pneumatic source or air gun suddenly injects a bubble of high pressure air (about 2000 pounds per square inch or 140 kilograms per square centimeter) into the water which commences to oscillate generating subsidiary

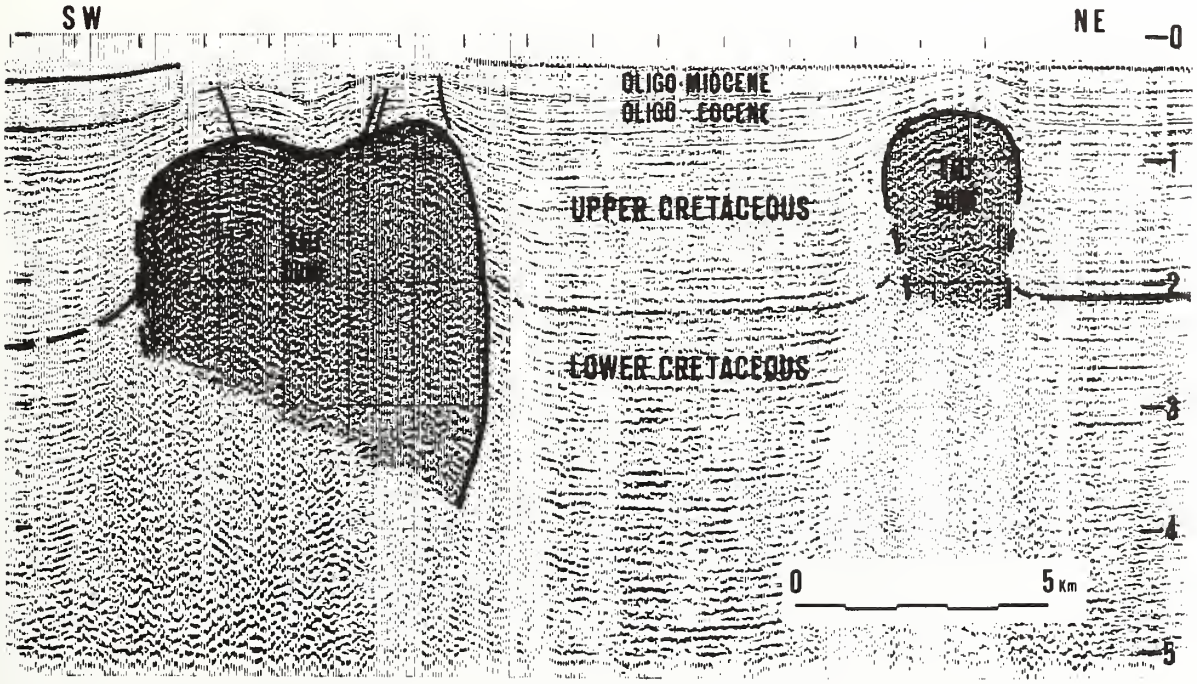

Figure 14. A low resolution, deep penetration (5 kilometers) seismic reflection profile shows salt domes (shaded) beneath the continental shelf off West Africa (From Templeton, 1970, fig. 7).

signals; the fundamental frequency and energy output is controlled by the volume of air which may be adjusted from 1 cubic inch or 16 cubic centimeters (about 50 Hertz) for shallow penetration to 2000 cubic inches or 32,800 cubic centimeters (about 5 Hertz) for deep penetration (fig. 15). Electric spark discharge sources generate an explosion by suddenly breaking water into its component gases which produces a broad bandwidth low-to-intermediate frequency (50-500 Hertz) signal achieving penetration to several kilometers depending on the electric energy used (100-120,000 Joules). The boomer is an electromechanical source consisting of two metal plates spring loaded against a coil which are suddenly separated by turning on and off a high voltage in the coil; the signal is of broad-bandwidth and intermediate frequency (500-2500 Hertz) capable of several hundred meters penetration. Piezo-electric and magnetostrictive sources transmit high frequency (hundreds to thousands of Hertz) signals of short duration to achieve high resolution and penetration of a few hundred meters. Sources can be used in concert to obtain mutual characteristics if the shipboard handling problems do not become too difficult.

In the operation of seismic profiling, a sound source and a receiver consisting of an array of pressure sensitive elements mounted inside an oil filled hose (fig. 15) are towed from the stern of a ship at speeds limited to about 20 kilometers per hour to reduce flow noise. The signals reflected from the ocean bottom and sub-bottom interfaces are received by the hydrophones, amplified, filtered, and continuously displayed on a graphic recorder (fig. 12). The reflected signals may also be recorded on magnetic tape to allow replaying and signal processing. The objective of signal processing is to increase the ratio of signal-to-noise by suppressing the noise and enforcing the signal (Silverman, 1967;

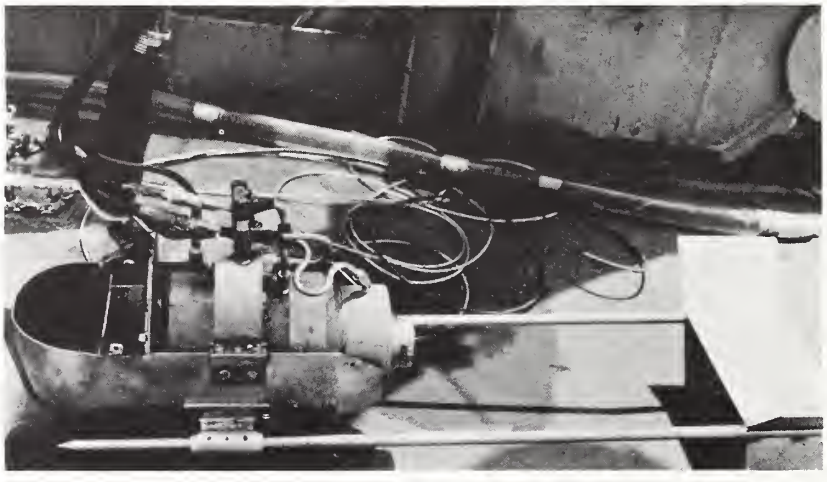

Figure 15. An air gun (30 cubic inch or 500 cubic centimeter capacity) mounted in a hydrodynamically stable towing vehicle about 1.5 meters long (foreground) is one type of sound source used in seismic reflection profiling. An array of hydrophones is mounted in an oil-filled clear plastic hose (background).

Neidell, 1968). Seismic signal processing has reached its most advanced development in the petroleum industry and has been neglected outside of industry owing to cost considerations (Schneider, 1971).

Reflection records are generally expressed in seconds of round-trip travel time to the reflector and back. The velocity of sound in the particular rock interval penetrated must be known in order to convert the travel time into thickness. Interval velocities are computed from information on the change in travel time with increase in distance between source and receiver utilizing a buoy-mounted hydrophone and radio transmitter (sonobuoy) to receive and transmit the reflected signal to the ship (Clay and Rona, 1967).

4.2 Seismic Refraction

Seismic refraction complements seismic reflection in providing a more generalized picture of the structures beneath the ocean bottom, deeper penetration, and a determination of sound velocities in major sediment and rock layers (fig. 16). Like seismic reflection, seismic refraction utilizes the fact that sound waves travel with different velocities in different materials. As in seismic reflection, the principle is to initiate such waves at a point and determine at another point the time of arrival of the energy. In refraction the sound wave is deflected from a straight line in passing obliquely from one sediment or rock layer into another of different velocity (fig. 11). In entering a layer of higher velocity the sound wave bends away from the higher velocity zone toward the zone of lower velocity by an amount proportional to the velocity difference between the zones, in a pattern that can be described according to principles of geometrical optics. Optical examples of refraction are the distortion of objects as seen through hot air or through the surface of water. From the measurements of the travel time of the sound wave from the sound source, through the water and rocks, and back to a receiver, the travel path can be reconstructed, and the position of boundaries between layers and sound velocities in the layers can be deduced (fig. 17).

The performance of seismic refraction involves the same basic components as reflection: 1) sound source, 2) receiver, 3) amplifiers and filters, 4) recorder. The major difference is in the configuration of source and receiver which must be separated at least several times the distance of the desired penetration in order to be in the path of the refraction returns (fig. 11). To accomplish this separation requires either two ships, a "shooting" and a "receiving" ship, or a sonobuoy which performs the listening function of the receiving ship (Hill, 1963). As the travel paths of the sound waves are much longer than in reflection the higher energy sources such as explosives or large air guns must be used. Various arrangements involving more than one receiver may be used in order to gain more information from different travel paths of each shot.

The practice of seismic refraction is limited to situations where each layer has a sound velocity higher than the layer immediately above

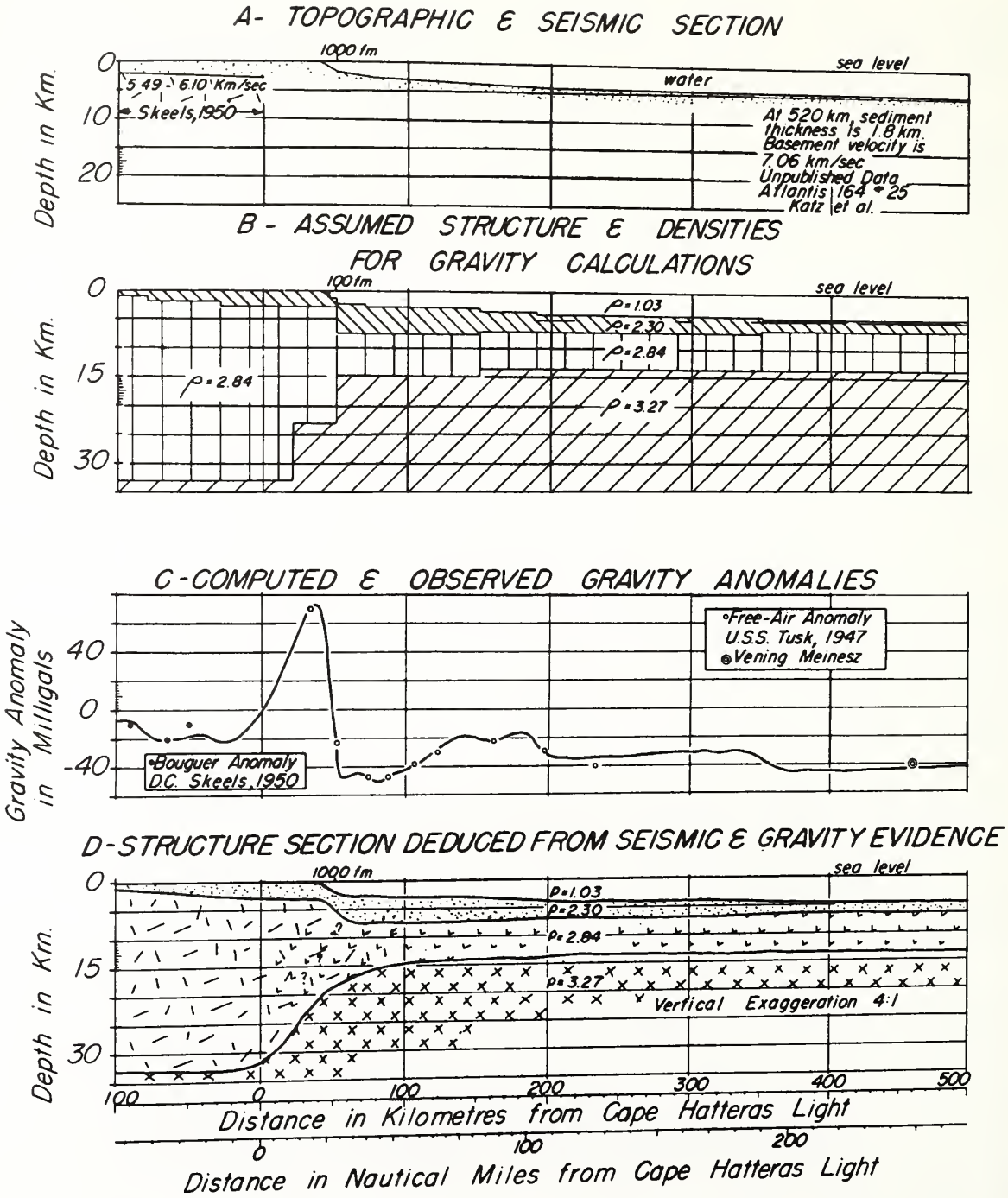

Figure 16. Seismic refraction profiles provide a generalized picture of major sediment and rock layers down to about 30 kilometers beneath the ocean bottom as in this example off Cape Hatteras, U.S.A. (From Worzel and Shurbet, 1955, fig. 8).

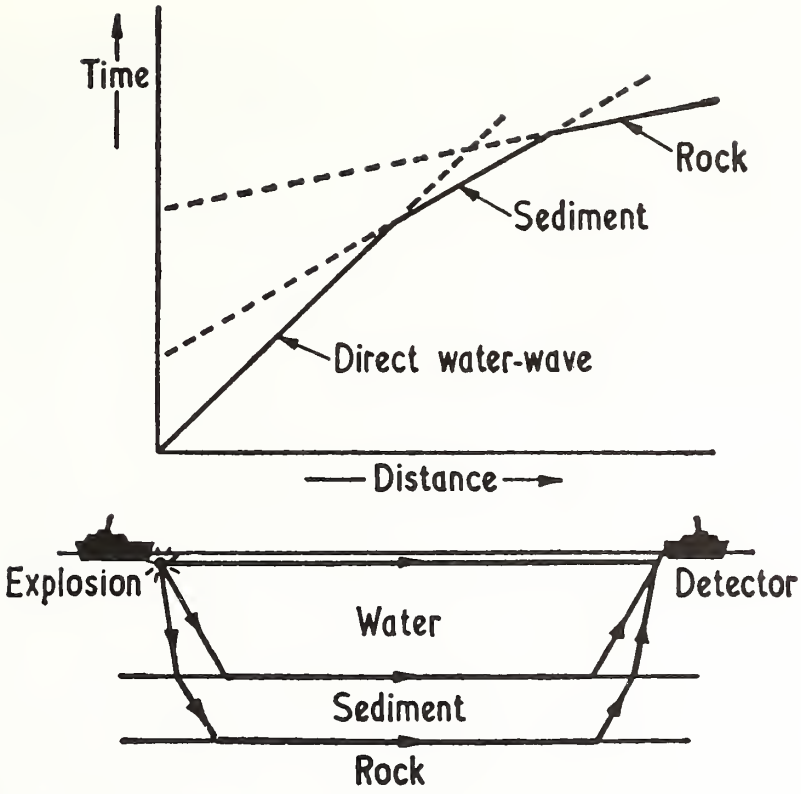

Figure 17. The travel times of sound waves refracted through water, sediment and rock layers are plotted on a time-distance graph. The sound velocities through the different materials are derived from the slopes of the corresponding segments of the time-distance curve and the thicknesses of the layers from their intercepts on the time axis (From Smith, 1968, fig. 2).

it, and where the velocity contrast between layers is sufficiently great to refract the energy. This means that the refraction method is blind to a lower velocity layer underlying higher velocity layers such as sediments underlying rocks.

4.3 Magnetic Method

The magnetic method is used to delineate geological structures associated with petroleum, to measure thickness of sediment above magnetic basement rocks, and to locate concentrations of magnetic (iron-bearing) minerals on or beneath the sea floor. The magnetic method depends on accurately measuring anomalies of the local geomagnetic field produced by variations in the intensity of magnetization residing in magnetized sediments and rocks. The magnetization is due partly to induction in the earth's magnetic field and partly to permanent (remanent) magnetization. The induced intensity depends primarily upon the magnetic susceptibility of the materials and the present magnetizing field. The susceptibility is almost entirely controlled by the quantity

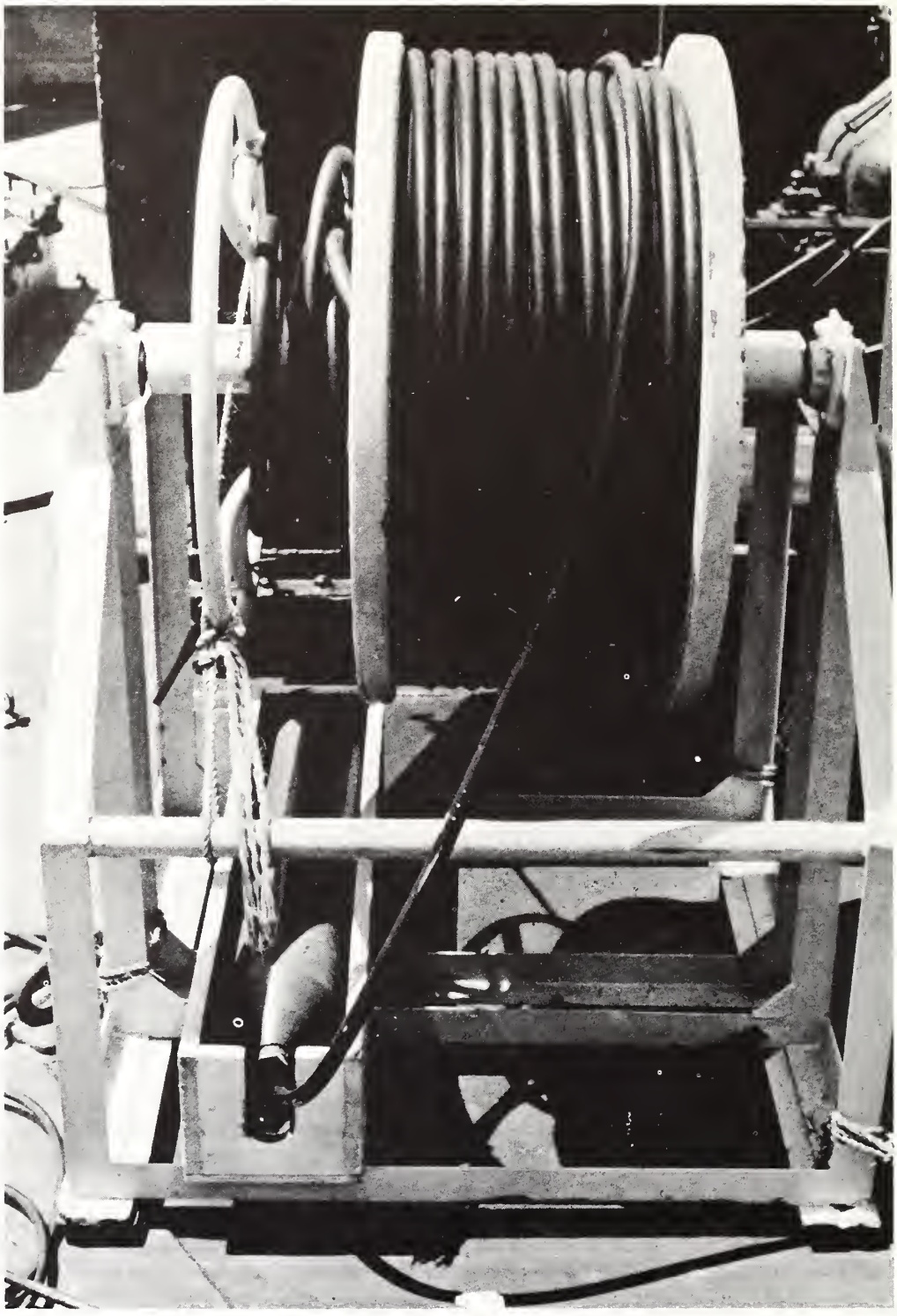

Figure 18. The sensor of the proton free-precession magnetometer is affixed to electrical cable by which it is towed behind a moving ship.

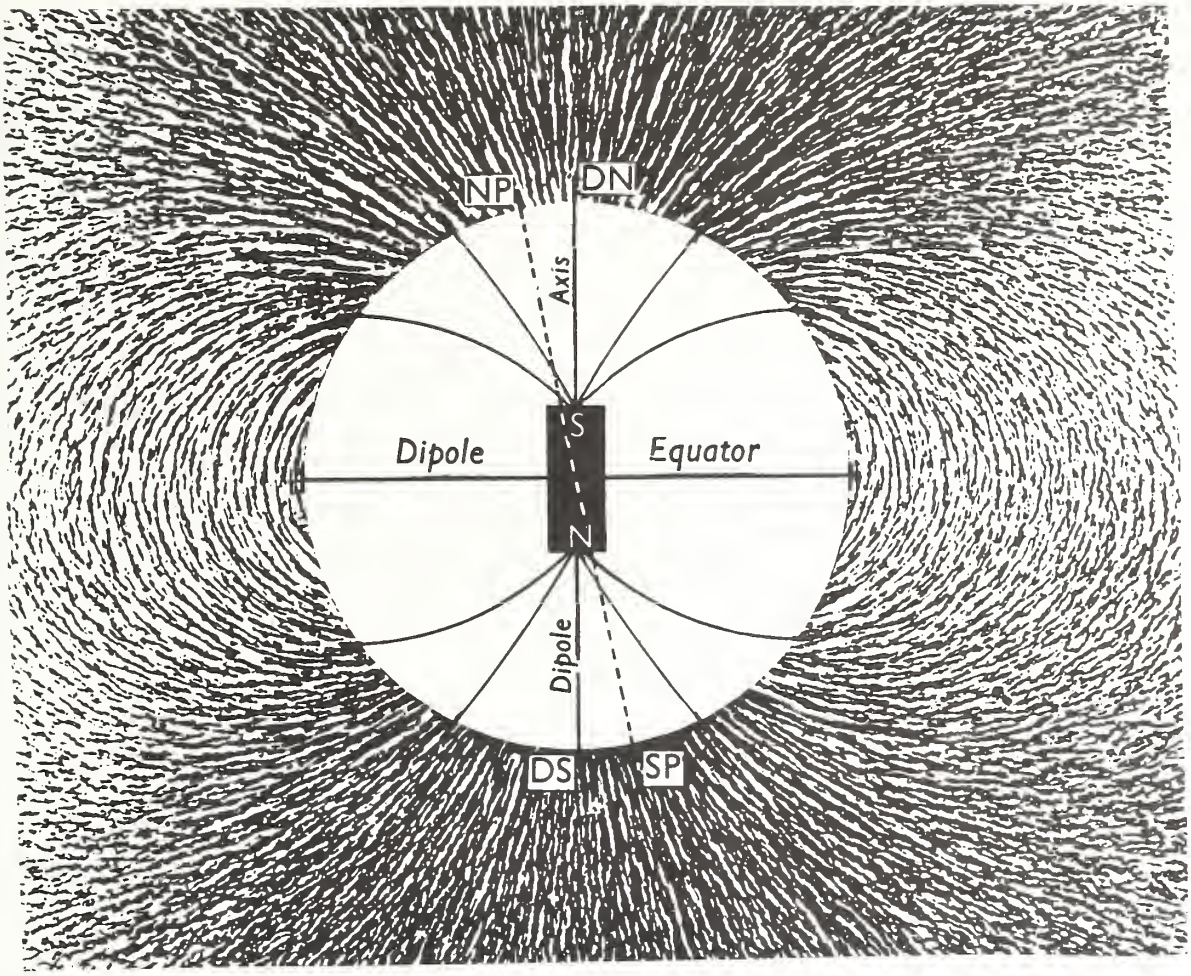

Figure 19. Lines of force of the earth's magnetic field are aligned as if generated by an internal bar magnet. DN and DS are the north and south geomagnetic poles; NP and SP are the geographical north and south poles. (Arthur Holmes, PRINCIPLES OF PHYSICAL GEOLOGY, Second Edition, The Ronald Press Company, New York, fig. 726. Copyright 1965).

of iron-rich minerals with magnetic properties, especially the mineral magnetite present in many volcanic rocks. Quartz, limestone, rock salt, and most sediments have very low magnetic susceptibilities. The permanent intensity is recorded in the materials from exposure to previous magnetic fields which have varied in the past.

Magnetic intensity measurements of the continental shelf are made with a magnetometer towed either by a ship or an airplane. The components of a magnetometer are the sensing element towed on an electrical cable, electronic components to convert the output of the sensor into units corresponding to magnetic intensity (gammas; 1 gamma = 10^{-5} gauss), and a recorder to display the values. Two types of magnetometers in common usage are the fluxgate and the proton free-precession (fig. 18).

Fluxgate magnetometers operate by sensing flux densities induced by the external magnetic field in certain materials of high electrical permeability. The fluxgate magnetometer measures relative magnetic intensity. Proton free-precession magnetometers (Hill, 1959) utilize the phenomenon of magnetic resonance of elementary particles. The proton free-precession magnetometer measures the magnitude of the total magnetic field consisting of the earth's regional field (fig. 19) plus the magnetic anomaly related to the materials of the ocean bottom (fig. 20). The earth's regional or reference field, known at all points (I.A.G.A., 1969), is subtracted from the total field leaving the residual field, which reveals anomalies associated with the sediments and rocks of the ocean bottom. The total field is measured along a set of tracks spaced for adequate coverage and residual values are plotted and contoured to delineate the magnetic anomalies (fig. 21).

Computer techniques have been developed to obtain the residual field from the total field (Cain and others, 1964) and to calculate models of crustal structure from the magnetic anomalies (Talwani and Heirtzler, 1964). Thicknesses of sediments and depth of burial and shape of rocks with magnetic properties can be deduced from the

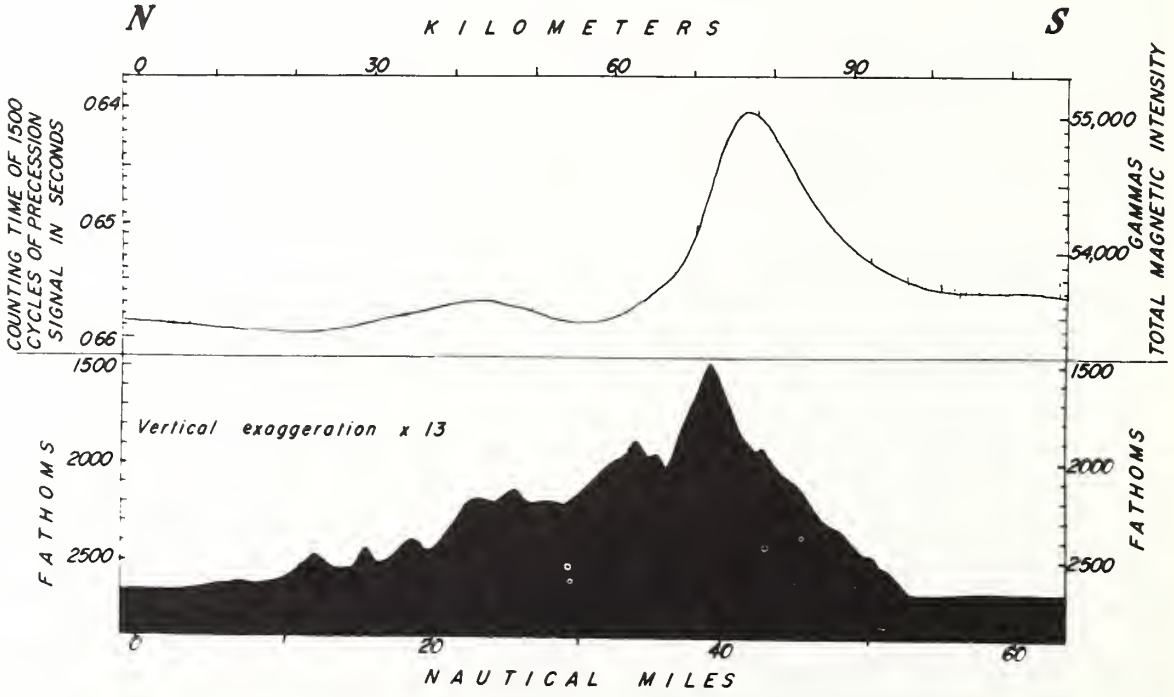

Figure 20. Profile of total magnetic intensity (top) made by a shipborne proton free-precession magnetometer over a seamount (bottom) (From Talwani, 1964, fig. 6).

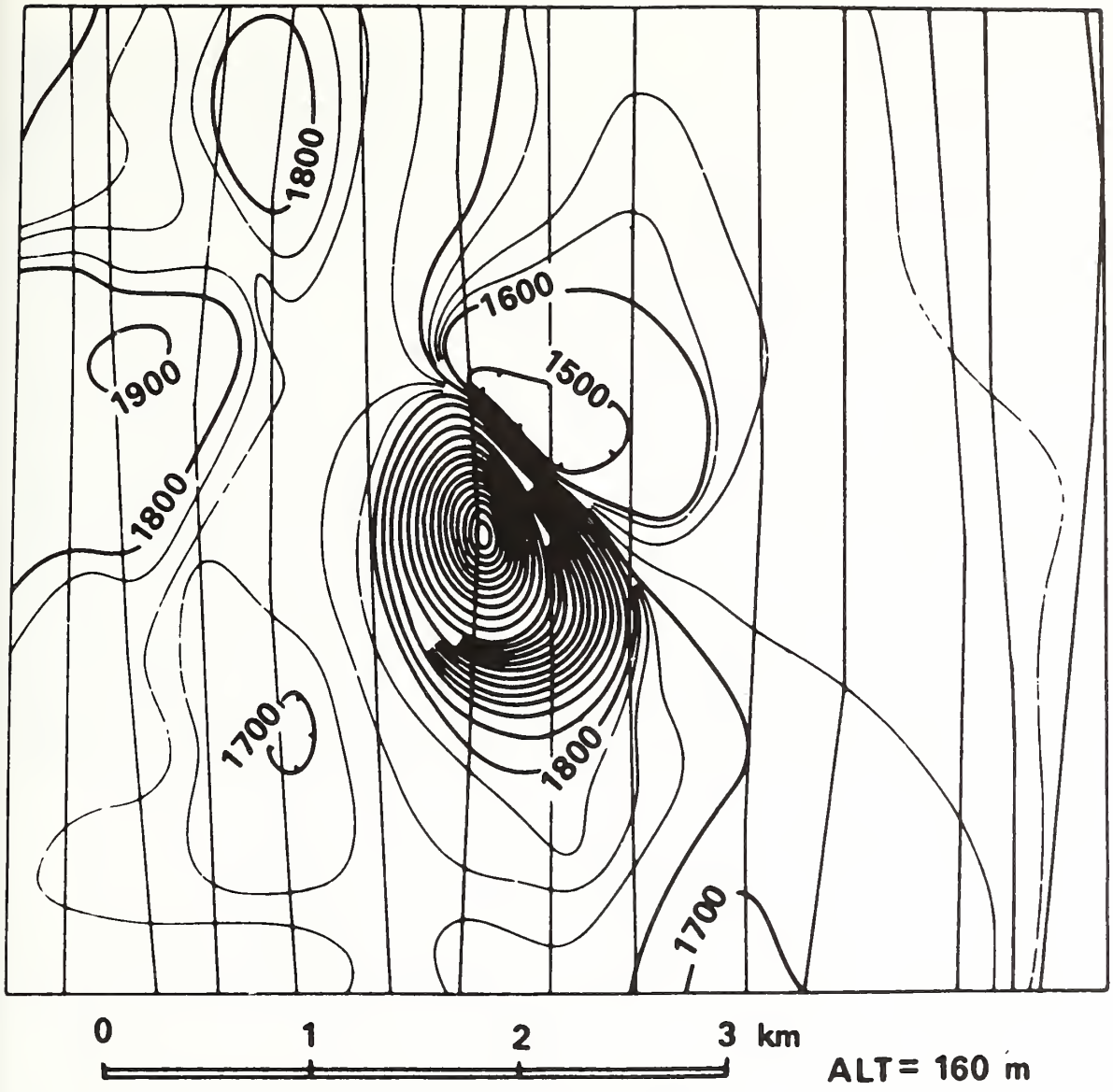

Figure 21. A residual intensity magnetic contour map (gammas) constructed from aeromagnetic profiles flown along north-south lines. An anomalous magnetic "high" (center) is associated with an iron-bearing deposit.

associated magnetic field. The interpretation of magnetic measurements is usually ambiguous. Many possible depths and shapes of magnetic source materials may account for the observed magnetic field (fig. 22). If either the depth or dimensions of the magnetic source materials is determined by seismic methods, then the other unknown quantity can be calculated from the associated magnetic field. Alternatively, the depths and dimensions of magnetic basement rocks can be determined empirically by comparing magnetic anomalies at locations where the basement rocks are known from drilling with anomalies over unknown sites in the same region.

4.4 Gravity

The gravity method, in common with the magnetic method, measures a field associated with the earth as a whole and influenced by local fluctuations. The local fluctuations in gravity relate to variations in the density of materials, in turn related to geologic features such as intrusions of light material like salt, or heavy material like basalt, or displacements of materials with contrasting densities in faults or folds.

Newton's law of gravitation states that the force of attraction between two objects is directly proportional to the product of their masses and is inversely proportional to the distance between them. Gravity measurements are expressed in milligals. One milligal is one thousandth of a gal, which is a unit of acceleration (1 centimeter/second^2) named after Galileo, and is roughly equal to one millionth of the total value of gravitational attraction exerted by the earth. The force of gravitational attraction exerted by the earth on an object of unit mass on its surface is not constant, but varies from place to place.

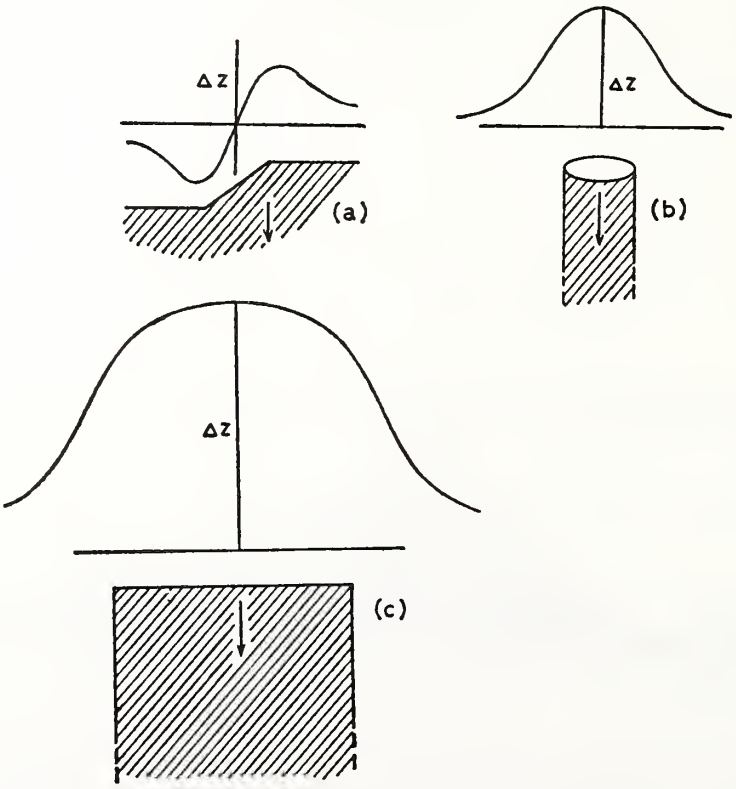

Figure 22. Curves of magnetic intensity and one of the many possible distributions of magnetic materials which could account for each of the curves (From Parasnis, 1962, fig. 6).

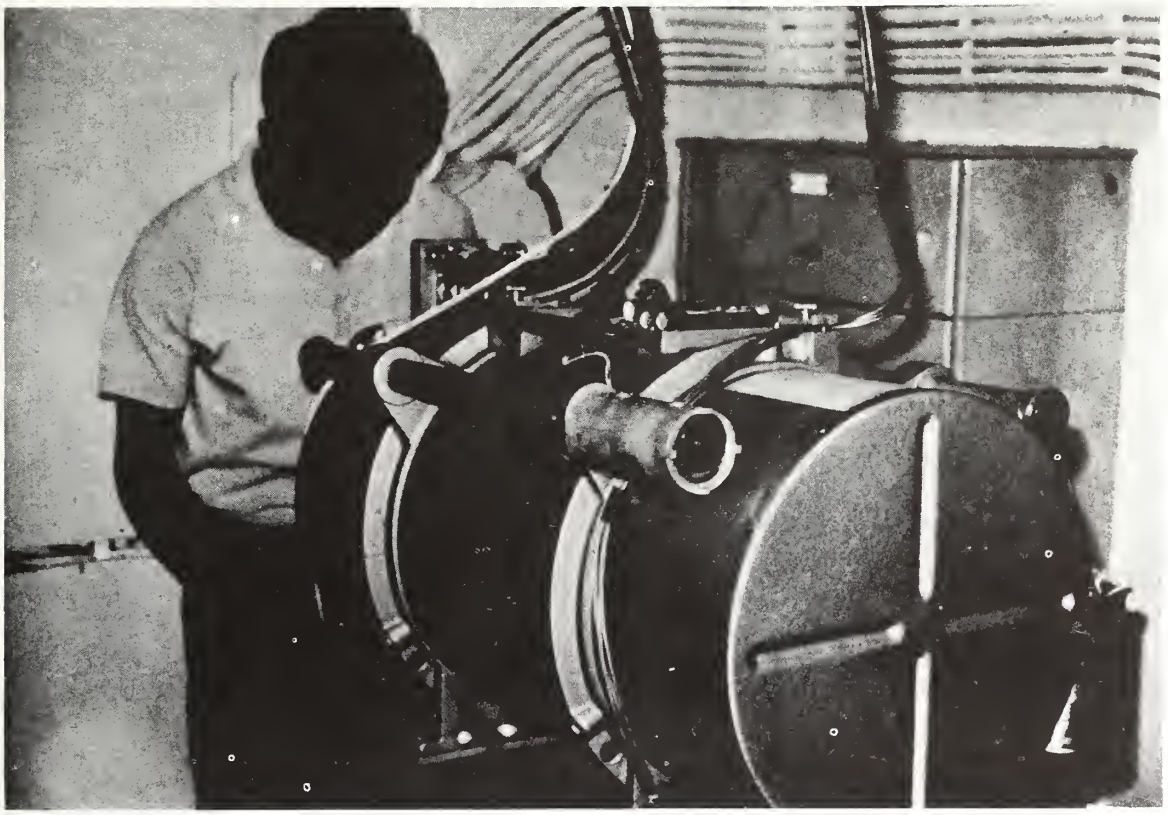

Figure 23. A scientist adjusting a Graf-Askania shipborne gravimeter (Courtesy of B. P. Dash).

A major part of this variation is related to the shape of the earth which is not a perfect sphere but is wider at the equator than at the poles and to the centrifugal force of a spinning earth. Superimposed on this gradual variation of the gravitational field are small variations caused by the density inhomogeneities in the earth's crust. The object of gravity measurements is to detect these small variations and relate them to geological structures.

Gravity measurements at sea are made with gravimeters installed on ships (fig. 23). The LaCoste-Romberg and the Graf-Askania are two types of gravimeters in common usage in which changes in the force of gravity are measured by its effect on a weight at the end of a spring; the former type of gravimeter measures the force displacing the weight from an equilibrium position and the latter type measures the force necessary to restore the weight to an equilibrium position (fig. 24). In order to cancel the effects of horizontal and vertical accelerations of ship motion, the Graf-Askania gravimeter is mounted on a gyro-stabilized platform and the LaCoste-Romberg may be gimbal mounted with an auxiliary pendulum to establish true vertical. Observations are fed to a computer which eliminates extraneous accelerations and produces the corrected observations due to gravity. The vibrating string is another

type of shipborne gravimeter which measures a change in frequency of vibration which is proportional to the acceleration of gravity (Wing, 1969). Ships larger than several thousand tons displacement are favored as platforms for making gravity measurements because of their stability. The problem of extraneous accelerations is averted and the highest accuracy is achieved in the sea-floor gravimeter which is encased in a water-tight chamber, placed on the ocean bottom, and operated by remote control through an electrical cable to the surface ship. Accuracy of navigation during gravity measurements is essential because the Eötvös correction arising from the Coriolis force experienced by moving bodies on a rotating earth varies significantly with ship's speed, course, and position (Worzel and Harrison, 1963).

The observed value of gravity minus the value predicted by the international formula for the earth's field gives the free-air anomaly (fig. 25). Bouguer anomalies are computed from the free-air anomalies after an allowance is made for the density deficit of water with respect to crustal materials and directly represent density variations below the sea floor. The corrected gravity measurements can be contoured to delineate gravity "highs" and "lows" if enough measurements over an area are available (fig. 26). Hypothetical reconstructions of buried geological structures can be computed from individual profiles. As in the magnetic method, the interpretation of gravity measurements is ambiguous

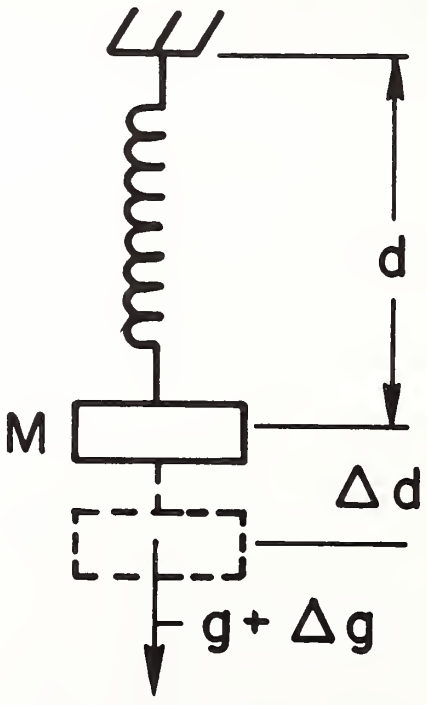

Figure 24. The Graf-Askania and La Coste-Romberg gravimeters measure the force of gravity (g) by its effect in displacing a weight (Δd) balanced by a spring (From Nettleton, 1971, fig. 6).

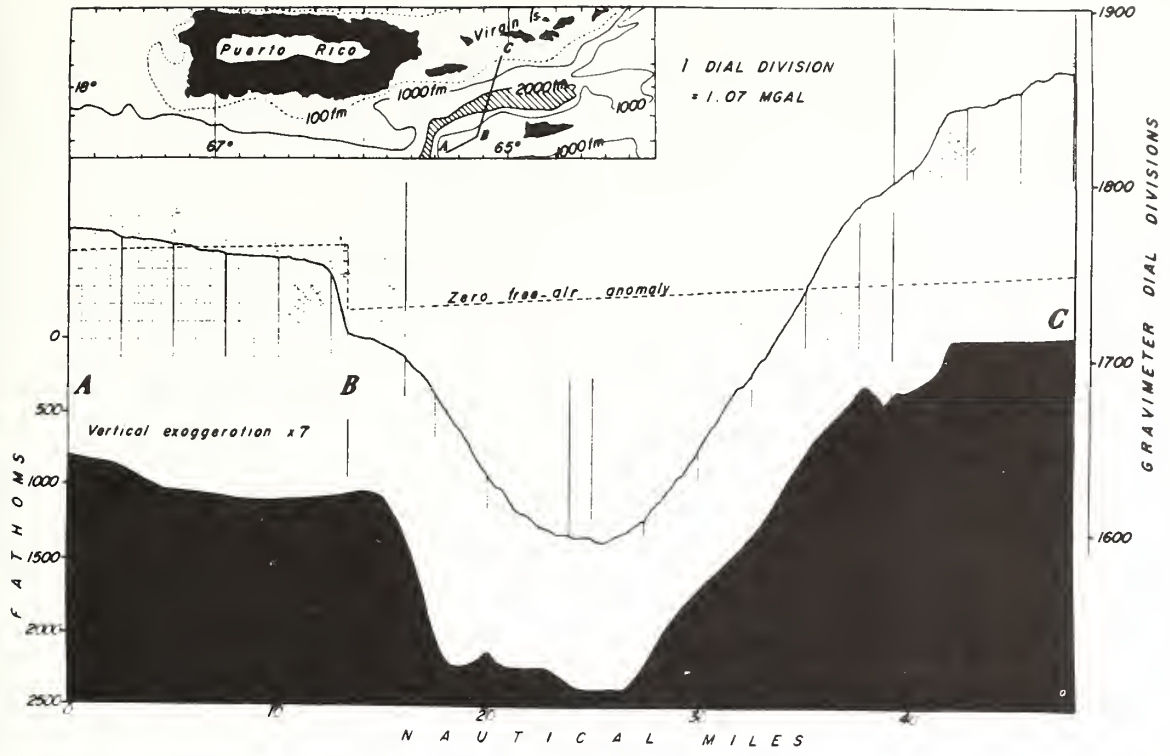

Figure 25. Profile made by a Graf-Askania shipborne gravimeter across a trough-shaped depression in the ocean bottom (shaded). The difference between the earth's gravity field (dashed line) and the observed value of gravity (solid line) is the free-air anomaly which closely corresponds to the shape of the ocean bottom (From Talwani, 1964, fig. 1). The slope of the zero free-air anomaly reflects the change of gravity with latitude and the step at B is caused by a change of Eötvös correction due to change in the heading of the ship.

because any gravitational field observed at the surface can be caused by an infinite number of different mass distributions, although every configuration of masses gives rise to a unique gravitational field (fig. 27). Gravity can only be interpreted if the number of possible solutions can be constrained by information on the size and depth of source materials obtained from seismic methods (fig. 16).

4.5 Electrical Methods

Electrical methods utilize natural electric fields flowing through the earth (self-potential and telluric), applied direct-current fields (resistivity and equipotential), and applied alternating fields (induced

polarization and induction), to locate small scale features such as electrically conductive ore bodies. Voltages due either to natural or artificial electrical currents flowing through the earth are measured between two electrodes inserted in the ocean bottom. Differences in electrical response between pairs of electrodes evidence differences in the resistivity of the intervening rocks. Electrical methods are commonly used on land and their application to the ocean bottom is presently in the stage of research and development.

The self-potential method involves placing electrodes into the ocean bottom and measuring naturally occurring anomalous potentials between them with a millivoltmeter or potentiometer. Anomalously high potentials result from electric currents flowing through sulfide and graphite ore bodies caused by associated naturally occurring electrochemical reactions. Self-potential anomalies have been observed associated with sulfide ore bodies beneath the continental shelf (Corwin et al., 1970).

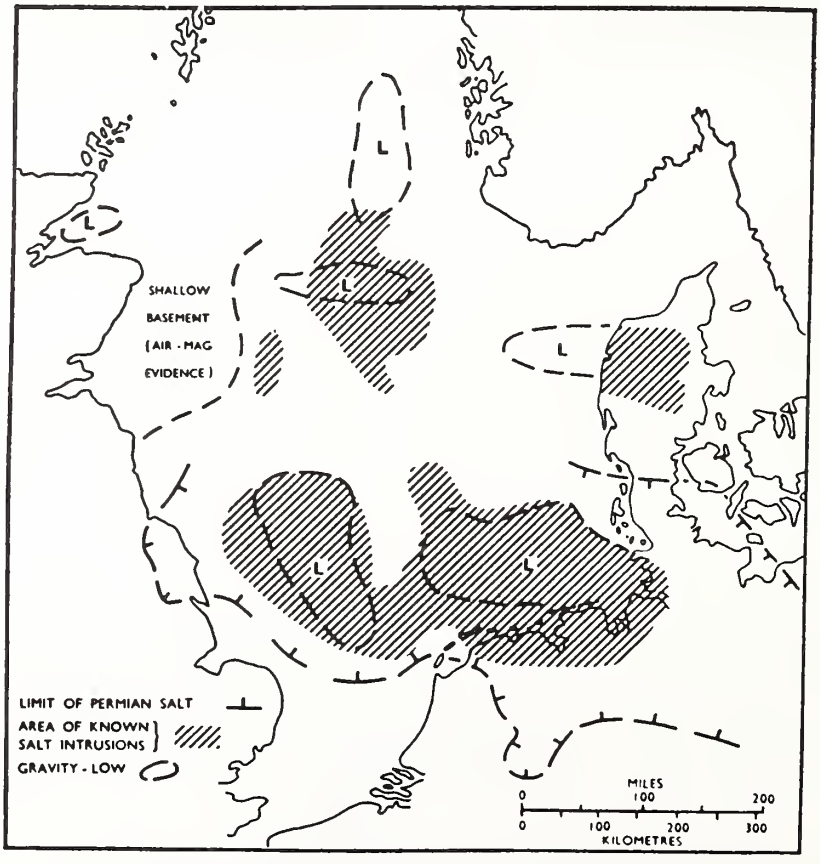

Figure 26. Gravity "lows" on a gravity map of the North Sea are associated with salt domes of lower density than surrounding materials (From Smith, 1968, fig. 6).

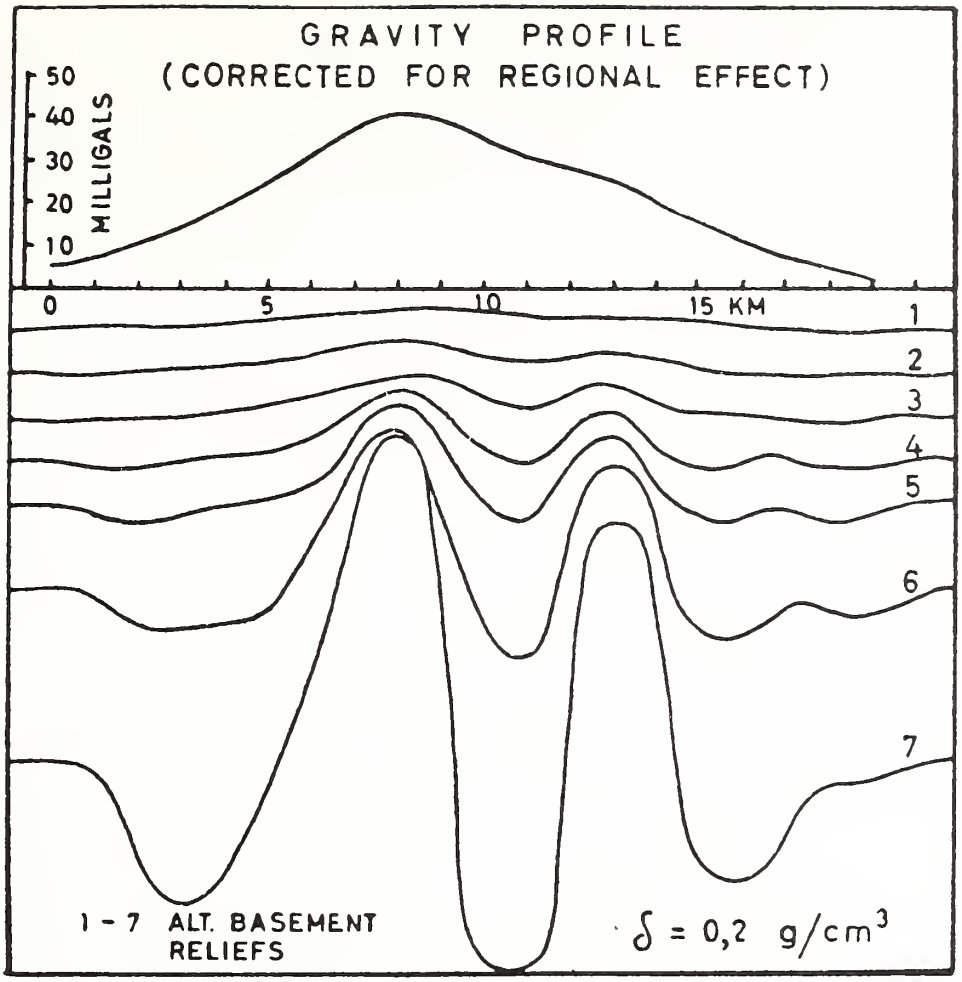

Figure 27. A given gravity anomaly (top) may be explained by each of the mass distributions shown below (From Parasnis, 1962, fig. 18).

Telluric currents are electric currents flowing naturally through the earth on a broad scale that can be detected with pairs of properly spaced electrodes. The telluric method has been used to detect large scale anomalies in conductivity such as salt domes.

Resistivity and equipotential methods consist of putting an electric current into the bottom with two electrodes and measuring the potential differences with two other electrodes. The results indicate the resistivity of a layer in the earth whose depth is proportional to the electrode spacing and whose dimensions are related to the symmetry of the lines along which the current flows.

In induced polarization a voltage is applied across two electrodes put into the bottom and shut off. The nature of the intervening material is inferred from the decay rate of the resulting current. Induced polarization and resistivity are generally limited in depth of penetra-

tion to twice the minimum dimension of the ore body sought.

In electromagnetic or induction methods an alternating current is set up in a wire loop. If a conducting body is present such a body of metallic ore, currents will flow in the body and can be detected with search coils. Electromagnetic methods have not yet been applied successfully at sea because of the high conductivity of sea water (Tooms et al., 1965).

4.6 Heat Flow

Heat is constantly being dissipated through the ocean bottom generated from the decay of radioactive elements within the earth. Hot spots may occur at sites of submarine volcanism, and very subtle temperature changes may be related to the heat conducting properties of local bodies of rock. For example, higher rates of heat dissipation would be expec-

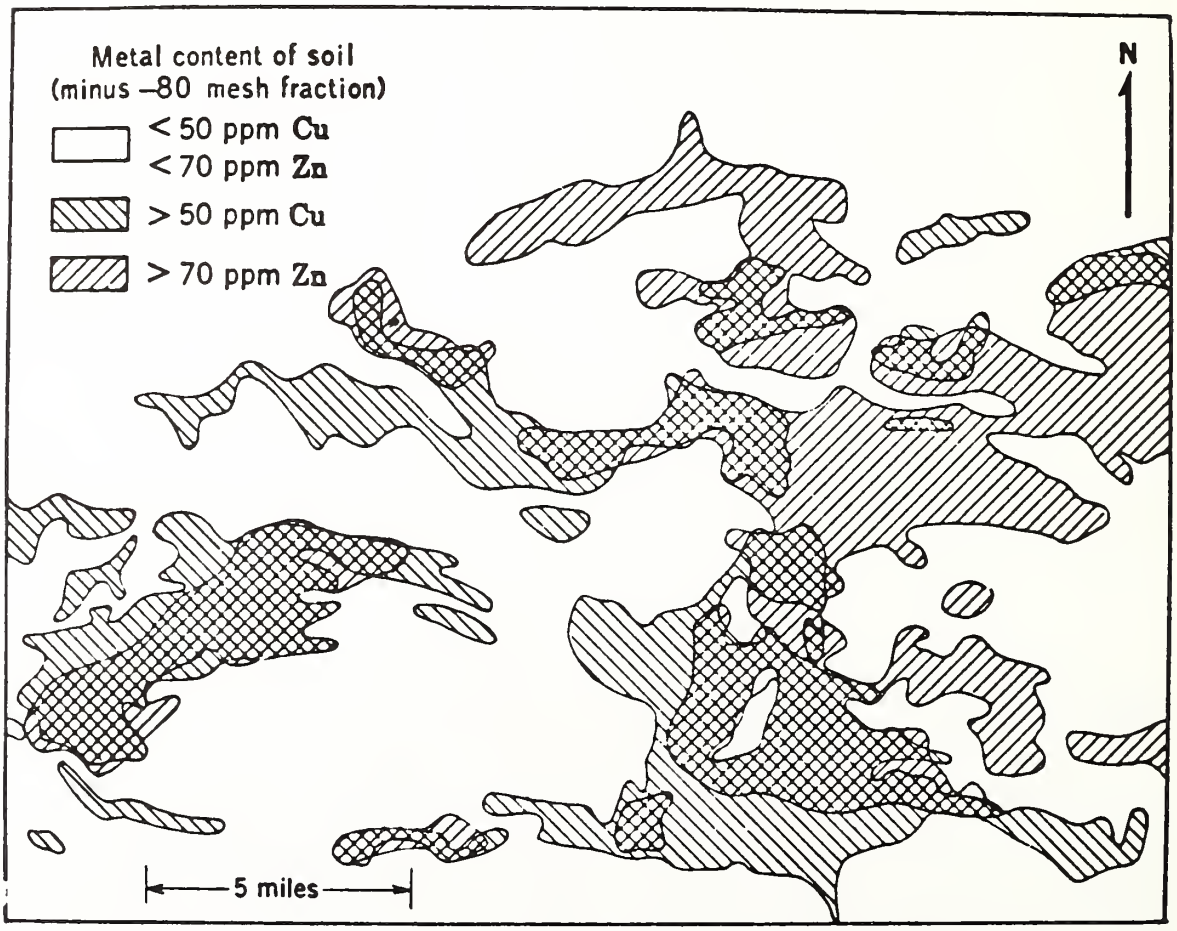

Figure 28. A geochemical map showing anomalous concentrations of copper and zinc measured in soil samples directly overlying buried ore bodies (Hawkes and Webb, GEOCHEMISTRY IN MINERAL EXPLORATION, Harper & Row Publishers, 1962. Data for this figure were supplied by Chartered Exploration Ltd.).

ted over metallic ore bodies of high conductivity than over salt domes of relatively low conductivity.

Measurements of the amount of heat flowing through the ocean bottom are made with a heat probe called a "thermograd", an instrument consisting of several heat sensors (thermistors) mounted at equal intervals along a cylindrical probe or along the barrel of a sediment coring device, which is vertically inserted into the sediments of the ocean bottom (fig. 8). The vertically spaced thermistors measure electrical

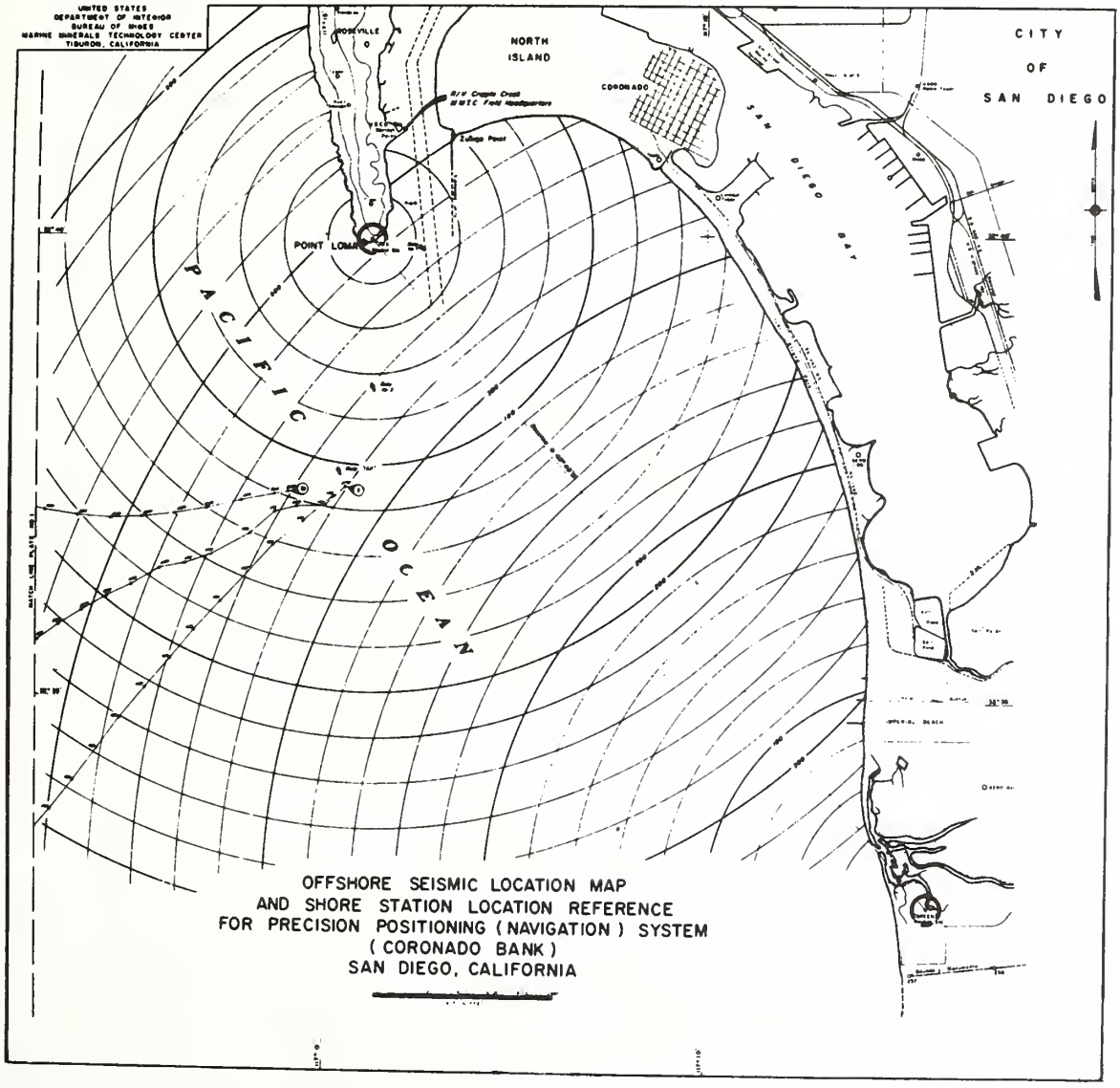

Figure 29. A range-range electronic navigation system in which a ship's position is at the intersection of two circles concentric about shore-based transmitting stations (From Barnes, 1970, plate 3). Each circle is the locus of all points equidistant from a transmitting station.

resistance which registers on an accompanying recorder calibrated to convert the resistances to temperature differences which may amount to several tenths of a degree Centigrade or more over a 10-meter vertical separation (Bullard, 1963; Gerard et al., 1962; Langseth, 1965). To obtain heatflow, the measured temperature gradients are multiplied by the value of the average thermal conductivity of the sediments between the thermistors. The thermal conductivity is routinely measured on-board ship in the simultaneously recovered sediment core (Von Herzen and Maxwell, 1959). The quantity determined is the amount of heat emerging through a unit area of the ocean bottom in a given time expressed as microcalories per second per square centimeter.

A spectacular association between submarine heat flow and valuable metallic ore bodies is described from the central rift of the Red Sea (Degans and Ross, 1969), where the temperature of bottom water is about 10°C higher than that of surface water. Heat flow is not presently used as a standard exploration method at sea largely because of the great

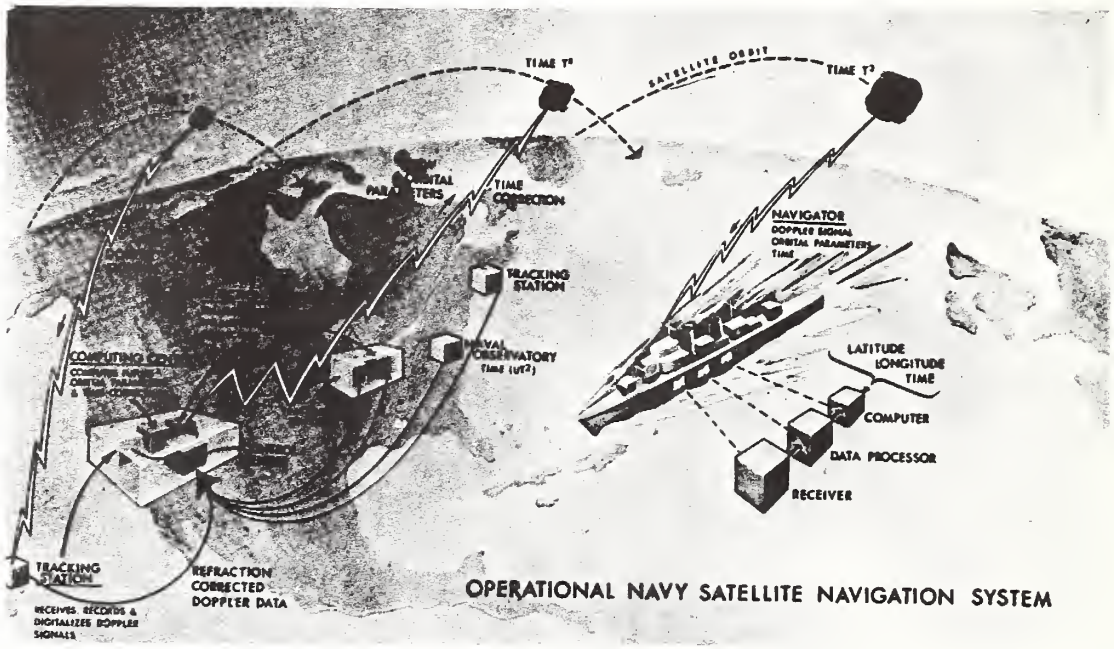

Figure 30. The satellite's signal is picked up by a tracking station (time[1]) which is relayed to the Computer Center. After computing future orbital parameters and a time correction, these are then relayed to an injection station which in turn transmits them to the satellite (time[2]). The satellite stores the information and transmits it to earth intermittently (time[3]). Shipboard systems with receiver-computer equipment combines position information of the satellite with information on the position of the ship relative to the satellite to determine the ship's position on earth (from Thomas, 1966, fig. 15.).

variation in values observed within small areas and the large changes in water temperature over continental shelves. Statistical analysis of many closely-spaced measurements at depth beneath the surface of the continental shelf is needed to accurately define anomalies.

4.7 Radioactive Methods

Radioactive methods are principally used to search for ores that are naturally radioactive or that are associated with radioactive minerals. They may also be used to locate minerals that emit characteristic radiation when artifically stimulated (see radiometric methods under Geochemical Methods).

Natural radioactivity occurs when certain atoms disintegrate, spontaneously emitting alpha particles (helium nuclei), beta particles (electrons and positrons), and gamma electromagnetic radiation. This phenomenon is confined principally to four radioactive series including the elements neptunium, thorium, and two types of uranium. The alpha and beta particles lose their energy in passing through matter and are not detectable under even a thin cover of sediments. The gamma rays can be detected through considerable thicknesses of material depending on the sensitivity of the instruments and the background effects due to

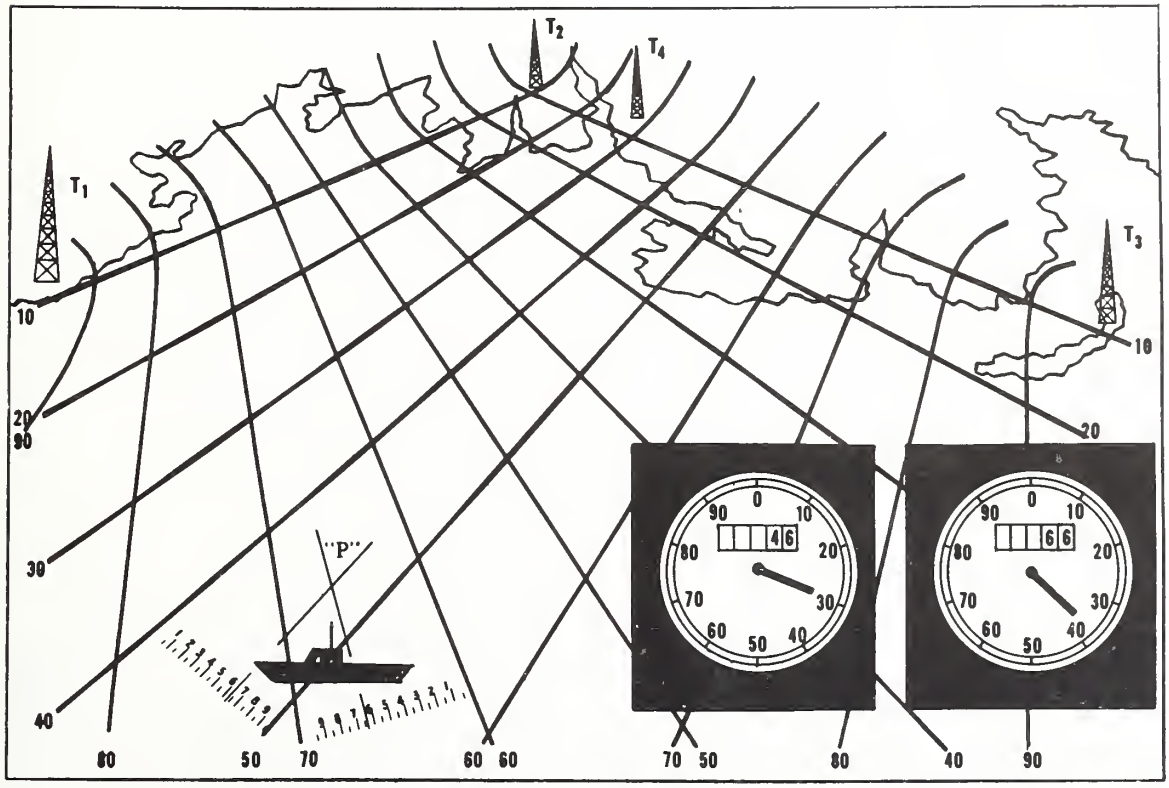

Figure 31. Hyperbolic electronic navigation system in which a ship's position "P" is at the intersection of two hyperbolae with foci at shore-based transmitting stations.

cosmic radiation. Characteristic gamma radiation may be stimulated when non-radioactive minerals are bombarded by neutrons from a radioactive source such as californium 252 in the method of neutron activation analysis.

Natural or stimulated radiation emanating from rocks is detected by Geiger and scintillation counters. Geiger counters detect gamma rays by their effect of ionizing gas contained in the instrument to produce an electric current. Scintillation counters detect gamma rays by their effect of causing certain substances to emit radiation. The radiation intensities may be recorded as counts-per-minute or millirontgens-per-hour.

Radioactive methods are used on land and have not yet been extensively applied to marine work. The Geiger or scintillation counter can be encased and towed near the sea floor, as has been done in exploration for submarine phosphorite nodules enriched in uranium (Tooms, 1969). A neutron activation analysis system designed for towing near the sea floor has been used experimentally to identify ore samples planted on the continental shelf (Ocean Industry, 1970; Noakes and Harding, 1971). Alternatively, shipboard measurements can be made on seawater, sediment, and rock samples.

5. GEOCHEMICAL METHODS

In geochemical prospecting the constituents in sediments and rocks and seawater are analyzed for indications of the presence of ore bodies and petroleum. The chemical property measured is usually the content of some element that occurs in minute "trace" quantities relative to other elements. The purpose of the measurement is the discovery of abnormal chemical patterns, or geochemical anomalies, related to mineralization. Geochemical prospecting is especially important in the search for minerals that occur in quantities too small to be resolved by most geophysical methods, as occurrences of such industrially important metals as molybdenum, tungsten, and vanadium.

Chemical indicators of the presence of a mineral deposit may disperse hundreds to thousands of meters away from the deposit. The indicators may disperse in solid, liquid, or gaseous phases. The concentration of the indicator will decrease away from the source giving rise to a concentration gradient that leads back toward the source. For example, hydrocarbon gases like methane, ethane, and propane, as well as brines from salt domes, may diffuse from petroleum deposits through overlying materials, to the ocean bottom (Kartsev and others, 1959). Metal ions in solution can migrate through the agencies of weathering, leaching, and transport in ocean currents resulting in dispersion halos around the parent ore body (Ginsburg, 1960). Dispersion patterns can be identified by the chemical analysis of samples systematically obtained on and beneath the ocean bottom and from the adjacent seawater.

Qualitative and semi-quantitative chemical methods are used to identify and estimate concentrations of the principal and indicator elements in samples. The reliability of geochemical prospecting depends on the sensitivity and precision of these measurements, which can vary depending on the method, the presence of impurities, and the competence of the geochemist. The analytical methods in most common use are summarized in table 3.

The results of sample analyses can be usefully portrayed by maps on which concentrations of different elements are contoured to delineate geochemical anomalies (fig. 28). The maps may reveal trends and gradients in concentrations of indicator elements, which may converge toward a source mineral deposit.

6. THE MARINE ENVIRONMENT

The continental shelf is covered by a layer of salt water up to about 200 meters thick. This means that a ship must be used as a stable platform for the execution of most exploration methods with the exception of magnetics, long-range photography, and certain electromagnetic techniques which can be flown (Powell, 1969; Undersea Technology, 1970, Oceanographic Ships and Submersibles of the World, Section E, p. 1-36). This also means that instruments immersed in sea water must be specially packaged against water, corrosion, and the pressure of submergence.

The progress of a ship over the sea or a submersible vehicle through the sea is less hampered by physical obstacles and, therefore, faster than that of a vehicle over most terrains on land. Sound energy transmitted to probe the earth is more effectively coupled through water than through soil zones on land. The ocean bottom is less contaminated by mechanical and electromagnetic noise than is the land, generally resulting in better signal-to-noise ratios in geophysical measurements at sea. Alternatively, operations at sea are even more weather sensitive than those on land because as soon as waves start building, the ship becomes unstable and the efficiency of men and instruments rapidly declines. Operations at sea frequently must be curtailed due to rough seas. The percentage of unfavorable weather conditions varies with region and time of year and can be approximately predicted from consideration of synoptic weather maps compiled from prior years.

The efficiency of shipborne seismic, magnetic, and gravity coverage generally results in cost savings over the application of corresponding methods on land. However, the cost of exploration drilling at sea is considerably greater than on land. The rapid rate of development of ocean exploration techniques acts to increase the prices of equipment and services (Luehrmann, 1971). Airborne exploration offers the most rapid and inexpensive way to gather certain information over a large area at sea, but is limited in methods, resolution, and positional accuracy.

*Table 3. Analytical Methods in Geochemistry **

FLAME SPECTROMETRY: Many elements emit characteristic radiation when vaporized in the heat of a flame. The elements are identified by the wavelength of the spectral lines and their quantity estimated by the intensity of the lines.

EMISSION SPECTROMETRY: Almost all elements emit radiation of characteristic wavelengths when vaporized and ionized in the intense heat of an electric discharge. As with flame spectrometry, the element is identified by the wavelength and the quantity present is determined by the intensity of the spectral line. Flame and emission spectrometry are the basic tools of geochemical prospecting because of their capacity to conveniently determine whole series of chemical elements.

GRAVIMETRY: Gravimetric methods involve weighing the separated constituent.

COLORIMETRY: A trace element is made to form a compound that, when dissolved or suspended in a suitable liquid medium, absorbs or scatters light of characteristic wavelengths.

TURBIDITY AND NEPHELOMETRY: These methods involve, respectively, the unselective absorption and the scattering of light of all wavelengths by suspended particles of a precipitate containing the element to be determined.

SPOT TESTS: Some trace elements may be made to form colored compounds that can be displayed on paper.

PAPER CHROMATOGRAPHY: Ions may be separated by their differential rates of movement in a solvent as it flows along a strip of filter paper and dries in different colored bands. The element is identified by color and the amount by width and color intensity of the band.

VISIBLE FLUORESCENCE: Samples containing uranium emit a visible luminescence under ultraviolet light when fused and cooled.

X-RAY SPECTROMETRY: The inner orbital electrons of atoms may be activated by x-rays in such a way that they re-emit x-rays of a wavelength that identifies the activated element.

RADIOMETRIC METHODS: Uranium, thorium and potassium are naturally radioactive. Non-radioactive elements may be made radioactive by exposure to neutrons generated in an atomic reactor. Both natural and artificial radioactive elements give off gamma radiation of characteristic energy. The element is identified from the gamma ray energy and the quantity is measured from the intensity.

ELECTRICAL MEASUREMENTS - Polarography: A number of analytical methods depend on instrumental determination of the electrical properties of solutions as a measure of the kind and concentration of ions dissolved in the solution.

*After Hawkes and Webb, 1962

7. NAVIGATION

Exploration and navigation go hand in hand because geological, geophysical, and geochemical information must be accurately located to be useful. The ship performing the exploration must be equipped with a position-keeping system capable of sufficient accuracy, repeatability, and range, to fulfill the requirements of a particular exploration problem.

Positions at sea are determined relative to known locations using visual and electronic instruments with accuracies varying from 1 meter to many kilometers depending on the method and the conditions of its use. Accuracies quoted by manufacturers of navigational systems are based on optimum conditions, and may be greater than accuracies achieved in actual operations.

The traditional methods of visual and celestial navigation are seldom adequate as primary navigation but are useful as verification and backup for more efficient electronic methods which utilize radio waves. Most electronic methods work by determining ranges from the ship to known locations, or the position of the ship on hyperbolic curves (Thomas, 1966; Chernof, 1971). The range methods utilize travel time or phase differences of electromagnetic signals transmitted between the ship and two radio transmitters at two different known locations to measure two ranges; the maximum operational distance is generally line-of-sight. The two ranges determine the radii of two circles, and one of the intersections of the circles is the position of the ship (fig. 29). Radar determines range and bearing relative to an object such as an anchored buoy or landmark which reflects electromagnetic signals. Satellite navigation systems determine the position of the ship relative to the known position of the satellite from information transmitted via radio from the satellite to a shipboard receiver and computer (fig. 30).

Hyperbolic methods utilize two pairs of transmitting stations at known locations and a receiver onboard the ship (fig. 31). The difference in arrival time or phase of electromagnetic signals received at the ship determines the position of the ship along a hyperbola, defined as the locus of all points along which the difference in distance to two foci (land-based transmitters) is equal. The ship's position is determined by the intersection of two hyperbolae.

Electronic navigational systems utilizing other than radio waves include doppler sonar and inertial. Doppler sonar systems utilize the reflection of sound waves from the ocean bottom in depths up to about 300 m (Buford, 1969). As the ship moves relative to the ocean bottom a hull-mounted sonar transducer continuously emits sound waves at a frequency which is shifted by a value proportional to the ships velocity (Doppler shift). This information is displayed as a velocity and direction and is integrated by a computer to provide distance and course from an independently known starting point. Inertial systems utilize a gyroscope to sense accelerations from which ships speed and direction are derived and integrated by a computer to provide distance and course from

an independently known starting point; the high cost of inertial navigation systems limits their application to exploration.

At present the only electronic navigational systems with worldwide coverage are satellite and Omega (hyperbolic). Several other hyperbolic systems have permanent installations but are limited in range up to about 2000 kilometers. Shorter range systems can be commercially obtained to suit specific tasks.

8. COMPOSITE EXPLORATION METHODS

The choice of an exploration method is guided by pure and practical considerations. The pure considerations emphasize the objective of the investigation and the type of information needed to fulfill the objective, including the geology of the region to be investigated and the anticipated mode of occurrence of the mineral deposit being sought (Table 1). Cost, anticipated economic return, the availability of funding, competent manpower, instrumentation, ships, navigational control, and the conditions of work (accessibility, weather, etc.) in a given region are important practical considerations.

An exploration campaign should employ several exploration methods both concurrently and sequentially (table 2). For example, bathymetric, seismic reflection, magnetic, and gravity methods can be run concurrently from a single moving ship to provide complementary information about the ocean bottom (Robinson, 1971). The aeromagnetic method can provide rapid regional reconnaissance. Shipborne geophysical methods can provide more information on selected areas and serve to guide geological and geochemical sampling. Estimates of additional field costs to obtain shipboard gravity, magnetic, and seismic refraction information in combination with seismic reflection data range as low as 10 percent (Dean and Kologinczak, 1970). The information gained from such a composite investigation reduces the uncertainties in interpretation and increases the probability of discovery.

9. BIBLIOGRAPHY

9.1 General

Brillouin, L. (1956), "Science and information theory," Academic Press, New York.

Dean, R. E. and J. B. Kologinczak (1970), "Total package exploration survey approach," Oil and Gas Journal, November 16 and 23.

Freitag, J. S., T. L. Holcombe and J. A. Pew (1969), "Oceanographic and data processing instrumentation aboard USNS KANE for Cruise Nine," UnderSea Technology, Handbook/Directory 1969, Section A, 31-44, Reprint E6.

Hill, M. N. (editor) (1963), "The Sea," 3, New York, Wiley - Interscience, 963 p.

Holmes, A. (1965), "Principles of physical geology," The Ronald Press, New York, 1288 p.

Long, F. S. (1969), "Redundancy gives RESEARCHER computer system high reliability," UnderSea Technology, August, 35-40, Reprint R290.

Luehrmann, W. H. (1971), "The high cost of offshore exploration," Oceanology, October, 24-29.

Maxwell, A. E. (editor) (1970), "The Sea," 4, Part 1, New York, Wiley - Interscience, 791 p.

Moody, G. B. (editor) (1961), "Petroleum exploration handbook," New York, McGraw-Hill, 25 chapters.

O'Hagan, R. M. (1968), "Digital computer applications in the marine sciences," UnderSea Technology, October, Reprint R227.

Powell, A. L. (1969), "The cost of government research ships," UnderSea Technology, Handbook/Directory 1969, Section A, 9-11, Reprint E3.

UnderSea Technology (1970) (yearly), Handbook/Directory, Compass Publications, Inc., Suite 1000, 1117 N. 19th Street, Arlington, Virginia 22209, U.S.A.

Turekian, K.K. (1968), "Oceans," Prentiss-Hall, Englewood Cliffs, N.J., 120 p.

Wang, F. F. H. and M. J. Cruickshank (1969), "Technologic gaps in exploration and exploitation of sub-sea mineral resources," Offshore Technology Conference, paper number OTC 1031, I-286-298.

9.2 Occurrence of Continental Shelf Mineral Deposits

Cruickshank, M. J. (1970), "Mining and mineral recovery 1969," UnderSea Technology Handbook 1970, A 11-21, Reprint E7.

Hess, H. D. (1965), "The Ocean: Mining's newest frontier," Engineering and Mining Journal, 166, No. 8, 79-96.

Mero, J. L. (1965), "The mineral resources of the sea," New York, Elsevier, 312 p.

McKelvey, V. E. and F. F. H. Wang (1969), "Preliminary maps, World Subsea Mineral Resources," U. S. Geological Survey, Miscellaneous Geologic Investigations, Map I-632.

United Nations (1970), "Mineral Resources of the Sea," United Nations, Secretariat, Department of Economic and Social Affairs, Resources and Transport Division, 49 p.

Worzel, J. L. (1968), "Survey of continental margins," Donovan, D. T. (editor), Geology of shelf seas, Edinburgh, Oliver and Boyd, 117-152.

9.3 Geological Methods

Chesterman, W. D., P. R. Clynick and A. H. Stride (1958), "An acoustic aid to sea bed survey," Acustica, 8, 285-290.

Clay, C. S., J. Ess and I. Weisman (1964), "Lateral echo sounding of the ocean bottom on the continental rise," Journal of Geophysical Research, 69, 3823-3825.

Emery, K. O. (1966), "Geological methods for locating mineral deposits on the ocean floor," Exploiting the ocean, Transactions of Second Marine Technology Society Conference, 24-43.

Emery, K. O. and L. C. Noakes (1968), "Economic placer deposits of the continental shelf," Technical Bulletin, ECAFE, 1, 95-111.

Johnson, G. L. and M. K. Jugel (1968), "Recent developments in hydrography," UnderSea Technology, Handbook/Directory 1968, Section A, Reprint H-3.

Kofoed, J. W. and R. J. Malloy (1965), "Bathymetry of the Miami Terrace," Southeastern Geology, 6, 159-165.

Owen, D. M. (1967), "A multi-shot stereographic camera for close-up ocean bottom photography," in Hersey, J. B. (editor), Deep-Sea Photography: Baltimore, Maryland, The Johns Hopkins Press, 310 p., 95-105.

Petroleum Engineer Publishing Co., Fundamentals of Rotary Drilling: latest edition, Dallas, Texas.

Rusby, S. (1970), "Long range side-scan sonar for use in the deep sea (G.L.O.R.I.A. Project)," Monaco, The International Hydrographic Review, 48, No. 2, 25-39.

Sanders, J. E., K. O. Emery and E. Uchupi (1969), "Micro-topography of five small areas of the continental shelf by side-scanning sonar," Geological Society of America Bulletin, 80, 561-572.

Shepard, F. P. (1963), "Submarine Geology," Second edition: New York, Harper and Row, 557 p.

Shepard, F. P. (1972), "Submarine Geology," Third edition: New York, Harper and Row, in press.

Shepard, F. P., K. O. Emery and H. R. Gould (1949), "Distribution of sediments on East Asiatic continental shelf," Allan Hancock Foundation Publication, Occasional Paper No. 9, 1-64.

9.4 Geophysical Methods

Barnes, B. B. (1970), "Marine phosphorite deposit delineation techniques tested on the Coronado Bank, southern California," Dallas, Texas, Offshore Technology Conference, paper number OTC 1259, II-316-330.

Bullard, E. C. (1963), "The flow of heat through the floor of the ocean," Hill, M. N. (editor), The Sea, 3, Interscience Publishers, Wiley, 963 p., 218-232.

Cain, J. C., S. J. Hendricks, W. E. Daniels and D. C. Jensen (1964), "Computations of the main geomagnetic field from spherical harmonic expansions," NASA Report X-611-64-316.

Clay, C. S. and P. A. Rona (1965), "Studies of seismic reflections from thin layers on the ocean bottom in the western North Atlantic," Journal of Geophysical Research, 70, 855-869.

Corwin, R. F., W. C. Ebersole and P. Wilde (1970), "A self potential detection system for the marine environment," Houston Offshore Technology Conference, OTC 1258.

Dobrin, M. B. (1952), Introduction to geophysical prospecting," New York, McGraw-Hill, 435 p.

Eve, A. S. and D. A. Keys (1956), "Applied geophysics in the search for minerals," Cambridge, The University Press, 382 p.

Gerard, R., M. G. Lanseth, Jr. and M. Ewing (1962, "Thermal gradient measurements in the water and bottom sediment of the western Atlantic," Journal of Geophysical Research, 67, 785-803.

Gurke, J. L. (1970), "Shipboard data acquisition - why use a computer?," Compass Publications, UnderSea Technology Handbook/Directory, A63-66, Reprint D8.

Heiland, C. A. (1963), "Geophysical exploration," New York, Hafner, 1013 p.

Hill, M. N. (1959), "A shipborne nuclear spin magnetometer," Deep Sea Research, 5, 309-311.

Hill, M. N. (1963), "Single-ship seismic refraction shooting," Hill, M. N. (editor), The Sea, 3, Interscience Publishers, Wiley, 39-46.

I.A.G.A. Commission 2, Working Group 4, (1969), "International Geomagnetic reference field 1965.0," Journal of Geophysical Research, 74, 4407-4409.

Jakosky, J. J. (1960), "Exploration geophysics," California, Trija Publishing Company, 1179 p.

Kramer, F. S., R. A. Peterson and W. C. Walter (1968), "Seismic energy sources 1968 handbook," Bendix, United Geophysical Corporation, 57 p.

Langseth, M., Jr. (1965), "Techniques of measuring heat flow through the ocean floor," in, Lee, W. H. K. (editor), Geophysical Monograph 8, American Geophysical Union, Washington, D.C., 58-77.

Neidell, N. S. (1968), "Data processing for controlled energy acoustic sources," UnderSea Technology, October, 28-29, 44-46.Reprint R231.

Nettleton, L. L. (1971), "Elementary gravity and magnetics for geologists and seismologists," Wuenschel, Paul C. (editor), Monograph Number 1, Society of Exploration Geophysicists, P. O. Box 3098, Tulsa, Oklahoma 74101, 121 p.

Noakes, J. E. and J. L. Harding (1971), "Marine mineral prospecting by neutron activation analysis (abstract)," Geological Society of America 1971 Meeting, Abstracts with Programs, 800 p, 661.

Ocean Industry (1968), "Sources of seismic energy for marine exploration," Ocean Industry, 3, Nos. 5-6, 36-41, 87-94.

Ocean Industry (1970), "Nuclear probe for underwater detection of minerals," Ocean Industry, 5, No. 10, 39-40.
Parasnis, D. S. (1962), "Principles of applied geophysics," New York, Wiley, 176 p.
Parasnis, D. S. (1966), "Mining Geophysics," New York, Elsevier, 356 p.
Paterson, N. R. (1967), "Underwater mining - new realms for exploration," Mining in Canada, April.
Robinson, W. B. (1971), "Geophysics is here to stay," American Association of Petroleum Geologists Bulletin, 55, No. 12, 2107-2115.
Romberg, F. E. (1961), "Exploration geophysics: A review," Geological Society of America Bulletin, 72, 883-932.
Schneider, W. A. (1971), "Developments in seismic data processing and analysis (1968-1970)," Tulsa Society of Exploration Geophysicists, Geophysics, 36, No. 6, 1043-1073.
Senftle, F. E., E. D. Duffey and P. F. Wiggins (1969), "Mineral exploration of the ocean floor by in-situ neutron absorption using a Californium-252 source," Marine Technology Society Journal, 3, No. 5, 9-16.
Silverman, D. (1967), "The digital processing of seismic data," Geophysics, 22, 988-1002.
Smith, D. T. (1968), "Physics and sea-floor minerals," Contemporary Physics, 9, 565-585.
Society of Exploration Geophysicists: P. O. Box 3098, Tulsa, Oklahoma 74101, Geophysics.
Talwani, M. (1964), "A review of marine geophysics," Marine Geology, Elsevier, Amsterdam, 2, 29-80.
Talwani, M. and J. R. Heirtzler (1964), "Computation of magnetic anomalies caused by two-dimensional structures of arbitrary shape," in Computers in the mineral industries, Proceedings of Third Annual Conference, Stanford and University of Arizona, Part 1, 480 p., 464-480.
Templeton, R. S. M. (1970), "Geology of the continental margin between Dakar and Cape Palmas," in Geology of the East Atlantic continental margin, Natural Environment Research Council, Institute of Geological Sciences, Report No. 70/16, 209 p., 43-60.
Tooms, J. S. (1969), "Some aspects of exploration for marine mineral deposits," London, Institute of Mining and Metallurgy, 9th Commonwealth Mining and Metallurgical Congress, 12 p.
Von Herzen, R. P. and A. E. Maxwell (1959), "The measurement of thermal conductivity of deep-sea sediments by a needle-probe method," Journal of Geophysical Research, 64, 1557-1563.
Wing, C. G. (1969), "MIT vibrating string surface-ship gravimeter," Journal of Geophysical Research, 74, 5882-5894.
Worzel, J. L. and J. C. Harrison (1963), "Gravity at sea," Hill, M. N. (editor), The Sea, 3, New York, Wiley - Interscience, 963 p. 134-174.
Worzel, J. L. and G. L. Shurbet (1955),"Gravity anomalies at continental margins," Proceedings U.S. National Academy of Sciences, 41, 458-469.

9.5 Geochemical Methods

Degens, E. T. and D. A. Ross (1970), "The Red Sea hot brines," Scientific American, 222, no. 4, 32-42.

Ginzburg, I. I. (1960), "Principles of geochemical prospecting," New York, Pergamon Press, 311 p.

Hawkes, H. E. (1957), "Principles of geochemical prospecting," United States Geological Survey, Bulletin 1000-F, 225-355.

Hawkes, H. E. and J. S. Webb (1962), "Geochemistry in mineral exploration," New York, Harper and Row, 415 p.

Kartsev, A. A., Z. A. Tabasaransky, M. I. Subbota and G. A. Magilevsky (1959), "Geochemical methods of prospecting and exploration for petroleum and natural gas," (translation from Russian) edited by P. A. Witherspoon and W. D. Romey: Berkeley, University of California Press, 349 p.

Rainwater, F. H. and L. L. Thatcher (1960), "Methods for collection and analysis of water samples," United States Geological Survey Water Supply Paper 1454, 301 p.

Shapiro, L. and W. W. Brannock (1956), "Rapid analysis of silicate rocks," United States Geological Survey, Bulletin 1036-C, 19-56.

Smales, A. A. and L. R. Wager (editors) (1960), "Methods in geochemistry," New York, Interscience Publishers, Wiley, 464 p.

Tooms, J. S., D. T. Smith, I. Nichol, P. Ong and J. Wheildon (1965), "Geochemical and geophysical mineral exploration experiments in Mounts Bay, Cornwall," in W. F. Whittard and R. Bradshaw (editors), Submarine geology and geophysics, London, Butterworths, 363-391.

Yoe, J. H. and H. J. Koch, Jr. (editors) (1957), "Trace Analysis," New York, Wiley, 672 p.

9.6 Navigation

Bauss, W. (1963), "Radio navigation systems for aviation and maritime use," New York, MacMillan.

Bigelow, H. W. (1965), "Electronic surveying: Accuracy of electronic positioning systems," Supplement to the International Hydrographic Review, 6 September.

Bowditch, N. (1966), American practical navigator," Washington, U. S. Naval Oceanographic Office, 1542 p.

Buford, W. H., Jr. (1969), "Doppler sonar - a new navigation tool," UnderSea Technology, March, Reprint R241.

Chernof, J. (1971), "Navigation and positioning systems," Oceanology International, April, 42-45.

Dunlap, G. D. (1969), "Dutton's navigation and piloting," 12th edition, Annapolis, United States Naval Institute, 715 p.

Radio aids to maritime navigation and hydrography (1956), Monaco, International Hydrographic Bureau, Special Publication No. 39, 481 p.

Radio aids to maritime navigation and hydrography (1965), Monaco, International Hydrographic Bureau, Supplementary Papers to Spec.Pub. 39.

Symposium on electronic distance measuring (1960), Journal of Geophysical Research, 65, 385-528.
Symposium on marine geodesy, Columbus, Ohio (1966), Washington, U. S. Environmental Science Services Administration.
Talwani, M. (1970), "Developments in navigation and measurement of gravity at sea," Geoexploration, 8, 151-183.
Thomas, P. D. (1966), "Terrestrial and earth satellite navigation systems," Washington, U. S. Naval Oceanographic Office, Technical Report No. 188, 139 p.; Table 4 contains a summary of electromagnetic and acoustic positioning systems including accuracies and costs.
Winston, E. J. (1970), "Underwater tracking systems," Ocean Industry, 5, No. 10, 49-52.

GPO 842-990

(Reprinted from Nature Physical Science, Vol. 239, No. 92, pp. 77–79, October 2, 1972)

Manganese Crusts of the Atlantis Fracture Zone

SUMMARIES of the transition element chemistry of oceanic ferro-manganese deposits report compositional trends related to water depth and to geographic proximity to continental margins[1–4]. Explanations of compositional variations include continental source influence[3,5,6], diagenetic environmental control of manganese mineralogy that regulates the trace metal composition[1,3,7], ionic mobility in interstitial solutions during diagenesis[3,8–10], and volcanic or hydrothermal influence[3,11–14]. Glasby[15] rejects a significant pressure control on manganese oxide mineralogy on thermodynamic grounds.

Manganese crusts were dredged from the Atlantis Fracture Zone (AFZ) by the NOAA ship Discoverer in 1971 as part of the Trans-Atlantic Geotraverse (TAG) (Figs. 1 and 2) and give evidence in support of a mineralogical control and a secondary volcanic influence on the manganese crust composition. Sufficient crusts for analytical work were recovered on the limestone outcrops on the Mid-Atlantic Ridge (MAR) (site 10G) and on the altered volcanic breccia ridge (site 2B) that offsets the AFZ at magnetic anomaly K-12 (ref. 16). Although this ridge at dredge site 2B obviously was volcanic and is a magnetic high, it is now aseismic without volcanic activity. AFZ encrustations are similar to oceanic seamount nodules: broad diffuse 2.4 and 1.4 Å X-ray diffraction peaks indicate poorly crystallized birnessite, an oxidized mineralogy compared to the todorokite found in less oxidized abyssal sea floor and continental margin nodules[1,17].

The average AFZ crust Fe/Mn ratio of 1.5 is close to the Atlantic average of 1.35 (Table 1). The Fe/Mn ratio is 1.9 on the MAR and 1.1 at 2B some 2,100 km to the east. The higher Fe/Mn ratio nearer the MAR conforms with the belt of nodules with high Fe/Mn ratios along the MAR[2]. Cronan[2] considers that this trend is related to volcanic or hydrothermal influence of the ridge; we agree. It seems doubtful that this regional trend could be controlled by Eh gradients[18] because in open sea water local Eh anomalies would be obliterated a

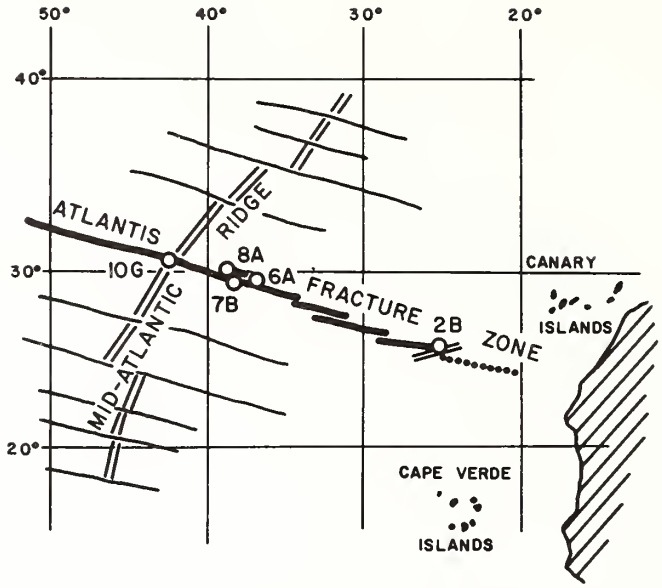

Fig. 1 Location of dredge sites where manganese crusts were encountered (open circles). Sufficient material for chemical analyses was recovered at sites 10G and 2B. The dotted line shows the extension of the AFZ under abyssal plain sediment. The parallel lines at dredge site 2B delineates the altered volcanic ridge discussed in the text.

short distance from a hydrothermal vent[19]. Mercury determinations also suggest volcanic influence: the MAR crust contains 130 p.p.b. Hg but upper 2B crusts have only 12–23 p.p.b. Hg, supporting the correlation of high Hg concentrations with local volcanic influence noted by Harriss[13]. Cronan[20] finds high Hg values in some MAR sediments but Aston *et al.*[21] find equally high Hg values unrelated to volcanic regions.

The strikingly similar Ni/Co ratios of Pacific oceanic seamount nodules (0.35) and AFZ crusts (0.40) are in contrast with those from Pacific abyssal sea floor (2.0) and marginal sea floor (5.7) nodules and all Atlantis nodules (0.96). Covariance of Ni and Co with Mn in fracture zone crusts (Table 1, Fig. 3) suggests substitution in or adsorption on birnessite. If several manganese phases with different trace metal affinities compete for Ni and Co, more complex elemental relationships occur[14]. Probably Ni/Co ratios are sensitively controlled by the different trace metal affinities of birnessite and todorokite so that todorokite nodules have higher Ni/Co ratios. The surface chemistry properties of manganese dioxides support

Table 1 Composition* of Manganese Crusts from the Atlantis Fracture Zone

Sample number		% Fe	% Mn	P.p.m. Ni	Co	Cu	V	Zn	P.p.b. Cr	Hg	Location of sample	Fe/Mn	Ni/Co	Fe/Cu × 10^{-2}
Dredge site 10G	10G4	16.5	9.2	1,200	2,160	780	500	320	45	—		1.80	0.55	2.1
	10G9	18.2	10.2	1,340	3,050	830	500	400	50	—	30° 08′ latitude north	1.78	0.44	2.2
	10G15	18.5	9.4	1,240	2,480	840	800	350	35	—	42° 29′ longitude west	1.97	0.50	2.2
	10G16	19.1	10.2	1,355	3,200	1,080	425	485	50	—	depth = 3,120 m	1.87	0.42	1.8
	10G3	—	—	—	—	—	—	—	—	129		—	—	—
Dredge site 2B	2B1	14.9	13.5	1,970	7,200	550	750	375	50	23	26° 07′ latitude north	1.10	0.27	2.7
	2B2	18.5	14.5	2,500	7,540	1,120	750	640	30	12	25° 21′ longitude west	1.27	0.33	1.7
	2B8	15.9	13.9	2,280	5,660	680	500	375	40	—	depth = 4,280 m	1.14	0.40	2.4
	2B9	14.9	14.4	2,060	8,380	460	1,000	365	90	—		1.04	0.25	3.2
Sequence of samples through crust of dredge site 2B	2B2–1	13.8	17.3	2,490	6,850	380	500	370	—	—	0.5 mm top	0.80	0.36	3.8
	2B2–2	13.9	17.2	2,340	8,890	410	575	380	—	—	2 mm	0.81	0.26	3.4
	2B2–3	17.0	13.4	1,850	4,700	615	675	400	—	—	8 mm	1.27	0.39	2.8
	2B2–4	18.7	11.9	1,650	3,170	735	525	430	—	—	18 mm	1.57	0.51	2.5
	2B2–5	20.6	12.8	1,670	2,990	765	550	460	—	—	28 mm	1.61	0.56	2.7
	2B2–6	20.0	13.2	1,640	2,660	780	575	500	—	—	38 mm	1.52	0.62	2.6
	2B2–7	19.3	13.7	1,610	2,420	745	575	490	—	—	48 mm	1.41	0.67	2.6
	2B2–8	18.4	13.1	1,790	2,070	800	450	470	—	—	55 mm bottom	1.40	0.86	2.3
Precision error		±0.4	±0.3	±30	±60	±40	±150	±40	±10	±5				
Average Pacific Oceanic Seamount[1]		13.4	17.4	4,100	10,600	1,000	—	—	—	—		0.77	0.39	1.3
Average Atlantic[2]		21.8	16.2	2,970	3,090	1,090	—	—	—	—		1.35	0.96	2.0

* By weight.

Analyses for Fe, Mn, Ni, Co, Cu, V, Zn and Cr by atomic absorption spectrophotometry and Hg by the cold-flow flameless atomic absorption method. The entire sample was dissolved by a HCl-HNO_3-HF treatment. Values for Al (atomic absorption) are less than 1.5 weight % indicating that negligible detrital clay was present. Locations of dredge sites 10G and 2B are given and the relative sample positions in crust 2B2 are indicated. Average Pacific oceanic seamount nodules and average Atlantic nodules are listed for comparison.

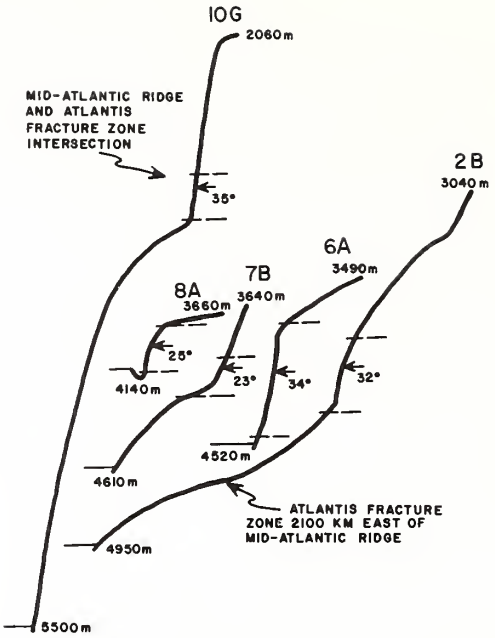

Fig. 2 Traces of PDR records showing the estimated positions of contact with outcrop by arrows and calculated average slopes in the interval dredged (within dashed horizontal lines). Depths in m. Vertical exaggeration is extreme. Traces are arranged west to east from left to right.

this conclusion[22–24] Also, compilations of all nodule types[1,2,4] or individual nodules of complex mineralogy[25] show inverse or no Fe–Cu correlation, but the simple mineralogy of fracture zone crusts shows a distinct Fe–Cu covariance (Table 1).

A stratigraphic record of the chemical environment of manganese crust growth is preserved if no postdepositional redistribution occurred. The 58 mm thick crust of dredge site 2B was sampled from the top (2B2-1) to the bottom (2B2-8). The chemistry of the older portion of the crust (2B2-4 to 2B2-8) is similar in Fe/Mn, Ni/Co, and Fe/Cu ratios to present day MAR crusts (Table 1 and Fig. 3). The chemistry of the upper 13 mm of 2B2 is distinctly different. The similarity between MAR manganese chemistry and older crusts at dredge site 2B may indicate a similarity of growth environments with an environmental change at site 2B during growth of the upper layers. From the ^{230}Th dating method using the top 1 mm of crust[26], the extrapolated time of environmental change was about 11 m.y. ago. It is doubtful

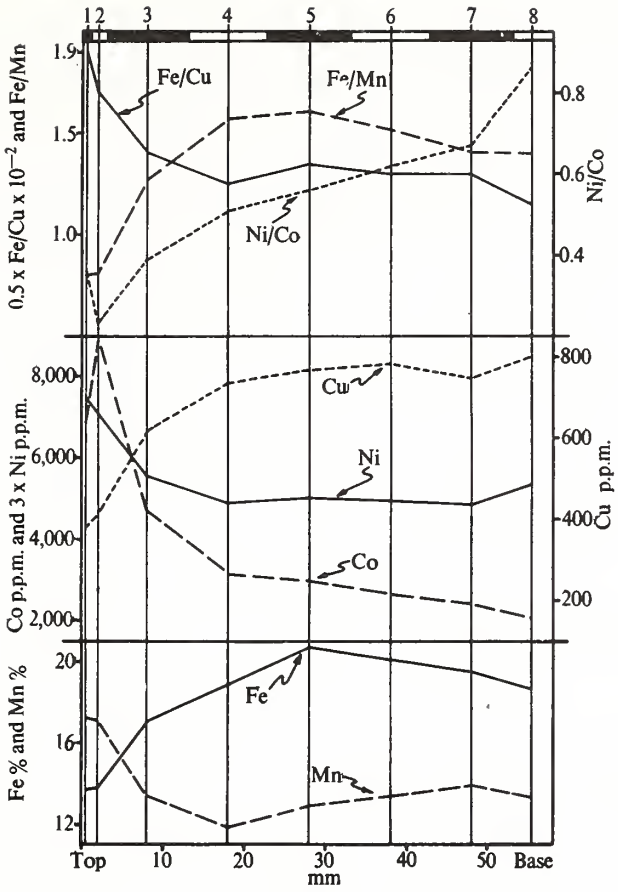

Fig. 3 Transition metal chemistry profile through the 58 mm thick manganese crust recovered at dredge site 2B. Note that the Ni and the Fe/Cu scales have been arbitrarily adjusted to the range of the graphs to facilitate comparisons of trends. Sample numbers and positions are marked at the top of the graph. The light and dark bars at the top of the graph indicate the intervals of crust removed so that the chemical value at each sample position refers to the integration of all values within each interval.

that the change in chemistry of the crust is related to migration away from the MAR volcanic influence because 11 m.y. ago 2B was 1,960 km from the MAR and has only moved 140 km since that time. It is more likely that the change in 2B chemistry is related to a cessation of local volcanic activity.

This study agrees with the contention[1,3,7] that a primary control of the trace metal composition of manganese deposits is the mineralogy formed in equilibrium with local Eh environmental conditions. Further, the results support the idea that a secondary influence[3,11–14] is related to volcanic activity by direct supply of metals or indirect environmental controls of metal extraction from seawater.

We thank Steven Levine and Janet Mathewson for analytical work, and Drs Bob Presley and David Cronan for criticism of the manuscript. This work was supported by grants from the NSF and AEC and by cooperation from NOAA.

ROBERT B. SCOTT

Texas A & M University,
Department of Geology,
College Station, Texas 77843

PETER A. RONA
LOUIS W. BUTLER

NOAA, 15 Rickenbacker Causeway,
Miami, Florida 33149

ANDREW J. NALWALK

University of Connecticut,
Marine Sciences Institute,
Groton, Connecticut 06340

MARTHA R. SCOTT

Texas A & M University,
Department of Oceanography,
College Station, Texas 77843

Received July 21, 1972.

[1] Price, N. H., and Calvert, S. E., *Marine Geol.*, **9**, 145 (1970).
[2] Cronan, D. S., *Science*, **235**, 171 (1972).
[3] Cronan, D. S., *Deep-Sea Res.*, **16**, 335 (1969).
[4] Tooms, J. S., Summerhayes, C. P., and Cronan, D. S., *Oceanogr. Mar. Biol. Ann. Rev.*, **7**, 49 (1969).
[5] Manheim, F. T., *Narragansett Mar. Lab. Occ. Pub.*, **3**, 217 (1965).
[6] Arrhenius, G., and Bonatti, E., *Progress in Oceanog.*, **3**, 7 (Pergamon, 1965).
[7] Cronan, D. S., *Trans. Amer. Geophys. Union*, **53**, 410 (1972).
[8] Lynn, D. C., and Bonatti, E., *Marine Geol.*, **3**, 457 (1965).
[9] Skornyakova, N. S., *Inter. Geol. Rev.*, **7**, 2161 (1965).
[10] Ku, T. L., and Glasby, G. P., *Geochim. Cosmochim. Acta*, **36**, 699 (1972).
[11] Arrhenius, G., Mero, J. L., and Korkisch, J., *Science*, **144**, 170 (1964).
[12] Bonatti, E., and Nayudu, Y. R., *Amer. J. Sci.*, **263**, 17 (1965).
[13] Harriss, R. C., *Nature*, **219**, 54 (1968).
[14] Corliss, J. B., *J. Geophys. Res.*, **76**, 8128 (1971).

[15] Glasby, G. P., *Nature Physical Science*, **237**, 85 (1972).
[16] Lattimore, R. K., Rona, P. A., and DeWald, O. E., *Trans. Amer. Geophys. Union*, **53**, 407 (1972).
[17] Buser, W., and Grutter, A., *Schweiz. Mineral. Petrog. Mitt.*, **36**. 49 (1956).
[18] Krauskopf, K. B., *Geochim. Cosmochim. Acta*, **12**, 61 (1957).
[19] Zelenov, K. K., *Doklady Akad. Nauk SSSR*, **155**, 1317 (1964).
[20] Cronan, D. S., *Canad. J. Earth Sci.*, **9**, 319 (1972).
[21] Aston, S. R., Bruty, D., Chester, R., and Riley, J. P., *Nature Physical Science*, **237**, 125 (1972).
[22] Healy, T. W., Herring, A. P., and Fuerstenau, D. W., *J. Colloid Interface Sci.*, **21**, 435 (1966).
[23] Morgan, J. J., and Stumm, W., *J. Colloid Sci.*, **19**, 347 (1964).
[24] Murray, D. J., Healy, T. W., and Fuerstenau, D. W., *Advances in Chemistry*, **79**, 74 (1968).
[25] Burns, R. G., and Fuerstenau, D. W., *Amer. Mineral.*, **51**, 895 (1966).
[26] Scott, R. B., Rona, P. A., Butler, L. W., Scott, M. R., Kennett, J. P., Nalwalk, A. J., Warme, J. E., and McCrevey, J. A., *Trans. Amer. Geophys. Union*, **53**, 529 (1972).

Printed in Great Britain by Flarepath Printers Ltd., St. Albans, Herts.

Reprinted from Marine Geology 12, 165-185.

Research Papers

SEISMIC RECONNAISSANCE OF POST-MIOCENE DEPOSITS, MIDDLE ATLANTIC CONTINENTAL SHELF—CAPE HENRY, VIRGINIA TO CAPE HATTERAS, NORTH CAROLINA

GERALD L. SHIDELER AND DONALD J. P. SWIFT[1]

Institute of Oceanography, Old Dominion University, Norfolk, Va. (U.S.A.)

(Received August 7, 1971)

ABSTRACT

Shideler, G. L. and Swift, D. J. P., 1972. Seismic reconnaissance of post-Miocene deposits, Middle Atlantic continental shelf – Cape Henry, Virginia to Cape Hatteras, North Carolina. *Mar. Geol.*, 12: 165–185.

A seismic reconnaissance survey was conducted to examine post-Miocene deposits on the Middle Atlantic Shelf between Cape Henry, Virginia and Cape Hatteras, North Carolina. Approximately 900 kilometers of continuous seismic reflection profiles were obtained, employing a 400-joule high resolution boomer system.

The post-Miocene section unconformably overlies a furrowed and discordant Tertiary substrate. The basal unconformity appears to be of regional extent, and its configuration supports the presence of an eastward-trending ancestral Albemarle fluvial channel near the present mouth of Albemarle Sound. A basal sedimentary sequence of pre-Wisconsinan and Early Wisconsinan age is widespread, and comprises most of the post-Miocene section. It contains both transgressive fluvial deposits, and regressive coastal barrier lithosomes. An overlying sequence of Late Wisconsinan age was deposited in a regressive paralic–neritic environment. Holocene deposits, unconformably overlying the Pleistocene sequence, form a discontinuous sand sheet whose upper surface is molded into a north- or northeast-trending ridge and swale topography.

The morphology of the outer shelf and shelf break is variable throughout the region. Prominent wave-cut terraces reflecting Pleistocene glacio-eustatic movements are present, except in the southern third of the region. Most areas of the outer shelf exhibit ridge and swale systems which appear to be polygenetic. Variations in shelf break morphology suggest differential rates of Holocene sedimentation and shelf development. Shelf upbuilding and progradation are minimal near Cape Henry, and maximal near Cape Hatteras where Diamond Shoals may be actively advancing eastward across the shelf.

INTRODUCTION

This paper presents the results of a regional seismic reconnaissance survey of post-Miocene deposits along the Middle Atlantic continental shelf between Cape Henry, Virginia and Cape Hatteras, North Carolina. This continuous seismic reflection survey was conducted during a 1969 cruise of the NASA telemetry vessel, "Range Recoverer", employing a 400-joule high resolution boomer system. Emphasis was placed on obtaining a high degree of resolution in the upper

[1] Present address: Marine Geology and Geophysics Laboratory, National Oceanic and Atmospheric Agency, 901 South Miami Avenue, Miami, Florida 33130.

30–45 m of shelf deposits, rather than on deep penetration. This reconnaissance study is an extension of a more detailed localized study of the post-Miocene section along the Inner Virginia Shelf southeast of Cape Henry (Shideler et al., in press).

Field procedures

Approximately 900 km of continuous seismic reflection profiles were obtained along the Middle Atlantic Shelf between Cape Henry and Cape Hatteras (Fig.1). The study area is located between 35°00′–37°00′ N latitude, and 74°30′–

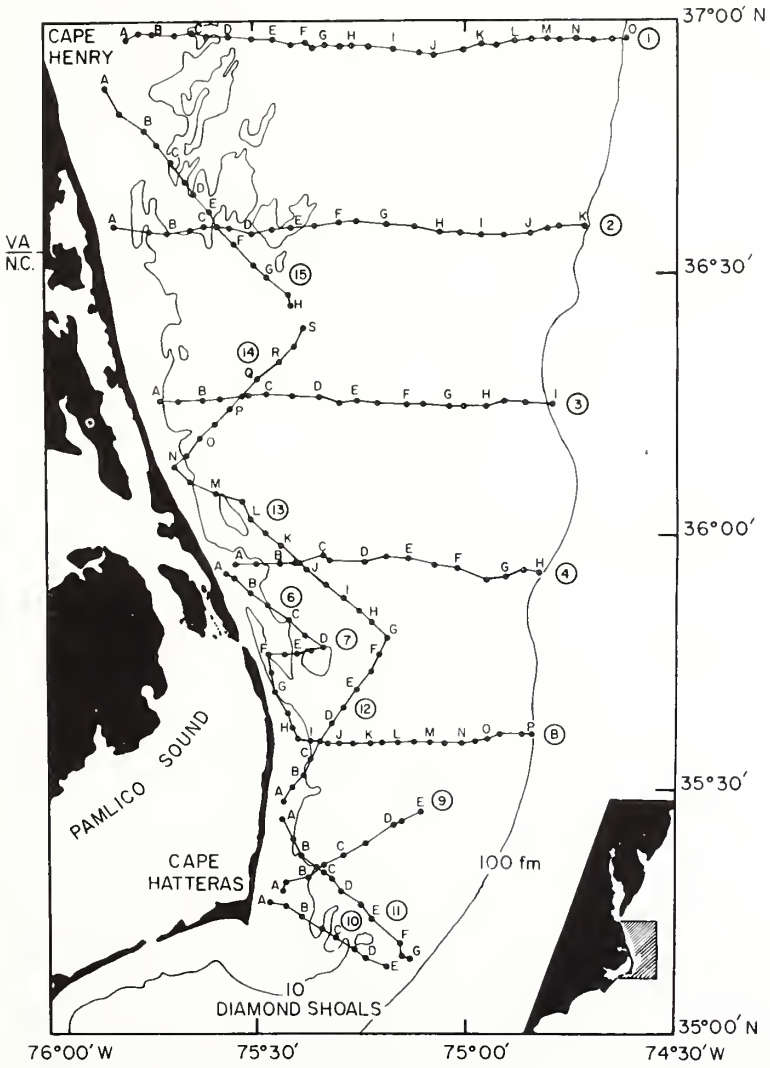

Fig.1. Index map of the study area illustrating the seismic profile network.

76°00′ W longitude. Profile traverses were run perpendicular to the shelf break, at approximately a 40-km interval. Individual traverses extend from the shelf break at the 200-m (100-fm) isobath to points as far shoreward as were possible under local bathymetric and sea state conditions. The perpendicular traverse network is augmented by a zigzag profile network along the inner shelf. The courses of the zigzag tracks were selected to provide coverage of interesting bathymetric features along the inner shelf, and to facilitate correlations between adjacent profiles of the perpendicular traverse network. Navigation fixes were obtained at 20-min intervals, employing a Loran A system; geographic locations are indicated as letters on the individual profiles.

Seismic instrumentation consisted of an EG and G 400-joule high resolution boomer, using a repetition rate of 640 msec. Occasionally, the system was operated at a 200-joule level, with a repetition rate of 320 msec. The output frequency spectrum of the transducer ranged from DC, to a maximum of 3 kHz; the resulting pulse had a peak pressure of 98.6 dB, referenced to 1 volt per microbar. Reflected energy was received by a linear array hydrophone (Type XOC-45), consisting of 10 elements equally spaced at 1-foot intervals. Received signals were passed through a Krohn-Hite external filter with a band pass of 250–40 kHz, and recorded on a Model 254 seismic recorder. Both hydrophone array and acoustic source were towed at the surface, approximately 8 m astern of the "Range Recoverer". The average surveying speed was approximately 6 knots, but varied with maritime traffic and sea state conditions.

Data processing

Seismic reflection data were processed manually. The original boomer records were fitted with transparent acetate overlays, and all reflecting horizons were traced with a marking pencil. Strong reflectors were marked with solid lines, while dubious reflectors were indicated by dashed lines. The acetate overlays of the individual boomer profiles were reduced to common vertical and horizontal scales on graph paper, and converted into stratigraphic line drawings (Fig.2, 3, 4). The vertical scale of the line drawings represents two-way reflection travel time in milliseconds. The approximate thickness and depth values presented in this paper are based on an assumed average seismic velocity of 1.5 km/sec for both the substrate and overlying water column. In view of the probable increasing velocity gradient within the substrate, the values presented should be regarded as minimal values; unless otherwise stated, all depth values are referenced to sea level. On the basis of the assumed seismic velocity, the line drawings exhibit a vertical exaggeration of approximately 133 ×. Enumerated fiducial marks along the top of each profile refer to the geographic reference points illustrated on Fig.1; the triangular fiducial marks indicate profile intersections.

The seismic line drawings illustrate the shallow post-Miocene stratigraphy and structure throughout the study area. Prominent reflectors which serve as

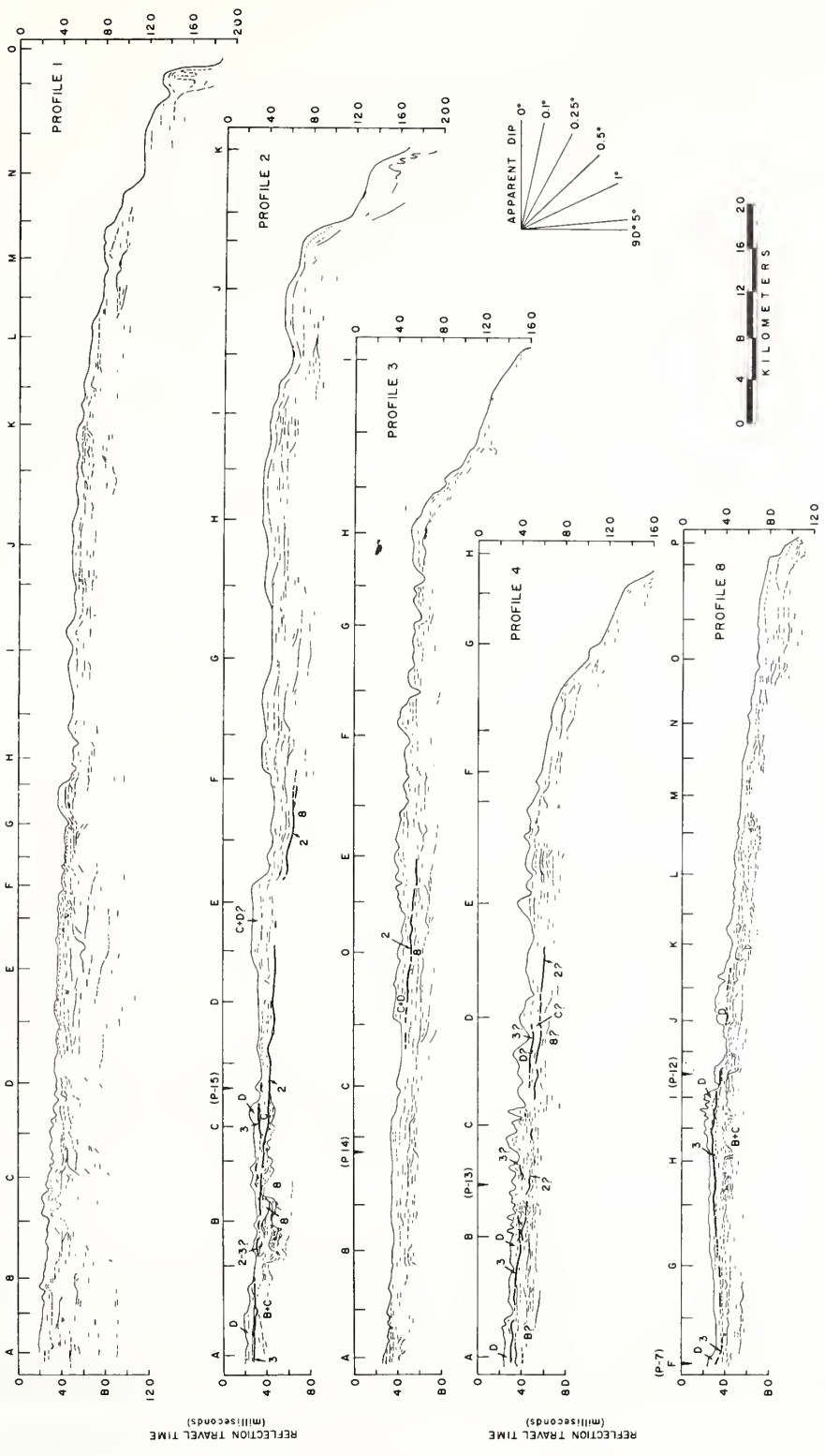

Fig.2. Stratigraphic line drawings of seismic profile records: profiles 1, 2, 3, 4, and 8. Millisecond scale illustrates two-way travel time.

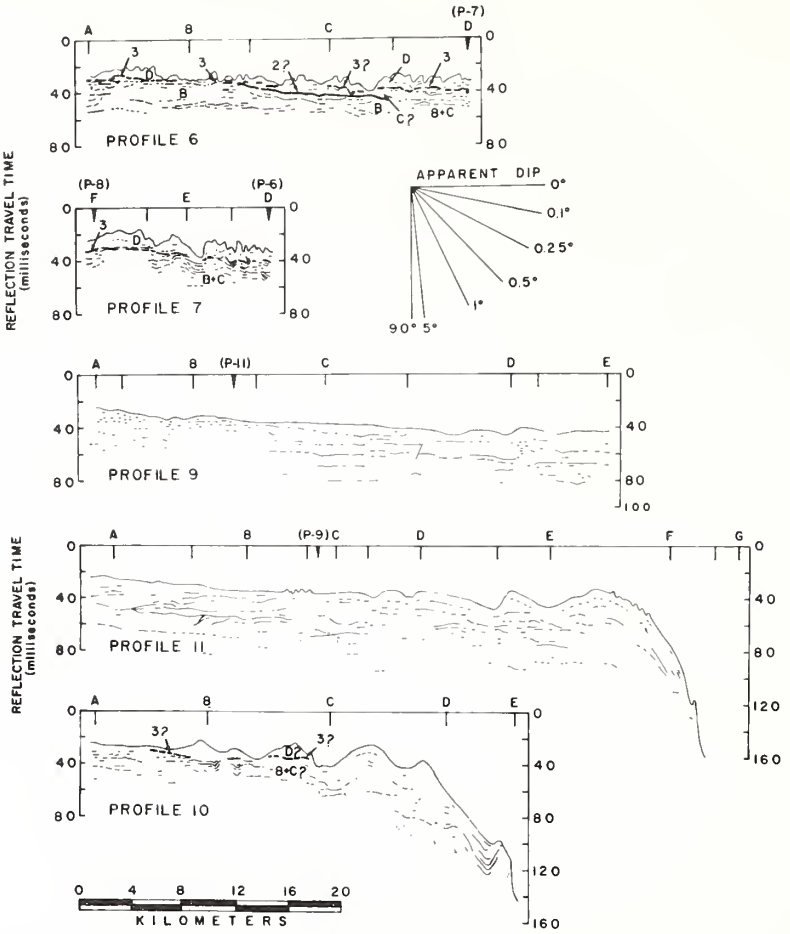

Fig.3. Stratigraphic line drawings of seismic profile records: profiles 6, 7, 9, 10 and 11. Millisecond scale illustrates two-way travel time.

stratigraphic marker horizons are numbered and indicated by bolder lines, while stratigraphic units are indicated by letters. Correlations between individual profiles are based on tie points at profile intersections, stratigraphic position, and structural similarities.

STRATIGRAPHY AND STRUCTURE

A proposed standard section for the Late Quaternary System established on the Inner Virginia Shelf (Shideler et al., in press) served as a stratigraphic focal point for this regional reconnaissance study. Along the Inner Virginia Shelf, four distinct sedimentary sequences separated by three prominent acoustic reflections

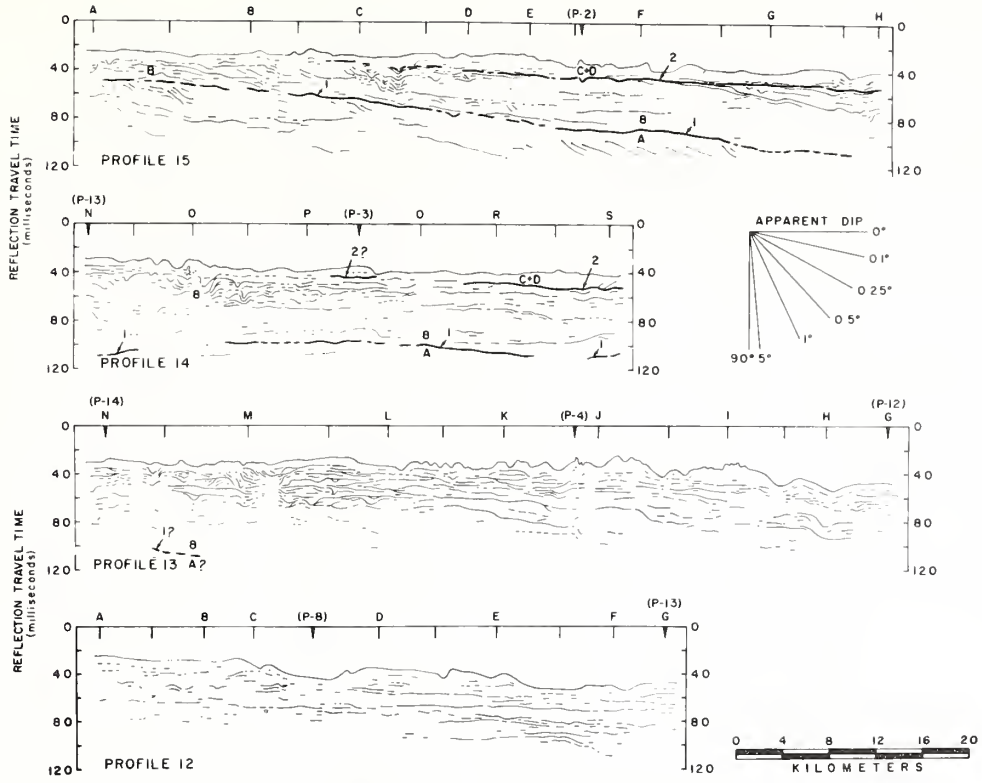

Fig.4. Stratigraphic line drawings of seismic profile records: profiles 12, 13, 14, and 15. Millisecond scale illustrates two-way travel time.

were identified. In ascending order, the four sequences were tentatively correlated as a Tertiary sequence (Unit A), a pre-Wisconsinan and Early Wisconsinan sequence (Unit B), a Late Wisconsinan sequence (Unit C), and a Holocene sequence (Unit D). The nature of these assemblages throughout the present study area, as delineated by the high resolution boomer profiles (Fig.2–6), are discussed individually. In general, optimum resolution and penetration of the stratigraphic section occur along the inner shelf. However, with increasing absorption by the water column along the deeper outer shelf, resolution and penetration of the substrate are substantially reduced.

Tertiary substrate

The deepest sedimentary sequence detected during the study is designated Unit A, which is defined as the sequence whose upper boundary is reflector *R1*, the deepest prominent acoustic discontinuity observed during the study. The absence of deep well data in the area of detection precludes a positive age determination at present. However, on the basis of its structural attitude and strati-

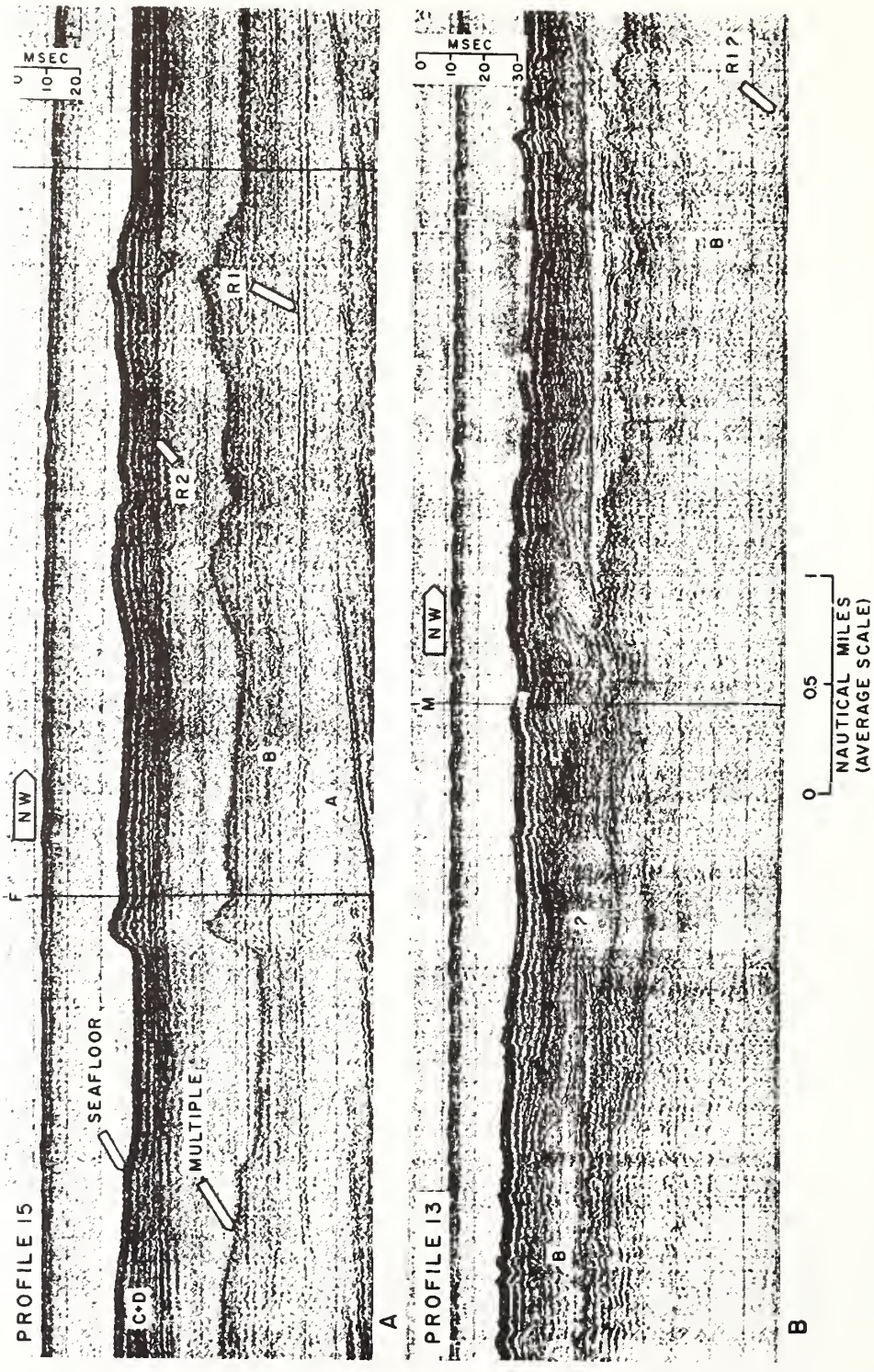

Fig.5. Selected portions of the original high resolution boomer records: Millisecond scale illustrates two-way travel time. A. Angular unconformity at the inferred Miocene and post-Miocene boundary (R1) near point *F* of profile 15. Note high reflectivity of R1, and subjacent discordant strata of Unit A. B. Prominent lenticular stratification of Unit B within part of the *N–L* interval of profile 13 suggests cut-and-fill structures of a possible ancestral Albemarle fluvial system. Structureless reef-like feature southeast of point *M* is probably a seismic shadow.

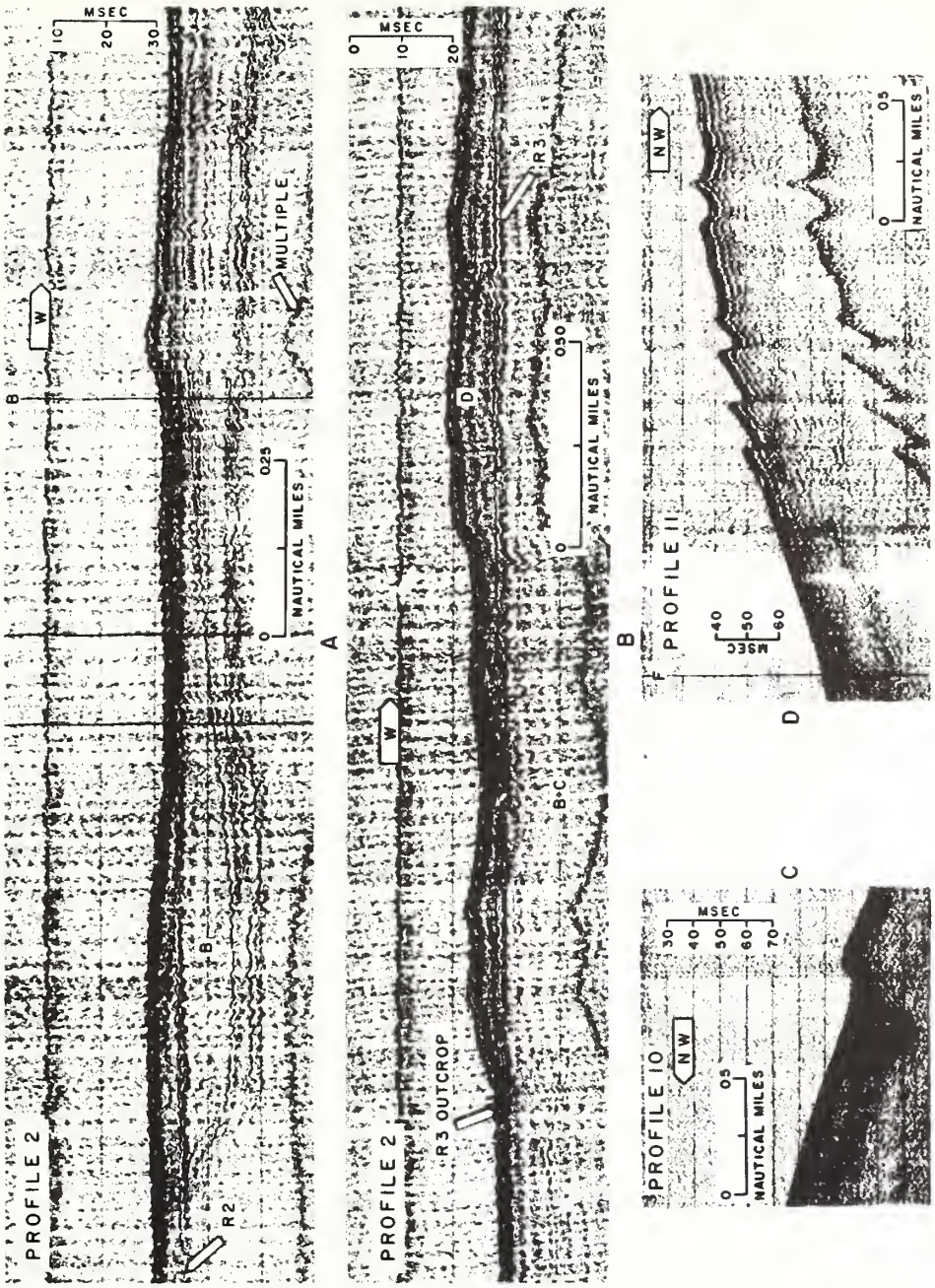

Fig.6. Selected portions of original high resolution boomer records: Millisecond scale illustrates two-way travel time. A. Prominent local channeling within Unit B near point *B* of profile 2. B. Eastern portion of the prominent Holocene ridge within the *A–B* interval of profile 2; the ridge exhibits a typical plano-convex cross section, and is part of the False Cape ridge system. C. Prominent cut-and-fill structure in the *D–E* interval of profile 10, suggesting that Diamond Shoals may be prograding over an older erosional surface. D. Sand waves on shelf edge north of Diamond Shoals in the *E–F* interval of profile 11.

graphic position, Unit A has been tentatively correlated as a Late Tertiary sequence, with reflector R1 constituting the Miocene and post-Miocene boundary (Shideler et al., in press).

Tertiary strata comprising Unit A were detected only in the northwestern segment of the study area. Their characteristics are well defined only on profile 15 (Fig.4, 5A), where the unit is characterized as a sequence of eastward dipping homoclinal strata, with dip angles notably greater than overlying units. The average dip rate is 3 m/km, corresponding to an apparent dip angle of less than 0.25 degrees. The angular discordance between Unit A and overlying strata is most apparent in the *E–G* interval of profile 15. The minimal total thickness value of Unit A is 35 m; however, its maximum total thickness was not determinable because of the limited penetration capabilities of the high resolution boomer system.

Pre-Wisconsinan and Early Wisconsinan deposits

The youngest post-Miocene sequence detected in the study area is designated Unit B. It is defined as the sequence above reflector R1, which is characterized by frequently lenticular stratification and prominent local channeling. The upper boundary is generally reflector R2, a prominent acoustic discontinuity which can be used to separate Unit B from strata of overlying Unit C. In the local absence of Unit C, the upper boundary consists of reflector R3 which occurs at the base of Unit D, the youngest assemblage comprising the post-Miocene section. On the basis of radiocarbon dating and stratigraphic position, Unit B has been correlated as an assemblage of pre-Wisconsinan and Early Wisconsinan age (Shideler et al., in press). It could represent the offshore partial equivalent of the Pleistocene Great Bridge Formation–Sand Bridge Formation sequence of the adjacent coastal plain; the unit might also contain partial correlatives of the Pliocene (?) Sedley and Bacons Castle formations which have been described by Oaks (1964) and Coch (1965).

Basal boundary reflector. The basal boundary reflector, R1, appears to be manifested in the study area as a prominent unconformity. It was detected at depths ranging from approximately 37 to 82 m below sea level, with a mean depth value of 70 m. Its burial depth beneath the sea floor ranges from 17 to 60 m, with a mean value of 47 m. The areal extent of reflector R1 detection during the study is confined to the northwestern segment of the surveyed area, where it was noted on profiles 14, 15, and possible 13 (Fig.4).

Along profile 15, reflector R1 is an irregular eastward-dipping surface with an average apparent dip rate of 1 m/km (less than 0.1°). It is manifested as an angular unconformity, as indicated by the angular discordance between Unit A and strata of overlying Unit B, a relationship best exemplified in the *E–G* interval (Fig.5A). A similar angular discordance was also observed within the shallow structure of the outer shelf and slope east of the present study area (Uchupi and

Emery, 1967; Uchupi, 1970), as well as further north along the shelf off the northeastern United States (Garrison, 1967; Knott and Hoskins, 1968), suggesting that reflector R1 may be of regional extent. Reflector 1 may correlate with Knott and Hoskins' (1968) "surface #1", which they describe as a relatively extensive angular unconformity occurring approximately 70 m below the seafloor, and exhibiting an average dip of about 0.1°; they suggest a possible Nebraskan age for the erosional surface.

Reflector R1 was also detected intermittently along profile 14. Along this transect, angular discordance is not apparent, and the reflector surface appears as a slight topographic high, with the crest occurring in the *O–Q* interval. The only other possible indication of reflector R1 occurs in the *M–N* interval of profile 13. The non-detection of reflector R1 on other profiles is not attributed to its absence, but rather to the low penetration capabilities of the high resolution boomer system. A structure contour map of reflector R1 over its limited area of detection suggests an undulose topographic surface (Fig.7). The contours indicate a prominent re-entrant east of the mouth of Albemarle Sound near the junction

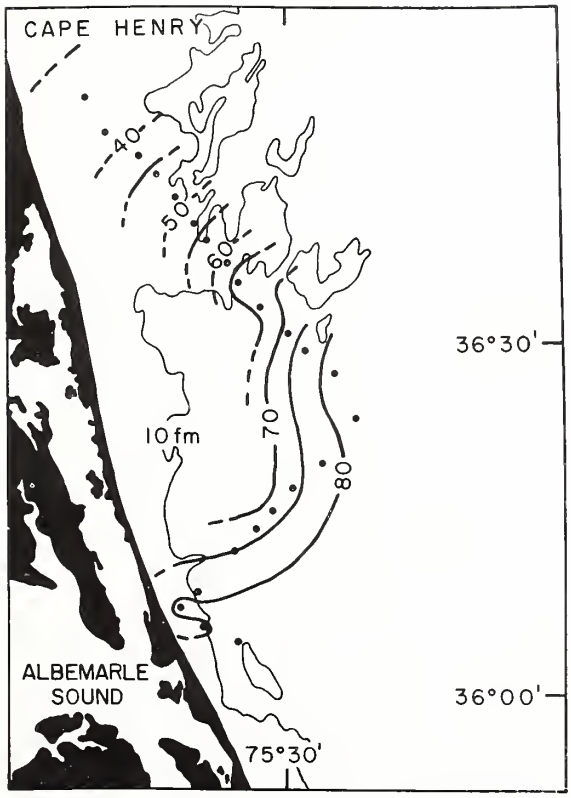

Fig.7. Structure contour map on reflector R1, which comprises the inferred Miocene and post-Miocene boundary. Contours are presented as meters below sea level.

of profiles 13 and 14, suggesting the possible presence of an ancestral Albemarle fluvial channel, such as advocated by Fisher (1967) on the basis of relict beach ridges in that vicinity. The presence of such a channel is further substantiated by the fluvial characteristics of overlying strata which exhibit pronounced lenticularity in this area (Fig.5B), suggesting the extensive development of cut-and-fill structures (*N–K* interval of profile 13). In addition, anomalous textural properties of sediments comprising the barrier island chain near this locality (Swift et al., 1971) further support the presence of a prominent eastward-draining ancestral Albemarle fluvial channel in this area.

The burial depth range of reflector R1 within its area of detection indicates an average total thickness value of 47 m for the overlying post-Miocene section along the inner shelf in the northwestern portion of the study area. The reflector is interpreted as prominent regional unconformity which truncates Miocene and older strata, and which may have developed during Late Tertiary or Early Pleistocene times.

Unit characteristics. Deposits comprising Unit B appear to be relatively widespread, as their presence is indicated on most profiles; however, differentiation of Unit B from adjacent strata by tracing its boundary reflectors was possible only on profiles 2, 3, 4, 6, 13, 14, and 15. The structures which characterize the unit are frequently lenticular stratification and prominent local channeling. Deposits of this facies frequently truncate a second distinct facies within the unit, which is characterized by more uniform stratification. The characteristic structures of Unit B are most apparent on profiles 2, 12, 14, and 15. Profile 2 denotes Unit B as a separate entity within the *B–F* interval. Lenticular stratification and prominent apparent channeling are present near the *B–C* interval (Fig.6A), where a strong internal reflector exhibits maximum local relief of up to 10 m. Although most of the structures in this interval indicate fluvial channels, similar structures might also result from the presence of topographic ridges, possibly accentuated by differential compaction. Profile 13 permits the partial differentiation of Unit B, where pronounced lenticular stratification within the *N–J* interval strongly suggests cut-and-fill structures of a fluvial assemblage (Fig.5B). The upper boundary of the unit was not delineated along this profile, and the pervasiveness of apparent cut-and-fill suggests that most of the section above reflector R1 may consist of Unit B deposits. The conspicuous reef-like structure near point *M* is enigmatic, but probably represents a "seismic shadow" resulting from the presence of some acoustically opaque material. However, the possible presence of a true organic reef structure must not be ruled out; apparent Late Pleistocene algal reefs have been noted on the North Carolina shelf south of Cape Hatteras (e.g., Menzies, 1966; Rona, 1969; Pilkey et al., 1971). Unit B is differentiable throughout much of profile 14, where lenticular stratification and channeling are most apparent in the *O–P* interval. In profile 15, Unit B is fairly well defined throughout the length

of the traverse. A large channel exceeding 16 km in width appears to be present in the *F–H* interval; the relatively great apparent width might be attributable to an oblique traverse across the trend of the channel. Other smaller-scale channeling is also apparent in the *C–D* interval.

Only along profiles 14 and 15, where both boundary reflectors are seen, could accurate total thickness measurements of Unit B be obtained. The total thickness along profile 14 averages approximately 43 m and is relatively constant, indicating a depositional strike section. However, the thickness along profile 15 ranges from approximately 21 m in the *B–C* interval, to 41 m in the *G–H* interval, indicating a general eastward (seaward) thickening along a dip section. Along profiles where only the upper boundary was delineated (profiles 2, 3, 4, 6), an average value of 20 m is obtained for the minimal unit thickness. In general, thickness values indicate that the majority of the post-Miocene section is comprised of pre-Wisconsinan and Early Wisconsinan deposits of Unit B.

Genetically, the deposits comprising Unit B have been interpreted as consisting primarily of a fluvial complex, overlain by a coastal barrier complex. The former appears to have developed during one or more pre-Wisconsinan interstadial transgressions, while the latter appears to represent a regressive assemblage developed during the Early Wisconsinan glacial sub-stage (Shideler et al., in press).

Late Wisconsinan deposits

Overlying Unit B with apparent unconformity are younger Pleistocene deposits which comprise Unit C. This unit is defined as the sedimentary sequence whose lower and upper boundaries are reflectors R2 and R3, respectively. On the basis of radiocarbon dating and stratigraphic position, Unit C is interpreted as a Late Pleistocene assemblage which developed during the regression that followed the mid-Wisconsinan Interstadial; the unit appears to have no known onshore correlatives (Shideler et al., in press).

Basal boundary reflector. The basal boundary reflector, R2, is detected at depths ranging from approximately 20 to 49 m below sea level, with a mean depth value of 34 m. Its burial depth beneath the seafloor ranges from 0 to 17 m, with a mean value of 8 m. Reflector R2 is an irregular eastward dipping surface, which exhibits an overall average apparent dip of 0.47 m/km. It is locally truncated by reflector R3. Genetically, reflector R2 has been interpreted as a prominent widespread unconformity throughout the study area. It may represent a composite erosional surface developed both by subaerial erosion during the Early Wisconsinan regression, as well as by surf erosion during the subsequent mid-Wisconsinan interstadial transgression (Shideler et al., in press).

Unit characteristics. The deposits comprising Unit C are characterized by relatively uniform stratification, compared with the lenticular and channeled nature of

underlying Unit B strata. Although the presence of Unit C is suggested on several profiles, the non-detection of both boundary reflectors frequently precluded its differentiation from adjacent units. It was detected as a distinct assemblage only on profiles 2, 4, and 6. Stratigraphically, Unit C on all three profiles appears to wedge out toward the west, as a result of truncation by overlying reflector R3. On all other profiles, Unit C is not totally differentiable from adjacent deposits.

Thickness values for Unit C are obtained only in the relatively few areas where both boundary reflectors are well defined. Detected thickness values range from zero, to a maximum of 8 m near point *C* on profile 2; the mean detected value is 3.2 m. The unit is relatively thin, but does exhibit a general thickening in an eastward (seaward) direction. The westward thinning of Unit C may be attributable to the combined effect of both depositional and erosional processes.

Genetically, Unit C is interpreted as a widespread Late Wisconsinan paralic–neritic assemblage, which developed during the regression that followed the mid-Wisconsinan interstadial (Shideler et al., in press). Since sea level at the end of the mid-Wisconsinan interstadial along the Atlantic Shelf was approximately at the position of present sea level (Milliman and Emery, 1968), the apparent absence of present onshore correlatives of Unit C suggests that Late Wisconsinan sedimentation may have been confined to areas seaward of the location of maximum interstadial strandline advance, and that their present absence might be less likely attributable to subsequent erosion.

Holocene deposits

The youngest sedimentary sequence detected during this study is designated Unit D, which is defined as the sequence above reflector R3, the shallowest prominent subsurface reflector observed during this study. The deposits comprising Unit D are the surficial sea floor sediments throughout much of the study area; consequently, the upper boundary reflector of the unit is the sediment-water interface, which is manifested as present sea floor topography. Detailed previous studies of Unit D in the northwestern quadrant of the present study area, employing cores, grab samples, and precise bathymetric data indicate that Unit D represents a Holocene transgressive sand sheet (Swift et al., 1970, 1972; Shideler et al., in press).

Basal boundary reflector. Reflector R3, which comprises the basal boundary of Unit D, is detected at a depth range of 19 to 39 m below sea level, with a mean depth value of 26 m. Its burial depth beneath the sea floor ranges from zero, to a maximum of 12 m, with a mean depth value of 5 meters. In many areas, reflector R3 appears to outcrop, and is coincident with the present sea floor (Fig.6B). It locally truncates reflector R2.

Reflector R3 is detected sporadically throughout much of the inner shelf, where it appears on profiles 2, 4, 6, 7, 8, and 10. Its non-detection on other profiles

is not necessarily due to its absence, but might be attributed to the following two factors: (*1*) reflector R3 frequently out crops, and is therefore coincident with the present sea floor and indistinguishable from it; and (*2*) excessive seismic ringing in the uppermost few meters of the profile records frequently obscured detection of shallow reflector R3. Regionally, reflector R3 is a nearly horizontal interface, with only a slight eastward (seaward) apparent dip, at an average rate of 0.34 m/km. Locally, the reflector is an irregular surface.

Genetically, reflector R3 is interpreted as a widespread unconformity, which represents the Pleistocene–Holocene boundary throughout the study area. It may represent a compound erosional surface, reflecting both subaerial erosion during the Late Wisconsinan regression, and subsequent shore face erosion during the following Holocene transgression (Shideler et al., in press).

Unit characteristics. The Holocene sand sheet of Unit D appears to be widely distributed throughout most of the inner shelf. Its presence could be established on all profiles where its basal reflector, R3, appears (profiles 2, 4, 6, 7, 8, 10). Conversely, its absence can be reasonably inferred in areas where reflector R3 appears to outcrop, thus exposing subjacent Pleistocene deposits. However, the non-detection of reflector R3 in many areas frequently precludes differentiation of Unit D from underlying deposits, and prevents accurate mapping of its areal distribution. In fact, the establishment of a precise distribution pattern for Pleistocene and Holocene sediments along the present shelf may ultimately be accomplished only by means of a high-density vibracore network, which is beyond the realm of this reconnaissance study.

Structurally, Unit D appears to be a relatively homogeneous assemblage compared to subjacent units, as indicated by the paucity of internal reflectors. The thickness of Unit D varies from zero, to a maximum of 12 m, with a mean value of 5 meters. Thickness variation of the unit are expressed topographically as ridge and swale systems throughout much of the study area. Thicker sections occur as ridges which are approximately plano-convex in cross section (Fig.6B), while the thinner sections and discontinuities are the intervening swales. Side slopes are 2 degrees or less. The *A–D* interval of profile 2 illustrates prominent ridge and swale topography exemplified by the False Cape–Virginia Beach ridge system, a system which has been previously studied in detail (e.g., Swift et al., 1972; Shideler et al., in press). Profile 8 exhibits a relatively uniform Unit D sand sheet within the *F–H* interval which parallels the trend of the ridges, but changes into conspicuous ridge and swale topography in the *H–K* interval. The ridges attain maximum local relief of 10 m near point *I*, and constitute the well-known Wimble Shoals; unit thickness varies from zero, at a probable reflector R3 outcropping in the *I–J* interval, to a maximum of 10 m at Wimble Shoals near point *I*. Profile 10, which parallels the north flank of Diamond Shoals off Cape Hatteras, illustrates prominent ridge and swale topography. However, a possible Unit D

could only be detected intermittantly within the *A–C* interval, where it exhibits maximum local relief of 14 m; unit thickness varies from zero, to a maximum of 9 m within the *B–C* interval. An alternate interpretation of profile 10 is that Unit D in the Diamond Shoals area is anomalously thick, and that reflector R3 was sufficiently deep to escape detection by the 400-joule boomer system. Although the delineation of reflector R3 and the differentiation of overlying Unit D was confined largely to the inner shelf during the present study, the presence of prominent sea floor ridge and swale topography along much of the outer shelf suggests that the unit may be more widely distributed.

The north-to-northeast-trending ridge and swale topography is the most striking and least understood morphologic feature of the Middle Atlantic Bight. The topography is prominent along the inner shelf, with ridges locally merging with the shore face at depths of 5–10 m. Shepard (1963) has implied that the ridges are relict strand lines marking stillstands of the transgressive Holocene sea. Uchupi (1968), however, has noted that in some sectors, the ridges are at substantial angles to the modern shoreline, and suggests that they are modern bedforms built by storm currents. Sanders (1962) examined the shore face ridge system at False Cape, and concluded that these were not Holocene features, but the offshore extensions of the northeast-trending Pleistocene barriers which had been mapped by Oaks (1964) on the adjacent coast. Moody (1964) mapped shore face ridges off Bethany Beach, Delaware, before and after the great Ash Wednesday Storm of March, 1962; he noted that the ridges had moved up to 70 m in the interim. Moody suggests that the offshore ridges are not relict beach ridges, but are rather quiescent, hydraulic bedforms of nearshore submarine origin, which may still be activated during storms. Recent detailed studies of the False Cape–Virginia Beach ridge system (profile 2) indicate that these ridges, like those reported by Moody, are maintained by the modern hydraulic regime (SWIFT et al., 1972; Shideler, in press). Employing the False Cape–Virginia Beach system as a prototype, it is believed that many of the ridges within the study area may have had a similar origin. A proposal model for generating the Unit D transgressive sand sheet incorporates Moody's concept of ridge evolution. The "relict" sand sheet of the shelf is seen as the product of shore face erosion of a retrograding barrier complex during the Holocene transgression. The sediments comprising Unit D may thus have accumulated as a lag deposit on the sea floor, molded by storm currents into a ridge and swale topography (Swift et al., 1970, 1972; Shideler et al., in press).

OUTER SHELF AND SHELF BREAK CHARACTERISTICS

The limited penetration capabilities of the high resolution boomer system precluded a detailed examination of the outer shelf and shelf break. However, the boomer profiles do illustrate the general sea floor morphology of this region, as

well as some shallow structural features. Traverses extending to the shelf break are illustrated by profiles 1, 2, 3, 4, 8, 10, and 11.

The sea floor morphology of the outer shelf and shelf break from Cape Henry southward to Cape Hatteras is variable, illustrating such physiographic features as terraces, ridges and troughs, and sand waves.

Profile 1 located east of Cape Henry illustrates an outer shelf characterized by a small-scale ridge and swale system, with relatively low local relief (less than 6 m). The profile also exhibits a gradually rounded shelf break, with the shoreward terminus of a prominent terrace occurring at point *N*. The terrace is approximately 6 km wide, and occurs at an average of 85 m, with its seaward terminus occurring at 95 m; it may correlate with the 95-m terrace noted by Uchupi (1968; p.13) off Atlantic City, New Jersey. The terrace is separated from the adjacent slope by a trough approximately 6 m deep. The shallow structure along profile 1 is not sufficiently resolved to permit genetic inferences. However, deeper seismic studies of the shelf break east of Cape Henry indicate that underlying strata are essentially parallel with the sea floor, indicating a depositional structure resulting from both shelf upbuilding and slope progradation (Moore and Curray, 1963; Uchupi and Emery, 1967; Rona, 1969; Uchupi, 1970). As noted by Dietz (1964), the profile east of Cape Henry may lie along the route of the ancestral Susquehanna fluvial system; this fluvial system could have produced an aggradational "Norfolk Apron", genetically similar to the Hudson Apron further to the north. Profile 1 does illustrate contorted strata near point O, suggesting possible mass movements along the shelf break. Such movements may have resulted in the development of the trough adjacent to the wave-cut terrace.

Further south along profile 2, the sea floor of the outer shelf is characterized by moderate relief. It exhibits a relatively broad ridge and swale topography, with maximum local relief of 12 m. The shelf break is gradually rounded, and exhibits a terrace whose seaward terminus occurs near point *K*. The terrace is 5 km wide and occurs at an average depth of 95 m, with its seaward terminus occurring at 100 m. The terrace might correlate with the 100-m terrace off Onslow Bay, North Carolina, as noted by Uchupi (1968; p.13); it could also correlate with the Franklin terrace of the Hudson Apron area (Veatch and Smith, 1939). Structurally, the faint traces of shallow strata tend to be concordant with the surface of the shelf break, suggesting Quaternary progradation along this segment of the shelf. Contorted strata near point *K* further suggest possible mass movements along the shelf break.

Profile 3 illustrates an outer shelf characterized by relatively high relief. It exhibits a prominent ridge and swale system, with maximum local relief of 15 m in the *F–G* interval. This particular ridge system appears to be largely of erosional origin, as indicated by some of the swales which truncate sub-bottom reflectors (e.g., *F–H* interval). A similar situation has been noted by Macintyre and Milliman (1970) for some of the ridges and swales south of the study area between Cape

Hatteras and Cape Fear; they interpret the topography as being largely an erosional surface produced by the pre-Holocene Gulf Stream. The shelf break along profile 3 exhibits a distinct change in morphology; it assumes a faceted appearance, relative to the more rounded shelf break further to the north. This appearance largely results from the presence of a relatively broad terrace, whose seaward terminus occurs near point *I*. The terrace is about 9 km wide and occurs at an average depth of 95 m, with its seaward terminus occurring at approximately 116 m; the terrace might correlate with the 120-m terrace noted by Uchupi (1968) off both Atlantic City and Onslow Bay.

The outer shelf along profile 4 is characterized by moderate relief, with ridges and swales exhibiting maximum local relief of 10 m near point *E*. The plano-convex nature of the ridge near point *E* suggests that outer shelf ridges of this system may be aggradational features, genetically similar to the prominent ridges in the *A–D* interval further to the west. The shelf break is faceted, with a wave-cut terrace present in the *G–H* interval. The terrace is 16 km wide and occurs at an average depth of 92 m; its seaward terminus occurs at 100 m, and it might correlate with the 100 m terrace noted by Uchupi off Onslow Bay. The faceted nature of the shelf breaks along both profiles 3 and 4 might reflect a predominantly erosional regime during the Quaternary. Although the internal structure observed along both profiles is inconclusive, a deeper profile of the shelf break along an intermediate transect does indicate truncation of shallow strata by a sub-bottom unconformity (Rona, 1969).

The outer shelf along profile 8 is relatively featureless, with maximum local relief of less than a few meters. The shelf break is not totally resolved along this profile, thus precluding genetic inferences. Structurally, the shallow strata tend to be concordant with the shelf break, thus suggesting Quaternary progradation.

The outer shelf along profile 11 is characterized by moderate relief. It exhibits a large-scale ridge and swale topography, with maximum local relief of 10 m in the *D–E* interval. Superimposed on the large-scale ridge and swale system are smaller-scale ridges which exhibit maximum relief of 3 m, and which appear to comprise a shelf-edge sand wave field (Fig.6D). The morphology of the shelf break is well rounded; it is also relatively abrupt, compared to the more gradual shelf breaks to the north. The structure of shallow strata is concordant with the surface of the shelf break, suggesting Quaternary progradation in this area.

Profile 10 is the southernmost traverse in the study area, and is located east of Cape Hatteras along the northeastern flank of Diamond Shoals. The outer shelf along the flank of Diamond Shoals is characterized by high relief. It exhibits a prominent large-scale ridge and swale system, which attains maximum local relief of 15 m near point *C*. Slightly south of profile 10 off Cape Hatteras, another outer shelf ridge system consisting of four ridges with intervening sediment-filled troughs has been reported. As noted by Rona (1969), calcareous algae with a radiocarbon date of 19,000 years B.P. have been sampled from the most seaward ridge of the

system (Menzies et al., 1966). Rona interprets this ridge system as either possible algal reefs, barrier beaches with an overgrowth of algae, or a combination of barrier beaches behind a shelf-edge organic reef. Alternately, this topography has also been interpreted as resulting largely from pre-Holocene Gulf Stream erosion (Macintyre and Milliman, 1970). The ridges observed along profile 10 may belong to the same system observed further to the south; however, the apparent absence of intervening sediment-filled troughs suggests a different genesis. These ridges may be similar to those of profile 11, possibly representing aggradational bedforms which develop in response to the modern hydraulic regime. Bathymetrically, the shelf break occurs at its shallowest depth in the study area along profile 10; its depth increases northward towards Cape Henry. This relationship was also noted by Uchupi (1968), who attributed this variation to sediment upbuilding off Cape Hatteras. The shelf break along profile 10 is abrupt, being analogous to adjacent profile 11. However, in contrast to the well-rounded shelf break configuration on profile 11, the profile 10 shelf break is angular. In addition, a small trough approximately 3 m deep is present within the *D–E* interval. The configuration of the shelf break, as well as the presence of prominent cut-and-fill structures in the *D–E* interval (Fig.6C), suggest that Diamond Shoals is actively prograding over a relict topography or has done so within the Holocene. Progradation in this area is further supported by a concordance of the shelf break surface with underlying strata to an acoustic penetration depth of about 280 m (Rona, 1969). The cut-and-fill structures of the *D–E* interval could reflect the infilling of a tributary from the Hatteras Canyon System, as outlined by Newton and Pilkey (1969). Alternately, the structures could also reflect the infilling and burial of an erosional surface scoured by a meandering pre-Holocene Gulf Stream, as suggested for areas of the shelf edge south of profile 10 (Macintyre and Milliman, 1970). The apparent capabilities of the Gulf Stream as an erosional agent south of Cape Hatteras along the Blake Plateau and Florida–Hatteras Slope have been noted (e.g., Pratt and Heezen, 1964; Pratt, 1966; Uchupi, 1967). Linear depressions along the western Blake Plateau and Florida–Hatteras Slope may represent the loci of maximum current axes of a meandering Gulf Stream during Pleistocene glacio-eustatic movements (Uchupi, 1967). It is equally feasible that the buried erosional surface along profile 10 may have had a similar origin. Although general progradation is indicated in the Diamond Shoals area, it is feasible that the seaward edge of the shoals may also experience occasional erosional episodes, possibly in response to minor variations in the Florida Current flow regime of the Gulf Stream System.

CONCLUSIONS

Post-Miocene deposits of the Middle Atlantic Shelf unconformably overlie a truncated Tertiary substrate. Although the limited penetration capabilities of

the high resolution seismic system allowed detection of the basal unconformity along only a small sector of the inner shelf, previous deeper studies of adjacent areas of the Atlantic shelf suggest that it is of regional extent. The basal unconformity appears to reflect widespread shelf emergence during Late Tertiary or Early Pleistocene time. The angular discordance and undulose topography of the basal unconformity within its area of detection suggest a major interval of subaerial erosion and subsequent crustal subsidence prior to post-Miocene sedimentation. During the erosional interval, a prominent eastward-trending channel of the ancestral Albemarle fluvial system was in existence along the coastal plain near the present mouth of Albemarle Sound.

Following the period of widespread shelf emergence during Late Tertiary or Early Pleistocene time, subsequent glacio-eustatic fluctuations associated with the Pleistocene resulted in the development of both transgressive and regressive sequences. Deposits of pre-Wisconsinan and Early Wisconsinan age comprise a widespread sequence which represents the majority of the post-Miocene section. The sequence appears to consist of both a fluvial complex, and a coastal barrier complex. The fluvial complex could reflect coastal alluviation in response to a rising base level associated with one or more interstadial transgressions, while the barrier complex may reflect coastal progradation during a regressive glacial substage.

Following deposition of the basal post-Miocene assemblage, a widespread unconformity was developed, possible as the result of both subaerial erosion during the Early Wisconsinan regression, and shore face erosion during the subsequent mid-Wisconsinan interstadial transgression. The overlying Pleistocene sequence of Late Wisconsinan age consists of a relatively thin, widespread assemblage of apparent paralic–neritic deposits, which developed during the regression following the mid-Wisconsinan interstadial.

The Pleistocene–Holocene boundary is manifested as a prominent widespread unconformity, possibly developed by both subaerial erosion during the Late Wisconsinan regression, and by shore face erosion during the Holocene transgression. The Holocene deposits comprise a discontinuous sand sheet which mantles the sea floor throughout much of the study area. The sand sheet appears to have been generated as a sea floor lag deposit resulting from the erosion of a retrograding shore face during the Holocene transgression, and to have been subsequently molded by currents of the Holocene hydraulic regime into prominent ridge and swale topography throughout much of the inner shelf.

The prominent ridges of the outer shelf appear to be polygenetic. Some appear to represent aggradational features molded by the Holocene hydraulic regime, similar to those of the inner shelf, while others may be of erosional origin, being related to the scouring action of a meandering pre-Holocene Gulf Stream. In addition, others may be manifestations of relict barriers or of organic reef structures. Morphological variations of the shelf break along the Middle Atlantic Bight indicates variable responses to Quaternary processes. The presence of wave-

cut terraces in the northern two-thirds of the study area indicate the influence of low stands of sea level during the Pleistocene. However, the absence of similar terraces in the southern third of the area suggests a more accelerated rate of Holocene sedimentation and shelf development toward the south, thus possibly masking previous Pleistocene eustatic effects. Variations in the configuration and depth of the shelf break further suggest differential shelf upbuilding and progradation during Holocene time, being minimal near Cape Henry and maximal near Cape Hatteras.

ACKNOWLEDGEMENTS

Financial support for this study was provided through research grants and contracts from the National Science Foundation (No. GA-13837), the Coastal Engineering Research Center (No. DACW-72-69-C-0016), the Old Dominion University Research Foundation (No. 8028), and the Marine Geology Office of the U.S. Geological Survey. The authors further express their appreciation to the National Aeronautics and Space Administration for the use of their vessel, "Range Recoverer", in conducting the seismic survey.

REFERENCES

Coch, N. K., 1965. Post-Miocene stratigraphy and morphology, inner coastal plain, southeastern Virginia. *Off. Nav. Res., Tech. Rep.*, 6: 97 pp.

Dietz, R. S., 1954. Wave-base, marine profile of equilibrium, and wave-built terraces: Reply. *Geol. Soc. Am., Bull.*, 75: 1275–1282.

Fisher, J. J., 1967. *Development Pattern of Relict Beach Ridges, Outer Banks Barrier Chain.* Thesis, Univ. North Carolina, N.C., 250 pp., unpublished.

Garrision, L., 1967. *Cretaceous–Cenozoic Development of the Continental Shelf South of New England.* Thesis, Univ. Rhode Island, Kingston, R.I., 100 pp., unpublished.

Knott, S. T. and Hoskins, H., 1968. Evidence of Pleistocene events in the structure of the continental shelf of the northeastern United States. *Mar. Geol.*, 6: 5–43.

Macintyre, I. G. and Milliman, J. D., 1970. Physiographic features on the outer shelf and upper slope, Atlantic continental margin, southeastern United States. *Geol. Soc. Am., Bull.*, 81: 2577–2598.

Menzies, R. J., Pilkey, O. H., Blackwelder, B. W., Dexter, D., Huling, P. and McCloskey, L., 1966. A submerged reef off North Carolina. *Int. Rev. Ges., Hydrobiol.*, 51: 393–431.

Milliman, J. D. and Emery, K. O., 1968. Sea level during the past 35,000 years. *Science*, 162: 1121–1123.

Moody, D., 1964. *Coastal Morphology and Processes in Relation to the Development of Submarine Sand Ridges off Bethamy Beach, Delaware.* Thesis, Johns Hopkins Univ., Baltimore, Md., 167 pp., unpublished.

Moore, D. G. and Curray, J. R., 1963. Sedimentary framework of the continental terrace off Norfolk, Virginia and Newport, Rhode Island. *Bull. Am. Assoc. Pet. Geologists*, 47: 2051–2054.

Newton, J. G. and Pilkey, O. H., 1969. Topography of the continental margin off the Carolinas. *Southeastern Geology*, 10: 87–92.

Oaks, R., 1964. Post-Miocene stratigraphy and morphology, outer coastal plain, southeastern Virginia. *Off. Nav. Res., Tech. Rep.*, 5: 241 pp.

Pilkey, O. H., Macintyre, I. G. and Uchupi, E., 1971. Shallow structures, shelf edge of continental margin between Cape Hatteras and Cape Fear, North Carolina. *Bull. Am. Assoc. Pet. Geologists*, 55: 110–115.

Pratt, R. M., 1966. The Gulf Stream as a graded river. *Limnol. Oceanogr.*, 11: 60–67.

Pratt, R. M. and Heezen, B. D., 1964. Topography of the Blake Plateau. *Deep Sea Res.*, 11: 721–728.

Rona, P. A., 1969. Middle Atlantic continental slope of United States: deposition and erosion. *Bull. Am. Assoc. Pet. Geologists*, 53: 1453–1465.

Sanders, J. E., 1962. North–south-trending submarine ridge composed of coarse sand off False Cape, Virginia (Abstr.). *Bull Am. Assoc. Pet. Geologists*, 46: 278.

Shepard, F. P., 1963. *Submarine Geology*. Harper and Row, New York, N.Y., 57 pp.

Shideler, G. L., Swift, D. J. P., Johnson, G. H. and Holliday, B. W., in press. A proposed standard section for Late Quaternary stratigraphy of the Inner Virginia continental shelf. *Geol. Soc. Am. Bull.*

Swift, D. J. P., Shideler, G. L., Avignone, N. F. and Holliday, B. S., 1970. Holocene transgressive sand sheet of the Middle Atlantic Bight: A model for generation by shore face erosion. *Abstr. with Programs, Geol. Soc. Am.*, 2: 757–759.

Swift, D. J. P., Sanford, R. B., Dill, Jr., C. E. and Avignone, N. F., 1971. Textural differentiation on the shore face during erosional retreat of an unconsolidated coast, Cape Henry to Cape Hatteras, western north Atlantic shelf. *Sedimentology*, 16: 221–250.

Swift, D. J. P., Holliday, B. W., Avignone, N. F. and Shideler, G. L., 1972. Anatomy of a shore face ridge system, False Cape, Virginia. *Mar. Geol.*, 12: 59–84.

Uchupi, E., 1968. Atlantic continental shelf and slope of the United States—physiography. *U.S. Geol. Surv., Prof. Pap.*, 529-C: 30 pp.

Uchupi, E., 1970. Atlantic continental shelf and slope of the United States—shallow structure. *U.S. Geol. Surv., Prof. Pap.*, 529-I: 44 pp.

Uchupi, E. and Emery, K. O., 1967. Structure of continental margin off Atlantic coast of United States. *Bull. Am. Assoc. Pet. Geologists*, 51: 223–234.

Veatch, A. C. and Smith, P. A., 1939. Atlantic submarine valleys of the United States and the Congo submarine valley. *Geol. Soc. Am. Spec. Pap.*, 7: 101 pp.

Reprinted from Geological Society of America Bulletin *83*, 1787-1804.

GERALD L. SHIDELER *Department of Geophysical Sciences, Old Dominion University, Norfolk, Virginia 23508*
DONALD J. P. SWIFT *Institute of Oceanography, Old Dominion University, Norfolk, Virginia 23508*
GERALD H. JOHNSON *Department of Geology, College of William and Mary, Williamsburg, Virginia 23185*
BARRY W. HOLLIDAY *Institute of Oceanography, Old Dominion University, Norfolk, Virginia 23508*

Late Quaternary Stratigraphy of the Inner Virginia Continental Shelf: A Proposed Standard Section

ABSTRACT

A continuous seismic reflection survey indicates that the post-Miocene section of the inner Virginia Shelf is 27 m in average thickness and unconformably overlies a discordant Tertiary substrate. Vibracore data and a faunal analysis reveal three distinct sedimentary sequences separated by prominent unconformities.

The oldest post-Miocene sequence has a radiocarbon age of more than 37,000 yrs B.P. It consists largely of a muddy, fine-grained sand and is characterized by lenticular stratification and prominent local channeling. It appears to represent a pre-Wisconsinan and early Wisconsinan assemblage, containing both a transgressive fluvial complex and a regressive coastal barrier complex.

The overlying sequence has a radiocarbon age ranging from 25,700 ± 800 yrs, to possibly as young as 20,400 ± 850 yrs B.P. It is comprised primarily of mud, and is characterized by relatively uniform horizontal stratification. The assemblage appears to represent a regressive paralic-neritic sequence developed at the end of the mid-Wisconsinan interstadial.

The youngest sequence of the section has yielded a radiocarbon age of 4,200 ± 140 yrs B.P. It is comprised of a discontinuous sand sheet that mantles the modern sea floor, and which appears to have been generated through the shore face erosion of a retrograding coastal barrier complex during the Holocene transgression. Evidence suggests that it accumulated as a lag deposit on the sea floor, where it was subsequently molded into a ridge and swale topography by the Holocene hydraulic regime.

INTRODUCTION

This paper presents the results of a study of the Quaternary structure and stratigraphy of the inner continental shelf off the Virginia Coast. The stratigraphic sequence established in the study area is intended to function as a standard marine section for a larger-scale regional reconnaissance study of post-Miocene deposits along the Middle Atlantic Shelf from Cape Henry, Virginia, to Cape Hatteras, North Carolina (Shideler and Swift, 1972).

The shallow Quaternary section of the inner Virginia Shelf was investigated during a 1969 cruise of the NASA telemetry vessel, *Range Recoverer*. Grab samples of surficial sediments were obtained throughout the study area. Subsurface deposits were investigated by a continuous seismic reflection survey, with emphasis placed on obtaining high resolution of the shallow Quaternary section. Supplemental subsurface stratigraphic data consisting of five vibracores were obtained in the study area during a 1970 cruise of the R/V *Eastward*. The core data aided in seismic interpretations and in the correlation of shelf stratigraphy with the stratigraphic section of the adjacent coastal plain.

METHODS

Field Procedures

The area under investigation is located between 36°30′–36°55′ N. lat, and 75°29′–75°55′ W. long (Fig. 1). The study area encompasses most of the inner Virginia Shelf south of Cape Henry, and includes a segment of the inner North Carolina Shelf. The sea floor in the study

Geological Society of America Bulletin, v. 83, p. 1787–1804, 12 figs., June 1972

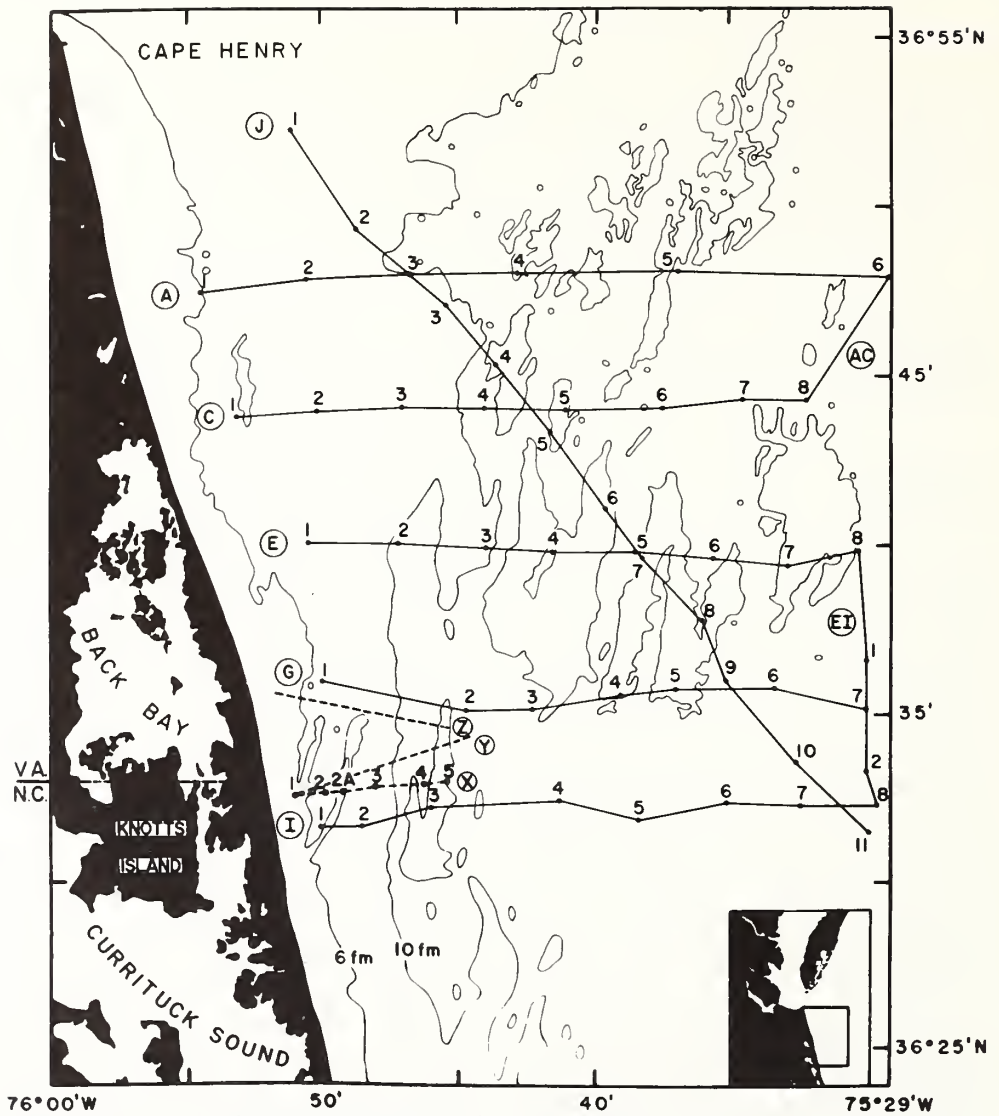

Figure 1. Index map of the study area southeast of Cape Henry, Virginia. The map illustrates the location of the seismic profile network and vibracore transect.

area is comprised of a north-trending ridge and swale system, as delineated by the 6- and 10-fm isobaths.

Continuous seismic reflection profiles were obtained along an east-west traverse network, spaced at approximately 8-km intervals (Fig. 1), of two north-trending profiles and one diagonal profile. The seismic system consisted of an EG and G 400-joule high resolution boomer, with a repetition rate of 640 milliseconds. Occasionally, the system was operated at a 200-joule level, with a repetition rate of 320 milliseconds. The output frequency spectrum of the transducer ranged from DC, to a maximum of 3 kHz; the resulting pulse had a peak pressure of 98.6 dB, referenced to 1 volt per microbar. Reflected energy was received by a linear array hydrophone (Type XOC–45), consisting of 10 elements equally spaced at 1-ft intervals. Received signals were passed through an external filter with a band pass of 250 to 40,000 Hz, and recorded on a model 254

seismic recorder. Both hydrophone array and acoustic source were towed at the surface, approximately 8 m astern of the *Range Recoverer*. The average surveying speed was approximately 6 knots but varied with maritime traffic and sea-state conditions.

Vibracoring operations were conducted on a cruise of the R/V *Eastward* during the summer of 1970. An east-west vibracore transect (profile X) was obtained east of the Virginia-North Carolina state line, approximately 2 km north of the 1 to 3 interval of profile I. The traverse was selected to provide detailed sub surface data regarding the structure of the prominant shore-tied ridge and swale system at False Cape in the southwestern corner of the study area. This locality is also the site of a detailed study concerning the structure and probable genesis of the ridge system (Swift and others, 1972). Vibracores were obtained along the traverse, ranging in length from 3 to 10 m. The cores are 10 cm in diameter, and were obtained with an Alpine Vibracore System (model 271) which employs an air-powered vibrator unit. After each core was extracted, it was segmented for ease of handling, sealed in polyethylene liners, and stored for laboratory analysis. Core 1 was obtained on the shore face, in 10 m of water, whereas the remaining cores were obtained from the False Cape ridge and swale system of the adjacent shelf floor. Core 2 was obtained from the first trough, core 3 from the seaward flank of the first main ridge, Core 4 from the trough between the two forks of the outer ridge, and core 5 from the seaward flank of the outer ridge. The five vibracores were supplemented by a sixth hand-driven core (2A) obtained from the crest of the first ridge during a scuba dive. Geographic positions of the coring sites were established using a combination of Loran A, fathometer readings, and radar navigation.

In addition to the seismic profiles obtained with the high resolution boomer system, three supplemental sub-bottom profiles were obtained at the False Cape locality, employing an EG and G 5 kHz acoustic profiler. The vibracore transect was profiled, as well as two other traverses to the north (profiles Y, Z). The three acoustic profiles were obtained from Ocean Science and Engineering's charter vessel *Wando River*, a shallow-draft coastal survey vessel, to gain more detailed stratigraphic data of the prominent False Cape ridge system.

Surficial sediments were also examined throughout the study area during the 1969 cruise of the *Range Recoverer*. Grab samples were obtained over a 2 km × 4 km sample net, employing a Shipek sampler. Grain-size frequency distributions of the samples were determined by means of a modified Woods Hole rapid sediment analyzer, as described by Sanford and Swift (1972).

Data Processing

Seismic reflection data were processed manually. The original boomer records were fitted with transparent acetate overlays, and all reflecting horizons were traced with a marking pencil. Strong reflectors were denoted with solid lines, while dubious reflectors were indicated by dashed lines. The acetate overlays of the individual boomer profiles were reduced to common vertical and horizontal scales on graph paper, and converted into stratigraphic line drawings. The vertical scale of the line drawings represents two-way reflection travel time in milliseconds. The approximate thickness and depth values presented in this paper are based on an assumed average seismic velocity of 1.5 km/sec for both the substrate and overlying water column. In view of the probably increasing velocity gradient within the substrate, the values presented should be regarded as minimal values. On the basis of the assumed seismic velocity, the line drawings exhibit a vertical exaggeration of approximately 133×. Enumerated fiducial marks along the top of each profile refer to the geographic reference points illustrated on Figure 1; the triangular fiducial marks indicate profile intersections. The three short acoustic profiles in the False Cape locality were processed in a similar manner but at a different horizontal scale, resulting in a vertical exaggeration of approximately 150×. Lithologic data and radiocarbon dates derived from the cores were superimposed on profile X, and extrapolated northward to profiles Y and Z.

The seismic line drawings illustrate the shallow Quaternary structure and stratigraphy throughout the study area. Prominent reflectors which serve as stratigraphic marker horizons are numbered and delineated by bolder lines, while stratigraphic units are indicated by letters. Correlations between individual profiles were based on tie points at profile intersections, stratigraphic position, and structural similarities. In correlating shelf stratigraphy with the adjacent subaerial coastal

plain, geologic sections of southeastern Virginia constructed by Oaks (1964) constituted the main source of onshore control. Additional control consisted of subsurface data north of Cape Henry near the mouth of Chesapeake Bay (Harrison, 1962; Harrison and Malloy, 1963; Harrison and others, 1965). The vibracore transect obtained in the southwestern corner of the study area (False Cape locality) during the present study also aided in stratigraphic interpretations.

In processing the vibarcores, the individual cores were longitudinally bisected. The lithologies of one-half of the cores were logged, and selected portions of that half were impregnated to preserve sedimentary structures. The impregnation medium consisted of an epoxy mixture described by Burger and others (1969). The other half was examined for its faunal content, and provided organic material for four radiocarbon dates, determined by Geochron, Inc.

In conducting the paleontological analysis, one-half of each core was divided into sections 15 cm long. Fifty-one sections were wet sieved with a -1 phi sieve, and the fossils removed. Species diversity, relative abundance, state of preservation, and stratigraphic distribution of each species were determined. Broken- and whole-shell materials of foraminifers, sponges, coelenterates, annelids, bryozoans, echinoderms, arthropods, and vertebrates were observed, but they were not included in the study. A total of 95 species of mollusks were identified. An environmental interpretation was then undertaken, based on data for living species from Abbot (1954), Brett (1963), Clench and Turner (1951), Lawrence and Raup (1963), and Parker (1955, 1956). The reconstruction was limited by sample size, paucity of definitive studies on living species and the cored assemblages, and by the broad environmental tolerances of many of the abundant species.

RESULTS

An analysis of high resolution boomer profiles indicates that the shallow stratigraphic section of the inner Virginia Shelf consists of four distinct sedimentary sequences separated by three prominent acoustic reflectors. In ascending order, the sedimentary assemblages are designated as units A, B, C, and D. The following is a description of each unit, as illustrated in Figures 2 and 3.

Unit A

The deepest and oldest sedimentary sequence detected within the study area, which can be considered a discrete stratigraphic entity, is designated unit A. This unit is defined as the sequence whose upper boundary is reflector 1, the deepest prominent acoustic discontinuity observed during the study.

Unit A appears to be a widespread sequence distributed throughout the study area, as indicated by its persistence along profile J. The unit consists of eastward-dipping homoclinal strata, with dip angles notably greater than those of the overlying units. The average dip rate is 3 m/km, corresponding to an average apparent dip angle of less than 0.25 degrees. The angular discordance between unit A and strata of overlying unit B is most apparent in the interval between points 9 and 11, profile J. The minimal thickness of unit A is 35 m; however, its total thickness was not determined.

The structural attitude and stratigraphic position of the unit suggest a late Tertiary age. It is believed that reflector 1 constitutes the Miocene–post-Miocene boundary, which is manifested throughout the study area as a widespread angular unconformity. A similar angular discordance has also been noted within the shallow structure east of the study area along the outer Virginia Shelf (Uchupi and Emery, 1967; Uchupi, 1970), suggesting that reflector 1 is of regional extent. Reflector 1 is also noted to the south of the study area (Shideler and Swift, 1972), although its angular discordance is not apparent in the latter area.

An area of subsurface control, where the Miocene–post-Miocene boundary has been well defined, occurs at the mouth of Chesapeake Bay north of Cape Henry, 28 km northwest of point 1 on profile J (Harrison, 1962; Harrison and Malloy, 1963; Harrison and others, 1965). The Miocene–post-Miocene boundary was established by them near the mouth of Chesapeake Bay as a subaerial erosion surface of Pliocene-Pleistocene age, dissected into strata of pre-Yorktownian Miocene age. Harrison and co-workers describe the unconformity as one of high relief, with buried channels of the Pleistocene Susquehanna fluvial system excavated to depths ranging from 30 to 48 m below mean low-water level. The interfluve areas range in depth from approximately 23 m on the north side of the bay mouth, to 14 m at

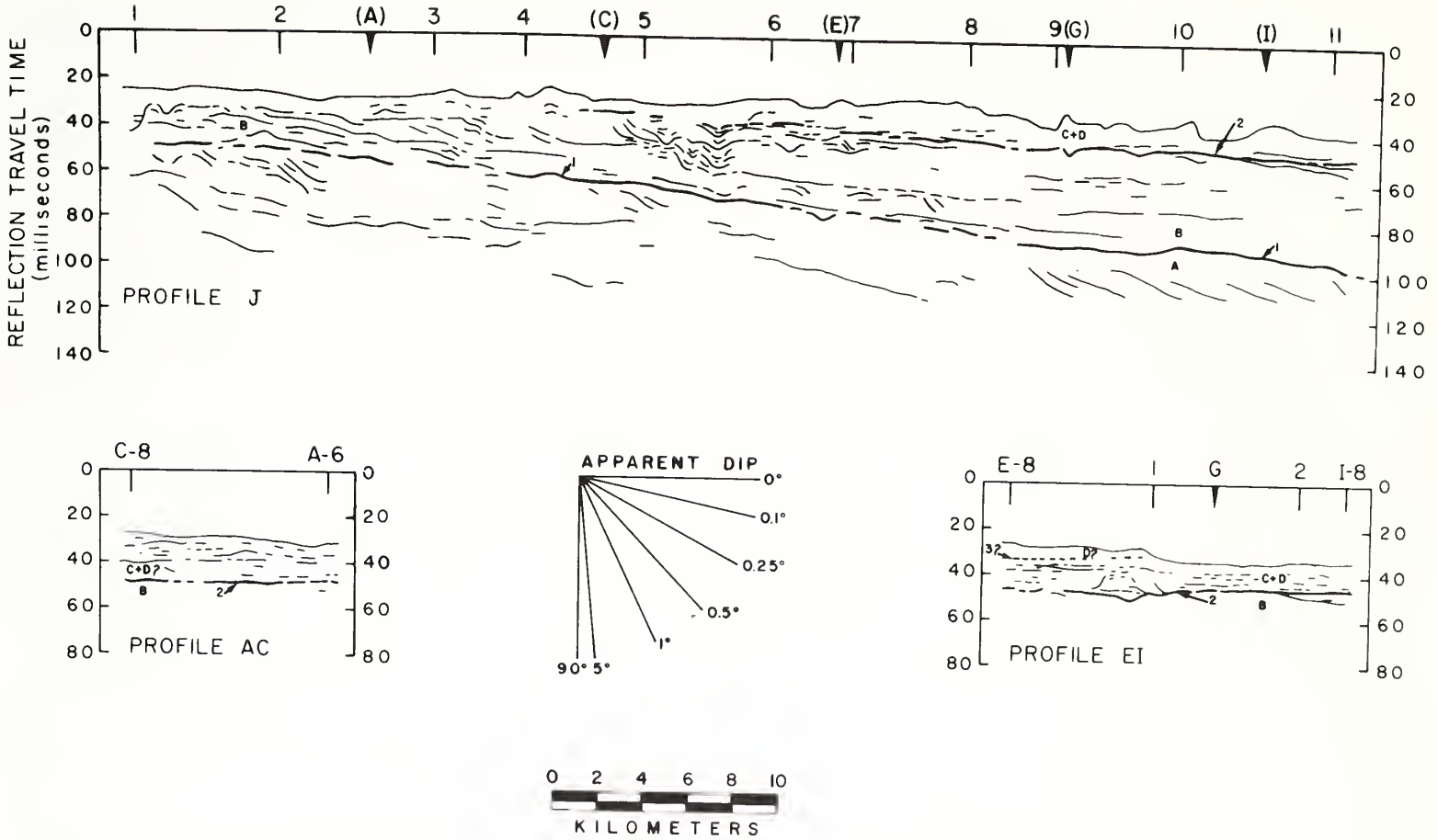

Figure 2. Stratigraphic line drawings of the north-trending boomer profiles. Prominent reflectors are numbered, while stratigraphic units are lettered. Vertical exaggeration is 133× (assumed velocity of 1.5 km/sec).

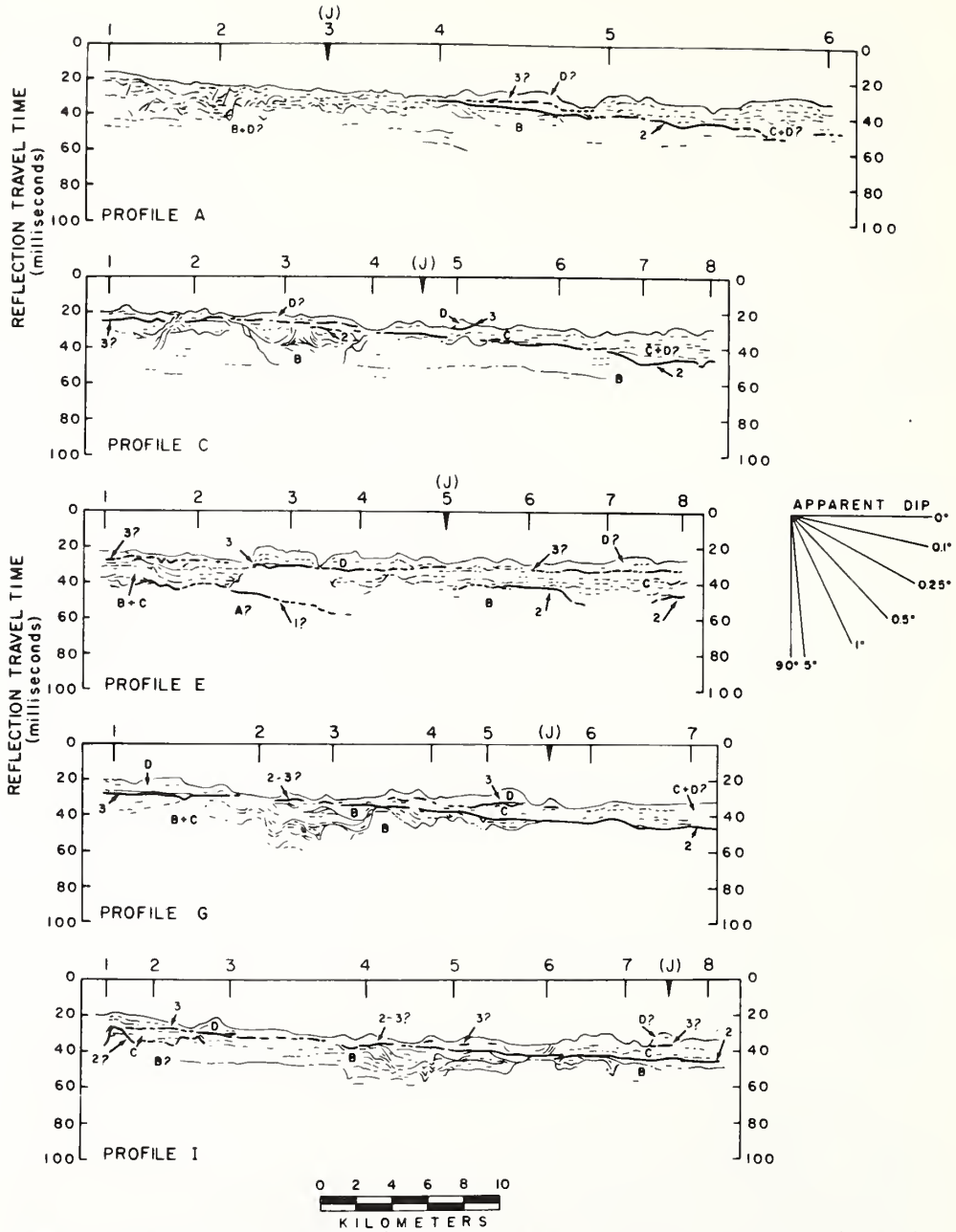

Figure 3. Stratigraphic line drawings of boomer profiles along the east-west traverse network. Vertical exaggeration is 133×. Assumed velocity of 1.5 km/sec.

Cape Henry. If the structural trend of reflector 1 on profile J were projected to the mouth of Chesapeake Bay at its apparent dip angle, it would occur at a depth of 16 m below sea level, in close agreement with the interfluve depth determined by Harrison and others (1965) near Cape Henry. A late Tertiary age for unit A is also suggested by the possible detection of reflector 1 on profile E. If extrapolated 9 km updip to the coastline, it would occur within 2

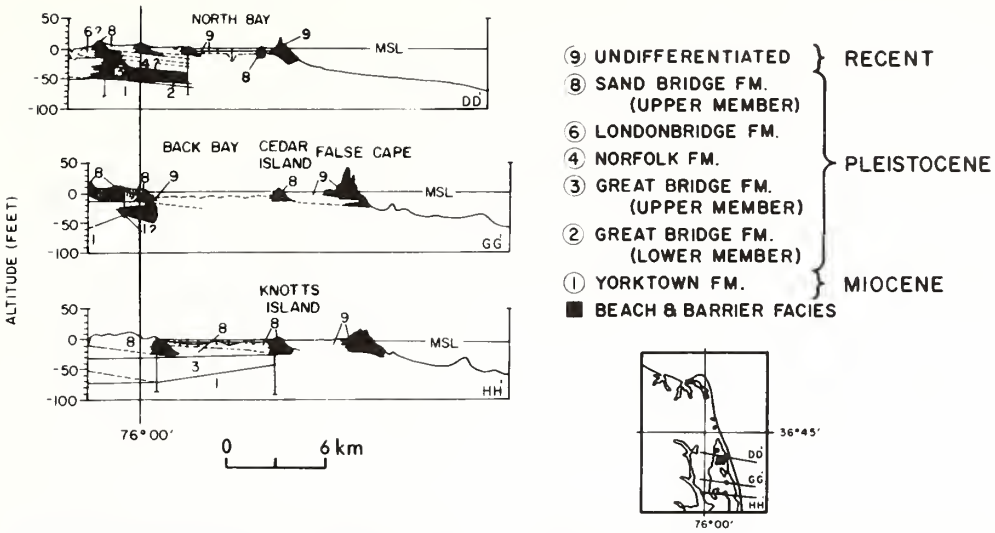

Figure 4. Three geologic cross sections of Quaternary deposits along the southeastern Virginia coastal plain adjacent to the study area. Vertical exaggeration is 108× (*modified from* Oaks, 1964).

m of the estimated depth to the top of the Miocene at the coast, as extrapolated along Oaks' (1964) geologic section DD′ (Fig. 4).

A Tertiary age for unit A is further suggested by the high reflectivity of reflector 1 on the original seismic records, which indicates a prominent acoustic impedance contrast between unit A and overlying unit B. Such a contrast has been noted between Pleistocene strata and over-consolidated Miocene strata in the Chesapeake Bay region, resulting in good reflective characteristics of the Miocene–post-Miocene unconformity (Harrison and Malloy, 1963; Harrison and others, 1965). On the basis of the foregoing evidence, unit A is interpreted as a sedimentary sequence of probable late Tertiary age. The sequence is truncated by reflector 1, which may represent an erosional interval of possible Pliocene–early Pleistocene age. This interpretation would result in an average total thickness of 27 m for the post-Miocene section of the inner Virginia Shelf.

Unit B

Unit B is defined as the sequence above reflector 1, whose seismic profiles are characterized by commonly lenticular stratification and prominent local channeling. The upper boundary is generally reflector 2, a prominent acoustic discontinuity which can be used to separate unit B from unit C. In the local absence of unit C, the upper boundary consists of reflector 3 which occurs at the base of unit D, the youngest sedimentary sequence within the study area.

Basal Boundary Reflector. Within the study area, basal boundary reflector 1 was detected along the entire length of profile J, at depths ranging from 30 to 75 m below sea level, and 10 to 44 m beneath the sea floor. It is characterized as an irregular interface, with maximum local relief of 3 m. It dips eastward at an average apparent rate of 1 m/km (less than 0.06°).

The nondetection of reflector 1 on other profiles throughout the study area is not attributed to its absence, but rather to the low penetration capabilities of the high resolution boomer system. The reflector is interpreted as a prominent angular unconformity of probable widespread distribution throughout the study area. A regional seismic reconnaissance study also indicates its presence along the inner shelf farther to the south of the study area, where it exhibits substantial relief (Shideler and Swift, 1972).

Seismic Characteristics. Unit B is distributed throughout most of the study area. Strata comprising unit B are characterized by commonly lenticular stratification and prominent local channeling. These features are best illustrated on profile C (interval 1 to 4), profile G (interval 2 to 5), and profile I (interval 4 to 7). The maximum relief exhibited by an individual channel is 18 m, occurring near point 3 on profile C. Unit B commonly has relatively

strong and persistent local reflectors, which appear to represent highly furrowed surfaces of substantial relief; such a reflector is illustrated in profile G (interval 2 to J), exhibiting maximum local relief of 10 m. Much of the prominent local relief observed within unit B results from channeling. However, some of the relief might also reflect the presence of topographic ridges, possibly accentuated by the differential compaction of adjacent sediments. Unit B, in addition to the channeled and lenticular strata, contains a second distinct facies. This facies is characterized by relatively uniform stratification and commonly appears to be truncated by the channel facies. This relation is most apparent in interval 2 to 5 of profile C. Unit B increases in thickness eastward, attaining a maximum detected thickness of 37 m at point 11 of profile J.

Core Analysis. The basal lithologic unit of the cored section (Fig. 5) is correlated with unit B, and consists of medium greenish-gray (5GY5/1) fine-grained, muddy sand. (Color was determined by the comparison of wet samples with the Geol. Soc. America Rock Color Chart.) The unit contains 10 to 20 percent silt and clay, and 3 to 8 percent very pale orange (10YR8/2) shell fragments. Primary structures consist of poorly defined mottling, and occasional poorly defined laminations. This general lithology is consistent through 10 m of core 4, and through 3.6 m of core 5. However, the unit is more variable in core 3; the uppermost 45 cm grades from grayish black (N2) at the top, to the normal medium greenish gray at the center. The dark pigment is probably "humate," leached from a soil zone which has since been removed by erosion. The humate immediately underlies reflector 2, which is manifested in the False Cape locality as a highly furrowed surface exhibiting prominent local channeling. It appears to be a prominent unconformity, indicating a substantial amount of weathering and erosion. Core 3 grades downward into coarse, shelly, yellowish-gray sand at the base, which may be a beach or near-beach

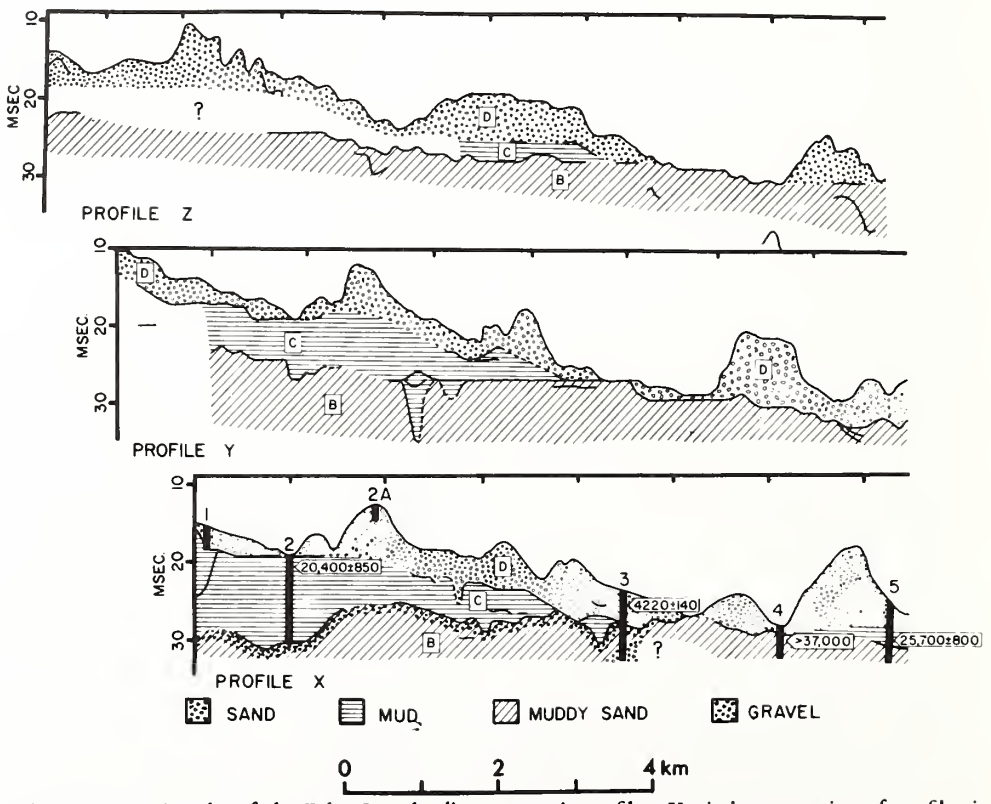

Figure 5. Stratigraphy of the False Cape locality, as revealed by cores (profile X) and three 5 kHz acoustic profiles. Vertical exaggeration of profiles is 150×.

deposit. Gravel and sand-sized shell fragments from the uppermost 2.6 m of core 4 were determined by radiocarbon methods to be older than 37,000 yrs B.P.

Faunal Analysis. Forty-four species of mollusks were recovered from the medium greenish-gray, muddy, fine sand of unit B. Shallow marine species such as *Macoma balthica*, *Mulinia lateralis*, *Abra equalis*, and *Ensis directus* are abundant and dominate the fossil assemblage. These forms are found today from the low tide line to a depth of 12 m. Most shells are disarticulated but do not show evidence of excessive abrasion, except locally in sandy zones. A faunal discontinuity between the coarse basal horizon and the overlying strata is especially striking in core 3 (Fig. 7).

Correlation. On the basis of its stratigraphic position and radiocarbon data, the unit is tentatively correlated as the offshore equivalent of the Pleistocene Great Bridge Formation–Sandbridge Formation sequence of the adjacent coastal plain, as mapped by Oaks (1964). The lower portion of unit B may be the partial equivalent of the Great Bridge Formation, which was noted by Oaks as being a relatively widespread subsurface formation throughout the adjacent coastal region of southeastern Virginia. Oaks describes the Great Bridge Formation as consisting of "coarse sand and peat of freshwater origin restricted to channels cut in the top of Miocene sediments and grading upward into widespread, unoxidized, soft, silty clay and silty fine sand." He interprets this stratigraphic pattern as a fluvial lithosome, grading upward into an estuarine-lagoonal lithosome. The closest onshore control, where the stratigraphic relations of the Great Bridge Formation are moderately defined, is Oaks' (1964) section HH′ (Fig. 4), which terminates at the coastline approximately 2 km northwest of core 1 on profile X. At the northern end of Knotts Island, approximately 8 km northwest of core 1, the Great Bridge Formation unconformably overlies the Miocene Yorktown Formation and is unconformably overlain by the Sandbridge Formation. If the lower portion of unit B is largely equivalent to the Pleistocene Great Bridge Formation, a possible age of Sangamonian or pre-Sangamonian is suggested (Oaks, 1964). The lower portion could thus reflect coastal inundation and alluviation associated with one or more pre-Wisconsinan interstadial transgressions. However, lower unit B may also include Pliocene deposits, which are possibly partial equivalents

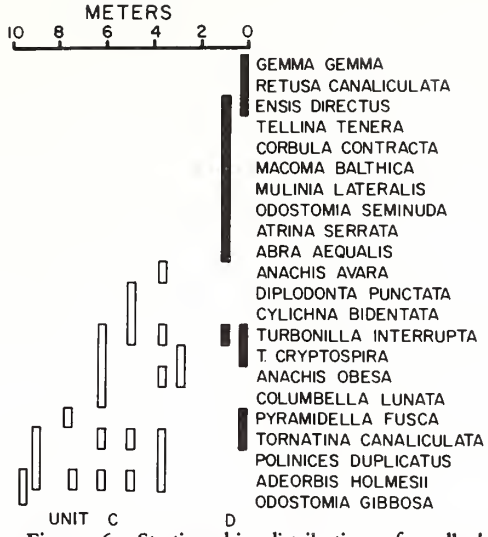

Figure 6. Stratigraphic distribution of mollusk species in core 2, arranged by first occurrence. Prepared by C. Stein and M. Simpson.

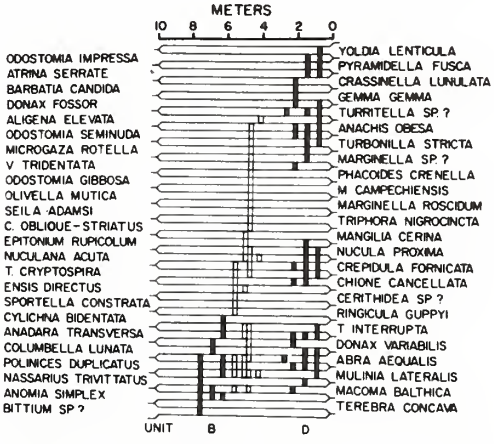

Figure 7. Stratigraphic distribution of mollusk species in core 3, arranged by first occurrence. In unit B, fauna of the lower coarse pebbly sand (dark) are distinguished from fauna of the upper fine sand. Prepared by C. Stein and M. Simpson.

of the Sedley and Bacon's Castle Formations (Coch, 1965) of the inner coastal plain.

The upper part of unit B may be the partial equivalent of the Sandbridge Formation, which is a widely distributed Pleistocene unit throughout the adjacent coastal region. Oaks (1964) describes the upper member of the

Sandbridge Formation as a regressive complex of barrier sand ridges, with intervening "mud flat" lithosomes (Fig. 4). The medium greenish-gray, fine muddy sand penetrated in cores 3, 4, and 5 appears to be Oaks' "mud flat" lithology, while the coarse shelly sand penetrated near the base of core 3 may represent the flank of a barrier. The fine, well-sorted muddy sand of unit B most nearly resembles the fine, well-sorted muddy sand facies of the modern shore face in unit D, which appears to have been deposited as clouds of fine sand drifting down the shore face from the surf zone during and after storms (Swift and others, 1971). Such muddy fine-sand blankets are normally thick and extensive on prograding shore faces. The unit B faunal assemblage of shallow open-water species, which exhibit very little mechanical abrasion, likewise suggests deposition on an aggrading shore face. It therefore seems more reasonable to infer that upper unit B in the vicinity of False Cape is composed of alternating barriers and shore-face deposits, rather than barriers and intervening backbarrier "mud flats."

Internal reflectors resembling channels and ridges are relatively abundant throughout unit B. We surmise that fluvial, estuarine, and lagoonal tidal channels, and barrier ridges are present; however, we do not feel that they can be distinguished from each other on the basis of reflector morphology alone. The most lenticular portions of unit B occur in a coast-parallel belt, which may be a barrier complex [submarine extension of Oaks' (1964) sand ridge complex], a structurally controlled coast-parallel fluvial complex, or a combination of both.

The Sandbridge constitutes the youngest Pleistocene formation mapped in the adjoining coastal region. Although it is beyond the realm of radiocarbon dating, tentative thorium-ionium dates indicate an age of 50,000 to 75,000 yrs B.P. (N. K. Coch, 1970, personal commun.). This would suggest an early Wisconsinan age for the upper portion of unit B, employing the Pleistocene stratigraphic classification of Illinois and Wisconsin (Frye and others, 1965). The upper portion of the unit might therefore represent a barrier complex, developed along a prograding coast during the regression associated with the Wisconsinan glacial stage. The entire unit B would thus be comprised of deposits representing both fluvial and strand plain complexes of pre-Wisconsinan and early Wisconsinan age.

Unit C

The next younger sedimentary sequence, unit C, is defined as the sequence with uniform horizontal stratification, whose basal and upper boundaries are reflectors 2 and 3, respectively.

Basal Boundary Reflector. The basal boundary reflector 2 of unit C is detected within an approximate depth range of 17 to 39 m below sea level, with a mean depth of 30 m. Its burial depth beneath the sea floor ranges from less than 1 m to a maximum of 19 m, with a mean value of 9 m. Reflector 2 is noted on all profiles within the study area. It is characterized as an irregular interface, exhibiting maximum local relief of 5 m. It is an eastward dipping reflector, with an average apparent dip rate of 0.48m/km (less than 0.03°).

With the exception of profile E, reflector 2 is well defined throughout the eastern half of all east-west profiles. However, in the west, it frequently appears to be truncated by overlying reflector 3, with which it exhibits notable angular discordance. This relation is apparent on profiles A, C, G, and I. Reflector 2 is interpreted as a prominent unconformity of widespread extent throughout the study area.

Seismic Characteristics. In portions of the study area where boundary reflectors 2 and 3 were detected, unit C is readily distinguished from deposits of underlying unit B and overlying unit D. It appears to be widely distributed throughout the study area. It is characterized by relatively uniform, horizontal stratification throughout, with only occasional indications of minor local channeling. Unit C appears to wedge out toward the west in the northern part of the study area, as indicated on profiles A and C. On profile I, the unit appears to wedge out in the 4 to 5 interval, but then reappears farther west in the 1 to 3 interval. The frequent wedge-out relation exhibited by unit C may be largely of erosional origin, resulting from truncation by reflector 3. The thickness of unit C ranges from zero, to a maximum detected value of 14 m in the 6 to 8 interval of profile E. Although the frequent nondetection of both boundary reflectors precludes accurate thickness determinations throughout much of the study area, the unit does exhibit a general thickening in an eastward (seaward) direction.

Core Analysis. In the False Cape cores, unit C's predominant lithology is brownish-gray (5YR6/1) to medium greenish-gray (5GY5/1) mud. The sediment is mud, both in the sense of

being a mixture of silt- and clay-sized particles, and in the sense of having a high water content (12 to 25 percent, versus 2 to 9 percent for underlying unit B). A single water analysis revealed a salinity of 20 parts per thousand (Thomas Gosink, 1970, personal commun.). At the stratigraphic top of the unit in core 1, and at its stratigraphic base in core 5, the unit consists of thick to very thin beds and laminae of fine to very fine-grained sand, alternating with very thin beds and laminae of mud (thickness terms from Ingram, 1954). When interbedded with sand, the mud layers tend to be light brownish gray. The bulk of unit C, as revealed in core 2, is an obscurely mottled to massive, medium greenish-gray mud (5GY5/1). In core 2, the base of the unit consists of 0.7 m of muddy gravel containing granules and fine pebbles. The nondetection of unit C in cores 3 and 4 indicates its discontinuous nature at the False Cape locality. The western segment of the unit penetrated by cores 1 and 2 might therefore represent an outlier, separated from the main body of the unit located to the east. Core 5 might therefore record the western terminus of the wedge-out indicated on the boomer profiles. Two radiocarbon dates were obtained for unit C. One date was obtained near the stratigraphic base of the unit in core 5; shell fragments of gravel and sand size were extracted from the basal 2.6 m, which dates at 27,700 ± 800 yrs B.P. The second date was obtained near the stratigraphic top of the unit in core 2; organic material from the uppermost 2.6 m dates at 20,400 ± 850 yrs B.P. Since sufficient shell fragments were not present in this interval, the date is based on total carbonate extracted from the sample.

Faunal Analysis. The watery mud of unit C in core 2 contains a limited assemblage of 12 mollusk species (Fig. 6). Besides having a distinctly smaller faunal diversity, the populations in the samples were numerically small. They were, however, exceptionally well preserved, without abrasion or corrosion. Most species are physically small forms, with greater surface area per unit weight—an adaptation for living in soft, low-density muds. Sessile epibenthos of the oyster family are absent. The assemblage is tolerant of reduced salinities. It occurs in depths ranging from low tide to 10 m, and may indicate a lagoonal environment. The unit C in core 5 contains a limited fauna of eight euryhaline species that are characteristic of the margins of lagoons and estuaries (Fig. 8). Most of these species have been reported by Brett (1963) from Bogue Sound, North Carolina.

Correlation. The presence of zones of homogeneous watery mud, interbedded mud and fine sand layers, and a shallow euryhaline fauna suggest that unit C, where cored, is the product of a restricted environment, such as an estuary or lagoon.

The two radiocarbon dates indicate a late Pleistocene age. The older date of 25,700 ± 800 yrs B.P. at the base of the unit, derived from shallow-water mollusks, was obtained at a mean depth of 25 m below modern sea level; this conforms to the curve of late Quaternary sea level fluctuations presented by Milliman and Emery (1968). These workers have reported similar dates from oölites in surficial sands of the Carolina Shelf to the south, and they refer the dates to the sea-level lowering associated with the end of the mid-Wisconsinan interstadial.

The younger date of 20,400 ± 850 yrs B.P. was obtained from the top of an apparent unit C outlier, at a mean depth of 15 m below modern sea level. It therefore falls along the younger margin of Milliman and Emery's (1968) envelope of dates for their curve of late

Figure 8. Stratigraphic distribution of mollusk species in core 5, arranged by first occurrence. Prepared by C. Stein and M. Simpson.

Quaternary sea levels. This date also indicates an age associated with the regression following the end of the mid-Wisconsin interstadial. However, it is feasible that this radiocarbon date, which is based on total carbonate content, may be anomalously old. In this event, the apparent outlier of unit C might actually represent lagoonal mud of early Holocene age, which has been overridden by the retrograding Currituck Spit during the Holocene transgression. Assuming that the younger radiocarbon date is valid, the entire unit C is interpreted as a regressive paralic-neritic sequence of late Wisconsinan age. Since the youngest Pleistocene deposit mapped by Oaks (1964) in the adjacent coastal region is the Sandbridge Formation of probable early Wisconsinan age, unit C has no apparent onshore correlatives.

Unit D

The youngest sedimentary sequence within the study area is designated unit D, which is defined as the sequence above reflector R3. This unit consists of the surficial sea-floor deposits of the study area, except locally, where units B and C outcrop.

Basal Boundary Reflector. Basal boundary reflector 3 is detected intermittently throughout the surveyed area, and it constitutes the shallowest prominent subsurface reflector noted during the study. Its burial depth beneath the sea floor ranges from zero to 9 m, with a mean depth of 3 m. In several localities, reflector 3 appears to outcrop and coincide with the present sea floor. This relation is especially apparent in the 1 to 6 intervals of both profiles C and G. In other areas, lack of detection of reflector 3 may be due to the seismic ringing which commonly obscured the upper few meters of the profile records. Regionally, reflector 3 can be characterized as a nearly horizontal interface, with only a slight apparent eastward dip; the average apparent dip rate is less than 0.20 m/km (less than 0.016°). Locally, the reflector is frequently irregular, exhibiting maximum local relief of as much as 3 m.

Profile G illustrates an angular discordance between reflector 3 and underlying reflector 2, with the former appearing to truncate the latter near the 2 to 3 interval. This same stratigraphic relation also appears to be illustrated on profiles A, C, and possibly I. In areas where reflector 2 has been truncated by reflector 3, unit C is absent, and the latter reflector also constitutes the upper boundary of unit B. Reflector 3 is interpreted as a prominent unconformity of widespread extent throughout the study area.

Seismic Characteristics. Unit D appears to be distributed throughout much of the study area; however, its detailed areal distribution is uncertain because of the intermittent detection of boundary reflector 3. The presence of unit D can be ascertained in areas where reflector 3 is clearly discernible; conversely, the absence of unit D can be reasonably inferred in areas where reflector 3 appears to crop out. However, in much of the study area, excessive seismic ringing precluded detection of reflector 3, thus rendering unit D undifferentiable. Differentiation of the unit is confined largely to the east-west profiles, where it is detected intermittently. Unit D is characterized as having a relatively homogeneous internal structure, as compared with underlying units; this is indicated by relatively fewer internal seismic reflectors within unit D. The thickness of the unit varies from zero, to a maximum of 9 m in the 2 to 3 interval of profile E. In general, thickness variations of unit D are expressed geomorphically as the north-trending ridges and swales, which comprise much of the present sea-floor topography within the study area. The thickest sections of the unit occur as plano-convex ridges, while the thinner sections occur as intervening swales (Fig. 9). The ridges may attain maximum local relief up to 8 m, with some of the more prominent examples occurring on profiles E, G, and I.

Core Analysis. The uppermost lithologic unit, penetrated by all six cores, is correlated with unit D. The unit consists of very fine-grained to coarse-grained sand, whose color ranges from medium dark gray (N5) through light olive gray (5Y6/1) to dark yellowish orange (10YR6/0). This color spectrum corresponds to a grain size range from very fine-grained sand, through medium-grained to coarse-grained sand. Brown sands, however, are also found within 1 m of the surface, in what appears to be an oxidized "soil zone." The brown and dark orange hues of the superficial sands on the Atlantic shelf have been considered a characteristic acquired during a former period of subaerial exposure (Emery, 1965; Sanders and others, 1970) or during weathering in the source area of the sediment (Judd and others, 1970). We have observed no evidence which directly contradicts these hypotheses. However, the close correlation of color with grain size suggests a simpler hypothesis. The color

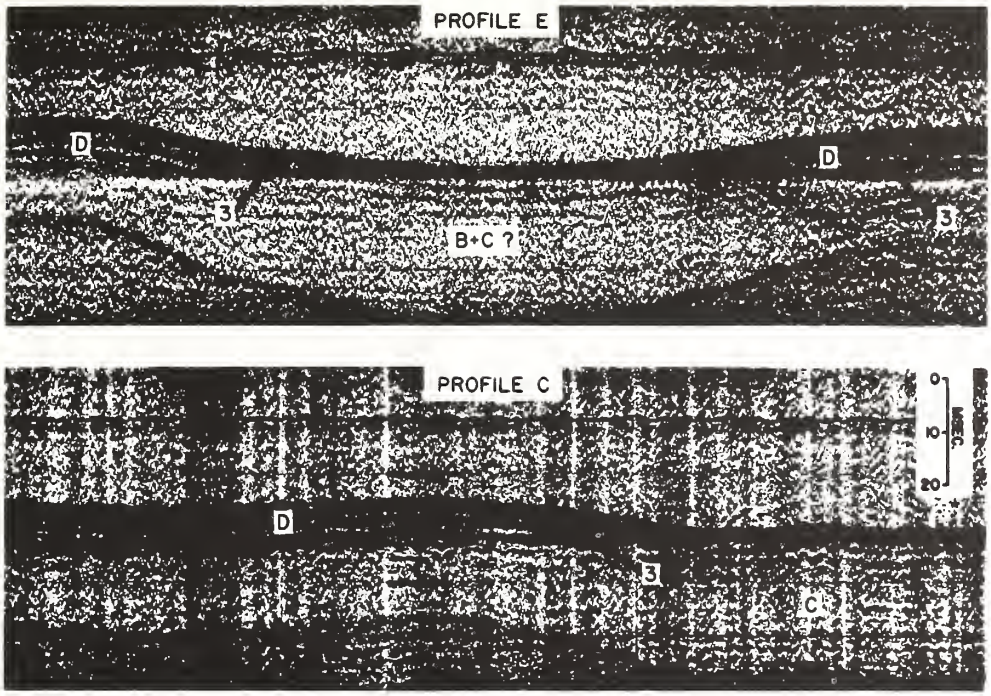

Figure 9. Original high resolution boomer records illustrating the plano-convex nature of some sand ridges comprising unit D: Top record illustrates the prominent swale and adjacent ridge flanks in the 3 to 4 interval of profile E. Bottom record illustrates the eastern edge of the prominent ridge near point 5 of profile C.

may be a function of permeability; finer sands are less permeable and may be reduced and darkened by interstitial organic matter, while the coarser, more permeable sands may be oxygenated by wave surge and stained orange and brown by iron oxides.

Grain sizes and primary structures of the sands observed in unit D reflect the subenvironments of the inner Virginia Shelf in which they were deposited. In core 1, fine and very fine sands of the shore face are penetrated, which consist of very thin to medium beds of upward fining sand, presumably winnowed from the surf zone. In cores 2 and 4, a thin, coarse-grained, pebbly and shelly sand is observed veneering older units; it appears to represent a lag deposit resulting from the storm-scouring of trough floors. A strongly cross-bedded fine- to medium-grained sand is observed on the crest of the inner ridge (core 2A), which is inferred to represent concomitant storm deposition. The finer sands observed along the ridges' seaward flanks (cores 3 and 5) are believed to have been winnowed from ridge crests by fair-weather wave surge. The genesis of these individual sand facies comprising unit D is considered in greater detail elsewhere (Swift and others, 1972). A single radiocarbon date was established for unit D. An articulated *Mercenaria* sp. extracted from core 3 at a depth of 1.7 m below the surface was dated at 4,220 ± 140 yrs B.P.

Faunal Analysis. The surfical sand sheet attains maximum faunal diversity with 47 species, and exhibits both horizontal and vertical variations. Species from core 1, and from the lower part of the unit elsewhere, indicate deposition in water depths ranging from intertidal to 8 m. However, the upper portion of the unit was deposited in deeper water; its species presently range from 5 to 16 m. Biofragmental sand lenses indicating a high energy environment are present in the basal strata, and shells in the entire unit show a greater degree of breakage, rounding, and corrosion than shells of the same species from lower stratigraphic units. It seems probable that some of the shells have been scoured from an older matrix, and have been reworked into the younger unit D deposits.

Genesis. The sand sheet of unit D is comprised of the surficial sea-floor deposits throughout much of the study area, except where local outcrops of subjacent units occur. Its upper surface is manifested as present sea-floor morphology, the genesis of which is one of the most critical aspects of the study area. The major morphological elements of the inner Virginia Shelf southeast of Cape Henry are illustrated by Figure 10. In the northwest, there is a smoothed area, which is the distal southern portion of the submarine "tidal delta" attributed by Payne (1970) to the tidal regime associated with the mouth of Chesapeake Bay. Southeast of this area, there is a system of subdued ridges (Virginia Beach Ridges), trending north-northeast. Individual ridges are continuous for a maximum distance of 10 km. The maximum relief is 10 m, and the side slopes are two degrees or less; crests are about 4 km or less apart. The ridges are interrupted to the south by a channel, 2 to 4 km wide, that extends in an arc from the tide-smoothed area of the northwest, toward the south and east. A ridge topography is again evident south of the channel (False Cape Ridges); these ridges merge into the shore face at depths as shoal as 6 m. Northeast of both ridge systems, a prominent scarp exists which may be an abandoned shoreline.

Fisher (1968) and Payne (1970) have suggested that the ridges of the study area are relict Pleistocene beach ridges. However, the radiocarbon date obtained from a depth of 1.7 m along the flank of one of the ridges comprising unit D is 4,220 ± 140 yrs B.P., indicating a Holocene age. In addition, a detailed analysis of the False Cape ridge system (Swift and others, 1972) indicates that the ridges are not relict features, but instead are large-scale hydraulic bedforms which probably formed in response to coast-parallel storm currents. Bottom current measurements along the innermost trough of the False Cape system suggest that the trough and the adjacent ridge may be in a state of active formation, nourished by the eroding shore face. We infer that the more seaward False Cape ridges were similarly formed in contact with the shoreline, and are now periodically reactivated by storm currents.

Our data permit us to tentatively extend this interpretation to the Virginia Beach ridge system north of the channel. Payne (1970) has interpreted the channel separating the two

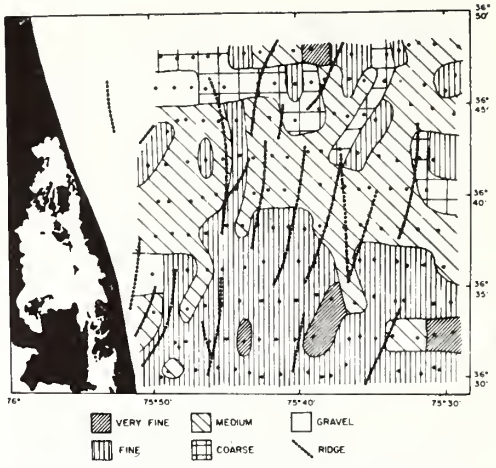

Figure 10. Grab sample net, and distribution of median diameters over the study area.

ridge systems as the course of an ancestral Susquehanna River. Although this may be its ultimate origin, there is reason to believe that, if this is the case, then there has been extensive modification of the topography since the channel was incised. The evidence is partly morphological and partly textural. The False Cape ridge system south of the channel consists of ridges nearly normal to the channel, with crestlines shoaling toward the south; the ridges also become steeper and better defined toward the south. Three ridges merge with the shore face, but the fourth terminates abruptly, in a relatively steep south-facing slope. Troughs contain a veneer of pebbly sand over a stiff, fine-grained substrate. Crests are comprised of wave-winnowed, well-sorted, medium-grained sand; whereas flanks are mantled with out-winnowed finer sand. The finer sand on the seaward flanks of the ridges thickens to the south, and the shore face south of the ridges has experienced considerable accretion of this material, indicating net sediment transport southward through the ridge system.

If the topography and grain-size pattern were primarily relict features dissected by a fluvial channel, one would expect to see topographic and grain-size gradients reversed north of the channel, with the Virginia Beach ridge system being a mirror image of the False Cape system. Instead, the Virginia Beach system resembles a simple northeast translation of the False Cape system. The crestlines of the Virginia Beach ridges climb to the south, peaking only a few hundred meters north of the

channel, and are terminated by relatively steep south-facing slopes. The 2 km × 4 km grab sample net over the study area is not sufficiently dense to clearly resolve the close correlation of median grain size to topography previously observed in the False Cape locality (Swift and others, 1972). However, the median diameter distribution map (Fig. 11) does illustrate a subtle small-scale "grain" of north-south trending sediment belts, thus suggesting topographic control of grain-size distribution. This small-scale variation is superimposed on a larger-scale pattern of northward coarsening throughout the study area. The high resolution boomer profiles indicate that the ridges of both the False Cape and the Virginia Beach systems are hemicylindrical sand mounds resting on a relatively flat substrate (Fig. 9). The substrate of both is mud to fine muddy sand; it is sporadically veneered with gravel, as confirmed by the False Cape cores, as well as by three cores taken from the Virginia Beach ridge system (Swift and others, 1972). Powers and Kinsman (1953) also reported coring this gravel bed across the northern part of the study area. They attributed it to postdepositional sorting of the Holocene sand sheet by wave surge; however, it is here interpreted as a sporadically distributed lag gravel which formed at the base of a Holocene transgressive sand sheet generated by erosion of a retreating shore face. The general coarsening of sediments toward the northern portion of the study area, as illustrated by the median diameter map (Fig. 11), suggests that sand is being swept off this basal gravel in the north, transported through the ridge system, and deposited in the southern portion of the area. Therefore, the Virginia Beach topography, like the False Cape topography, appears to be at least in part a response to the modern hydraulic regime.

The nature of the causative hydraulic mechanisms may be inferred from the topography. Detailed mapping of the False Cape ridge system has revealed second-order ridges on the flanks of major ridges. They are asymmetrical toward major ridge crests, suggesting that the ridge system is maintained by coast-parallel currents organized into helicoidal flow cells, with bottom-current divergences in the troughs, and convergences on the crests (Swift and others, 1972). Mapping of the Virginia Beach ridge system has not yet been sufficiently precise to reveal the presence or absence of ridge asymmetry; however, there is evidence

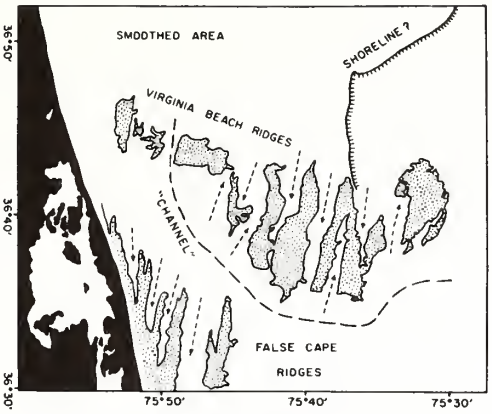

Figure 11. Major morphological elements of the sea floor on the inner Virginia Shelf southeast of Cape Henry. Arrows indicate the shoaling direction of individual trough thalwegs between adjacent ridges. Northward shoaling troughs are suspected to be flood tidal channels, while southward shoaling troughs may be ebb tidal channels.

for a related current regime that could produce similar longitudinal bedforms. One of the Virginia Beach ridges is organized into a tight "Z" pattern, opening to the north and south (Fig. 10). Elsewhere in the ridge complex, some trough thalwegs slope toward the south, while adjacent troughs slope toward the north. This basic pattern has also been reported from the southern bight of the North Sea (Van Veen, 1936; Houbolt, 1968), where it has been interpreted as an ebb-flood channel system, resulting from residual ebb and flood tidal currents respectively dominating paired troughs; the troughs shoal and close in the direction of the dominant residual. Semidiurnal tidal currents are presently too weak in this ridge area to be considered by themselves as ridge-forming currents. The zig-zag pattern of the topography may instead reflect an earlier period when the channel was a tide-dominated estuary mouth and the Virginia Beach ridges were an associated inner shelf shoal.

Unit D is thus interpreted as a Holocene transgressive sand sheet. Its basal reflector, 3, constitutes the Pleistocene-Holocene boundary, which is manifested in the study area as a prominent unconformity. Stratigraphically, unit D overlies the modern shore face along the western margin of the study area during fair-weather conditions. However, along the shore face, it is an ephemeral deposit which is periodically removed by intense storm activity

(Swift and others, 1972). Farther seaward of the modern shore face, unit D consists of a discontinuous sand sheet with a locally developed basal gravel bed, which unconformably overlies a Pleistocene substrate. The sand sheet appears to have been generated through the shore face erosion of a retrograding coastal barrier during the Holocene transgression (Swift and others, 1970, 1972). It appears to have accumulated as a lag deposit on the sea floor, where it was subsequently molded into ridge and swale topography by coast-parallel storm surge currents and perhaps by interaction of these currents with an estuary mouth shoal. Its mixed faunal assemblage consists of abraded shells scoured out of underlying deposits, plus modern species living in and on the sand sheet. Faunal diversity is further increased as a consequence of the relatively greater textural fractionation of this current-winnowed lag concentrate, in contrast to the more texturally homogeneous subjacent deposits.

Vertical and Horizontal Faunal Variations

While relative abundance of species varies among localities and within each core, approximately 30 percent of the species constitute a common element in the various faunas. When the faunas are arranged by first (lowest) occurrence of species, they show a progressive upward change in species composition within the core. The shift in species composition reflects environmental changes that took place during the deposition of each of the sedimentary units. The pattern of vertical change is similar from core to core, but the faunal composition cannot be readily correlated through a given stratigraphic horizon. This anomalous situation presumably reflects the greater sensitivity of some of the organisms to low-order environmental changes that did not significantly alter the distribution pattern of the sediments. A majority of the species show a preference for a given sediment type, but only a few rare forms are restricted to a single stratigraphic unit. The faunal homogeneity of the section is a measure of the similarity of successive late Quaternary environments, and perhaps also the extent to which older fossils have been reworked into younger units.

The species diversity varies with the texture of the sediment (Fig. 12). In general, the species diversity and the absolute abundance of individuals in a fossil assemblage decreases with decreasing grain size of the sediment. The ratio of infauna to epifauna remains constant throughout this trend, but the relative abundance of filter feeders with respect to detritus feeders decreases, thus reflecting the effect of the increasing clay content on the filtering mechanisms of the fauna.

CONCLUSIONS

The Quaternary stratigraphy of the inner Virginia Shelf reflects eustatic events associated with continental glaciation. Widespread emergence of the inner Virginia Shelf during late Tertiary–early Pleistocene time resulted in the development of a prominent unconformity on top of Miocene deposits. An overlying sedimentary assemblage of pre-Wisconsinan and early Wisconsinan age may reflect both transgressive and regressive deposition, as manifested by the presence of apparent fluvial and coastal barrier complexes. The presence of fluvial deposits could reflect an aggrading stream system along an inundated coastal plain during one or more pre-Wisconsinan interstadial transgressions, while the overlying barrier complex appears to reflect regressive strand plain deposits of a prograding coast developed during the early Wisconsinan glacial substage.

The subsequent mid-Wisconsinan interstadial transgression appears to be manifested throughout the inner Virginia Shelf as a widespread unconformity. The absence of a transgressive record might be attributed to the relatively

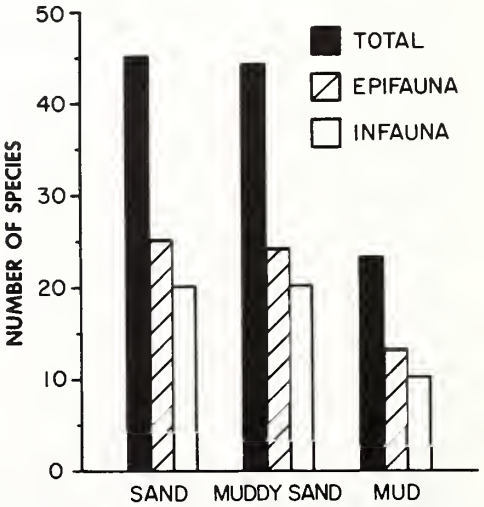

Figure 12. Distribution of fauna, as related to sediment type.

short time interval associated with the mid-Wisconsinan interstadial, as well as to the destruction of paralic deposits by the transgressing sea, in a manner described by Fischer (1961). Following the mid-Wisconsinan interstadial, an apparent paralic-neritic regressive assemblage developed during the late Wisconsinan glacial substage.

The late Wisconsinan regressive sequence was then subjected to erosion, resulting in the development of a second prominent unconformity within the Quaternary section. This unconformity constitutes the Pleistocene-Holocene boundary, and may represent a compound erosional surface, possibly reflecting both subaerial erosion during the late Wisconsinan regression, and subsequent shore face erosion during the following Holocene transgression. The Holocene section consists of a discontinuous transgressive sand sheet, with a locally developed basal gravel. The section was apparently generated as a sea-floor lag concentrate, resulting from the erosion of a retrograding shore face. The lag deposit appears to have been subsequently molded by south-trending coast-parallel storm surge currents into the prominent ridge and swale topography which characterizes the present inner Virginia Shelf.

Initially, these currents may have interacted with tidal currents associated with a former Susquehanna River mouth to form estuary mouth shoals. At present, however, only the storm currents are sufficiently intense to mobilize sea-floor sediment. The topography may date in part from an earlier, tide-dominated period, but the surficial grain-size distribution is adequately explained simply as a response to the modern regime of intermittent storm currents.

The numerous common mollusk species throughout much of the Quaternary section reflect the basic similarity of the successive depositional environments. The faunal differences which are present reflect both the higher turbidity and lower salinity of the pre-Holocene deposits, as well as the higher energy level and more extensive textural fractionation of the Holocene transgressive sand sheet.

ACKNOWLEDGMENTS

This study was financially supported by research grants and contracts from the National Science Foundation (No. GA-13837), the Coastal Engineering Research Center (No. DACW-72-69-C-0016), the Old Dominion University Research Foundation (No. 8028), and the Marine Geology Office of the U.S. Geological Survey. The authors are also indebted to the National Aeronautics and Space Administration for the use of their vessel, *Range Recoverer*. R. Sheridan and his colleagues at the University of Delaware allowed us to include our vibracoring operation in their cruise (C-18B-70) aboard the Duke University ship R/V *Eastward*. Operation of the *Eastward* is supported by National Science Foundation Grant CB-17545. The acoustic profiler survey at False Cape was conducted for us by Lt. K. R. Bitting of the U.S. Army Mobility Equipment Command, Fort Belvoir, Virginia. Carol Stein and Michael Simpson assisted in the paleontological analysis.

REFERENCES CITED

Abbott, R. T., 1954, American seashells: New York, D. Van Nostrand, 541 p.

Brett, C. E., 1963, Relationships between invertebrates, infauna distribution, and sediment type distribution in Bogue Sound, North Carolina [Ph.D. dissert.]: Chapel Hill, Univ. North Carolina, 202 p.

Burger, J. A., Klein, G. deVries, and Sanders, J. E., 1969, A field technique for making epoxy relief-peels in sandy sediments saturated with saltwater: Jour. Sed. Petrology, v. 39, p. 338–341.

Clench, W. J., and Turner, R. D., 1951, The genus *Epitonium* in the Western Atlantic: Johnsonia, v. 2, p. 284–293.

Coch, N. K., 1965, Post-Miocene stratigraphy and morphology, inner coastal plain, southeastern Virginia: Office Naval Research, Geography Branch, Tech. Rept. 6, 97 p.

Emery, K. O., 1965, Geology of the continental margin off eastern United States, *in* Whittard, W. F., and Bradshaw, R., eds., Submarine geology and geophysics: London, Butterworths, p. 1–20.

Fischer, A. G., 1961, Stratigraphic record of transgressing seas in the light of sedimentation on the Atlantic Coast of New Jersey: Am. Assoc. Petroleum Geologists Bull., v. 45, p. 1656–1660.

Fisher, J. J., 1968, Preliminary quantitative analysis of surface morphology of inner continental shelf surface—Cape Henry, Virginia to Cape Fear, North Carolina, *in* Margolis, A. E., and Steere, R. C., eds., National Symposium on Ocean Sciences and Engineering of the Atlantic Shelf, trans.: Washington, D. C., Marine Technology Soc., p. 143–149.

Frye, J. C., Willman, H. B., and Black, R. F., 1965,

Outline of glacial geology of Illinois and Wisconsin, *in* Wright, H. E., Jr., and Frey, D. G., eds., The Quaternary of the United States: Princeton, Princeton Univ. Press, p. 43–61.

Harrison, W., 1962, Pleistocene record in the subsurface of the Norfolk area, Virginia, *in* Harrison, W., Virginia Acad. Sci. 40th Meeting, Gen. Pub. Ser., Guidebook for field trips: Norfolk, College of William and Mary, p. 37–61.

Harrison, W., and Malloy, R. J., 1963, Reconnaissance geological echo profiler (GEP) survey in lower Chesapeake Bay: Am. Geophys. Union Trans., v. 44, p. 68.

Harrison, W., Malloy, R. J., Rusnak, G. A., and Terasmae, J., 1965, Possible late Pleistocene uplift Chesapeake Bay entrance: Jour. Geology, v. 73, p. 201–229.

Houbolt, J.J.H.C., 1968, Recent sediment in the southern bight of the North Sea: Geologie en Mijnbouw, v. 47, p. 245–273.

Ingram, R. L., 1954, Terminology for the thickness of stratification and parting units in sedimentary rocks: Geol. Soc. America Bull., v. 65, p. 937–938.

Judd, J. B., Smith, W. C., and Pilkey, O., 1970, The environmental significance of iron stained quartz grains on the southeastern United States Continental Shelf: Marine Geology, v. 8, p. 355–362.

Lawrence, D. R., and Raup, D. M., 1963, Paleoecology of Pleistocene mollusks from Martha's Vineyard, Massachusetts: Jour. Paleontology, v. 37, p. 476–481.

Milliman, J. D., and Emery, K. O., 1968, Sea level during the past 35,000 years: Science, v. 162, p. 1121–1123.

Oaks, Robert, Jr., 1964, Post-Miocene stratigraphy and morphology, outer coastal plain southeastern Virginia: U. S. Office Naval Research Tech. Rept. No. 5, 241 p.

Parker, R. H., 1955, Changes in the invertebrate fauna apparently attributable to salinity changes in the bays of central Texas: Jour. Paleontology, v. 29, p. 193–211.

—— 1956, Macro-invertebrate assemblages of central Texas coastal bays and Laguna Madre: Am. Assoc. Petroleum Geologists Bull., v. 43, p. 2161–2166.

Payne, L. H., 1970, Sediments and morphology of the continental shelf off southeastern Virginia [M.S. thesis]: New York, Columbia Univ., 70 p.

Powers, M. C., and Kinsman, B., 1953, Shell accumulations in underwater sediments and their relations to the thickness of the traction zone: Jour. Sed. Petrology, v. 23, p. 229–234.

Sanders, J. E., Friedman, G. M., Caldwell, D., and Kumar, N., 1970, Stratigraphic relationships, brown and gray relict Quaternary shelf sediments: Geol. Soc. America, Abs. with Programs (Ann. Mtg.), v. 2, no. 7, p. 672–673.

Sanford, R. B., and Swift, D.J.P., 1972, Comparison of sieving and settling techniques for size analysis, using a Benthos Rapid Sediment Analyzer: Sedimentology (in press).

Shideler, G. L., and Swift, D.J.P., 1972, Seismic reconnaissance of post-Miocene deposits, Middle Atlantic continental shelf—Cape Henry, Virginia, to Cape Hatteras, North Carolina: Marine Geology (in press).

Swift, D.J.P., Shideler, G. L., Avignone, N. F., and Holliday, B. W., 1970, Holocene transgressive sand sheet of the Middle Atlantic Bight—a model for generation by shore face erosion (Discussion paper): Geol. Soc. America, Abs. with Programs (Ann. Mtg.), v. 2, no. 7, p. 757–759.

Swift, D.J.P., Sanford, R. B., Dill, C. Z., Jr., and Avignone, N. F., 1971, Textural differentiation on the shore face during erosional retreat of an unconsolidated coast, Cape Henry to Cape Hatteras, western North Atlantic Shelf; Sedimentology, v. 16, p. 221–250.

Swift, D.J.P., Holliday, B. W., Avignone, N. F., and Shideler, G. L., 1972, Anatomy of a shoreface ridge system, False Cape, Virginia: Marine Geology, v. 12, p. 59–84.

Uchupi, Elazar, 1970, Atlantic continental shelf and slope of the United States—shallow structure: U.S. Geol. Survey Prof. Paper 529-I, 44 p.

Uchupi, Elazar, and Emery, K. O., 1967, Structure of continental margin off Atlantic Coast of United States: Am. Assoc. Petroleum Geologists Bull., v. 51, p. 223–234.

Van Veen, J., 1936, Onderzoekingen in de Hoofden in Verband met de gesteheid der Nederlandse Kust. Neiuwe Verhandelingen Van het Bataafsch Gehootschap Voor Proefondervindelikje wigs begurte to Rotterdam: Tweede Reeks, elfde deel.

Manuscript Received by the Society June 21, 1971

Revised Manuscript Received November 19, 1971

Authors' Present Addresses: NOAA/AOML, 901 South Miami Avenue, Miami, Florida 33130 (Swift). Department of Oceanography, Texas A & M University, College Station, Texas 77843 (Holliday)

PRINTED IN U.S.A.

Reprinted from Shelf Sediment Transport, edited by Swift, Duane, and Pilkey, © Dowden, Hutchinson and Ross, Inc., Stroudsburg, Pa., 363-371.

CHAPTER 17

Implications of Sediment Dispersal from Bottom Current Measurements; Some Specific Problems in Understanding Bottom Sediment Distribution and Dispersal on the Continental Shelf— A Discussion of Two Papers

Donald J. P. Swift

National Oceanic & Atmospheric Administration
Atlantic Oceanographic & Meteorological Laboratories
15 Rickenbacker Causeway
Miami, Florida 33149

ABSTRACT

The emphasis of Creager and Sternberg (1972) and also Sternberg and McManus (1972) on the wind-drift component of shelf storm currents is valid, since this component is a major, if not dominant, cause of unidirectional currents over large portions of most nontidal shelves. In view

of the genetic complexity of the current velocity field over the shelf, however, an operational distinction is better made between storm-generated bottom currents in which a unidirectional component of compound origin is dominant, and the surge-dominated flow, which characterizes but is not confined to the fair-weather hydraulic regime. This division recognizes that shelf currents are frequently of compound origin, and is keyed to the interpretation of substrate response elements. Such an approach may encourage examination of the very real role of waves as a contributing factor in shelf sediment transport.

A simple random walk model for sediment transport across the shelf does not, as noted by Sternberg and McManus (1972) and by Creager and Sternberg (1972), accurately describe the advective component of sediment transport. It does, however, accommodate the diffusive component. The more flexible Markov-process model is valid for both components.

CONCEPTUAL MODELS

Creager and Sternberg (1972) have found an ideal key with which to review the broad field of the study of bottom sediment distribution and dispersal on continental shelves. They seek the paradigm, or conceptual framework with which their colleagues order reality. Unfortunately, the more successful conceptual models, like other valuable tools, are easily misused. They can be treated as closed systems, which cease to create new order and reason, but merely recirculate the old; that is, they lead to circular reasoning whereby relationships predicted in the model are too hastily "found" in nature, then cited as the model's verification. Creager and Sternberg are concerned with such use and misuse of conceptual models for shelf sediment transport.

Probably the best defense for those of us brought to task for our complicity in thus detaching reasoning from reality is Griffiths' (1967) "stochastic convergence" model for the advancement of knowledge. Griffiths notes that major scientific advances are based on preceding concepts (Fig. 141) and that while a given concept may be erroneous, it is generally less erroneous than its predecessor, portions of which it tends to incorporate. In his example, historical estimates for the age of the earth range from approximately zero to infinity, but converge towards a "true value" (which itself is time variant). The fine structure of the process is significant. A "vertical breakthrough" often contains many erroneous concepts, yet gives impetus to its field. Those who follow in the pioneer's footsteps spend most of their efforts in tidying up his structure of thought; eventually the reordering is thoroughgoing enough to constitute a new breakthrough which, despite its freshness, contains elements of the old. Our own field of shelf sediment transport affords a classic example. The turn of the century students, of whom D. W. Johnson (1919) was a noted example, conceived of the equilibrium shelf profile and its corollary, the size-graded shelf. Shepard (1932) sharply questioned the corollary on the basis of map notations, and Emery's (1952) classification of shelf sediments restructured the Johnson model in such a systematic fashion as to constitute a new breakthrough. The concept

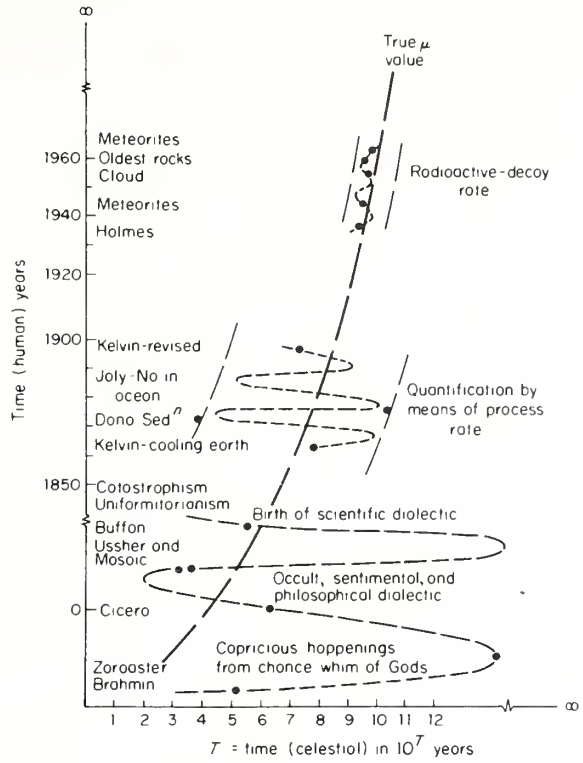

Figure 141.

Estimation of the age of the earth as an example of stochastic convergence toward some true value (from Griffiths, 1967).

of relict sediments is one which I and others in the phase of consolidation have attempted to qualify; yet without the conceptual platform provided by both Johnson's and Emery's models, we could only move painfully toward these points of departure.

SHELF VELOCITY FIELD: WAVE-DRIFT AND WIND-DRIFT COMPONENTS

With this perspective I would like to take advantage of my early acquaintance with both the Sternberg-McManus and the Creager-Sternberg manuscripts and their request for clarification of some of my earlier statements. Clarification is necessary, for several of us (Swift, 1970; Swift, Stanley, and Curray, 1971) seem (with some provocation) to have become straw men in a debate on the relative merits of wind-drift and wave-drift velocity components as agents of

shelf sediment dispersal. Both papers were written at a time when a major issue had been defined by the exchange between Dietz (1963) and Moore and Curray (1964) as to whether or not any significant movement at all occurred on the shelf. Consequently, no major attempt to assess relative competence of wave- and wind-drift velocity components was undertaken. Instead, we invoked evidence wherever we found it to indicate that sediment is moving on shelves. The lengthy discussion of oscillatory wave, tidal, and storm surge movements, and their residual components (Swift et al., 1971a, p. 324-325) was introduced to help prove that movement occurred. I note that we place "direct wind input" first among energy inputs into the shelf velocity field, although the effect is somewhat marred by later unfortunate references to "wave-dominated" shelves. Weather-dominated shelves is a preferable term. We clearly distinguished between tide-dominated shelves and weather-dominated shelves (Swift, 1970, p. 17; Swift et al. 1971a, p. 324) before discussing the catastrophic fine structure of storm-driven sedimentation on the latter (p. 324), hence we were presumably applying this generality with the caution required by Creager and Sternberg.

Since completion of the manuscript, "Relict Sediments: a Reconsideration," I have been investigating hydraulic process and substrate response on portions of the Atlantic continental shelf. The latter studies have progressed more rapidly than the former; although I have acquired only a small store of hydraulic data, I now have a great awareness of the appalling logistics of *in-situ* recording of the hydraulic regime. My substrate studies (Swift et al., 1971b, 1972a, 1972b; Duane et al., 1972) have provided considerable circumstantial evidence for southward sediment transport on the inner central Atlantic shelf. I have attributed these to storm-generated currents rather than to the fair-weather wave regime, and have been considerably influenced in my thinking by theoretical considerations set for by Harrison et al. (1964) in their study of circulation in the Chesapeake bight of the Atlantic shelf. These authors postulated south-flowing currents on the inner shelf as a consequence of a barotropic response to wind set-up during northeasters. Consequently when, during the oral presentations of this symposium, a wind- versus wave-current controversy was referred to and it became apparent that I was expected to defend the latter end of it, I was rather startled. However, after reviewing my 1970 and 1971 papers I note that while a clear distinction between wind- and wave-drift velocity components was made, wave-drift components were stressed, and that wind-drift components were not discussed in detail. The papers in this volume by Sternberg and McManus and Creager and Sternberg are justifiably concerned with this imbalance. Their review of the problem is a service to our readers and has sharpened my own thinking. However, my thoughts, thus sharpened, have led to doubts concerning a simple division between wave-drift and wind-drift currents.

One concern is in part semantic. The total instantaneous shelf velocity field at a point of measurement, and the succession of these fields through time are

the only realities. Velocity components are fictional though useful abstractions. My own work on the central Atlantic shelf (Swift et al., 1972b; Duane et al., 1972) has led me to conclude that brief, intense, storm-generated pulses are the most significant factor associated with observed forms of substrate response such as large and small bedforms and sand size-distributions. The wind-drift velocity component presumably dominates these currents, but they are probably never purely wind-drift currents in the sense of being solely due to direct wind stress on the water surface. They are most nearly such on the outer shelf during storms, when in the generating area, the waves are high and steep but also of wavelength too short to reach to the outer shelf floor. The surface currents thus generated, theoretically a pure wind-drift component for deep water gravity waves, may eventually reach the shelf floor; either directly through he downward transfer of momentum by turbulent diffusion, or indirectly, in the form of compensatory currents. However, complex wind waves are the least amenable to the linear approximations of classical wave theory, and the wave-drift component of the surface current cannot be accurately assessed. An additional significant wave-drift component, likewise mathematically intractable, occurs as a consequence of the breaking of the crests of the steep storm waves.

Other velocity components are present in this situation. Galt (1971) has devised a model for pressure-induced storm surges over the continental shelf that indicates a velocity component form this cause on the order of 10 cm sec^{-1} near the shelf break, with the possibility of considerably larger components in the vicinity of submarine canyons. Finally, if long period waves unrelated to the present storm are arriving, the bottom may be directly affected by wave surge and an associated residual velocity component. During this time, the central and inner shelves, if within the storm area, are experiencing a similar velocity field, with the oscillatory and residual wave components intensified on the bottom in proportion to the decreasing depth.

It may be more helpful for the interpretation of shelf-floor response elements to distinguish not between such genetic concepts as wind-drift and wave-drift currents, but instead between two operational bottom regimes; namely a unidirectional, storm-generated current in which the wind-drift component is a major residual and dominates over oscillatory wave surge; and surge-dominated flow, which characterizes (but is by no means limited to) the fair-weather hydraulic regime. The response element corresponding to surge-dominated bottom flow is, of course, an oscillation ripple field (Komar et al., 1972). The response elements associated with dominantly unidirectional storm currents have been little investigated, but on the central Atlantic shelf they appear to include asymmetric transverse ripples up to 20 cm high, asymmetric transverse forms up to 3 m high, and longitudinal sand ridges up to 10 m high (Swift et al., 1972).

Of concern also is the problem of over-reaction. The emphasis of Sternberg

and McManus and Creager-Sternberg on the importance of the wind-drift component in high-competence currents on nontidal shelves seems reasonable, but the advent of this ray of light on one aspect of the hydraulic climate is all the more reason to get a better fix on the significance of waves in shelf sediment transport. Part of the present emphasis on unidirectional shelf currents stems from our mode of observation; generally by means of Savonius rotor meters which are poorly designed for resolving wave surge. As noted by Creager and Sternberg, "If waves from severe storms on rare occasions influence the sediment distributions on the central and outer shelf, this is not detectable in the parameters studied." However, the problem is basically one of conceptual approach, since other workers in the same general area, with access to similar equipment, have come to very different conclusions concerning the role of wave action in sediment transport (Komar et al., 1972).

This role is thus at present ambiguous. Creager and Sternberg (1972) detect a wave-dominated zone landward of the 50-m isobath on the Washington shelf, while Komar et al. conclude that there is a significant wave-driven component of sediment transport as far seaward as rippling occurs on the adjacent Oregon shelf, or to depths in excess of 200 m. However, Komar et al., (1972), following the model of Bagnold (1963) stress that wave surge is an efficient mover of sediment mainly in conjunction with a superimposed unidirectional current. Not only does wave surge serve to entrain sediment, but as noted by Keulegan (1948), Scott (1952), and Bagnold (1963), complex synergistic effects occur whereby the movement of various size fractions of the pulsating sediment stream across a wave-rippled surface tends to be rectified, or even reversed. Here is a further potentially misleading aspect of the wave-drift versus wind-drift controversy. We are justly proud of our present concern with the hydraulic regime, but the outlines and dimensions of shelf sediment transport will continue to elude us until we undertake to directly monitor the sediment flux itself by sediment traps, tracers, time lapse photography, microbathymetric time series, or other means.

In the middle Atlantic bight, unidirectional, storm-generated currents appear to control constructional shelf topography well landward of Creager and Sternberg's 50-m boundary. The characteristic response element, the ridge and swale topography, appears as far inshore as the 10-m isobath, where it gives way to the wave-smoothed shore face. It appears to result in part from a helicoidal flow structure of storm-generated currents in the shallow-water generating zone. In the seaward sectors, the topography itself probably impresses this flow pattern on storm currents and consequently would tend to be maintained by it. Here surge-dominated flow serves primarily to degrade wave crests between storms, although Creager (personal communication) has made the interesting observation that the mid-shelf divergence of bottom drift noted by Bumpus (1962) in the Middle Atlantic Bight may reflect to some extent the shoreward residual compo-

nent of bottom wave surge on the inner shelf, as well as the salinity-driven circulation.

But any comparison of the east- and west-coast shelves must consider their respective regimes and substrates. The east-coast shelf is in the lee of the continent with respect to the prevailing westerlies, and has a very different and less intense wave climate, whereas the west-coast shelf has a high, rocky coast, whose shore face may be less suitable for the generation of a constructional ridge topography. Thus the ridge-building propensity of the east-coast shelf may tend to overshadow its response to wave-driven components of the hydraulic regime, just as the apparent inability of the west coast inner shelf to build ridges may tend to disguise the importance of the unidirectional component of storm-generated currents in that area.

PROBABILITY MODELS: ADVECTIVE VERSUS DIFFUSIVE SEDIMENT TRANSPORT

Creager and Sternberg object to Dunbar and Rodgers' (1957, p. 11) vivid, intuitive picture of drift currents generated by storms (quoted by Sternberg and McManus, 1972), presumably because the wave-versus-wind dichotomy is not considered. However, Sternberg and McManus' Fig. 4 (1972) is basically this quotation given flesh. It has been impressively quantified, but we still know only that sediment must have been moved first "one way, then another," and very little about the channels of energy transfer. Here, in our respective attitudes to the Dunbar and Rodgers quotation, lies a more basic difference in viewpoint than any emphasis on wave-drift or wind-drift velocity components. Flume studies show that bedload sand grains travel in a series of short trajectories punctuated by periods of rest. Dunbar and Rodgers (1957) inferred, and Sternberg and McManus (1972, Fig. 78) have demonstrated that on weather-dominated shelves, there is a higher order of intermittent storm-driven trajectories punctuated by rest intervals. In this hierarchy of intermittent movements, the role of diffusive sediment transport is large relative to that of advective transport, particularly in the large-scale movements. As noted by Sternberg and McManus, there is a net transport direction, but the variation among directions of successive trajectories is high. In consequence, the deterministic relationships expressed by the laws of classical sediment hydraulics can never fully resolve the regional sediment budget, and probabilistic analysis must be an important aspect of any such study.

In my 1970 paper, "Quaternary shelves and the return to grade," I considered a simple, qualitative, diffusion model for shelf sediment transport. I wanted to show that in the simplest case, with random movement of sediment on the shelf, there ensued a net cross-shelf transport to the shelf-edge sink. However, the random walk scheme that I described is a framework for conceptualization

and ultimately for calculation, and is not to be confused with a real process "associated" with residual currents "in some unstated manner" (Sternberg and McManus, 1972). As the model does not have the ability to simulate advective transport and preferred directions of movement, its virtue lies in its ability to accommodate the diffusive component of sediment transport. In our 1971 paper (Swift et al., 1971), we developed, on a qualitative basis, the more flexible general case, a Markov process model which permits preferred directions and paths of sediment movement. A first step in quantifying this model has been taken in this volume (Chapter 9). Thus when Creager and Sternberg represent me as saying on one hand that shelf transport is random and on the other hand that all significant components of the sediment transport scheme have onshore residuals, I can only reply that I hold neither of these opinions. I would suggest instead that the direction of residual currents depends on the climate and configuration of the shelf in question, that the role of diffusive processes is a strong one on some shelves, and that a probabilistic analysis of these processes is rewarding.

Advective shelf sediment transport is in fact probably shelf-parallel or nearly so in most cases (Swift et al.; Smith and Hopkins, 1972; McCave, 1972), due to the tendency of oceanic water movements to parallel pressure gradients. Cross-shelf diffusion may be volumetrically insignificant on some modern disequilibrium shelves. Ancient shelves, however, must frequently have had higher coastal sediment input, and the rate of cross-shelf diffusion of the finer grades of sand and silt, which travel largely by suspension, may have been much higher, as is probably the case today off large deltas.

There once transpired a debate between Nils Bohr and Albert Einstein concerning the role of probability in the universe (Cline, 1965). Einstein rejected a universe in which probabilistic laws played a significant role as being unworthy of its Creator, and considered probabilistic laws as merely expedient shortcuts to deterministic reality. Bohr noted that "blind chance" followed laws of precision and symmetry. He felt that these laws correspond to a deep level of reality, and considered them a credit to the Creator. Shelf geologists, faced with the complexities of diffusive sediment transport, must look thankfully to Bohr as a spokesman for a probabilistic approach.

REFERENCES

Bumpus, D. F. (1965). Residual drift along the bottom on the continental shelf in the middle Atlantic area. *Limnology and Oceanography* **10**[Suppl.], R50-R53.

Bagnold, R. A. (1963). The mechanics of marine sedimentation. *In* "The Sea Vol. 3 of The Earth Beneath the Sea." (M. N. Hill, ed.), p. 507-525. Wiley, Interscience, New York.

Cline, B. L. (1965). *Men who made the new physics*. 223 pp., Signet Science, New York.

Creager, J. S., and Sternberg, R. W. (1972). Some specific problems in understanding bottom sediment dispersal and distribution on the continental shelf. *In* "Shelf Sediment Transport:

Process and Pattern" (D. J. P. Swift, D. B. Duane, and O. H. Pilkey, eds.). Dowden, Hutchinson and Ross, Stroudsburg, Pa.

Dietz, R. S. (1963). Wave-base, marine profile of equilibrium and wave built terraces, a critical appraisal. *Geol. Soc. America Bull.* **74**, 971-990

Duane, D. B., Field, M. E., Meisburger, E. P., Swift, D. J. P., and Williams, S. J. (1972). Linear shoals on the Atlantic inner continental shelf, Florida to Long Island. *In* "Shelf Sediment Transport: Process and Pattern" (D. J. P. Swift, D. B. Duane, and O. H. Pilkey, eds.). Dowden, Hutchinson and Ross, Stroudsburg, Pa.

Dunbar, C. O., and Rodgers, J. (1957). "Principles of Stratigraphy." 356 pp., Wiley, New York.

Emery, K. O. (1952). Continental shelf sediments off southern California. *Geol. Soc. America Bull.* **63**, 1105-1108.

Galt, J. A. (1971). A numerical investigation of pressure induced storm surges over the continental shelf. *J. Physical Oceanography* **1**, 82-91.

Galt, J. A. (1971). A numerical investigation of pressure induced storm surges over the continental shelf. *J. Physical Oceanography* **1**, 82-91.

Griffiths, J. C. (1967). "Scientific Method in Analysis of Sediments." 508 pp. McGraw-Hill, New York.

Harrison, W., Norcross, J. J., Pore, N. A., and Stanley, E. M. (1967). Circulation of shelf waters off the Chesapeake Bight. *Environmental Science Services Administration Prof. Paper* **3**, 82 pp.

Johnson, D. W. (1919). "Shore Processes and Shoreline Development." 584 pp. Hafner, New York (1965 facsimile).

Keulegan, G. H. (1948). An experimental study of submarine sand bars. *Beach Erosion Board Tech. Rept.* **3**, 42 pp.

Komar, P. D., Neudeck, R. H., and Kulm, L. D. (1972). Observations of deep water oscillatory ripple marks on the Oregon continental shelf. *In* "Shelf Sediment Transport: Process and Pattern" (D. J. P. Swift, D. B. Duane, and O. H. Pilkey, eds.). Dowden, Hutchinson and Ross, Stroudsburg, Pa.

Moore, D. J., and Curray, J. R. (1964). Wave base, marine profiles of equilibrium, and wave built terraces: discussion. *Geol. Soc. America Bull.* **75**, 1267-1274.

Scott, T. (1954). Sand movement by waves. *Beach Erosion Bd. Tech. Memo.* **48**, 37 pp.

Shepard, F. P. (1932). Sediments on the continental shelves. *Geol. Soc. America Bull.* **43**, 1017-1039.

Sternberg, R. W., and McManus, D. A. (1972). Implications of sediment dispersal from long term, bottom-current measurements on the continental shelf of Washington. *In* "Shelf Sediment Transport: Process and Pattern" (D. J. P. Swift, D. B. Duane, and O. H. Pilkey, eds.). Dowden, Hutchinson and Ross, Stroudsburg, Pa.

Swift, D. J. P. (1970). Quaternary shelves and the return to grade. *Marine Geology* **8**, 5-30.

Swift, D. J. P., Holliday, B. W., Avignone, N., and Shideler, G. (1972). Anatomy of a shoreface ridge system, False Cape, Virginia. *Marine Geology* **12**, 59-84.

Swift, D. J. P., Stanley, D. J., and Curray, J. R. (1971a). Relict sediments on continental shelves: a reconsideration. *J. Geol.* **79**, 322-346.

Swift, D. J. P., Sanford, R. B., Dill, C. E., Jr., and Avignone, N. F. (1971b). Textural differentiation of the shore face during erosional retreat of an unconsolidated coast, Cape Henry to Cape Hatteras, western North Atlantic shelf. *Sedimentology* **16**, 221-250.

Reprinted from Bulletin of Geological Society of America *83*, No. 4, 877-883.

DONALD J. P. SWIFT
W. RICHARD BOEHMER
Institute of Oceanography, Old Dominion University, Norfolk, Virginia 23508

Brown and Gray Sands on the Virginia Shelf: Color as a Function of Grain Size

ABSTRACT

Brown iron-staining on coarse shelf sands has been taken as evidence of subaerial weathering, either in the source area or at the depositional site. However, we note that iron-staining can occur subaqueously, as well. We have found a close correlation between grain size and color on the inner Virginia shelf, with finer sands being olive-gray, and coarser sands being brown. We suggest that the sand-grain surfaces are in chemical equilibrium with their environment. The coarser sands are permeable, and are kept oxygenated by wave surge. The finer sands are relatively inpermeable, and are reduced by interstitial organic matter. While in any given case, brown iron-staining may have occurred sub-aerially, it may also have occurred in the modern marine environment. Hence brown iron-staining is not a definitive criteria for a relict origin or subaerial exposure of shelf sand.

INTRODUCTION

When Emery (1952) first categorized shelf sands as relict, residual, organic, authigenic, or modern detrital, he noted that one of the relict sediment masses on the California shelf was "medium- to coarse-grained brown sand that is iron stained and coarser than most of the other sediments." He later stated (Emery, 1965, 1968) that coarseness, a high degree of sorting, iron-staining, and solution pitting are characteristic of shelf sands relict from Pleistocene low stands of the sea. The reason for the coarseness and iron stain is not made explicit, although it is possible to infer that the pigment was generated by Pleistocene subaerial weathering, perhaps of associated heavy minerals, while the sorting and coarseness is a consequence of winnowing by the returned Holocene sea.

Since the initial observations of Emery, some workers have utilized coarseness and brown pigment to map and interpret "relict" sands on continental shelves. Pilkey and Frankenberg (1964) mapped the relict-recent sediment boundary on the Georgia coast by these criteria. James and Stanley (1968) noted that the Holocene "neosands" of the dunes of Sable Island on the Nova Scotia shelf were buff-gray (2.5Y7/4) and were relatively rich in opaque heavy minerals (40 to 60 percent of total heavy minerals) while the Pleistocene "paleosands" were red to orange (10YR6/6) and were relatively depleted of opaque heavy minerals (20 to 50 percent of total heavy minerals). They concluded that the paleosands were stained by weathering of the heavy minerals. They further noted (James and Stanley, 1968) that the reddish iron-stained sand grains of Sable Island Bank gave way to greenish, iron-stained sand grains in the muddy sands of the basin landward of the bank, below 132 meters. Stanley (1969) later considered the distribution of sediment color along the entire Atlantic continental shelf.

Judd and others (1970) were the first to attack the problem of iron-staining directly. They found that on the southeastern United States shelf, anomalously high percentages of iron-stained sand grains were found off river mouths. They further noted that beach sands of this province were characteristically iron-stained, despite presumed intense abrasion. They concluded that the pigment was generated in the piedmont source, rather than by Pleistocene subaerial weathering on the shelf depositional site.

Finally, Sanders and others (1970) inferred that brown shelf sands are the consequence of *in situ* Pleistocene weathering, while gray sands "were never extensively exposed above the water table"; and that relict coastal land forms may be traced by mapping sediment color.

Our studies of sediment distribution and morphology of the Virginia shelf (Swift and others, 1971, 1972a, 1972b) has caused us to be

Geological Society of America Bulletin, v. 83, p. 877–884, 4 figs., March 1972

wary of generalizations concerning pigment and grain size as criteria of "relict" versus "modern" sand. We note that the gray "nearshore modern sands" with their characteristic seaward decrease in grain size, are in our area confined to a narrow zone on the upper shore face between the breaker and the 10-m isobath (Swift and others, 1971). We believe that this belt of fine sand is most aptly described as a surf fallout, settled out of clouds of fine sand which drift down the shore face from the surf zone during periods of high waves (Cook, 1969). The sand on the adjacent sea floor consists of both the coarse brown types and the finer gray types, distributed over the subdued ridge and swale topography characteristic of the middle Atlantic shelf. We have noted (Swift and others, 1972a) that brown, coarse-grained, poorly sorted sand occurs on ridge crests, while gray, fine- to very fine-grained, well-sorted sand occurs on the ridge flanks (Fig. 1). We have interpreted this distribution as the interaction of storm-generated currents which scour out the troughs and aggrade the ridges, with fair-weather wave surge which winnows ridge crests and aggrades the flanks. We have concluded that the "modern" shoreface sands, and the "relict" sea-floor sands are each relict in the sense that they both are autochthonous sands derived by erosion of the pre-recent substrate, and are each modern, in the sense that they both exhibit textural gradients which reflect modern hydraulic processes.

During the course of our studies, we collected 5 vibracores as much as 10 m long, on a transect from shore to 15 km out. We noted that many cores contained brown sand in their upper meter, but all were a uniform medium dark gray below this surficial zone.

As a consequence of this observation, we propose a hypothesis concerning the significance of iron-stained shelf sands that we believe to be more economical than those previously cited, although it does not necessarily contradict these previous hypotheses. We suggest that while the pigment may ultimately stem from *in*

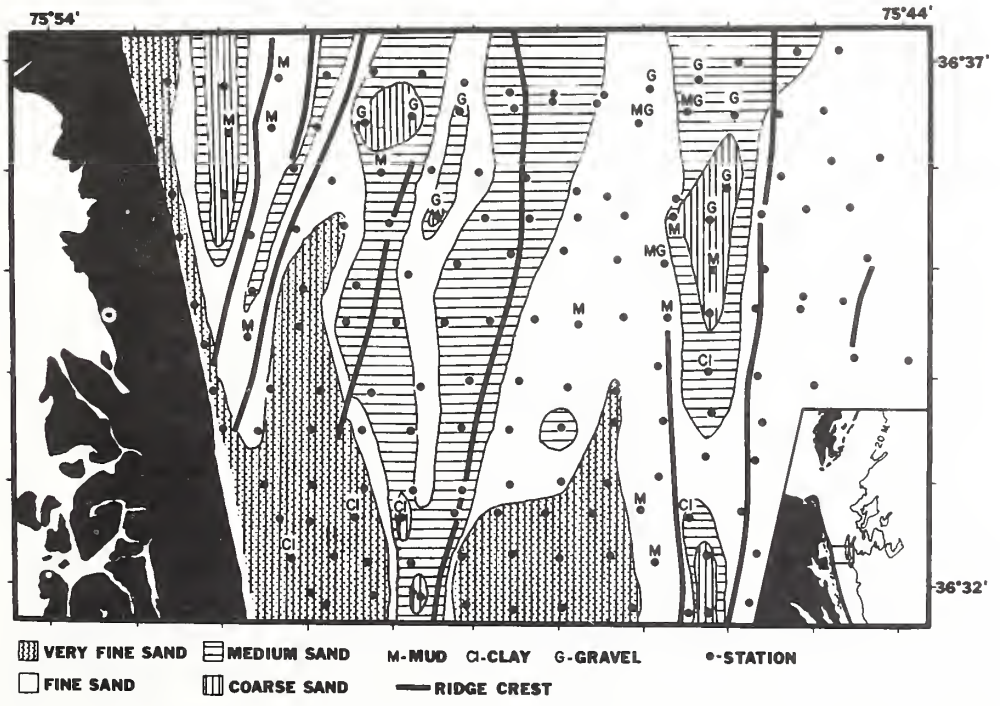

Figure 1. Distribution of median diameters over the False Cape ridge system. One km sample net is just able to resolve correlation of textural variation with topography. "Clay" refers to pre-Holocene substrate exposed in troughs. "Mud" consists of thin, ephemeral, fair-weather lenses that fill bottom depressions.

situ subaerial weathering, or weathering in the piedmont source area, it is immediately a function of grain size, and of the consequent chemical microenvironment at the depositional site.

To evaluate this hypothesis, we will trace the cycle of iron-stained shelf sand as described in the literature and then present a statistical analysis of the relation of pigment to grain size in our study area.

CYCLE OF IRON-STAINED SANDS

The surfaces of quartz grains are chemically active, due in part to unsatisfied bond on the surfaces of the silicate polymer. In fact, quartz grains whose surfaces have been stripped of their inert coatings by acid become so charged with static electricity that they appear "wet" and sticky, and will not sieve properly (J. C. Ludwick, 1969, personal commun.). As a consequence of this phenomenon, quartz grains are prone to acquire surficial coatings of hydrous iron oxides, iron-bearing clay minerals, and other materials during any stage of their sedimentary history (Fig. 2). The first possible stage is in the source area, either in an iron-precipitating B horizon of a metamorphic or igneous terrane which is serving as a primary source of quartz detritus and ferrous ions, or in the vadose zone of a coastal plain sand unit (Spoljaric, 1971). Under moist, oxidizing conditions, the precipitate is initially ferric hydroxide [$Fe(OH)_3$] which recrystallizes relatively rapidly to the mineral goethite ($HFeO_2$) (Schmalz, 1968). Dehydration may convert the yellow or brown hydroxide to red hematite (Fe_2O_3) if the climate includes periodic dry seasons. Under proper conditions, iron-bearing clays may also form on the surface of the quartz grain.

Oxidizing river waters transporting iron-stained sand have relatively little effect on the coatings on quartz grains, other than minor

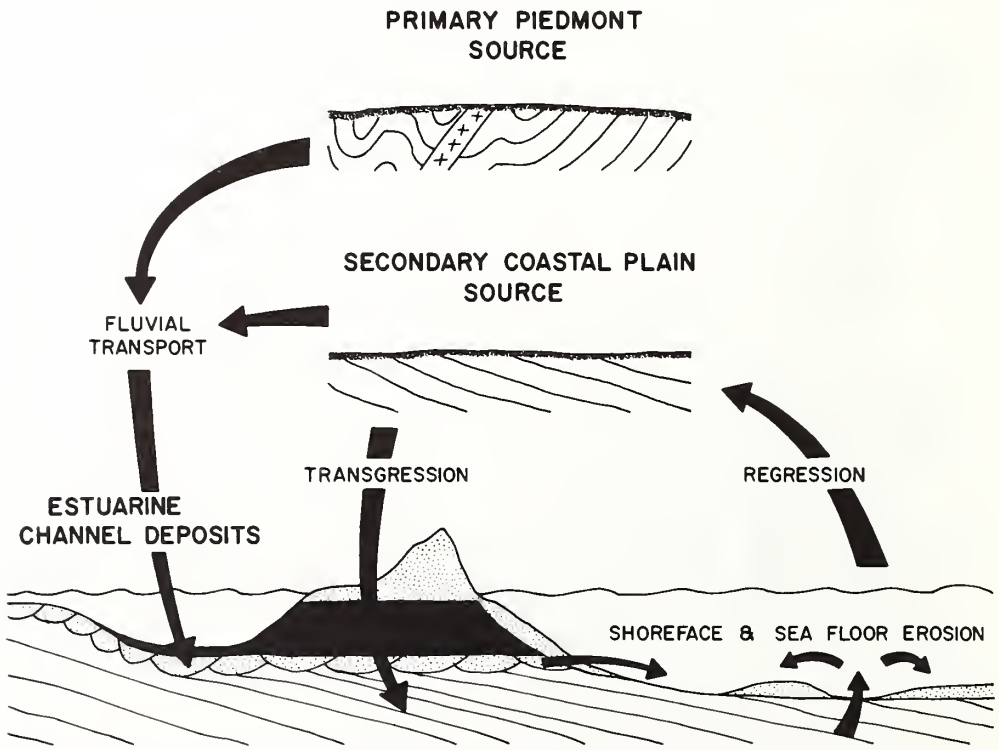

Figure 2. Proposed cycle of iron-stained sand on a Quaternary shelf. Sand from a piedmont or coastal plain source may travel downriver to be trapped in an estuary mouth, and be buried by a retrograding barrier. The retreat of the shore face results in the release of the estuarine sand, and also sand from subjacent older strata. Regression of the sea exposes the sand sheet thus formed to further subaerial erosion, and the cycle begins again. Iron precipitation on grain surfaces may occur at any stage.

mechanical abrasion. However, the effect of arrival of the grain at the river mouth is more complex. In addition to being bound to grain surfaces, iron also travels downstream as a colloid, stabilized by organic matter (Krauskopf, 1967). The colloid is flocculated as hydrous ferric ion at the river mouth (Lowman and others, 1965). If sea level is falling at this stage, the river mouth may have the configuration of a delta. The quartz bedload may be delivered to littoral drift with little effect on the surface coating except further slight abrasion, and the flocculated iron may be bypassed seaward. However, during rising sea level, the sand may be trapped out at the head of tide with mud, flocculated iron, and organic material accumulating in the interstices (Coonley and others, 1971). The resulting estuarine deposit may undergo diagenesis whereby the iron compounds are transmuted to hydrotroilite and ultimately pyrite or marcasite. If there is some movement of pore water or mechanical reworking at this stage, the quartz grain surface may actually be cleaned of the more mobile ferrous iron; otherwise it may simply have its coating transformed to greenish iron silicate or black iron sulphide.

If sea level continues to rise, estuarine and lagoonal sand deposits are transgressed by the surf. Erosion of the shore face releases these deposits for dispersal over the shelf. Sea-floor erosion also releases older coastal plain sands which are thus contributed to the sea floor directly, without having undergone fluvial transport. Sand grains released to the sea-floor blanket of reworked or "relict" sand from estuarine deposits may have their coatings reoxidized. Grains lying at the water-sediment interface may receive further iron hydroxide coatings, either from the overlying water column, or from interstitial waters. In extreme situations, iron concretions may form (Manheim, 1965, p. 225), or limonite oölites (Borchert, 1965). Ultimately, if the sea withdraws, the iron-stained shelf sands will become a secondary coastal plain source, delivering iron-coated grains and colloidal iron to the fluvial transport system.

It is noteworthy that the geochemical cycle for manganese is very similar to that for iron. Manganese colloids may conceivably be flocculated farther seaward in estuaries than is iron. However, manganese oxides are easily reduced in the presence of organic matter, and its sulfide and carbonate are too soluble to remain long in contact with seawater except where Mn^{++} is usually concentrated (Krauskopf, 1967, p. 268). Hence most brownish stains are probably predominantly iron. However, manganese crusts and manganese-stained coarse sediments have been reported from the Gulf of Maine and the shallow banks off New England and Maritime Canada (Manheim, 1965).

EVOLUTION OF IRON-STAINED SANDS ON THE CONTINENTAL SHELF

So few data as are presently available suggest that quartz sands, once released on the continental shelf, undergo further intermittent transport in response to periodic, storm-generated currents. Thus a given grain may be first buried under several feet of sand, exposed at the water-sediment interface, then buried again. The reworking process affects the size-frequency distribution of the matrix of grains in which a particular grain is encased; hence the grain may find itself in a coarse deposit at one time, and in a fine deposit at another. The color of a grain at any given time is a function of the thickness and composition of coating inherited from the preceding stage, the *p*H, Eh, ionic concentration, and other parameters of the chemical environment, and the relation of the grain's residence time in that stage to the time needed for the coating to attain chemical equilibrium.

We infer that most pigmented shelf sand grains have coatings that are relatively rich in iron, and that the rate of intermittent dispersal by periodic storm currents is low relative to the time required for the grain to come into equilibrium with its chemical environment. Hence the immediate chemical environment becomes the predominant control of pigment. Friedman and others (1968) have cored the Long Island shelf. They noted that Eh values were positive above the water-sediment interface and decrease below this interface to values as low as −85 mv. We suggest that in the uppermost layer of the shelf floor that is penetrated by a grab sampler, chemical environment is primarily a function of grain size. Coarse sands are inherently more permeable than fine sands and are consequently better aerated by sea-floor wave-surge currents. The tendency is augmented in our study area by the fact that coarse sands on wave-agitated ridge crests are better sorted than are the finer sands of ridge flanks (Swift and others, 1972a). The permeability of the fine flank sands is further reduced by the fact that these deposits

may contain as much as 15 percent clay, and their Eh is probably further reduced by an abundance of clay-sized organic matter. To the extent that these deductions are correct, coarse bottom sands should have the most oxidized coatings and should be the most nearly yellow-brown, while fine sands should be the least oxidized, and should be pigmented in some shade of green or blue (partially reduced iron) or neutral (totally reduced iron). The fine sands might be further pigmented a dark hue by their characteristically higher percent of heavy minerals and organic-rich clay fraction.

CORRELATION OF GRAIN SIZE AND COLOR, VIRGINIA SHELF SANDS

Methods

In order to test this hypothesis, we measured the grain size and color of 149 samples of sand collected from False Cape submarine sand ridge system on the Virginia shelf off False Cape, Virginia. The samples had been collected during a study of the ridge system in order to relate grain size to topography (Swift and others, 1972a). The samples were collected with a Shipek grab sampler on a 1 km grid (Fig. 1). This sample collection was selected for study because grain size varied through 4 phi units in an area so small that regional petrographic gradients influencing color might be excluded. Median diameter of the −1 to 4 phi fraction was determined by means of a modified Woods Hole rapid sediment analyzer (Sanford and Swift, 1972). The samples had been stored for a year before color coding, which according to Stanley (1969) should shift hue to slightly more yellow values. Color was determined by means of visual comparison of wet samples with "the Munsell Book of Color" (Munsell Color Co., 1929–1960), in terms of hue, value, and chroma. All estimations were made under an overhead fluorescent light. Fifteen of the samples were selected at random for a "main effects" test, to determine the effect of various petrographic components on color. They were wet-sieved to determine percent fines, and their heavy fractions were extracted by means of bromoform flotation. Their carbonate fractions were removed by acid digestion. The colors were estimated before and after the removal of fines and heavies. Color was not estimated after the removal of carbonate, since the acid solution became strongly discolored, and had clearly removed much of the iron-staining as well.

Results

In order to assess the relation of grain size to color, stepwise multiple linear regression was performed, with grain size as the dependent variable, and hue, value, and chroma as the independent values. Correlation coefficients calculated in the course of this test indicated that grain size varies in sympathy with hue but not with variation in value and chroma. Figure 3 represents the scatter of hue–grain size values, with a regression line calculated with grain size as the independent parameter. The correlation coefficient for the two sets of data is 0.61, indicating that hue is positively correlated with phi median diameter. The regression coefficient (slope of line in Fig. 3) is 0.32. An F test indicates that it is significant at the 99 percent confidence level (there is less than one chance in a hundred that the regression line as estimated has zero slope). Due to the method used for estimating color, only four hue classes are present (Table 1). Presumably, the correlation would have been stronger if a more sensitive method of determining hue were used. Figure 4 shows that for the two main color classes, hue is

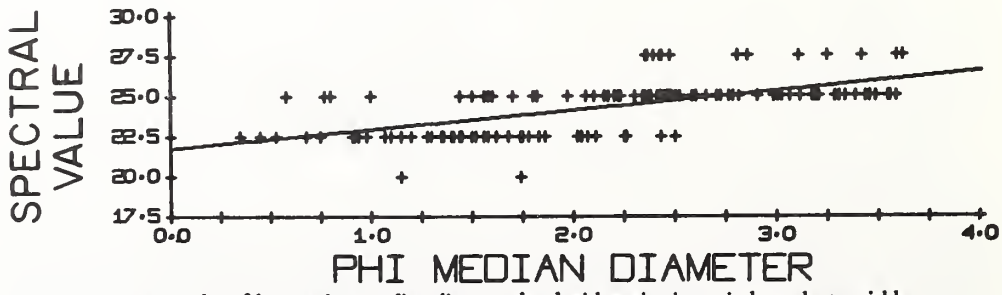

Figure 3. Scatter plot of hue against median diameter for False Cape samples, and regression line calculated with grain size as independent variable.

TABLE 1. CHARACTERISTICS OF HUE CLASSES

Hue notation	Spectral value	Name	Average Phi median diameter	Range, Phi median diameter	Number of samples
1.0YR	20.0	Reddish-brown	1.44	1.15–1.74	2
2.5Y	22.5	Brown	1.58	0.58–3.55	40
5.0Y	25.0	Olive	2.61	0.35–2.50	94
7.5Y	27.5	Olive-gray	2.79	2.39–3.61	13

continuously distributed with an approximately normal distribution through the grain size spectrum.

The compositional analysis of the "main effects" 15 samples indicated that they contained 0.7 to 8.5 percent clay, 0.2 to 2.6 percent heavy minerals, and 1.0 to 17.7 percent of acid-soluble material (Table 2). The acid-soluble material, by inspection mainly carbonate, was randomly distributed through the grain-size spectrum. Many of the coarser shell fragments were strongly iron stained.

The percent of fine and heavy minerals increase with decreasing grain size. The fine fraction was medium gray (N5) to light olive-gray (5Y5/2). A heavy mineral analysis of the area (Swift and others, 1972b) indicates that dark-green amphibole is the most abundant translucent heavy mineral in the finer sands. The fine and heavy mineral fractions could conceivably form part of the pigmentation of the olive and olive-gray sands. However, only two of the 15 samples changed color (from olive to brown) during the sequential removal of these components.

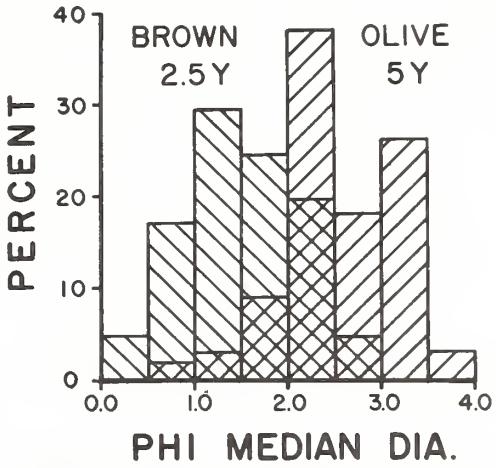

Figure 4. Histograms of median diameters for brown and olive sands.

TABLE 2. ACCESSORY COMPONENTS OF 15 SAMPLES

Phi grain size	Initial color	Percent fine minerals	Percent heavy minerals	Percent carbonate
0.45	5Y3/2	0.48	0.52	1.15
0.53	2.5Y4/2	0.88	0.20	0.96
0.92	2.5Y4/2	1.26	0.26	5.38
1.15	2.5Y4/2	0.79	0.17	2.06
1.35	2.5Y3/2	3.76	0.26	17.99
1.44	5Y3/2	8.01	0.27	3.78
1.58	5Y4/2	1.74	0.57*	1.15
1.62	2.5Y4/2	0.75	0.13	2.02
2.06	5Y3/2	1.31	1.35	3.51
2.25	2.5Y3/2	2.55	0.46	1.19
2.47	2.5Y3/2	2.45	0.43	1.80
2.52	5Y3/2	2.68	0.71*	1.80
2.81	5Y4/1	4.99	2.59	1.95
3.20	5Y3/2	6.32	0.79	3.73
3.45	5Y3/2	8.51	1.69	17.71

* *Removal of heavy minerals shifted color to 2.5Y4/2.*

CONCLUSIONS

On the inner Virginia shelf, sand pigmentation is correlated with median grain size. Coarse- and medium-grained sands exhibit a brown hue, while fine- and very fine-grained sands exhibit an olive or olive-gray hue. The pigment may be ultimately inherited from the source area, may be the result of *in situ* subaerial precipitation, may be the product of modern submarine precipitation, or may reflect all three factors. In every case however, the iron pigment appears to be in equilibrium with the interstitial chemical environment as determined by grain size, and hence permeability of the sand. In our study area, the systematic distribution of brown pigmented "relict" sands reflects only a systematic distribution of grain sizes which are a consequence of the hydraulic regime of the returned Holocene sea (Swift and others, 1972b). Consequently, we conclude that iron-staining by itself is not a definitive criterion for a relict origin of shelf sands.

ACKNOWLEDGMENTS

The samples used in this study were collected in the course of an examination of the inner Virginia shelf supported by Contract DACW–

72–69–C–0016, of the Coastal Engineering Research Center; by Grant GA–13837 from the Oceanography Section, National Science Foundation; and by the Office of Marine Geology, U.S. Geological Survey. Our study has profited from our discussions with J. C. Ludwick and W. Smith of the Institute of Oceanography, Old Dominion University, and with John Sanders and Naresh Kumar of Columbia University.

REFERENCES CITED

Borchert, H., 1965, Formation of marine sedimentary iron cores, *in* Riley, J. P., and Skirrow, G., Chemical oceanography, Vol. 2: New York, Academic Press, p. 159–204.

Cook, D. O., 1969, Sand transport by shoaling waves [Ph.D. dissert.]: San Diego, Southern California Univ., 148 p.

Coonley, L. S., Baker, E. B., and Holland, H. D., 1971, Iron in the Mullica River and in Great Bay, New Jersey: Chem. Geology, v. 7, p. 51–63.

Emery, K. O., 1952, Continental shelf sediments off southern California: Geol. Soc. America Bull., v. 63, p. 1105–1108.

—— 1965, Geology of the continental margin off eastern United States, *in* Whittard, W. F., and Bradshaw, R., eds., Submarine geology and geophysics: London, Butterworths, 464 p.

—— 1968, Relict sediments on continental shelves of the world: Am. Assoc. Petroleum Geologists Bull., v. 52, p. 445–464.

Friedman, G. M., Fabricand, B. P., Imbimbo, E. S., Brey, M. E., and Sanders, J. E., 1968, Chemical changes in interstitial waters from continental shelf sediments: Jour. Sed. Petrology, v. 38, p. 1313–1319.

James, N. P., and Stanley, D. J., 1967, Sediment transport on Sable Island, Nova Scotia: Smithsonian Misc. Colln., v. 152, 33 p.

—— 1968, Sable Island bank off Nova Scotia: Sediment dispersal and recent history: Am. Assoc. Petroleum Geologists Bull., v. 52, p. 2208–2230.

Judd, J. B., Smith, W. C., and Pilkey, O. H., 1970, The environmental significance of iron-stained quartz grains on the southeastern United States Atlantic Shelf: Marine Geology, v. 8, p. 355–362.

Krauskopf, K. B., 1967, Introduction to geochemistry: New York, McGraw-Hill, 721 p.

Lowman, F. G., Quinones, L., Miro, M., Oliver De Padovani, I., Ramos, E., Roman De Vega, V., and Bielen, H. J., 1965, Investigations of trace element distribution in marine waters and sediments: Pan American Union, Inter-American symposium on the peaceful application of nuclear energy, 5th, Washington, D. C., p. 233–259.

Manheim, F. T., 1965, Manganese-iron accumulations in the shallow marine environment, *in* Schink, D. R., and Corless, J. T., *eds.*, Marine geochemistry: Rhode Island Univ. Graduate School Oceanography Occasional Pub. 3, p. 217–276.

Pilkey, O. H., and Frankenberg, D., 1964, The recent-relict sediment boundary on the Georgia continental shelf: Georgia Acad. Sci. Bull., v. 22, p. 1–4.

Sanders, J. E., Friedman, G. M., Caldwell, D., and Kumar, N., 1970, Stratigraphic relations, brown and gray relict Quaternary shelf sediments: Geol. Soc. America Abs. with Programs, v. 2., p. 672–673.

Sanford, R. B., and Swift, D.J.P., 1972, Comparison of sieving and settling techniques for size analysis, using a Benthos Rapid Sediment Analyzer: Sedimentology (in press).

Schmalz, R. F., 1968, Formation of red beds in modern and ancient deserts: Discussion: Geol. Soc. America Bull., v. 79, p. 277–280.

Spoljaric, N., 1971, Origin of colors and ironstone bands in the Columbia Formation, Middletown-Odessa Area, Delaware: Southeastern Geology, v. 12, p. 253–266.

Stanley, D. J., 1969, Atlantic continental shelf and slope of the United States—color of marine sediments: U.S. Geol. Survey Prof. Paper 529–D, p. D1–D14.

Swift, D.J.P., Sanford, R. B., Dill, C. E., Jr., and Avignone, N. F., 1971, Textural differentiation on the shore face during erosional retreat of an unconsolidated coast, Cape Henry to Cape Hatteras, western North Atlantic shelf: Sedimentology, p. 221–250.

Swift, D.J.P., Holliday, B. W., Avignone, N. F., and Shideler, G. L., 1972a, Anatomy of a shore face ridge system, False Cape, Virginia: Marine Geology (in press).

Swift, D.J.P., Dill, C. E., Jr., and McHone, F., 1972b, Hydraulic fractionation of heavy mineral suites on an unconsolidated retreating coast: Jour. Sed. Petrology (in press).

MANUSCRIPT RECEIVED BY THE SOCIETY JUNE 11, 1971

AUTHORS' PRESENT ADDRESSES: ATLANTIC OCEANOGRAPHIC AND METEOROLOGICAL LABORATORIES, NATIONAL OCEANIC AND ATMOSPHERIC ADMINISTRATION, MIAMI, FLORIDA 33130 (SWIFT). MARINE AFFAIRS PROGRAM, UNIVERSITY OF RHODE ISLAND, KINGSTON, RHODE ISLAND 02852 (BOEHMER)

Reprinted from Shelf Sediment Transport, edited by Swift, Duane and Pilkey © Dowden, Hutchinson and Ross, Inc., Stroudsburg, Pa., 195-223.

CHAPTER 9

Shelf Sediment Transport: A Probability Model

Donald J. P. Swift,* John C. Ludwick,† and W. Richard Boehmer‡

ABSTRACT

For many purposes the most useful conceptual framework for the study of detrital sediments is that of the sediment transport system. A system is comprised of a sediment source, and a dispersal zone which is at once a conduit and sink. Sediment transport systems impress granulometric and other petrographic gradients on their deposits by means of progressive sorting and similar mechanisms.

Markov process modeling is a versatile and illuminating method for testing assumptions concerning sediment-transport systems. Transition probabilities are employed as operational substitutes for incompletely understood physical mechanisms. In particular, the granulometric evolution of a detrital sediment stream through a dispersal zone may be examined stage by stage.

A simple, one-dimensional model consists of a Markov chain of nine transient states with nonzero transition probabilities between adjacent states only. Each transient state has associated with it an absorbing state from which the system (sand grain) cannot exit. For all trials, the transient state on the left side of the model (proximal state) has an initial state probability of unity. This fixes the place of sediment introduction. Ten transition probability matrices, one for each half-phi fraction of a hypothetical input sand, are used in ten successive trials. Calculation of the limiting state probability distribution permits the further calculation of simulated sediment size frequency distributions across a hypothetical shelf.

The model shows that progressive size sorting will occur along a sediment transport system

*Atlantic Oceanographic and Meteorological Laboratories, National Oceanic and Atmospheric Administration, 15 Rickenbacker Causeway, Miami, Florida 33149.

†Institute of Oceanography, Old Dominion University, Norfolk, Virginia 23508

‡Marine Affairs Program, University of Rhode Island, Kingston, Rhode Island 02892

if the transport is occurring over a depositional surface. If the input size distribution is not approximately normal, the distribution will evolve towards that configuration during the sorting process. In several variants of the model, standard deviation tends to decrease and kurtosis to increase. Skewness may increase, especially if the transport competence declines across the system.

While a one-dimensional Markov model of shelf sediment transport is useful for analyzing the textural or compositional evolution of sediment, two-dimensional models should permit evaluation of depositional topography, and the hydraulic mechanisms that produce shelf sand bodies.

INTRODUCTION

The study of sediments has witnessed an evolution of the central conceptual model of the discipline, from a stratigraphic product model, in which attention was primarily focused on the distribution of lithologies in three dimensions, to a stratigraphic process model based on the characteristics of depositional environments which produced the lithologies, and the changes of these characteristics through time. A further evolution of the model appears to be occurring as our accumulated knowledge of ancient sediments is increasingly supplemented by hydraulic analysis of modern sedimentary environments. This trend is concerned with dynamic systems of sediment transport. Its ultimate goal is not total resolution of the depositional environment, but instead analysis of sediment flux and quantification of the sediment budget.

The study described below is our initial attempt at development of a probability model of shelf sediment transport, as a tool in the analysis of shelf-transport systems and effects on grain-size distributions. However, because we have had to start at a very fundamental level, we find that our model is adaptable to almost any transport system.

SEDIMENT TRANSPORT MODELS

A basic conceptual model of a sediment transport system requires a planetary surface. In our own case, we are concerned with interfaces between the earth's several fluid envelopes and the lithosphere. The model is driven mainly by solar energy expended in the presence of a gravitational field. The surface is conveniently divided into a sediment-source area, a sediment conduit or gradient (Tanner, 1962), and a sediment sink. A slightly more advanced model recognizes that the second two elements are to a large extent synonymous; hence the model might be more realistically divided into a source area and a dispersal zone.

A real-world sediment-transport system may consist of any of the following: (a) an eroding headland, a zone of littoral drift, plus the expanding tip of a spit; (b) a drainage basin, its river net, plus a marine delta; (c) a shelf with relict sediment, a canyon and submarine fan, plus an aggrading abyssal plain; or (d) a desert deflation surface and adjacent dune belt.

Such sediment-transport systems may be identified in nature on the basis of circumstantial evidence, since the systems serve as filters whose sediment outputs differ systematically from their sediment inputs. The differences are usually observed as gradients in grain-size parameters, mineral composition, or other easily measured petrographic attributes within the sediment transport system. Most of these petrographic gradients have been attributed to "progressive sorting," whose effects have been described by Russell (1939) as:

> Shown by progressive changes in the characteristics of sediments, and can be detected by the analysis of a series of samples taken in the direction of transportation. . . . Progressive sorting may produce a progressive decrease in the mean grain size of sediments. There appear to be two possible causes of such a decrease; a progressive decrease in the competency of the transporting agent, and the lagging behind of the larger particles due to fluctuations in competency.

The latter idea has been expressed more succinctly as "the fines outrun the coarser particles." The concept of a sediment transport system identified by petrographic gradients appeared very early in sedimentological literature, and is ably summarized in the chapter on dispersal in Pettijohn's second edition (1957) of *Sedimentary Rocks*; but has received little notice in the interim. Since then attention has been focused on regional patterns of bedforms as indicators of sediment transport or "paleocurrent systems." More recently, examination of modern sediment transport systems has resulted in renewed interest in diagnostic petrographic gradients of sediment transport systems. Some recent studies of modern sediment transport systems revealed by petrographic gradients are the reports of Northrup (1951) on the southern New England shelf, of Stride (1963) on the sand streams of the western European shelf, Allen's (1965) analysis of prodelta sands on the Nigerian shelf, the studies by James and Stanley (1968) on sediment transport on the Nova Scotian shelf, and Beall's (1970) study of the fractionation of fine sand in the Mississippi River delta. These studies suggest that the "graded shelf" hypothesis of Johnson (1919) and the "relict shelf" hypothesis of Shepard (1932) and Emery (1952) are both partly correct. It appears that with time, continental margins tend to develop integrated cross-margin sediment transport systems. Systems of modern shelves have been disrupted by the Pleistocene sea-level fluctuations, but textural grade may be beginning to return (see Swift et al., 1971). We are not concerned here with larger implications of this premise, but merely note that textural gradients do locally exist in shelves, and propose a probabilistic model for their generation.

At this large scale of observation, the deterministic laws of sediment transport, as elucidated by hydraulic engineers and experimental sedimentologists, are not directly useful. Modeling of sediment-transport systems calls rather for a sort of statistical mechanics in which the element processed is seen as a population of particles whose behavior is best predicted by a probabilistic model. Deterministic laws of sedimentation have allowed us to estimate the behavior of a single-

sediment particle entrained by a fluid on the basis of such parameters as grain size, shape, and density; and water temperature, density, and viscosity. Aggregate behavior is commonly inferred from single grain calculations. Probabilistic models postulate individual grain behavior, but permit direct evaluation of aggregate behavior, by focusing on a fundamental characteristic of entrained sediment; the propensity of individual particles to travel in a sequence of discrete, independent trajectories of varying orientation punctuated by periods of rest. These trajectories occur on at least two scales. At the smallest scale, saltating or rolling grains entrained in moving turbulent fluids undergo intermittent movement, with mean travel times on the order of seconds. Migrating bedforms impose residence times of their constituent grains of minutes to centuries. Grains suspended by fluids are subject to small-scale turbulence, and their trajectories may be viewed as a sequence of discrete steps separated by infinitely small residence times. A probabilistic model of sediment transport in random steps has recently been devised by Yang (1971a,b).

But sediment transport of the scope described on previous pages is intermittent on a larger scale. Rivers move most of their sediment during floods, and shelf surfaces are quiescent between storms, while hemipelagic environments are dependent on intermittent turbidity currents for sand input.

DIFFUSION MODEL

Thus a basic probabilistic model of sediment transport is a diffusion model. This is not to imply that the mean transport vector in such a system is zero. A case commonly studied in thermodynamics is a cylinder, partitioned into two chambers, one of which is evacuated. Air molecules in the remaining chamber are characterized by successive movements whose path lengths and orientations may be described as randomly distributed. If the partition is removed, the molecules redistribute themselves uniformly throughout the cylinder by means of these random movements. During the redistribution process, however, there is a net movement from one part of the cylinder to another. A simple geological analogy would be a hypothetical shelf with fluvial sediment input linearized by littoral drift. Sand escaping this linear source may then be distributed over the shelf by intermittent storm-generated currents of widely varying orientation and intensity (Swift, 1970). Net sand transport, however, must be directed seaward across the shelf in this hypothetical example.

But this example is unrealistic, since winds are systematically distributed within storms, and storm tracks are systematically distributed over the earth's surface. Therefore, a preferred sediment transport direction is to be expected. However, probabilistic methods are amendable to anisotropic situations, and are generally preferable to deterministic ones when the diffusive component

(short term, variable movements) in the transport process is large with respect to the advective ("mean current") component.

Diffusion is a process by which matter is transported from one part of a system to another as a result of random motions (Crank, 1957). The simplest diffusion model would consist of a surface with polar coordinates and a point sediment source at the origin. If a coefficient of diffusion, D, is assigned to the sediment, then the concentration C of sediment over the surface at time T and distance x is given by

$$C = \frac{1}{2(\pi DT)^2} e^{\frac{-x^2}{4DT}}$$

Figure 82, showing concentration-distance curves for successive values of DT, is of particular interest to sedimentologists, for if different values of D are assigned to different size classes of sediment, and these classes are allowed to diffuse simultaneously, then the set of values C_{D1}, C_{D2}, C_{D3} . . . C_{Dn} for each successive value of x would correspond to the successive-size frequency distributions of a sediment-transport system in which progressive sorting is occurring.

As presented, the model is inadequate for the analysis of sediment transport. Preferred directions of movement cannot be programmed. A more subtle but equally serious problem is that the model makes no provisions for the withdrawal of sediment from the system into permanent storage, analogous to deposition. The result is that a sequence of ephemeral states may be observed, in which different geographic stations have different size frequency distributions. However, in the equilibrium state the model has been depleted of all sediment,

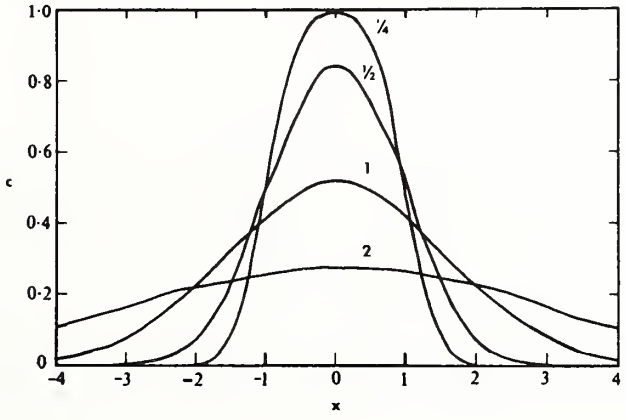

Figure 82.

Concentration-distance curves for a diffusion model. x = distance; c = concentration. Successively flatter curves are for successively larger values of DT.

or if it is a closed system with reflecting boundaries, the concentration for each size class is homogeneous throughout the model and size distributions at every point are equivalent to that of the input distribution. As noted by Pettijohn (1957, p. 541) this problem has disconcerting implications for Russell's (1939) concept of progressive sorting, in which the "fines outrun the coarse particles." The problem can be restated in graphic terms by considering an expressway at rush hour, whose traffic consists of cars and trucks. The onset of rush hour is signaled by a truck-free wave of the faster cars. However, after the arrival of the first slow-moving trucks at the point of observation, the mix of trucks and cars must remain constant, as long as the supply and speeds of each are constant. Clearly, for progressive sorting to occur in a sediment transport system, the sediment conduit must also be a sediment sink. Sediment particles must be selected for permanent deposition, and some sizes of particle must have higher probabilities of being so selected than others.

More advanced diffusion models overcome these difficulties. The simplistic geometry of Fig. 82 can be manipulated, and diffusion constants can be made to vary in time and space so as to simulate advective transport (Jost, 1960). Aspects of diffusion theory relating to heat sinks may be used to simulate selective deposition of sediment. However, the mathematics are abstruse, and it is difficult to intuitively grasp the evolution of particle populations modeled in this fashion.

MARKOV PROCESS MODEL

An alternative model using Markov processes permits ready visualization of aggregate-grain behavior during sediment transport. A Markov process model consists of states, which for the purposes of a sediment-transport model are locations on a Cartesian surface (Fig. 83). The term "state" is unfortunate in that it commonly has a time rather than a space connotation, but it is thoroughly established in Markov literature. Each state has associated with it a probability of transition to every other state in the chain. For a sediment transport model, these transition probabilities have nonzero values only between adjacent states. An important aspect of first-order Markov models is that they exhibit the Markov property: the probability p_j of the "system" (sand grain, for our purposes) occupying a given state, j, after having occupied the previous state i, is dependent on the probability $p_{i \rightarrow j}$, the probability of moving from state i to state j. First-order Markov models, therefore, have short "memories" extending for only a single transition. Higher order Markov processes "remember" more than one transition; since each state has associated with it probabilities for two or more successive steps.

Markov models, like diffusion models, may attain equilibrium. As well as transition probabilities, each state in a Markov chain has associated with it

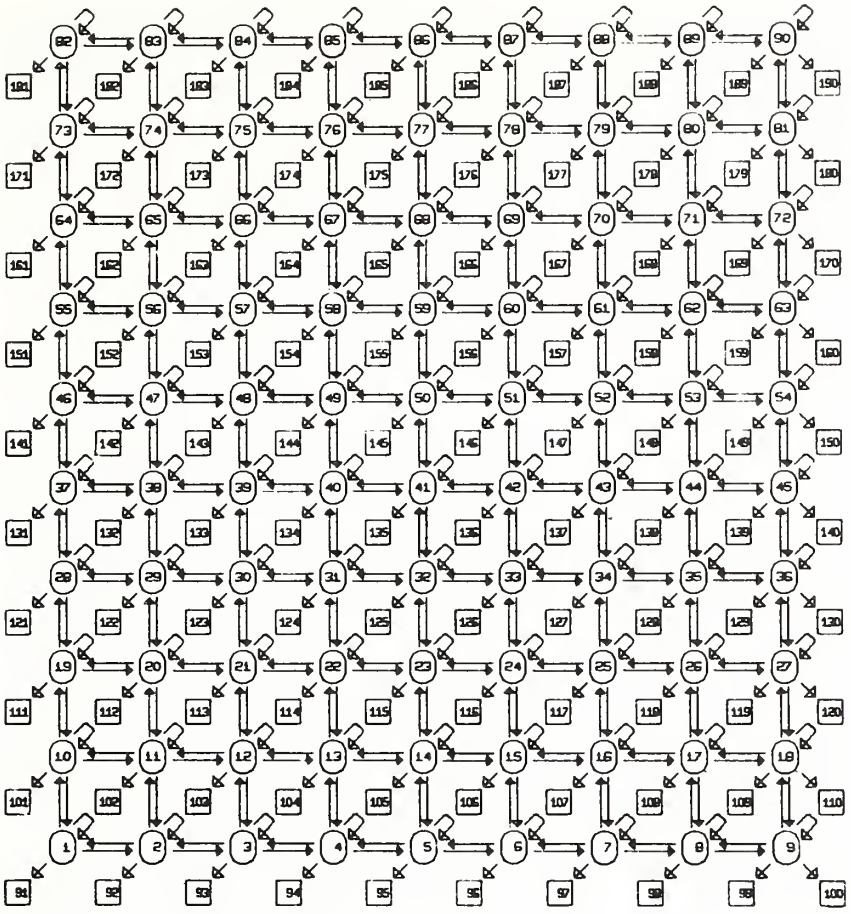

Figure 83.

A two-dimensional Markov model for simulating shelf sediment transport. Arrows are paths of transition between states. Circles are transient states which the system (a sand grain) can both enter and exit. Squares are absorbing states, with entrance paths but no exit paths. Transition probabilities for each path are associated with the source state. State probabilities, also associated with states, are the probabilities of the system occupying respective states after n transactions.

a state probability, or the probability of the system being that state after n transitions. With successive transitions, the state probability of a given state may asymtotically approach the limiting-state probability. For the Markov model of the kind shown in Fig. 83, the equilibrium distribution of probabilities is homogeneous only if all transition probabilities are equal. For a sediment transport model, the constraint that nonzero probabilities may occur only between adjacent states in the model means that strictly speaking, a uniform distribution of equilib-

rium probabilities will be impossible; there will always be boundary effects. Boundary states must have fewer permissible transitions; hence at least some of the associated transition probabilities must be larger than those of interior states.

This Markov model (Fig. 84) can be visualized as a sediment transport system by allowing a sand grain to work its way through it. Any state may be chosen as the starting state. The permissible exits from each state are given equal probabilities, and are assigned numbers one through four for north, east, west, and south transitions. The successive transitions may be selected by means of a random number table. If a large number of grains are introduced simultaneously, then "sediment" in a state of random diffusion is simulated. Preferred directions and pathways of sediment movement can be programmed into the model by specifying the appropriate initial state, and an appropriate matrix of transition probabilities.

A significant virtue of a Markov model is its ability to simulate an open system, whereby in the case of a sediment transport model, sediment is permanently lost at appropriate sites to deposition and burial. This is accomplished by adding states whose only nonzero transition probability is to itself: an autotransition. In the Markov models shown in Figs. 83 and 84, such absorbing states are represented as squares. For the sake of a sediment-transport model, they can be pictured as existing in a plane below the plane of the transient states.

The introduction of absorbing states into a Markov model renders it nonergodic; that is, the limiting state probability distribution is now dependent on the selection of the starting state. The "equilibrium" attained by a nonergodic Markov model simulates a static rather than a dynamic equilibrium. An input-sediment load, simulated by many trials, diffuses through such a chain until all grains are in absorbing states, rather like the conclusion of pin ball game. Thus, in a nonergodic Markov model of sediment transport, both deposits and sediment in transit are simulated.

PROGRESSIVE SORTING IN A MARKOV PROCESS MODEL

A Progressive Sorting Model

The Markov process model for sediment transport described in the previous section may be used to further explore Russell's concept of progressive sorting. For simplicity's sake, a section (Fig. 84) through the two-dimensional model of Fig. 83 has been selected to simulate a generalized bedload transport system. State 1 is the *initial state* or sediment source where successive "grains" may be introduced. States 1 through 9 are transient states representing a sediment pathway. The pathway is leaky since each transient state is associated with an absorbing state (states 10 through 18), and a final absorbing state, 19 represents

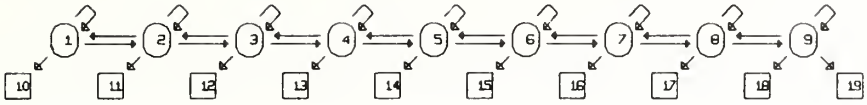

Figure 84.

A one-dimensional Markov model, equivalent to a cross section through Fig. 83. Circles are transient states; squares are absorbing states. Each set of one transient state and subjacent absorbing state comprises one geographical station in the Markov model. Farthest left station is shoreline, farthest right station, consisting only of an absorbing state, is the shelf edge.

Table XII
Size-Probability Matrix, Distribution Linear with Size and Invariant with Distance

	Grain size class									
	Coarsest ←									→ Finest
	1	2	3	4	5	6	7	8	9	10
Forward[a]	0.20	0.23	0.26	0.29	0.32	0.35	0.38	0.41	0.44	0.47
Backward[b]	0.20	0.23	0.26	0.29	0.32	0.35	0.38	0.41	0.44	0.47
Autotransition[c]	0.30	0.27	0.24	0.21	0.18	0.15	0.12	0.04	0.06	0.03
Trap[d]	0.30	0.27	0.24	0.21	0.18	0.15	0.12	0.04	0.06	0.03

[a] Doubled for first station, 0.000 for east station.
[b] 0.000 for first and last stations.
[c] 1.000 for last station.
[d] 0.000 for last station.

a sink at the end of the sediment pathway. Thus the 19 states combine to form a linear series of 10 geographical stations. This generalized system is for our purposes, a cross-shelf transect with a river mouth, aggrading shelf floor, and shelf edge; but it could be with suitable modifications a river, a littoral drift cell, a submarine fan valley, or any other conceivable transport system. In order to simulate progressive sorting in this Markov model it is necessary to consider a family of ten matrices of transition probabilities, one for each half Phi size class. The matrices are designed so that "very coarse sand" is most prone to being trapped, and "very fine sand" is the least prone. For simplicity, we have chosen a family of matrices with a linear relationship (Table XII) although in nature, the expression for the mobility of successive grain sizes must be a power function.

Procedure

The simplest method of determining the size frequency distributions of the deposits in absorbing states 10 through 19 would be to conduct, with the aid of a random number table, thousands of trials for each of the 10 matrices, then determine the relative proportions of trapped grains in equivalent states of each. This is an impractical procedure, and the same result can be obtained

by calculating instead the limiting state probabilities of the states (Howard, 1960; pp. 3-7) for each of the 10 matrices. The initial state probability distribution for the Markov model of Fig. 84 can be expressed as a row vector; [1 0 0 0 . . . 0] indicating that when the system (sand grain) is in its initial state, there is a unit probability that it is in state 1. The state probability vector after the first transition S(1) can be found by post-multiplying the initial state probability vector S(0) by the transition probability matrix, P. Thus

$$S(1) = S(0)P$$

Likewise

$$S(2) = S(1)P = S(0)P^2$$

In general, the state probability vector of any transition S(n) can be found by post-multiplying the initial state probability vector S(0) by the nth power of the transition probability matrix P.

$$S(n) = S(0)P^n$$

In each state of the chain the successive state probabilities associated with successive transitions forms a sequence that asymptotically approaches the limiting state probability, thus

$$S(L) = S(0)P^{\infty}$$

Limiting state probability distributions can be calculated by recursion, by solving simultaneous equations, or by means of a zeta transform (Howard, 1960, pp. 3-12).

Sorting of a Rectangular Input Distribution

In order to model progressive sorting, ten transition probability matrices (see Tables XII and XIII) were designed to simulate the diffusion of 10 half phi sand classes through the Markov model of Fig. 84. Since the limiting-state probabilities values of the 10 chains were equally weighted a rectangular (uniform) input distribution has been assumed.

Limiting state probability distributions generated by these transition probability distributions are presented in Fig. 85a as percentages, indicating the distributions of different grades of sand across the "shelf." Figure 85a indicates that within each size class, the sediment is distributed according to a negative exponential function of the variety $Y = e^{-ax}$ where Y is the percent of sand present at distance x, e is the base of natural logarithms, and "a" is a coefficient determining the rate of sediment size decrease. This coefficient must become larger for successively finer-grained size classes.

Strong boundary effects are present at the ends of the geographic distributions.

Table XIII
Transition Probability Matrix for Size Class 1, Distribution Linear with Size and Invariant with Distance

From station	To station																	
	1	2	3	4	5	6	7	8	9	10	11	12	13	14	15	16	17	18	19
1	0.30	0.40								0.30									
2	0.20	0.30	0.20								0.30								
3		0.20	0.30	0.20								0.30							
4			0.20	0.30	0.20								0.30						
5				0.20	0.30	0.20								0.30					
6					0.20	0.30	0.20								0.30				
7						0.20	0.30	0.20								0.30			
8							0.20	0.30	0.20								0.30		
9								0.20	0.30									0.20	0.30
10										1.00									
11											1.00								
12												1.00							
13													1.00						
14														1.00					
15															1.00				
16																1.00			
17																	1.00		
18																		1.00	
19																			1.00

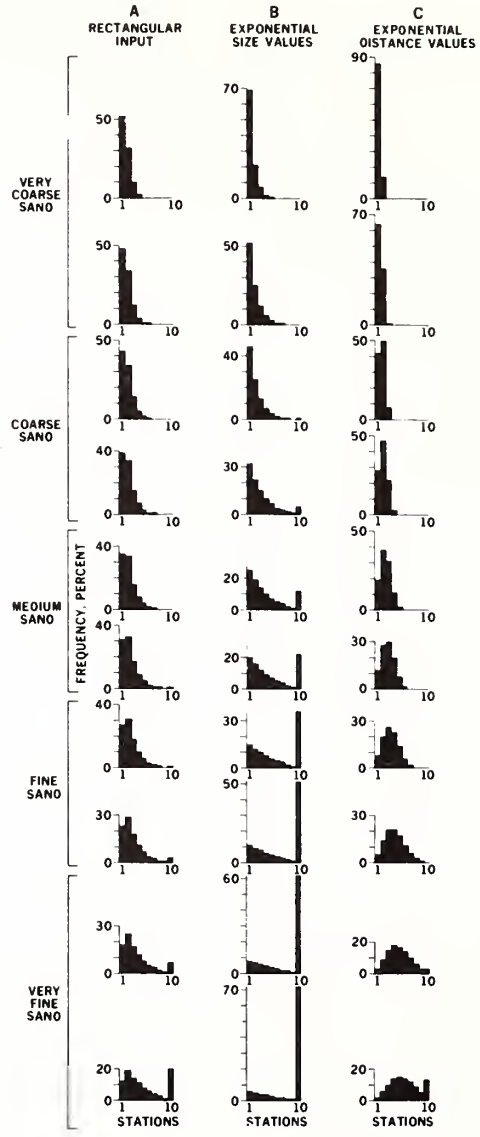

Figure 85.

Percent deposition of sand by geographic station for each of the 10 sizes classes, as calculated for the 4 variants of the model. Each distribution is a cross-section through the model, showing where most of the sand of that particular size class was deposited.

The "river mouth" (station 1) is an area of retarded deposition due to the fewer exit paths of its transient state and the necessarily higher probabilities associated with them, a not unrealistic feature in that real estuaries often have

scour trenches associated with their mouths. The last station (10) corresponding to the upper continental slope, has an anomalously high deposition as a consequence of having no exit paths. The anomalies are the most pronounced for the finest, most mobile sediment class. They appear in plots of size parameters against distance (Fig. 87), as well in the geographic and grain size distributions of Figs. 85a and 86a.

Vertical sections through each of the size classes of the 10 geographical distributions are recalculated to 100% in Fig. 86a. These constitute the grain size frequency distributions of sand deposited at these stations.

In successive stations, the mode may be seen to progress through the sequence of size frequency distributions in a wavelike fashion, and the variation in mean size (Fig. 87) indicates that this mathematical model does indeed simulate progressive size sorting. The concavity in the decreasing curve for mean and the steady decrease in the standard deviation (Fig. 87) results from autotruncation of the distribution as the wavelike progression of the mode reaches the lower limit of the initial size distribution.

It is noteworthy that the initial "rectangular" distribution appears to evolve toward a normal distribution during the sorting process. The size distribution at station 1 consists of a linear decrease in relative sand abundance toward the fine end of the distribution. At stations 2 and 3 however, a mode or maximum may be seen, with frequencies decreasing away from it in both directions. By station 6, the mode has reached the finest class. However, continued evolution towards a more nearly normal distribution is apparent as a gain in modal frequency at the expense of the remaining classes, and as an increasingly steeper exponential form for the coarse side.

Sorting of a Normal Input Distribution

A major unrealistic aspect of the Markov model as described above is that it operates on an input with a rectangular size distribution. The distribution appears to evolve toward normality, but the sediment-transport path as defined by the model is too short and the number of size classes is too limited for the process to attain completion. This matter is remedied in post facto fashion by multiplying the size frequency distributions by weighting factors calculated from the normal distribution function (Hald, 1952). The resulting size frequency distributions (Fig. 86b) are the same as they would have been if the input distribution were normally distributed through 3 standard deviations on either side of the mean. Geographic distributions remain the same as for the rectangular input.

The effect of this transform is that the shift in mean and the variation in shape parameters is greatly muted (Fig. 87). The cyclic variation that does occur in the parameters of higher moment (standard deviation, skewness, kurtosis) is best understood by dissection of the size frequency curves into two components

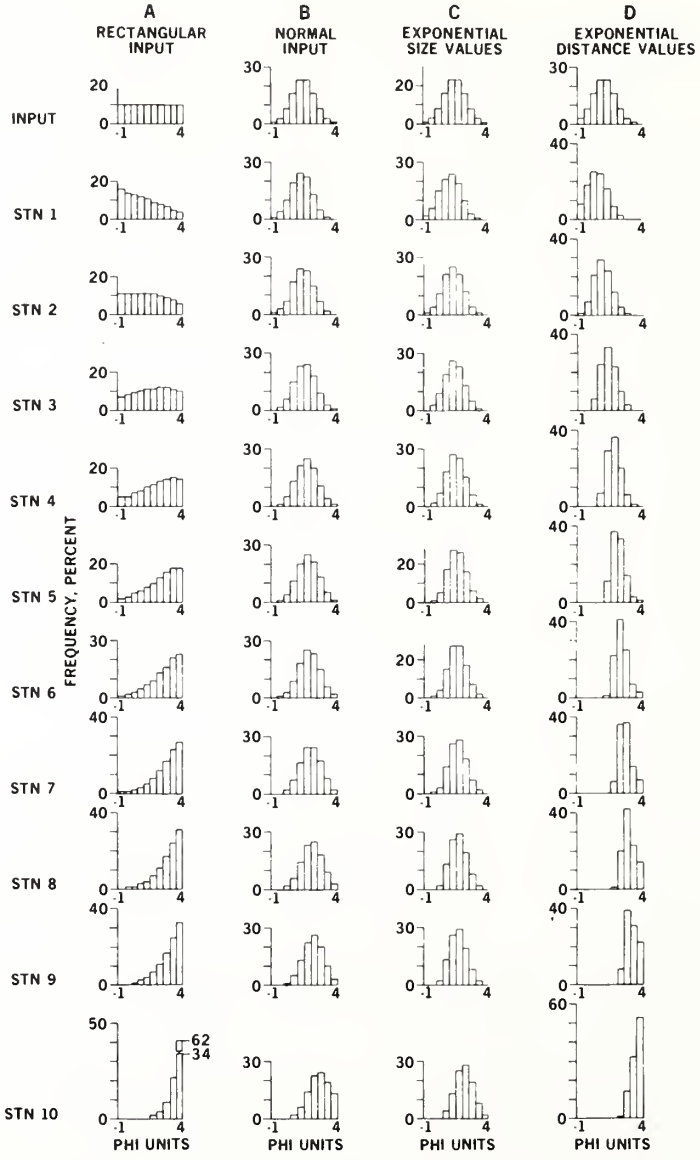

Figure 86.

Size frequency distributions at the 10 geographic stations of each of the 4 variants of the model described in this paper.

(Fig. 88): (a) An initially rectangular distribution through which a modal wave is seen to progress as successive frequency distributions are viewed, and (b) an invariant normal curve that has been imposed on each distribution by means of weighting factors. This curve represents the normally distributed input which the modal wave is modifying.

The modal wave may in turn be resolved into a central peak or zone of relative sand gain, and two flanking troughs, or zones of relative sand loss. In each zone, sand has been lost or gained relative to the baseline provided by the modal wave's initially rectangular shape.

The effect of the progression of the tripartite modal wave on the moment parameters of the normal distribution is a consequence of the mathematical and geometrical properties of these parameters. The normal curve may be viewed as the first member of a series of successive derivative curves, such that each curve represents a higher moment about the mean; the moment parameters are functions of these moments (Krumbein and Pettijohn, 1938, p. 25, p. 253). Skewness, for instance, is a function of the third moment about the mean, and of the second derivative of the normal distribution function. As such it is sensitive to changes in the four segments of the normal curve defined by its mode and inflection points, namely the distal coarse admixture, proximal coarse admixture, and proximal and distal fine admixtures (Fig. 88). In particular it is sensitive to changes in these segments that effect the symmetry or "tailedness" of the curve.

In station 1, for example, the forward zone of sand loss has developed over the fine admixture, while the distal zone of sand loss has developed over the coarse admixture (Fig. 88). These losses and gains are strongest over the distal portions of the admixtures. The result, barely discernable in the histogram of Fig. 86b, is that the coarse side of the curve has flattened (developed a tail) and the fine side has steepened (become truncated); skewness has become negative. In station 2, the central zone of sand gain now effects the proximal-fine admixture as well as the coarse admixtures; only the distal-fine admixture is now suppressed. The dominant effect is the differential modification of the two fine admixtures; with the proximal one amplified and the distal one suppressed, this side of the curve is rotated into a more nearly vertical position; skewness is more negative than in station 1. At station 3, however, the near zone of loss dominates the distal coarse admixture while the central zone of gain dominates the fine admixture (Fig. 88). The effect is to coarse truncate the distribution and to generate a tail on the fine side noticeable in the histogram of Fig. 86b as an additional fine class. Skewness is now positive. At station 4, the near zone of loss is now suppressing the proximal coarse admixture as well as the distal coarse admixture; steepening of this side is less effective, and skewness is not as positive as at the previous station.

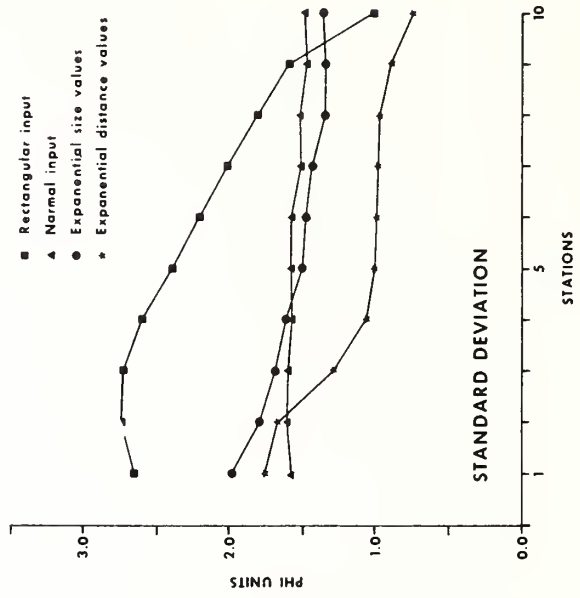
Rectangular input
Normal input
Exponential size values
Exponential distance values
STANDARD DEVIATION
PHI UNITS
3.0
2.0
1.0
0.0
1
5
10
STATIONS

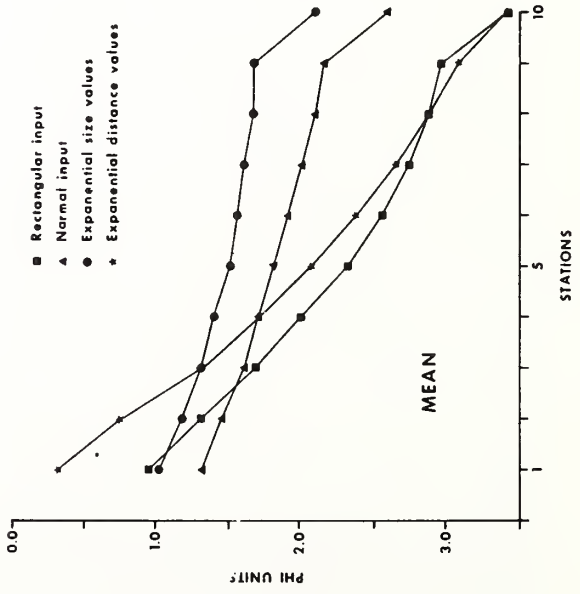
Rectangular input
Normal input
Exponential size values
Exponential distance values
MEAN
PHI UNITS
0.0
1.0
2.0
3.0
1
5
10
STATIONS

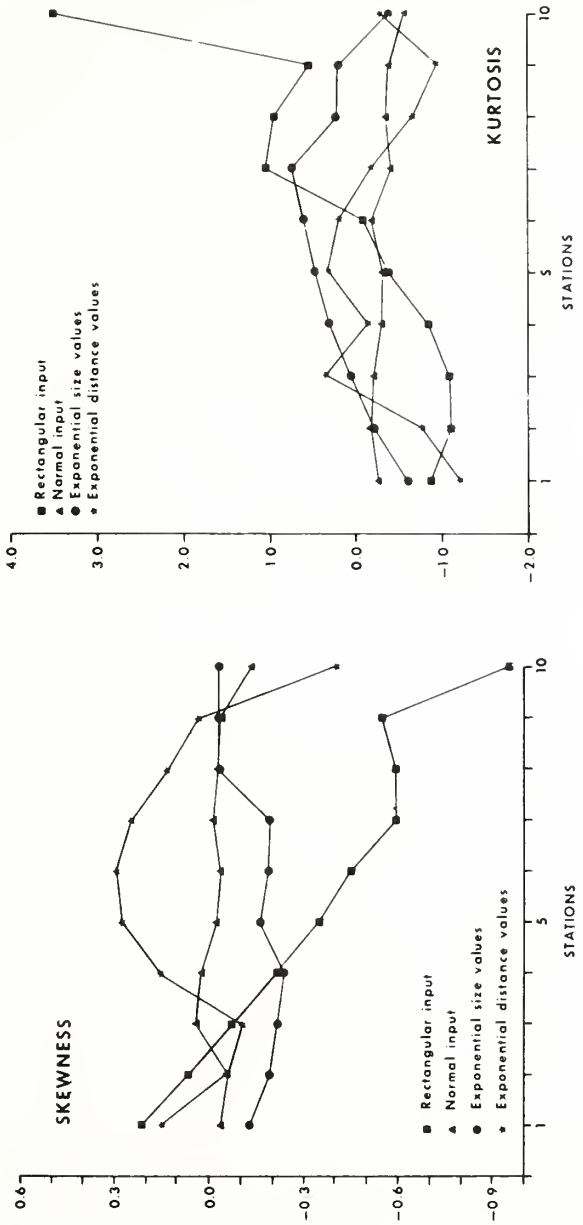

Figure 87.
Phi moment parameters for the 4 versions of the one-dimensional Markov process model described in this paper.

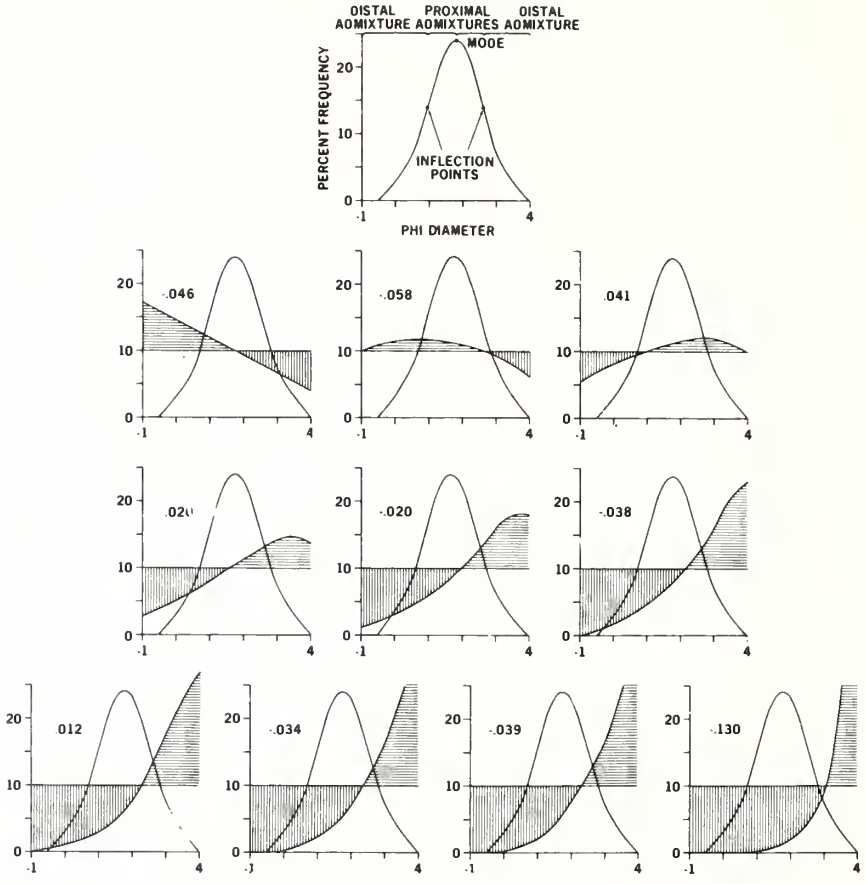

Figure 88.

Diagram illustrating interaction of zones of relative loss and gain of "modal wave" with distal and proximal admixtures of normal input curve. Ruled areas are defined by initial rectangular distribution and its subsequent modification by progressive sorting. Horizontally ruled sector is zone of relative sand gain; vertically ruled areas are forward and rear sectors of sand loss. The normal curve is the weighting distribution used in the experiment, and is invariant from station to station. Numbers are values of moment skewness for the resultant distribution.

Thus as the modal wave progresses through the normal input curve its 3 zones interact with the 4 curve segments so that the distribution's "tails" become more pronounced first on one side then on the other. Small-scale fluctuations must simultaneously occur in the other higher moment parameters, since the changes in curve shape also effect the spread of curve area about the mean (standard deviation), and the hollowness of the sides of the curve (kurtosis).

Table XIV
Size-Probability Matrix, Distribution Exponential with Size and Invariant with Distance

	Grain size class									
	Coarsest ←									→ Finest
	1	2	3	4	5	6	7	8	9	10
Forward [a]	0.196	0.321	0.362	0.432	0.459	0.475	0.485	0.491	0.494	0.496
Backward [b]	0.196	0.321	0.362	0.432	0.459	0.475	0.485	0.491	0.494	0.496
Auto-transition[c]	0.304	0.179	0.138	0.068	0.041	0.025	0.015	0.009	0.006	0.004
Trap[d]	0.304	0.179	0.138	0.068	0.041	0.025	0.015	0.009	0.006	0.004

[a] 0.000 for last station.
[b] 0.000 for first and last station.
[c] 1.00 for last station.
[d] 0.000 for last station.

Sorting with an Exponential Size Probability Distribution

A further unrealistic aspect of the Markov model is its family of transition matrices which have been assigned a linear relationship as a function of grain size. Experimental work has suggested that transport rates bear an exponential relationship to grain size (for instance Einstein, 1950). In this initial experiment we have not distributed the probabilities in accordance with any particular bedload function such as Einstein's, since the shelf regime that we are modeling is not one of continuous flow, but instead one of short periods of intensive movement, followed by long periods of quiescence. Thus the distribution of bed shear stress with time would be at least as important as the laws governing water-grain interaction under conditions of continuous flow in determining the transport rates of successive grain size classes. We are, therefore, free to adopt any size probability function of the general form $Y = 0.5 - e^{-axb}$ where Y is the probability of a grain moving forward or backward out of a station, x is here a number between 1 and 10 representing the 10 grain sizes in the model, and "a" and "b" are constants determining the shape of the curve. An "a" of 0.5 and a "b" of 1 were used to calculate the probabilities shown in Table XIV. The probability of a grain moving forward is Y/2, as is the probability of moving backward, and the probability of staying in place is 0.5 − Y/2, as is the probability of a grain being trapped out.

With probability distributions thus exponentially distributed by size, the size distributions and geographic distributions of Figs. 85b and 86c result. Standard deviation decreases and kurtosis increases as the size range decreases with passage through the system. Skewness is negative in the near stations. Early losses in *both* the proximal and distal coarse admixtures of the size distribution result in a decrease in slope of the coarse side of the frequency curve. The skewness

becomes less negative in the far stations. The greater difference in transport probabilities assigned to the coarser sand results in greater efficiency of sorting on that side of the curve, and progressive steepening of that side.

Sorting with an Exponential Distance Probability Distribution

Variations in size parameters in the sediment transport model now resemble those of actual sediment transport systems, with the principal exception of skewness. Many transport systems have a tendency to separate into two textural provinces defined by the skewness of the size frequency distributions produced; a proximal province of negatively skewed (coarse-tailed) lag deposits, and a distal province of positively skewed (fine-tailed) sediment. Beach sands tend to be negatively skewed, while derivative sands, in the back-beach dune on one side (Shepard and Young, 1961) and on the shore face on the other (Swift and others, 1971) are positively skewed. Crestal sands of shelf shoals are coarse-tailed while flank sands are fine-tailed (James and Stanley, 1970). Some notable exceptions occur. Sands of the Cretaceous Shelf of the Carolinas were initially fine-tailed, and trended toward symmetry with distance across the shelf (Swift and others, 1969). These sands were muddy, with 10% or more of silt and clay, hence the initial positive skewness. Since all sizes finer than gravel were present in the proximal deposits, progressive sorting could only reduce the skewness by autotruncation.

Transport systems whose deposits vary systematically from negative to positive skewness along the transport path are characterized by a downstream decline in competence. The proximal coarse-tailed lags are generated on high-energy shoals, while the distal fine-tailed deposits accumulate in deeper, quieter water. This characteristic can be simulated in our model by means of an exponential decrease in the transport probabilities for each grain size with distance through the system. The equation cited previously is used to generate probabilities, but in this case the distance-probability distribution rather than the size-probability distribution is obtained. The x is again a number between 1 and 10, this time representing the 10 stations. The "a" is now a grain-size coefficient and is itself exponentially distributed according to the formula $a = S(^{2-n})$ where S is an arbitrary starting value, and n is the number in the series. To prepare the probability distributions of Tables XV and XVI, S was set equal to 2, resulting in the series, 2, 1, 1/2, 1/4. . . . For each of these values of the size constant "a" a distance-probability distribution was determined, using a curve-determining constant "b" of 2.

Application of the resulting distance-variant transition probability matrices to the model generates sediment size frequency distributions (Fig. 86d) in which skewness increases through the transport system (Fig. 87) until the trend is reversed at the last few stations by autotruncation of the distribution. We conclude

that if a sediment-transport system, for instance a modern shore face (Fig. 89), is characterized by increasing positive skewness in its distal portion, then this trend is probably the consequence of a down-current decrease in energy level.

Other benefits accrue from the distance-variant model. Progressive size sorting is enhanced; the curve for mean-grain size in Fig. 87 is as steep as for the rectangular distribution. The trend of mean diameter with distance through the transport system (Fig. 87) is no longer nearly linear, but becomes an exponential decay curve of the sort $Y = e^{-ax}$, similar to the dispersal curves seen in nature (Pettijohn, 1957, p. 525-577). For the first time there is a real geographic separation of size classes (Fig. 85c).

An Alternative Characterization of Progressive Sorting

In preceding sections a model for the progressive size sorting of a sediment population has been examined. During the examination, the observer has in effect moved with the sediment, by viewing populations at successive downstream stations. In this section an alternative approach is used, wherein probability vectors and frequency distributions are considered from the vantage point of a single station.

For the purpose of the ensuing discussion, we propose the following terms and associated definitions:

system input frequency distribution denotes the grain-size distribution of sediment introduced into a model at one end as if from a source;

local input frequency distribution denotes the altered grain-size distribution that is available to enter a given local geographic location or site downstream from the point of system input;

admittance vector denotes an orderly arrangement of admittances each of which is a probability that a particle of stated characteristics and present in a local input can enter a local geographic site. Different admittances in the vector correspond to particles of different size, or shape, or density;

Table XV
Size-Probability Matrix, Distribution Exponential with Size and Distance, Station 1

	Grain size class									
	Coarsest ←									→ Finest
	1	2	3	4	5	6	7	8	9	10
Forward	0.034	0.184	0.303	0.389	0.444	0.470	0.485	0.492	0.492	0.498
Backward	0.000	0.000	0.000	0.000	0.000	0.000	0.000	0.000	0.000	0.000
Autotransition	0.500	0.500	0.500	0.500	0.500	0.500	0.500	0.500	0.500	0.500
Trap	0.432	0.316	0.197	0.011	0.059	0.030	0.015	0.008	0.004	0.002

Table XVI
Transition Probability Matrix for Size Class 5, Distribution Exponential with Size and Distance

From station	To station																	
	1	2	3	4	5	6	7	8	9	10	11	12	13	14	15	16	17	18	19
1	0.500	0.441							0.059										
2	0.303	0.197	0.303							0.197									
3		0.162	0.338	0.162							0.338								
4			0.068	0.432	0.068							0.432							
5				0.022	0.478	0.022							0.478						
6					0.006	0.494	0.006							0.494					
7						0.001	0.499	0.001							0.499				
8								0.500								0.500			
9									0.500								0.500		
10										0.100									
11											0.100								
12												0.100							
13													0.100						
14														0.100					
15															0.100				
16																0.100			
17																	0.100		
18																		0.100	
19																			0.100

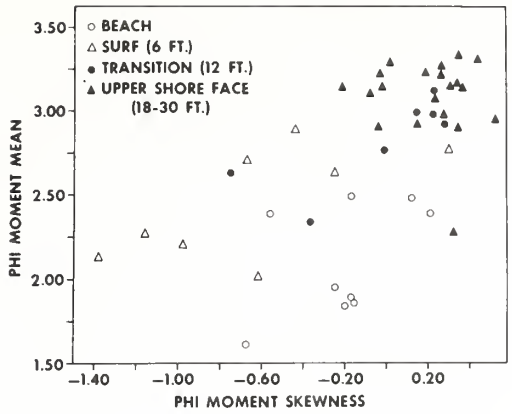

Figure 89.

Distribution of skewness on the shore face, Virginia-North Carolina coast. Data from Swift et al., 1971.

exit vector denotes an orderly arrangement of numbers each of which gives the probability that a particle of stated characteristics present at a local geographic site can exit, or leave, that site. Different probabilities corresponding as before to particles of different size, or shape, or density;

retention vector denotes an arrangement of probabilities each of which is obtained by subtracting the corresponding element in an exit vector from unity; and

retained distribution denotes a population of particles that were admitted by a geographic site and did not exit from that site.

If p_{jn} is an element in an admittance vector, where j denotes the jth station and n denotes one of 10 grain-size classes, and if p'_{jn} is a corresponding element in an exit vector for the same station, then the product of the two probabilities, $p_{jn}\ (1-p'_{jn})$, gives the probability that a particle in the local input enters and does not leave station j, and hence is present in the retained distribution at that site. The product of all corresponding elements in the admittance and retention vectors for a station gives a probability density function for that station (Fig. 90).

It is likely, but not necessary, that the admittance and exit vectors at a site are identical. Thus the probability entering and not leaving a station can be rewritten as $p_{jn}\ (1-p_{jn})$. There is no requirement that either vector should be linear. It is to be noted that if transportability of a given particle size is so great that admittance at a station is certain, then $p_{jn} = 1$, and the probability of retention at that station is nil, and the particle moves through and on to the next station. Also note that if transportability of a given particle size is so small that admittance is zero, then particles of that size cannot occur in the retained distribution at that station.

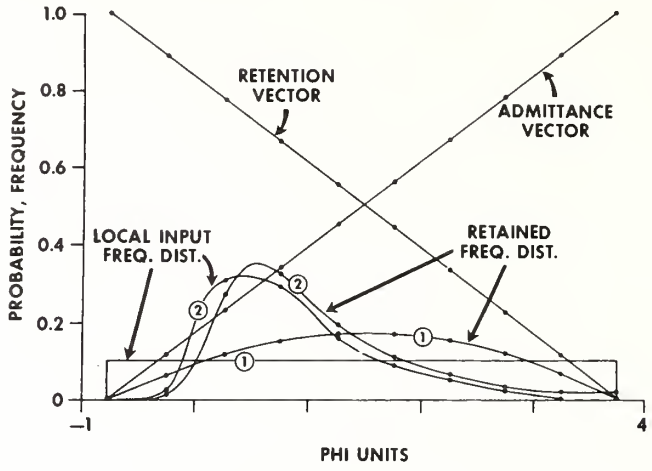

Figure 90.

Grain-size distribution at a station. For simplicity a local admittance vector and retention vector are linear and complementary. Local input distribution 1 is uniform; the shape of the corresponding retained distribution, 1, is solely dependent on the action of local admittance vector and retention vector. Local input distribution 2 is an arbitrary positively skewed, bell-shaped distribution; the corresponding retained distribution, 2, is altered in skewness by the action of the local admittance vector and retention vector.

The array of probabilities, p_{jn} $(1 - p_{jn})$, n = 1, 2, . . . , 10, for a station does not necessarily indicate the form of a retained distribution, because what is retained is dependent also on shape of the local input distribution. If the local input is uniform, the array of probabilities referred to above gives the shape of the retained distribution. In general, the local input distribution is not uniform, and this causes a skewing of the form of the retained distribution. If I_{jn} is the frequency of occurrence of grains of size n in the local input to station j, then

$$R_{jn} = \frac{I_{jn} P_{jn} (1 - p_{jn})}{\sum_{n=1}^{n=10} I_{jn} P_{jn} (1 - p_{jn})}, \qquad n = 1, 2, \ldots, 10$$

is the frequency of grains of size n in the retained distribution at station j. The local output from station j would usually be different than the local input to station j, because of the unequal partial removal of various grain-size classes.

The retained grain-size frequency distribution is, in this context, comprised of two significant parts: a coarser-grained part; and a finer-grained part. The extreme of the coarser-grained part is comprised of those available grains whose

transportability is barely great enough for their entry into location j. The tail of the finer-grained part is comprised of those grains that although mobile were not quite mobile enough to escape location j. The central part of the retained distribution is less amenable to interpretation and reflects the crossing point of the admittance and retention vectors and biasing by the shape of the local input distribution. Grain-size sorting of the retained distribution might also better be conceived of as consisting of two measures: coarse-end sorting, or spread of the coarse tail of the retained grain-size distribution; and fine-end sorting, or spread of the fine tail of the retained grain-size distribution. These measures reflect the function of the admittance and retention vectors.

It is noteworthy that in the special case when the grain-size distribution of the local input matches the distribution, $p_{jn}(1-p_{jn})$, no change in grain-size distribution occurs with passage through location j. Ultimately all the sediment would be deposited along the transport path; however, the analysis described in the preceding few paragraphs does not deal with absolute amounts of sediment transported or deposited, but only with a progressive grain-size fractionization process.

Admittance and exit vectors are expressions for sediment transportability at station j, and relate to effects of fluid motions on sediment. It is the joint interaction of local input with these fluid motions that determines what is deposited. In the end the probability, p_{jn}, or admittance, is an alternative characterization of a sediment transport rate. A decrease in this rate with distance along a transport path will result in net deposition.

The evolution of a rectangular input frequency distribution towards a normal distribution, noted in a previous section, may now be seen as the consequence of the repeated application of complimentary admittance and retention vectors, or of a repeated "sorting event" (Middleton, 1968), in which a modal class is repeatedly selected for at the expense of distal classes. However, the phrase "[evolving] . . . towards a normal distribution" must be used with caution. The initially rectangular distribution of Fig. 86a is evolving toward a normal distribution to the extent that sorting is favoring the central portion (ultimately the fine distal admixture) at the expense of the distal portions. The application of successive admittance vectors to the coarse admixture causes its frequencies to become exponentially distributed, resulting in the sigmoidal shape characteristic of the sides of the normal distribution. No comparable process modifies the fine admixture, however, whose shape is determined primarily by the local retention vector. As a result, the retention distribution becomes more asymmetrical at successive stations, and, judged by the criterion of skewness, becomes increasingly less normally distributed. Thus, while the simplest version of the model modifies distributions toward more centralized patterns, a process inherent in the model inhibits the development of truly normal distributions.

CONCLUSIONS

Our Markov process model for simulation of a one-dimensional sediment-transport model has provided us with some fundamental insights into the generation and evolution of sediment size frequency distributions. We have watched rectangular input distributions evolve toward more centralized distributions. We have noted that progressive size sorting of normal size distributions will occur as long as the transport surface will accept grains for permanent deposition. If sediment mobility decreases exponentially with increasing size, there will be a concomitant down-current decrease in standard deviation and increase in kurtosis. If competence decreases with distance through the system, skewness will become markedly positive. These specific insights have been helpful, but the most valuable result of all has been a change in our conceptual approach to the interpretation of grain-size distributions from descriptive, statistical viewpoint to the probabilistic analysis of population dynamics.

We feel that we have by no means exhausted the possibilities of our model. To date we have attempted simulation of the simpler sort; we have changed our probability distributions in an arbitrary but reasonable way, until we obtained results that imitate those of nature. We have not yet attempted to work in the other direction; namely to obtain from the literature experimental and observational assessments of sediment movement probabilities, then to apply these to the model. A logical next step would be to mate our quantitative probabilistic model to the qualitative hydraulic approach of Inman (1944) to the nature of sediment sorting.

Real sediment transport systems may have more than one source (Cronan, 1972). Tributary sediment streams may join the trunk, resulting in hybrid size frequency distributions. This situation is easily modeled by attaching tributary sequences of states to the model of Fig. 84.

Two-dimensional models, such as the one in Fig. 83, may represent much more complex systems with several superimposed gradients. On open coasts the nearly coast-parallel, time-continuous surf-driven, littoral drift system is linked to the intermittent storm-driven system of coast-parallel currents seaward of the surf, by coast-normal processes such as rip currents, and the mid-depth return flow, and bottom wave-drift currents (Swift et al., 1971; Duane et al., 1972). Here longshore bars and troughs would be modeled by axes of convergence of transition probabilities; sand-circulation cells (Ludwick, 1972) by axes of convergence and shear. In two-dimensional models, matrices of limiting state probability distributions could be contoured for mean diameter or other textures. With some modifications isopleth maps of percent of total sediment deposited could be prepared, and interpreted as bathymetric maps of depositional topography. In these ways the dynamics of coastal and shelf morphology may be studied.

However, it is important to point out that Markov process models are subject to severe limitations. Like all wholly defined systems they constitute zero sum games. Considerable structural detail and precision is possible, but it is gained at the expense of dynamic realism, since it is difficult and perhaps ultimately impossible to translate real processes into probabilities. In the two-dimensional models stationarity promises to be an obstacle; bedload-substrate interactions occur as complex feedback systems, and in Markov terms, the transition probabilities must change with time. Higher order chains with multiple-dependence relationships must be explored. Ultimately, potential-flow theory must be added to the presently more limited forms of sediment transport modeling (Tanner, 1962, p. 114; Harbaugh and Bonham Carter, 1970, p. 205-254).

LIST OF SYMBOLS

Symbol	Definition
a	Shape constant for exponential curve
b	Shape constant for exponential curve
C	Concentration
C_{Dn}	Concentration for a given value n of D
D	Coefficient of diffusion
e	Base of natural logarithms
I_{jn}	Frequency of occurrence of grains of size at station j
i, j	Geographic stations in a Markov model
P	Transition probability matrix
p_{jn}	Probability of occurrence of grains of size at station j
R_{jn}	Frequency of occurrence of grains of size n in retained distribution at station j
S (L)	Limiting state probability vector
S (n)	State probability vector after n transitions
S (O)	Initial state probability vector
T	Time
x	Distance; grain size class; geographic stations
y	Transition probability between 2 transient states

REFERENCES

Allen, J. R. L. (1965). Late Quaternary Niger Delta, and adjacent areas: sedimentary environments and lithofacies. *Am. Assoc. Petroleum Geologists Bull.* **44**, 547-600.

Beall, A. O., Jr. (1970). Textural differentiation within the fine sand grade. *J. Geology.* **78**, 77-93.

Belderson, R. H., and Stride, D. H. (1966). Tidal current fashioning of a basal bed. *Marine Geology.* **4**, 237-257.

Crank, J. (1957). "The Mathematics of Diffusion." Oxford Univ. Press (Clarendon), London and New York.

Cronan, D. S. (1972). Skewness and kurtosis in polymodal sediments from the Irish Sea. *J. Sed. Petrology.* **42**, 1-2-106.

Duane, D. B., Field, M. E., Meisburger, E. P., Swift, D. J. P., and Williams, S. J. (1972). Linear shoals on the Atlantic inner continental shelf, Florida to Long Island. *In* "Shelf Sediment Transport: Process and Pattern" (D. J. P. Swift, D. B. Duane, and O. H. Pilkey, eds.). Dowden, Hutchinson and Ross, Stroudsburg, Pa.

Einstein, H. A. (1950). The bed-load function for sediment transportation in open channel flows: *U.S. Dept. of Agriculture, Soil Conservation Serv. Tech. Bull.* **1026**, 71 pp.

Emery, K. O. (1952). Continental shelf sediments off southern California. *Geol. Soc. America Bull.* **63**, 1105-1108.

Hails, J. R., and Hoyt, J. R. (1969). The significance and limitations of statistical parameters for distinguishing ancient and modern sedimentary environments of the lower Georgia Coastal Plain. *J. Sed. Petrology.* **34**, 559-580.

Hald, A. (1952). "Statistical Tables and Formulas." 97 pp, Wiley, New York.

Hjulstrom, F. (1939). Transportation of detritus by moving water. *In* "Recent Marine Sediments." (P. D. Trask, ed.), Am. Assoc. Petroleum Geologists, Tulsa.

Howard, R. A. (1960). *Dynamic programming and Markov processes.* Cambridge, M.I.T. Press, Cambridge, Massachusetts and Wiley, New York.

Inman, D. L. (1949). Sorting of sediments in the light of fluid mechanics. *J. Sed. Petrology.* **19**, 51-70.

James, N. P., and Stanley, D. J. (1968). Sable Island bank off Nova Scotia: sediment dispersal and recent history. *Am. Assoc. Petroleum Geologists Bull.* **52**, 2208-2230.

Johnson, D. W. (1919). *Shoreline processes and shoreline development.* (Facsimile, 1965), Hafner, New York.

Jost, W. (1960). *Diffusion in Solids, Liquids and Gases.* Academic Press, New York.

Kemeny, J. G., Snell, J. L., and Knapp, A. W. (1966). "Denumerable Markov Chains." Van Nostrand, Princeton, New Jersey.

Ludwick, J. C. (1972). Migration of tidal sand waves in Chesapeake Bay entrance. *In* "Shelf Sediment Transport: Process and Pattern" (D. J. P. Swift, D. B. Duane, and O. H. Pilkey, eds.). Dowden, Hutchinson and Ross, Stroudsburg, Pa.

Middleton, G. V. (1968). The generation of the log normal size frequency distribution in sediments. *In* "Problems of Mathematic Geology." Science Press, Leningrad.

Northrup, J. (1951). Ocean bottom photographs of the neritic and bathyal environmental south of Cape Cod, Massachusetts. *Geol. Soc. America Bull.* **62**, 1381-1383.

Pettijohn, (1957). "Sedimentary Rocks" (2nd ed.). Harper, New York.

Plumley, W. J. (1948). Black Hills terrace gravels: a study in sediment transport. *J. Geology.* **56**, 526-577.

Shepard, F. P. (1932). Sediments on the continental shelves. *Geol. Soc. America Bull.* **43**, 1017-1039.

Shepard, F. P. (1961). Distinguishing between beach and dune sands. *J. Sed. Petrology.* **31**, 196-214.

Spiegal, M. R. (1961). *Statistics.* Schaum, New York.

Swift, D. J. P. (1970). Quaternary shelves and the return to grade. *Marine Geology.* **8**, 5-30.

Swift, D. J. P. (1971). Relict sediments on continental shelves: a reconsideration. *J. Geology.* **79**, 322-346.

Swift, D. J. P., Heron, S. D., Jr., and Dill, C. E., Jr. (1969). The Carolina cretaceous: petrographic reconnaissance of a graded shelf. *J. Sed. Petrology.* **39**, 18-33.

Swift, D. J. P., Sanford, R. B., Dill, C. E., Jr., and Avignone, N. F. (1971). Textural differentiation of the shore face during erosional retreat of an unconsolidated coast, Cape Henry to Cape Hatteras, Western North Atlantic. *Sedimentology* **16**, 221-250.

Swift, D. J. P., Stanley, D. J., and Curray, J. R. (1971). Relict sediments on continental shelves: a reconsideration. *J. Geology* **79**, 322-346.

Tanner, W. F. (1962). Geomorphology and the sediment transport system. *Southeastern Geology* **4**, 113-126.

Yang, C. T., and Sayre, W. W. (1971). Longitudinal dispersion of bed-material particles. *J. Hydraulics Div. Proc. Am. Soc. Civil Engineers* **97**, 907-921.

Yang, C. T., and Sayre, W. W. (1971). Statistical model for sand dispersion. *J. Hydraulics Division, Am. Soc. Civil Engineers* **71**, 265-273.

Reprinted from Journal of Sedimentary Petrology 42, No. 1, 122-134.

SIZE ANALYSIS OF FINE-GRAINED SUSPENDED SEDIMENTS: A REVIEW[1]

DONALD J. P. SWIFT[2]
Radioecology Program, Puerto Rico Nuclear Center, Mayaguez, Puerto Rico

J. R. SCHUBEL
Chesapeake Bay Institute, Johns Hopkins University, Baltimore, Maryland

RAYMOND W. SHELDON
Fisheries Research Board of Canada, Marine Ecology Laboratory, Bedford Institute, Dartmouth, Nova Scotia, Canada

ABSTRACT

Particle size analysis is one of the potentially most powerful tools available for the interpretation of any population of sedimentary particles. The size distribution characterizes the particles as a product, providing information on the actual particle sizes, and also is a prerequisite to understanding their roles in a set of sedimentary processes. Fine-grained suspended sediments are the least amenable to size analysis because of the difficulty of preserving the natural state of aggregation throughout sampling and analysis.

Fine suspended sediments are composed of inorganic mineral matter and living and dead organic matter which occur as individual particles, and as agglomerates and aggregates. The projected areas, volumes, and diameters of the particles are highly variable as are their electrical and optical properties. The various methods of size analysis measure very different properties of the particle population. The basic methods of sizing fine suspended sediments described in this paper are microscopic analysis, optical-sedimentation analysis, direct optical analysis, and electronic (Coulter Counter) analysis.

The microscopic method is the only one which permits direct visual observation of the particles, but yields a number frequency distribution rather than a weight or volume-size distribution. Optical-sedimentation methods permit analysis of the hydraulic behavior of the sediment in its natural medium, but at present are limited by concentration and size range. The Coulter Counter method is in some respects the most versatile method, but it yields a volume distribution which can not be directly related to settling velocity.

STATEMENT OF PURPOSE

This paper describes four methods of size analysis which have proved useful in characterizing populations of fine-grained suspended sediment both as products and as participants in a set of sedimentary processes. Schubel has prepared a section on microscopic methods. Sheldon has prepared a section on electronic methods. Swift has discussed direct optical and optical-sedimentation methods, and has assembled the paper. Sonic methods (Interagency Committee on Water Resources, 1963; Flammer, 1962), nuclear methods (Interagency Committee on Water Resources, 1963), and gas adsorption methods (Irani and Callis, 1963) are not considered. The section on microscopic methods is based on work supported by the Department of Chesapeake Bay Affairs, State of Maryland and the Bureau of Commercial Fisheries, Fish and Wildlife Service, Department of the Interior, through Public Law 88-309 funds. The section on optical methods is based on a study undertaken by the Radioecology Program, Puerto Rico Nuclear Center, Mayaguez, Puerto Rico, for the Battelle Memorial Institute and the Atomic Energy Commission. The senior author would like to acknowledge the logistical support and technical advice of F. G. Lowman, head of the Radioecology Program, which sustained that portion of the study.

[1] Manuscript received April 6, 1971; revised September 21, 1971.

[2] Present Address: NOAA, Atlantic Oceanographic and Meteorological Laboratories, Miami, Fla. 33130.

INTRODUCTION

Particle size analysis is one of the potentially most powerful tools available for the interpretation of any population of sedimentary particles. The size distribution characterizes the particles as a product, providing information on the actual particle dimensions, and also is a prerequisite to understanding their roles in a set of sedimentary processes. The size distribution may also yield information on the origin of the sediment. Special techniques and judicious interpretation of the results are required to realize this diagnostic potential when dealing with small samples of suspended sediment. The range of particle sizes encountered in a sample frequently extends from those in the Newtonian "macro-world" dominated by gravity and momentum, to the "micro-world" of "Gibbsian" forces where parameters such as surface area, viscosity, and electrostatic charges are very significant. The division corresponds approxi-

mately to the sand-silt boundary. (See Went, 1968, for a development of this concept.)

Despite these difficulties, the interest of sedimentologists and civil and industrial engineers in size analysis has been sufficient to develop a variety of operational methods (Krumbein and Pettijohn, 1939; Milner, 1962) that are at least reproducible, even if the ultimate meaning of the results is not always clear. The various methods of size analysis measure very different properties of the particle population—properties more or less closely related to the actual physical dimensions of the particles. The size of a particle may be defined as any measure characteristic of the fineness of its subdivision. The measure most commonly chosen is a "diameter." But since natural particles are irregular and have no unique diameter in the mathematical sense, it is necessary to construct a set of "equivalent particle diameters" which are compatible with the measurements generated by the various methods of analysis. The "diameter" most commonly determined by microscopy is an equivalent projected diameter, the diameter of a circle with cross-sectional area equal to that of the particle. Sedimentation analyses are based upon a relationship between particle size and settling velocity and are generally expressed in terms of an hydraulic or Stokes equivalent diameter, the diameter of a sphere having the same density and the same settling velocity as the particle. The Coulter Counter measures a kind of equivalent volume diameter, by determining the electrical resistance of particles in an electrolyte.

One of the most difficult problems in any size analysis of fine-grained suspended sediment is the preservation of the naturally occurring size distribution throughout sampling and analysis. Ideally particle size would be measured by means of an *in situ* analyzer. Barring this, samples should be analyzed on board ship without changing concentration, salinity, or other parameters of the water-sediment system. If the particles must be extracted from the water, as in the microscopic method, it must be done with great care so that the composite particles are neither destroyed nor increased in number. The ultimate size distribution, which is obtained by dispersing the suspension by means of peptizing agents, has very limited diagnostic value in the interpretation of sedimentary processes. The practice of peptizing was initiated by students of ancient sediments who sought the "ultimate" size distribution, since the size distribution at the time of deposition could not be recovered.

An associated problem that the investigator must face is the choice of analytical technique. The same sample will yield very different size frequency distributions depending on whether microscopic, sedimentation, optical, or electronic methods are used, because of the heterogeneous nature of the particles. Suspended fines are generally believed to consist of four compositional components: silt-size tectosilicate particles, primarily quartz; clay mineral particles; siliceous and calcareous tests of unicellular organisms; and amorphous living and dead organic material. The physical chemistry of colloidal systems has long been understood (Kruyt, 1952). The sensitive response of clay particles to increasing electrolyte concentration and their consequent flocculation is a process that follows clearly formulated physical laws and may easily be studied in the laboratory. Many workers who have considered these laws adequate explanation for the behavior of suspended sediment in coastal water. Krone (1962) has shown that water-clay systems are dynamic systems in which the grain size of clay floccules is in a state of equilibrium with fluid shear, sediment concentration, and salinity. Whitehouse and others (1960) have discussed the differential flocculation of clay mineral type. It has been suggested, however, that the role of organisms in pelleting and agglutinating fine sediments has been greatly underrated. If so, then the structure of suspended sediment particles may be as variable as their composition. A single sample might contain platy particles consisting of clay minerals held together by electrostatic charges, ellipsoidal particles consisting of clay minerals tightly packed by passage through an invertebrate gut, and tenuous, irregularly shaped aggregates of degraded organic material held together by algal mucus or bacterial slime. Such variations in structure cause variations in water content (density), shape, and cohesiveness, and resistivity that generate very different results when different methods of analysis are applied. Silt sized quartz fragments have a specific gravity of 2.5, and are subspherical. Clay floccules with the same geometric diameter may contain up to 95% water and a clay floccule with a diameter of 500 microns may settle with the velocity of a quartz sphere of 20 microns. Thus sedimentation and microscopic techniques will give very different results.

Postma (1961) has been particularly concerned with the difference in behavior of suspended organic material relative to inorganic material. Like some clay floccules, organic aggregates may consist of up to 95% water; hence may settle much more slowly. The effect is aggravated if living or dead plankters are among the organic particles, since these organisms of-

ten have irregular shapes designed to assist in floatation. Optical methods of size analysis are also effected by the presence of organic material. Since organic aggregates are so diffuse, a given dry weight of organic material will much more efficiently intercept light than will the same weight of inorganic sediment. The discrepancy is reduced to a certain extent by the lower refractive index and greater transparency of organic matter (Postma, 1961).

Clearly, in reporting the results of a size analysis the techniques must be explicitly stated. The purpose of the investigation should be firmly in mind before an analysis is undertaken and should dictate the method and techniques used.

MICROSCOPIC PARTICLE SIZE ANALYSIS

Introduction

Microscopic sizing is the most direct method of particle size analysis available. Large numbers of particles can be readily measured and counted with one of the automatic microscopic sizing instruments such as the Quantimat Micro-Image Analyzer (Jarrel—Ash Co., 590 Lincoln St., Waltham, Mass.), or the Flying Spot Particle Resolver (Cinema Television, Ltd., London, England). These instruments are expensive ($10,000–$25,000), however, and do not provide information on particle shape, composition, or degree of agglomeration.

The two instruments which we have found most effective for microscopic studies of natural populations of fine-grained suspended sediment are a photo-micrographic analyzer, the Zeiss Particle Size Analyzer TGZ-3 (Carl Zeiss, Inc., 444 Fifth Ave., New York, N.Y.), and a semiautomatic analyzer, designed and built by the Chesapeake Bay Institute, which couples directly to the microscope (Schubel and Schiemer, 1967).

Sample Collection

Samples of suspended sediment for microscopic size analysis by either of these two methods are obtained by filtration of water samples through 0.22 microns APD cellulose membrane filters immediately after collection. For microscopic analysis the ideal sample is a single particle layer with no particle touching another. Although such samples are necessarily very small, they are sufficiently large to ensure stability of the statistics associated with the number-size distribution (Schubel, 1968, 1969).

Slides of suspended sediment samples are prepared by clearing portions of the filters with a liquid which has a refractive index equivalent to that of the cellulose (n 1.51). The particles are then either directly sized under the microscope with the CBI particle size analyzer or photographed for analysis with the Zeiss Particle Size Analyzer TGZ-3. With either technique phase microscopy is desirable because many suspended particles are nearly colorless and have indices of refraction close to 1.5.

The Chesapeake Bay Institute Particle Size Analyzer: This instrument, built by coupling a Vickers Image Splitting Eyepiece (Vickers Instruments, Inc., 15 Waite Court, Malden, Mass.) with electrical impulse counters, provides a semiautomatic particle size analyzer with which particles can be sized, sorted into classes, and counted accurately and quickly. By incorporating a modified Mach-Zehnder interferometer between the microscope objective and its own eyepiece, the Vickers eyepiece splits each particle image into two identical coplanar images which can be superimposed or displaced with respect to each other and whose displacement can be accurately measured with a micrometer screw. In the CBI analyzer the necessity of reading the micrometer is eliminated by connecting it through an electrical bridge to sixteen electrical impulse counters, each of which corresponds to a certain displacement of the micrometer. One half of the bridge, a high resolution potentiometer coupled to the micrometer, generates a voltage analog of the micrometer setting. The other half of the bridge is a logarithmic voltage divider. When a particle image is appropriately "split," the operator depresses a footswitch activating a stepping switch, and the micrometer-generated analog voltage is compared with the increasing voltage scale which represents the desired size intervals. When the micrometer-generated voltage is equalled or exceeded, the differential amplifier detector closes its relay, triggering a silicon controlled rectifier which connects a charged capacitor to the proper counter via another section of the stepping switch. For a complete description of the instrument and its circuit, see Schubel and Schiemer, 1967.

Since 1966 when the CBI analyzer was built, Fleming Instruments (Fleming Instruments, Ltd., Stevenage, England) has constructed a similar analyzer with variable class limits, but with fewer classes. This instrument, the Particle Size Micrometer and Analyzer, is imported and distributed by Vickers, Inc.

These instruments can be used to measure particle lengths, widths, or "diameters." A "diameter" is most commonly chosen as a measure of particle size, and the most useful diameter is an equivalent projected diameter—the diameter

of a circle with cross-sectional area equal to that of the particle. Particles with circular cross-sections are easily sized by "splitting" the two images until they are tangent. The equivalent diameters of irregular particles, although more difficult to determine, can be reliably estimated with the aid of a graphic guide showing, for various shapes of particles, the correct displacement of one image relative to the other for the determination of the equivalent projected diameter "Schubel and Schiemer, 1967). An operator can, with a few hours of practice, size more than 500 particles in less than 30 minutes.

The Zeiss Particle Size Analyzer TGZ-3. The Zeiss analyzer is a semiautomatic device for sizing particle images on photomicrographs. The principal components are a light source, a lens system, and an adjustable diaphragm which is correlated via a commutator with 48 telephone counters, each counter corresponding to a certain aperture interval of the iris diaphragm. The counters can be switched into either a linear or a logarithmic sequence. The iris diaphragm, illuminated from below, is imaged as a sharply defined circular light spot in the plane of the plexiglass plate which supports a photomicrograph. The photograph is moved by hand until the "center of gravity" of a particle image lies at the center of the measuring mark. The particle image is then measured by adjusting the diaphragm until the light spot has an area equal to that of the image. A foot switch is depressed, the proper counter is activated, a hole is punched in the particle image, and the total registered on the cumulative counter is increased by one. The diameter measured is the equivalent projected diameter, D_m.

The photographic procedures (Schubel, 1968, 1969) must be rigidly controlled because of their effects on the apparent particle size distribution (Loveland, 1959).

The photomicrographic sizing technique using the Zeiss TGZ-3 is less fatiguing on the operator than the direct sizing method. The additional step of photography offers the advantages of providing a permanent record and attaining desired magnifications. But it involves considerable work and expense if a large number of samples are to be analyzed. A more serious disadvantage of the photomicrographic method is that the focus is fixed at the time of exposure. For particle populations with broad size distributions, it may be necessary to make multiple photographs of each field with different focal settings. Great care is required in combining the results from several photographs of the same field to ensure that each particle is measured once and only once.

DISCUSSION

Microscopic size analysis, involving the actual measurement of a small sample of individual particles, affords and estimate of the parent particle populations *number-size distribution*—the relative frequency of particles whose equivalent projected diameters fall within certain size classes. The number-size distribution has its greatest significance in characterizing the suspended particle population as a product and may yield little or misleading information regarding the behavior of the constituent particles in the active sedimentation processes (Schubel, 1969). The microscopic sizing procedure can be greatly facilitated with either the CBI analyzer or the Zeiss particle size analyzer.

The complete description of a particle population requires, in addition to the number-size distribution, the determination of either the volume or weight-settling velocity ("size") distribution. These distributions have their greatest significance in characterizing the particles as participants in sedimentation processes and must be determined directly (Schubel, 1969). Transformation of microscopically determined number-size data to volume-size data by assuming that the particle population is a polydisperse system of spheres is usually unsatisfactory, except for very narrow size distributions, because of the distorting effects produced by a few large particles when their "diameters" are cubed.

OPTICAL METHODS

Introduction

Light passing through turbid water is attenuated. It has long been known such attenuation consists of two distinct processes; scattering, which may be defined simply as the deviation of light from rectilinear propogation, and absorption, in which radiant energy is degraded into simpler forms. In addition, the light is polarized during its passage. Optical methods of the analysis of suspended fines may be divided into four categories on the basis of two parameters. These are 1) whether optical methods are used in conjunction with sedimentation methods, or whether they are used by themselves and, 2) whether absorption or scattering is the parameter measured. The manner in which a suspension depolarizes transmitted light has been used as a means determining a size-frequency distribution curve (Atherton, 1952). However, only absorption and scattering methods will be considered here.

Theory

The earliest comprehensive theory of scattering of light was set forth by Lord Rayleigh in

1871. Rayleigh theory states that a particle in a beam of light becomes an oscillating dipole, radiating in all directions (Rayleigh, 1871, Stutz, 1930, Jerlov, 1968, p. 22). For the case of particles which are small relative to the wavelength of light, isotropic, and distributed at random, the radiant intensity perpendicular to the light is

$$I = \frac{Kd^6}{\lambda 4}$$

where K is a constant, d is particle diameter, and λ is wavelength.

Rayleigh theory presents a valid picture of the scattering of light in pure water by water molecules and of the scattering of light by extremely small suspended particles (Tabibian and others, 1956, p. 211–212, Burt, 1955, p. 36). For particles over .01 micron in diameter, a more rigorous theory of scattering has been developed by Mie (1908). Mie theory defines the intensity of light scattered in a given direction in terms of particle diameter, wavelength of incident light, and refractive index of the particle. These parameters are related by means of Bessel functions to produce a series which converges rather slowly for particles as large as several wavelengths in diameter (Van De Hulst, 1957). The calculations are generally done by computer.

Mie theory is difficult to comprehend in simple terms. A parameter of Mie theory which is of considerable importance for the analysis of suspened sediments is a dimensionless quantity known as the effective area coefficient, K, sometimes called tthe scattering area ratio or the efficiency factor. It is the number by which the geometric cross-sectional area of a particle must be multiplied in order to determine its effectiveness in attenuating light by scattering and absorption. K, therefore, equals the energy lost by the incident beam divided by the energy of the pencil of light that is geometrically obstructed by the particle, K is a function of α $(= \pi^d/\lambda)$ and $n(1 - ik)$ where n is the refraction index, R is radius, λ is wavelength, i is the square root of negative one, and k is the bulk absorption coeffi cient. Burt (1956) has presented a useful scattering diagram which shows the effective area coefficient K as a function of grain size, wavelength, and relative refractive index. For a more detailed discussion of Mie theory, see Van De Hulst, 1957 and Jerlov, 1968.

Optical—Sedimentation Methods

Introduction. Size analysis of fine sediments has commonly been undertaken by means of sedimentation according to Stokes Law (Stokes, 1851), and Oden's theory of sedimenting systems (Oden, 1915). In this technique, a sample, suspended in water, undergoes size differentiation by gravity settling. Sediment concentration is sensed synoptically at a series of depth intervals, or more commonly is sensed through time at a single horizon. In both cases, the sensing may be accomplished by actually extracting a sub-sample, drying, and weighing it (pipette methods, first used in this country by Jennings, Thomas, and Gardner, 1922), by hydrometer methods (Buoyocos, 1928), or by optical methods.

Concentration Requirements: Most sedimentation methods have concentration requirements which severely limit their direct use in the analysis of suspended sediments. For the pipette and hydrometer methods, a concentration of 15 g/l is optimum (Folk, 1961, p. 37), and 5 g/l is a lower limit below which error is excessive.

It is possible to artificially increase the concentration of a suspended sediment sample by means of decantation (Krumbein and Pettijohn, 1938, p. 147–150). The turbid water sample is allowed to undergo sedimentation within its container until the density in the lower portion exceeds the desired value. The supernatant liquid is then siphoned off. Preliminary concentration by decantation has serious limitations. The size distribution is fine-truncated by drawing off the liquid above the limiting surface of critical density. During the period of concentration, coarser particles have come to rest on the container floor, and unless these are resuspended, the distribution will be coarse-truncated as well. Fine-truncated is often an acceptable limitation; most of the significant information is contained in the coarse part of the curve, and many other methods result in fine-truncated curves. If the larger particles are sturdy enough to stand resuspension (as is often the case; Sheldon, 1968, p. 75), then preliminary concentration may be feasible.

The direct sedimentation method which has the lowest concentration requirement is the bottom withdrawal tube method of the Interagency Committee on Water Resources (1943A, 1957, 1958). The lower limit of concentration required by this method is .3 g/l.

Optical-sedimentation methods are more sensitive than direct settling methods. The senior author has obtained reproducible sedimentation curves from initial concentrations as low as .07 grams per liter, using a photoextinction technique (Swift and Pirie, 1970). The lower concentration limit of optical-sedimentation methods, depending on incident light intensity, photocell

sensitivity, and sedimentation cell width, have not been established.

Sampling Technique: While suspended sediment particles may be collected on filters with minimal damage if care is shown, resuspension of quantities sufficient for optical-sedimentation analysis is generally impractical. Sampling for this method therefore is accomplished by means of fixed-volume samples or continuous pumping.

The older literature on suspended sediment sampling has been ably summarized by the Interagency Water Resources Committee (1940). After preparing this summary, the committee designed a series of suspended sediment samplers and developed techniques for using them (Interagency Water Resources Committee, 1941, 1952, 1961, 1962, 1966). The committee determined that the sampler must 1) have an intake nozzle that protrudes from the sampler and points up current, 2) fill in a steady and continuous manner, rather than with an initial rush, and 3) have an intake velocity equal to current velocity, if sand as well as fine sediment is to be sampled. Keeping these requirements in mind, the committee designed fixed-volume, point-integrating samplers, fixed-volume depth-integrating samplers, and continuous pumping systems.

Both the fixed-volume and continuous pumping samplers were designed primarily for determining suspended sediment concentration rather than size distribution, and probably neither are ideal for size analysis. Fixed-volume samplers are containers which are lowered to sampling depth. Their orifices are opened, then closed, and the sampler is brought back to the surface. During this period the sample is no longer subjected to flow, the sediment settles, and may stick to the sample wall (Interagency Committee on Water Resources 1941, p. 72). Pumping systems bring the sediment to the surface under conditions more or less similar to the original flow field, but the suspended sediment must pass through the rotor of the pump. However, experience on the part of the senior author suggests that a pumping system such as that designed by Jordan (Jordan, 1965, Swift and Pirie, 1970) is the most practical and efficient method of sampling suspended sediment for size analysis.

The Photoextinction—Sedimentation Method

Morison (1919) seems to have been the first to simplify the sedimentation method of size analysis of suspended fines by using an optical sensing technique for determining the variation in density with time at a given horizon in the settling column. (See also Richardson, 1934, 1936.) This modification has the virtue of simplicity (no sampling to disturb the column; no dryings or weighings) and it permits the use of automatic recording equipment.

The photoextinction-sedimentation method offered so many possibilities that considerable research effort was spent on it in England where it was subsequently developed on a sound mathematical and experimental basis by Rose (1953). Rose has drawn on Mie theory to show that when a beam of light is passed through a settling suspension, the intensity of the incident light bears the following relationship to the intensity of the transmitted light:

$$\ln I_0/I = kC1 \sum_{d=0}^{D} Knd^2$$

where k is the bulk absorption coefficient, C is the concentration in grams per cubic centimeter, n is the number of particles, 1 is the width of the sedimentation cell, and K is the effective area coefficient. In any particular experimental situation, k, C, and 1 are constants, and values for K may be obtained from Roses's curve. Readings of I may be taken at successive times, which can be related to certain grain diameters by means of Stokes Law. By multiplying the change in $\ln I_0/I$ by the average diameter, it is possible to determine the percent by weight of a grain size class. The result is then divided by the effective area coefficient to given the true weight percent of particles in the size class. See Simmons, 1959, and McKenzie, 1963, for further discussion of the calculations.

The equipment generally used for the photoextinction method consists of a light source, a lens, collimating stops, sedimentation cell, and a micro-ammeter (fig. 1). Bradley (1956) has designed a very simple turbidometer using a light bulb, bottle, camera light meter, and variable voltage transformer. McKenzie (1963) has presented a method of adopting a colorimeter for the photoextinction-sedimentation method. McKenzie was able to analyze a sample down to five microns in a half hour, and compute weight percentages in 10 minutes.

Burt and Beardsley (1969) have noted some of the potential sources of error in such systems. One of the most serious problems is temperature variation. It seems that temperature

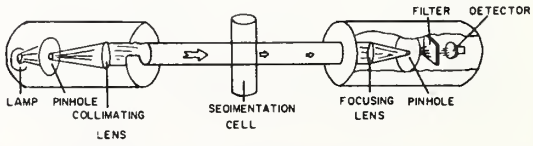

FIG. 1.—Generalized model of apparatus for grain-size analysis by the photo-extinction—sedimentation method. Modified from Burt and Beardsley, 1969.

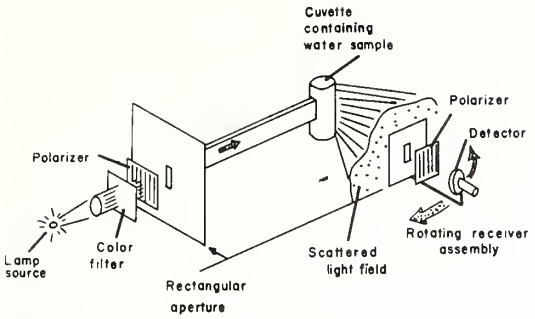

FIG. 2.—Generalized model of apparatus for grain-size analysis by the photo-scattering—sedimentation method. After Burt and Beardsley, 1969.

sensitivity is an inherent feature of all photoelectric transducers. The effect is so great that variations in output of 10 percent, 50 percent, and even more are common when the photodetector temperature changes from 0 to 30°C.

To have a finite amount of optical power fall on the photosensitive surface of the detector, the acceptance angle of the detector must be non zero, but this acceptance angle admits a portion of the scattered light into the detector surface. Burt and Beardsley state that recent measurements indicate that up to 90 percent of the particulate scattering may be contained in a cone 5° in diameter about the forward direction.

If white light is used, the beam transmittance is averaged across the entire spectrum. Burt and Beardsley remark that the concept of average transmission is difficult to apply in optical calculations.

In spite of these theoretical difficulties, Simmons (1959) and McKenzie (1963) were able to achieve a high degree of reproducibility and were able to closely correlate their results with microscopic analyses of the same material. However, the method as practiced by these two authors has two practical limitations. Both authors were concerned with only the silt range and Rose's curve for K values, as reproduced by Simmons, probably cannot be used below this range. This limitation no longer holds, since Burt (1956) has published a table giving K values down to 0.01 microns.

A second limitation is concentration of the sample being analyzed. This instrument-imposed problem of a lower limit for concentration has been previously discussed. Probably the best way to increase the sensitivity of the photo-sedimentation method and accurately measure low concentrations is to measure scatterance rather than transmittance (fig. 2). Tolman and others (1919) built a "tyndallmeter" that measured scattering at right angles to the transmitted beam. They remarked that it was sensitive to concentrations of less than .01% (100 mg/l) "suspensions which appeared transparent to the naked eye."

This is not an especially low concentration for coastal waters; in fact, it is rather high, but perusal of the paper suggests that this is merely the lowest concentration that they tried and not necessarily the lowest concentration to which the "tyndallmeter" would react.

Stamm and Svedberg (1925) devised a scatterance sedimentation meter in which the sensor consisted of a series of photographic plates exposed at intervals during sedimentation. A photometer was utilized in determining density from the negatives.

The Interagency Committee on Water Resources (1963) has built a unique optical-sedimentation system for size analysis that utilizes scattered light. It consists of a pump, a recirculating system, sedimentation chamber, and a General Electric recording turbidometer which contains a turbidity detector and a recorder. Turbidity is measured by a photovaltaic cell in the detector and interpreted in the recorder as the ratio of the light scattered by the particles in the liquid to the light transmitted through the liquid.

The transmitted light is measured for 15 seconds, the scattered light for 45 seconds, and the ratio is computed and recorded. The cycle is repeated continuously. Stability of the ratio measurement is achieved by using a single light source and a single photovoltaic cell.

The device measures both concentration and particle size distribution. Turbidity of a sample being pumped through the detector is recorded continuously to establish concentration. The flow is then stopped, and turbidity is recorded against time in the sedimentation cell. The machine is thus adoptable to field measurements of both concentration and size distribution. It can be adjusted to measure concentration ranges of either 0 to 10 PPM or 0 to 1000 PPM, and measures particle diameters from 0.020 to 0.120 mm. Finer particles require an excessively long time to measure, while coarser particles require a taller sedimentation chamber.

Inquiries to General Electric on the part of the senior author during the spring of 1967 revealed that General Electric has stopped making the turbidometer. An inquiry to St. Anthony Falls Hydraulic Laboratory, headquarters of the Interagency Committee on Water Resources, indicated that the committee has halted development of this apparatus, in part because they experienced poor reproducibility among samples of differing compositions. This was per-

haps due to differing absorption coefficients. Theirs is nevertheless the most sophisticated use of the optical-sedimentation method, and persons interested in continuing this line of development should contact the St. Anthony Falls Hydraulic Laboratory, Minneapolis, Minnesota.

Direct Optical Measurements

Direct optical measurements of grain size utilize the fact that according to both Rayleigh and Mie theory, percent transmission varies with grain size. Burt (1955) has used a Beckman spectrophotometer to measure both suspended sediment concentration and grain size in Chesapeake Bay. The spectrophotometer reads in optical density, E_λ, which is defined as the negative logarithm to the base 10 of the fraction of light energy which passes through the cell. For N spherical particles per cubic centimeter with constant radius in centimeters.

$$0.23\,E\lambda = \pi R^2\,NK$$

To determine the radius of monodisperse systems, Burt measured optical density of a sample at different wavelengths, then divided each value by E_{600}. The result, when plotted as a curve of $f(E_\lambda)$ versus λ, is independent of concentration and is directly comparable to a family of curves of f(K) versus λ that Burt has calculated. Burt determined particle radius by superimposing the experimental curve on the calculated curves and interpolating. By comparing experimental $f(E_\lambda)$ curves with synthetic $f(E_\lambda)$ curves for known size frequency distributions, Burt was able to apply his method to polydisperse systems and to estimate the spread of grain size values about the mean.

Postma (1961) has experimented with grain-size measurements by means of Secchi disc. He has shown that the relationship between Secchi disc visibility (D), concentration of suspended inorganic matter (G), and particle diameter (d) is

$$1/D = 0.1\,5\,\frac{G}{d}$$

Postma concluded that the optical grain-size values that he determined by this method were half of the values obtained by microscopic means due to the differing optical properties of organic and inorganic suspended matter.

Biggs (1968) has developed a direct optical method of determining grain size using a "Lumitron" model 402E colorimeter to determine transparency of water samples. Duplicate water samples were collected for filtration in order to establish the concentration of suspended sediment in milligrams per liter. Determination of the median "optical" grain-size from the transparency and weight data involved transforming transparency to the volume attenuation coefficient as follows (Tyler and Presisendorfer, 1962).

$$\alpha = \frac{1}{L}\ln\frac{N_\gamma}{N_o}$$

where α is the volume attenuation coefficient per cm, L is path length in cm, N is radiance at distance R from source, and N γ is source radiance. Jones and Willis (1956) empirically determined the relationship between Secchi disc visibility, weight, and median diameter of seston was given by

$$\frac{\alpha}{4.38} = \frac{1}{D}$$

substituting $\frac{\alpha}{4.38}$ for $\frac{1}{D}$ in Postma's equation, Biggs arrived at

$$d = \frac{.657G}{\alpha}$$

so that by measuring α and G, he could obtain an estimate of grain size. Comparison of optical data with microscope data indicated that the latter values were 30% coarser.

ELECTRONIC METHODS FOR PARTICLE-SIZE MEASUREMENT

Introduction

The Coulter Counter is the only instrument currently available that uses an electrical property directly for particle measurement. Many other kinds of instrument use electrical components, but these usually measure some variable which itself does not depend on electrical properties.

The Coulter Counter was developed about 15 years ago for rapid, routine counting of blood cells, but since then it has found many other applications. The early instruments were not easy to apply to materials other than blood cells or particle systems with similar characteristics, but recent developments have overcome most of the disadvantages. The new instruments can be applied to almost any situation that calls for counting and measuring of particles in the size range from 0.5 microns to 1.0 mm.

The principle and operation of the instrument have been described many times during the past decade. The most recent and comprehensive accounts are those of Interagency Committee on Water Resources (1964), Allen (1966), and Sheldon and Parsons (1967). The basic principle is very simple. If an electric field is maintained in an electrolyte, then a particle passing

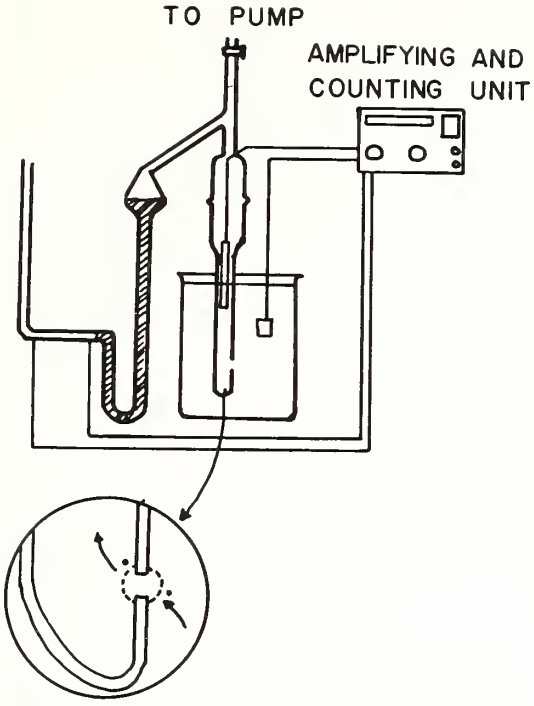

FIG. 3.—Diagrammatic arrangement of the components of a Coulter Counter. The approximate extent of the electrically sensitive zone is shown on the enlarged diagram of the aperture.

into this field will cause a change in it if the electrical properties of the particle differ from those of the electrolyte. The particle displaces its own volume of electrolyte and therefore the change produced is proportional to particle volume.

In practice and electrically sensitive zone is restricted by means of a nonconducting barrier pierced by an aperture (fig. 3). This zone has a volume about three times that of the aperture and consists of the aperture itself and two hemispheres of similar volume (Mattern, *et. al.*, 1957). Particulate material is dispersed in a suitable electrolyte and is made to flow through the aperture. As each particle passes through, the electrical properties of the sensing zone change and these changes are scaled and counted as voltage pulses. By means of electrical filters voltage pulses smaller than or larger than any two predetermined values are ignored. Therefore, by setting the filters (called "thresholds") to correspond to pulses produced by, say, 10 microns and 12 microns particles, all particles smaller than 10 microns or larger than 12 microns will be ignored and only particles between 10 microns and 12 microns will be counted. Discrimination between any two sizes can be made within the measuring range of a particular aperture (for limitations see Sheldon and Parsons, 1967).

Two limitations are imposed by the basic principle and by the physical structure of the instrument. The first is that the resistivity of the particles must differ from that of the electrolyte. For geological applications this limitation is of no consequence. Most particulate materials have very high resistivity and most electrolytes have very low resistivity. If the particle resistivity is large compared to the electrolyte resistivity all particles of the same size will produce the same instrument response. Variation in resistivity between particles is not important (Sheldon and Parsons, 1967). The second is that particles should pass through the aperture one at a time. This means that very small samples have to be taken, or, if large samples are used, suspensions must be diluted. For instance, a suspension of sediment prepared for analysis by the pipette method would have to be diluted about 1000 times before it could be analyzed with a Coulter Counter.

Grade Scales and Frequency Distributions

As the Coulter Counter measures particle volume and as most of the instrument settings progress by a factor of 2, it is convenient to use a grade scale such that particle volume varies by a factor of 2 in successive grades (Sheldon and Parsons, 1967, p. 17, Sheldon, 1969). This means that particle diameter varies by $2^{1/3}$ (or ⅓ phi) in successive grades. It is near enough to the standard quarter phi scale commonly used with other techniques for the results of Coulter Counter and other analytical methods to be compared (fig. 4).

The experimental details of techniques for determining grain-size distributions of material

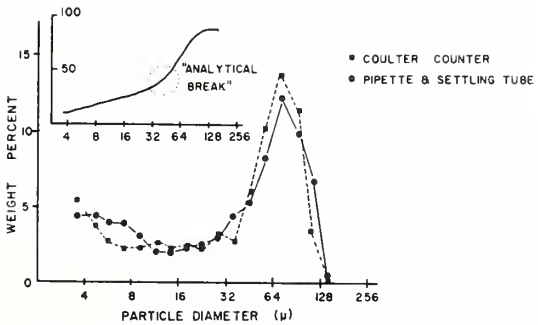

FIG. 4.—Grain-size distribution of sediment from an estuarine mud-flat (River Crouch, Essex, England). Squares indicate analysis by pipette (3–60 microns) and Emery settling tube (30–256 microns). Inset: Data re-cast as a cumulative curve to show the supposed "analytical break."

carried in suspension have been described (Sheldon and Parsons, 1967, Sheldon, 1968).

Discussion

For the grain-size analysis of sediments, the Coulter Counter has no intrinsic advantage over the conventional techniques of sieve or of settling tube and pipette analysis. However, it is very much more rapid than these. An analysis in the size range 1 micron to 50 microns can be carried out in less than ½ hour, and an analysis in the size range 1–500 microns takes less than 1 hour. When the new instruments which are currently being developed become generally available, an analysis over the size range 1 micron to 500 microns will be possible in less than ¼ hour.

The size of sample needed for a complete grain-size analysis by Coulter Counter is very much less than that needed for analysis by other methods. For fine-grained sediments (particle size range 1 micron to 100 microns) the sample need be no larger than a match head, and should the nature of the work demand it, it can be very much smaller than this. For sands, rather larger samples are required, but even these need to be no more than 0.1 gm to 0.2 gm. Although the necessity for small samples can be a disadvantage and can lead to sampling problems, in some circumstances small samples can be an advantage. It is possible to measure grain-size distributions of samples taken in close proximity; for instance, the individual laminae of varves (Sheldon and Parsons, 1967).

One considerable advantage of analysis by Coulter Counter is that the same parameter (particle volume) is measured over the whole size range. However, this is also true of a settling tube/pipette analysis (settling velocity), and, following the recent development of sieves with mesh spacings to 5.5 microns, could also be true of sieve analysis, although the latter may be technically difficult. It is of interest to note that the so-called "analytical break" which occurs at 30–50 (Fig. 2), and was originally considered to be due to difference in analytical technique for small and large particles (Krumbein and Pettijohn, 1938), is a real feature of fine-grained sediments. This was first noted by Belderson (1964), who used sieves over the size range 250 microns to 18 microns and found the "analytical break" still occurred. It was clearly not due to change in analytical method. Belderson suggested that it was caused by the formation of aggregates in samples. This is only partially true. The "break" is caused by aggregates, but these are formed during transport of the sediment, not during the analysis (Sheldon, 1968).

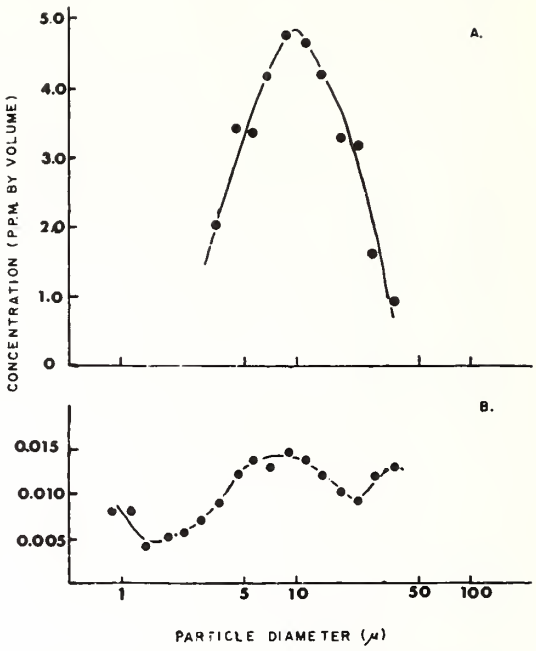

FIG. 5.—Frequence distributions of suspended material. A: Crouch estuary, England, 17 June, 1965. B: Sargasso Sea, 29°22'N, 64°03'W, 29 November, 1968. The ordinate represents the Concentration of particulate matter in a third phi diameter range.

There seems to be no foreseeable limit to the application of the Coulter Counter to the study of suspended particulate material. It has been used to measure both concentration and particle size with concentrations of material in the 1–40 micron range in excess of 30 PPM in environments ranging from a turbid estuary (Sheldon, 1968) to the gin-clear waters of the Sargasso Sea, where the concentration of material of similar size is typically less than 0.2 PPM (fig. 5).

CONCLUSIONS

Four basic methods have been described for the determination of the particle size distribution of fine-grained suspended sediment. It should be clear that no method is ideal; each measures a different property more or less closely related to particle "size." The objectives of the size analysis should dictate both the mode of analysis and the specific techniques employed within that framework.

The microscopic method, involving the actual measurement of particle images, is the most direct approach to size analysis and should be employed, at least as a supplementary method, in any serious study of a suspended sediment population. In some ways it is the most restrictive

method. In removing the suspended particles from a small volume of water by filtration weakly bound composite particles may be flattened or completety disrupted destroying the naturally occurring size distribution. Measurement of the particle images using the common microscopic techniques with graticules or micrometers is time consuming and tedious and the number of particles sized is generally small. The method of Schubel and Schiemer (1967) greatly increased the speed and precision of the microscopic method and has removed many of these objections.

A more serious limitation of the microscopic method is that it generates a number-size distribution. For many purposes the volume or weight-size distribution is more valuable, and it usually cannot be satisfactorily obtained by transformation of the number-size data.

Optical-sedimentation methods have two distinct advantages over the microscope method. The sample is not removed from its natural medium, and an hydraulic, rather than a projected diameter is obtained. Problems of size range and concentration have not yet been resolved although they are within the scope of existing technology. The problem of varying absorption coefficients for different materials has not been adequately treated in the literature. The continuous-pumping, optical-sedimentation meter that was developed by the Federal Interagency Committee on Water Resources that measures the ratio between transmitted and scattered light, is one of the most promising of its kind. Unfortunately it has been abandoned during development.

Direct optical methods likewise permit the sediment to be analyzed in its natural medium. They offer a rapid means of determining median diameter, but yield little further information on the size distribution. Two workers utilizing this method have increased the rigor of their observations by using monochromatic light (Burt, 1955, Biggs, 1968). Burt's spectrophotometer technique is the simplest, as it is independent of concentration.

The Coulter Counter is in many respects the most versatile and satisfactory instrument for analyzing the size-frequency distribution of suspended sediments. The natural medium is retained, the size range (1 mm to 0.5 microns) is the widest. The method is rapid, and may be completed on shipboard. There is a lower concentration limit, but it is probably rarely attained in nature. This limit may be .05 PPM in the 1–40 micron range. For larger particles there is a limit, depending on particle size. At 250 microns, it is about 1 particle per 10 ml. The major drawback of the method is the nature of the distribution which is based on a volume diameter rather than settling velocity or an hydraulic diameter.

Each basic method of size analysis is sufficiently limited that the final choice should depend upon the purpose of the investigation rather than upon the experience and personal prejudice of the investigator.

REFERENCES

Allen, T., 1966, A critical evaluation of the Coulter Counter. *In* Particle size analysis: London, Soc Analytical Chemistry, p. 110–127.

Atherton, E., 1952, Photoelectric turbidometer for particle size distribution: Jour. Textile Inst. Trans., v. 43, p. T173–T178.

Belderson, R. H., 1964, Holocene sedimentation in the western half of the Irish Sea: Marine Geology, v. 2, p. 147–163.

Bond, G. C., and Meade, R. H., 1966, Size distribution of mineral grains suspended in Chesapeake Bay waters: Jour. Marine Research, v. 14, p. 33–46.

Biggs, R. B., 1968, "Optical grain-size" of suspended sediment in upper Chesapeake Bay: Chesapeake Sci., v. 9, p. 261–266.

Buoyocoz, G. J., 1928, The hydrometer method for studying soils: Soil Sci., v. 25, p. 365–369.

Burt, W. V., 1955, Interpretation of spectrophotometer readings on Chesapeake Bay waters: Jour. Marine Research, v. 14, p. 33–46.

Burt, W. V. and Beardsley, G. F., 1969, Underwater optical measurements: Oceanology, May-June, p. 35–39.

Flammer, G. H., 1962, Ultrasonic measurement of suspended sediment: U. S. Geol. Survey Bull. 1141-A, 48 p.

Folk, R. L., 1961, Sedimentary petrography: Austin, Texas, Hemphills Bookstore, 325 p.

Gripenberg, S., 1938, Mechanical analyses. *In* P. D. Trask, *editor,* Recent marine sediments: Am. Assoc. Petroleum Geologists, p. 532–557.

Herdon, G., 1953, Small particle statistics: New York, Elsevier, 234 p.

Interagency Committee on Water Resources, 1940, Field practice and equipment used in sampling suspended sediment: Report No. 1, Minneapolis, St. Anthony Falls Hydraulic Laboratory, 175 p.

———, 1941A, Analytical study of methods of sampling suspended sediment: Report No. 3, Minneapolis, St. Anthony Falls Hydraulic Laboratory, 52 p.

———, 1941B, Methods of analysing sediment samples: Report No. 4, Minneapolis St. Anthony Falls Hydraulic Laboratory, 203 p.

———, 1941C, Laboratory investigation of suspended sediment samples: Report No. 5, Minneapolis, St. Anthony Falls Hydraulic Laboratory, 99 p.
———, 1943, A study of new methods for size analysis of suspendtd sediment samples: Report No. 7, Minneapolis, St. Anthony Falls Hydraulic Laboratory, 102 p.
———, 1952, The design of improved types of suspended sediment samples: Report No. 6, Minneapolis, St. Anthony Falls Hydraulic Laboratory, 103
———, 1953, Accuracy of sediment size analyses made by the bottom withdrawal tube method: Report No. 10, Minneapolis, St. Anthony Falls Hydraulic Laboratory, 115 p.
———, 1961, The single stage sampler for suspended sediment: Report No. 13, Minneapolis, St. Anthony Falls Hydraulic Laboratory, 105 p.
———, 1962, Operation and maintenance of USP-46 suspended sediment sampler: Minneapolis, St. Anthony Falls Hydraulic Laboratory, 59 p.
———, 1963, A summary of the work of the Interagency Sedimentation Project: Report S, Minneapolis, St. Anthony Falls Hydraulic Laboratory, 29 p.
———, 1964, Electronic sensing of sediment: Report R, Minneapolis, St. Anthony Falls Hydraulic Laboratory, 80 p.
Irani, R. R., and Callis, C. F., 1967, Particle size, measurement, interpretation, and application: New York, John Wiley and Sons, 165 p.
Jennings, D. S., Thomas, M. D., and Gardners, W., 1922, A new method of mechanical analysis of soils: Soil Sci., v. 14, p. 485–499.
Jerlov, N. G., 1959, Maxima in the vertical distribution of particles in the sea: Deep-Sea Research, v. 5, p. 173–184.
———, 1968, Optical oceanography: New York, Elsevier, 194 p.
Jones, P., and Willis, M. S., 1956, The attenuation of light in the sea and estuarine waters: Marine Biol. Assoc. United Kingdom Jour., v. 35, p. 431–444.
Jordan, R. R., 1965, Notes on technique for sampling suspended sediment: Southeastern Geology, v. 7, p. 9–13.
Krone, R. B., 1962, Flume studies of the transport of sediment in estuarial shoaling processes: Berkeley, Hydraulic Engineering Laboratory, University of California, 110 p.
Krumbein, W. C., and Pettijohn, F. J., 1938, Manual of sedimentary petrography: New York, Appleton-Century-Crofts, 549 p.
Kruyt, H. R., *Editor*, 1952, Colloid Science I: New York, Elsevier, 338 p.
Loveland, R. P., 1959, Methods of particle-size analysis, p. 57–86. *In:* Symposium on Particle Size Measurement, 1958, Am. Soc. Testing Materials, Spec. Tech. Pub. 234, 303 p.
Mattern, C. F. T., Brackett, F. S., and Olson, B. J., 1957, Determination of number and size of particles by electrical gating of blood cells: Jour. Appl. Physiology, v. 10, p. 56–70.
McKenzie, K. G., 1963, The adoption of a colorimeter for measuring silt-sized particles—a rapid photo-extinction (P_E) method: Jour. Sed. Petrology, v. 33, p. 41–48.
Mie, G., 1908, Beiträge zur optik Trüber Medien, speziell Kolloidalen Metall-lösungen. Annals Physik, v. 25, p. 377–381.
Milner, H. B., 1962, Sedimentary petrography, v. 1, Methods in sedimentary petrography: New York, MacMillan, 643 p.
Morrison, C. G. T., 1925, The effect of light on settling suspensions: Royal Soc. [London] Proc., v. 108A, p. 280–284.
Oden, S., 1915, Eine nue methode zur Mechanischen Bodenanalyse: Int. Mitt. f. Bodenkunde, v. 5, p. 257–311.
Payne, R. E., 1948, The measurement of particle size of subsieve powders: Third national Conference of the American Instrument Society, p. 133–148.
Postma, H., 1961, Suspended matter and secchi disc visibility in coastal waters: Netherlands Jour. Sea Research, v. 1, p. 359–390.
———, 1967, Sediment transport and sedimentation in the estuarine environment. *In* Lauff, G., *editor,* Estuaries: Am. Assoc. Adv. Sci. Pub., p. 158–179.
Rayleigh, Lord, 1871, On the scattering of light by small particles: Philos. Mag., v. 41, p. 447–454.
Richardson, E. G., 1934, An optical method for mechanical analysis of soils, etc.: Jour. Agricultural Sci., v. 24, p. 457–468.
———, 1936, A photo-electric apparatus for delineating the size frequency distribution of clays or dusts: Jour. Sci. Instruments, v. 13, p. 229–233.
Rose, H. E., 1953, The measurement of particle size in very fine powders: London, Constable and Company, 309 p.
Schubel, J. R., 1968, Suspended sediment of the northern Chesapeake Bay: Johns Hopkins Univ., Chesapeake Bay Inst. Tech. Rep. 35, Ref. No. 68–2.
———, 1969, Size distributions of the suspended particles of the Chesapeake Bay turbidity maximum: Netherlands Jour. of Sea Research, v. 4, p. 283–309
Schubel, J. R., and Schiemer, E. W., 1967, A semiautomatic microscopic particle size analyzer utilizing the Vickers image splitting eyepiece: Sedimentology, v. 9, p. 319–326.
Sheldon, R. W., 1968, Sedimentation in the estuary of the River Crouch, Essex, England: Limnology and Oceanography, v. 13, p. 72–83.
———, 1969, A Universal Grade Scale for Particulate Materials, Geol. Soc. London Proc., 1659, p. 293–295.
——— and T. R. Parsons, 1967, A Practical Manual on the Use of the Coulter Counter in Marine Science: Coulter Electronics, Toronto, p. 66.
Simmons, 1959, The photo-extinction method for the measurement of silt-sized particles: Jour. Sed. Petrology, v. 29, p. 233–245.
Stokes, G. G., 1851, On the effect of the internal friction of liquids on the motion of pendulums: Cambridge Philoso. Soc. Proc., v. 9, p. 8–106.

STOMM, A. J., AND SVEDBERG, T., 1925, The use of scattered light in the determination of the distribution of size of particles in emulsion: Jour. Am. Chem. Soc., v. 47, p. 1582–1596.
STUTZ, G. F. A., The scattering of light by dialectrics of small particle size: Jour. Franklin Institute, v. 210, p. 67–85.
SWIFT, D. J. P., AND PIRIE, R. G., 1970, Fine sediment dispersal in the Gulf of Panama: A reconnaissance: Jour. Marine Research, p. 65–95.
TABIBIAN, R. M., HELLER, W. AND EPEL, J. A., 1956, Experimental investigations of the light scattering of colloidal spheres: Jour. Colloid Science, v. 11, p. 195–213.
TOLMAN, R. C., REYERSON, L. H., VLEIT, E. B., GERKE, R. H., AND BROOKS, A. P., 1919, Relations between the intensity of the Tyndall beam and concentration of suspensions and smokes: Jour. Am. Chem. Soc., v. 41-I, p. 300–303.
VAN DE HULST, H. C., 1957, Light scattering by small particles: New York, John Wiley and Sons, 470 p.
WENT, F. W., 1968, The size of man: Am. Scientist, v. 56, p. 400–413.
WHITEHOUSE, V. G., JEFFREY, L. M., AND REBRECHT, J. D., 1960, Differential settling tendencies of clay minerals in saline waters: Proc. 7th Natl. Conf. Clays, Clay Minerals, p. 1–79.

Reprinted from Geotimes, 12-14.

Deep Sea Drilling Project

Leg 16

by the scientific staff

Chief scientists on Leg 16 of the Deep Sea Drilling Project, which is supported by the National Science Foundation: Tjeerd H. van Andel and G. Ross Heath—both from Oregon State University, Corvallis. (Van Andel is shown at center above, and Heath at right, with Dell Redding of Phillips Petroleum Co., cruise operations manager.) Sedimentologists: Richard H. Bennett (N.O.A.A. Atlantic Oceanographic & Meteorological Laboratories, Miami, Fla.), Santiago Charleston (Instituto Mexicano del Petróleo, Mexico City), David S. Cronan (University of Ottawa), Kelvin S. Rodolfo (University of Illinois at Chicago Circle), Robert S. Yeats (Ohio University, Athens). Paleontologists: David Bukry (U.S. Geological Survey, La Jolla, Calif.), Menno Dinkelman (Oregon State University, Corvallis), Ansis Kaneps (Scripps Institution of Oceanography, La Jolla, Calif.).

On Leg 16 of the Deep Sea Drilling Project in February and March, the *Glomar Challenger* sailed from the Panama Canal to Hawaii. We had these main objectives: 1) to examine the ages of basement, stratigraphic sections and depositional histories of the ridges surrounding the Panama Basin, and 2) to complete a series of holes begun on Legs 5, 7, 8, and 9 to delineate the tectonic and depositional history of the eastern equatorial Pacific. We drilled 9 sites on Leg 16 of which 8 were successful (see table) and the ninth had to be abandoned because we encountered hard formation at the surface. Experimentation with the new reëntry system took place at the last site.

Panama Basin—This basin is bordered by the Cocos and Carnegie ridges in the west and south (see chart). Its northern limit is the continental margin of Central America; its eastern limit, northeastern South America. A rift zone, trending east-west, lies between the Carnegie and Cocos ridges; the sea floor of the western part of the basin is the result of spreading from this rift during the last 10 million years.

The rift is offset by fracture zones oriented north-

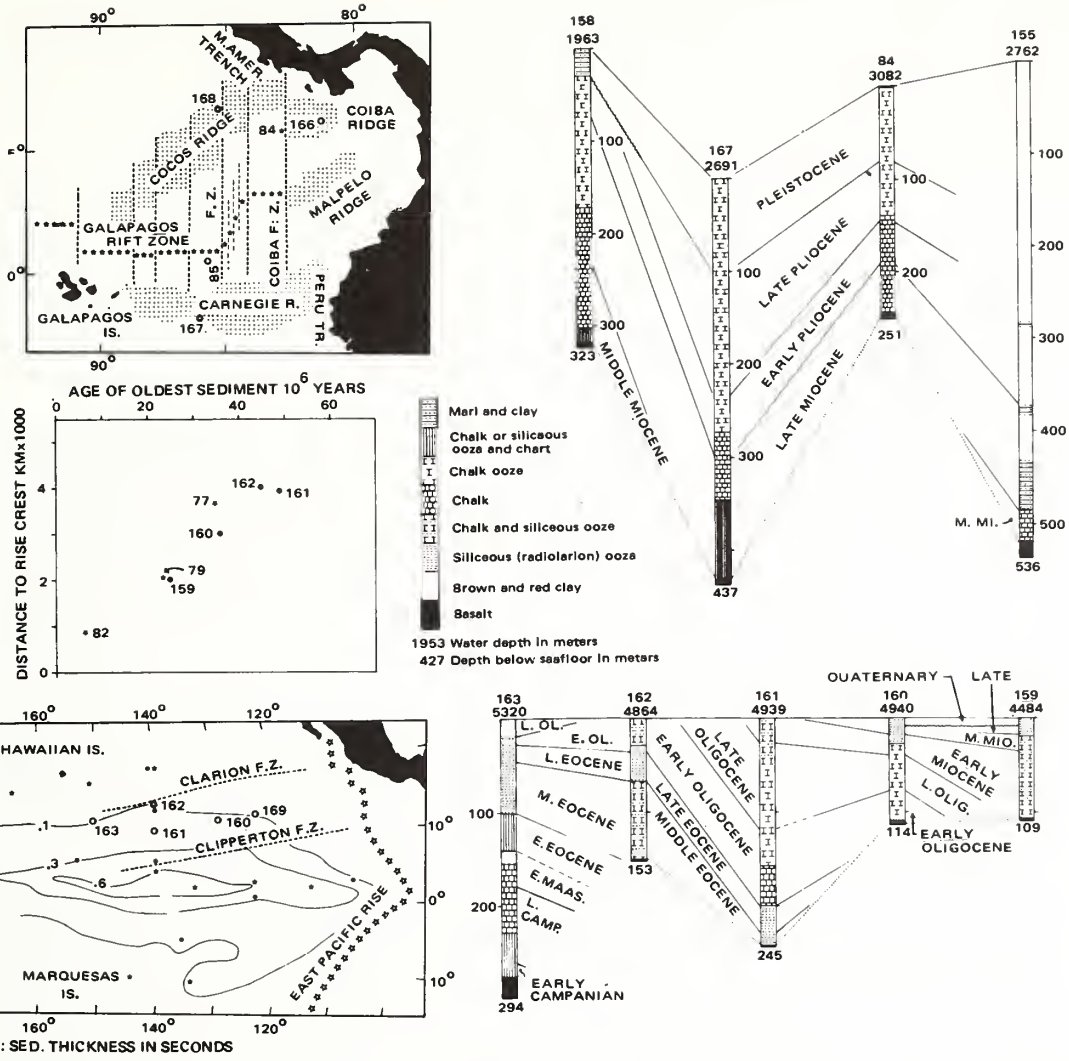

south. The Cocos and Carnegie ridges and some high blocks in the eastern part of the basin are structurally similar and have a sediment cover that is distinct from that of the deeper and younger basins. Based on geophysical evidence, van Andel and others have postulated that these high blocks once formed an ancestral Carnegie Ridge, which was split lengthwise by the formation of the Galapagos Rift Zone before the late Miocene. Rifting originated in the east, and successive blocks, now forming the Malpelo, Coiba, and segments of the Cocos Ridge, moved northward. When these blocks collided with the eastern extension of the Middle America Trench, they sealed the subduction zone. Isostatic rebound may then have led to the uplift of the Panamanian Isthmus. If this model is correct, the basal sediments of the blocks should be identical, and should then diverge in character upward as a consequence of the northward migration of the northern blocks into different waters. Sites 155-158 were chosen to test this hypothesis. Site 84 (see April 1970 *Geotimes*) provides a sedimentary section of the rift zone itself.

The findings at Sites 155-158 are in general accord with the hypothesis. At all 3 sites, the oldest deposits are chalks typical of the equatorial zone of high productivity. Commonly, they contain chert layers and nodules in the lower part. At the Carnegie site (157) a nannofossil chalk of equatorial type continues throughout the entire section. At the others, the chalk is replaced first by calcareous oozes indicative of less productive waters and finally by deposits rich in clay and volcanic ash probably derived from the nearby continental margin. Sedimentation rates confirm this model; they are high in the lower section at all 3 sites, then at 155 and 158 they decrease in the middle portions before increasing again in the upper part. At Site 157, on the other hand, the sedimentation rate shows no intermediate decrease and remains close to that to be expected under the equatorial-current system. The transitions to the regimes of somewhat reduced sedimentation and subsequent more rapid deposition occur considerably earlier at Site 155 than at site 158, as predicted by the tectonic hypothesis. The basement age at both 155 and 158 is middle Miocene. Unexpectedly, the basement at Site 157 is much younger

(late Miocene). Perhaps this young basalt is derived from the Galapagos volcanic center.

West Flank, East Pacific Rise—3 principal factors govern the depositional history of the eastern equatorial Pacific. Sea-floor spreading moves the crust westward from the shallow crest, where carbonates accumulate, into the deeper water of the lower flank, which lies below the calcite compensation depth and receives only biogenous silica and some inorganic detritus. A general northwestward shift of the Pacific plate, which appears to have continued since the early Cenozoic, carries the sea floor from a zone of slow deposition in the South Pacific through the equatorial zone of high productivity and rapid deposition into the north-central Pacific where deposition is again slow. The resulting sequence of deposits changes from siliceous to calcareous to siliceous. Finally, the calcite-compensation level—the depth below which calcite is completely dissolved—moved from a relatively shallow position during the Eocene to a depth in the Oligocene at least 1,000 m greater than the present 4,600 m or so. The interaction of these 3 factors has determined the arrangement in time and space of calcareous (rapid deposition above compensation depth), biogenous siliceous (moderate deposition below compensation depth), and red and brown clay (slow deposition below compensation depth) facies in the equatorial zone.

To unravel these interactions and to determine the depositional, tectonic, and oceanographic history of the eastern equatorial Pacific, a series of sites was drilled on Legs 8 and 9. Sites 159-162 of Leg 16 complete this series (see chart), which provides several north-south and east-west traverses across this critical region. Results from Sites 42 and 70-75 showed that the Oligocene calcareous belt was wider and its axis situated farther north than the corresponding Miocene facies (see February 1970 *Geotimes*). Sites 161 and 162, unlike those drilled earlier, succeeded in penetrating through the Eocene chert into volcanic basement, and show the extent of this shift during the Oligocene and Eocene. The thickest lower Oligocene lies north of the axis of deposition of the upper Oligocene, and the upper and middle Eocene zones of maximum thickness follow successively farther north. The calcareous zone appears to have been widest during the Oligocene and narrowed in the Miocene. The upper Eocene, although showing a distinct thickening near Site 162, is mainly siliceous although the middle Eocene shows a calcareous facies only at its thickest point. The northward migration of the equatorial belt of thickest deposits is thus well documented; the marked reduction in carbonate content of sediments from even the zone of maximum accumulation in the middle and late Eocene points to shoaling of the calcite compensation depth, with a possible shallowest position in the upper Eocene.

Sites 159-162 also show the effect of westward sea-floor spreading, both by the increasing age of deposits immediately overlying the basement (which is extrusive in all cases) and by a westward reduction in carbonate content in each stratigraphic interval as the sea floor became progressively deeper. The results confirm the existence of widespread regional erosion on the lower flank of the Rise; westward, progressively older formations occur at the surface.

Sea-floor spreading—The ages of the sediments immediately overlying the extrusive basalts make possible an estimate of the rates of sea-floor spreading if we assume that the rift axis was located at the present crest of the East Pacific Rise (see graph). Within the limits of error of the age determinations and distance estimates, they indicate an average spreading rate of about 8 cm/year. This value is much higher than the 5-6 cm/year that has prevailed since the late Miocene. Our values confirm the estimates provided by Leg 9 sites and earlier estimates based on ages of surface cores.

Site 163—The results from this site do not match those of the sites farther east. A mainly siliceous Oligocene-Eocene section overlies a mainly calcareous upper Cretaceous sequence indicative of equatorial deposition. The two biogenous sequences are separated by almost barren Maestrichtian zeolitic clay with chert layers. Because the cherts prevent recovery of intervening soft sediments, the nature of the Cretaceous-Tertiary transition is unknown; no sediments in the interval from early Maestrichtian to middle Eocene were recovered. The basement age of approximately 78 million years exceeds the extrapolated age of 65 million years calculated from the spreading rate given above, and the position of the calcareous Cretaceous is well south of the inferred equatorial position during the early Cenozoic and does not agree with the depositional history postulated above. The crust between Sites 161/162 and Site 163 is marked by a zone of highly fractured basement and very thin sediment. The significance of Site 163, similar to some sites drilled farther west on Leg 7, requires further consideration.

Holes drilled on Leg 16

site	latitude	longitude	date	water depth (m)	penetration (m)	number of cores	terminated in
155	06°07.4'N	81°02.6'W	Feb. 6-8	2,752	536	15	Middle Miocene basalt
156	01°40.8'5	85°24.1'W	Feb. 11-12	2,369	4	2	Manganese crust
157	01°45.7'5	85°54.2'W	Feb. 12-15	2,591	437	49	Late Miocene basalt
157A	01°45.7'S	85°54.2'W	Feb. 15-16	2,591	27	3	Pleistocene chalk ooze
158	06°37.4'N	85°14.2'W	Feb. 18-20	1,953	323	36	Middle Miocene basalt
159	12°19.9'N	122°17.3'W	March 1-3	4,484	109	14	Late Oligocene basalt
160	11°42.3'N	130°52.8'W	March 5-7	4,940	114	14	Early Oligocene basalt
161	10°40.3'N	139°57.2'W	March 9-11	4,939	126	14	Early Oligocene chalk
161A	10°40.3'N	139°57.3'W	March 11-13	4,939	245	15	Middle Eocene basalt
162	14°52.2'N	140°02.6'W	March 15-17	4,854	153	17	Middle Eocene basalt
163	11°14.7'N	150°17.5'W	March 20-25	5,320	294	29	Early Campanian basalt
163A	11°14.7'N	150°17.5'W	March 25-26	5,320	151	2	Early Maestrichtian clay

Reprinted from Remote Sensing of the Troposphere, edited by V. E. Derr, U. S. Dept. of Commerce and the Electrical Engineering Dept., University of Colo., Boulder, Colorado.

Chapter 22 REMOTE SENSING OF THE OCEAN

Kirby J. Hanson
National Oceanic and Atmospheric Administration
Atlantic Oceanographic and Meteorological Laboratories
Sea-Air Interaction Laboratory
Miami, Florida

22.0 Introduction

Progress in remote sensing of the oceans has been slow since the satellite era began more than a decade ago. The reasons for this are numerous. However, I believe the over-riding reason is that, although satellite experiments were designed to study both meteorological and ocean variables, the atmospheric variables (such as cloudiness) were clearly distinguishable and had great utility for meteorologists. For the oceanographer, the satellite provided useful sea surface temperature measurement only over a small fraction of the world's oceans where upwelling and western boundary currents cause horizontal temperature gradients which were large enough to be detectable above atmospheric and measurement noise. It is little wonder the oceanographic community has been slow to respond to the potential offered by satellite platforms.

In spite of the difficulty in interpreting sea surface temperature over broad oceanic areas, considerable progress has been made in the past five years. That progress is discussed in the first section of this chapter.

Studies of the possibility of global measurement of other oceanic variables have continued, mainly supported by NASA. These studies have led to a great deal of optimism about the possibility of remote sensing of salinity, temperature, surface roughness, foam, sea spray, sea ice coverage, and phytoplankton in the surface mixed layer of the ocean. Passive microwave and ocean color measurements may make these global measurements possible. They are discussed in the second and third sections of this chapter. A shortcoming of this chapter is that it does not include a discussion of the potential of active microwave sensing, or remote sensing of heat flux from the ocean surface as exemplified by the work of McAlister and his colleagues of Scripps, University of California, San Diego.

Because of the rapid development in these three areas, there is no single document which gives students a statement of present knowledge. To attempt to fill this need, this chapter gives the reader the parametric relationship between oceanic variables and the electromagnetic energy either emitted or reflected from the ocean surface. It also discusses what the major uncertainties are today.

The atmosphere is not transparent to all electromagnetic energy and measurement systems for remote sensing of the ocean must make use of windows in the absorption spectra of the active atmospheric gases (mainly H_2O, CO_2, O_3, O_2) in order to detect energy from the ocean. The principal atmospheric windows for visible, IR and microwave radiation are listed in (T22.1).† The boundaries of the windows are difficult to define because the transmissivity depends both on concentration of the active absorbing gases, and on path length of the radiation through the atmosphere.

22.1 Infrared Detection–Sea Surface Temperature

22.1.1 Satellite Experiments

When the first infrared (IR) window data were obtained from TIROS II in November, 1960, the interest of the investigators was meteorological; they examined the space and time variation in surface temperature over continental regions (e.g., Fritz, 1963, Rao and Winston, 1963). They also investigated the remote detection of cloud top heights for use in synoptic meteorology. Small attention was given to oceanography in the analysis of these early TIROS Medium Resolution IR (MRIR) data.

In 1964 the High Resolution Infrared Radiometer (HRIR) on NIMBUS-I provided an improved resolution of 5 n mi at the sub-satellite point. This was a great step forward for oceanography because it gave better resolution of horizontal temperature gradients along ocean current boundaries and upwelling regions than was possible with TIROS MRIR data. Table (22.2) shows the improvement of resolution in the IR window sensors as the satellite program evolved.

†The radiation windows can also be seen in the atmospheric transmissivity curve in the top of (F22.24).

Table 22.1 Principal Atmospheric Windows of the Electromagnetic Spectrum

Window	Wavelength	Frequency (GHz)	Absorbing Gas	
			Lower Boundary†	Upper Boundary†
Visible	0.3 to 0.9 μm	–	O_3	H_2O
Near IR	1.5 to 1.6 μm	–	H_2O	H_2O
Near IR	2.0 to 2.3 μm	–	H_2O	H_2O
Intermediate IR	3.5 to 4.5 μm	–	H_2O	H_2O
Far IR	8.0 to 9.0 μm	–	H_2O	O_3
Far IR	10.0 to 12.5 μm	–	O_3	CO_2
Microwave	0.3 to 0.36 cm	100 to 80	H_2O	O_2
Microwave	0.7 to 1.0 cm	45 to 30	O_2	H_2O
Microwave	2.0 to > 30 cm	15 to < 1	H_2O	–

† Refers to wavelength

An analysis of surface temperatures of the Gulf Stream, shown in (F22.3), is another example of significant oceanic temperature gradients (Allison, et al., 1967). These data are also from the NIMBUS II HRIR experiment. Studies of ocean current boundary detection and movement have been done by Warnecke, et al. (1967), Hansen and Maul (1970), and Maul and Hansen (1971).

These and other data from NIMBUS II provided hope for the remote detection of sea-surface temperature on a global scale to delineate major current boundaries and upwelling regions. But they also introduced the difficult task of properly interpreting sea-surface temperature from IR window measurements. This requires an understanding of how active atmospheric gases, clouds, and aerosols modify radiation emitted by the sea surface. The major progress of a number of investigators on these problems is reported in subsequent sections of this chapter.

In the period from 1966 to 1970 there was great improvement in displaying, mapping, and brightness enhancing IR satellite data. In 1970 ITOS-I provided many spectacular views of horizontal gradients in sea temperature which mark current bodies. Figure (22.4) shows the position of the north wall of the Gulf Stream on February 15, 1971. Relatively cold water outlines the Bahama Banks and coastal water in the Gulf of Mexico.

In (F22.5) cold air is moving off the east coast from New York to Florida causing cloudiness to develop over the Gulf Stream. The colder surface water south of Cape Hatteras appears to be moving eastward into the warm Gulf Stream in two large swirls under the influence of this offshore flow.

The scanning radiometers (SR) of ITOS-I and NOAA-I have 4 n mi resolution at nadir.† Future NOAA satellites, beginning with ITOS-D, are expected to have improved resolution with the addition of a Very High Resolution Radiometer (VHRR) which has resolution of 0.5 n mi at nadir (McClain, 1970).

Data from the NIMBUS-I HRIR experiment were used by many investigators for oceanographic studies. The radiometer contained a lead selenide photo-conductive cell which was radiatively cooled to -75 °C and responsive to radiation in the 3.4-4.2 μm region. The radiometer field of view was 0.5 degrees. A scanning mirror, rotating in front of the detector, scanned normal to the orbital path. A sample of the detector output over two complete scans is shown in (F22.1). During each complete scan, the detector viewed space, the satellite housing, and the earth scene below. Data from space and the radiometer housing are useful in earth locating and evaluating the data. A complete description of the experiment is given in NASA, (1966).

NIMBUS satellites are in a noon/midnight local sun time orbit. This provides global coverage twice a day. However, only night-time coverage is useful for surface temperature determination with HRIR data, because a sufficient amount of reflected solar radiance is present at 3.4-4.2 μm during the daytime to contaminate the IR measurements.

In using NIMBUS HRIR data, it was natural for investigators to look for ocean temperature features which have large horizontal temperature gradients. One example is that due to upwelling along the Somali coast, as shown in (F22.2) from Allison and Kennedy (1967). Here the temperature varies by 25 °F over only a few degrees latitude. Similar studies have recently been reported by Warnecke, et al. (1971).

†Nadir: the point of the earth's surface intersected by a line between the satellite and the earth's center.

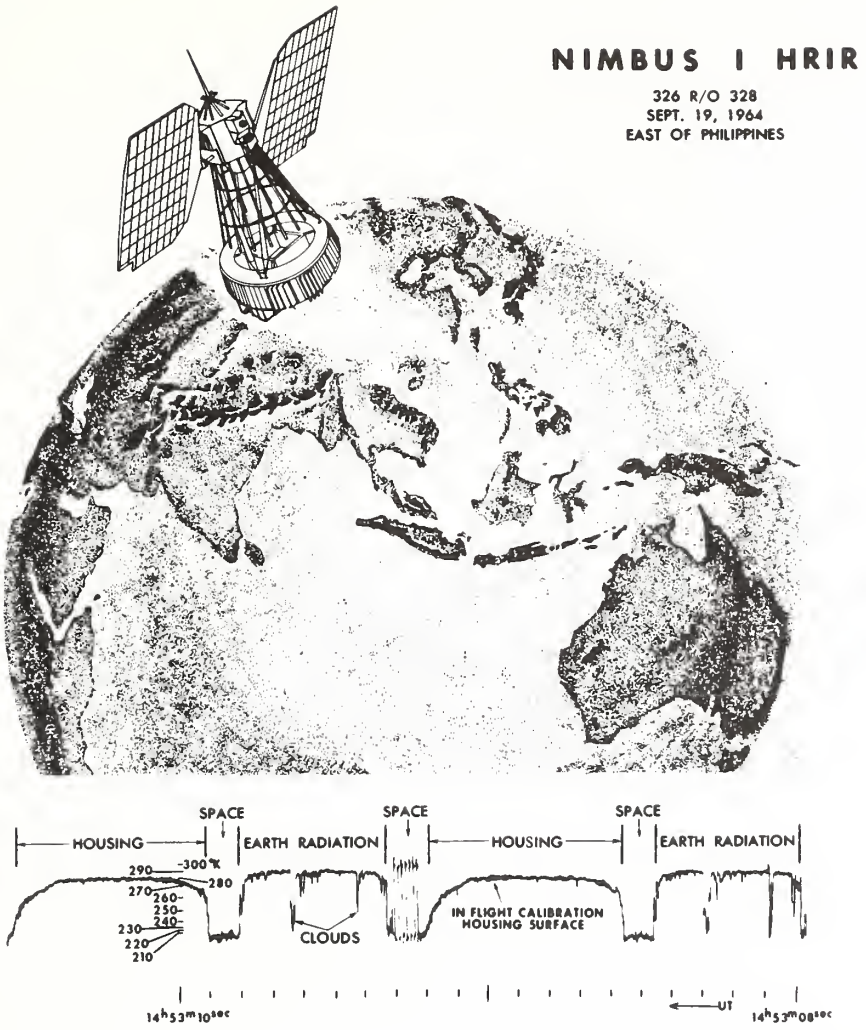

Figure 22.1 *Portion of an HRIR analog record of NIMBUS I. In the example, the mirror made two complete revolutions, scanning the effective radiation temperature of space and the radiometer housing as well as the earth. The space and radiometer housing data are useful in positioning the satellite and calibrating the radiometer (after LaViolette and Chabot, 1968).*

An example of sea surface temperature mapping, in (F22.6), is from a computer automated technique for global monitoring of sea surface temperature (Leese, 1971b) being developed at the National Environmental Satellite Service, NOAA. The two left polar projections show mean temperatures on a grey scale from 270-304 °K. The two right polar projections indicate the number of days which have elapsed since new satellite data have been added to the mean temperature value for each location. The grey scale for the two right projections ranges from (a) greater than 5 days (light grey); (b) 2-5 days (medium grey); (c) 1 day (black). Complete coverage from each satellite orbit is not possible because the computer program has certain rejection criteria when the effect of clouds is present in the data. A description of the experimental model for obtaining these temperature maps from ITOS-I is given by Leese, et al., (1971a). In (F22.6) there are numerous grey areas which indicate no satellite coverage was possible for more than 5 days due to clouds. This difficulty of cloud contamination of the data should improve as the very high resolution IR sensors are added in the NOAA satellite series and 0.5 n mi radar resolution is obtained with these sensors.

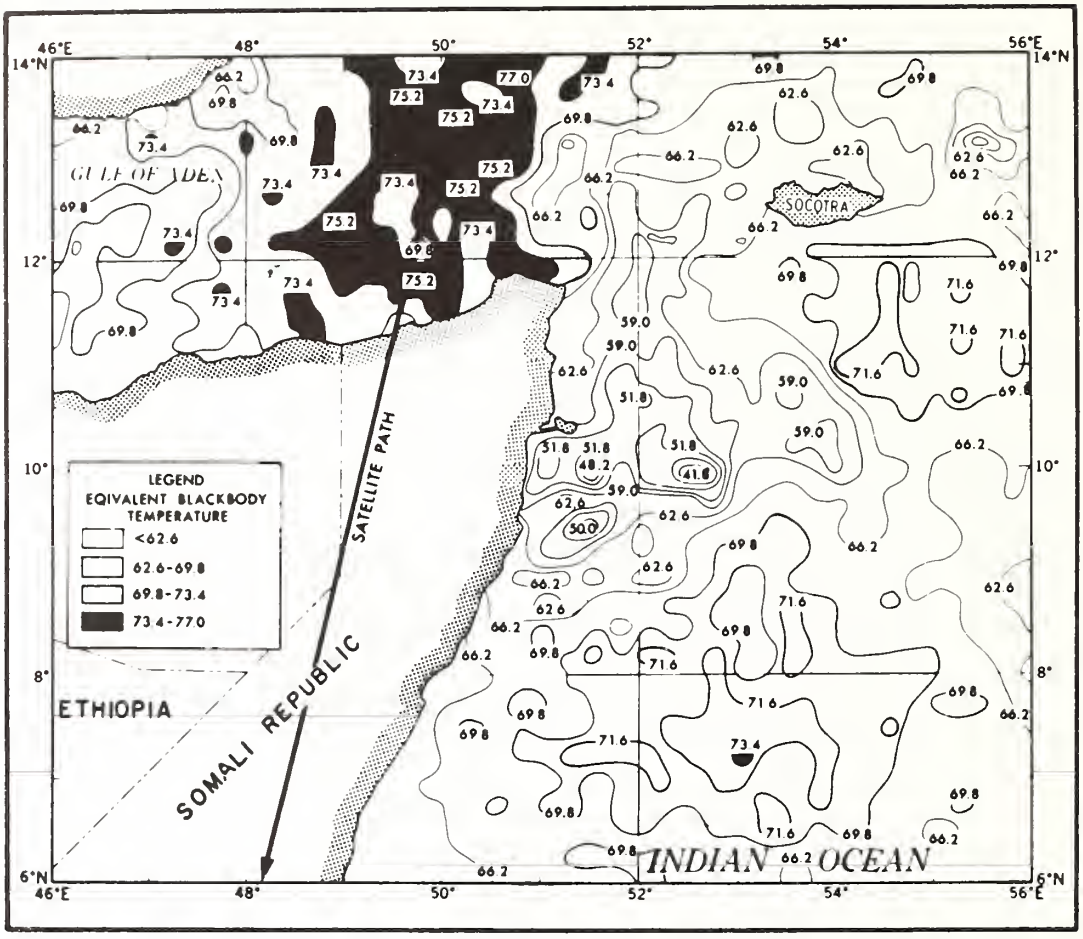

Figure 22.2 *NIMBUS I determination of sea surface isotherms (°F) along the Somali coast related to upwelling of cold water in that region (after Allison and Kennedy, 1967).*

22.1.2 Theory

The notation and some of the discussion in this section follows that of Holter (1970). The fundamental radiation equation of Plank (1900) gives the spectral distribution of radiation from a self-emitting perfect radiator, called a blackbody, with uniform temperature. This theoretical law agrees with experimental results and applies to all regions of the electromagnetic spectrum. Plank's law, stated in terms of spectral radiant emittance, is

$$W_{B\lambda} = C_1 \lambda^{-5} [\exp(C_2/\lambda T) - 1]^{-1} \tag{22:1}$$

and has units of erg/cm^2 sec μm. C_1 and C_2 are well known radiation constants; λ is wavelength and T is the temperature of the emitting surface.

Because most objects are not perfect radiators, a radiative efficiency factor, ϵ_λ, termed spectral emissivity, is defined as

$$\epsilon_\lambda = W_\lambda / W_{B\lambda} \tag{22:2}$$

where W_λ is the spectral radiant emittance of an imperfect radiator, called a greybody. Depending on the

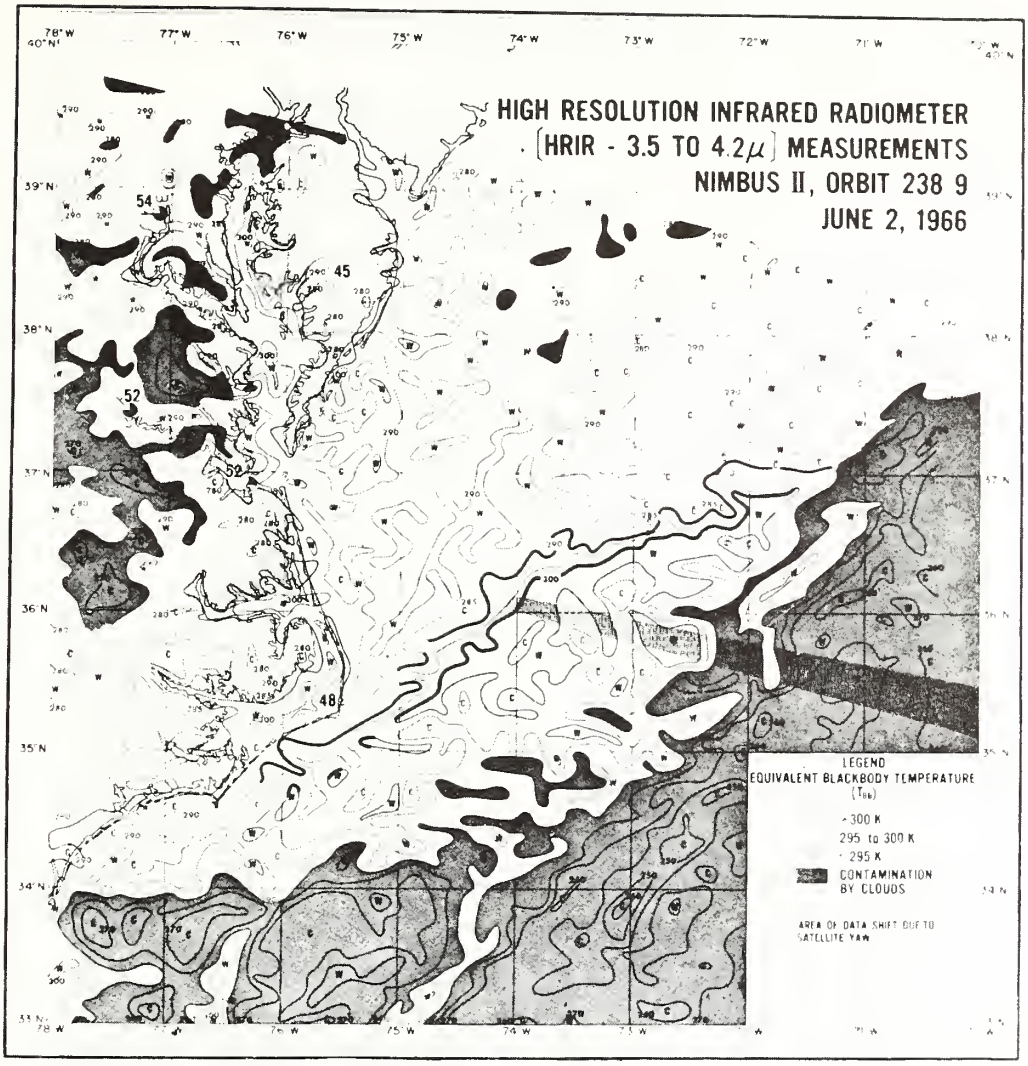

Figure 22.3 *Northern boundary of the Gulf Stream as observed by NIMBUS II (after Allison, et al., 1967).*

radiative efficiency of a surface, the spectral emissivity ranges from near zero for poor radiators to unity for perfect radiators. Using (22:1) and (22:2) calculations can be obtained of the spectral radiant emittance of any surface of known temperature and spectral emissivity.

However, the spectral radiant emittance of a surface does not describe completely the electromagnetic energy emanating from that surface. The reason for this is that greybody surfaces reflect as well as emit energy. This is shown by a form of Kirchhoff's law which states that if a surface is optically opaque, then the spectral reflectivity, ρ_λ, and spectral emissivity, ϵ_λ, of that surface have the simple relation of

$$\rho_\lambda = 1 - \epsilon_\lambda \tag{22:3}$$

Thus, infrared radiation from a surface is due both to self-emission of the surface and reflection of a portion of the radiation incident on the surface.

Figure 22.4 *ITOS-1 scanning radiometer IR picture over the East coast of the United States, February 15, 1971, orbit No. 4853. The northern boundary of the Gulf Stream is clearly visible. Temperature gradients over the Bahama Banks and in the Gulf of Mexico are also visible (after Watson, 1971).*

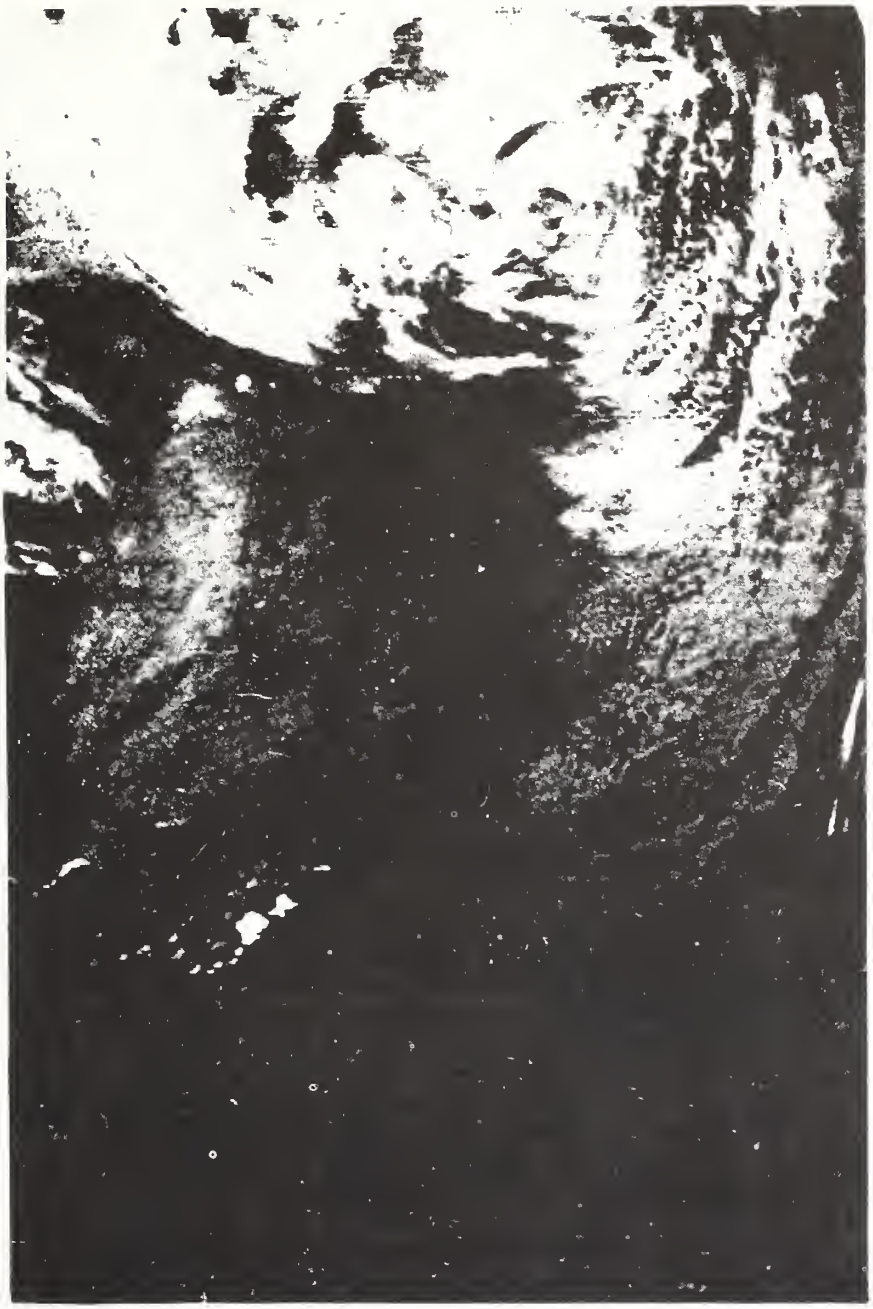

Figure 22.5 *ITOS-1 scanning radiometer IR picture over the East coast of the United States, March 5, 1971, orbit No. 5078. Cold water eddies appear to penetrate the northern boundary of the warm (dark) Gulf Stream east of North Carolina, as cold polar air moves off the entire east coast of the United States (after Watson, 1971).*

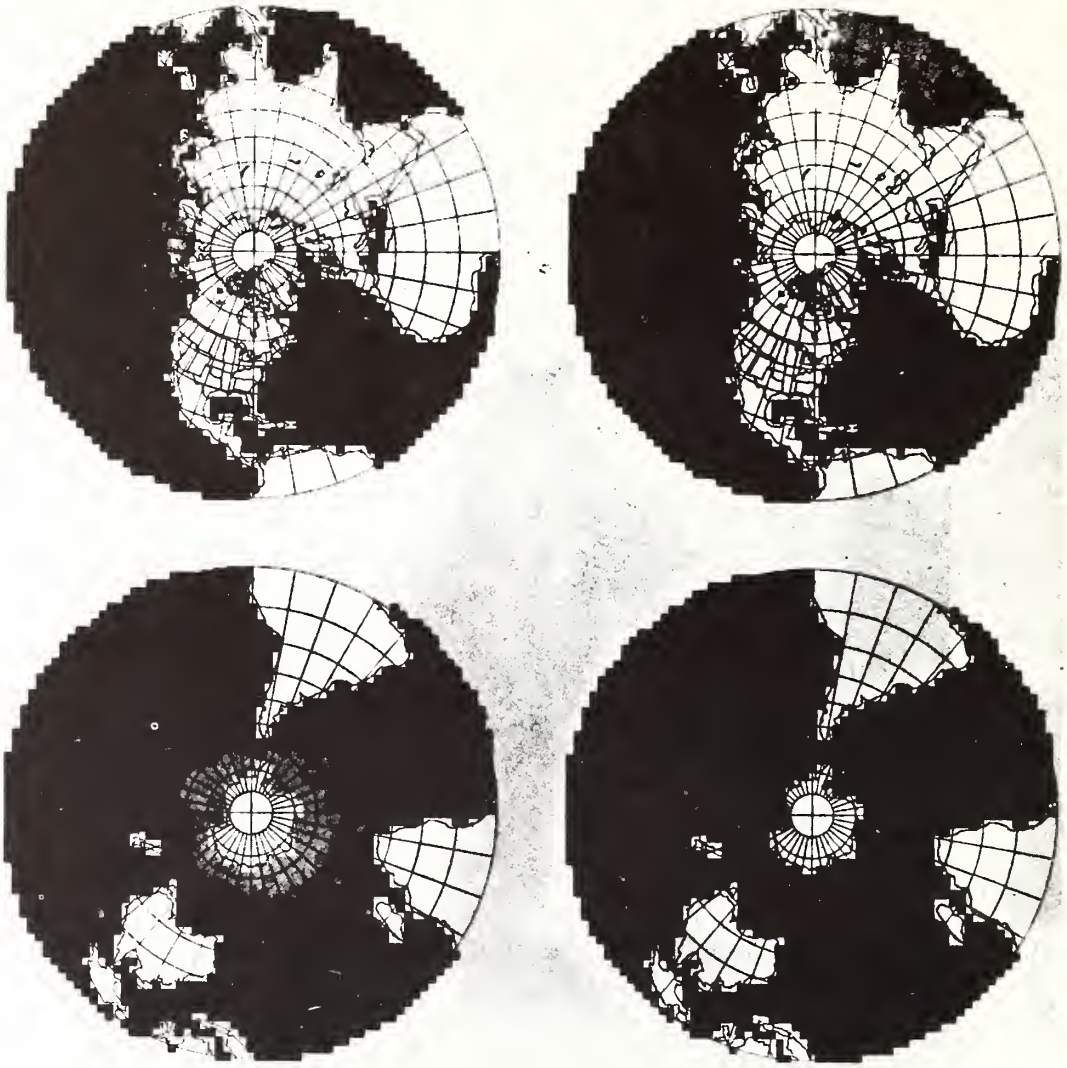

Figure 22.6 *Average sea-surface temperature from ITOS-1 obtained by computer automated technique developed at the National Environmental Satellite Service, NOAA (Leese, 1971b). Temperature maps (left) indicate temperatures from 270-304°K. Maps (right) indicate the frequency with which new satellite data have been used to update the mean temperature (Leese, 1971a).*

If these radiation principles are applied to an ocean surface, it follows from the previous statement that infrared radiation emanating from the ocean surface is due both to self-emission of the top few micrometers of the ocean and to reflection by the ocean surface of infrared radiation from such natural atmospheric sources as clouds, water vapor, carbon dioxide, and aerosols. The sum of these two radiation components is defined as the effective spectral radiance emittance of the sea surface, $W_{e\lambda}$.

$$W_{e\lambda} = \epsilon_\lambda W_{B\lambda} + \rho_\lambda W_{a\lambda} \tag{22:4}$$

where the self-emission component is $\epsilon_\lambda W_{B\lambda}$ and the surface reflection component is $\rho_\lambda W_{a\lambda}$.

If a determination of the effective spectral radiant emittance of the sea surface is to be obtained from satellite measurement, then account must be made of infrared absorption and emission by atmospheric water vapor, carbon dioxide, and ozone. At satellite height, the upward spectral radiance at a given zenith angle, θ, and wavelength, λ, is given by

$$N_\lambda(\theta) = W_{e\lambda}(T_s)\,\tau_{\lambda a}(\theta) + \int W_{a\lambda}(T_a)\,d\tau_\lambda(\theta) \qquad (22:5)$$

Where: $W_{e\lambda}$, the effective spectral radiant emittance of the sea surface at temperature T_s; $\tau_{\lambda a}$, the spectral transmissivity through the entire atmosphere; τ_λ, the spectral transmissivity through a layer which extends from any height in the atmosphere to the top of the atmosphere; $W_{a\lambda}$, the spectral radiant emittance of the atmosphere at temperature, T_a. The first term on the right side of (22.5) is the radiant emittance of the sea surface to space, and the second term is the emittance of a cloudless atmosphere to space. The integration is carried out from the ocean surface to satellite height.

In the real atmosphere, clouds and aerosols attenuate the radiant emittance of the ocean surface and emit radiation as well. Realistic radiative transfer models of the combined effects of clouds, aerosols and gaseous absorbers are needed, because at present experimental results do not agree with theoretical transfer calculations based on pure gaseous atmospheres (Kuhn, 1963, 1972) (Kuhn and Stearns, 1971, 1972).

At infrared wavelengths, molecular absorption by atmospheric gases is important. The active absorbing gases in the infrared are H_2O, CO_2, N_2O, and O_3 and other minor absorbers. Where one or more of these gases are strongly absorbing in the infrared, the atmosphere is essentially opaque. A region of weak absorption by these gases is called an atmospheric window.

As shown in (F22.7) these regions are difficult to define because the wings of the absorption bands cause partial absorption in the upper and lower wavelength portion of the window. Satellite systems for sensing sea-surface temperature make use of these atmospheric windows. The wavelength region of the window is of primary consideration in selecting the wavelength region of satellite IR detectors of sea-surface temperature. Table (22.2) shows that the 3.4-4.2, 8-12, and 10.5-12.5 μm regions have been employed successfully in satellite IR sensors. A second consideration in selecting sensor wavelength is the amount of radiant energy in that portion of the spectrum. As previously discussed, the amount of energy radiated by a blackbody surface is given by Planck's function (22:1) and is shown in (F22.8). Clearly, the 8-12 μm window region has the advantage of maximum emitted energy at temperatures near 300 °K. In the 3.4-4.2 μm window, roughly comparable amounts of reflected sunlight and emitted radiation are

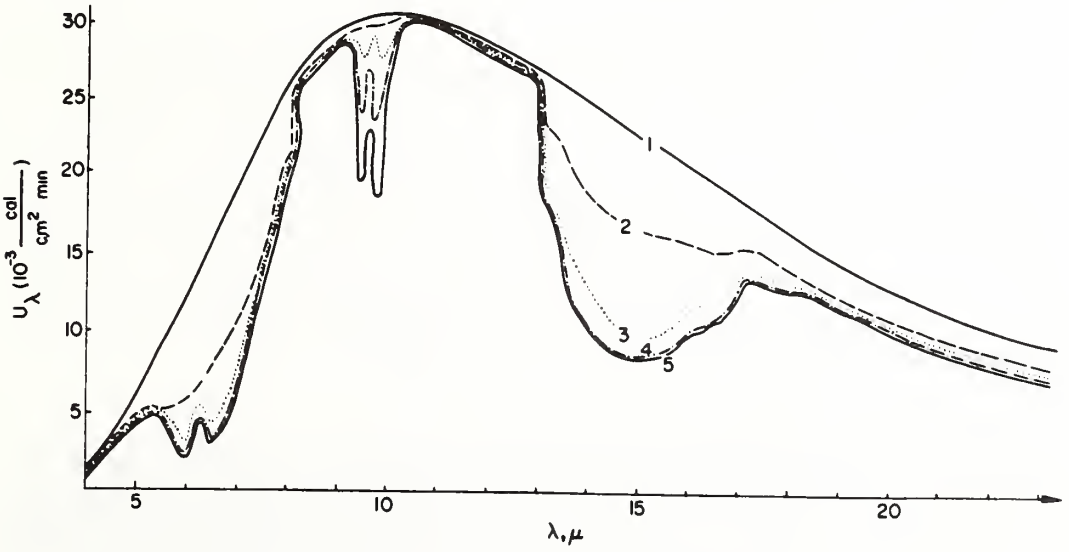

Figure 22.7 *Spectral intensities of the up going radiation from zenith at different levels in the atmosphere at 2000 hr., Nov. 14, 1963, Rostov-on-Don. (1) at the level 1,000 mb (100 m); (2) 575 mb (4, 600 m); (3) 275 mb (10,000 m); (4) 75 mb (18,000 m); (5) 17.5 mb (28,000 m) (after Kondratyev, 1969).*

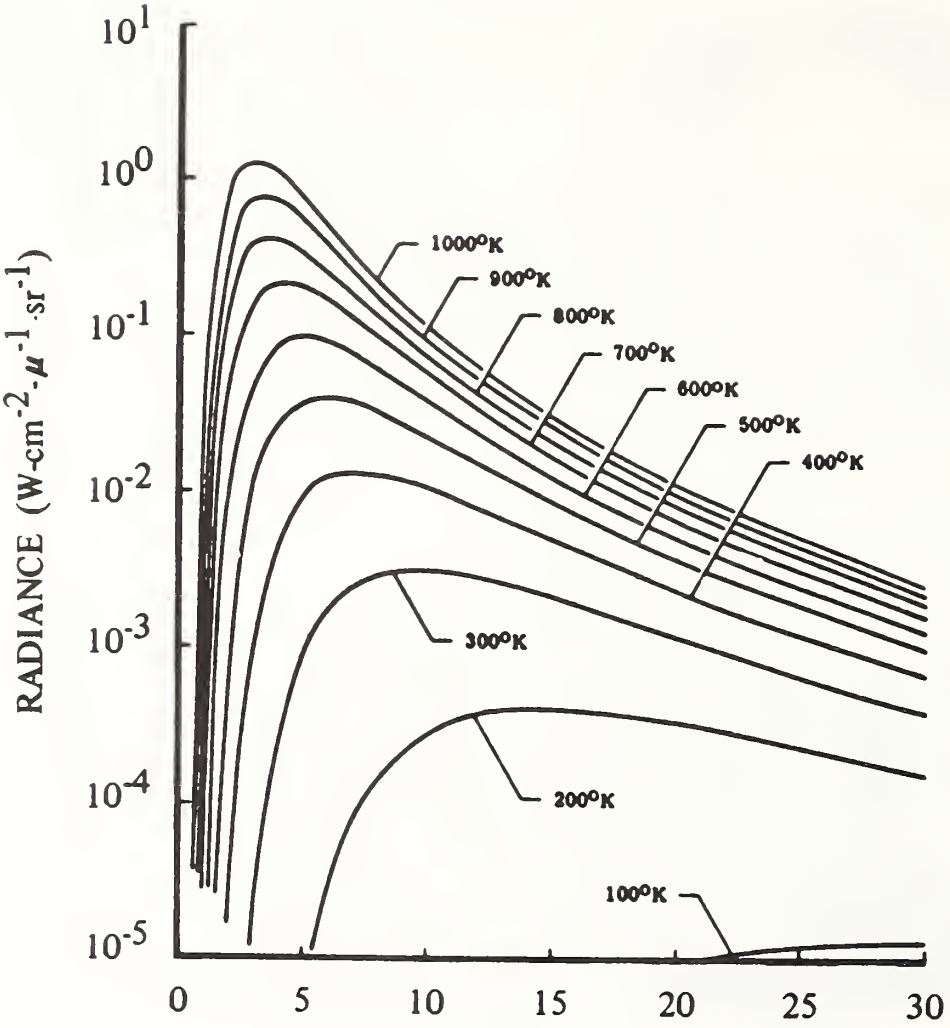

Figure 22.8 *Spectral radiance from a blackbody versus wavelength, in micrometers, with temperature as a parameter (after Wolfe, 1965).*

present in the daytime. This is apparent from (F22.9) which compares these two radiation sources for various reflectivity and emissivity values. Because of this reason the NIMBUS HRIR 3.4-4.2 μm data are contaminated with sunlight during the day-side of the orbit. ITOS-I and NOAA-I have side stepped this problem of solar contamination by using the 10.5-12.5 μm wavelengths.

22.1.3 Atmospheric Correction Models

In order to obtain accurate sea-surface temperature information from satellite IR window data, it is necessary to correct the measurement for the effect of the atmosphere on the upward IR radiance from the sea surface. That effect is to absorb and re-emit a portion of the sea surface radiance. To determine the error introduced by the atmosphere, some investigators have made theoretical calculations with radiative transfer models of the upward spectral radiance in the atmosphere. They have examined the error under various (a) assumed model atmospheres with varying temperature and water vapor and (b) zenith angles. They have incorporated the significant absorbing gases. Two such studies have been reported in the past year; these will be discussed here. To my knowledge, they are the most useful attempts at solution of the atmospheric problem which have been reported to date.

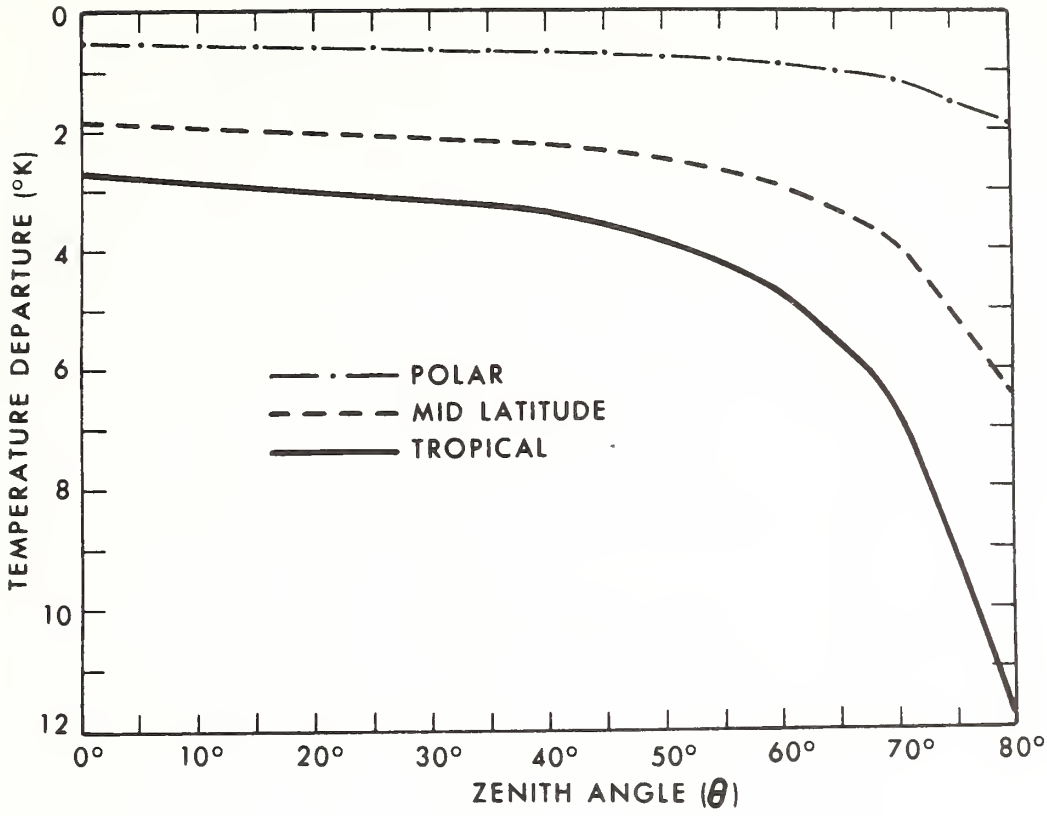

Figure 22.10 *Calculated departure of NIMBUS HRIR (3.8 μm) temperature from ground surface temperature as a function of local zenith angle for three model atmospheres (after Smith, et al., 1970).*

temperature, when the height of the emitting clouds is varied from 1000 to 300 mb and the latitude is varied by the use of these 3 model atmospheres. Smith, et al., (1970), indicate "this is due to the fact that water vapor and carbon dioxide attenuation is naturally correlated with the surface radiating temperatures since it decreases with increasing cloud height and increasing latitude." They point out that this characteristic of the atmosphere makes it possible to predict the surface to satellite temperature difference from only two parameters: the satellite observed temperature; and the zenith angle of the measurement. They have presented this relationship for satellite observed temperatures from 210 to 300 °K and for zenith angles of less than 60° as

$$\Delta T = [a_0 + a_1(\theta/60°)^{a_2}\ 1n(100/300\text{-}T_{so}) \qquad (22:6)$$

where: $a_0 = 1.13$, $a_1 = 0.82$, a_2 - 2.48, θ is the local zenith angle of measurement, and T_{so} is the satellite observed temperature in °K.

Athough it would have been possible to estimate probably accuracy of this single band model using dependent data, the authors have not given an error figure. A summary of the important features of the single band model is given in (T22.3).

22.1.3.2 Double Band Model

The other recent work with an atmospheric correction model is that of Anding and Kauth (1970). They have used a radiative transfer model, described by Anding and Kauth (1969), capable of including

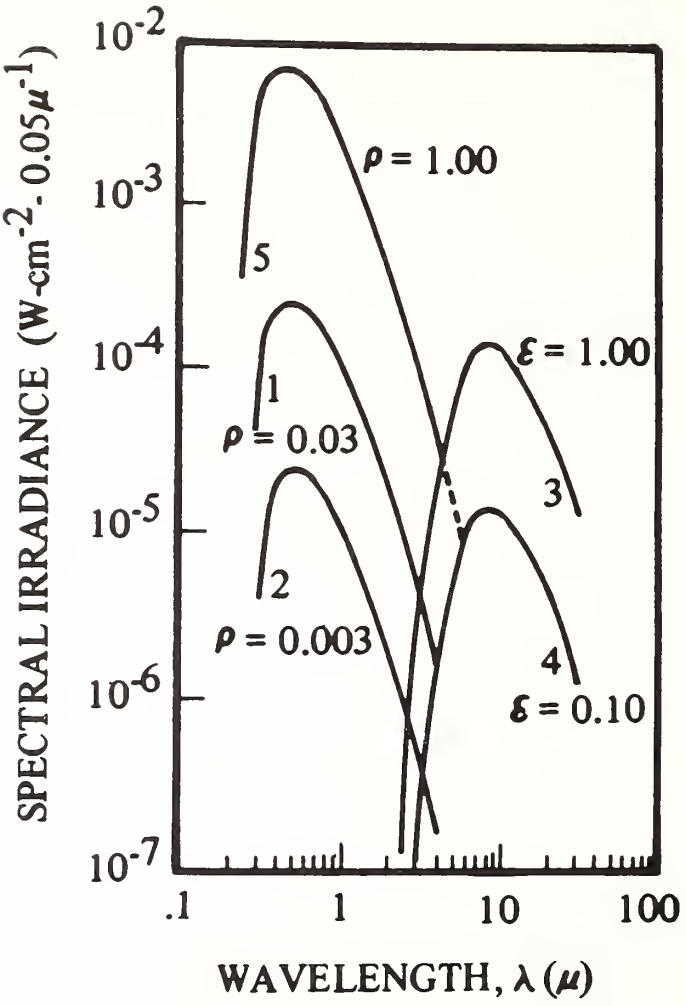

Figure 22.9 *Comparison of reflected sunlight and emitted radiation for various emissivity, ϵ, and reflectivity, ρ, values and a surface temperature of 300°K (after Holter, 1970).*

22.1.3.1 Single Band Model

Smith, et al. (1970) have used a radiative transfer model to calculate the upward radiance at 3.8 μm. The model accounts for H_2O and CO_2 absorption and emission. They have utilized three model atmospheres (polar, midlatitude, and tropical) with total water vapor amounts 0.15, 1.2, and 4.7 cm., respectively. Using this model they have calculated the temperature difference between the surface and the effective radiative temperature at satellite height. The resulting temperature differences are shown in (F22.10) as a function of zenith angle (θ) for each model atmosphere. It is clear that the temperature error increases with increasing zenith angle. The tropical atmosphere has a greater error than the polar atmosphere. For these calculations the atmosphere was assumed to be cloud-free.

Smith et al. (1970) also obtained calculations in which the radiating surface was raised from 1000 to 300 mb for the three model atmospheres. His calculations simulate what may be expected with clouds (ground) which have an emissivity of unity and completely fill a radiometer field of view. The results of these calculations with clouds which vary in height and latitude are shown in (F22.11). The temperature differences (surface minus satellite) are plotted as a function of satellite observed temperature. It is apparent that a high correlation exists between the temperature difference and satellite observed

Table 22.2 U.S. Satellites with IR Window Sensor Experiments

Satellite	TIROS II, III,IV,VII	NIMBUS I	NIMBUS II	NIMBUS III	ITOS-1 (TIROS-M)	NIMBUS IV	NOAA1 (ITOS-A)	ITOS-D
Launch	1960-63	8/28/64	5/15/66	4/14/69	1/23/70	4/8/70	12/11/70	Planned 7/72
Orbit Inclination and Altitude (n. mi.)	48-58° 350	Sun Syn. 400	Sun Syn. 600	Sun Syn. 600	Sun Syn. 790	Sun Syn. 600	Sun Syn. 790	Sun Syn. 790
IR Window Sensors	MRIR[2]	HRIR[1]	HRIR[1] MRIR[2]	HRIR[1] MRIR[2]	SR[4]	THIR[3]	SR[4]	SR[4] VHRR[5]
Resolution (n. mi.)	20	5	5 30	5 30	4	4	4	4 0.5
Sensor Spectral Response (μm)	8-12	3.4-4.2	3.4-4.2 10-11	3.4-4.2 10-11	10.5-12.5	10.5-12.5	10.5-12.5	10.5-12.5

1 - High Resolution Infrared Radiometer
2 - Medium Resolution Infrared Radiometer
3 - Temperature-Humidity Infrared Radiometer
4 - Scanning Radiometer
5 - Very High Resolution Radiometer

Table 22.3 Summary of Atmospheric Correction Models

			Theoretical Radiative Transfer Model		Model Atmosphere			
Model	Band	Assumes	Accounts for	Zenith Angle(°)	Temperature Profile	Water Vapor Profile	Range of Cloud Height	Error
Single band (Smith et al., 1970)	3.8 μm	Surface Emissivity of Unity	H_2O CO_2	0-60	Polar Midlatitude Tropical	0.15 cm 1.2 cm 4.7 cm	Surface to 300 mb.	Not given
Two band (Anding and Kauth, 1970)	9.1 and 11.0 μm	Cloudless	H_2O CO_2 O_3 NO_2	0 60 75	Summer Winter Mean 30°N	Wet Dry Mean 30° N	Clouds not included	±0.15°C (on dependent data)

water vapor, carbon dioxide, ozone, methane, nitrous oxide, and haze. In the computations, atmospheric gas concentrations were held constant and only water vapor and temperature were varied through the use of five model atmospheres, indicated in (T22.4). The temperature and water vapor profiles for these model atmospheres are shown in (F22.12) and (F22.13).

Calculations were carried out for all combinations of (a) five model atmospheres, (b) three zenith angles (0, 60, and 75°), and (c) five ocean surface temperatures (280, 285, 290, 295, and 300 °K). A total of 75 spectra were calculated. An example of the spectral radiance calculation for the summer wet model atmosphere and zenith angle of 60° is shown in (F22.14). Each spectral radiance curve in (F22.14) is that of a greybody water surface, at the temperature indicated, modified by the summer wet model atmosphere. Emissivities were based on Buettner and Kern (1965). The 0 °K surface temperature was included by Anding and Kauth (1970) to show the emission of the atmosphere alone. In the intense absorbing regions, the spectra are the same regardless of the surface emission because the atmosphere is opaque in these regions.

Atmospheric attenuation affects the radiance in both the 9.1 and 11.0 μm channels, although the effect on the radiance at 9.1 μm is greater. Since a high correlation exists between the two spectral radiance values, Anding and Kauth (1970) have plotted the 9.1 μm radiance versus the 11.0 μm radiance for various ocean surface temperatures (F22.15). The results show that given the radiance in these two spectral bands, the surface temperature can be predicted with high accuracy, providing the viewing angle, sea temperature, and atmospheric conditions are similar to one of the 75 combinations tested. The surface temperature is simply interpolated between the isothermal lines in (F22.15).

An estimate of error in ocean temperature determination has been obtained using the 75 radiance pairs (which are dependent data, i.e., correlated) to predict the surface temperature. The rms error quoted by Anding and Kauth (1970) is ±0.15 °C, which is very encouraging for oceanography.† It should be remembered, however, that this two channel model does not include the effect of clouds. Anding and Kauth (1970) have indicated they are working on the addition of clouds in their model; this will require the addition of one or more spectral bands. They have indicated also the method of regression coefficients is unworkable if the cloudiness exceeds 25 percent.

Table 22.4 Summary of Model Atmospheres

(after Anding and Kauth, 1970)

No.	Model Atmosphere Name	Temperature Profile	Water Vapor Profile
1.	Summer Wet	Summer	Summer Wet
2.	Summer Dry	Summer	Summer Dry
3.	Winter Wet	Winter	Winter Wet
4.	Winter Dry	Winter	Winter Dry
5.	Mean, 30° N.	Mean	Mean

22.1.4 Satellite Experimental Methods

In attempting to remove the effects of clouds and the atmosphere in obtaining satisfactory data on sea surface temperatures, investigators have employed several simple statistical techniques on the data. In some cases the investigators have not evaluated the error of the technique, perhaps because of lack of suitable ground truth data. In these cases, the results are presented here to show the history of these attempts at obtaining useful data.

†An error of 0.15°C is reasonable only if the absorption coefficients for water vapor are known accurately. A realistic error is undoubtedly higher than this figure.

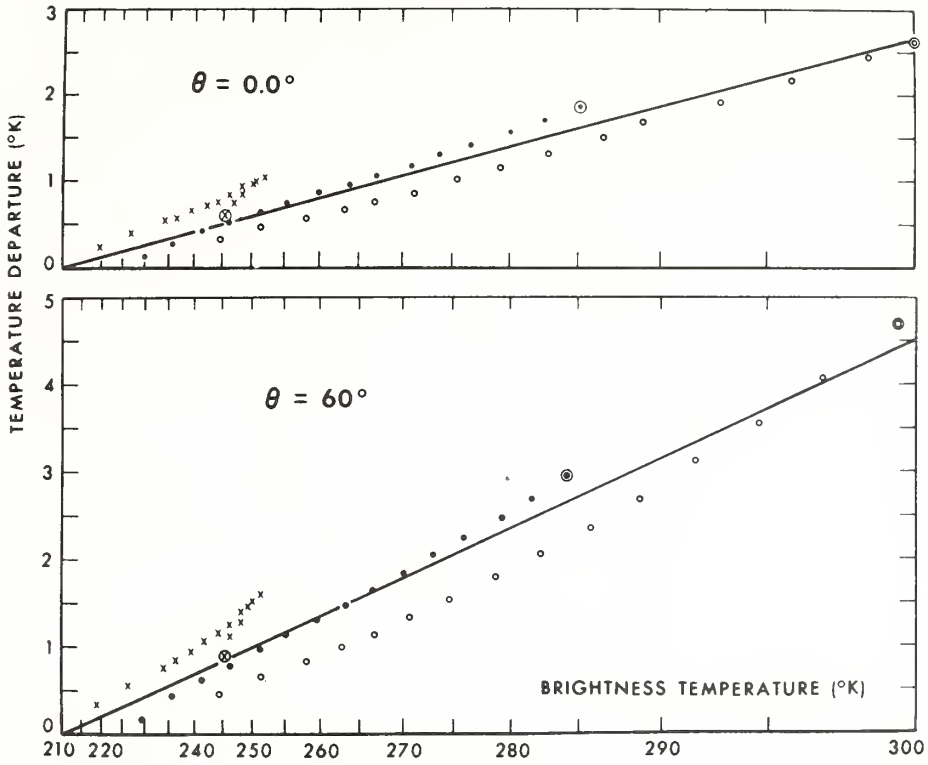

Figure 22.11 *Departure of NIMBUS HRIR brightness temperature from ground and cloud radiating temperature as a function of "observed" brightness temperature. The crosses, dots, and open circles pertain to the polar, midlatitude, and tropical model atmospheres, respectively (after Smith et al., 1970).*

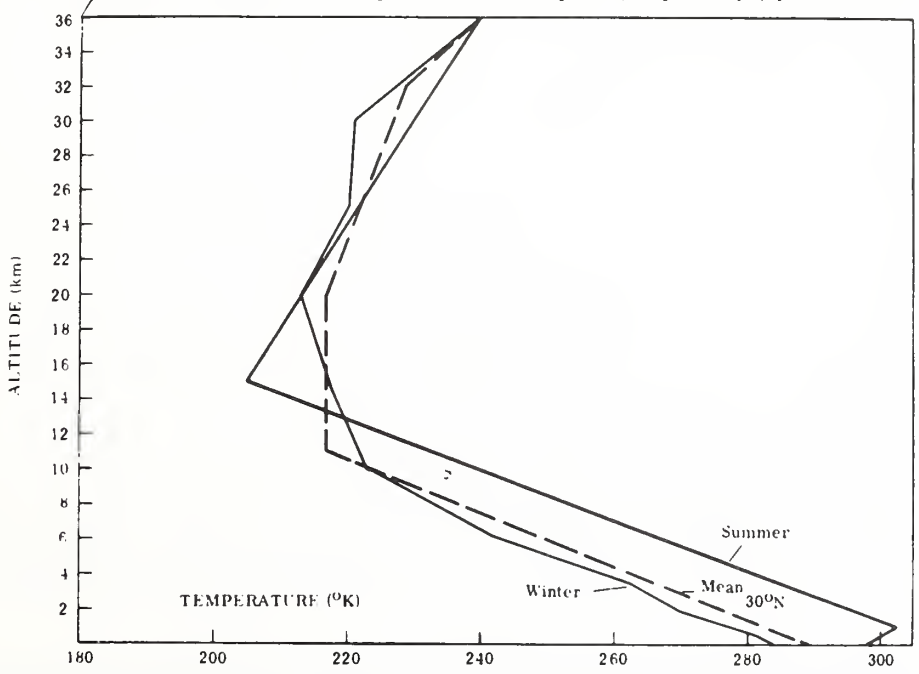

Figure 22.12 *Temperature profiles for model atmospheres used for double band model radiance calculations (after Anding and Kauth, 1970).*

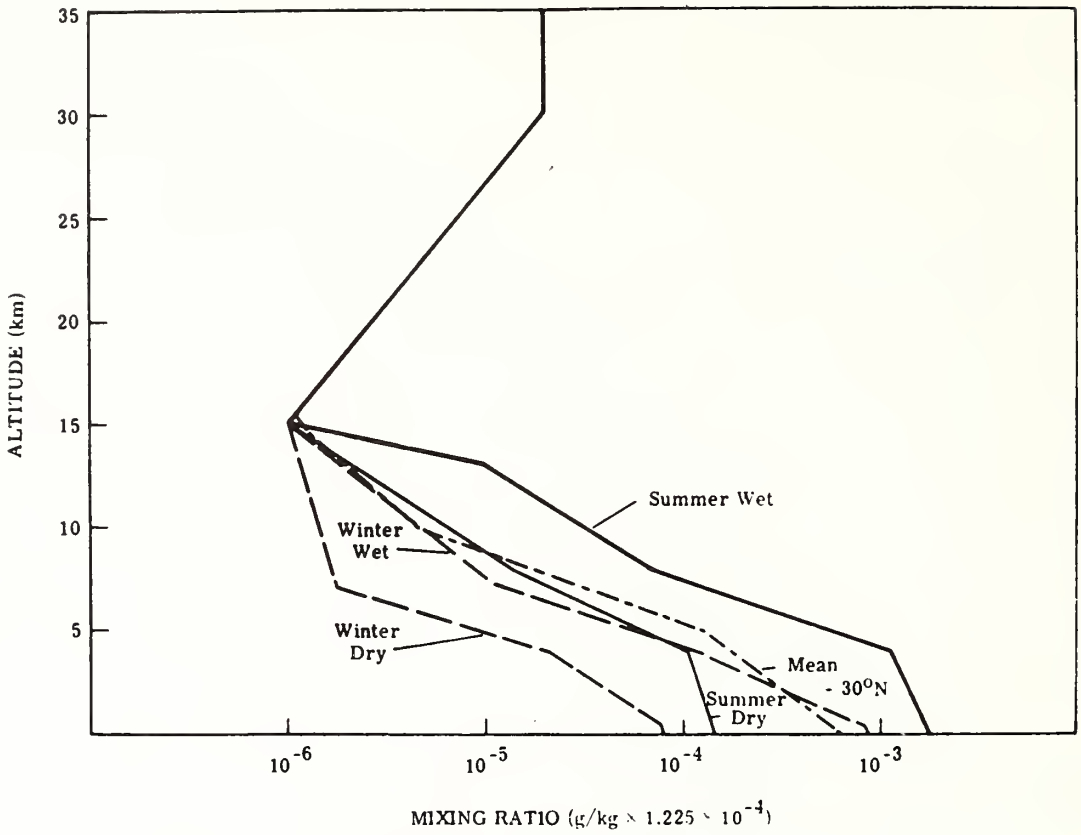

Figure 22.13 *Water vapor profiles for model atmospheres used for double band model radiance calculations (after Anding and Kauth, 1970).*

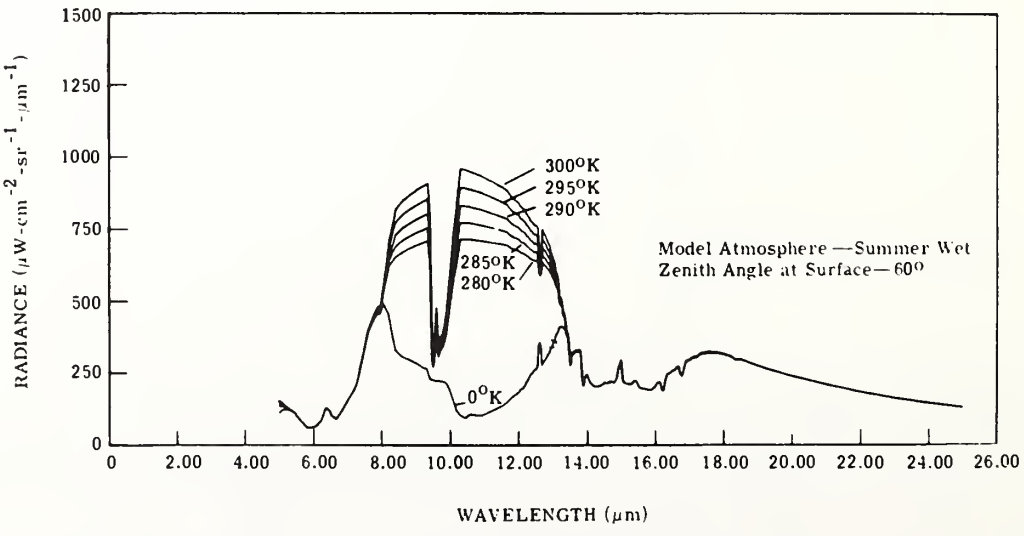

Figure 22.14 *Upward spectral radiance at 100 Km with sea temperature as a parameter (after Anding and Kauth, 1970).*

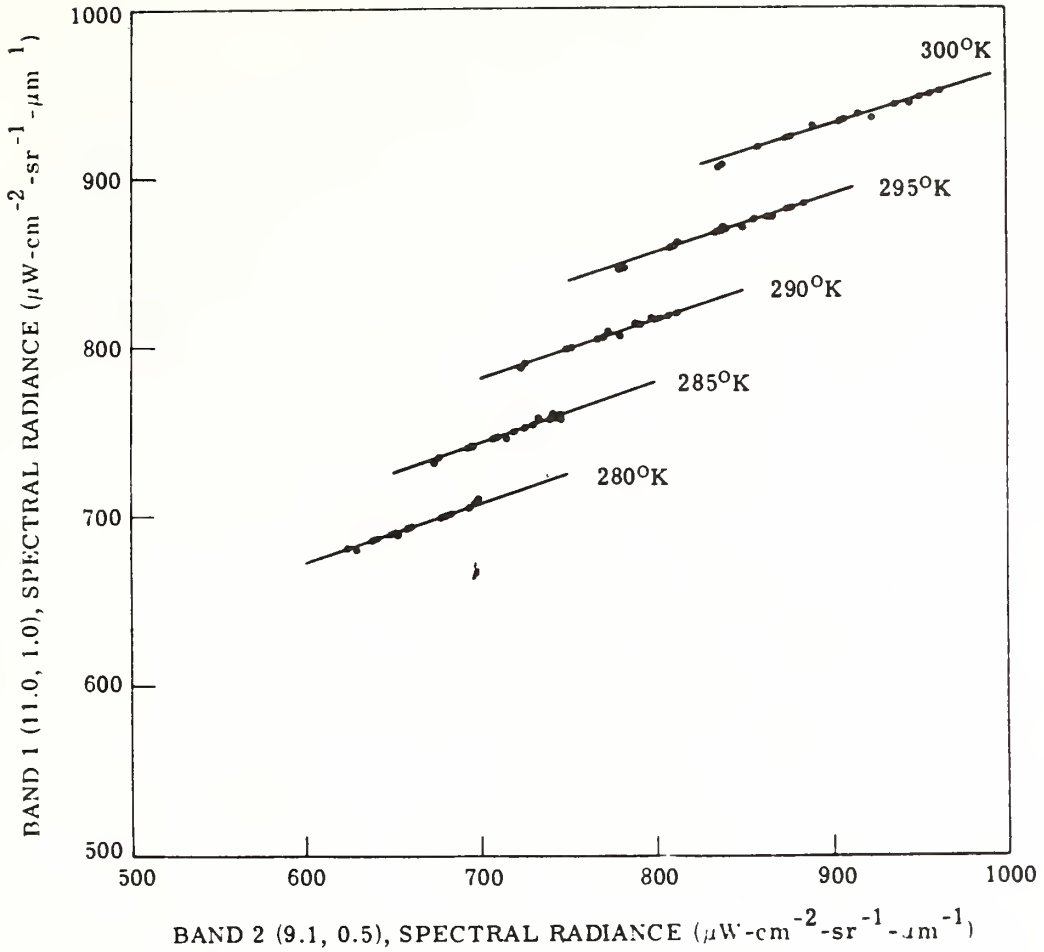

Figure 22.15 *Spectral radiance at 9.1 μm for various ocean surface temperatures (after Anding and Kauth, 1970).*

22.1.4.1 Data Averaging Techniques

Some of the early experimental data have shown much detailed structure in the temperature pattern; this was believed to result from sensor noise.† Some examples of this fine scale structure are shown in (F22.3) and (F22.16). In an attempt to remove this noise, Curtis and Rao (1969) have averaged NIMBUS II HRIR data over one-half degree latitude/longitude rectangles. Beginning with the data shown in (F22.16), Curtis and Rao (1969) have applied an averaging technique and arrived at the smoothed temperature field shown in (F22.17). The Gulf Stream boundary is preserved in the smoothed analysis as is the strong gradient between the cold, cloudy region and the warm Gulf Stream. The influence of clouds is not removed by simple data averaging, although sensor noise is suppressed. Others have also used simple averaging techniques.

†E. J. Williamson (unpublished manuscript, 1968) has shown from NIMBUS II HRIR housing scan data that the noise-equivalent temperature is about 2°K (at 280-300°K) (cited by Curtis and Rao, 1969).

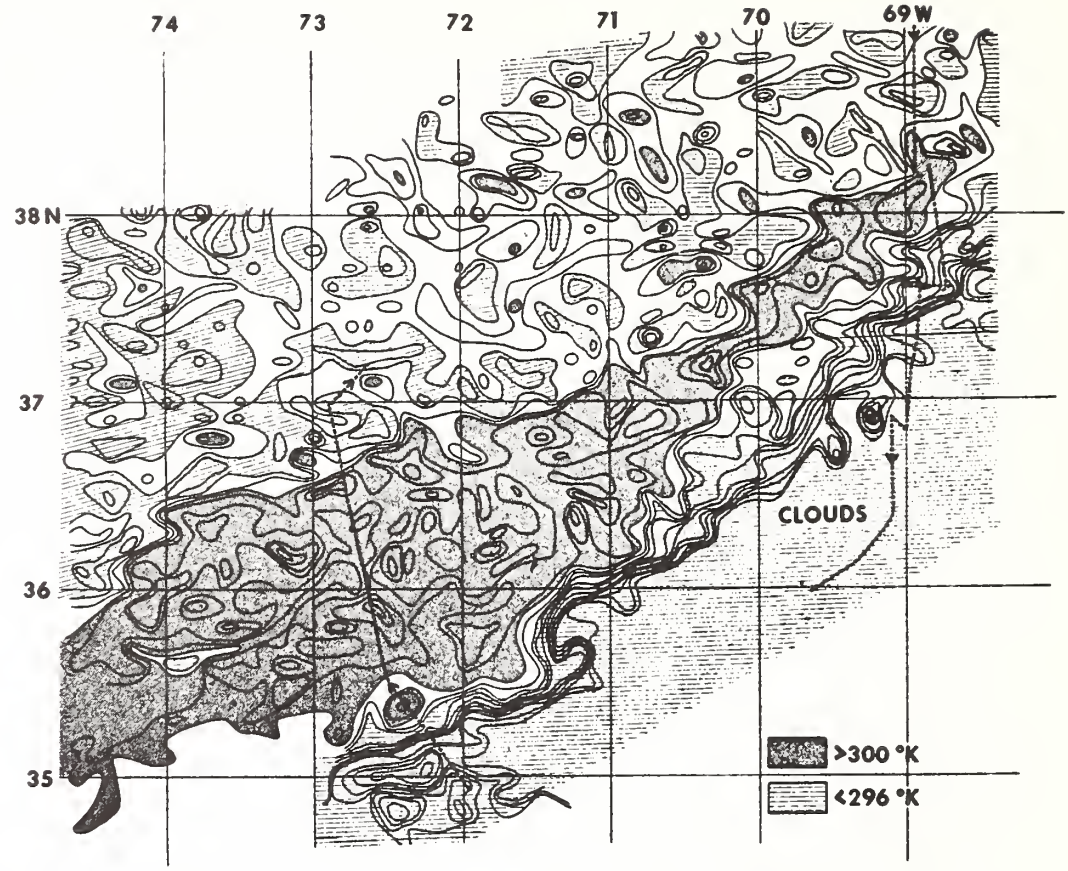

Figure 22.16 *The Gulf Stream from the analyses of digitized HRIR data from NIMBUS 2, orbit 504, June 22, 1966, 0430 UT (after Curtis and Rao, 1969).*

22.1.4.2 Highest Daily Value Technique

Because clouds tend to reduce satellite-observed sea temperatures, a technique has been used by a number of investigators to select only the highest temperature in a given area as representative of the surface temperature. Curtis and Rao (1969) have used this method on the data set in (F22.16); the results are illustrated in (F22.18). Temperatures are 2-4 °K higher than with the averaging technique (F22.17) and probably indicate a sensor noise of this magnitude. In the boundary of the cloudy region of (F22.17), the temperature has increased as much as 13 °K by using the highest value technique. Apparently most measurements representing clouds are eliminated by this method, depending on the degree of cloudiness. A part of the cloudy area in (F22.17) still remains in (F22.18).

Selecting the highest reading in a region practically guarantees that detector noise will make the reading higher than the true temperature. In addition, if the detector noise is 2-4 °K, the sea surface temperatures are of little value other than for climatological studies.

LaViolette and Chabot (1969)†, used a similar highest daily value technique. HRIR scan spot data within the range of climatological sea surface temperature were averaged over 2,205 square mile areas. Data outside the temperature range were excluded from the average. For each day this included about 10 scan spots per area. A five-day composite was obtained by selecting the highest daily average for each area. The result is shown in (F22.19). The basic idea of this technique is that clouds are transient and sea temperature is horizontally homogeneous and relatively constant with time. Thus, the likelihood is small that clouds would cover the same area for many days. This region, Baja California, is one of the most cloud-free regions on earth—so one would expect optimum results there.

†Cited by LaViolette and Seim (1969).

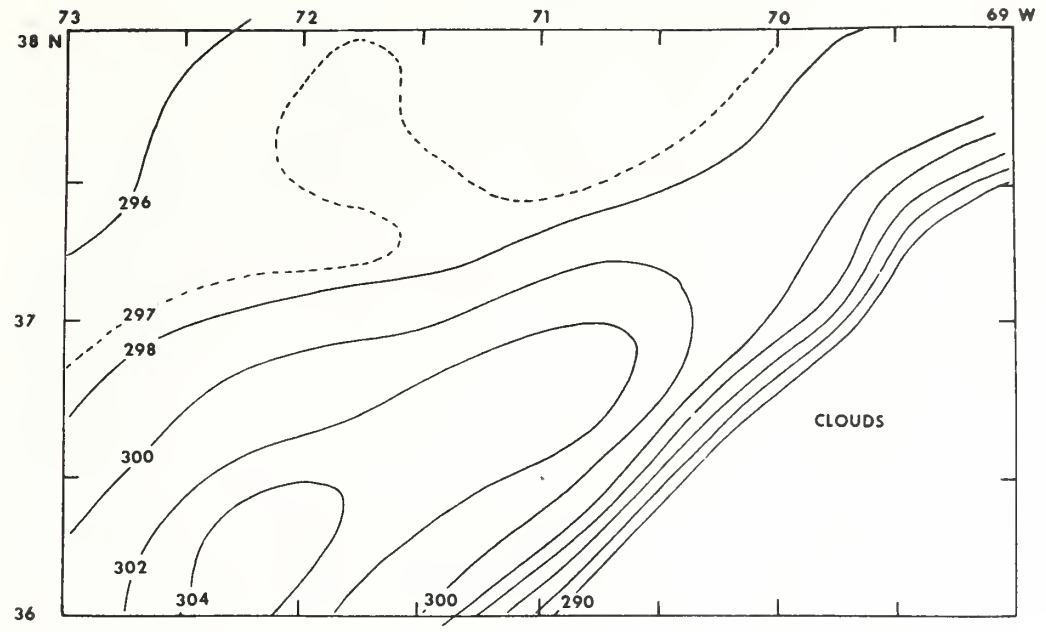

Figure 22.17 *Sea-surface temperature analysis made by using the average values in each half-degree latitude/longitude box from NIMBUS 2 HRIR data, orbit 504, June 22, 1966, 0430 UT (after Curtis and Rao, 1969).*

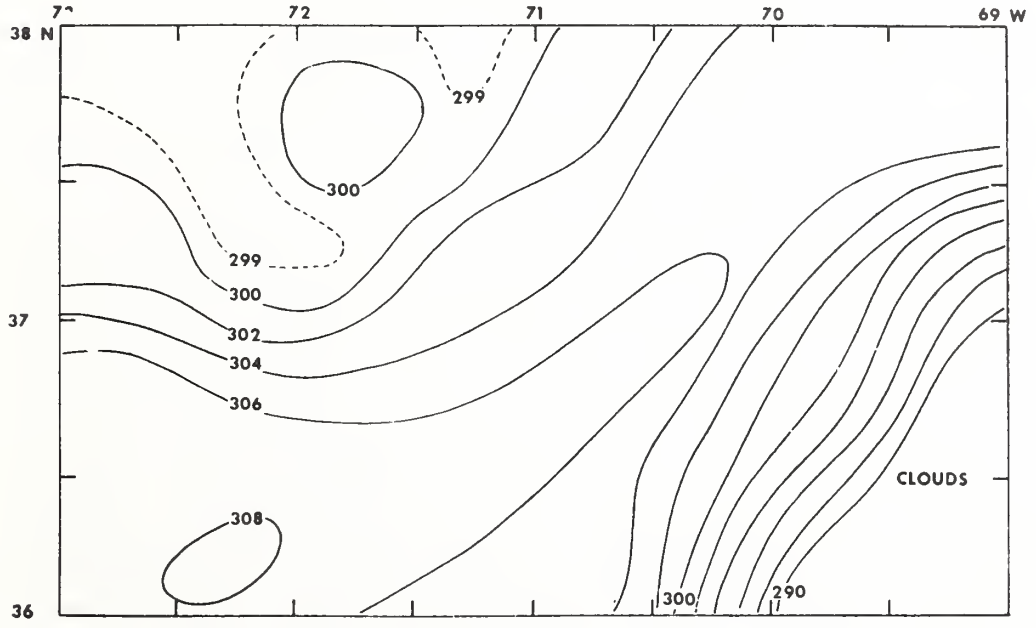

Figure 22.18 *Sea-surface temperature analysis made by using only the highest value in each half-degree latitude/longitude box from NIMBUS 2 HRIR data orbit 504, June 22, 1966, 0430 UT (after Curtis and Rao, 1969).*

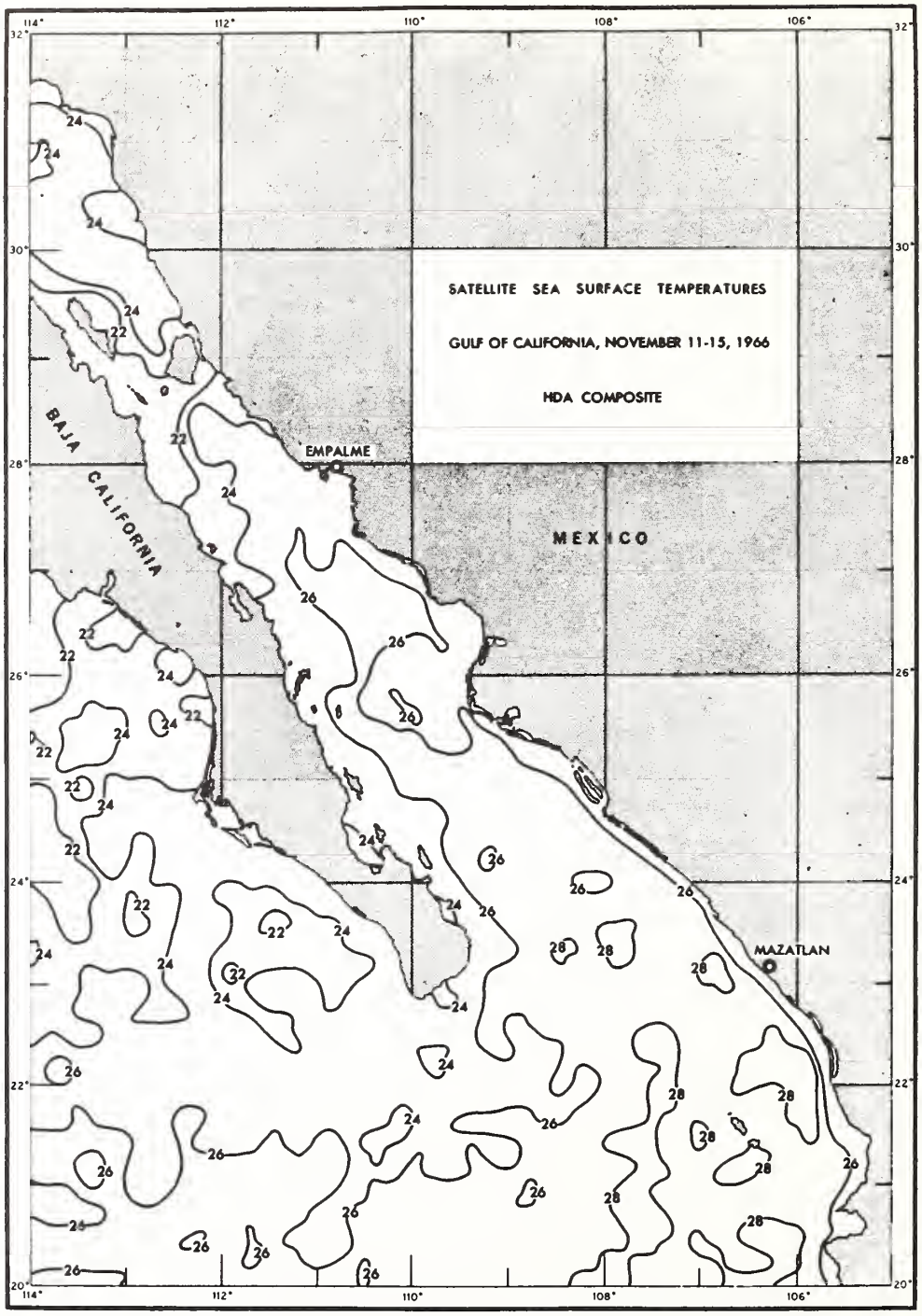

Figure 22.19 *Highest temperatures of a 5-day period of sea-surface temperatures derived from NIMBUS II HRIR data, Nov. 11-15, 1966 (after LaViollette and Chabot, 1969).*

Smith, et al. (1970) have used a similar maximum temperature technique on NIMBUS III HRIR data over the BOMEX area near Barbados. In that study the highest satellite observed temperature was selected in each one degree latitude/longitude square. Results are shown in (F 22.20). Ship ground truth sea surface temperature data are given by an asterisk. The investigators have commented that "the highest temperatures are extremely spatially unstable due to cloud and instrument noise. As a result, they do not provide any useful information on the true sea-surface temperature distribution."

22:1.4.3 Histogram Technique

The basis of the histogram technique lies in the fact that a HRIR sensor has random noise which will given an otherwise constant signal a Gaussian distribution on a frequency of occurrence diagram. An example of the use of this technique is given in (F22.21) by Smith, et al. (1970) based on NIMBUS HRIR data. These diagrams show the frequency of occurrence of satellite observed temperature for two areas, each with dimensions of 2.5 x 2.5° latitude/longitude. The warmest side of the distribution curve is least affected by clouds and is somewhat Gaussian in shape because of the random sensor noise. The investigators have indicated that at one standard deviation the standard error is 1.5 °K for the NIMBUS HRIR sensor at these temperatures. The most probable sea-surface temperature for both histograms (F22.21) is 302.5-1.5 = 301.0 °K. When this technique is applied to the previously mentioned NIMBUS data for the BOMEX area, the set of temperatures in (F22.22) is produced. As can be seen by comparing the 5 BOMEX ship observations with the satellite derived surface temperatures, these data are in much closer agreement than resulted from the high temperature technique illustrated in (F22.20).

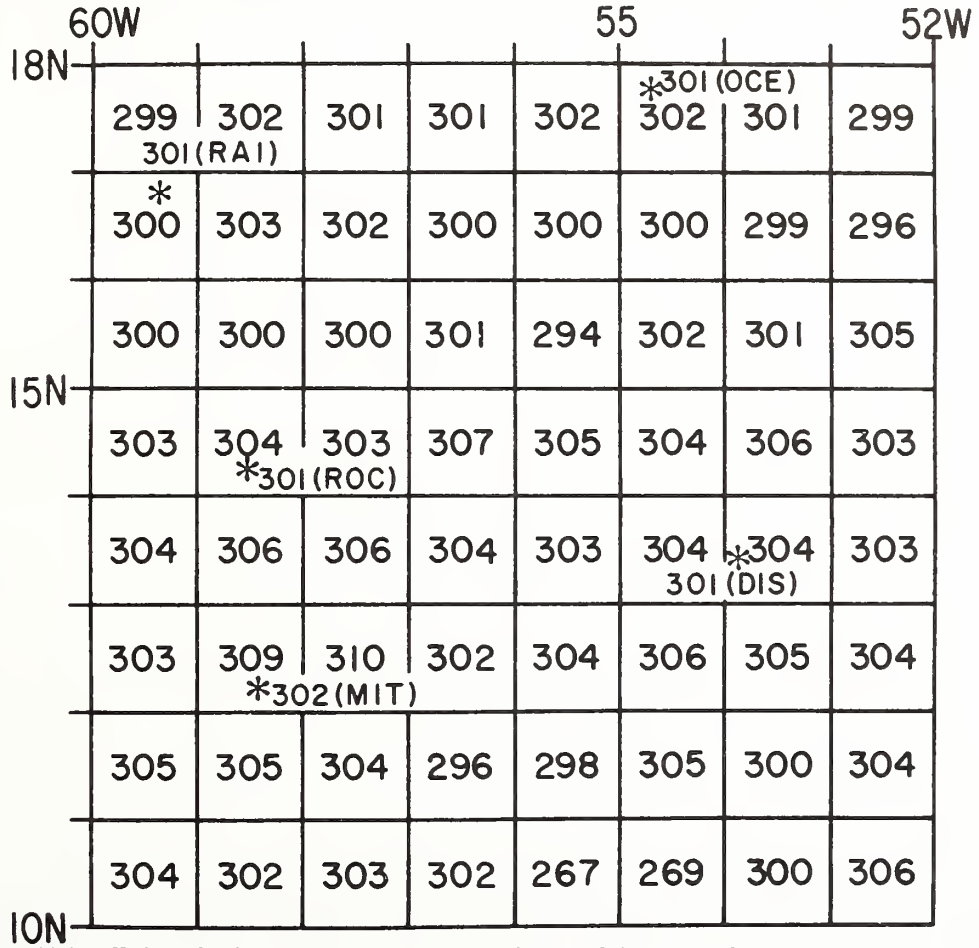

Figure 22.20 *Highest brightness temperatures in each latitude/longitude box from NIMBUS 3, HRIR, nighttime, orbit 681, on June 4, 1969 (after Smith et al., 1970).*

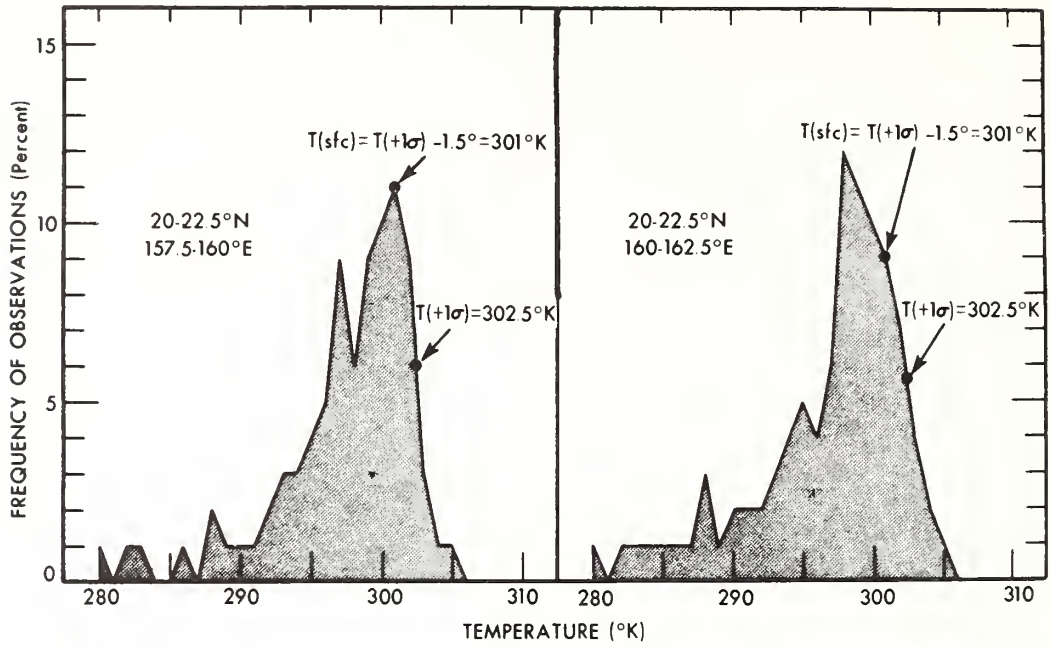

Figure 22.21 *Sample histograms of corrected NIMBUS HRIR data showing their relation to sea-surface temperature (after Smith et al., 1970).*

To test the histogram technique on additional data, Smith, et al. (1970) have derived sea temperature data for the North Pacific from HRIR data and compared them with ship reported temperatures. The rms difference of 97 observations was 1.71 °K. The scatter diagram of the comparison is shown in (F22.23). The relative discrepancy between satellite and ship data is less than 1 °K.

22.1.5 Cloud Problem

Although the data averaging technique does not remove the influence of clouds on the upwelling spectral radiance, both the high temperature technique and the histogram technique remove the influence of clouds to some extent, depending on the nature of the cloudiness.

In addition, it was mentioned in the discussion on the two-band model 22.1.3.2 for correcting atmospheric effects that there is a possibility of correcting for certain cloudiness with the addition of one or more spectral bands, perhaps in the visible portion of the spectrum. This is probably the best hope for removing the influence of clouds to the extent that absolute sea temperature can be obtained to ±0.5 °K.

This section was written while at sea in the sub-tropics on a cruise of three weeks. During that time I made a special effort to observe the horizontal spacing of trade cumulus, and smaller fragments of these clouds, relative to the scan spot size of IR sensors. It is my personal feeling that the concept of "looking between the clouds" with a 4 n mi resolution satellite radiometer is close to pure fiction for many areas of the tropics; even with a 0.5 n mi resolution sensor the occurrence of truely cloud-free data will be extremely rare. Perhaps there are regions over the earth's oceans which are systematically cloud free, but it is my impression that over most of the tropical and sub-tropical oceans trade cumulus and small cloud fragments exist a high percentage of the time. With present techniques it is not possible to remove the effect of these clouds which are much smaller than the field of view of the satellite sensor. Their effect must be evaluated.

Many of the initial problems of remote sensing of sea surtace temperature have been solved by the investigators whose work has been summarized here. The cloud problem has been partially solved but is still a serious limitation on achieving the accuracies needed for oceanography. There is a continuing need for theoretical studies of radiative transfer in realistic atmospheres including both clouds and aerosols, and for experimental studies to evaluate the influence of clouds, particularly those smaller than the radiometer field of view, on the spectral radiant emittance of the earth and atmosphere.

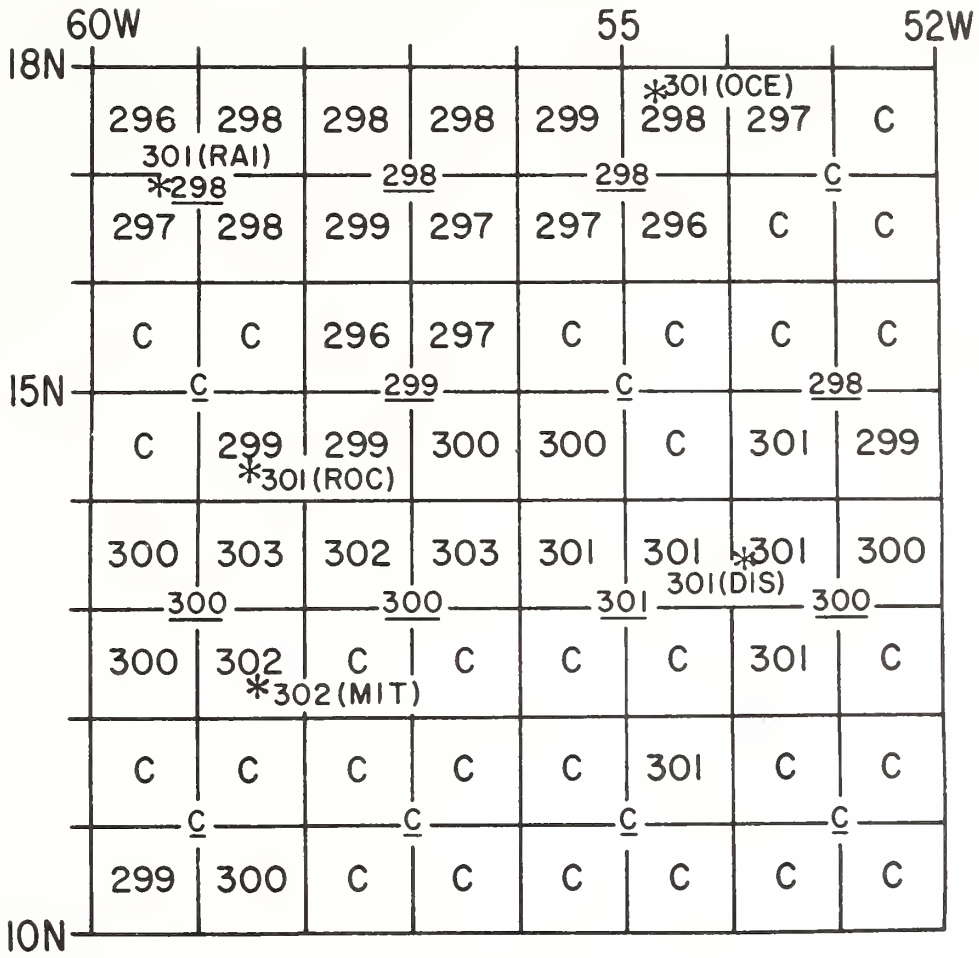

Figure 22.22 *Surface temperatures, °K, derived from NIMBUS 3 HRIR nighttime data orbit 681 on June 4, 1969. Centered values in each box were derived from 1° latitude/longitude histograms, underlined values from 3° histograms. Asterisks are BOMEX ship observations and C denotes indeterminate temperatures due to excessive cloudiness (after Smith et al., 1970).*

22.2 Passive Microwave Detection

Passive microwave detection is clearly distinguished from active microwave detection. An active microwave system, such as a radar, emits microwave frequency energy which is reflected from natural surfaces; the characteristics of this reflected energy can be used to identify the properties of the surfaces from which it was reflected or backscattered. Passive microwave detectors measure the intensity of microwave energy emitted by natural surfaces.

Present microwave technology evolved with the science of radio astronomy. The first successful measurement of radio frequency thermal radiation from an extra-terrestrial source (the Milky Way Galaxy) was obtained in 1931 using a radio receiver at 20.5 MHZ and 30 MHZ. Radar research during and after World War II has provided many studies of the propagation of radio waves, microwave absorption and scattering in the atmosphere, emission of the sea surface, and improved technology of microwave radiometers. An excellent summary of the historical development of microwave radiometry is given by Paris (1969).

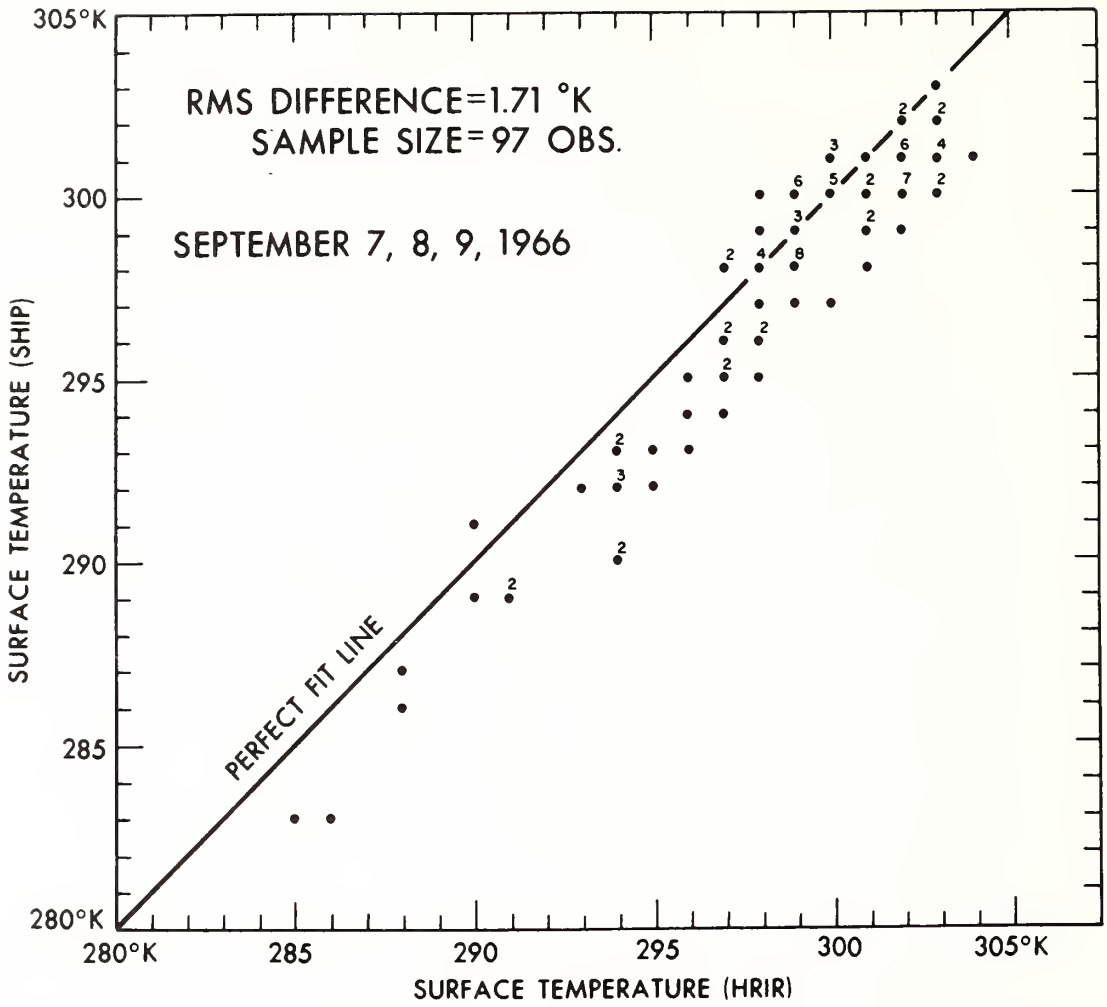

Figure 22.23 *Scatter diagram of surface temperatures obtained from ships and inferred from NIMBUS II HRIR data (after Smith et al., 1970).*

The basic problem in passive microwave remote sensing is to measure the microwave radiance of the ocean and atmosphere (N) and to infer from it the physical state of these media. In addition to temporal variation, there are three useful detection parameters which provide data for interpretation. These are microwave frequency, ν, both horizontal and vertical polarizations, P, and nadir angle, Ψ.

A number of oceanic and atmospheric variables control the upward microwave radiance, N (ν, P, Ψ); they are sea-surface temperature, T_S, salinity, S_S, roughness, R_S, and foam, F_S. When present, sea ice provides a different microwave emittance than that of the sea surface. Atmospheric water vapor, WV_a, liquid water, LW_a, and molecular oxygen, MO_a, also modulate the upwelling microwave emission from the sea and atmosphere. In parametric form this may be written as,

$$N(\nu, P, \Psi) = f(T_S, S_S, R_S, F_S, LW_a, WV_a, MO_a) \qquad (22:7)$$

Figure 22.24 shows how the oceanic and atmospheric variables depend on frequency, ν, alone. Since P and Ψ have not been specified in this figure, the curves are qualitative and are intended only to give the reader an indication of the microwave frequencies at which oceanic variables have the greatest effect on microwave emission. The temperature sensitivity curve, for example, is defined as the ratio of the change in microwave brightness temperature to the change in molecular temperature of the ocean surface, $\Delta T_B/\Delta T_S$. Because of the emissive properties of water, maximum temperature sensitivity occurs at a frequency of 5-6 GHz.†

In the case of salinity sensitivity, (F22.24), maximum sensitivity occurs at a frequency of about 1 GHz. At higher frequencies the microwave brightness temperature is practically insensitive to salinity variations.

Wind increases both the roughness and extent of foam coverage on the ocean surface, and both of these variables have an effect on the emitted microwave brightness temperature. (F22.24) shows that the greatest combined effect of roughness and foam occurs at the higher frequencies indicated, about 10 GHz and above, and that roughness and foam have a smaller effect at frequencies near 1 GHz. The effect of roughness and foam is one of the most difficult areas to interpret; some of the complications are discussed in 22.2.4.

Microwave emittance of water is much less than of thick ice, and the difference is only slightly dependent on frequency (F22.24). Studies of sea ice have shown that two characteristic types of sea ice have different emittances (Wilheit, et al., 1971). One type of relatively smooth, thin ice termed "first year ice" has ice" has a lower emittance than the second type described as "multi-year, heavily hummocked ice." This may lead to some ambiguity in determining the percentage of ice cover by passive microwave detection, unless polarization measurements are obtained.

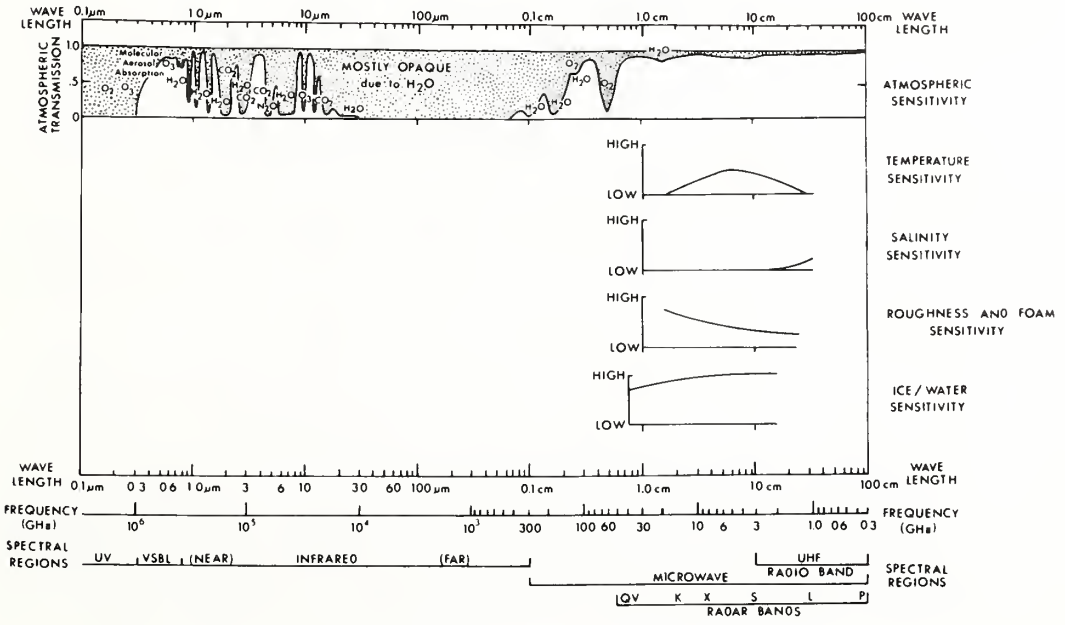

Figure 22.24 *Quantitative atmospheric transmission curve, adapted from Huston, (1971), and qualitative relationships between microwave brightness temperature and various oceanic variables.*

†GHz = 10^9 cycles per second (one giga Hertz).

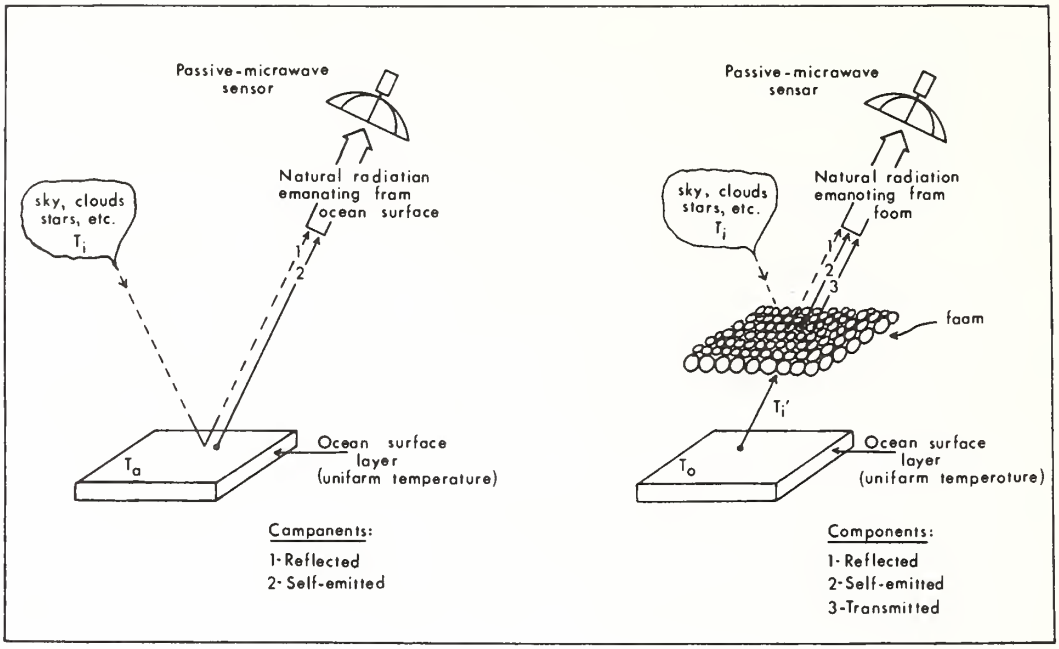

Figure 22.25 *Natural microwave radiation emanating from a smooth ocean surface (left) and a foam covered ocean surface (right) (adapted from Holter, 1970).*

The atmospheric transmission curve, (F22.24), shows the effects of water vapor and molecular oxygen on microwave transmission. An atmospheric window is located at 80-100 GHz and a strong molecular oxygen absorption band at 60 GHz. The highest frequency window in which satellite microwave measurements can be obtained presently is 30-45 GHz, because at 80-100 GHz flyable low-noise radiometers are not yet available (Huston, 1971). The window at 30-45 GHz is somewhat affected by the water vapor absorption band centered at 22.235 GHz. The effect of this band must be considered to frequencies as low as 10 GHz, below which water vapor is relatively transparent.

Water droplets in the atmosphere, in clouds and rain, also have an effect on microwave propagation. Both absorption and emission due to cloud water droplets increase as the square of the microwave frequency. The result is that the presence of water droplets increases atmospheric absorption and emission in the 35 to 90 GHz windows, but has a much less significant effect at frequencies in the window below 10 GHz.

The curves presented in (F22.24) are intended to give the reader a simple interpretation of the frequency dependence of changes in temperature, salinity, and other variables of the ocean. Subsequent sections will provide further discussion on these variables and will show that in addition to being frequency dependent, they are dependent on polarization, P, and viewing angle, Ψ. So the reader should be aware that the magnitude of the sensitivity functions in (F22.24) will change for other combination of P and Ψ.

22.2.1 Theory

As in 22.1.2, the notation and some of the discussion in this section follows that of Holter (1970) and Simon (1966).

Planck's fundamental radiation equation, presented in (22:1) gives the spectral distribution of radiation from a perfect radiator, called a blackbody, with uniform temperature. An approximation valid for long wavelengths is obtained from (22:1) by expanding the exponential function and retaining only the

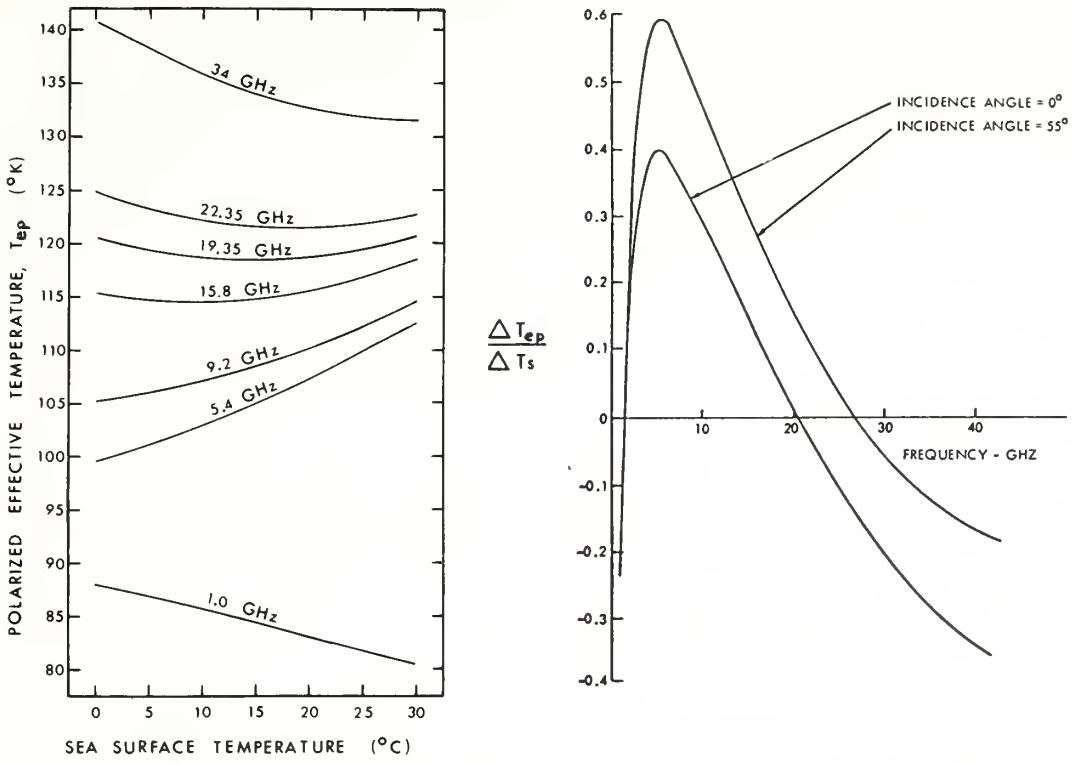

Figure 22.26 *The polarized emissive temperature of a flat sea surface versus the thermometric temperature of the sea surface for frequencies of 1, 5.4, 9.2, 15.8, 19.35, 22.235, and 34 GHz and for a salinity of 35 °/₀₀ (after Paris, 1969).*

Figure 22.27 *Radiometric temperature sensitivity to changes in molecular temperature, for calm sea, vertical polarization, $270 < T_s < 303$ °K (after Huston, 1971).*

first-order term:

$$W_{B\lambda} = \frac{C_1}{C_2} \frac{T_S}{\lambda^4} \tag{22:8}$$

This is the *Rayleigh-Jeans Law*† which is a good approximation when the product λT_S is greater than 10^5 micron degrees, and is valid for microwave emission from the earth's surface which is the order of 10^7 micron degrees. The importance of this approximation in microwave work is that the spectral radiant emittance of a surface, W_λ, is proportional to the first power of the absolute temperature. This simplifies the notation and many calculations.

22.2.1.1 Brightness Temperature

A commonly used term in microwave work is brightness temperature, T_B. This is often termed effective target temperature by investigators to refer to the case where a target does not completely fill the field of view of the sensor. The definition of brightness temperature evolves from basic radiation principles, discussed in 22.1.2, that radiation emanating from a surface is made up of three parts: a self-emitted component, a reflected component, and a transmitted component. These are shown schematically in

†This approximation and Planck's law are given in most basic textbooks on modern physics.

(F22.25). By (22:8) the self-emitted microwave component is proportional to the molecular temperature, T_o. Thus, an effective temperature of a surface can be defined as

$$T_e = \epsilon_\lambda T_o \tag{22:9}$$

Similarly, effective temperature contribution, T_ρ and T_τ, due to the surface spectral reflectance, ρ_λ, and transmittance, τ_λ, can be written as,

$$T_\rho = \rho_\lambda T_i \tag{22:10}$$

$$T_\tau = \tau_\lambda T_i' \tag{22:11}$$

where T_i and T_i' are terms proportional to the radiation incident on the surface from above and below, respectively. The brightness temperature, is thus the sum of these three terms, i.e.,

$$T_B = \epsilon_\lambda T_o + \rho_\lambda T_i + \tau_\lambda T_i' \tag{22:12}$$

This is the surface temperature which would be measured with a remote microwave sensor having an ideal antenna, assuming no atmospheric attenuation. It would agree with the molecular temperature only if the surface was a blackbody, in which case $\rho_\lambda = \tau_\lambda = 0$ and $\epsilon_\lambda = 1$.

Applying these principles to the ocean surface, one can visualize from (F22.25) that if the ocean has a smooth surface, without foam, and if the molecular temperature is constant in the near surface (active) layer, then the brightness temperature has only two components: the self-emitted and reflected components. In this special case, $\tau_\lambda = 0$. However with foam, all three components are present: the self-emitted component is radiation from the foam; the reflected component is microwave radiation from the atmosphere and cosmic sources reflected by the foam; and the transmitted component is radiation from the near-surface active layer of the ocean transmitted by the foam. Second order terms are present but are not shown here for simplicity.

Theoretical radiative transfer models have been developed by a number of investigators in order to calculate the three components of brightness temperature. Particularly valuable work has been done by Paris (1969, and 1971), Hidy, et al., (1971), Stogryn (1967), Lewis, et al., (1954), and McMahon (1950), among others.

22.2.1.2 Polarization

Because the emitted microwave radiation is polarized, it is convenient to divide the radiance field into two components—the vertical and horizontal polarized radiance. Then the total spectral radiance is the sum of the two polarized spectral radiance components, i.e.,

$$N_\lambda = N_{\lambda h} + N_{\lambda v} \tag{22:13}$$

where N_λ has units of ergs/cm^2 sec sr μm. In general, $N_{\lambda h}$ and $N_{\lambda v}$ are not equal.

For purposes of notation the subscript P will be used whenever either horizontal or vertical polarization is applicable. For example, the effective temperature, T_e can be expressed as the polarized effective temperature, T_{eP}, if it represents either of the two polarized components. Similarly, the brightness

temperature, T_B, can be termed polarized brightness temperature T_{BP} if it expresses either polarized component.

22.2.2 Ocean Temperature

Some investigators have developed radiative transfer models in order to study how the microwave radiant emittance of an active surface layer varies with temperature and dielectric properties of the layer. With such models, these investigators are able to determine how the microwave component varies with the detection parameters of frequency, ν, polarization, P, and nadir angle, Ψ. Such models are particularly useful because they allow one to simulate a wider range of conditions that occurs in nature or to examine problems which cannot be investigated easily in nature.

A simple model used by Paris (1969) and others is that of a smooth sea-air interface and an active surface layer which reflects, absorbs, and emits microwave energy and is homogeneous in both temperature and dielectric properties. This active layer has a thickness of only a few wavelengths. For the case of a smooth interface, one may use Fresnel's Law to predict the polarized components of reflectance and emmitance, which leads directly to a calculation of the polarized effective temperature, T_{eP}. Calculations with this model have been carried out by Paris (1969) for molecular temperatures ranging from 0 to 30 °C and for various microwave frequencies. The results, shown in (F22.26), indicate that at some frequencies the sea surface temperature does not uniquely determine the polarized effective temperature. At 15.8, 19.35, and 22.235 GHz, for example, two sea surface temperatures yield the same polarized effective temperature value. Another interesting feature of (F22.26) is that at 5.4 GHz the polarized effective temperature increases with surface temperature, but at 1.0 GHz it decreases with surface temperature. Obviously, the emissivity of a flat sea surface is dependent on both microwave frequency and molecular temperature. These computations also show that maximum sensitivity to surface temperature change occurs near 5 GHz. This is shown more clearly in (F22.27) which indicates a sharp maximum in the ratio of the change of polarized effective temperature to that of molecular temperature. The maximum is located at 5-6 GHz. However, above 20 and below 2 GHz the ratio becomes negative, indicating that warmer water appears to be colder and vice-versa.

Additional measurement information can be obtained by utilizing the detection parameters of polarization and nadir angle. (F22.28), which is derived from the calculations of Lewis, et al. (1954) shows that the spectral emittance of a smooth ocean surface depends on both these detection parameters. For these calculations T_s = 293 °K and ν = 23 GHz. Maximum emittance is obtained with a nadir angle of about 80 degrees with vertical polarization.

The calculations in this section assume a perfectly smooth surface, however the reader should keep in mind that surface roughness will affect the polarized microwave emission from sea water. This is described in detail in 22.2.4.

22.2.3 Salinity

Salinity is an important oceanic parameter which is studied on a global scale and affects microwave emission at certain frequencies. To illustrate this frequency dependence of brightness temperature on salinity, Paris (1969) has made calculations of polarized brightness temperature assuming: (1) T_s = 10 °C; (2) a smooth sea surface; (3) Ψ = 0; (4) a standard, cloudless atmosphere; and (5) a measurement height of 1 Km. His results are shown in (F22.29). It is apparent that salinity variation affects the polarized brightness temperature for a frequency of 1 GHz, but the affect is insignificant at higher frequencies. This suggests that multifrequency techniques may be employed for measurement of sea surface molecular temperature and other parameters, with one channel near 1 GHz in order to asses the salinity of the active layer.

Other studies have shown that the maximum effect of salinity on polarized brightness temperature occurs when Ψ = 0 (Sirounian, 1968), and that this effect increases with sea surface temperature (Paris, 1969).

Some investigators have proposed using the S-band frequency of 2.69 GHz to determine molecular temperature of the ocean surface. They must therefore consider the possible uncertainty due to salinity. A set of such uncertainty curves has been derived by Hidy et al. (1971) and is presented in (F22.30). This shows the uncertainty in measured molecular temperature due to variation in salinity for certain water

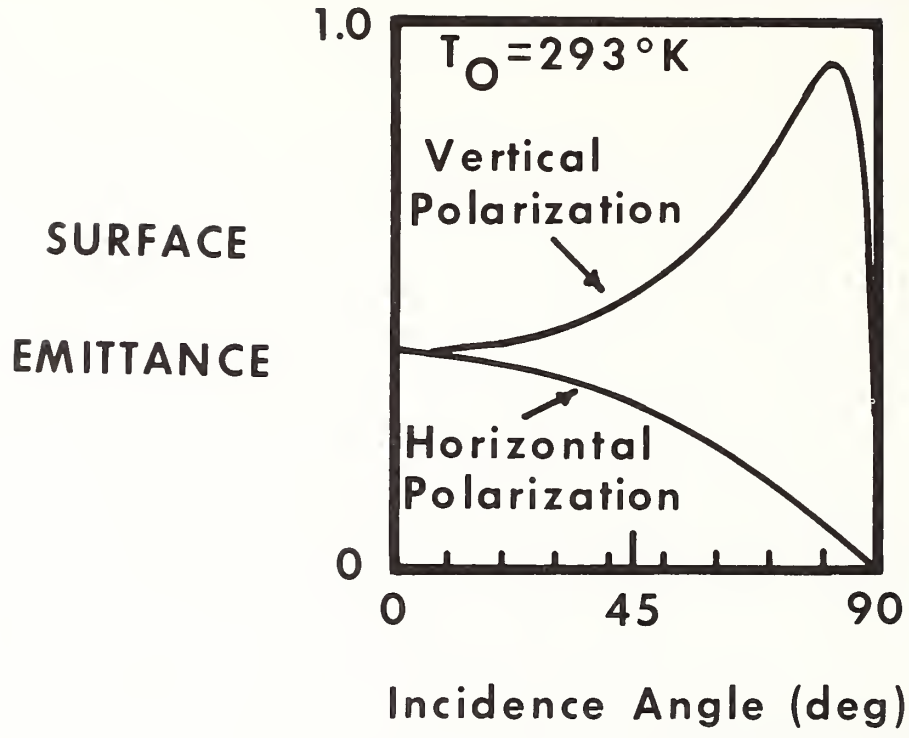

Figure 22.28 *Calculated emittance of a water surface, T_s = 293 °K and ν = 23 GHz (after Lewis et al., 1954).*

temperatures and a frequency of 2.65 GHz. They have also indicated that the uncertainty is inversely proportional to frequency, so by doubling the frequency, the uncertainty is reduced by approximately a factor of 2.

There is geographical variation in salinity as shown in F22.31. The change in salinity from equator to pole is about 10 percent which would cause an orbiting microwave 2.65 GHz radiometer to observe a molecular temperature change of 3 °K. If this is compared to the actual sea surface temperature change of 35 °K between the equator and pole, it is apparent that first order corrections for the geographical variation of salinity must be applied.

Hidy, et al., (1971) have also studied the temporal variations of salinity and find them large enough to be significant. Daily variations of 0.5 percent in mid-oceans surface salinity lead to an uncertainty in molecular temperature of 0.1-0.2 °K. Seasonal and year-to-year variations produce an uncertainty in surface temperature of 0.5 °K.

Thus, geographical and temporal salinity variation in the world's oceans represents a small but significant uncertainty in interpreting S-Band 2.65 GHz radiometer observations for sea surface temperature. However, these variations are correctable to first order with known geographical and temporal variation (Hidy, et al., 1971).

22.2.4 Sea State–Roughness and Foam

If either sea surface temperature or wind speed is to be inferred from microwave brightness temperature, it is essential that the effect of sea state on microwave emission be adequately understood for the range of environmental conditions of the world's oceans. At present only first order theoretical calculations have been carried out on the effect of surface roughness, i.e., wave slope, and there is no physical theory that is adequate to describe the effective dielectric constant of an ocean surface covered with foam. Theoretical and experimental data which are available suggest that the brightness temperature

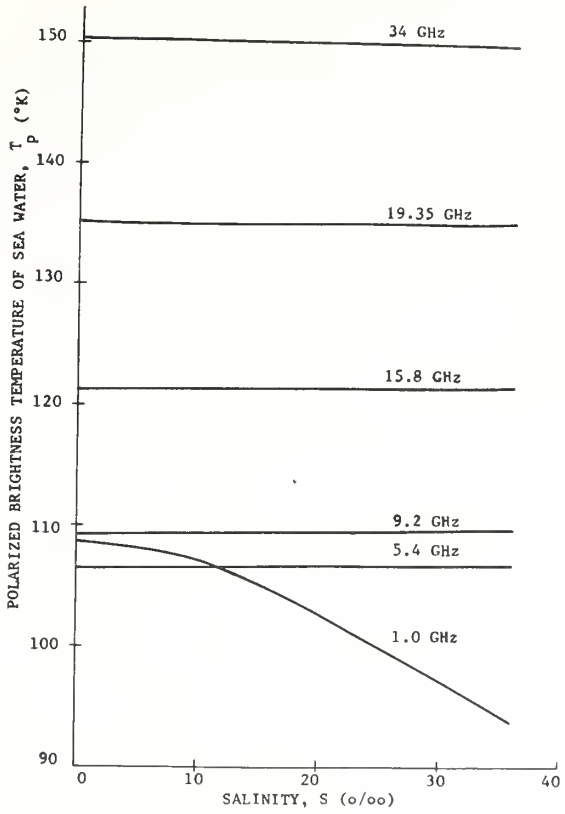

Figure 22.29 *The polarized brightness temperature of sea water versus salinity for a water temperature of 283 °K, for an incidence angle of 0°, for frequencies of 1, 5.4, 9.2, 15.8, 19.35, and 34 GHz and for an altitude of 1 km (after Paris, 1969).*

increases with increasing wind speed, although this relationship is critically dependent on polarization and viewing angle. At lower wind speeds, without foam, the brightness temperature depends on the RMS wave slope, whereas when foam is present the brightness temperature increases appear to be influenced primarily by foam.

22.2.4.1 Roughness

Investigators, such as Stogryn (1967) and Hidy, et al. (1971), have developed geometric optics models which include the effect on microwave emission of roughening of the sea surface by wind. The procedure is to assume Fresnel's Law of reflection is valid at a particular point on the surface, and to compute mean polarized emissivities by integration of the wave slope distribution, as described by Buettner et al. (1968). The wave slope distribution given by Cox and Munk (1954a, 1954b) is used for expressing the wave slope as a function of wind speed.

The potential use of detection parameters, P and Ψ, in determining the distribution of wave slopes was demonstrated first by Stogryn (1967). He calculated the brightness temperature versus incidence angle for both polarizations at 19 GHz, and for the following conditions:

1. An active ocean layer with homogeneous temperature and salinity of 17 °C and $36^0/_{00}$ (which are representative of midlatitude conditions).
2. An ARDC standard atmosphere,
3. A sensor height of 1 km, and,
4. Surface wind speeds of 0, 4, 8, and 14 ms^{-1}.

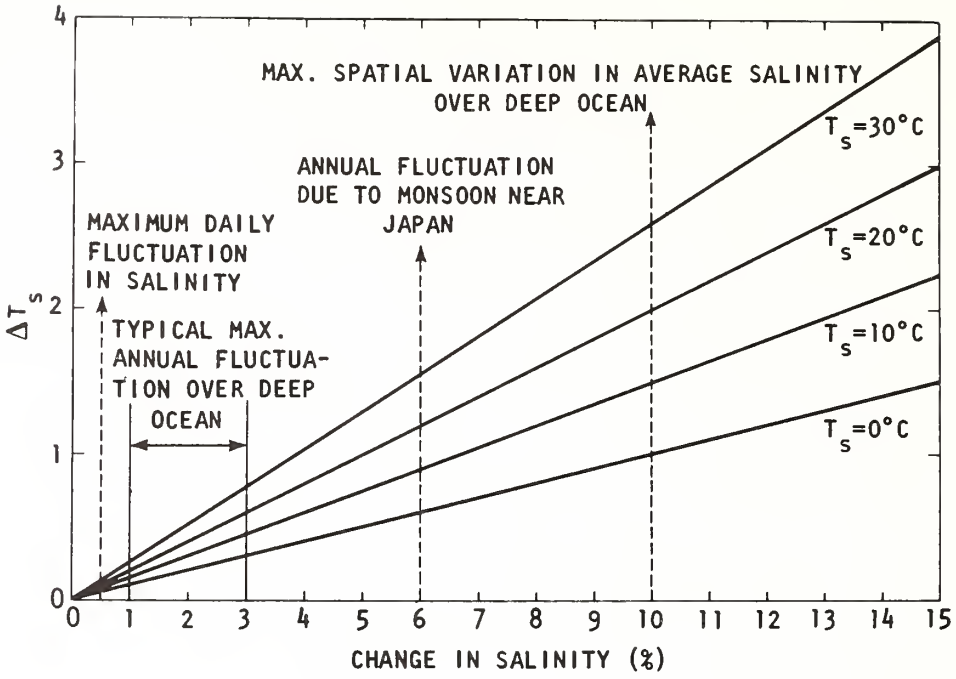

Figure 22.30 *Uncertainty in molecular temperature T_s, measured by a 2.65 GHz radiometer, due to changes in salinity of the world's oceans (after Hidy et al., 1971).*

Stogryn's calculations, illustrated in (F22.32), show a number of significant features. Brightness temperature strongly depends on polarization, as previously shown for the smooth ocean case in (F22.28) (Lewis et al., 1954). For vertical polarization, roughness of the ocean tends to increase the brightness temperature at $\Psi < 55°$, but decreases it at $\Psi > 55°$. The fact that vertically polarized brightness temperature is independent of wind speed at $\Psi = 55°$ may be used to advantage in multi-frequency scanning from satellites. For horizontal polarization, ocean roughness produces insignificant changes in brightness temperature at $\Psi = 0$ and has maximum change at Ψ values near 60°. The principle cause of this phenomenon, appearing in both vertically and horizontally polarized brightness temperature, is the change in the source of reflected sky radiation which results from wind roughening of the surface.

The theoretical calculations of Stogryn have been partially substantiated in experimental studies by Hollinger (1970). Using an 8.36 and 19.34 GHz radiometer from an ocean tower near Bermuda, Hollinger obtained polarized brightness temperatures for nadir angles from 0-75° and for wind speeds of 1.6 and 7.4 ms^{-1}. His results, in (T22.33), show no significant difference between the measurements at these two frequencies. They verify the reversal in wind effect on vertically polarized brightness temperatures at $\Psi = 55°$ as calculated by Stogryn. They are in excellent quantitative agreement with the same effect on horizontally polarized brightness temperature at $\Psi = 55°$, as is evident by comparison of the appropriate $\Delta T_{Bh}/\Delta v$ values in (F22.5). The only significant difference is the wind effect on horizontally polarized temperatures at small values of Ψ. Stogryn's theoretical calculations showed minimal wind effect as Ψ approached 0°; whereas Hollinger's experimental data show a diminishing but yet significant wind effect at $15° < \Psi < 55°$. The data at $\Psi \leqslant 15°$ may be anomalous due to the presence of the tower in Hollinger's data (Hollinger, 1970).

The theoretical calculations also predict very little dependence of the wind effect on microwave frequency. However, other experimental work by Hollinger (1971) shows that the wind effect at 1.41 GHz is only about 1/3 of that at 19.34 GHz, based on wind speeds in the range 0.5-13.5 m/sec. The appropriate numerical values are given in (T22.5). Thus, there is an important discrepancy between theory and experiment on the degree to which ocean roughness effects are frequency dependent.

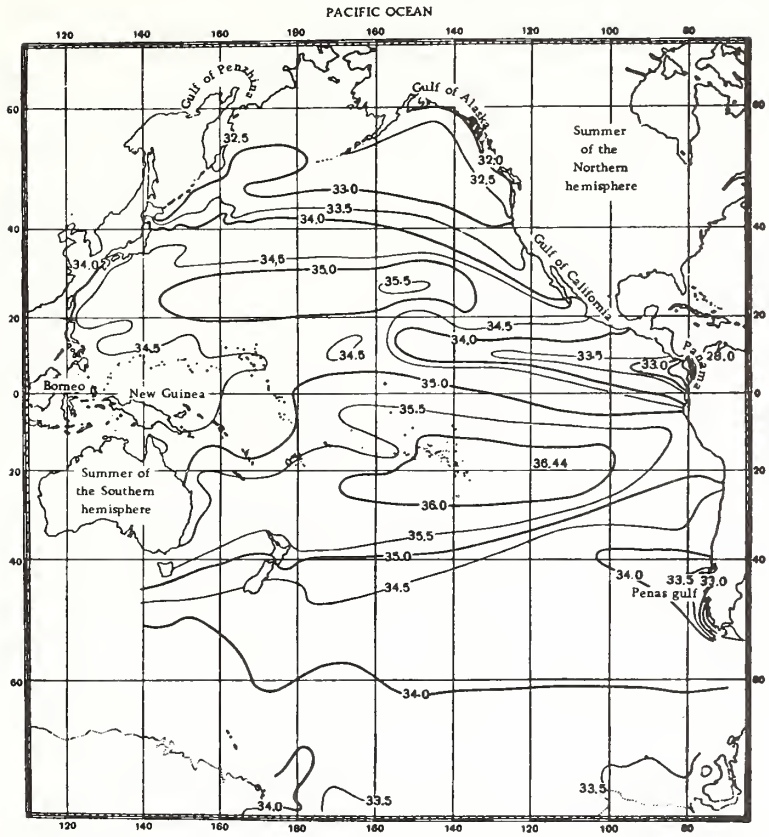

Figure 22.31 *Average distribution of sea-surface salinity for the Pacific Ocean in parts per thousand (after Muromtsev, 1963).*

22.2.4.2 Foam

The emissivity of foam is much higher than that of the sea surface. This was first suggested by Williams (1969) based on experimental data, and was supported theoretically on the basis of a physical model for foam by Droppleman (1970). Recent experimental data, reported by Ross et al. (1970) and Nordberg et al. (1971), indicate that over typical oceanic whitecaps the brightness temperature may by 100 °K higher than over adjacent foam-free ocean areas. Such a temperature anomaly indicates that foam may act as both an error source for molecular temperature measurement and a possible useful indicator of wind speed.

Both theoretical and experimental studies show there is a significant increase in whitecap coverage and spray density, beginning at 6-7 ms^{-1} (Monahan 1969, and Cardone, 1969). Similarly, the aircraft microwave radiometer data by Nordberg, et al. (1971) suggest a significant increase in microwave brightness temperature begins at about 6-7 ms^{-1}. They used a horizontally polarized 19.34 GHz radiometer and from a time series of measurements were able to show an increase in brightness temperature as a function of wind speed for speeds of <5 to 25 ms^{-1} with the sensor looking directly at the nadir. Their results in (F22.34) suggest that at wind speeds >7 ms^{-1} the increase in brightness temperature is due to an increase in foam coverage. It is apparent from their study that a determination of foam coverage is critical because only a few percent foam coverage can cause brightness temperature anomalies of about 2 °K.

The natural variation in foam coverage on a global scale has been investigated by Blanchard (1963) and is shown in (F22.35). In the tropics and mid-latitudes one would expect 2 percent or more foam coverage in both summer and winter, but as much as 8-9 percent at higher latitudes. A first order correction in brightness temperature will be necessary at certain angles and polarization in order to correct for foam.

Table 22.5 Summary of Brightness Temperature Sensitivity to Wind Speed

INVESTIGATOR	ν (GHz)	ψ (deg.)	Wind Speed Range (ms^{-1})	$\Delta T_B/\Delta v$ Vertical ($°K/ms^{-1}$)	$\Delta T_B/\Delta v$ Horizontal ($°K/ms^{-1}$)
Theoretical					
Stogryn (1967)	19.34	30	0-14	+0.4	+0.4
	19.34	55	0-14	0	+1.4
Experimental					
Hollinger (1970)	19.34	55	1.6-7.4	-0.1	+1.3
Hollinger (1971)	1.41	55	0.5-13.5	+0.02	+0.34
	8.36	55	0.5-13.5	+0.04	+0.60
	19.34	55	0.5-13.5	-0.06	+1.06
Nordberg et al. (1971)	19.34	0	6-25	–	+1.2
	19.34	70	6-25	–	+1.8

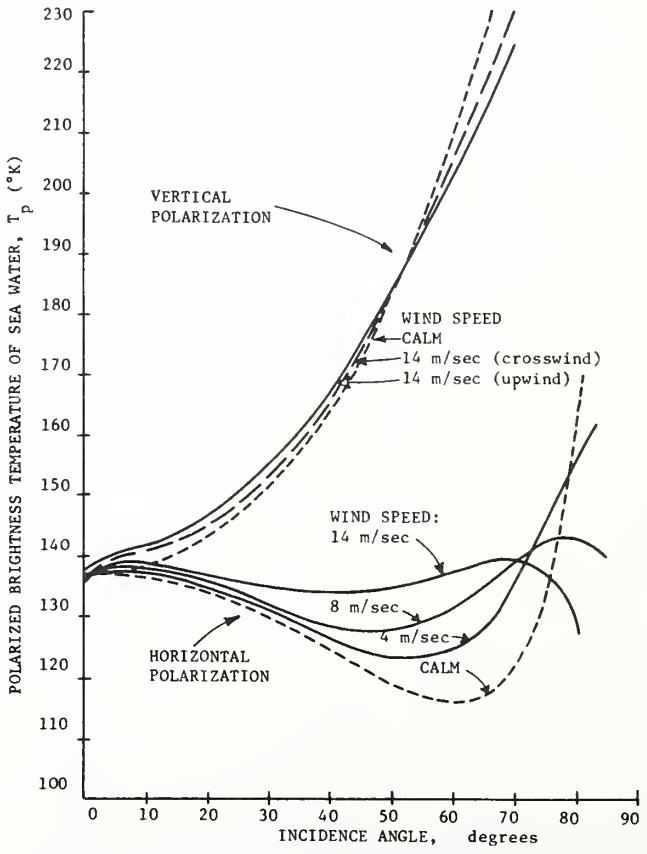

Figure 22.32 *The polarized brightness temperatures of sea water versus incidence angle for horizontal and vertical polarization, for fully developed sea driven by surface winds of 0, 4, and 14 m/sec, an altitude of 1 km, and a frequency of 19.4 GHz (after Stogryn, 1967).*

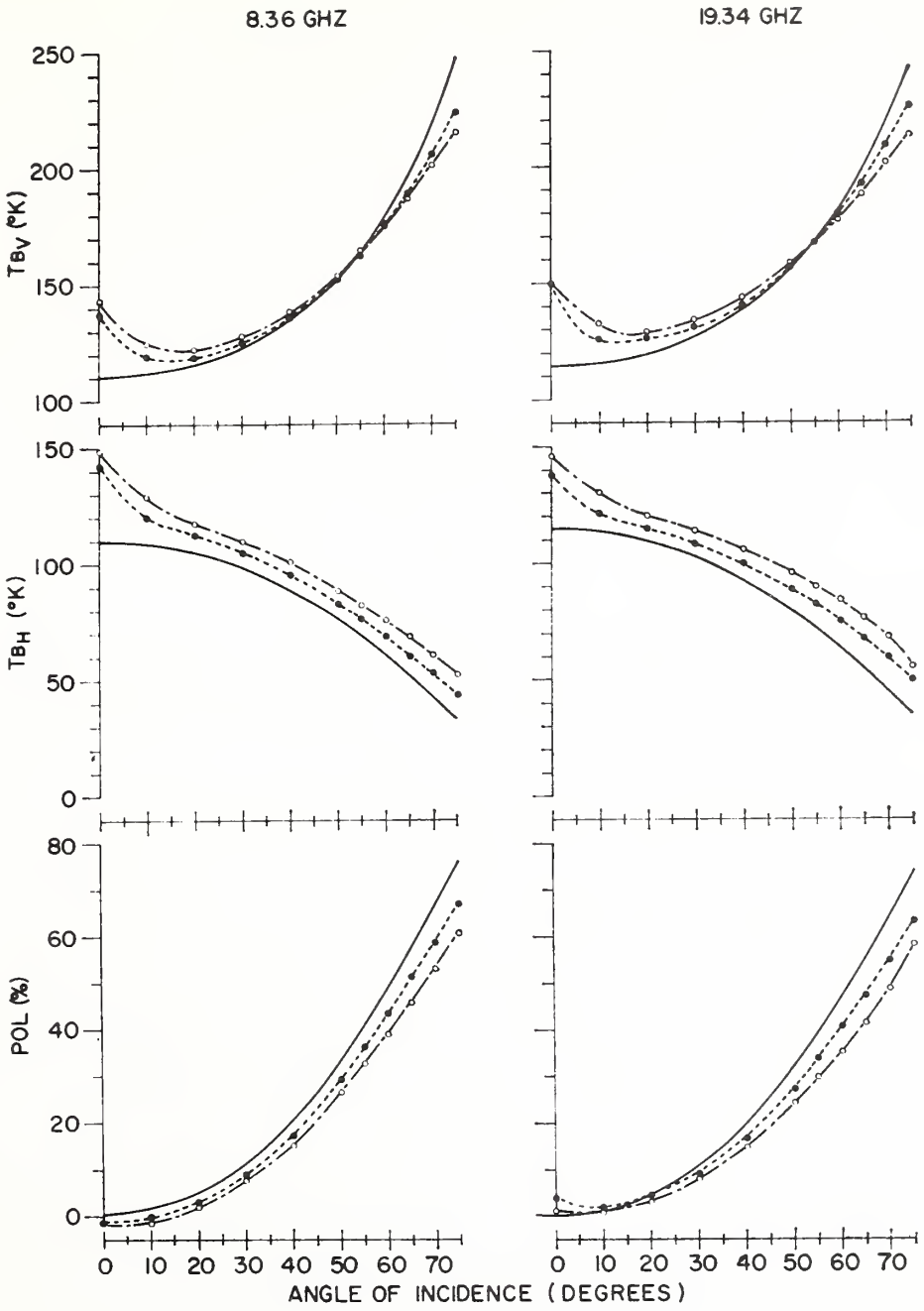

Figure 22.33 *The vertical and horizontal components of brightness temperature of the sea and the percentage of polarization (defined as the ratio of the difference of these two components of their sum) at 8.36 and 19.34 GHz are plotted as a function of incidence angle for two groups of measurements comprising the lowest and highest sea conditions encountered. The solid circles represent average sea conditions of 2.6 m/sec winds with 1.6 meter waves; the open circles, 7.4 m/sec winds with 1.9 meter waves. The solid line has been calculated for a specular surface (after Hollinger, 1970).*

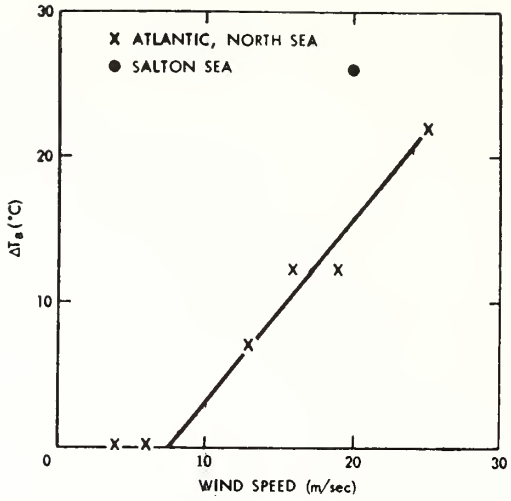

Figure 22.34 *Brightness temperature differences between observations made at wind speeds <5 m sec^{-1} and higher wind speeds as a function of wind speed (after Nordberg et al., 1971).*

22.2.5 Ice

There have been many excellent studies, such as that of Pascalar and Sakamoto (1965), which show that the brightness temperature contrast between ice and water is quite large because the emissivity of optically thick ice is in the range 0.8-1.0, whereas that of water is only about 0.4-0.5. This natural difference in their emissivities might possibly be employed in remote sensing to determine the extent of open water in the arctic ice pack.

Studies by Badgley (1966) of polar ocean areas have suggested that the heat flux from the ocean to the atmosphere is at least two orders of magnitude greater in open water areas of the ice pack than through the ice pack itself. Other studies have indicated that at any time of the year as much as 10 percent of the Arctic Ocean may be open water, resulting from polynyas (large cracks) and leads (small cracks) in the ice pack (Wittman and Schule, 1966).† Hence the ocean to air heat flux in ice covered ocean regions may be monitored through microwave sensing by measurement of the relative amount of open water.

Because the open water leads may be relatively narrow, antenna beamwidths must be small enough to resolve them. With the restrictions imposed by space craft on antenna sizes, this requires high frequencies. However the attenuation due to water vapor and oxygen limit the choices. The window centered near 37 GHz is the highest frequency range which can be used successfully because of the attenuating and emitting effects at higher frequencies of molecular oxygen and water droplets in the atmosphere.

Recently in experimental studies, Wilheit, et al., (1971) discovered that year-old, smooth ice has a lower emissivity than older, more heavily hummocked ice. This would lead to an ambiguity in determining the relative amount of open water by observation of emissivity contrast. Fortunately, the difference in emissivity between the two ice types is relatively independent of polarization and is proportional to frequency (up to 37 GHz), whereas the emissivity contrast between water and ice is strongly dependent on polarization. Thus, with a measurement of both polarizations, the environmental variables can be resolved.

The large emissivity contrast between ice and water has been used by the U. S. Coast Guard to locate and track icebergs in the North Atlantic Ocean (Roeder, 1967). Such an iceberg target must be sufficiently large within the field of view to give a detectable emissivity contrast from the ocean background.

†cited by Wilheit et al., (1971).

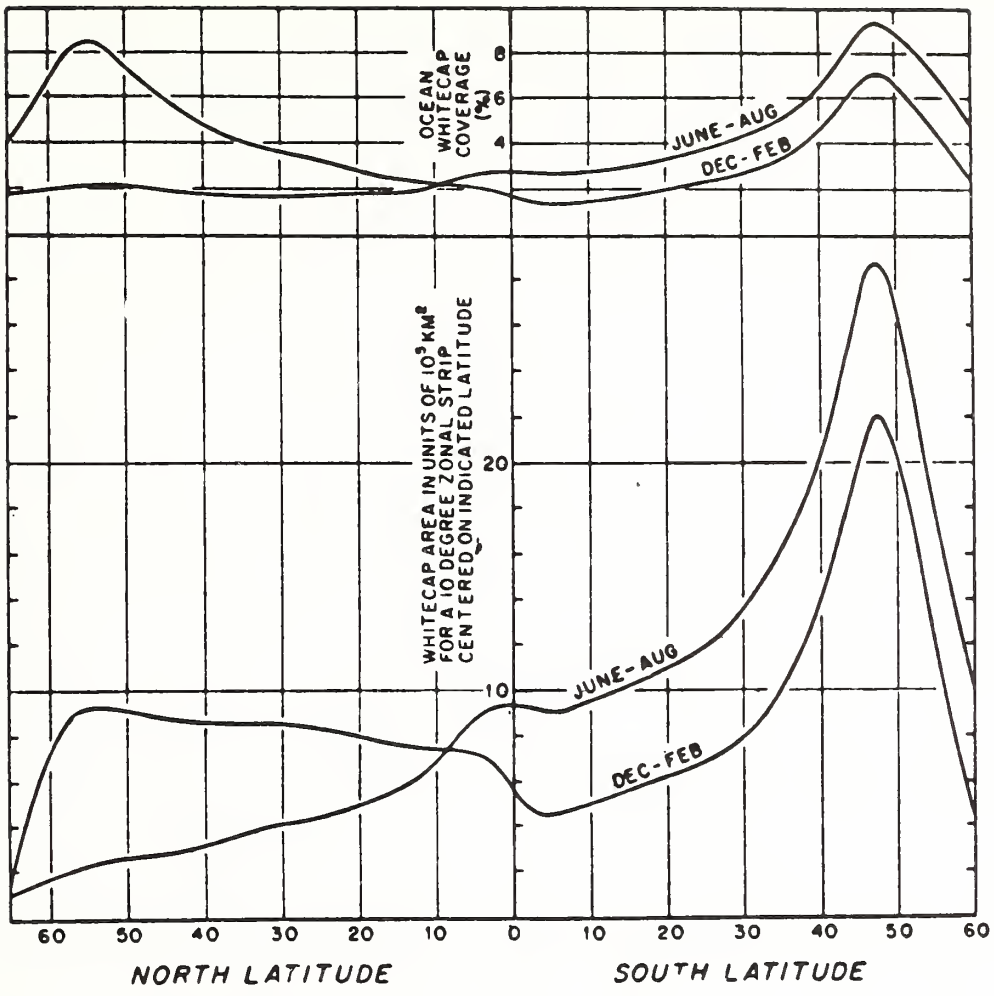

Figure 22.35 *The latitudinal variation of the world ocean whitecap distribution. The upper set of curves give the percentage coverage during the winter and summer seasons. The lower set gives the area of the sea surface that is covered with whitecaps. The bump in the June-August curves near the equator reflects the monsoons in the Indian Ocean (after Blanchard, 1963).*

22.2.6 Atmospheric Extinction and Emission

Microwave emission by the atmosphere affects remote sensing of oceanographic variables in two ways. One is that the atmosphere itself is a source of microwave illumination for the ocean surface, and because of the relatively high reflectivity of the surface, a remote detector would receive the combined microwave emission of the ocean and atmosphere. Clearly the atmospheric portion must be evaluated in order to interpret the emission from the ocean alone. Secondly, the atmosphere attenuates microwave radiation from the ocean surface, tending to limit the information available for detecting oceanographic variables. Only a limited discussion of these atmospheric effects will be presented here because they are discussed in other chapters of this volume.

The reader will recall from (F22.24) there are two relatively broad atmospheric windows on either side of the 60 GHz oxygen absorption band; these windows are shown in greater detail in (F22.36). Although the 80-90 GHz window has a high transmissivity, it has only limited usefulness because of the relatively large influence of liquid water drops at those frequencies. Thus, the window on the lower

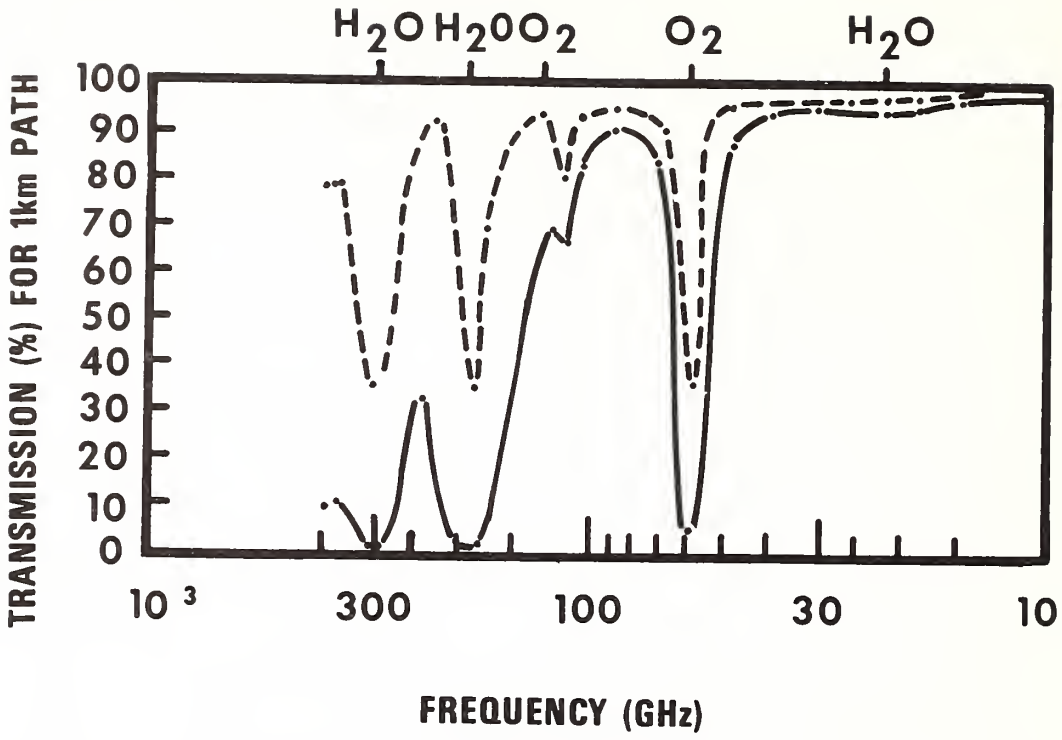

Figure 22.36 *Transmission for 1 Km path. Attenuation due to atmospheric oxygen and water vapor. Solid curve: p = 760 mm Hg.; T = 20 °C; water vapor = 7.5 gm/M³ (adapted from Meyer, 1966).*

frequency side of the 60 GHz absorption band is most promising for passive microwave sensing. Here transmissivities are relatively high at frequencies below 40 GHz. However, a water vapor absorption line is centered at 22.235 GHz, as shown in (F22.37), and it has a significant influence on atmospheric absorption at frequencies as low as 5-10 GHz, depending on the amount of water vapor.

Galactic and cosmic background radiation becomes relatively large at frequencies below 1 GHz and can usually be ignored at frequencies above 2 GHz (Hidy, et al., 1971).

As long as liquid water droplets in clouds are much smaller than microwave wavelengths, scattering is assumed negligible and the absorption of cloud water is (1) approximately proportional to the square of the frequency, (2) directly proportional to liquid water content in the path, and (3) independent of the drop size distribution (Huston, 1971). Calculations by Gunn and East (1954) indicate the absorption of ice in clouds is roughly an order of magnitude less than that for liquid water.

It is considerably more difficult to evaluate the influence of hydrometeors in microwave attenuation than to evaluate the influence of cloud droplets because hydrometeors are large enough to approach microwave wavelengths. Thus, both scattering and absorption must be considered. Gunn and East (1954) obtained calculations of radiation attenuation with precipitation and found that (1) attenuation was roughly proportional to precipitation rate, and (2) snow fall effects are at least two orders of magnitude less than liquid water.

22.3 Ocean Color Detection–Chlorophyll

A discussion of ocean color introduces a new aspect to remote sensing beyond the physics of light alone–that is, use of color stimulation of the human eye for discrimination of differences in scene illumination. Probably the first remote sensing of the sea was by early sailors who used color to discriminate ocean depth. This technique is still used today.

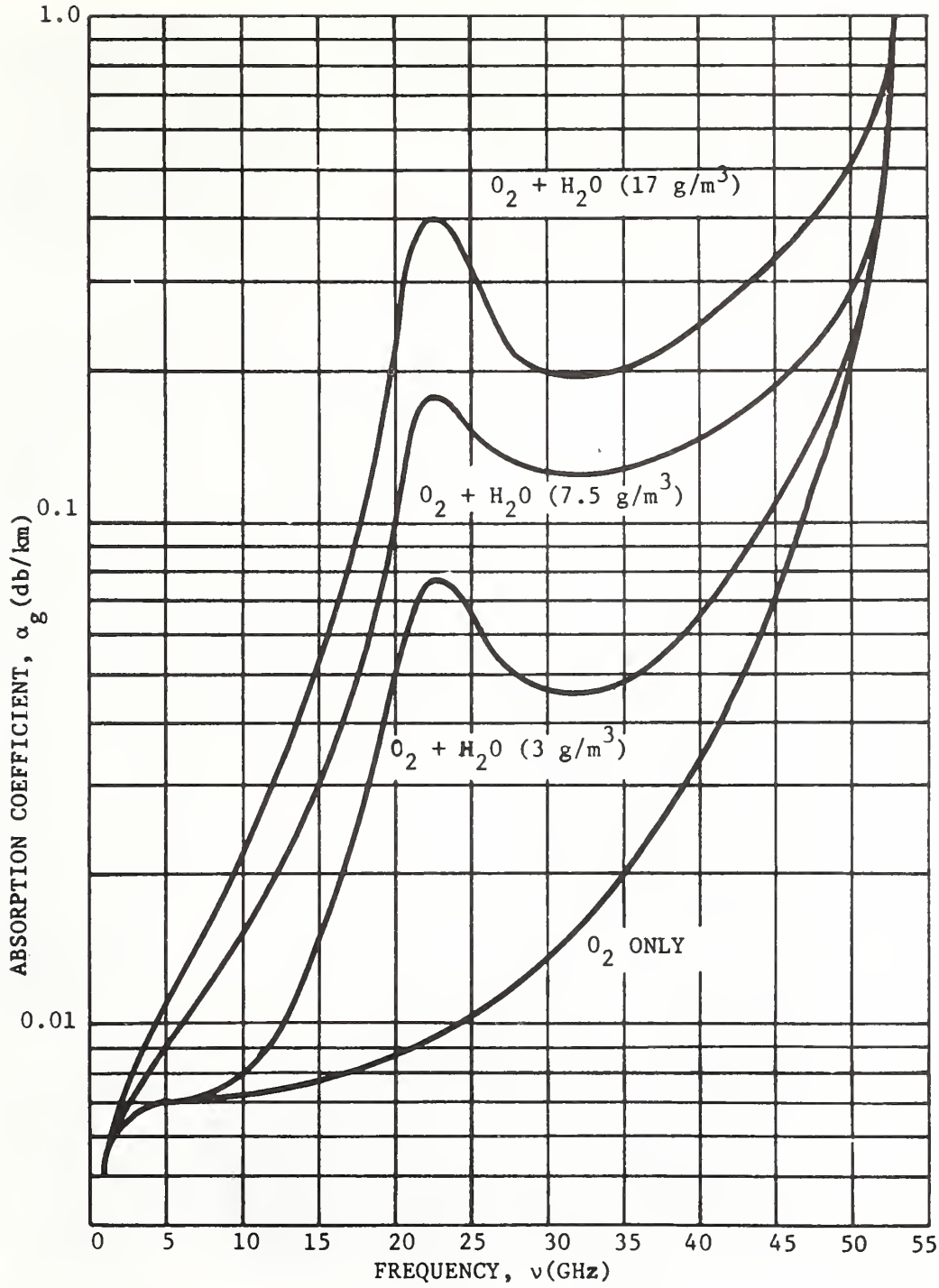

Figure 22.37 *The absorption coefficient of molecular oxygen and water vapor at sea level versus frequency for a temperature of 293 °K and for water vapor densities of 0, 3, 7.5, and 17 grams per cubic meter (after Paris, 1969).*

Figure 22.38 *Color of the sea as indicated in percent of yellow according to the Forel scale (according to Schott (1942) from Sverdrup, et al., (1942)).*

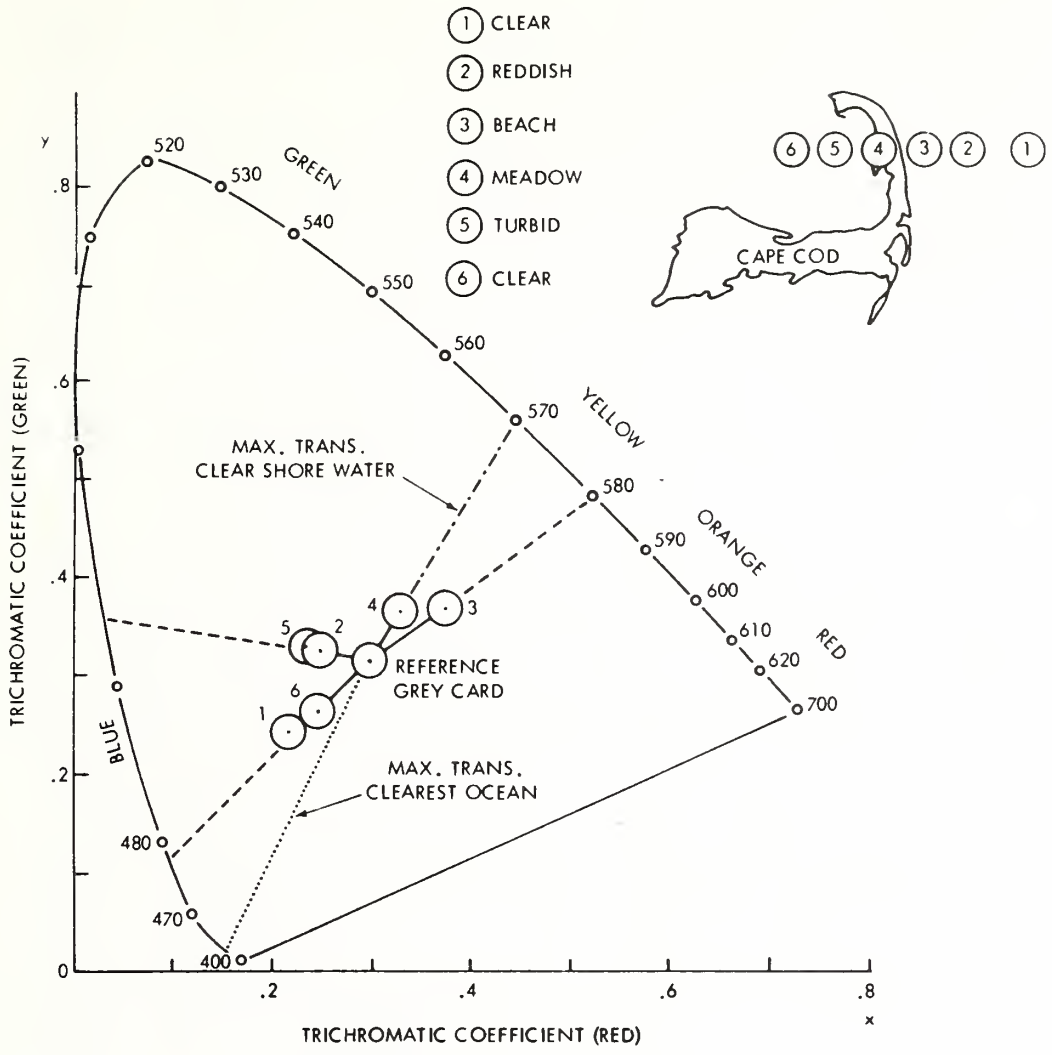

Figure 22.39 *Chromaticity Diagram (after Ewing, 1969).*

Solar radiation that penetrates the sea makes possible photosynthesis in green plants which are primarily phytoplankton. Because the production of all marine creatures depends on the growth of phytoplankton, it is important to assess the possibility of measuring the concentration of phytoplankton in the world's oceans by remote sensing techniques.

Although direct measurement cannot be made, it is known that light which penetrates the sea is absorbed and scattered by the particulates and dissolved materials, of which chlorophyll is an active absorber. Because high concentrations of chlorophyll are known to contain large populations of phytoplankton, color of light emerging from the ocean may be used to discriminate concentration of phytoplankton, and hence regions of high productivity (Clarke, et al., 1969).

22.3.1 Color Perception Methods

Oceanographers, over the past decades, have obtained measurements of ocean color and clarity for use in ocean watermass analysis. These color determinations have been obtained by lowering a Secchi disc one meter below the surface and comparing the apparent color of the disc with each of eleven tubes

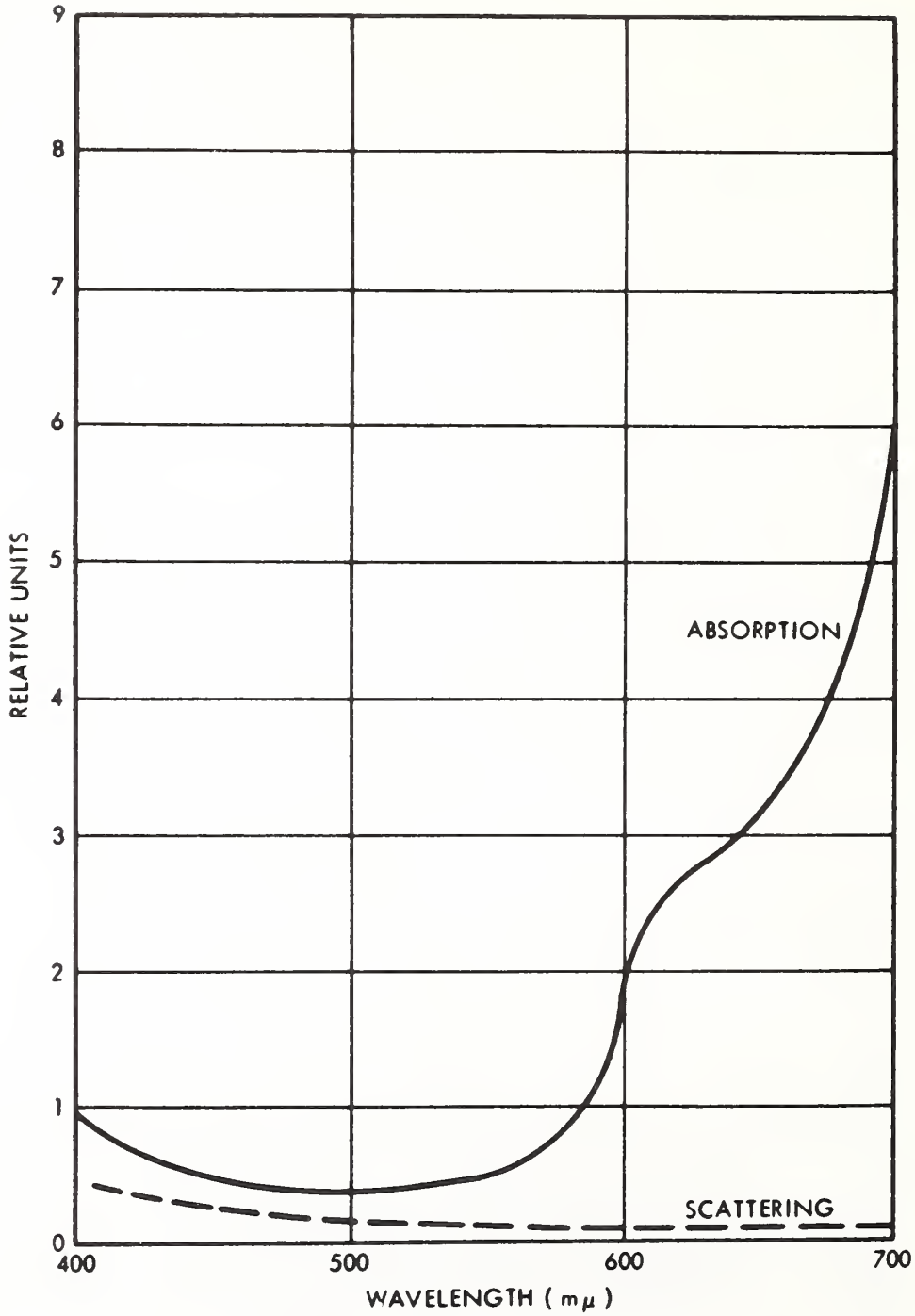

Figure 22.40 *Absorption and Scattering of Distilled Water (after Hulbert, 1945).*

containing colored water samples ranging from blue to green. The advantage of such a technique is that it is affected to only a minor degree by the atmosphere. However, it is deficient because it is based on a subjective judgment, has a color resolution of only one part in eleven, presents serious global sampling problems, and varies as a function of cloud cover.

The Forel Scale† color determinations were begun in the late 1800's and were improved by Kalle (1938) with the development of a comparitor which allowed the observer to produce a color with red, green, and blue filters matching that observed in the sea. The three colors represent the primary colors of the color triangle of the Young-Helmholtz theory of color vision (Neumann and Pierson, 1966 and Jerlov, 1968).

In spite of the areal sampling problem with ocean color measurements, Schott (1942) has shown that the distribution of color over the Atlantic Ocean ranges from deep blue, Forel Scale 0, in the Sargasso Sea to greenish or yellow-green colors in equatorial regions, near shore, and at high latitudes. Schott's map is shown in (F22.38). Neumann and Pierson (1966) point out that this map reveals a close relationship with a map (not shown here) of the vertical extinction coefficient of surface water in the Atlantic Ocean obtained by Joseph and Wattenberg (1944). This provides evidence of an apparent large-scale relationship between oceanic particulates and ocean color, and also provides some hope for satellite remote detection on this spatial scale.

22.3.1.1 Chromaticity Coordinates

A completely objective method of determining color is by color analysis in C.I.E. chromaticity coordinates (Anonymous, 1957). This numerical definition of color is based on tristimulus values of the spectrum colors, red, green, and blue. Each color has standardly defined spectral response values. The green values are identical with the standard luminosity curve for photoptic vision of the human eye (Committee on Colorimetry, 1966). A plot of pure color in chromaticity coordinates is called the spectrum locus and defines a horseshoe-shaped boundary of the color space (see F22.39). The chromaticity coordinates are taken nominally as the red and green trichromatic coefficients. By definition white light is located only at the central coordinate point (.333, .333).

Ewing (1969) has presented on a chromaticity diagram an example of the color variation of backscattered light from the ocean and from the land at Cape Cod, Mass., obtained by aircraft measurements at 500 ft. altitude. The diagram is shown in (F22.39). Clearly there is a distinct color separation between the measurements over and adjacent to Cape Cod, 2-5, as compared to those over clear ocean water, 1 and 6. The dominant wavelength is another term associated with the chromaticity diagram and is defined by extending a line from the central (white light) point, through the point in question to the spectrum locus. In (F22.39) the clear ocean points, 1 and 6, have a dominant wavelength of .478 μm. This is slightly higher than the wavelength of maximum transmission for the clearest oceans, about .470 μm (Jerlov, 1968).

The chromaticity coordinate technique appears to be a useful but laborious method for discriminating color information from either properly obtained photographic data or spectral radiance data.

22.3.2 Spectral Radiance

Apart from human color perception, it is possible to specify color objectively as the spectral radiance of a particular scene. In this definition, color need not be restricted to the visible portion of the spectrum and could include, for example, spectral radiance in the near IR as well. This section will discuss the use of spectral radiance in remote detection of ocean chlorophyll and productivity. The established convention of relating color to wavelength is given in (T22.6).

It is of interest to consider the path of solar radiation before it reaches a remote sensor. Of the solar illumination impinging on the upper atmosphere, about 75 percent of this broad-band radiation reaches and is transmitted downward through the ocean surface. Once in the ocean photic zone†† the

†Forel (1895 and 1901).

††Photic zone is defined as the oceanic layer with upper limit at the surface and lower limit at a level where the irradiance is reduced to 1 percent of the surface value.

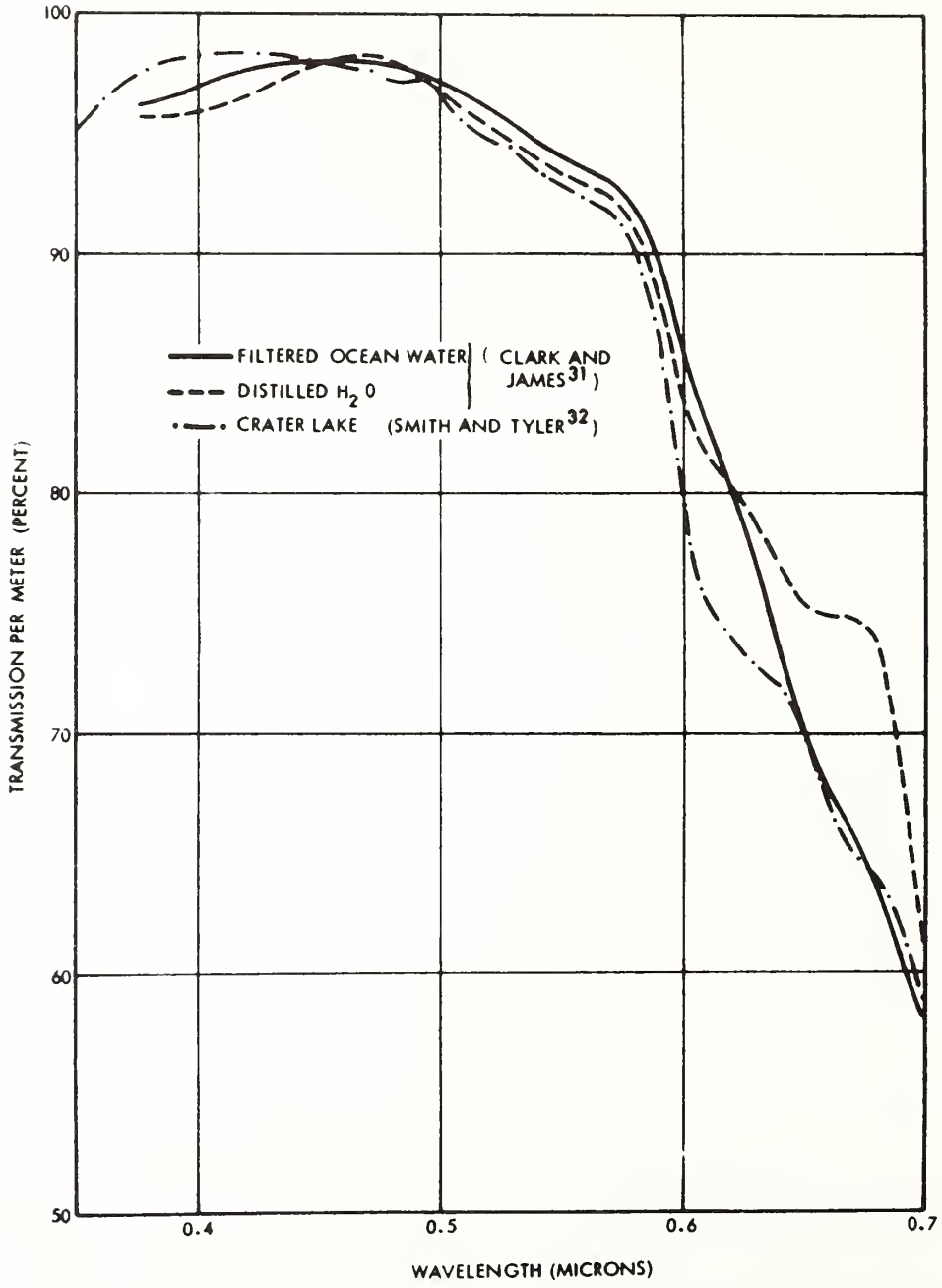

Figure 22.41 *Percent Transmission of Clear Waters (according to Clarke and James (1939) and Smith and Tyler (1967), after Ramsey, 1968).*

radiaton is scattered and absorbed by particles, solutes, and the water itself in a complex way. A large portion of the radiation is scattered forward; a small but spectrally significant portion is back-scattered to the surface. The color of this backscattered light is critically dependent on the concentration of particles and solutes in the water. Pure water backscatters predominantly blue light with a dominant wavelength near .470 μm; however, particulates including chlorophyll, and solutes including yellow substance, in some ocean waters, tend to shift the dominant wavelength toward higher values causing the ocean to appear green, yellow-green, or brown. This relatively small back-scattered light which emerged from the sea surface traverses the atmosphere with some attenuation, finally reaching the remote aircraft or satellite detector. Also reaching the detector is light from two other sources; (1) that reflected by the sea surface, and (2) that scattered upward by atmospheric molecules and aerosols. Thus, remote sensing of oceanic chlorophyll requires the interpretation of upwelling spectral radiance which is the sum of three components, one of which varies, in part, because of variations in chlorophyll.

Only the backscattered spectral radiance of the photic zone will be discussed in the following sections. For a discussion of the sea surface and atmospheric radiation components, the reader is referred to an excellent review of the subject by Ramsey (1968).

22.3.2.1 Absorption and Scattering of Pure Ocean Water

Progress in the investigation of the attenuation of pure water was relatively slow, because the measurements were handicapped by the difficulty of preparing pure water. However, it is generally thought that Clarke and James (1939) have been successful in preparing pure water, and their values of attenuance (beam attenuation) for the visible region are representative (Jerlov, 1968).

A comparison of the attenuance data by Clarke and James and the scattering data for pure water by LeGrand (1939) indicates that the attenuation is primarily due to absorption rather than scattering. This is also verified by the data of Hulbert (1945) shown in (F22.40). Pure water has highly selective absorption properties and acts essentially as a monochromator for blue light near .470 μm, as shown in the transmittance curve, (F22.41), for distilled water from Clarke and James (1939).

The question arises whether the addition of sea salts changes the attenuance of pure water. To answer this, Clarke and James filtered clear ocean water from the Sargasso Sea and compared its transmittance with that of pure water. They found,(F22.41), no significant difference between the pure water and filtered Sargasso Sea water. Their finding was verified by Sullivan (1963). The conclusion is that sea salts exert little or no influence on visible light attenuation. Slight effects have been studied by Morel (1966).

22.3.2.2 Absorption by Yellow Substance and Chlorophyll

Natural ocean water contains both solutes and particles which alter significantly the radiative properties of pure water. This became apparent from the work of Clarke and James who obtain transmittance spectra on filtered water samples from turbid, coastal areas as well as from Sargasso Sea water. They found (F22.42) that even after careful filtration and removal of all suspended matter, the extinction of light remained much greater in filtered coastal water than for both pure water and filtered Sargasso Sea water. This indicates that turbid matter, remaining in the coastal water after filtering, is the major cause of selective extinction at short wavelengths (blue).

Evidence suggests that filter-passing turbidity matter is probably due to dissolved organic substances. Kalle (1938) has shown that sea water, especially in coastal areas, contains soluble pigments of yellow color which are chemically related to humic acids. This yellow substance represents fairly stable metabolic products, mainly carried into the sea by rivers but probably also produced in ocean water as a result of plankton metabolism (Neumann and Pierson, 1966). Yellow substance plays an important part in explaining the transition of the color of sea water from blue to green. The spectral absorption data for yellow substance (F22.43) show a strong increase in absorption at shorter wavelengths, which tends to shift the wavelength of maximum transmission of light in water from near 0.470 μm, blue, to the longer yellow or green wavelengths.

Although the absorption spectrum of plant leaves is relatively well known, that for living phytoplankton has had much less attention. Yentsch (1960, 1962) has provided particularly useful information in this area. He has examined the absorption of various living phytoplankton groups and compared them with a natural population of phytoplankton sampled from ocean water near Woods Hole,

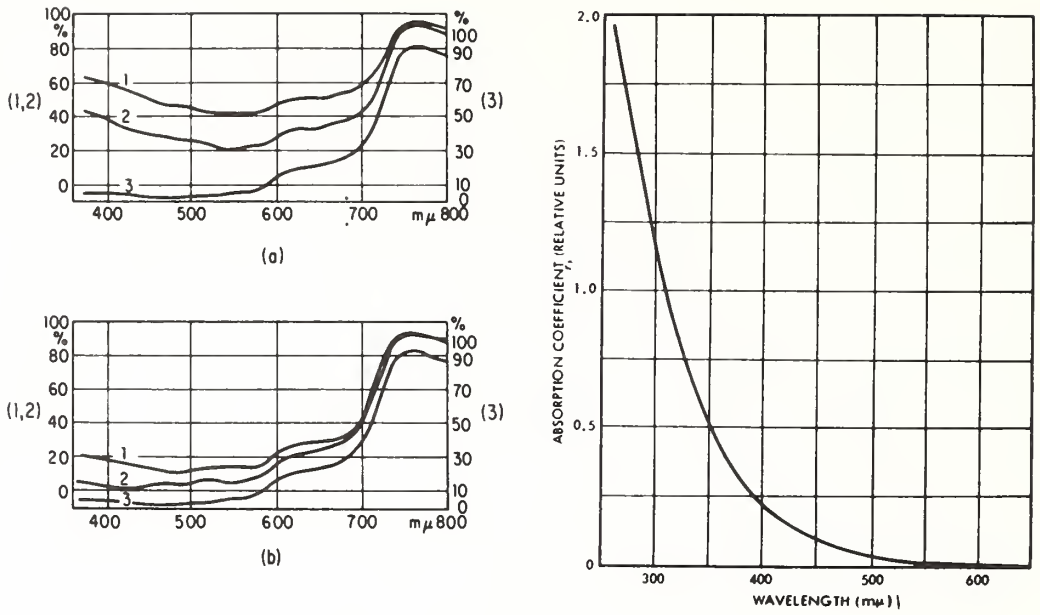

Figure 22.42 *(a) Spectral extinction of coastal water (1) before and (2) after filtering, in comparison with double-distilled water (3). (b) Spectral extinction of Sargasso Sea water (1) before and (2) after filtering, in comparison with double-distilled water (3). The scale for curve 3 (double-distilled water) is on the right-hand side of the figures and vertically displaced with respect to the scale for curves 1 and 2 (according to Clark and James (1939), after Newmann and Pierson (1966)).*

Figure 22.43 *Absorption curve of yellow substance (after Jerlov, 1948).*

Massachusetts (Yentsch, 1960). His results, in (F22.44) show that all of the populations exhibit (1) a strong, broad absorption maximum in the blue related to chlorophyll and carotenoid absorption, (2) an absorption minimum in the green, and (3) a minor absorption maximum at .680 μm due to chlorophyll *a* (Yentsch, 1960). This suggests that naturally occurring phytoplankton populations in the oceans may have sufficiently uniform absorption properties that their concentration can be detected and quantified by spectral signature or radiance integral inversion techniques.

In order to improve the computational utility of his data, Yentsch(1960) determined the combined absorption coefficient of pure water and chlorophyll in varying concentration from 0.5-200 mg/m^3. His spectral absorption curves, in (F22.45), show clearly the strong, broad absorption band in the blue and the sharp absorption peak at .680 μm. Of particular interest is the shift in minimum absorption from the blue-green to the green-yellow part of the spectrum. It may be of interest to the reader mentally to combine the pure water absorption in (F22.40) with the phytoplankton absorption in (F22.44) in order to see the similarity of the result of this combination with Yentsch's combined absorption in (F22.45).

22.3.2.3 Calculations of Backscattered Light

Hulbert (1943) derived a general expression for back-scattered light from the sea, including also the effect of surface reflection. Ramsey (1968) has used this expression together with Yentsch's absorption coefficient for pure water and plant pigments, (F22.45), in order to calculate the spectral reflectance of the deep ocean for a given solar zenith angle and atmospheric turbidity. His results, in (F22.46), show the change from blue color with low chlorophyll concentrations to the predominant green and yellow colors for heavy chlorophyll concentrations.

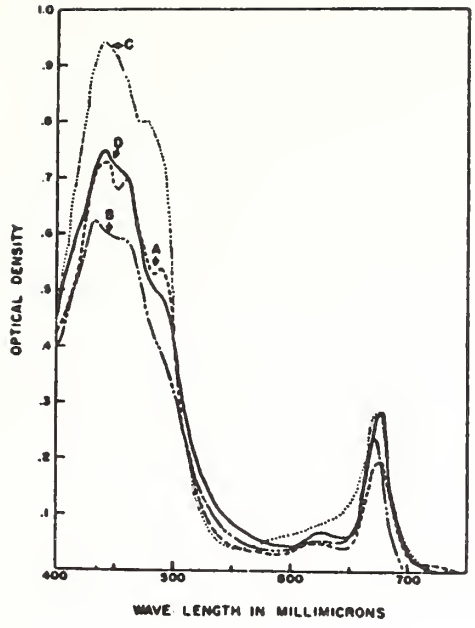

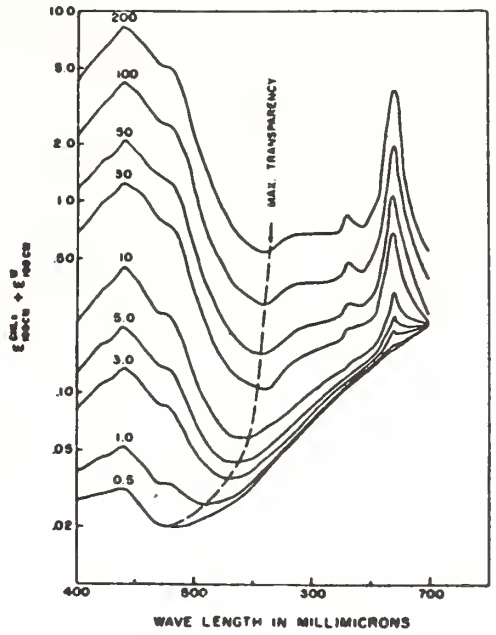

Figure 22.44 *Pigment Spectra of Living Phytoplankton, (a) Diatom Cyclotella sp., (b) Dinoflagellate, amphidium sp., (c) green Flagellate chlamydomonas, (d) Natural population sampled from Woods Hole waters (after Yentsch, 1960).*

Figure 22.45 *Combined absorption coefficient for pure water and plant pigments. Numbers adjacent to the curves indicate the chlorophyll concentration in mg/m^3 (after Yentsch, 1960).*

In the blue-green spectrum, 0.4-0.5 μm, of F22.46, increasing chlorophyll concentration from 0 to 10 mg/m^3 causes a systematic reduction in backscattered light. However, for concentrations $>$ 10 mg/m^3, the amount of backscattered light appears to be relatively constant. This suggests there is little or no information content in this part of the spectrum for chlorophyll concentrations of 10 to 100 mg/m^3, although the backscattered light is particularly sensitive to changes of low chlorophyll concentrations.

In the green-yellow-red spectrum, 0.5-0.7 μm, however, the reflectance systematically increases for concentrations from 0 to 100 mg/m^3. This portion of the spectrum appears to be useful for remote detection of all concentration levels.

22.3.2.4 Experimental Measurement of Backscattered Light

An important question is whether the calculations of Ramsey (1968), using Hulbert's theoretical expression for upwelling light from the sea and Yentsch's (1960) absorption data for pure water and phytoplankton, can be verified with experimental data.

In order to attempt such a verification, investigators at Woods Hole Oceanographic Institution (WHOI) have obtained measurements of upwelling spectral radiance by aircraft and also obtained simultaneous *in situ* measurements of chlorophyll content over the range 0.1 to 3.0 mg/m^3. Their results have been published by Clarke, et al. (1970 and 1971) and Ewing (1971) and are shown in (F22.47). The locations of the samples, chlorophyll concentrations, and mean square slopes of the spectral reflectance curves are also given in that figure. Clarke and Ewing's data show that with increasing concentrations of chlorophyll the energy in the blue region of the spectrum decreased markedly, whereas the energy at longer wavelengths, green, tends to increase a small amount. Ewing (1971) says that "these effects can be explained by the well-known absorption of chlorophyll *a* which is particularly large in the blue (Yentsch, 1960)."

To examine the question of experimental verification of Ramsey's calculations, it is of interest to compare (F22.46) and (F22.47). One sees the slopes of the reflectance curves are in general agreement but differ in some detail. For example, the relatively strong absorption band for plant pigments near .450 μm in Ramsey's calculations do not show up as strongly in the aircraft data. Another difference in the curves is the point of reversal in reflectance which, in Ramsey's calculations, is centered near 0.500 μm but is somewhat uncertain in the aircraft data. Perhaps this could be resolved if it were true that the A station water was deficient in yellow substance compared to stations B-D, (which is reasonable considering the source and distribution of yellow substance). If true, the A station curve would be displaced toward shorter wavelengths which would allow the aircraft data to support a reversal in reflectance at about 0.500 μm. The aircraft data also suggest that at stations B-D water is relatively high in yellow substance, because the measured values of backscattered light are considerably lower than those of Ramsey's calculations which did not include the absorption of yellow substance.

The high negative correlation between chlorophyll concentration and mean squared slope of the spectral radiance curve (Table in F22.47) is extremely promising for those interested in remote detection of chlorophyll. These data also suggest that other natural variables which scatter and absorb light in the ocean, such as yellow substance, must be better understood before either theoretical calculations or empirical relations between spectral radiance and chlorophyll can be used to support global surveys of ocean chlorophyll.

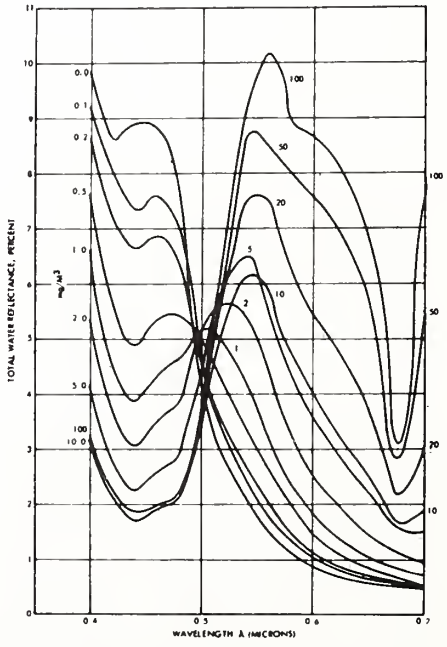

Figure 22.46 *Calculated spectral reflectance of deep ocean with varying amounts of chlorophyll, clear sunny day – 45° solar zenith angle, includes surface reflection from smooth ocean with turbid atmosphere (after Ramsey, 1968).*

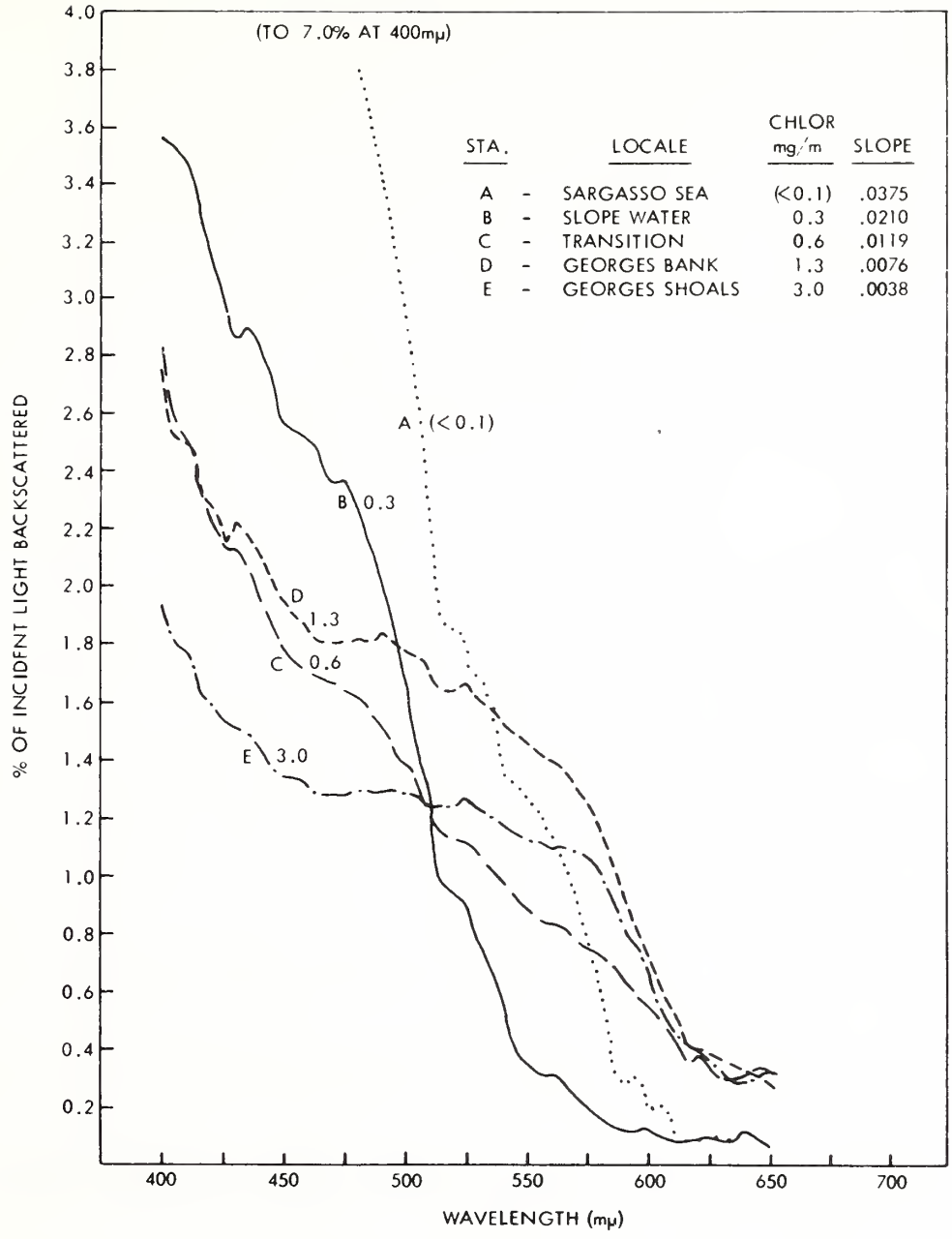

Figure 22.47 *Spectra of backscattered light measured from the aircraft at 305 m on 27 Aug. 1968 at the following stations and times (all E.D.T.): Station A, 1238 hours; Station B, 1421 hours; Station C, 1428.5 hours; Station D, 1445 hours; Station E, 1315 hours. The spectrometer with polarizing filter was mounted at 53° tilt and directed away from the sun. Concentrations of chlorophyll a were measured from shipboard as follows: on 27 Aug., Station A, 1238 hours; on 28 Aug., Station B, 0600 hours; Station C, 0730 hours; Station D, 1230 hours (after Ewing, 1971).*

Table 22.6 Colors and Corresponding Electromagnetic Wavelengths

(After Kondratyev, 1969)

Color	Wavelength Interval mμ	Typical Wavelength mμ
Violet	390-455	430
Dark blue	455-485	470
Light blue	485-505	495
Green	505-550	530
Yellow-green	550-575	560
Yellow	575-585	580
Orange	585-620	600
Red	620-760	640

22.4 References

Allison, L. J., L. L. Foshee, G. Warnecke and J. C. Wilkerson (1967), An analysis of the north wall of the Gulf Stream utilizing NIMBUS II High resolution infrared measurements, (paper presented at the 48th meeting of the American Geophysical Union, April 17, 1967, Washington, D. C.).

Allison, L. J. and J. S. Kennedy (1967), An evaluation of sea surface temperature as measured by NIMBUS 1 high resolution infrared radiometer, TN D-4078, NASA, Washington, D. C.

Anding, D., and R. Kauth (1969), Atmospheric modeling in the infrared spectral region: Atmospheric effects on multispectral sensing of sea-surface temperature from space, Report 2676-1-P, Willow Run Laboratories, Institute of Science and Technology, The University of Michigan, Ann Arbor, Michigan.

Anding, D. and R. Kauth (1970), Estimation of sea surface temperature from space, Remote Sensing of Environment, *1*, 217-220.

Anonymous, 1957: *International Lighting Vocabulary – Comm. Intern. Eclairage, Publ.* 1(1): 136 pp.

Aukland, G. C., P. J. Caruso, Jr., and W. H. Conway (1969), Remote sensing of the sea conditions with microwave radiometer systems, Proceedings of the Sixth International Symposium on Remote Sensing of Environment, *II*, Univ. of Michigan, Ann Arbor, 709-720.

Badgley, F. J. (1966), Heat budget of the surface of the Arctic Ocean, Proceedings of the Symposium on the Arctic Heat Budget and Atmospheric Circulation, Edited by J. O. Fletcher, The Rand Corporation, (RM-5233-NST).

Blanchard, D., 1963: *Electrification of the atmosphere, Progress in Oceanography*, Vol. I, M. Sears (Ed.) Pergmon Press, N. Y., p. 151.

Bristor, C. L. (1968), Computer processing of satellite cloud pictures, NESC TM3, NESC, ESSA, Washington, D. C.

Buettner, K. J. K., (1968), On the uses of intermediate infrared and microwave infrared in meteorological satellite, Semi-annual report, Contact NASA NSG-632, 25 pp., Univ. of Washington, Seattle.

Buettner, K. J. and C. D. Kern (1965), The determination of infrared emissivities of terrestrial surfaces, J. Geophys. Res., *70*(6).

Cardone, V. J. (1969), Specification of the wind field distribution in the marine boundary layer for wave forecasting, Geophysical Sciences Lab., New York University, Report TR 69-1.

Clarke, G. L., 1961: The significance of spectral changes in light scattered by the sea, *Remote Sensing in Ecology*, Ed. P. J. Johnson, Univ. of Georgia Press, Athens.

Clarke, G. L. and H. R. James (1939), Laboratory analysis of the selective absorption of light by sea water, J. Opt. Soc. Amer., *29*, 43-55.

Clarke, G. L. and G. Ewing (1971), Remote sensing of ocean color from aircraft, Third annual Earth Resources Program Review, Vol. III, Section 59, NASA, MSC, Houston, Texas.

Clarke, G. L., Ewing, G. C., and Lorenzen, C. J. (1969), Remote measurement of ocean color as an index of biological productivity, Proc. of the Sixth International Symp. of Remote Sensing of the Environment, University of Michigan, Ann Arbor, Michigan, *2*, 991-1001.

Clarke, G. L., G. Ewing and C. Lorenzen (1970), Spectra of backscattered light from the sea obtained from aircraft as a measure of chlorophyll concentration, Science, *167*, 3921.

Committee on Colorimetry, 1966: *The Science of Color*, 6th Ed. Opt. Soc. Amer., Washington, D. C. 385 pp.

Cox, C. and W. Munk (1954a), Measurements of the roughness of the sea surface from photographs of the sun's glitter, J. Optical, Soc. Amer., *44*, 838-850.

Cox, C. and W. Munk (1954b), Statistics of the sea surface derived from sun glitter, J. Marine Res., *13*, 198-227.

Curtis, W. R. and P. K. Rao (1969), Gulf Stream thermal gradients from satellite, ship and aircraft observations, J. Geophy. Res., *74*, 28, 6984-6990.

Droppleman, J. D., Mennella, R. A., and Evans, D. E. (1970), An airborne measurement of the salinity variations of the Mississippi River outflow, J. Geophysical Res., *75*, 30, 5909-5913.

Ewing, G. (1969), The color of the ocean, Report of the Conference, 5-6 Aug. 1969, Woods Hole Oceanographic Institution, Cambridge, Mass.

Ewing, G. (1971), Remote spectrography of ocean color as an index of biological activity, Proceedings of the Symposium on Remote Sensing in Marine Biology and Fisheries Resources, Remote Sensing Center, Texas A&M University, College Station, Texas.

Forel, F. A. (1895), LeLeman: Monographic Limnologique, Vol. II, Lausanne, F. Ronge, 651 pp.

Forel, F. A., 1901: *Handbook der seenkunde: Allegemeine Limnologie*, Stuttgart, 249 pp.

Frederick, M. A. (1970), An atlas of secchi disc transparency measurements and forel-ule color codes for the oceans of the world, Naval Postgraduate School Thesis, 188 pp., AD-718 333.

Fritz, S. (1963), The diurnal variation of ground temperature as measured from TIROS II, J. Appl. Meteorol. *2*:5, 645-648.

Gunn, K. L. and T. W. R. East (1954), Microwave properties of precipitation particles, Quarterly J. Royal Meteorol. Society, *80*, 522-545.

Hansen, D. and G. Maul, (1970), A note on the use of sea surface temperature for observing ocean currents, Remote Sensing of Environment, *1*, 161-164.

Hidy, G. M., W. F. Hall, W. N. Hardy, W. W. Ho, A. C. Jones, A. W. Love, M. J. VanMelle, H. H. Wang and A. E. Wheeler (1971), Development of a satellite microwave radiometer to sense the surface temperature of the worlds oceans, S-BAND Radiometer, Final Report, Contract No. NAS 1-10106, Space Division, North American Rockwell.

Hollinger, J. P. (1970), Microwave measurements of sea surface, J. of Geophy. Res. *75*:27, 5201-5214.

Hollinger, J. (1971), Passive microwave studies, Third annual Earth Resources Program Reviewer, Vol. III, Sect. 69, NASA, MSC, Houston, Texas.

Holmes, R. W. (1971), The secchi disc in turbid coastal waters, Limn. and Ocean., to be published.

Holter, M. (1970), Chapter 3, Imaging with non-photographic sensors, in *Remote Sensing with Special Reference to Agriculture and Forestry*, National Academy of Sciences, Washington, D. C.

Hulbert, E. O. (1943), Propagation of radiation in a scattering and absorbing medium, J. Opt. Soc. Amer., *33*, 42-45.

Hulbert, E. O. (1945), Optics of distilled and natural water, J. Optical Soc. Amer., *35*:11, 698-705.

Huston, W. B. (study manager) (1971), Earth observatory satellite (EOS), Definition Phase Report, Vol. 1, Goddard Space Flight Center, Greenbelt, Md.

Jerlov, N. G. (1948), Opticai studies of ocean water, Reports of the Swedish Deep Sea Expedition, Vol. III, Physics and Chemistry, No. 1.

Jerlov, N., 1968: *Optical Oceanography*, Elsevier Publishing Company. Amsterdam, London, New York.

Joseph, J. and H. Wattenberg, 1944: Untersuchungen uber die optischen verhaltnesse inn Meere. Mitteilungen Chef Hydr. Dienstes, Oberkomm, d. Kriegsmarine (Berlin).

Kalle, K. (1938), Zum problem der meerliasserfarbe, Ann. d. Hydr. u. Maril, Meteorol., *66*, 1.

Kondratyev, K. Ya., 1969: *Radiation in the Atmosphere,* International Geophysical Series, Vol. 12, Academic Press, New York and London.

Kuhn, P. (1963), Soundings of observed and computed IR flux, Journal of Geophysical Research, *68*:5, 1415-1420.

Kuhn, P., 1972: Parameterizing continuum radiation to remove the calculated-observed radiative transfer discrepancy, in Sea Surface Topography From Space, Key Biscayne, Florida, Oct., 1971.

Kuhn, P. and L. Stearns (1971), Radiative transfer observations and calculations during BOMEX, NOAA Technical Report, ERL 203- APCL 19, April, 1971, 171 p.

Kuhn, P. and L. Stearns (1972), Radiosonde humidity retrieval by simultaneous radiation measurements, Journal of Applied Meteorology, *11*, 1.

LaViolette, P. E. and P. L. Chabot (1968), NIMBUS II satellite sea surface temperature versus historical data in a selected region: A comparative study, Deep Sea Research, *15*, 617-622.

LaViolette, P. E. and P. L. Chabor (1969), A method of eliminating cloud interference in satellite studies of sea-surface temperature, (unpublished).

LaViolette, P. E. and S. E. Seim (1969), Satellites capable of oceanographic data acquisition – a review, TR-215, U. S. Naval Oceanographic Office, Washington, D. C.

LeGrand, Y. (1939), The penetration of light into the sea. Annales l'Inst. Oceanogr. (Monaco), *19*, 393-436.

Leese, J. (1971), National Enviornmental Satellite Center, NOAA, Wash. D. C. (private communication).

Leese, J., W. Pichel, B. Goddard and R. Brower (1971), An experimental model for automated detection, measurement and quality control of sea-surface temperatures from ITOS IR data. Proc. of the Intl. Symposium on Remote Sensing of the Environment, Univ. of Michigan, Ann Arbor.

Lewis, E. A., J. P. Casey, and A. J. Vaccaro (1954), Polarized radiation from certain thermal emitters, Electronics Research Directorate, Air Force Cambridge Research Center, AFCRL Tech. Rep. No. 54-G.

Maul, G. and D. Hansen (1971), An observation of the Gulf Stream surface front structure by ship, aircraft and satellite, Remote Sensing of Environment, *2*.

McClain, P. (1970), Applications of environmental satellite data to Oceanography and Hydrology, ESSA Technical Memorandum NESCTM 19, U. S. Dept. of Commerce, ESSA, NESS, Washington D. C.

McMahon, H. O. (1950), Thermal radiation from partially transparent reflecting bodies, J. Opt. Soc. Amer. *40*, 376-380.

Meyer, J. W. (1966), Radio astronomy at millimeter and submillimeter wavelength, Proc. IEEE. *54*, 484-492.

Monahan, E. C. (1969), Freshwater whitecaps, J. Atmos. Sci. *26*, 1026-1029.

Morel, A. (1966), Étude expérimental de la lumière par l'eau les solutions de chlorure de sodium et l'eau de mer optiquement pures, J. Chim. Phys., *10*, 1359-1366.

Mount, Wayne, D. (1969), Use of the millimeter wave radiometry to remotely measure atmospheric stability, Proceedings of the Sixth International Symposium on Remote Sensing of Environment, *I*, Univ. of Michigan, Ann Arbor, 469-491.

Muromtsev, A. M. (1963), The principal hydrological features of the Pacific Ocean (Trans. of Osnovnye Cherty gidroogii Tikhogo Okeana, Gidrometeor – ologicheskoe Iz datel'stoo, Lenigrad 1958) Israel Program of Sci. Trans, Jerusalem.

NASA (1966), NIMBUS II User's Guide, Aracon Geophysics Company, Goddard Space Flight Center, Greenbelt, Maryland.

Neumann, G. and W. Pierson, Jr., 1966: *Principles of Physical Oceanography*, Prentice-Hall, Inc., Englewood Cliffs, N. J.

Nordberg, W., Conaway, J. W., Ross, D. B., and Wilheit, T. (1971), Measurement of microwave emission from a foam covered, wind driven sea, J. Atmos. Sci., *28*, 3, 429-435.

Paris, Jack F. (1969), Microwave radiometry and its application to marine meteorology and oceanography, Ref. No. 69-IT, Dept. of Oceanography, Texas A&M University, College Station, Texas, January.

Paris, J. F. (1971), Transfer of thermal microwaves in the atmosphere, Vols. I and II, Dept. of Meteorology, Texas A&M University, College Station, Texas, Contract Final Report, NASA Grant NGR 44-001-098, NASA, GSFC, 211 pp.

Pascalar, H. G. and R. T. Sakamoto (1965), Microwave radiometric measurements of ice and water, Proc. 3rd Symp. Remote Sensing of Environ., Ann Arbor, Mich., 803-812.

Plank, M. (1900), Ann. Phys. *4*:533.

Polaym, F. (1971), Measurements of water depth by multispectral ratio techniques, Third Annual Earth Resources Program Review, Vol. III, Section 61, NASA, MSC, Houston, Texas.

Porter, Ronald A. and Frank J. Wentz III. (1971), Microwave radiometric study of ocean surface characteristics, Contract 1-35140, Radiometric Technology, Inc., Wakefield, Mass. 01880.

Ramsey, R. C. (1968), Study of the remote measurement of ocean color, Final Report, Prepared by TRW for NASA Headquarters, Washington, D. C., Contract NASW-1658.

Rao, P. K. and J. S. Winston (1963), An investigation of some synoptic capabilities of atmospheric "window" measurements from satellite TIROS II, J. Applied Meteorol. *2*, 1, 12-23.

Roeder, R. S. (1967), Airborne measurements with an AN/AAR-33 radiometric search set, Sperry Microwave Electronics Company, A Division of Sperry Rand Corporation.

Ross, D. B., V. J. Cardone, J. W. Conaway, Jr., (1970), Laser and microwave observations of sea-surface conditions for fetch-limited 17-25-M/s winds, IEEE Transactions on Geoscience Electronics, *GE-8*, 4, 326-336.

Ross, D. S. (1969), Enhanced oceanographic imagery, Proceedings of the Sixth International Symposium on Remote Sensing of Environment, Vol. II, Univ. of Michigan, Ann Arbor, 1029-1044.

Ross, D. S., and Jensen, R. C. (1969), Experiments in oceanographic aerospace photography: Ben Franklin special filter tests: NASA, 2nd Annual Earth Resources Aircraft Program Status Review, Vol. III, Houston, Tex., 51-1 to 51-32.

Schott, G., 1942: *Geographic des Atlautischen Azeans*, C. Boysen, Hamburg, 3rd Edition (1942; reprinted in 1944).

Sherman, J. W. III, 1969: Passive microwave sensors for satellites, Proceedings of the Sixth International Symposium on Remote Sensing of Environment, *II*, Univ. of Michigan, Ann Arbor, 651-670.

Simon, I., 1966: *Infrared Radiation*, Van Nostrand Company, Inc., Princeton, New Jersey.

Sirounian, V. (1968), The effect of temperature, angle of observation, salinity and thin ice on microwave emission of water, J. Geophys. Res., *73*, 14, 4481-4486.

Smith, R. C. and J. E. Tyler (1967), Optical properties of clear natural water, J. Opt. Soc. Amer., *57*, 5, 589-595.

Smith, W. L., P. K. Rao, R. Koffler, and W. R. Curtis, (1970), The determination of sea-surface temperature from satellite high resolution infrared window radiation measurements, Monthly Weather Review, *98*, 8, 604-611.

Stogryn, A. (1967), The apparent temperature of the sea at microwave frequencies, IEEE Trans. Ant. Prop. *AP-15*, 2, 278-286.

Sullivan, S. A. (1963), Experimental study of the absorption in distilled water, artificial sea water, and heavy water in the visible region of the spectrum, J. Opt. Soc. Amer. *53*, 963-967.

Sverdrup, H. U., M. W. Johnson and R. H. Fleming, 1942, 1st edition; 1946 2nd edition: *The Ocean, Their Physics, chemistry and General Biology*. Prentice Hall, Englewood Cliffs.

Tyler, J. E. (1968), The secchi disc, Limn. and Ocean., *13*, 1, 1-6.

Vary, W. (1969), Remote Sensing by aerial color photography for water depth penetration and ocean bottom detail, in, Proceedings of the Sixth International Symposium on Remote Sensing of Environment, *II*, Univ. of Michigan, Ann Arbor, 1045-1060.

Warnecke, G., L. J. Allison and L. L. Foshee (1967), Observation of sea surface temperatures and ocean currents from NIMBUS II, NASA Report X-622-67-435, Greenbelt, Maryland.

Warnecke, G., L. Allison, L. McMillin, K. H. Szekulda (1971), Remote sensing of ocean currents and sea surface temperature changes derived from the NIMBUS II satellite, J. of Phys. Oceanogr., *I*, 1, 45-60.

Watson, L. A. (1971), National Environmental Satellite Center, NOAA, Washington, D. C. (private communication).

Wilheit, T., J. Blim, W. Campbell, A. Edgerton, N. Nordberg (1971), Aircraft measurements of microwave emission from arctic sea ice, X651-71-417 (preprint) NASA, Goddard Space Flight Center, Greenbelt, Md.

Williams, G. F., Jr. (1969), Microwave radiometry of the ocean and the possibility of marine wind velocity determination from satellite observations, J. Geophys. Res., *74*, 4591-4594.

Wittman, W. and J. Schule (1966), Comments on the mass budget of Arctic pack ice, Symposium on the Arctic Heat budget and atmosphere circulation, edited by J. O. Gletcher. The Rand Corporation (RM-5233-NSF).

Wolfe, W. L. (ed.) (1965), Handbook of Military infrared technology, Office of Naval Research, Washington, D. C.

Yentsch, C. S. (1960), The influence of phytoplankton segments on the color of sea water, Deep Sea Res., *7*, 1-9.

Yentsch, C. S. (1962), Measurement of visible light absorption of particulate matter in the ocean, Deep Sea Res., *6*, 207-217.

Yost, Edward and Sondva Wenderoth (1969), Agricultural and oceanographic applications of multispectral color photography, Proceedings of the Sixth International Symposium on Remote Sensing of Environment, *I*, Univ. of Mich., Ann Arbor, 145-173.

LIST OF SYMBOLS

Symbol	Name	Dimension, Units or Value
c_1	radiation constant	3.7415×10^{-5} erg cm^2 s^{-1}
c_2	radiation constant	1.4388 cm K
N_λ	spectral radiance	erg cm^{-1} s^{-1} sr^{-1} μm^{-1}
P	polarization	
S_s	salinity of active layer	$^\circ/_{oo}$
T	molecular temperature	C, K
T_B	brightness temperature	K
T_{BP}	polarized brightness temperature	K
T_e	effective temperature	K
T_{eP}	polarized effective temperature	K
T_o	molecular temperature of active layer	C, K
T_a	temperature of the atmosphere	C, K
T_s	sea surface molecular temperature	C, K
T_{so}	satellite observed temperature	K
v	wind velocity	ms^{-1}
$W_{a\lambda}$	spectral radiant emittance of the atmosphere	erg cm^{-2} s^{-1} μm^{-1}
$W_{B\lambda}$	spectral radiant emittance of a blackbody	erg cm^{-2} s^{-1} μm^{-1}
$W_{e\lambda}$	effective spectral radiant emittance	erg cm^{-2} s^{-1} μm^{-1}
W_λ	spectral radiant emittance of a greybody	erg cm^{-2} s^{-1} μm^{-1}
ϵ_λ	spectral emissivity	–
θ	zenith angle	deg.
λ	wavelength	μm
ν	frequency	GHz
ρ_λ	spectral reflectivity	–
τ_λ	spectral transmissivity through a layer which extends from a given level in the atmosphere to the top of the atmosphere	–
$\tau_{\lambda a}$	spectral transmissivity of the entire atmosphere	–
Ψ	nadir angle	deg.

Reprinted from Conference on Atmospheric Radiation, August 7-9, 1972, Fort Collins, Colo. (AMS, Boston, Mass.).

ATTENUANCE OF BROAD-BAND SOLAR IRRADIANCE IN THE OCEAN

Kirby J. Hanson
and
Monte F. Poindexter

National Oceanic and Atmospheric Administration
Atlantic Oceanographic and Meteorological Laboratories
Sea-Air Interaction Laboratory
Miami, Florida

1. INTRODUCTION

It has been pointed out by Jerlov (1948) that the distribution of particles and yellow substance controls the solar irradiance attenuance in the sea. These distributions are controlled by the large scale dynamical processes in the sea. Thus, it would be expected that the solar irradiance profiles in the near surface waters form a pattern which broadly correspondes to the general oceanic circulation. The maximum attenuance occurs in upwelling regions and minimum in nutriant-poor areas such as the eastern Mediterranean and tha Sargasso Sea.

In this paper we are presenting solar irradiance profiles obtained along the southweatern side of the Sargasso Sea during the IDOE Mixed Layer Experiment by this Laboratory in September-October 1971. The profiles obtained are in good agreement with Jerlov's clearest ocean cass, as would be expected for that region.

2. IDOE MIXED-LAYER EXPERIMENT

This experiment was conducted from the U. S. R/V DISCOVERER approximately 200 miles NNW of Puerto Rico from September 28 - October 13, 1971. The ship followed two slowly drifting buoys in the area near 21.0°N, 66.8°W as shown in Figure 1. The purpose of the experiment was to measure directly the diurnal heat budget of the mixed layer of the ocean and to compare the change in heat storage with the energy gains and losses to the ocean.

In this connection continuous solar and IR radiation measurements were obtained over the two week period. The schematic diagram in Figure 2 shows the deployment of the radiation sensors. In this paper we are presenting the combined data from the upfacing pyranometer on the bow boom and an underwater pyranometer which was used to obtain irradiance profiles.

2.1 Instrumentation

The bow-boom pyranometer was an Eppley PSP (Model 2) with wire wound thermopile and receiver coated with Parsons-black coating. The receiver is covered with two concentric WG-7 glass hemispheres. The underwater sensor, shown in Figure 3, is identical to the PSP-type pryanometer except the body is made of monel metal to prevent corrosion. The thermopile leads are brought out from tha bottom of the body through an Electro-Oceanics underwater connector.

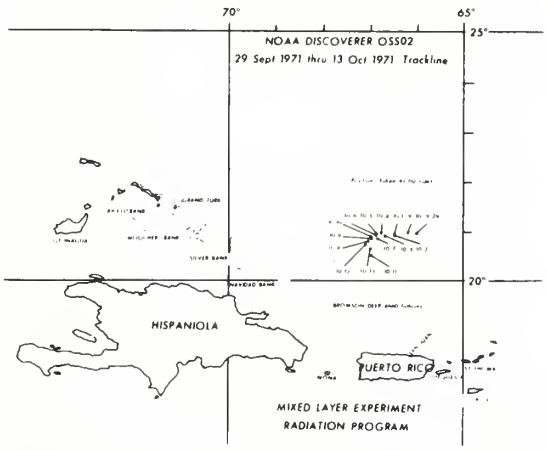

Fig. 1. Drift of the R/V DISCOVERER during the IDOE Mixed Layer Experiment.

A neutral density underwater platform was designed for mounting the underwater pyranometer. The platform shown in Figure 4 provides vertical stability for the pyranometer. A pressure transducer, shown just below the pyranometer in Figure 4, was included to provide continuous measurement of depth.

Fig. 2. Schematic diagram of the radiation instrumentation during the IDOE Mixed Layer Experiment.

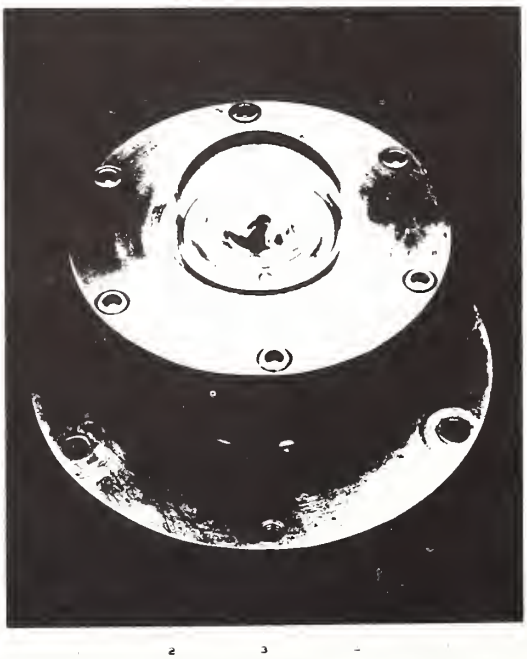

Fig. 3. An Eppley manufactured pyranometer model PSP modified by Eppley Laboratory for use underwater.

2.2 Measurement Procedure

Underwater solar irradiance profiles were obtained by positioning a small boat approximately 100 yards off the bow of the DISCOVERER and using scuba equipped divers to vary the depth of the underwater pyranometer (as shown in Fig. 2). Measurements were obtained at standard depths from 5 to 30 meters. Measurements were obtained for approximately two minutes at each level, both descending and ascending.

Fig. 4. Neutral density underwater platform with pyranometer and pressure transducer attached. Mr. Monte Poindexter is holding the platform.

2.3 Transmittance Definition

For the purpose of presenting these data a transmittance of the oceanic mixed layer will be defined from the irradiance terms.

H_s - Irradiance incident on the ocean surface

H_{ss} - Irradiance immediately below the ocean surface,

$$H_{ss} = H_s \times (1\text{-Albedo})$$

H_Z - Irradiance at depth Z in the ocean.

The transmittance, τ, is defined as the ratio H_Z/H_{SS}. Thus, τ represents the transmittance of broad-band solar irradience in the mixed layer without the effect of surface albedo.

2.4 Measurement Results

The transmittance, τ, defined in this way clearly will depend on the solar zenith angle, because the path length of the direct solar beam changes with zenith angle. This dependence is shown in the data of Table 1 for various depths. Thus, the transmittance profile will vary over certain limits during the day because of the changing zenith angle of the sun.

TABLE 1

Transmittance values as a function of solar zenith angle for various depths

Depth (m)	SOLAR ZENITH ANGLE (deg.) 35.1	39.9	55.0	70.7
	T			
5	.210	.197	.198	.164
10	.171	.164	.154	.128
15	.129	.125	.111	.097
30	.080	.070	.061	.052

We have used profiles on six days during the Mixed Layer Experiment and one profile each from the Gulf Stream and Tongue of the Ocean in order to calculate a mean transmittance profile, shown in Figure 5. The solid curves with error bars show the profile for downward and upward irradiance*. It can be seen that the upward irradiance is between one and two orders of magnitude less than the downward irradience for these particular depths. At much greater depths, these two components become very nearly equal.

Also in Figure 5 are the transmittance curves as given by Jerlov (1948). The I, II, and III curves indicate the oceanic water profiles, and the 1-5 curves indicate the coastal water profiles.

Our curve for downward irradiance has somewhat lower transmittance values than Jerlov's I curve. This may be due to the "emersion effect" of the instrument, which is discussed by H. Gordon in a companion paper in this publication. If we accept his contention that the sensor reads too low when emersed in water and use a correction factor of 1.5, our curve in Figure 5 is moved just to the right of (but in good agreement with) Jerlov's I curve for clearest ocean water. This would be expected for data obtained in the Sargossa Sea, Gulf Stream and Tongue of the Ocean.

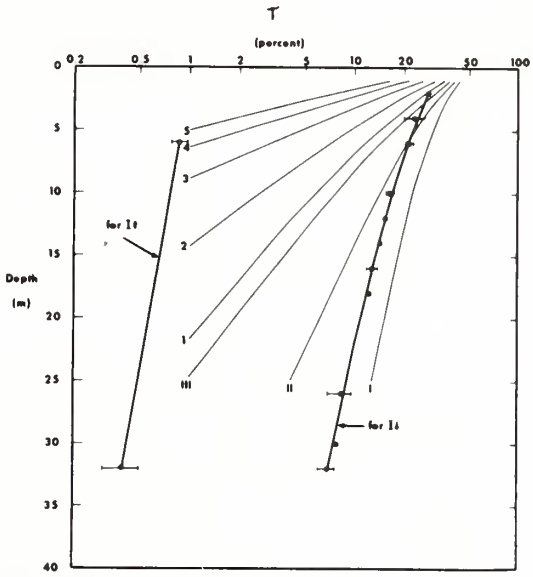

Fig. 5. Transmittance profiles for downward and upward irradiance from IDOE Mixed Layer Experiment data, and profiles I-III and 1-5 from Jerlov (1948).

An indication of the magnitude of the irradiance attenuance when integrated over the sun lite portion of the day is given in Figure 6. The downward irradiance at the ocean surface, 509 cal/cm^2 day, is the mean value for the six profile days during the Mixed Layer Experiment. Of this amount, 32 cal/cm^2 day are reflected upward at the interface, approximately four of which were scattered upward from the water column.

From these irradiance values, fractional absorption values have been determined and are shown in the right of Figure 6. It is seen that 71.5 percent of the solar energy which enters the water column is absorbed in the first two meters, with much diminished absorption below two meters. Approximately 7 percent is absorbed below 32 meters. The fractional absorption of upward directed irradiance is very small; only 0.5 percent is absorbed between 6 and 32 meters.

* The upward irradiance was obtained by inverting the pyranometer and platform

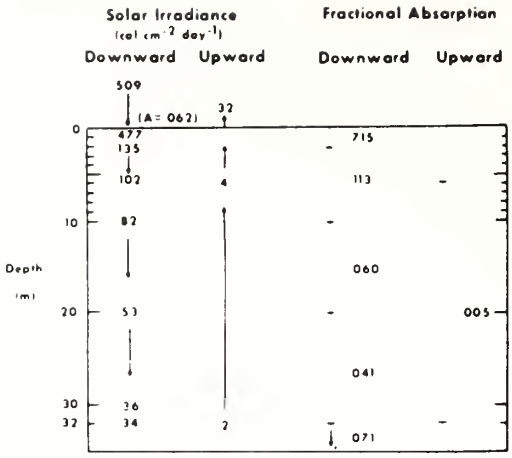

Fig. 6. Solar irradiance integrated daily values and fraction absorption based on IDOE Mixed Layer Experiment data.

Finally, this large absorption in the near surface (two meter) layer causes a similer profile for radiative heating of the water column. In Figure 7 is shown the radiative heating of the water column to 32 meters, with integrated heating over two meter increments of depth. Radiative heating of the upper two meters is 1.7°C/12 hours. At all depths below two meters the heating is less than 0.1 °C/12 hours. The actual temperature change profile in the open ocean is normally very different than the profile of this radiative forcing function. The reason being that wave action mixes the water and distributes the near surface radiative heating by sunlight. An indication of how the radiative and actual temperature change profiles compare can be seen in Figure 7 which is based on the IDOE Mixed Layer Experiment.

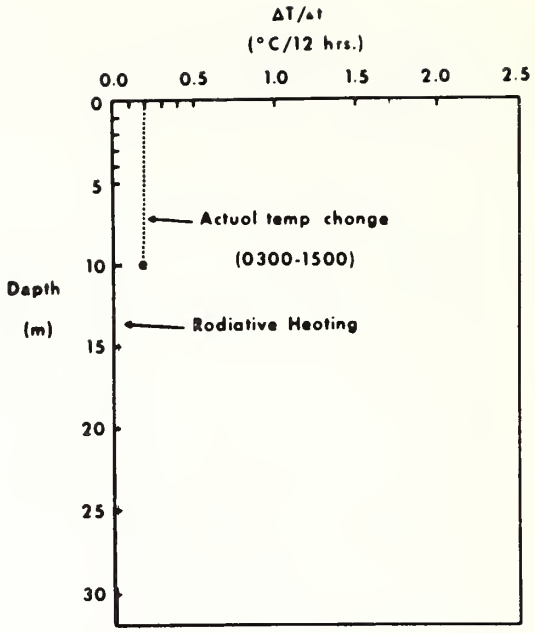

Fig. 7. Radiative and actual heating profiles based on IDOE Mixed Layer Experiment Data.

3. REFERENCES

Jerlov, N. G. (1968), Optical Oceanography, Elsevier Publishing Company, New York.

Tyler, J. and R. Smith (1970), Measurements of Spectral Irradiance Underwater, Gordon and Breach Publishers, New York.

U.S. DEPARTMENT OF COMMERCE
National Oceanic and Atmospheric Administration
Environmental Research Laboratories

NOAA Technical Memorandum ERL AOML-16

THE SOLAR IRRADIANCE ENVIRONMENT OF FLORIDA COASTAL WATER DURING FLARE

Kirby J. Hanson
Monte F. Poindexter

Sea-Air Interaction Laboratory

Atlantic Oceanographic and Meteorological Laboratories
Miami, Florida
October 1972

TABLE OF CONTENTS

	Page
ABSTRACT	1
1. INTRODUCTION	1
2. SOLAR IRRADIANCE MEASUREMENTS DURING FLARE	2
2.1 Ocean Surface and Shelf Surface Measurements	2
2.2 Profile Measurements	10
2.3 Discussion	11
3. RADIATIVE PROPERTIES OF THE COASTAL OCEAN WATER	14
3.1 Surface Reflectance	14
3.2 Transmittance	17
4. INSTRUMENTATION	18
5. IMMERSION EFFECT OF THE UNDERWATER PYRANOMETERS	21
6. REFERENCES	22
APPENDIX - Daily Solar Irradiance Curves	23

THE SOLAR IRRADIANCE ENVIRONMENT OF FLORIDA COASTAL WATER DURING FLARE

Kirby J. Hanson and Monte F. Poindexter

Solar irradiance measurements both above and within the mixed layer were obtained at three ocean sites along the southeastern Florida coast from Miami Beach (Government Cut) to Key Largo during the Florida Aquanaut Research Expedition of February - March, 1972. The results show that even though the transmittance of the water varied considerably from day-to-day due to changes in turbidity, the average transmittance at the sites was nearly the same.

The turbidity of the Florida coastal water causes a slight increase in the heating rate due to absorbed solar radiation (0.36^{o}C/12 hr) compared to the clear water of the Sargossa Sea (0.31^{o}C/12 hr) over a column from the surface to 13 m depth.

The reflectance and transmittance of the water column are also examined. The reflectance varied from 3.5 percent at midday to 15-20 percent in early morning and late afternoon. The transmittance of the water from the surface to 13 m depth is dependent on the zenith angle of the sun. With solar zenith angles of 30^{o}, the transmittance was 7-8 percent; this decreased to 5 percent with solar zenith angles of $60\text{-}70^{o}$. A surprising feature of the measurements was that, as the solar zenith angles approached 90^{o}, the transmittance increased to about 8 percent. Higher transmittance values (up to 17 percent) were also associated with cloudy sky conditions.

Results of studies of the immersion effect of the underwater pyranometer are discussed but have not been applied to the basic irradiance data.

1. INTRODUCTION

During the winter and early spring of 1972 solar irradiance measurements were obtained along the southeast Florida coast as a portion of the NOAA[1] program FLARE[2]. These measurements were made both above the ocean surface and in the water column; they represent spectrally integrated solar irradiance. This report presents the results of these measurements and discusses the physical properties of the coastal shelf water and the influence of turbidity of the water on solar irradiance reaching the shelf and coral reefs.

---

[1]National Oceanic and Atmospheric Administration

[2]Florida Aquanaut Research Expedition

The program was carried out from the R/V LULU that was moored at four locations from February 22 to April 16, 1972; these locations are shown in figure 1. The periods in which useful radiation data have been obtained at these locations and the approximate positions are:

Site	Location	Dates (1972)
1. Government Cut (Miami Beach)	25.8°N, 80.1°W	2/22 - 2/23
2. Pacific Reef-A	25.4°N, 80.2°W	2/26 - 3/1
3. Elbow Reef	25.2°N, 80.3°W	4/3 - 4/9
4. Pacific Reef-B	25.4°N, 80.2°W	4/12 - 4/16

2. SOLAR IRRADIANCE MEASUREMENTS DURING FLARE

There were two types of solar irradiance measurements obtained during FLARE. The first type is that of continuous measurement of incident and reflected solar irradiance at the ocean surface from a boom attached to the R/V LULU, and of the subsurface solar irradiance incident on the shelf and coral reefs. The latter measurement was obtained approximately 150 ft south of the R/V LULU to eliminate the shadowing influence of the ship. The second type is that of profile measurements from about 1 m above the shelf to 3 m below the ocean surface, in steps of 3 m in order to obtain the profile. Approximately 45 min were required to obtain a complete profile. On most days one or two profiles were obtained.

A schematic view of the deployment of radiation sensors is shown in figure 2. The habitat (EDELHAB) was not used in the radiation program and is shown for reference only.

2.1 Ocean Surface and Shelf Surface Measurements

Continuous measurement of the incident and reflected irradiance components were obtained just above the sea-air interface, and continuous measurement was obtained of the incident irradiance component at the shelf surface. The dates on which these measurements are available at the various sites is shown in table 1.

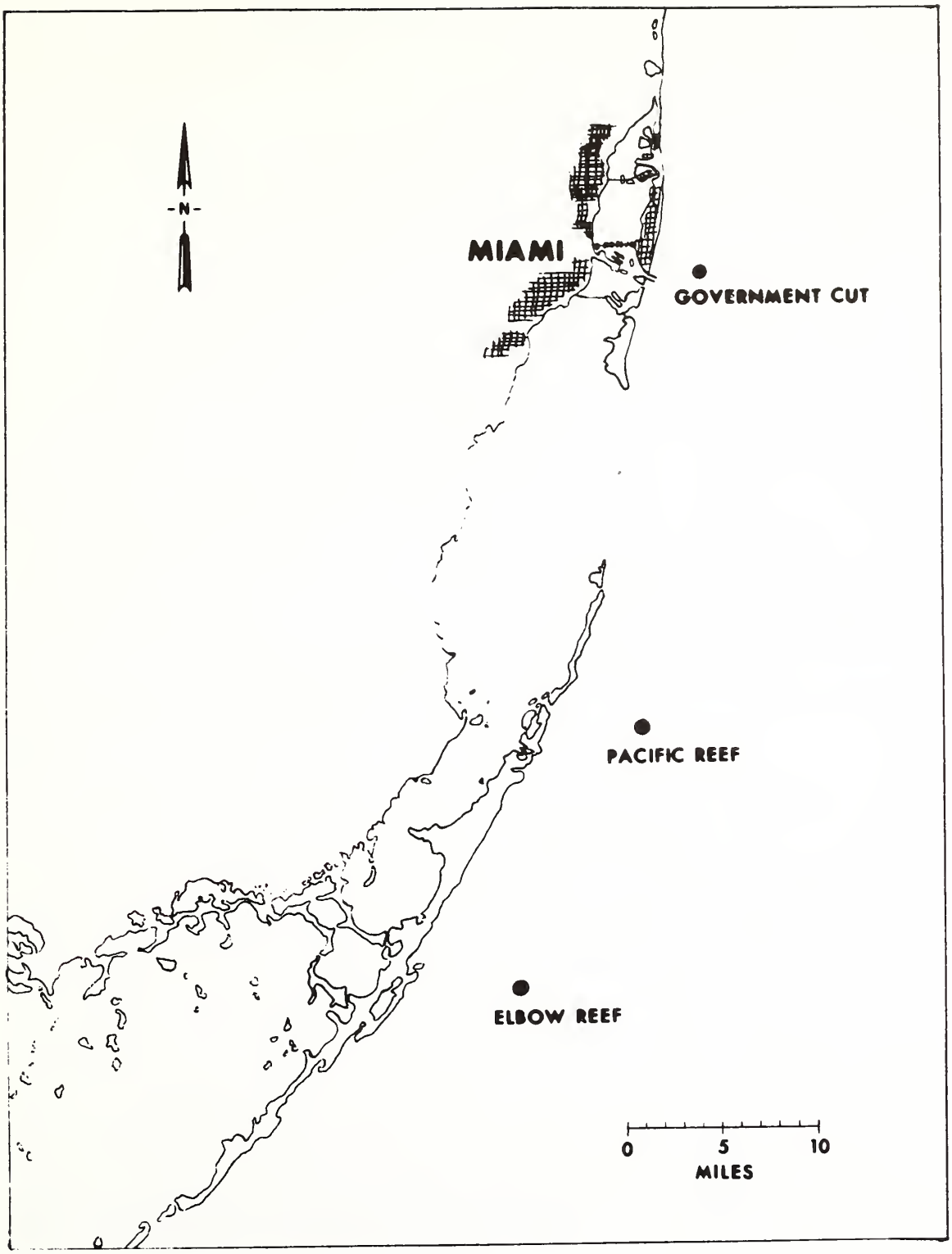

Figure 1. Site in southeast Florida for the Florida Aquanaut Research Expedition (FLARE), February-April, 1972.

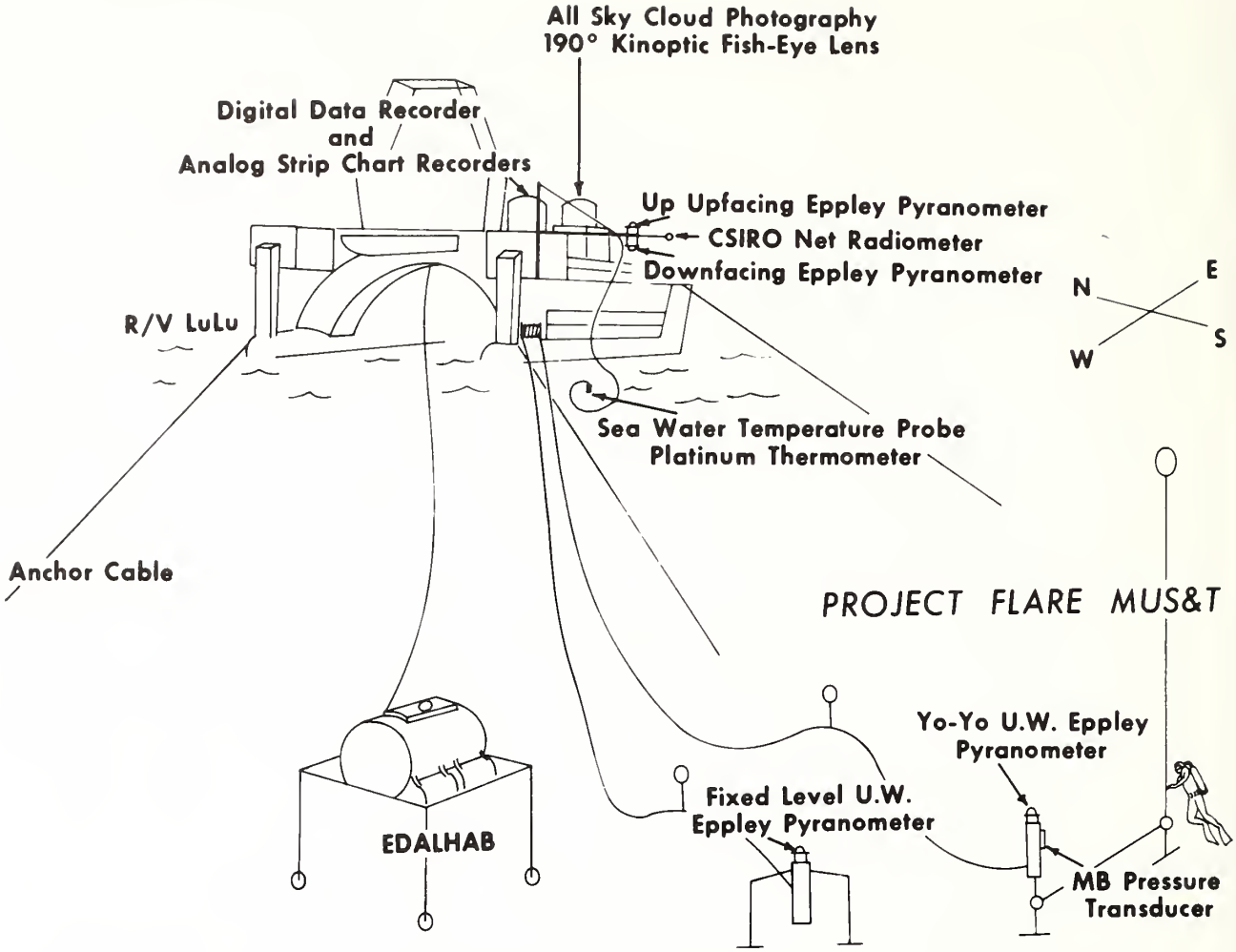

Figure 2. Schematic diagram of the radiation program instrumentation during FLARE, February-April, 1972.

Hourly totals of these three radiation components are given in tables 2, 3, and 4; daily sums and hourly means for the entire period are also given. These hourly means are plotted in figure 3, showing that only a small portion of solar irradiance that reaches the ocean surface is reflected from the ocean surface or reaches the shelf surface. The averages in tables 2, 3, and 4 show that of the 530 cal/cm^2 day, which was incident at the ocean surface. Only 25 cal/cm^2 day, or 4.8 percent, was reflected from the ocean surface, and only 35 cal/cm^2 day, or about 6.6 percent, reached the shelf surface and coral reefs at an average depth of 13 m; thus, the bulk of the solar energy entering the ocean is used to warm the ocean water.

Table 1. Solar Irradiance Data Obtained During the FLARE Program

Location	Date (1972)	Incident Irradiance	Reflected Irradiance	Fixed Depth Irradiance	Underwater Irradiance Profile
Government Cut (Miami Beach)	2/22	X	X	X	X
	2/23	X	X	X	X
Pacific Reef-A	2/26	-	-	X	X
	2/27	X	X	-	X
	2/28	X	X	X	X
	2/29	X	X	X	X
	3/1	X	X	X	X
Elbow Reef	4/3	X	X	X	X
	4/4	X	X	X	X
	4/5	X	X	X	X
	4/6	X	X	X	X
	4/7	X	X	X	X
	4/8	X	X	X	X
	4/9	X	X	X	X
Pacific Reef-B	4/12	X	X	-	-
	4/13	X	X	X	X
	4/14	X	X	X	X
	4/15	X	X	X	X
	4/16	X	X	X	X

Table 2. Solar Irradiance Incident at Ocean Surface During FLARE (cal/cm^2 hour)

	FEB					MAR					APRIL								Hourly
	22	23	27	28	29	1	3	4	5	6	7	8	9	12	13	14	15	16	Avg.
Hour ending (EST)																			
7	0.5	0.7	-	1.2	1.4	2.2		0.6	0	0.8	0	4.4	4.7	-	1.7	1.6	0.6	1.5	1.9
8	4.0	11.5	-	13.7	12.4	16.5		10.1	3.7	15.5	8.4	20.8	21.0	-	18.1	17.3	14.5	16.5	14.3
9	9.5	27.3	-	32.9	28.3	36.8		24.9	31.9	36.2	28.4	40.4	41.1	-	37.8	26.5	34.4	38.0	32.2
10	26.7	59.8	-	49.0	51.1	52.4		39.1	53.4	54.3	47.5	58.5	59.3	-	56.1	58.3	52.8	54.6	51.9
11	45.2	67.5	63.2	62.2	66.4	67.7		65.8	52.0	69.2	67.8	72.6	73.3	-	70.2	71.6	69.4	68.5	66.1
12	33.0	67.9	72.3	69.3	73.4	75.0	80.6	79.9	74.4	77.8	79.3	80.7	81.4	-	79.2	79.8	78.5	79.1	74.2
13	33.6	78.3	74.3	72.3	78.0	78.4	84.3	75.9	78.6	79.9	83.6	83.1	84.0	-	81.9	81.4	81.4	81.8	77.1
14	62.6	72.9	69.5	66.7	72.1	73.6	82.2	75.0	74.7	76.0	78.6	79.3	49.0	-	78.2	76.8	78.2	78.0	73.1
15	54.7	61.4	58.6	56.1	56.4	64.9	72.2	63.9	65.3	65.2	65.7	69.6	3.7	65.1	67.9	65.8	68.4	65.3	60.6
16	25.1	41.9	42.4	40.7	42.3	-	54.2	47.3	47.5	49.0	48.0	54.8	16.6	51.2	52.6	49.3	54.0	-	44.8
17	13.8	18.7	23.5	22.2	23.0	-	29.4	26.9	15.7	28.5	27.1	33.9	12.2	32.1	32.6	29.5	35.4	-	25.3
18	4.4	2.4	5.6	4.6	4.7	-	10.5	5.6	8.6	8.2	7.4	13.5	6.6	10.7	11.3	8.2	14.2	-	7.9
19	-	-	-	-	-	-	-	-	-	-	-	0.9	0.8	0	0.3	-	0.5	-	0.5
Daily Summary	313	510	-	491	509	-	616	515	506	561	542	613	454	-	588	566	583	-	530

The ocean heating rate can be calculated from these irradiance data, as shown in figure 4, on the basis of conservation of energy. For this calculation it is necessary to assume an average reflectance of the shelf surface of 20 percent. The result gives an average heating of the water column of $0.36^{o}C/12$ hr.[1] Thus, the heating rate of these Florida coastal waters is approximately 15 percent greater than that of the Sargasso Sea, which is one of the least turbid regions of the world's oceans.

A basic question which the experiment sought to answer was whether there were significant differences in the transmittance of the water at these sites and whether such differences were related to human activities. The irradiance data in tables 2, 3, and 4 have been used for this purpose. The transmittance (T) of the water was calculated from

$$T = H_z/(H-H_r) \qquad (1)$$

where H_z is the irradiance at depth Z and H and H_r are the incident and reflected solar irradiance at the ocean surface, respectively.

Transmittance values based on tables 2, 3, and 4 have been calculated for each day at the three sites and are given in table 5. The mean transmittance values are given for each site, and standard deviations are given for Pacific and Elbow Reefs where the sample is relatively large. At Pacific Reef the standard deviations is 18 percent of the mean transmittance, whereas at Elbow Reef it is 31 percent. Because only 2 days of data are available for Government Cut, it is not possible to obtain an idea of the daily variability in transmittance of the water at that location.

Because the depth of the shelf surface varied from one site to another, it is necessary to normalize the transmittance data to a single depth in order to make comparisons between sites. We have chosen 13 m as a depth for normalization and used the log transmittance profile of the following section to extrapolate the measurements to this standard depth. Table 6 lists the depths at each site, the mean transmittance normalized

[3]Hanson and Poindexter (1972) measured the heating rate due to absorption of solar radiation over various depths about 200 miles NW of Puerto Rico in October 1971.

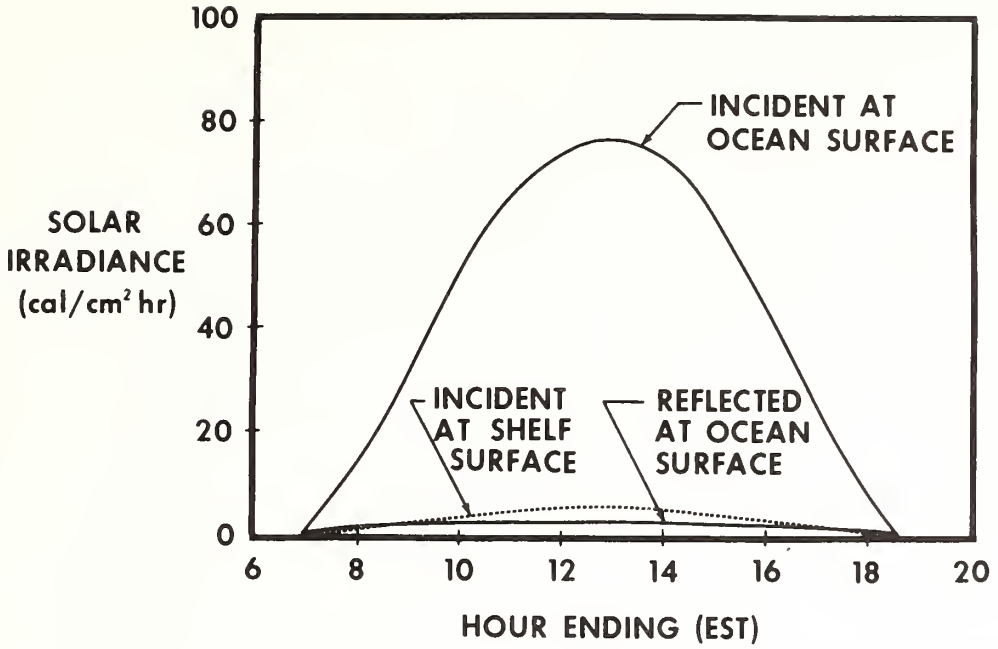

Figure 3. Integrated hourly solar irradiance data for the entire FLARE period.

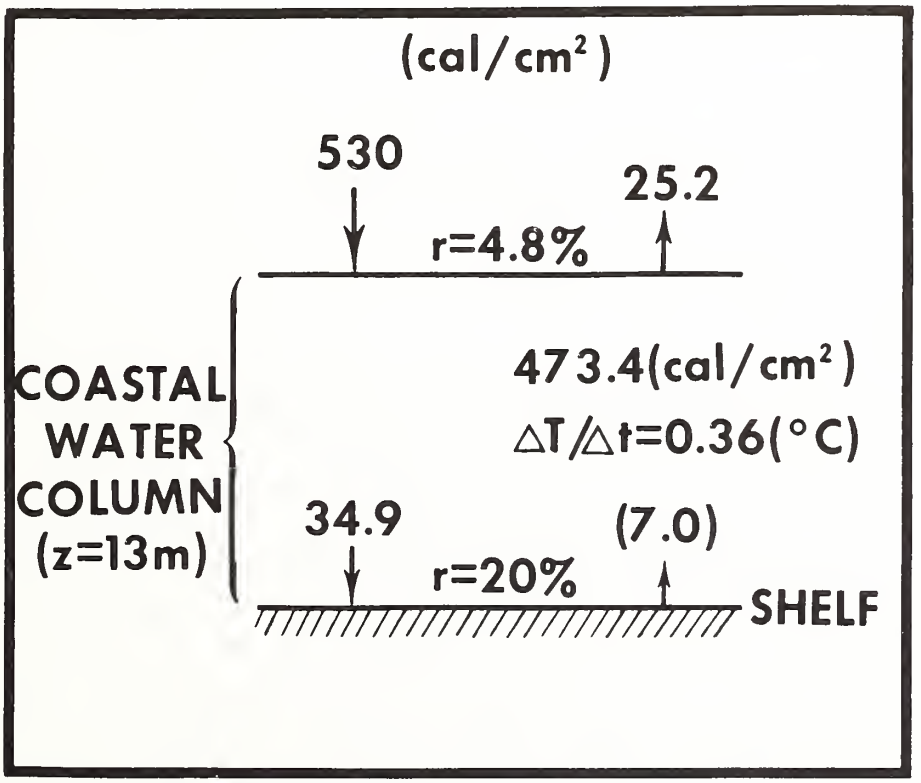

Figure 4. Integrated daily solar irradiance, mean for the entire FLARE period. Heating rate of the water column to 13 meters is also given.

Table 3. Solar Irradiance Reflected From the Ocean Surface During FLARE (cal/cm² hour)

	FEB					MAR					APRIL							Hourly
	22	23	27	28	29	1	3	4	5	6	7	8	9	12	13	14	15	16	Avg.
Hour ending (EST)																			
7	0.1	0	-	0.4	0.3	0.4		0.5	-	1.1	0.2	1.3	1.5	-	0	0	0	0	0.4
8	0.2	1.9	-	3.5	2.3	2.5		2.9	(0.7)	3.1	2.5	2.8	3.0	-	0.9	1.2	0.8	0.9	1.9
9	0.5	2.0	-	3.1	2.6	2.8		2.3	2.0	2.5	2.8	2.7	2.6	-	1.9	1.4	2.0	2.0	2.2
10	1.3	1.8	-	2.2	3.1	3.3		2.4	1.8	2.0	1.9	2.6	2.5	-	2.0	2.3	2.1	2.1	2.2
11	1.3	2.7	2.5	2.2	3.0	3.4		2.7	1.6	2.1	2.1	2.9	2.4	-	2.3	2.6	2.4	2.3	2.4
12	1.4	2.5	2.7	2.3	3.0	3.5	2.5	2.7	2.4	2.2	2.3	3.0	2.8	-	2.6	3.1	2.8	2.6	2.6
13	1.4	2.9	2.8	2.3	3.3	3.8	2.7	2.6	2.4	2.3	2.8	3.1	3.2	-	3.0	3.1	3.0	2.7	2.8
14	2.7	3.0	3.0	2.8	3.1	3.5	2.7	2.6	2.3	1.8	3.0	3.3	2.0	-	3.1	2.8	2.9	2.7	2.8
15	2.3	2.8	3.0	2.8	3.3	3.5	2.8	2.3	2.1	1.2	2.8	3.1	0.3	1.8	2.7	2.5	2.5	2.5	2.5
16	1.3	2.7	2.7	2.7	3.1	-	2.4	2.3	1.8	1.3	2.6	2.8	1.0	1.7	2.1	2.2	2.3	-	2.2
17	1.4	2.2	2.5	2.7	3.0	-	2.3	2.2	1.0	1.6	2.5	2.7	0.9	1.6	2.0	2.1	2.1	-	2.1
18	0.7	0.3	0.9	0.8	0.9	-	1.6	1.0	0.9	0.9	1.2	1.9	0.6	0.7	1.7	1.2	1.7	-	1.1
19	-	-	-	-	-	-	-	-	-	-	-	0.4	0.3	0	0.5	-	0.4	-	0.3
Daily Summary	15.2	24.9	-	27.7	31.1	-	24.1	26.4	19.0	22.1	26.7	32.7	23.1	-	24.9	24.4	25.2	-	25.2

Table 4. Solar Irradiance Incident at Shelf Surface During FLARE (cal/cm² hour)

	FEB					MAR					APRIL							Hourly
	22	23	27	28	29	1	3	4	5	6	7	8	9	12	13	14	15	16	Avg.
Hour ending (EST)																			
7	0	0	-	0	0.1	0	-	0.1	0.1	-	0.1	0	0	-	-	0.5	0	0.2	0.1
8	0.1	0.4	-	0.4	0.6	1.0	-	0.9	0.7	(2.9)	0.8	0.1	0.1	-	-	1.5	0.4	1.0	0.8
9	0.2	1.1	-	1.5	1.5	1.9	-	2.0	2.6	(3.0)	2.1	1.1	0.8	-	-	2.4	1.5	2.2	1.8
10	1.8	1.3	-	2.7	3.3	3.4	-	2.9	4.5	4.0	3.4	2.3	2.1	-	-	5.0	3.5	4.0	3.2
11	2.9	3.4	-	4.0	4.4	4.1	-	4.4	4.6	5.3	4.9	3.7	3.0	-	-	6.5	4.7	5.4	4.5
12	2.2	4.8	-	4.9	5.9	5.5	5.1	6.1	6.3	6.5	6.5	4.0	-	-	-	6.3	6.2	7.1	5.5
13	2.0	5.5	4.5	5.4	5.7	5.2	5.6	5.7	6.1	6.6	6.0	3.7	-	-	-	6.5	5.4	7.0	5.4
14	3.9	4.6	3.2	4.6	5.0	4.0	5.0	6.3	5.6	5.8	-	3.4	-	-	6.2	5.7	3.3	6.4	4.9
15	3.2	3.3	2.0	3.4	3.8	-	4.8	4.9	4.7	5.2	-	3.0	-	-	5.4	4.1	3.3	4.9	4.0
16	1.7	2.2	0.6	2.2	2.8	-	3.6	3.8	3.3	4.0	-	2.3	-	-	4.1	2.6	2.5	-	2.7
17	.9	1.0	0	1.0	1.3	-	2.0	2.4	1.5	2.2	-	1.3	-	-	2.4	1.1	1.7	-	1.4
18	.3	0	0	0.3	0.3	-	0.9	1.2	0.9	0.9	-	0.4	-	-	1.1	0.1	0.9	-	0.6
19	-	-	-	-	-	-	-	-	-	-	-	-			-	-	-	-	-
Daily Summary	19.3	27.6	-	30.3	34.7	-	-	40.5	40.9	46.4	-	25.3	-	-	-	42.4	33.6	-	34.9

Table 5. Daily Transmittance by Sites

Date (1972)	Government Cut	Pacific Reef	Elbow Reef
Feb. 22	.065		
23	.057		
27		(.045)	
28		.065	
29		.072	
Mar. 1		(.065)	
Apr. 3			(.068)
4			.083
5			.084
6			.086
7			.072
8			.044
9			(.032)
13		(.081)	
14		.078	
15		.060	
16		(.082)	
Mean	.061	.068	.067
Std.dev.	-	.012	.021

Table 6. Mean Transmittance by Sites (based on fixed depth pyranometer)

Site	Depth (m)	Mean Transmittance At Indicated Depth	Mean Transmittance Normalized to Depth of 13 Meters	Standard Deviation
Government Cut	14.3	.061	.070	
Pacific Reef	10.7	.068	.055	.012
Elbow Reef	15.2	.067	.081	.021

to the standard depth, and the standard deviation of the daily transmittance values.

It is surprising to see that the mean transmittance at Government Cut (0.070) is higher than that at Pacific Reef (0.055), because pollution at Government Cut and the more turbid outflow water of Biscayne Bay were thought to increase the turbidity at Government Cut. Table 6 shows the mean transmittance values for the sites are in the range 0.06 to 0.08, and the variation from day to day is 0.01 to 0.02; thus, considering the large standard deviation of the transmittance at the sites, it appears that the difference in mean transmittance between the sites is not statistically significant. From another point of view, if man-made changes in turbidity of the water are present at Government Cut, then they are so small compared to the natural occurring variation in turbidity that they are undetectable with the present data sample. Perhaps a much longer record at these sites may show a statistically significant difference between sites.

2.2 Profile Measurements

Measurement of the downwelling solar irradiance at various depths within the water column were obtained with a single pyranometer, which was raised and lowered in a series of steps to obtain a profile. These measurements are not continuous during the day, as are those of the fixed-depth pyranometer, but were obtained one or more times a day on the days indicated in table 1. It required about 45 min to obtain a profile. Most profiles were made between 10 am and 3 pm local time.

The transmittance of the water has been calculated from these data, according to equation 1, and from the incident and reflected solar irradiance at the surface. The individual transmittance profiles are listed in tables 7, 8, and 9 for Government Cut, Pacific Reef, and Elbow Reef, respectively. Means and standard deviations for each site are given in the tables. The mean profiles are also shown in figure 5 with the standard deviations for Pacific Reef.

These mean transmittance profiles show that differences between sites are small compared to the day-to-day variation in transmittance, as indicated by the standard deviation at Pacific Reef, which is shown as error bars in figure 5.

Table 7. Solar Radiation Profile Measurements - Government Cut

Time(GMT)	FEB. 22 1742	22 1954	23 1559	23 1634	23 1830	Avg.	Standard Deviation
Depth (m)	Transmittance						
3.0	.207	.249	.164	-	.180	.210	.032
6.1	.186	.138	.125	.128	.137	.140	.016
9.1	.139	.142	.098	.099	.105	.117	.019
12.2	.122	-	.073	.097	.067	.090	.020
13.1	.110	.062	-	-	-	.086	.021

Table 8. Solar Radiation Profile Measurements - Pacific Reef

	FEB.								MAR	APRIL										
	27	27	28	28	28	28	29	29	1	13	14	14	14	15	15	15	16	16	16	
TIME (GMT)	1758	2010	1523	1551	1801	1836	1523	1851	1526	1816	1537	1714	1928	1558	1718	1918	1541	1710	1901	Avg
Depth (m)	TRANSMITTANCE																			
3.0	.253	.263 .310	.273 .199	.199 .189	.201 .189	.168 .153	.238	.262 .237	.253	.234 .241	.224	.237 .227	.241 .242	.195 .193	.182 .178	.182 .184	.210 .198	.182 .208	.196	.216
6.1	.178	.185	.080	.094	.095	.089	.185	.169	.184	.151	.154	.164	.157	.140	.132	.103	.133	.143	.134	.141
9.1	.138	.136	.032	.046	.057	.045	.119	.118	.134	.112	.113	.123	.105	.102	.095	.067	.102	.106	.100	.098
10.7	-	-	-	-	-	-	-	-	-	.088	.098	.104	.086	.088	.075	.051	.089	.091	.082	.085
12.2	.116	.127	-	-	-	-	-	.098	.099	-	-	-	-	-	-	-	-	-	-	-

	Standard Deviation
	.035
	.034
	.033
	.014
	-

Table 9. Solar Radiation Profile Measurements - Elbow Reef

	APRIL											
	3	4	4	5	6	7	8	8	9	9		
Time (GMT)	1930	1652	1710	1523	1858	1700	1629	1654	1616	1740	Avg	Stand. Deviation
Depth (m)	Transmittance											
3.0	.203	.214	.229	.159	.264	.259	.170	.161	.197	.106	.196	.049
6.1	-	.167	.179	-	.189	-	.128	.117	.128	.095	.143	.035
9.1	-	.144	.134	-	.140	-	.105	.107	.098	.077	.115	.025
12.2	-	.119	.124	-	.108	-	.080	.076	.084	.073	.095	.022
15.2	-	.108	.108	-	.091	-	.070	.071	.074	.059	.083	.020

2.3 Discussion

During the FLARE program, two solar radiation pyranometers were used to measure the irradiance underwater. One sensor obtained continuous measurements at the shelf surface and the other obtained irradiance profiles in the water. Transmittance values determined from both measurements show that the mean transmittance value at the Pacific Reef site is lower than at the other two sites. This can be seen by comparing table 6, based on continuous measurement, and table 10, based on profile measurements. Differences between sites are small, however, in comparison to the day to day variations in transmittance.

Large variations in transmittance at the sites are thought to result from changes in turbidity caused by coastal currents, wind driven currents, and tidal currents. For example, very low transmittance values were observed on February 28, 1972, at Pacific Reef (table 8), and on April 8-9, 1972, at Elbow Reef (table 5). Strong currents were observed on those days.

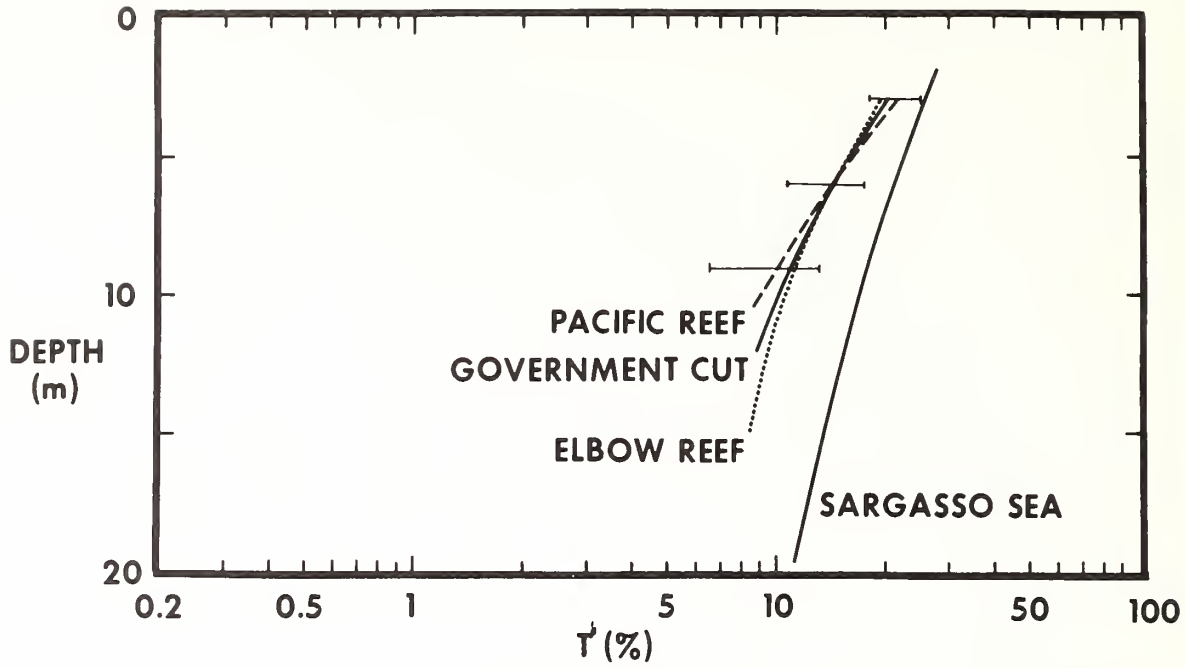

Figure 5. Mean transmittance profiles by sites in comparison to that for the Sargasso Sea. The brackets indicate the standard deviation of the daily transmittance values at three levels at Pacific Reef.

The data suggest that at Government Cut the effect of pollution on the amount of sunlight reaching the reefs is so minimal that it is undetectable in the present data set. The transmittance data also suggest that the natural variation in turbidity of the water caused by currents is considerably larger than variations caused by human activities.

For biological and other studies it may be useful to estimate the variation that may be expected in the daily integrated solar irradiance reaching the shelf surface and coral reefs. The information for this estimate is presented in table 11. This shows from a previous study for Miami that cloudiness in the atmosphere has a large influence (27 percent) in modulating the amount of solar energy which reaches the ocean surface from day to day. In addition, the present study has shown (table 5) that ocean roughness and turbidity have a significant effect (18-31 percent) in modulating the amount of solar energy transmitted by the water and reaching the coral reefs. These natural variations of the atmosphere and ocean taken together suggest that the day to day variability in solar irradiance reaching the coral reefs may be 45-58 percent. In addition there are other causes of variability, such as

those associated with astronomical (diurnal and seasonal) changes. Thus, the natural variation in radiation reaching the reefs is relatively large and any possible man induced variation must be significantly large to be detectable. In the present case it is too small to be detected.

Future studies should be directed toward establishing the cause and effect relationship between currents and the radiation environment of the reefs, as well as attempting to obtain a sufficiently long data sample that the effect of pollution might be detected.

Table 10. Mean Transmittance by Sites (based on profile pyranometer)

Site	Depth (m)	Mean Transmittance	Standard Deviation
Government Cut	9.1	.117	.019
Pacific Reef	9.1	.098	.033
Elbow Reef	9.1	.115	.025

Table 11. Variability in Daily Solar Irradiance Due to Various Sources

Variability at Ocean Surface due to Cloudiness	27%	(from Hanson (1971))
Variability at Shelf Surface due to Ocean Roughness and Turbidity	18-31%	(from Table 5)
Estimated Variability in Solar Irradiance at Shelf Surface due to Cloudiness, Ocean Roughness and Turbidity	45-58%	

3. RADIATIVE PROPERTIES OF THE COASTAL OCEAN WATER

Of the basic properties of sea water, the two which can be evaluated from the present study are reflectance and transmittance of irradiance. They are given in the following sections.

3.1 Surface Reflectance

The continuous measurements of incident and reflected solar irradiance at the sea surface, given in tables 2 and 3, have been used to determine surface albedo. In this calculation, the albedo has been evaluated as the ratio of the reflected to the incident irradiance. The albedo values were further stratified into "clear" or "cloudy" sky categories. The criteria for determining cloudy sky was that incident irradiance be less than 60 percent of maximum incident irradiance during the entire period of observation (fig. 6). If this case did not apply, the albedo data were included in the clear sky category.

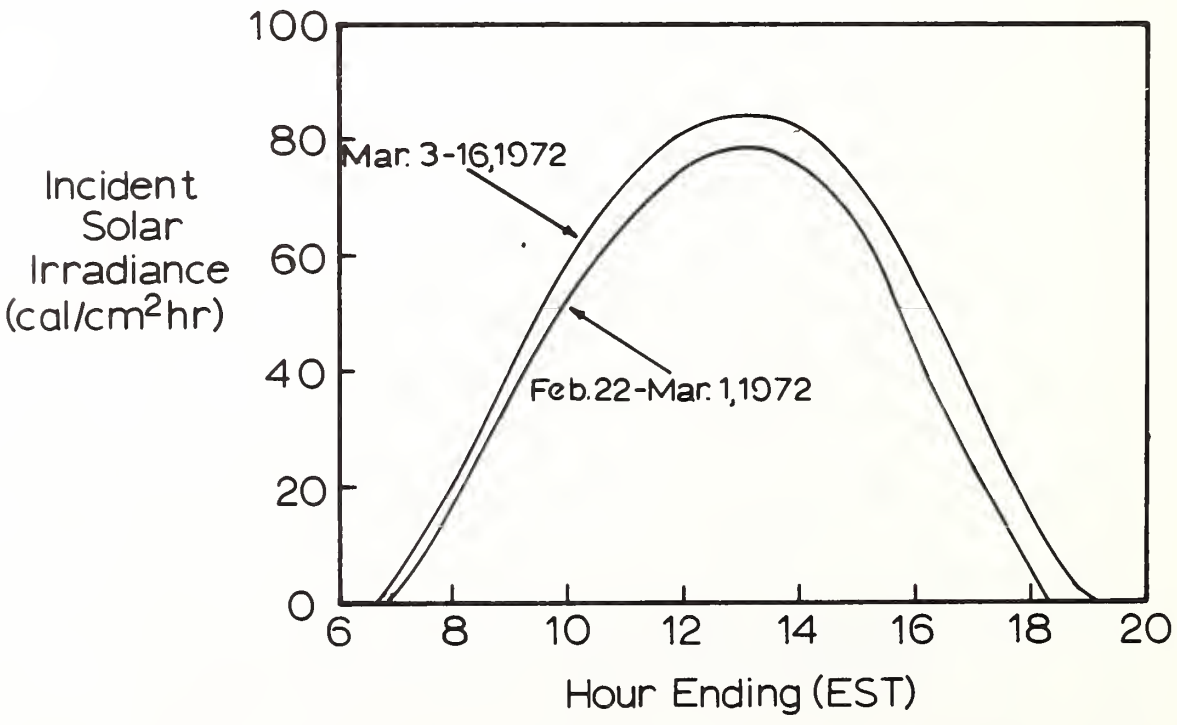

Figure 6. Maximum incident irradiance for two periods during FLARE. The curves simulate clear sky conditions.

Resulting hourly mean albedo values for the two cloud categories are given in table 12 and are plotted in figure 7. Albedo varies with time of day and is nearly symmetrical about solar noon with lowest values (3.5 percent) occurring near midday and higher values (15-20 percent) in early morning

Table 12. Mean Hourly Albedo Values for Clear and Cloudy Sky

Hour Ending (TST)	Clear Sky Albedo	N	Cloudy Sky Albedo	N
07	.217	7	-	-
08	.149	13	.168	2
09	.068	12	.065	4
10	.041	14	.055	2
11	.036	15	.042	2
12	.035	16	.042	1
13	.036	16	.042	1
14	.038	16	.049	1
15	.041	17	-	-
16	.049	14	.055	2
17	.085	13	.079	3
18	.145	13	.131	3

The distinction between clear and cloudy sky is defined in the text. N is the number of hourly albedo values on which the mean is based

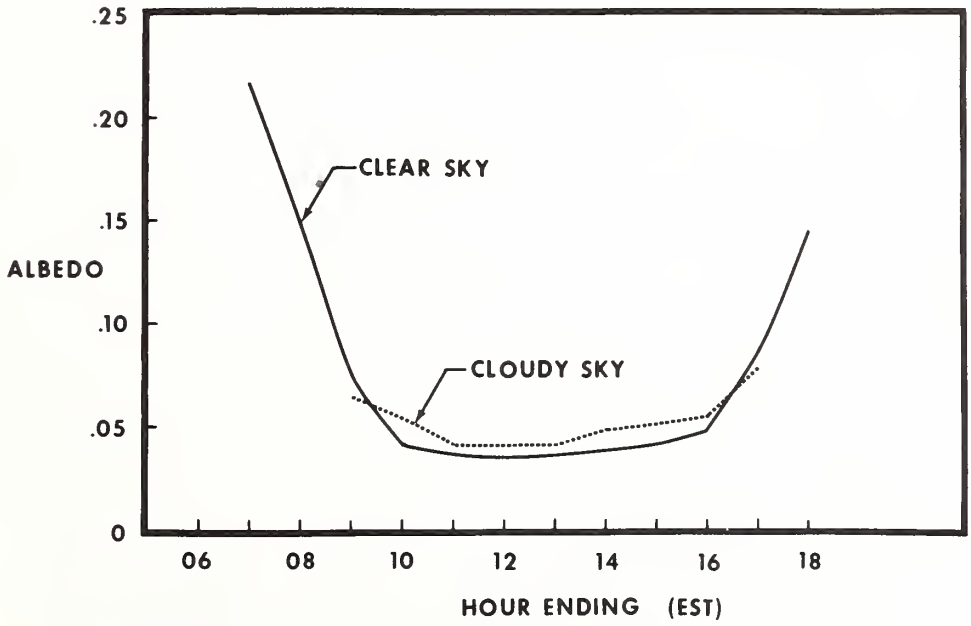

Figure 7. Mean hourly albedo of the ocean surface for all sites during FLARE.

and late afternoon. This effect of solar zenith angle on albedo of a smooth water surface has been evaluated by many others in earlier studies, e.g., see List (1958), Jerlov (1968) Table XVIII, and Anderson (1954).

During mid-morning the albedo appear to be slightly lower than during mid-afternoon. If this is real, it may be a result of the wave slope distribution with predominantly easterly wind and swell or caused by increased turbidity and ocean reflectance in the afternoon.

The dependence of albedo on zenith angle, as determined in this study, is given in table 13 and figure 8. The data agree within a few percent of those for smooth water surfaces given by Jerlov (1968) and List (1958).

Table 13. Clear and Cloudy Sky Albedo Values as a Function of Solar Zenith Angle

Zenith Angle (deg.)	Clear Sky Albedo	Cloudy Sky Albedo
28.5	.036	.042
35.2	.037	.046
45.6	.041	.063
57.8	.059	.060
70.8	.117	.124
84.2	.181	-

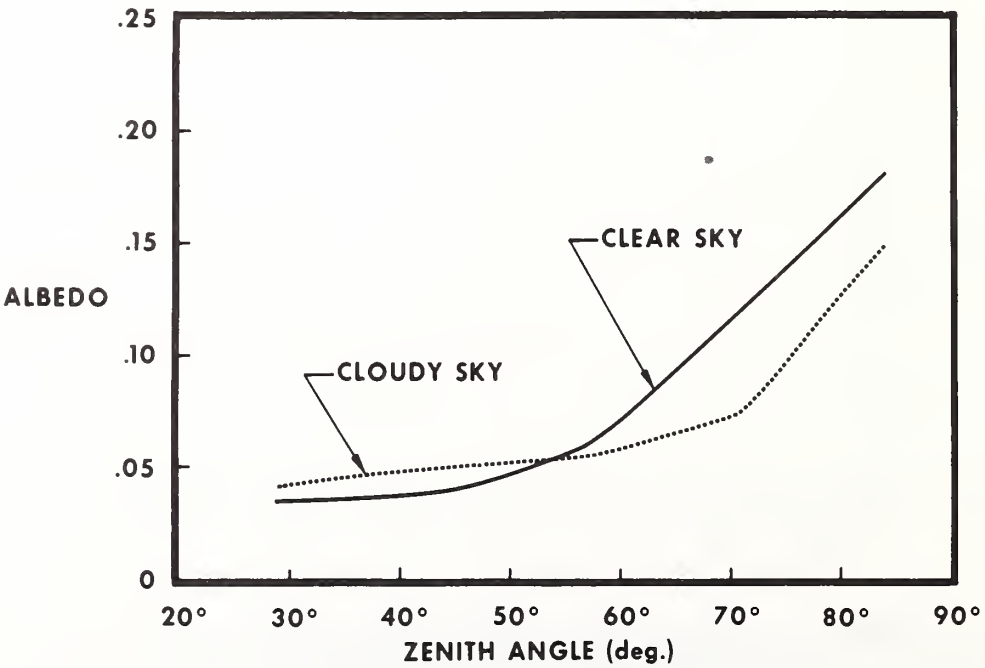

Figure 8. Albedo as a function of solar zenith angle during FLARE.

3.2 Transmittance

The continuous measurements of solar irradiance incident, reflected at the sea surface and incident at the shelf surface, as given in tables 2, 3, and 4, have been used to calculate the transmittance of the coastal water column. The transmittance (T) was calculated from equation 1. As previously discussed for albedo, the transmittance data were further stratified into clear and cloudy sky categories. The resulting hourly mean transmittance values for these two categories are given in tables 14 and 15 and are shown in figures 9 and 10.

In these figures it is apparent that the ocean transmittance varies with time of day and is relatively symmetrical about solar noon. The transmittance of the water column to 13 m with clear skies is highest at local noon, 7-8 percent, and decreases to about 5 percent at zenith angles of 60-70 degrees. As the zenith angle further increases from 70 to 90 degrees, an increase in the transmittance is observed. With cloudly skies the transmittance of the water column increases continuously as the zenith angle increases. A comparison between clear and cloudy sky transmittance values can also be made. This shows that the transmittance is considerably higher in the cloudy sky situation, particularly at higher zenith angles. For example, at 60 degrees and higher the cloudy sky value is larger by a factor of two than with clear skies.

A possible explanation for the increase in transmittance (1) during cloudy conditions and (2) with zenith angles from 70-90 degrees is connected with the spectral distribution of sunlight reaching the ocean surface. In

Table 14. Mean Hourly Transmittance Values for Clear and Cloudy Sky The distinction between clear and cloudy sky is defined in the text. N is the number of hourly transmittance values on which the mean is based.

Hour Ending (TST)	Clear Sky Transmittance	N	Cloudy Sky Transmittance	N
07	.080	9	.167	1
08	.049	9	.134	3
09	.049	8	.108	4
10	.064	11	.091	2
11	.069	11	.081	2
12	.076	13	-	-
13	.071	14	-	-
14	.066	15	-	-
15	.063	14	-	-
16	.054	13	-	-
17	.053	11	.095	2
18	.077	11	-	-

Table 15. Clear and Cloudy Sky Transmittance Values as a Function of Solar Zenith Angle

Zenith Angle (deg.)	Clear Sky Transmittance	Cloudy Sky Transmittance
28.5	.074	-
35.2	.068	.081
45.6	.064	.091
57.8	.052	.108
70.8	.051	.114
84.2	.078	.167

both cases the amount of near-infrared sunlight relative to the total will decrease because of atmospheric absorption; thus, the relative amount of visible sunlight is greater, and,because water transmits visible sunlight better than near-infrared sunlight, the apparent transmittance of the water will increase.

Future studies should include measurement of the relative spectral distribution of solar irradiance both above the surface and within the water column. This will answer the question of whether the apparent increase in ocean transmittance at zenith angles approaching 90 degrees and under cloudy conditions are a result of changing spectral distribution of the source or not. In addition, relative solar irradiance spectra in the ocean and the absolute pyranometer measurements provide a means for obtaining absolute spectral values, as suggested by the National Academy of Sciences (1969). This is a simple means of solving the difficult problem of obtaining absolute values of spectral distribution of solar irradiance in the ocean.

4. INSTRUMENTATION

The radiation measurements above the ocean surface were obtained with Model 2 pyranometers manufactured by the Eppley Laboratory. The sensing element of these pyranometers is a wire-wound thermopile. Its receiving surface is coated with Parsons black lacquer. The receiving surface is protected from the elements by a pair of precision ground concentric hemispheres of Schott optical glass (WG7) which are transparent from 0.28 to 2.8 micrometer wavelengths.

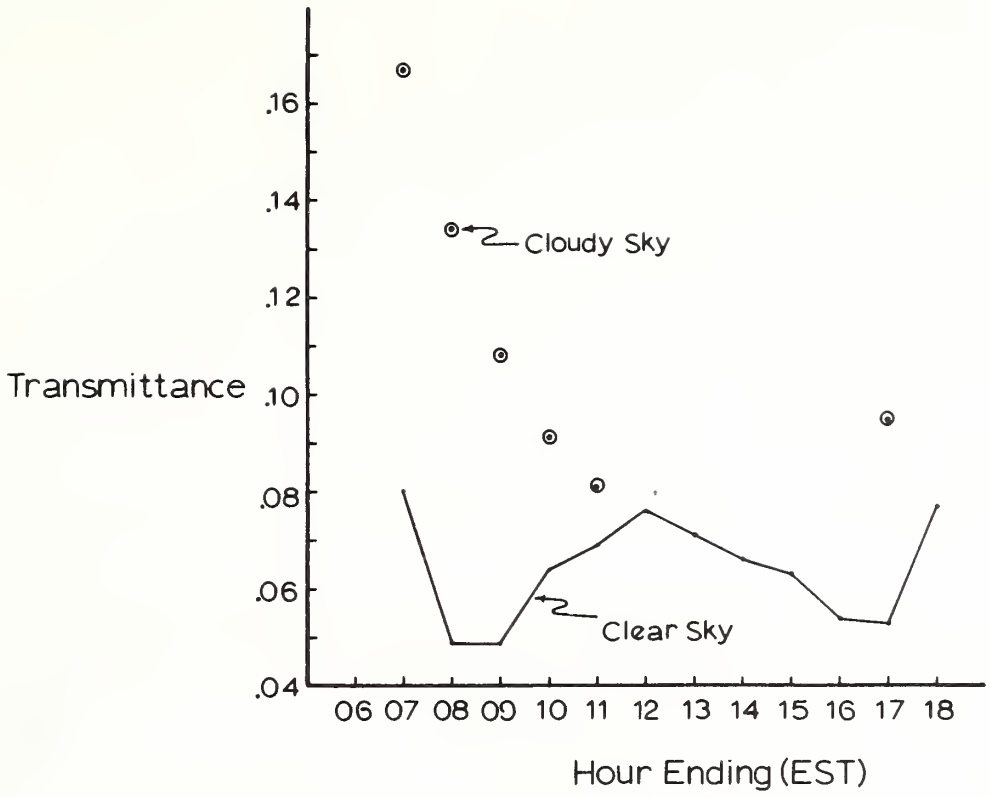

Figure 9. Mean hourly transmittance of the water for all sites during FLARE.

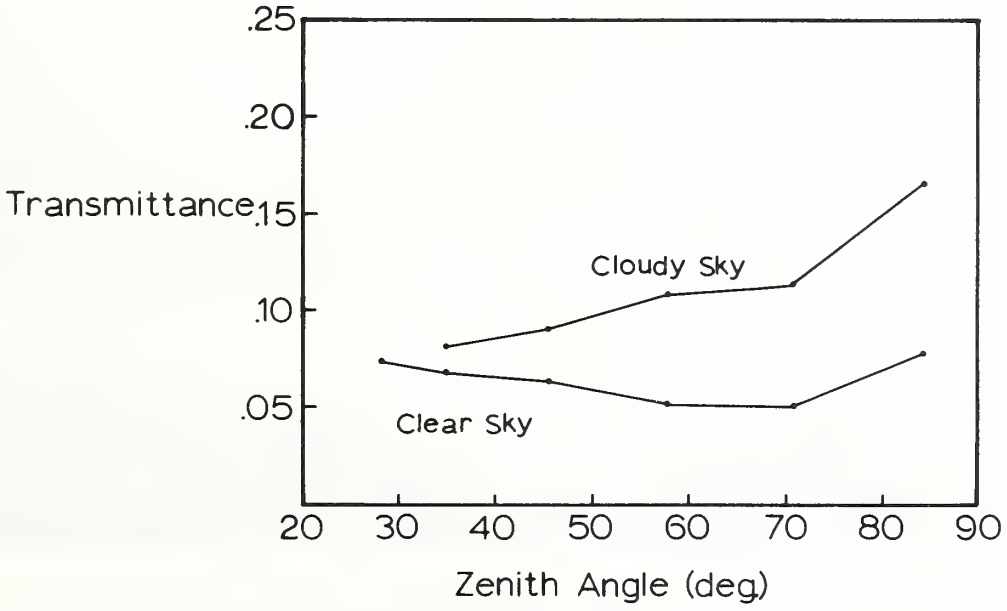

Figure 10. Transmittance of the water as a function of solar zenith angle during FLARE.

The underwater radiation measurements were obtained with pyranometers which have been adapted by the Eppley Laboratory for use underwater. They are identical with the Model 2 pyranometers, except they employ a three pound monel body as a heat sink and have an 0-ring seal and underwater connector to make them water tight. Both pyranometers are shown in figure 11.

A net radiometer of the Funk type was also used during the experiment to measure the net (solar and IR) radiation. The data are not included in the present analysis, although the daily curves are included in the Appendix. The radiometer is also shown in figure 11.

Table 16 is a summary of the radiation sensors employed and the sensitivities which were used in processing the measurements.

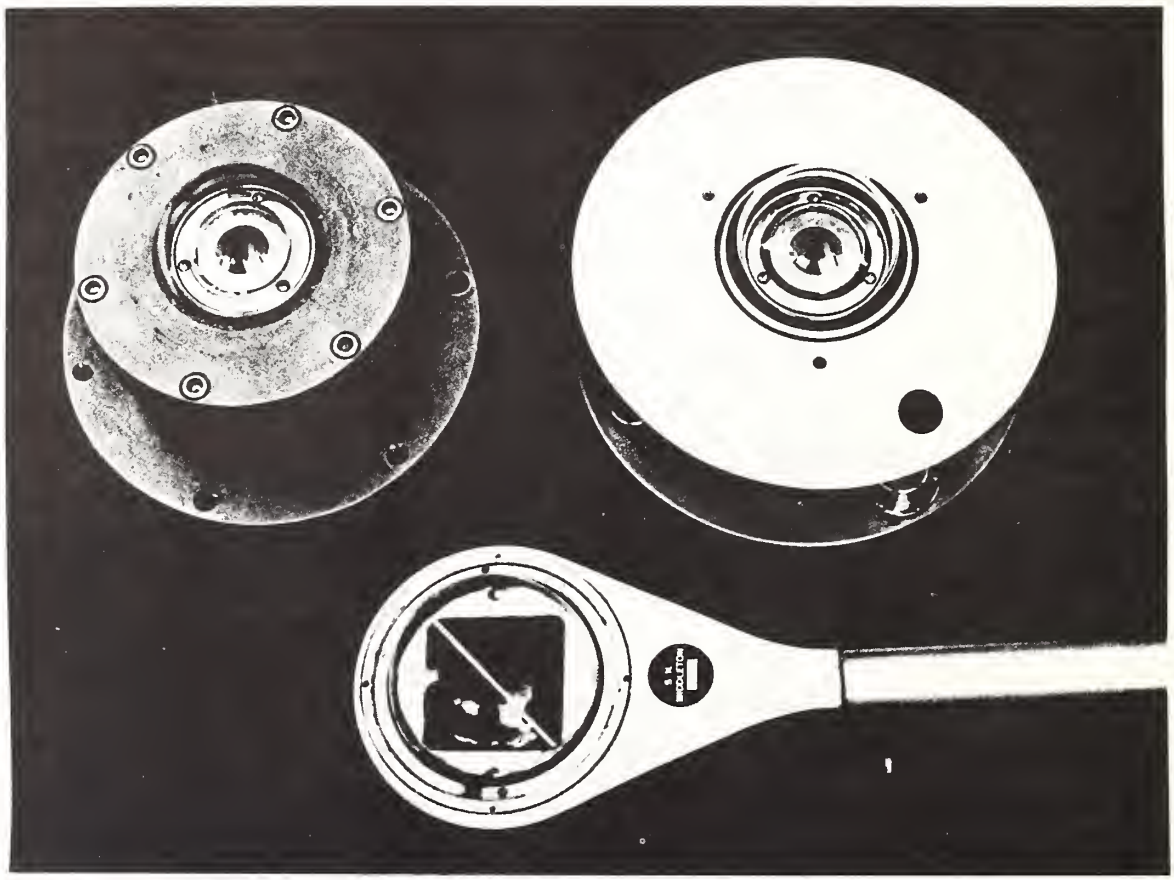

Figure 11. Underwater pyranometer (left) and Model 2 pyranometer (right). Both instruments are manufactured by the Eppley Laboratory and were used in the FLARE program. The Funk-type net radiometer is shown below.

Table 16. Summary of Radiation Sensors Used in FLARE Radiation Program

Sensor	Measurement	Mfgr.	Sensor Number	Sensitivity ($mv/cal\ cm^{-2}min^{-1}$)
Pyranometer	Incident Solar Irradiance	Eppley	9862	4.109
Pyranometer	Reflected Solar Irradiance	Eppley	9863	3.936
Net Radiometer	Net Radiation	Middleton & Co.	465	21.85
Underwater Pyranometer	Solar Irradiance, Fixed Depth	Eppley	9860	4.366
Underwater Pyranometer	Solar Irradiance, Profile	Eppley	9861	4.626

5. IMMERSION EFFECT OF THE UNDERWATER PYRANOMETERS

The underwater pyranometers used in this study have an immersion effect that must be determined before one can evaluate the absolute value of the measurements. Originally the sensors were calibrated in the air with the sun as a source by direct comparison with another pyranometer. Use of the instrument underwater changes the optical characteristics of the instrument from those in air in two ways – this is called the immersion effect. The first change results from a difference between the reflectivity of the outer hemisphere in water as compared to air. At normal incidence the reflectivity is

$$r = \left[\frac{n_1 - n_2}{n_1 + n_2}\right]^2 \qquad (2)$$

where n_1 is the index of refraction for the medium adjacent to the glass hemisphere and n_2 is that of the hemisphere. Because the indices of refraction of air, water, and glass have values of approximately 1.00, 1.33, and 1.5, respectively, it is apparent that the reflectance of the outer hemisphere will be smaller in water than in air. Although this effect is relatively small (about 3 percent), it will cause the instrument to measure too large an irradiance value.

The second change is caused by the lens properties of the outer hemisphere when used underwater. The hemisphere acts as a diverging lens which will cause the instrument to measure too small an irradiance value. A study of this effect is bing done by Gordon and Brown (1972), who have indicated that, for the indices of refraction given above, the correction factor necessary to increase the measurements to their proper value is 1.76 for solar zenith angles of 0-30 degrees and increased values at larger zenith angles. Thus, the second change caused by the lens effect is considerably more significant than the first caused by reflection.

In the present study no corrections have been applied to the data for the immersion effect. When present studies of this effect have been completed, and an adequate model for applying the corrections has been determined, the basic irradiance data will be revised. This will not alter the results given here based on relative measurements.

6. REFERENCES

Anderson, E. R. (1954), Energy-budget studies. In Water Loss Investigations: Lake Hefner Studies, U. S., Geol. Surv., Prof. Paper, 269, 71-117.

Gordon, H. R. and O. B. Brown (1972), Immersion corrections for the Eppley underwater pyranometer, Conf. on Atmospheric Radiation, Amer. Meteorol., Soc., Ft. Collins, Colorado, August, 1972.

Hanson, K. J. (1971), Studies of cloud and satellite parameterization of solar irradiance at the earth's surface, Proc. of the Miami Workshop on Remote Sensing, NOAA, ERL, Boulder, Colorado, July, 1971.

Hanson, K. J. and M. F. Poindexter (1972), Attenuance of broadband solar irradiance in the ocean, Conf. on Atmospheric Radiation, Amer. Meteorol., Soc., Ft. Collins, Colorado, August, 1972.

Jerlov, N. G. (1968), Optical Oceanography, Elsevier Publishing Company, New York.

List, R., (Ed.) (1958), Smithsonian meteorological tables, 6th Revised Edition, Smithsonian Institution, Washington, D. C.

National Academy of Sciences (1969), Recommended procedures for measuring the productivity of plankton standing stock and related oceanic properties, prepared by the Biological Methods Panel, Committee on Oceanography, Division of Earth Sciences, National Research Council.

Reprinted from ICES Symposium on "Physical Variability in the North Atlantic" held in Dublin, Ireland, September 1969.

Paper 8

*Observation of Laminae in the Termocline of the Tropical Atlantic**

FEODOR OSTAPOFF

National Oceanic and Atmospheric Administration
Atlantic Oceanographic and Meteorological Laboratories
Miami, Florida, 33130

Abstract A 15-hour time series was obtained in the tropical Atlantic (10°30′ N and 43°20′ W). The sampling period was five minutes and the principle tool used was the Expendable Bathythermograph (XBT). The data is presented in form of depth variation of selected isotherms, of temperature variations at selected depth and of depth variation of two selected features in the vertical temperature profiles.

INTRODUCTION

During the Atlantic Tradewind Expedition (ATEX) last winter the USC&GS Ship *Discoverer* drifted for 18 days within the tradewinds and carried out a multidisciplinary research program. The primary objective of the expedition, in which four research ships from three nations participated (see Figure 1), was the investigation of air–sea interaction processes in the tropical Atlantic Ocean. The main program consisted of 8 meteorological balloon ascent per day sounding the atmosphere up to 7 kilometers height with simultaneous oceanographic soundings down to 500 meters. Eight expendable bathythermographs (XBT) were dropped daily to obtain temperature profiles to 450 meters. In this way it was hoped to record temperatures vs. depths at 90-minute intervals.

On February 16 a program was initiated which would record temperature profiles at 5-minute intervals for 15 hours in order to study the variability of temperature and internal waves with periods up to 3 hours. Simultaneously,

* Presented at the ICES Symposium on "Physical Variability in the North Atlantic" held at Dublin, Ireland in September, 1969.

a salinity-temperature-depth sensing unit (STD) was suspended at 40 meters depth for the first 5 hours, at 100 meters for the next 5 hours and at approximately 275 meters for the last 5 hours. The purpose of these STD measurements was to investigate the variations in temperature and salinity in the mixed layer (40 m), the most intense part of the thermocline, (100 m), and the region below the thermocline (275 m).

After the termination of this program the routine 3-hourly XBT and STD program was resumed until the end of the expedition on February 22, 1969. This paper will present only the preliminary results from the oceanographic data obtained during the 15 hours of recording on February 16–17 at 10° 30′ N and 43° 20′ W (Figure 1).

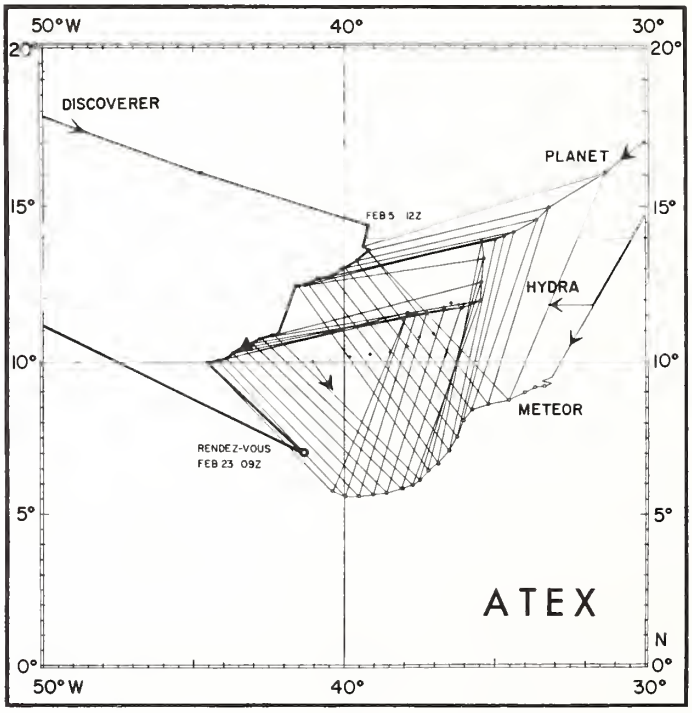

Figure 1 Solid triangle indicates the position at which the XBT Times Series was obtained during the Atlantic Tradewind Expedition 1969 (ATEX)

INSTRUMENTATION

The principle instrument used to gather the data for this study was the expendable bathythermograph (XBT) manufactured by Sippican Corporation. The XBT system is a thermistor embedded in the nose of a streamlined

body that is released from a launcher on board ship. The probe falls through the water with a constant velocity of 7 m/sec. The time constant for the thermistor is $\frac{1}{10}$ sec. Trailing wire connection transmits the signal back to the recorder. After reaching design depth (in this case 450 meters) the wire breaks, and the recording ends. Although the probe is designed for underway operation with ship speeds up to 30 knots, in this study it was used to obtain vertical profiles at one location in rapid succession.

The other instrument used in this study was the STD, also called the bathysonde. The particular model (Bissett–Berman Model 9006) records temperature, salinity, sound velocity, and pressure as a function of time. According to the manufacturer, the time constant for the temperature probe is 0.35 seconds.

THE OBSERVATIONS

The basic characteristics of the vertical temperature distribution are shown in Figure 2. The surface layer is well mixed and extends to 63 meters in this profile. The mixed-layer depth during the entire period varied between 40 and 70 meters. The main thermocline exhibits a mean temperature gradient of 10 °C/60 m or 0.17 °C/m. However, the structure in the thermocline is such that layers with high gradients alternate with layers of either low gradients or constant temperature, resulting in a step-like temperature distribution with depth. Locally, the gradient reaches values of at least 1 °C/m and it may exceed the limits of our observational tool. Laminae or nearly uniform layers occur about at a rate of 5 per 50 meters in the upper part of the thermocline. Similar features have been observed by White (1967) in the thermocline, in much deeper layers by Stommel and Fedorov (1967) and on a smaller scale by Woods (1968).

Also shown in Figure 2 are two laminae, one around 75 meters in the upper thermocline (labeled 1) and another one most prominent near 150 m (labeled 2). This extensive laminar layer of up to 30 meters thickness separates the upper part of the thermocline from the lower part. This lower part has a mean temperature gradient of 1 °C/24 m or 0.042 °C/m. Again, the temperature distribution shows step-like features all the way down to the termination of the last 450 meters.

Figure 3 shows the first 13 complete temperature profiles out of some 180. Each profile was obtained at a 5-minute interval, hence the figure shows complete profiles for one hour. The continuity of the major laminar is obvious.

As mentioned earlier, the STD sensor was kept for a period at each of three depths. From inspection of the pressure record, it is seen that the

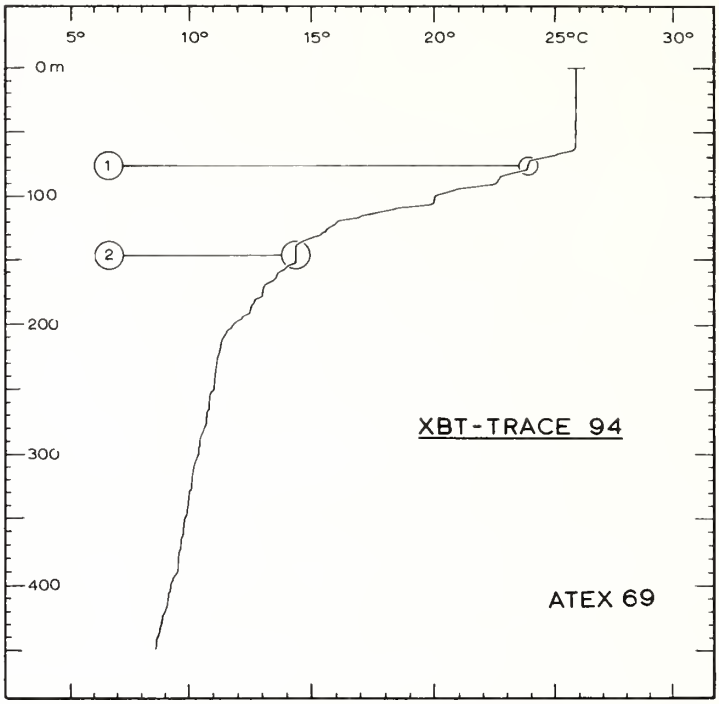

Figure 2 A typical XBT profile showing principle features of normal stratification on February 16, 1969 0315 L.T. at 10°30′ N and 43°20′ W. Features 1 and 2 are the two predominate laminae and are referred to in Figure 7

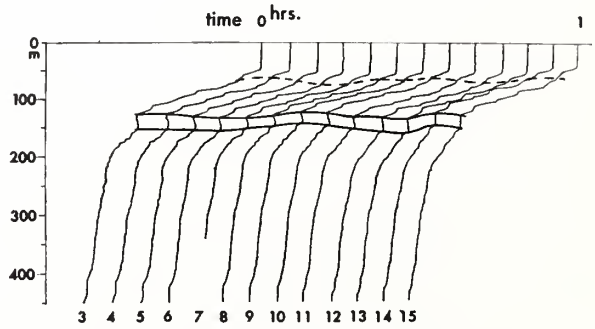

Figure 3 Reproduction of XBT traces for the first hour of the 15-hour time series. Mixed layer temperatures about 26°C and 400 meter temperatures about 9°C. Dashed line indicates feature 1 and solid lines show feature 2 in Figure 2

instrument moved up and down with an amplitude of about 2 meters and a period of about 7 seconds due, no doubt, to heaving of the ship. While the temperature trace shows at times a high "noise" level attributed to a strong vertical temperature gradient, at other times the record looks quiet on all channels except the pressure. The most likely explanation seems to be the movement of a lamina through this depth level. Obviously, in this case the temperature record will reflect no vertical motion resulting from internal waves, which would have much longer periods than seven seconds.

In order to investigate whether the XBT time series at the chosen 5-minute sampling period reproduces the major fluctuations, temperature values at 30-second intervals were read from the STD record after smoothing of the high frequency noise. The solid line in Figure 4 represents the temperature variations at 100 meters from the STD record. The circles are XBT 100 meter temperatures and the triangles represent XBT 95-meter temperatures. The width of the shaded area between these, therefore, shows the mean temperature interval between 95 and 100 meters. It is clearly seen that periods of strong gradients alternate with periods of weak gradients during which time a lamina is moving through that depth range. It is also seen that the agreement between the XBT and STD data is particularly good during periods of weak gradients (within 0.2 °C). In general, the STD curve lies within the hatched area and all major features are reproduced by the XBT data. This is quite remarkable, especially in view of the large temperature fluctuations of more than 2 °C in 5 to 10 minutes.

The remaining figures represent various ways to reduce the XBT data. First, the conventional procedure is applied, namely, to plot the depth distribution of individual isotherms. In Figure 5, depth variations of the 25°-, 20°-, and 15°-isotherm are presented. The thin curves show running one-hour means while the thick lines represent the mean depth of each isotherm. Amplitude variations of more than 10 meters in 20 minutes, sometimes more than 20 meters, occurred quite frequently and were more pronounced for the 15°-isotherm than the 25°-isotherm. Although all three isotherms behaved similarly as far as the trend is concerned, the coherence in the high frequency variations is rather low. A striking example is the downward departure of the 15° isotherm from the hourly mean by 24 meters at 11 hr 10 min whereas the 20°-isotherm as well as the 25°-isotherm coincide exactly with the hourly mean. Large oscillations of the 15°-isotherm near 12 hours are not all followed by the 25°-isotherm.

The results of a second method of reducing the original data are presented in Figure 6. Here temperature is plotted versus time for several individual depth levels (60, 80, 100, 120, and 200 meters). Thick horizontal lines represent the mean temperatures for the corresponding depth levels during

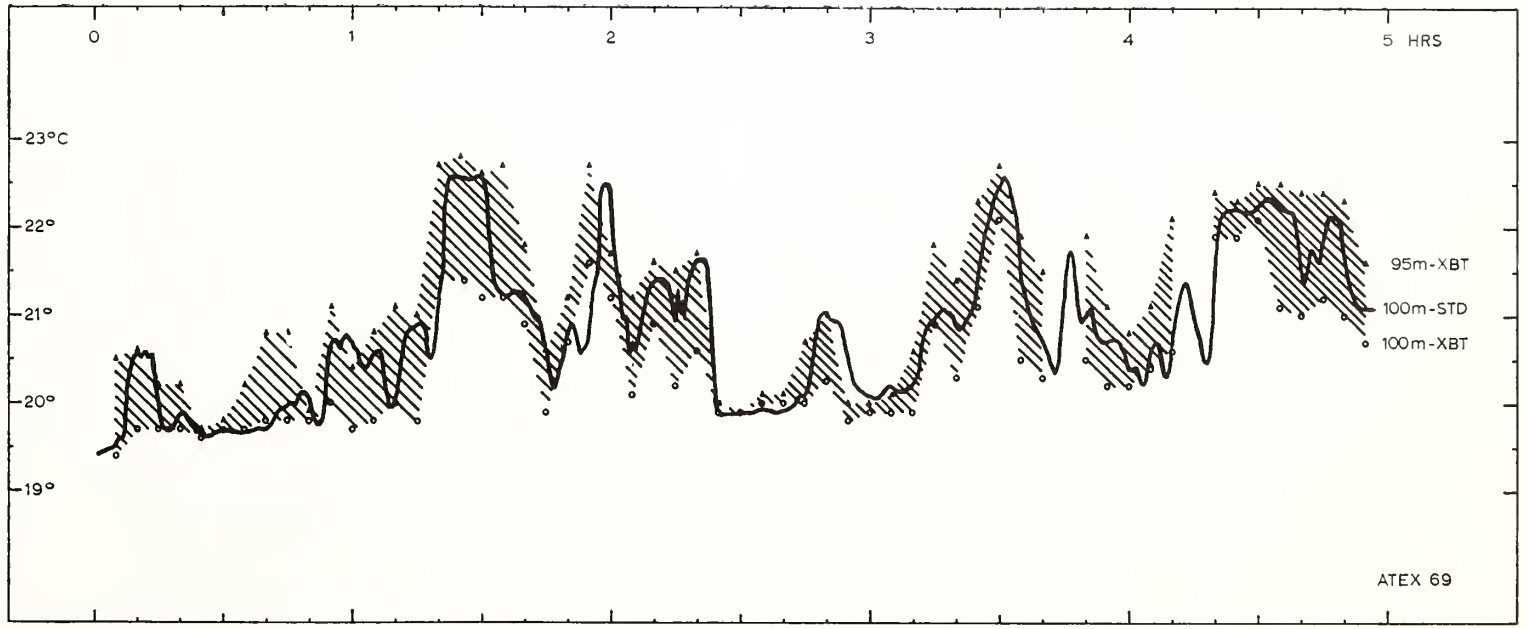

Figure 4 Comparison of simultaneous STD (solid line) at 100 meters and XBT temperatures at 100 meters (circles and 95 meters (triangles). The STD values were plotted at 30 second intervals

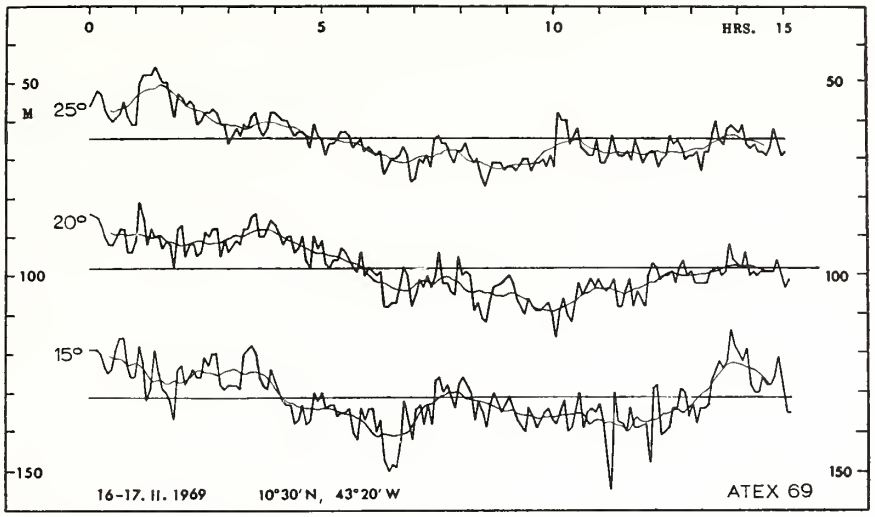

Figure 5 Depth variation of the 25°-, 20°- and 15°-isotherms for a period of 15 hours on February 16–17, 1969 at 10°30′ N and 43°20′ W

the 15 hour period. Their spacing represents the mean temperature gradient. As seen from the top curve, the surface mixed layer penetrated below 60 meters after 5 hours and remained for the rest of this time series. To some degree the deepening of the mixed layer is also reflected in the temperature record at 80 meters. The largest amplitude temperature variation is found at 100 and 120 meters with more than 5 °C amplitude. At and below 140 meters these changes do not exceed more than 2.5 °C. This is consistent with the mean temperature structure as shown in Figure 2. The small temperature variations at 140 meters can be attributed to the presence of a thick extensive lamina near this level seen in Figure 2.

Finally, the depth distributions of features 1 and 2 of Figure 2 have been followed as function of time. Figure 7 shows the vertical extent and depth of the 23° lamina and the 14° lamina. This should be the best evidence available for internal wave studies inasmuch as no specific assumption concerning the local temperature gradient is required in transforming temperature fluctuations at a given level into vertical motions. This record, more than any other, demonstrates little correlation between these two features. Moreover, at times the upper boundary and the lower boundary of either lamina vary with different amplitude and phase. The 23° lamina is growing thicker with time and, at the same time, cooling, while the 14° lamina is decaying and warming.

This discussion has been limited to a data presentation; the next step will consist of the detailed analysis of the various time series, their power spectra,

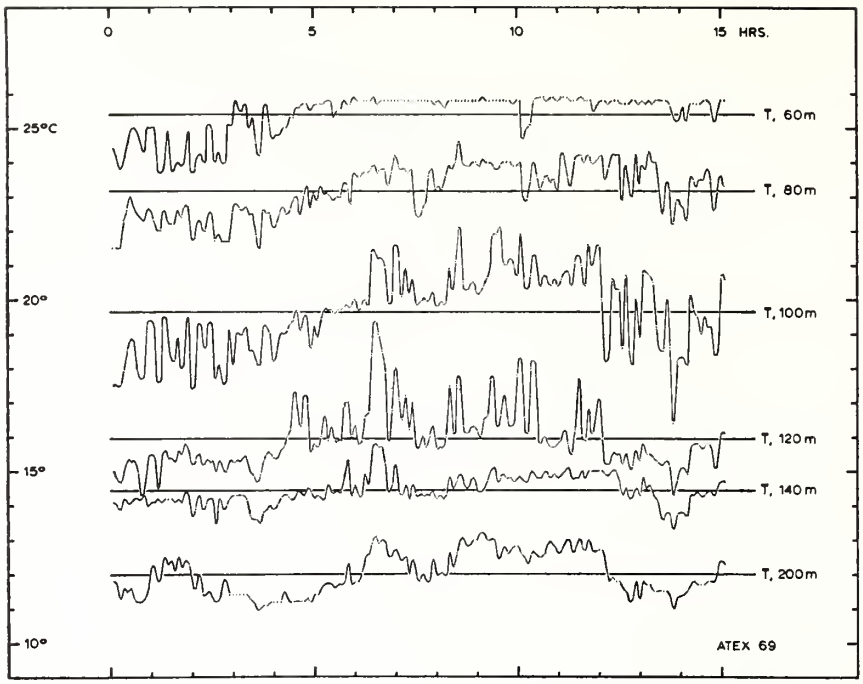

Figure 6 Temperature fluctuations at selected depth levels for a period of 15 hours on February 16–17, 1969 at 10°30′ N and 43°20′ W. The horizontal lines indicate the mean temperatures for the entire period at the respective depths

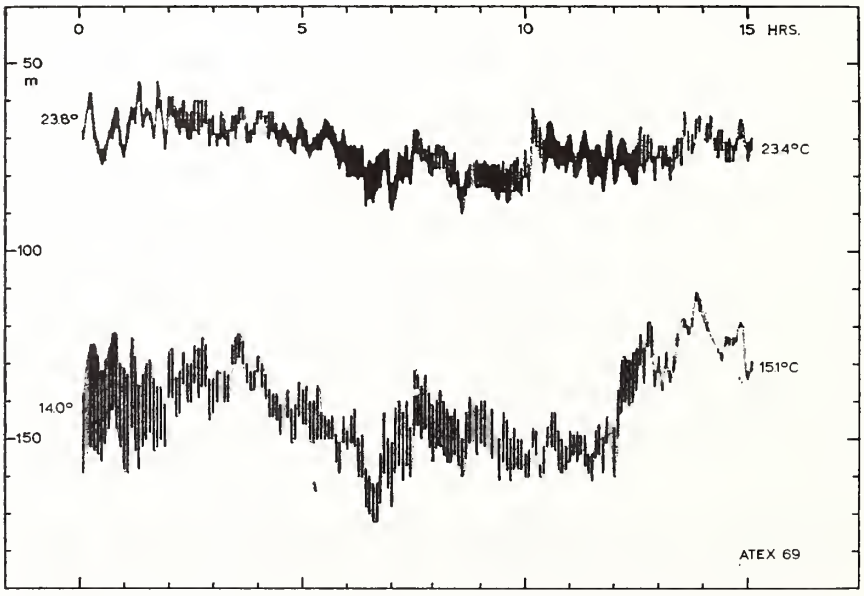

Figure 7 Thickness and depth variations of two selected features in the vertical temperature distribution (see Figure 2)

correlations, and coherences, which will be published elsewhere. Most interesting should be the comparison of the various time series in an effort to determine which represents the best approach to studying internal waves in the open ocean.

CONCLUSION AND SUMMARY

On the basis of a 15-hour time series of temperature profiles at 5-minute intervals the following conclusions can be made.

(1) The XBT is a useful tool to study the thermal structure of the thermocline in regions of strong vertical gradients.
(2) Large temperature variations at a given depth with amplitudes up to 5°C were found in the region of a strong thermocline.
(3) The vertical temperature structure in this region exhibits layering of sheets with strong gradients interrupted by layers of nearly uniform temperature. The temperature profile resembles a step-like function.
(4) If temperature records are obtained at preselected depths for studying internal waves, it is important to record not only the temperature fluctuations but also simultaneously temperature gradients. This is essential in regions with strong gradients and laminae.

References

White, R.A., The vertical structure of temperature fluctuations within an ocean thermocline. *Deep-Sea Res.*, **14**, pp. 613–623, 1967.

Stommel, H. and K.N.Fedorov, Small scale structure in temperature and salinity near Timor and Mindanao. *Tellus*, **19** (2), 1967.

Woods, J.D., Wave-induced shear instability in the summer thermocline. *J. Fluid Mech.*, **32** (4), pp. 791–800, 1968.

☆ U.S. GOVERNMENT PRINTING OFFICE: 1973—780-382